Lagrangian Modelling of gas/particle pollutant dispersion for atmospheric flows within stable, neutral and unstable situations

Guilhem Balvet

To cite this version:

Guilhem Balvet. Lagrangian Modelling of gas/particle pollutant dispersion for atmospheric flows within stable, neutral and unstable situations. Fluids mechanics [physics.class-ph]. École des Ponts ParisTech, 2024. English. NNT : 2024ENPC0011 . tel-04729860

HAL Id: tel-04729860
https://pastel.hal.science/tel-04729860v1

Submitted on 10 Oct 2024

École des Ponts
ParisTech

THÈSE DE DOCTORAT
de l'École des Ponts ParisTech

Modélisation lagrangienne de la dispersion de polluants gazeux/particulaires dans des écoulements atmosphériques stables, neutres et instables

Lagrangian Modelling of gas/particle pollutant dispersion for atmospheric flows within stable, neutral and unstable situations

Doctoral school $N^o 531$, - Sciences, Ingénierie et Environnement (SIE)

Speciality : Fluid dynamics

Thesis prepared in the CEREA laboratory, in "Mécanique des fluides, Energie et Environnement" department of EDF R&D

Jury version for the thesis defense on 15th March 2023, by
Guilhem BALVET

Jury composition:

Anne Taniere Professeure, LEMTA-Université de Lorraine	*Rapporteur*
Jacek Pozorski Professor, Polish Academy of Sciences, IMP Gdańsk	*Rapporteur*
Mireille Bossy Directrice de recherche, Inria d'Université Côte d'Azur	*Examiner*
Meissam, Bahlali Research Associate, Faculty of Engineering, Dpt of Earth Science & Engineering- Imperial College London	*Examiner*
Benjamin Loubet Directeur de recherche, INRAE	*Examiner*
Yelva Roustan Chargé de recherche, CEREA-Ecole des Ponts et Chaussées	*Thesis Director*
Martin Ferrand Maître de conférences, CEREA-EDF R&D	*Surpervisor*

Foreword

Acknowledgements

First of all, I would like to thank Anne Tannière and Jacek Pozorski for agreeing to be rapporteur of this thesis and for their valuable discussions and detailed corrections. I also express my gratitude to Benjamin Loubet for his kindness, willingness and advice as Chair of my thesis jury and as member of my CSIT. I am also very grateful to Mireille Bossy and Meissam Bahlali for their benevolence and their interesting questions as members of my jury.

I would like to mention the people I have worked with over the last few years and without whom this thesis would not have been possible. First of all, I want to sincerely thank my thesis director Yelva Roustan for the time he spent supervising my work, but also for his patience and kindliness. His pedagogy and assistance were of great help in clarifying and redirecting me whenever my reasoning and presentations became confused. I also want to thank him for his useful overview on transport and atmospheric physics. I express my deep gratitude to my EDF supervisor Martin Ferrand, for his dedication and for always making himself available when necessary even with an overbooked agenda. The guidance and answers he provided in the overall reasoning, scientific and technical background but also on simulation setups were of paramount importance in the progress of this work. I also truly thank Jean-Pierre Minier, for the many fruitful discussions we had. The latter enabled me to better understand Lagrangian stochastic methods and related issues but also broader topics such as the work and world of researchers. Finally I would like to thank Christophe Henry for his good will but also for always being friendly and attentive as a member of my CSIT and in our work discussion. It has been a real pleasure to work with each of you and I hope to have the opportunity to continue in the future.

I also thank all the colleagues from the CEREA, MFEE and I8F/H whom I had the opportunity to meet. These interactions were very pleasant and I learned a lot from them on scientific and non-scientific matters. A special thanks is of order to the past and present PhD students of 0314, the second league CFD magician and the CEREA team in Chatou. I would also like to thank Anne Peuré and Lydie Periac for their availability and help in all administrative matters, but also to Youngseob Kim for always being kind and taking the time to solve any IT problem.

On a more personal level, I deeply thank my partner Hélène for her constant support throughout this period of ups and downs. I would also like to thank my parents, without whom I would not be here today and my brother for showing me the excitement that a scientific and technical subject can bring. I would also like to thank my friends for being there and for the support they gave without even noticing (with a special big up to Céliandre who pretty much noticed the support she gave when correcting an earlier version of this work).

I would also like to sincerely thank all the teachers I met who have passed on the joy of learning, analysing, studying and understanding.

Summary in English & Résumé en Français

Summary in English

Title: Lagrangian Modelling of gas/particle pollutant dispersion for atmospheric flows within stable, neutral and unstable situations.

Key words: fluid dynamics; GLM stochastic approach; atmospheric flows; atmospheric stability; atmospheric dispersion.

This thesis aims at studying the atmospheric dispersion of pollutants at the micro-scale. In this context, we are focusing on the modelling of pollutant dispersion using stochastic Lagrangian methods developed for high-Reynolds number flows. In these methods, the pollutants and/or the carrier fluid are simulated by means of a large number of stochastic particles, enabling to reproduce the statistic properties of the turbulence. A hybrid approach is used in which the mean carrier fields (e.g. the mean velocity) are obtained on a mesh using external solutions (analytical ones or finite volume ones). We are also interested in the influence of atmospheric stability on the dispersion of pollutants, particularly in the lower layer of the atmosphere. The aim of this thesis is threefold: firstly, to study the numerical errors inherent to such methods, secondly, to improve the modelling of atmospheric surface-boundary-layer flows, and finally, to observe the influence of these elements on the modelling of plumes obtained by simulating only the particles originating from local pollutant sources. To this end, the simulations were carried out using the open-source computational fluid dynamics (CFD) code developed by EDF R&D: code_saturne.

Firstly, with a view to limiting numerical errors during integration over long time steps, a time step splitting algorithm is presented. This is used to dynamically and optimally update the mean carrier fields at each particle location as it enters a cell. In order to avoid anticipation errors due to the stochastic nature of these particles, deterministic virtual particles are used to obtain the travel times in each cell. In addition, a detailed study of the spatial errors that occur when considering surface boundary layer flows is carried out, along with proposals for limiting them. It is shown that these errors are caused by the interpolation of the mean carrier fields at the position of the particles impacting the dynamics of the latter, but also by the estimation of the statistics from these particles on a mesh.

In addition, with a view to improve the modelling of surface-boundary-layer flows, the necessity to use an an-elastic rebound condition near wall for the instantaneous velocity and potential temperature was verified. Without the latter, not only the gradients, but also the turbulent fluxes close to the wall plummet, in opposition to the physics of parietal flows. Furthermore, a description consistent with the choice of modelling was derived based on algebraic solutions and numerical resolution of the turbulent kinetic energy dissipation rate. This description is consistent with the asymptotic solutions associated to the Monin–Obukhov theory and is coherent with the results of code_saturne in the stable case. For convective flows, a study of the role of turbulent kinetic energy diffusion remains to be carried out.

Finally, the effects of this work on pollutant dispersion have been verified, in the neutral case, using experimental results from a channel flow both in the absence of an obstacle and in the presence of an obstacle. It is shown that the most important factors are the estimation of the mean carrier fields and the choice of the model considered. Furthermore, in a thermally stratified case, the influence of atmospheric stability and the modelling of thermal effects on the shape of the plumes were verified by means of a qualitative study.

Résumé en Français

Titre: Modélisation lagrangienne de la dispersion de polluants gazeux/particulaires dans des écoulements atmosphériques stables, neutres et instables.

Mots clefs : dynamique des fluides, approche stochastique GLM, écoulement atmosphérique, stabilité atmosphérique, dispersion atmosphérique.

Ce travail de thèse vise à étudier la dispersion atmosphérique de polluants à l'échelle locale. Dans ce contexte, nous nous concentrons sur la modélisation de la dispersion de polluants en utilisant des méthodes lagrangiennes stochastiques à haut Reynolds. Au sein de ces méthodes, les polluants et/ou le fluide porteur sont simulés par le biais d'un grand nombre de particules stochastiques permettant une représentation des propriétés statistiques de la turbulence. Une approche hybride est utilisée au sein de laquelle les champs porteurs moyens (par exemple la vitesse moyenne) sont obtenus sur un maillage par le biais de solutions externes (solutions analytiques ou calcul volumes finis). Par ailleurs, nous nous intéressons à l'influence de la stabilité atmosphérique sur la dispersion de polluants, en particulier dans la couche inférieure de l'atmosphère. L'objectif de cette thèse est triple : premièrement, il vise à étudier les erreurs numériques entachant de telles méthodes, deuxièmement, à améliorer la modélisation des écoulements de couche limite de surfaces atmosphériques, et finalement, à observer l'influence de ces éléments sur la modélisation de panaches obtenus en ne simulant que les particules issues de sources locales de polluants. A cette fin, les simulations sont réalisées à l'aide du code CFD open-source code_saturne qui est développé par EDF R&D.

Premièrement, dans l'optique de limiter les erreurs numériques durant l'intégration sur de longs pas de temps, un algorithme de découpage en sous-pas de temps est présenté. Celui-ci permet de mettre à jour de façon dynamique et optimale les champs porteurs associés à chaque particule, lorsqu'elle rentre dans une cellule. Afin d'éviter des erreurs d'anticipation dues à la nature stochastique de ces particules, des particules virtuelles déterministes sont utilisées pour obtenir les temps de parcours dans chaque cellule. Par ailleurs, une étude poussée sur les erreurs spatiales apparaissant lorsque l'on considère des écoulements de couche limite de surface est réalisée, et des solutions pour limiter celles-ci sont proposées. Il est montré que ces dernières sont dues à des erreurs lors de l'interpolation des champs porteurs à la position des particules impactant la dynamique de celle-ci, mais aussi lors de l'estimation sur un maillage des statistiques issues de ces particules.

Par ailleurs, dans l'optique d'améliorer la modélisation des écoulements de couche limites de surface, la nécessité d'utiliser une condition de rebond anélastique en proche paroi pour la vitesse et la température potentielle instantanée a été vérifiée. Sans celle-ci, les gradients, mais aussi les flux turbulents en proche paroi s'effondrent, en opposition avec la physique des écoulements pariétaux. Par ailleurs, une description cohérente avec le choix de modélisation sélectionnée a été dérivée grâce à l'obtention de solutions algébriques et à la résolution numérique du taux de dissipation d'énergie cinétique turbulente. Celle-ci permet de bien retrouver les solutions asymptotiques associées à la théorie de Monin–Obukhov et est cohérente avec les résultats de code_saturne dans le cas stable. Pour les cas instables, une étude sur le rôle de la diffusion d'énergie cinétique turbulente reste à réaliser.

Finalement, l'effet de ce travail sur la dispersion de polluant a été vérifié en cas neutre grâce à des essais expérimentaux en canal plan, à la fois en l'absence et en présence d'un obstacle. Il est montré que les éléments ayant un poids majoritaire restent l'estimation des champs porteurs et le choix du modèle considéré. Par ailleurs, dans un cas thermiquement stratifié, l'influence sur la forme des panaches de la stabilité atmosphérique et de la modélisation des effets thermiques a été vérifiée grâce à une étude qualitative.

Contents

List of Figures

List of Tables

Nomenclature

Superscripts

$+$	Adimensionalized value
$\dagger$	Vector projected on a plane
$\ddagger$	Quantity to model
B	Associated to the background flow
$\mathcal{G}$	Associated to buoyant redistribution terms
(i)	Index of a given particle
in	Particle entering domain after rebound near wall
c	Value stored at the center of gravity of the cell
k	Element index in a partition of time
$[m]$	Current sub-iteration
n	Current time step
out	Particle leaving domain before rebound near wall
P	Associated to the pollutant
pl	Associated to the position of the rebound plane
r	Associated to rapid redistribution terms
S	Associated to the flow issued from the source of pollutant
s	Associated to slow redistribution terms
T	Associated to the total flow

Subscripts

$\alpha,\ \beta$	Spatial direction without summation

η	Associated to Kolmogorov scale
Θ	Associated to the thermal effects
θ	Associated to the turbulent heat fluxes
Ψ	Associated to the scalar Ψ
ω, Ω	Associated respectively to the volumes ω, Ω
E	Associated to the Eulerian Standpoint
f	Associated to the carrier fluid
i,j,k,l	Spatial direction with Einstein summation convention
inj	Value at pollutant source
L	Associated to the Lagrangian Standpoint
p	Associated to the particle set

Abbreviations

ABL	Atmospheric boundary-layer
BC	Boundary condition
CFD	Computational fluid dynamics
CFL	Courant-Friedrichs-Lewy
DNS	Direct numerical simulation
DRSM	Differential Reynolds stress model
EDF	Electricité de France
EVM	Eddy viscosity model
FDF	Filtered density function
GLM	Generalized Langevin model
IEM	Interaction by exchange with the mean
LES	Large eddy simulation
LHS	Left hand side
LMSE	Linear mean square estimation
LRR	Launder-Reece-Rodi
LRR-IP	Launder-Reece-Rodi with isotropisation of production
LRR-L	LRR-IP with isotropisation of production for the scrambling term
MDF	Mass density function
MO	Monin-Obukhov

PBL	Planetary boundary-layer
PDF	Probability density function
$\underline{\boldsymbol{RHS}}$	Vector on the rhs of matrix system
RANS	Reynolds averaged Navier-Stokes
RHS	Right hand side
SBL	Surface boundary layer
SDE	Stochastic differential equation
SGDH	Simple gradient diffusion hypothesis
SLM	Simplified Langevin model
SSG	Speziale-Sarkar-Gatski
TKE	Turbulent kinetic energy
UV	Ultraviolet
WBC	Wall Boundary condition

Greek symbols

$\tilde{\alpha}$	Mean particle volumetric fraction
α	Coefficient in Lagrangian wall-boundary condition
$\upalpha_i$	Algebraic model constants
β_0	Dilatation coefficient $= \frac{1}{\Theta_0}$ for ideal gas (in K^{-1})
$\upbeta_i$	Algebraic model constants
γ	Heat capacity ratio of perfect gas $= \frac{\mathrm{c}_p}{\mathrm{c}_v}$
$\underline{\boldsymbol{\Gamma}}$	Given surface (in m^2)
$\upgamma$	Constant associated with the dissipation rate equation
Δ	Numerical step
Δt	Time step (in s)
Δx	Spatial step (in m)
$\Delta\uptheta$	Angular step (in °)
δ_L	Turbulent "memory" length scale $= U^c T_L$ (in m)
δ	Kronecker symbol
$\tilde{\updelta}$	Dirac delta function
$\underline{\underline{\boldsymbol{\epsilon}}}$	TKE Dissipation rate tensor (in $\mathrm{m}^2\,\mathrm{s}^{-3}$)
ϵ	TKE Dissipation rate $= \frac{1}{2}\mathrm{tr}(\underline{\underline{\boldsymbol{\epsilon}}})$(in $\mathrm{m}^2\,\mathrm{s}^{-3}$)

ζ	Monin-Obukhov similarity parameter $= \frac{z}{L_{M0}} = \frac{z\kappa g\beta_0\theta_*}{u_*^2}$
η	Relative remaining integration time
Θ	Potential temperature (in K)
θ	Fluctuations of potential temperature (in K)
$\uptheta$	Angle value (in °)
κ	Von Kármán constant taken = 0.42
$\upkappa$	Bulk viscosity (in $\mathrm{kg\,m^{-1}\,s^{-1}}$)
λ	A given constant
$\mathit{\lambda}$	Thermal conductivity (in $\mathrm{kg\,m\,s^{-3}\,K^{-1}}$)
$\uplambda$	Algebraic model constant
$\widetilde{\uplambda}_\alpha$	Toy model anisotropy coefficient
μ	Dynamic viscosity (in $\mathrm{kg\,m^{-1}\,s^{-1}}$)
$\upmu$	Algebraic model constant
ν	Kinematic viscosity (in $\mathrm{m^2\,s^{-1}}$)
ν_T	Turbulent viscosity (in $\mathrm{m^2\,s^{-1}}$)
ξ	Random number drawn following a normal centred distribution
$\underline{\underline{\boldsymbol{\Pi}}}$	Pressure-strain correlation tensor (in $\mathrm{m^2\,s^{-3}}$)
ρ	Density
$\underline{\underline{\boldsymbol{\sigma}}}$	Stress tensor (in $\mathrm{kg\,m^{-1}\,s^{-2}}$)
σ_{wall}	Stress tensor at wall (in $\mathrm{kg\,m^{-1}\,s^{-2}}$)
$\upsigma_\Psi$	Coefficient of turbulent diffusion term in Ψ equation
$\widetilde{\upsigma}$	Standard deviation
$\mathcal{T}$	Characteristic timescale (in s)
$\mathcal{T}_\Theta$	Integral turbulent timescale associated to the temperature (in s)
$\mathcal{T}_k$	Integral turbulent timescale $=\frac{k}{\epsilon}$ associated to the turbulence (in s)
$\mathcal{T}_p$	Particle inertial relaxation timescale (in s)
$\underline{\underline{\boldsymbol{\tau}}}$	Viscous stress tensor (in $\mathrm{kg\,m^{-1}\,s^{-2}}$)
$\underline{\underline{\boldsymbol{\Upsilon}}}$	Given Tensor
Φ	Given variable
ϕ	Fluctuation of $\phi = \Phi - \langle\Phi\rangle$ or $\Phi - \overline{\Phi}$
$\upphi$	Latitude (in °)

φ_h	Monin-Obukhov temperature universal function
φ_m	Monin-Obukhov momentum universal function
Ψ	Given variable
ψ	Fluctuation of Ψ: $\psi = \Psi - \langle\Psi\rangle$ or $\psi = \Psi - \overline{\Psi}$
ψ_m	Monin-Obukhov momentum integral universal function $=\int \frac{\varphi_m}{z}\mathrm{d}z$
ψ_h	Monin-Obukhov temperature integral universal function $=\int \frac{\varphi_m}{z}\mathrm{d}z$
χ	Random number drawn from a normal centred distribution
$\underline{\boldsymbol{\Omega}}$	Earth rotation angular frequency $\underline{\boldsymbol{\Omega}} = \Omega\left(\cos(\phi)\underline{\boldsymbol{e_2}} + \sin(\phi)\underline{\boldsymbol{e_3}}\right)$ with $\underline{\boldsymbol{e_2}}$ the south-north unitary vector, $\underline{\boldsymbol{e_3}}$ the upward vertical one, and $\Omega = \frac{2\pi}{T_{\text{Earth}}} \simeq 7.210^{-5}\ \mathrm{s}^{-1}$
Ω	Given volume (in m^3)
ω	Given smaller volume (in m^3)
$\tilde{\omega}$	Dummy volume used to model micro-mixing (in m^3)
$\widehat{\omega}$	Turbulent frequency $= \frac{\epsilon}{k}$ (in s^{-1})
$\underline{\underline{\boldsymbol{\omega}}}$	Rotation tensor: the anti-symmetric part of the velocity gradient (in s^{-1})
ω_θ	Angular velocity

Roman symbols

A	Acceleration (in $\mathrm{m\,s^{-2}}$)
$\underline{\underline{\boldsymbol{a}}}$	Anisotropy tensor $a_{ij} = \frac{\overline{u_i u_j}}{k} - \frac{2}{3}\delta_{ij}$
$\mathscr{A}^{\text{face}}_{f,i,j}$	Boolean test asserting the alignment of a displacement with an oriented face
$\underline{\boldsymbol{\mathcal{A}}}$	Drift vector in diffusion process
$\underline{\underline{\boldsymbol{\mathcal{B}}}}$	Diffusion matrix in diffusion process
$\underline{\boldsymbol{b}}$	Specific body forces (in $\mathrm{m\,s^{-2}}$)
C	Concentration (in $\mathrm{kg\,m^{-3}}$)
c	Fluctuations of concentrations $= C - \langle C\rangle$ or $C - \overline{C}$ (in $\mathrm{kg\,m^{-3}}$)
$\mathcal{C}_{(.)}$	Model constant
c_D	Drag coefficient
c_p	Heat capacity at constant pressure (in $\mathrm{m^2\,s^{-2}\,K^{-1}}$)
c_v	Heat capacity at constant volume (in $\mathrm{m^2\,s^{-2}\,K^{-1}}$)
$\underline{\underline{\boldsymbol{\mathscr{C}}}}$	Reynolds stress Coriolis terms (in $\mathrm{m^2\,s^{-3}}$)
$\underline{\underline{\boldsymbol{\mathscr{D}}}}$	Structure functions (in $\mathrm{m^2\,s^{-2}}$)
$\underline{\underline{\tilde{\boldsymbol{\mathscr{D}}}}}$	Diffusivity term in diffusion process $= \underline{\underline{\boldsymbol{\mathcal{B}}}} \cdot \underline{\underline{\boldsymbol{\mathcal{B}}}}^T$

$\mathcal{D}$	Reynolds stress diffusive term (in $\mathrm{m^2\,s^{-3}}$)
d	diameter (in m)
$\mathscr{E}$	Energy spectrum function (in $\mathrm{m^3\,s^{-2}}$)
e^t	Specific total energy (in $\mathrm{m^2\,s^{-2}}$)
e	Specific internal energy (in $\mathrm{m^2\,s^{-2}}$)
$\mathscr{F}$	Functional term
$\mathcal{F}$	Specific forces (in $\mathrm{m\,s^{-2}}$)
$\mathscr{f}$	Universal function considering similarity theory
F	Mass density function (in kg)
$f^{\mathscr{C}}$	Coriolis parameter = $= 2\Omega \sin \phi$ (in $\mathrm{s^{-1}}$)
$\underline{\boldsymbol{g}}$	Gravity acceleration vector $= -g\underline{\boldsymbol{e_3}}$ with $\underline{\boldsymbol{e_3}}$ the upward vertical unitary vector
g	Gravity acceleration norm considered uniform $\simeq 9.81\ \mathrm{m\,s^{-2}}$
$\underline{\underline{\boldsymbol{G}}}$	GLM drift modeling
$\underline{\underline{\boldsymbol{G}}}^*$	Anisotropic part of the GLM drift modeling
$\mathscr{G}$	Functional term
$\underline{\underline{\boldsymbol{\mathcal{G}}}}$	Reynolds stress gravity production or destruction term (in $\mathrm{m^2\,s^{-3}}$)
$\mathcal{G}$	Kinetic energy gravity production or destruction term $= \frac{1}{2}\mathrm{tr}(\underline{\underline{\boldsymbol{\mathcal{G}}}})$ (in $\mathrm{m^2\,s^{-3}}$)
h	Specific enthalpy (in $\mathrm{m^2\,s^{-2}}$)
H	Obstacle height (in m)
I	Stochastic integral
$\mathscr{k}$	Wavenumber associated to turbulent eddies $= \frac{2\pi}{\ell}$ (in $\mathrm{m^{-1}}$)
k	Turbulent kinetic energy $= \frac{1}{2}\mathrm{tr}(\mathcal{R})$ (in $\mathrm{m^2\,s^{-2}}$)
K	Molecular diffusivity (in $\mathrm{m^2\,s^{-1}}$)
K_t	Turbulent diffusivity (in $\mathrm{m^2\,s^{-1}}$)
ℓ	Length scale of turbulent eddies (in m)
$\mathcal{L}$	Length scale of the large eddies (in m)
L_{MO}	Monin-Onukhov length scale $= \frac{u_*^2}{z\kappa g\beta_0\theta_*}$ (in m)
$\mathscr{L}_{i,j}^{\mathrm{edge}}$	Boolean test asserting if a crossing point is on the left of an oriented edge
$\mathcal{M}$	Markov process
$\mathscr{M}$	Sample space value taken by a Markov process

$\mathpzc{m}$	particle mass (in kg)
M	total mass (in kg)
Ma	Mach number $= \frac{U}{c}$
N	Number of elements or time step
n	Number of elements
P	Pressure (in $\mathrm{kg\,m^{-1}\,s^{-2}}$)
p	Fluctuations of pressure $= P - \langle P\rangle$ or $P - \overline{P}$ (in $\mathrm{kg\,m^{-1}\,s^{-2}}$)
$\underline{\underline{\boldsymbol{\mathcal{P}}}}$	Reynolds stress production term (in $\mathrm{m^2\,s^{-3}}$)
$\mathcal{P}$	Kinetic energy production term $= \frac{1}{2}\mathrm{tr}(\underline{\underline{\boldsymbol{\mathcal{P}}}})$ (in $\mathrm{m^2\,s^{-3}}$)
$\mathscr{P}$	Probability function
$\mathpzc{p}$	Probability density function (PDF)
$\mathbb{P}$	Given set of particle
$\mathsf{P_n}$	Polynomial interpolation at the order n
Pr	Prandtl number $= \frac{\nu}{K_\Theta}$
Pr_t	Turbulent Prandtl number$= \frac{\nu_t}{K_{\Theta_t}}$
Q	Flow rate (in $\mathrm{kg\,s^{-1}}$)
q	Heat flux (in $\mathrm{kg\,s^{-3}}$)
r	radius (in m)
$\underline{\boldsymbol{\mathpzc{r}}}$	Ratio between Reynolds tensor diagonal terms and TKE $\mathpzc{r}_\alpha = \frac{\langle u_\alpha u_\alpha\rangle}{k}$
$\mathscr{R}$	Auto-correlation function
R	Perfect gas constant associated to a given gas (in $\mathrm{m^2\,s^{-2}\,K^{-1}}$)
$\mathsf{R}_{(\Phi)}(\underline{\boldsymbol{X}})$	Reconstruction of Φ at the location $\underline{\boldsymbol{X}}$ based on its value at the center of the cell $\underline{\boldsymbol{X}}^c$
$\underline{\underline{\boldsymbol{\mathcal{R}}}}$	Reynolds tensor $= \underline{\boldsymbol{u}} \otimes \underline{\boldsymbol{u}}$ (in $\mathrm{m^2\,s^{-2}}$)
Re	Reynolds number $= \frac{U^c L^c}{\nu}$
Ri	Richardson number $= \frac{g\beta\delta\Theta L^c}{(U^c)^2}$
Ri_f	Flux Richardson number $= -\frac{\mathcal{P}}{\mathcal{G}}$
Ri_g	Gradient Richardson number $= g\beta\frac{\frac{\partial\langle\Theta\rangle}{\partial z}}{\left(\frac{\partial\langle U\rangle}{\partial z}\right)^2}$
$\underline{\underline{\boldsymbol{S}}}$	Deformation rate tensor: symmetric part of the velocity gradient (in $\mathrm{s^{-1}}$)
$\underline{\underline{\boldsymbol{s}}}$	Deformation rate tensor fluctuations $= \underline{\underline{\boldsymbol{S}}} - \langle\underline{\underline{\boldsymbol{S}}}\rangle$ or $\underline{\underline{\boldsymbol{S}}} - \overline{\underline{\underline{\boldsymbol{S}}}}$ (in $\mathrm{s^{-1}}$)
s	Time integration parameter (in s)

$\mathscr{S}$	Surfacing element
$\mathscr{s}$	entropy
$\mathcal{S}$	Source or sink term
Sc	Schmidt number $\frac{\nu}{K}$
Sc_t	Turbulent Schmidt number
T	Temperature (in K)
t	Time (in s)
$\underline{\boldsymbol{U}}$	Velocity vector (in $\mathrm{m\,s^{-1}}$)
U	Velocity in the streamwise direction (in $\mathrm{m\,s^{-1}}$)
u	Fluctuations of velocity in the streamwise direction $=U - \langle U \rangle$ or $U - \overline{U}$ (in $\mathrm{m\,s^{-1}}$)
$\mathfrak{u}$	Eddy characteristic velocity (in $\mathrm{m\,s^{-1}}$)
V	Velocity in the spanwise direction (in $\mathrm{m\,s^{-1}}$)
v	Fluctuations of velocity in the spanwise direction $=V - \langle V \rangle$ or $V - \overline{V}$ (in $\mathrm{m\,s^{-1}}$)
$\underline{\boldsymbol{\mathcal{V}}}_p$	Sample space value of the particle velocity vector (in $\mathrm{m\,s^{-1}}$)
$\underline{\boldsymbol{\mathcal{V}}}_s$	Sample space value of the particle velocity seen vector (in $\mathrm{m\,s^{-1}}$)
W	Velocity in the normal direction (in $\mathrm{m\,s^{-1}}$)
w	Fluctuations of velocity in the normal direction $=W - \langle W \rangle$ or $W - \overline{W}$ (in $\mathrm{m\,s^{-1}}$)
$\mathcal{W}$	Wiener process (in $\mathrm{s^{-\frac{1}{2}}}$)
$\underline{\boldsymbol{X}}$	Position vector associated to the particles (in m)
$\underline{\boldsymbol{x}}$	Fluctuations of position vector associated to the particles $=\underline{\boldsymbol{X}} - \langle \underline{\boldsymbol{X}} \rangle$ (in m)
X	Position in the streamwise direction associated to the particles (in m)
x	Eulerian location in the streamwise direction (in m)
Y	Position in the spanwise direction associated to the particles (in m)
y	Eulerian location in the spanwise direction (in m)
$\underline{\boldsymbol{\mathcal{Y}}}_p$	Sample space value of the position vector (in m)
z	Height: Eulerian location in the spanwise direction (in m)
z^+	Dimensionless height in the surface flow $= \frac{z u_*}{\nu}$
z_0	Surface roughness length (in m)
$\underline{\boldsymbol{\mathcal{Z}}}$	State vector
$\mathcal{Z}$	Element of the state vector

Operator

$\cdot$	Scalar product
d	Infinitesimal increment
div	Divergence (in m^{-1})
$\equiv$	Boolean equivalent
$\frac{\mathrm{d}(.)}{\mathrm{d}t}$	Material derivative $\frac{\partial(.)}{\partial t} + \left(\underline{\boldsymbol{U}} \cdot \underline{\mathbf{grad}}\right) \underline{\mathbf{(.)}} = \frac{\partial(.)}{\partial t} + U_i \cdot \frac{\partial(.)}{\partial x_i}$ (in s^{-1})
$\frac{D(.)}{Dt}$	Material derivative transported only by mean velocity= $\frac{\partial(.)}{\partial t} + \left(\underline{\langle \boldsymbol{U} \rangle} \cdot \underline{\mathbf{grad}}\right) \underline{\mathbf{(.)}} = \frac{\partial(.)}{\partial t} + \langle U_i \rangle \cdot \frac{\partial(.)}{\partial x_i}$ (in s^{-1})
$\underline{\mathbf{grad}}$	Gradient (in m^{-1})
$[(.)]$	Interpolation operator
$\langle (.) \rangle$	Ensemble average operator
tr	Trace
$\otimes$	Tensor product
$\overline{(.)}$	RANS average operator
$\prod$	Product
$\propto$	proportional to
$\sum$	Sum
$\wedge$	Vector product
$o(.)$	Negligible compared to

CHAPTER 1

Introduction

Contents

1.1 Context

Major accidents, such as encountered at Chernobyl or at Fukushima Daiichi in the nuclear context; but also, in conventional situations the fire at the AZF factory near Toulouse; or more recently the fire at Lubrizol factory or at Bolloré Logistics warehouse both near Rouen and more iconically the Notre-Dame cathedral of Paris fire, have raised a major concern among the public regarding the impacts of atmospheric release of pollutant. Such a concern is not limited to accidental setups but also includes the emissions from industrial site in their normal operating system. Indeed, their emission might have a repercussion on the health of the surrounding populations, as recalled recently by the complaint addressed against Sanofi factory in Mourenx, but also on the environment.

In the context of pollutant releases by local sources, the proper characterisation of the resulting plumes is of paramount importance. From a safety perspective, it may be used as part of an emergency response, enabling to create maps with exclusion zones on the path of the plumes. Moreover, before any accident, the fine understanding of pollutant dynamics may be used to predict such risks and enable to develop both technical and legal solutions accordingly. For these reasons, such a subject is of major interest for EDF (Électricité de France), the most important European electricity producer. Indeed, as all industrial companies, it has to ensure the surety of its installation but also has to assess their potential impacts on the surroundings. This analysis is necessary to be able to prepare risk scenarios in accidental situations but also to estimate the repercussion of operating releases as illustrated recently by the Taishan power plant degassing process. In this context, this work has been realised within a CIFRE contract in collaboration between EDF R&D and the academic laboratory CEREA (Centre d'Étude et de Recherche en Environnement Atmosphérique) whose main subject of research is centred around atmospheric studies. The present work focuses on the numerical modelling of pollutant dispersion in the so-called local scale. The latter, also referred as micro-scale, is characterised by a spatial range from the metre to a few kilometres and a temporal scale from a few seconds to some dozens of minutes. The description of plumes at this scale remains a complex consideration as it depends on multiple factors such as the properties of the fluid released and of the pollutant source which are often complex to estimate (see e.g. Hutchinson et al. [2016]), the topography (see e.g. Britter and Hanna [2003], Bahlali et al. [2019]), but also the local meteorological situations (see e.g. Stull [1988], Arya [1999]). In the latter case, two main elements should be tackled: first the mean wind velocity characterising mostly the mean transport but also the atmospheric stability having a great impact on the turbulent plume diffusion. A main concern of this study will be to properly take into account this second aspect. Moreover, classical hypotheses assumed in Gaussian methods, often used in long range dispersion, such as the local vertical uniformity of the mean velocity and turbulence and the low effect of the topography are not valid at the micro-scale (see e.g. Stockie [2011], Leelóssy et al. [2018]). Due to these complexities, the estimation of the local phenomena at stake is necessary and computational fluid dynamics (CFD) simulations are considered. The latter are identified by the resolution of Navier–Stokes based equations on very refined meshes. In this scope, and in the continuation of the thesis presented by Bahlali [2018], this work focuses on the description of pollutant plumes in dry surface-boundary-layer flows using Lagrangian stochastic methods developed for high Reynolds-number flows.

In Lagrangian stochastic methods, also referred to as Lagrangian probability density function (PDF) methods (or simply as PDF methods in this work), the PDF associated to selected variables of interest, which form the particle state vector, is estimated, in a weak sense, by Monte Carlo methods from a large number of 'stochastic particles' as introduced in the fundamental work of Pope [1985]. These approaches belong to the category of reduced statistical descriptions (see Minier [2016]) in which a Lagrangian standpoint is adopted to model and simulate single-phase, as well as poly-disperse two-phase, turbulent flows and where the eliminated degrees of freedom are replaced by stochastic models. As indicated by their name, one-particle PDF models have an intrinsic Lagrangian nature from which one-point one-time Eulerian PDFs are automatically derived, using a one-way-street procedure, to obtain mean fields. The theoretical framework has been developed in the 1980s and 1990s, mostly by Pope and co-workers (see Haworth and Pope [1986], Pope and Chen [1990], Pope [1991, 1994a,b]) and were later extended to the disperse two-phase flow situation by Minier and co-workers (see Minier and Pozorski [1997], Pozorski and Minier [1998], Minier and Peirano [2001], Minier et al. [2004], Minier [2015, 2016, 2021]) and is now well-established. The ability of PDF methods to treat without approximation convection as well as chemical source terms (and, more generally, the mean value of any function, however complex or non-linear, of the variables entering the particle state vector) makes them attractive candidates to simulate pollutant dispersion and/or reactive flows (see e.g. Sabelfeld [2012]). This has long been recognised in the atmospheric (see Rodean [1996], Wilson and Sawford [1996], Thomson and Wilson [2013]) and combustion (see Pope [1979, 1981, 1983]) communities. Yet, historically, the formulation considered has been scarcely used in atmospheric flows. In this context an approach proposed by Sawford [1986] and Thomson [1987], where flow statistics are assumed known and injected directly in the model instead of being results of the simulation are often used. These methods requiring more information about the carrier flow compared to Pope's approach, are not studied in this work. Furthermore, a grid-based hybrid formulation is tackled, i.e., the mean quantities required to transport the particles are provided by an external solver: either from (pseudo-)analytical solutions or finite volume simulations and are estimated at first on a mesh.

The main goal of the work presented is threefold:

I First, we aim at presenting an in-depth analysis of numerical errors that may arise in the context of grid-based Lagrangian stochastic methods and solutions developed to reduce them.

II A second axis of study is to improve the modelling of neutral or stratified dry surface-boundary-layer flows.

III Finally, the impacts of these numerical and modelling issues on the results obtained when modelling only the pollutant plumes with Lagrangian stochastic methods are investigated.

This manuscript is constituted as follows:

- First, in the following of Chapter 1, an overview of the physical and modelling background in which this work takes place is presented.
- In Chapter 2, the entanglement between spatial and temporal errors is discussed. A time-splitting method enabling, for each particle, to dynamically update the mean carrier fields when it enters a cell is implemented to lower numerical error. As we consider a stochastic method based on an Itô formulation, a specific treatment to avoid anticipation error is provided and a discussion on such error is proposed.
- In Chapter 3, the numerical study is continued for neutral flows. A focus is given to the spatial errors that may impair interpolation of the mean fields at particle location and the estimation of the ensemble statistics from the set of particles. A detailed analysis of these issues is addressed as well as solutions to mitigate them. Moreover, in the spirit of providing a proper modelling of wall-modelled flows, the necessity to use an an-elastic rebound boundary condition to treat wall boundary condition is presented.

- The modelling of linear source dispersion in the context of neutral flow is then presented in Chapter 4, based on the experimental setup of Gamel [2015]. It is shown that, modelling only the pollutant, it is possible using hybrid moment/PDF methods to estimate the mean concentration but also the scalar turbulent fluxes and scalar variance. The different sources of error impacting such simulations are then put forward.

- In Chapter 5, the treatment of stratified surface-boundary-layer flows is investigated. First, a method to estimate the mean carrier fields in coherence with the modelling selected is presented. This method is based on the solutions of the algebraic model considered and on the iterative solution of the turbulent kinetic energy dissipation rate equation. It is followed by an extension of the analysis provided in Chapter 3 to thermally stratified flows. Afterward, the effects of the thermal stability and of its modelling on the pollutant dispersion are qualitatively assessed.

- Finally, in Chapter 6 the conclusions of this work are drawn, and perspectives are presented.

This work led to the publication of two scientific articles (see Balvet et al. [2023a] and Balvet et al. [2023b]). Respectively Chapter 2 and Chapter 3 are based on these papers and elements from both of them are used in Chapter 1.

1.2 Physical Background

Contents

1.2.1 Introduction to the Fundamental Equations of Fluid Dynamics

The present subsection goal is to provide a short introduction to fluid dynamics. It does not aim at being exhaustive. The interested reader may refer, e.g., to Tennekes and Lumley [1972], Monin and Yaglom [1971, 1975], Landau and Lifshitz [1987], Pope [2000], for further information.

1.2.1.1 From Continuum Mechanics to Navier–Stokes Equations

1.2.1.1.1 Continuum Mechanics

First, we aim at presenting the fundamental equations of fluid dynamics, in the scope of the continuum mechanics theory. This theory consists in a description of material bodies assumed to be "continuously filled" with matter. In order to consider such bodies, a smoothing of the intrinsically discrete microscopic interactions between very small elements (such as atoms or molecules) is assumed. Thus, a description at molecular scales is outside the scope of continuum mechanics and will not be treated in this work as it requires to consider a whole other field of physics: the quantum theory. The smoothing of molecular-scale discrete interactions is achieved by spatially averaging these interactions over elementary volumes whose dimensions greatly exceed the molecular interaction length scales. These elementary volumes correspond then to the lowest scale at which the continuum mechanics is valid. However, their size remains sufficiently small for any macroscopic properties to be considered uniform within them and to be able to apply differential calculus. The laws of continuum mechanics stem from conservation of given quantities. These laws are applicable only in closed systems, i.e., systems containing a given fixed mass.

Lagrangian and Eulerian Point of View

Two points of view can be employed to track the evolution of systems. The first one, referred as Lagrangian point of view, consists in following the evolution of given mass over their displacement knowing their state at an anterior time t^0. In this case, for any elementary volume, the position $\underline{\boldsymbol{X}}(t, \underline{\boldsymbol{Z}}^0)$ and any fluids property $\Psi(\underline{\boldsymbol{X}}(\underline{\boldsymbol{Z}}^0, t); t, \underline{\boldsymbol{Z}}^0)$ are variables depending on the time t and on their precedent state $\underline{\boldsymbol{Z}}^0 = (\underline{\boldsymbol{X}}^0,\ \Psi^0)$. In this notation, followed e.g., by Pope [2000], the semicolon is used to separate the location at a given time which is a variable from the initial state and time which are parameters. In the Lagrangian referential, i.e, the one following the volume tracked, the temporal evolution characterised by a material derivative corresponds to the temporal partial derivative along particle trajectories. The second point of view is the Eulerian one within which we consider the evolution of properties $\Psi(t, \underline{\boldsymbol{x}})$ at given location $\underline{\boldsymbol{x}}$. In this case, the location is no longer a time dependent variable but a fixed parameter. In this referential, so as to consider the temporal evolution of a closed system, it is necessary to take into account not only the local temporal derivative within the Eulerian control volume but also the spatial variation caused by the mass advected by the velocity in this volume. Thus, in the fixed Eulerian referential the material derivative is written $\frac{\mathrm{d}\Psi}{\mathrm{d}t}(\underline{\boldsymbol{X}}(t) = \underline{\boldsymbol{x}}; t) = \frac{\partial \Psi}{\partial t}(t, \underline{\boldsymbol{x}}) + (\underline{\boldsymbol{U}} \cdot \underline{\mathbf{grad}})\Psi(t, \underline{\boldsymbol{x}})$. Let's put emphasis that no point of view is intrinsically superior to the other, they are both equivalent and provide similar pieces of information.

To better understand the differences between the two points of view let us use a small analogy. Assuming one wants to describe the evolution of a procession of demonstrators in a road full of anxious shopkeepers, two points of view could be followed. The first one, the Lagrangian one, is the point of view of the demonstrators which are walking with the group and following its displacement in time. For them, the evolution of the behaviour of the procession evolves only on time as they go by. The second one, the Eulerian one, is the point of view of the shopkeepers remaining in their store and monitoring the flow of protesters from their windows.

The evolution of the protest in front of them will depend on the evolution of behaviour of the protesters, which are currently in front of them, but also on the difference of behaviour with the protesters to come. Once we have gathered at any time the information of each protester and each shopkeeper it is possible to extract the same description of the flow of protesters (in this analogy it is assumed that both protesters and shopkeepers remain objective and are not biased regarding the evolution of the procession).

Remark 1.2.1. Before going any further, let us make a small remark on the notation and operator used in this work. The Einstein notation is considered, i.e. there is a summation on all spatial directions when we have repeated Roman subscripts such as $_{i},_{j},_{k},_{l}$ for two side-by-side elements. The latter will be kept as subscripts only to characterise spatial directions. Except if otherwise stated we place ourselves in the Cartesian basis $(\underline{\boldsymbol{e_1}},\ \underline{\boldsymbol{e_2}},\ \underline{\boldsymbol{e_3}}) = (\underline{\boldsymbol{e_x}},\ \underline{\boldsymbol{e_y}},\ \underline{\boldsymbol{e_z}})$ with $x_1 = x,\ x_2 = y,\ x_3 = z$. Note that there is no implicit summation if the subscripts considered are Greek letters. For example, considering a second-order tensor $\underline{\underline{\boldsymbol{\Upsilon}}}$, a vector $\underline{\boldsymbol{\Psi}}$ and a scalar Φ we have:

$$\Psi_i = \underline{\boldsymbol{\Psi}} \cdot \underline{\boldsymbol{e_i}}, \tag{1.1a}$$

$$\mathrm{div}\underline{\boldsymbol{\Psi}} = \sum_{\alpha=1}^{3} \frac{\partial \Psi_\alpha}{\partial x_\alpha} = \frac{\partial \Psi_i}{\partial x_i}, \tag{1.1b}$$

$$\underline{\mathbf{grad}}\Phi = \sum_{\alpha=1}^{3} \frac{\partial \Phi}{\partial x_\alpha}\underline{\boldsymbol{e_\alpha}} = \frac{\partial \Phi}{\partial x_i}\underline{\boldsymbol{e_i}}, \tag{1.1c}$$

$$(\underline{\boldsymbol{U}} \cdot \underline{\mathbf{grad}})\Phi = \sum_{\alpha=1}^{3} U_\alpha \frac{\partial \Phi}{\partial x_\alpha} = U_i \frac{\partial \Phi}{\partial x_i}, \tag{1.1d}$$

$$\underline{\mathrm{div}}(\underline{\underline{\boldsymbol{\Upsilon}}}) = \sum_{\alpha=1}^{3}\sum_{\beta=1}^{3} \frac{\partial \Upsilon_{\alpha\beta}}{\partial x_\beta}\underline{\boldsymbol{e_\alpha}} = \frac{\partial \Upsilon_{ij}}{\partial x_j}\underline{\boldsymbol{e_i}}, \tag{1.1e}$$

$$\underline{\underline{\mathbf{grad}}}\underline{\boldsymbol{\Psi}} = \sum_{\alpha=1}^{3}\sum_{\beta=1}^{3} \frac{\partial \Psi_\alpha}{\partial x_\beta}\underline{\boldsymbol{e_\alpha}} \otimes \underline{\boldsymbol{e_\beta}} = \frac{\partial \Psi_i}{\partial x_j}\underline{\boldsymbol{e_i}} \otimes \underline{\boldsymbol{e_j}}, \tag{1.1f}$$

$$\frac{\mathrm{d}\Psi_i}{\mathrm{d}t} = \frac{\partial \Psi_i}{\partial t} + U_j \frac{\partial \Psi_i}{\partial x_j} = \frac{\mathrm{d}\Psi_\alpha}{\mathrm{d}t} = \frac{\partial \Psi_\alpha}{\partial t} + \sum_{\beta=1}^{3} U_\beta \frac{\partial \Psi_\alpha}{\partial x_\beta} \quad \text{with} \quad _i =_\alpha . \tag{1.1g}$$

A last notation remark: except otherwise stated, the components of the velocity vector $\underline{\boldsymbol{U}}$ are $\underline{\boldsymbol{U}} = U\underline{\boldsymbol{e_x}} + V\underline{\boldsymbol{e_y}} + W\underline{\boldsymbol{e_z}}$, with $U_1 = U_x = U, U_2 = U_y = V$ and $U_3 = U_z = W$.

Conservation Equations

In order to characterise the evolution of a continuous medium, we will consider the conservation laws of the mass, the momentum and the energy first in a Lagrangian point of view. Let us consider a mass δm contained in the elementary volume $\delta\Omega$ defined by the closed surface $\delta\Gamma$ oriented towards the exterior. The deformation of this material volume is characterised by its dilatation rate $\frac{1}{\delta\Omega}\frac{\mathrm{d}\delta\Omega}{\mathrm{d}t}$ following:

$$\frac{1}{\delta\Omega}\frac{\mathrm{d}\delta\Omega}{\mathrm{d}t} = \mathrm{div}(\underline{\boldsymbol{U}}). \tag{1.2}$$

The considered conservation laws per unit of volume can be written as:

$$\begin{aligned}
\frac{1}{\delta\Omega}\frac{\mathrm{d}\delta \mathscr{m}}{\mathrm{d}t}(\underline{\boldsymbol{X}}(t);t) &= \frac{\mathrm{d}\rho}{\mathrm{d}t}(\underline{\boldsymbol{X}}(t);t) + \frac{\rho}{\delta\Omega}(\underline{\boldsymbol{X}}(t);t)\frac{\mathrm{d}\delta\Omega}{\mathrm{d}t}(\underline{\boldsymbol{X}}(t);t) = 0, && \text{(1.3a)}\\
\frac{1}{\delta\Omega}\frac{\mathrm{d}\delta \mathscr{m} U_i}{\mathrm{d}t}(\underline{\boldsymbol{X}}(t);t) &= \frac{\mathrm{d}\rho U_i}{\mathrm{d}t}(\underline{\boldsymbol{X}}(t);t) + \frac{\rho U_i}{\delta\Omega}(\underline{\boldsymbol{X}}(t);t)\frac{\mathrm{d}\delta\Omega}{\mathrm{d}t}(\underline{\boldsymbol{X}}(t);t)\\
&= \frac{\partial\sigma_{ij}}{\partial x_j}(\underline{\boldsymbol{X}}(t);t) + \rho b_i(\underline{\boldsymbol{X}}(t);t), && \text{(1.3b)}\\
\frac{1}{\delta\Omega}\frac{\mathrm{d}\delta \mathscr{m} e^t}{\mathrm{d}t}(\underline{\boldsymbol{X}}(t);t) &= \frac{\mathrm{d}\rho e^t}{\mathrm{d}t}(\underline{\boldsymbol{X}}(t);t) + \frac{\rho e^t}{\delta\Omega}(\underline{\boldsymbol{X}}(t);t)\frac{\mathrm{d}\delta\Omega}{\mathrm{d}t}(\underline{\boldsymbol{X}}(t);t)\\
&= \frac{\partial\sigma_{ij}U_i}{\partial x_j}(\underline{\boldsymbol{X}}(t);t) - \frac{\partial q_j}{\partial x_j}(\underline{\boldsymbol{X}}(t);t) + \mathcal{S}_e(\underline{\boldsymbol{X}}(t);t). && \text{(1.3c)}
\end{aligned}$$

where ρ is the density, $\underline{\boldsymbol{U}}$ the velocity, $\underline{\underline{\boldsymbol{\sigma}}}$ the Cauchy tensor, $\underline{\boldsymbol{b}}$ the gathering of the specific body forces affecting the system, e^t the specific total energy, $\underline{\boldsymbol{q}}$ the specific heat flux and $\mathcal{S}_e$ a source term of heat. In the atmospheric context, the latter may be caused for example by radiation emissions and absorptions, by chemical reactions (either endothermic or exothermic) or due to water change of state (e.g., exothermic condensation or endothermic evaporation). The first equation, Eq. (1.5a) is the conservation of mass also referred as mass continuity equation or simply as continuity equation. The second one, Eq. (1.5b) is the conservation of momentum written using Cauchy's first law of motion derived from Newton's fundamental principle of dynamics for deformable bodies. The third equation Eq. (1.5c) is the conservation of energy described by the first law of thermodynamics. It is worth noticing that in the right-hand side (RHS) of these equations two kinds of terms do appear. On the one hand, there is b gathering all the body forces such as the gravity force, the Coriolis or electromagnetic forces that interact within the volume of the elements. On the other hand, there are terms inside a divergence such as the stress tensor $\underline{\underline{\boldsymbol{\sigma}}}$ or the heat flux $\underline{\boldsymbol{q}}$. They correspond to surface interactions with the surroundings taking place on the surface $\delta\Gamma$ of the volume considered. A fundamental theorem used in continuum mechanics to replace the surface integrals by the corresponding volumetric ones is the divergence theorem which states for any field $\underline{\boldsymbol{\Psi}}$:

$$\iiint_{\delta\Omega} \mathrm{div}(\underline{\boldsymbol{\Psi}})\mathrm{d}\mathscr{V} = \oiint_{\delta\Gamma} \underline{\boldsymbol{\Psi}}\cdot\underline{\boldsymbol{n}}\mathrm{d}\mathscr{S}, \tag{1.4}$$

where $\underline{\boldsymbol{n}}$ is the local normal vector directed towards the exterior.

The equilibrium assumption being true in all point, we can pass from the Lagrangian standpoint to the Eulerian one by estimating these equations in $\underline{\boldsymbol{X(t)}} = \underline{\boldsymbol{x}}$. Doing so, replacing the volume dilatation rate by Eq. (1.2) and the other time derivative using Eq. (1.1g), we obtain in the Eulerian standpoint:

$$\begin{aligned}
&\frac{\partial\rho}{\partial t}(t,\underline{\boldsymbol{x}}) + U_j(t,\underline{\boldsymbol{x}})\frac{\partial\rho}{\partial x_j}(t,\underline{\boldsymbol{x}}) + \rho(t,\underline{\boldsymbol{x}})\frac{\partial U_j}{\partial x_j}(t,\underline{\boldsymbol{x}}) = 0, && \text{(1.5a)}\\
&\frac{\partial\rho U_i}{\partial t}(t,\underline{\boldsymbol{x}}) + U_j(t,\underline{\boldsymbol{x}})\frac{\partial\rho U_i}{\partial x_j}(t,\underline{\boldsymbol{x}}) + \rho U_i(t,\underline{\boldsymbol{x}})\frac{\partial U_j}{\partial x_j}(t,\underline{\boldsymbol{x}}) = \frac{\partial\sigma_{ij}}{\partial x_j}(t,\underline{\boldsymbol{x}}) + \rho b_i(t,\underline{\boldsymbol{x}}), && \text{(1.5b)}\\
&\frac{\partial\rho e^t}{\partial t}(t,\underline{\boldsymbol{x}}) + U_j(t,\underline{\boldsymbol{x}})\frac{\partial\rho e^t}{\partial x_j}(t,\underline{\boldsymbol{x}}) + \rho e^t(t,\underline{\boldsymbol{x}})\frac{\partial U_j}{\partial x_j}(t,\underline{\boldsymbol{x}}) = \frac{\partial\sigma_{ij}U_i}{\partial x_j}(t,\underline{\boldsymbol{x}}) - \frac{\partial q_j}{\partial x_j}(t,\underline{\boldsymbol{x}}) + \mathcal{S}_e(t,\underline{\boldsymbol{x}}). && \text{(1.5c)}
\end{aligned}$$

These equations can then be written as:

$$\boxed{\begin{aligned} \frac{\partial \rho}{\partial t} + \frac{\partial \rho U_j}{\partial x_j} &= 0, \\ \frac{\partial \rho U_i}{\partial t} + \frac{\partial \rho U_i U_j}{\partial x_j} &= \frac{\partial \sigma_{ij}}{\partial x_j} + \rho b_i, \\ \frac{\partial \rho e^t}{\partial t} + \frac{\partial \rho U_j e^t}{\partial x_j} &= \frac{\partial \sigma_{ij} U_i}{\partial x_j} - \frac{\partial q_j}{\partial x_j} + \mathcal{S}_e. \end{aligned}} \qquad \begin{aligned} &(1.6a) \\ &(1.6b) \\ &(1.6c) \end{aligned}$$

In the previous equation and in the following one the explicit dependence on $(\underline{\boldsymbol{x}}; t)$ is not written for the sake of clarity and to simplify the notation. Yet let us keep in mind these dependencies and that for now on we have made the choice to consider a Eulerian description. This is the set of conservation equations provided by the continuum mechanics written in a conservative form.

1.2.1.1.2 Navier–Stokes Equations and Thermal equations

Now that we have seen the conservation equations provided by the continuum mechanics, we will see how they can be applied to model fluid dynamics and in particular ideal gas. The continuity equation Eq. (1.6a), will be first considered as such and we will focus on the momentum and energy equations in the context of compressible flows.

Compressible Flows

Momentum: The body forces considered will only be the weight and the Coriolis effects; (additional forces such as long-range electromagnetic interactions could be considered). We have then:

$$b_i = g_i - 2\Omega_k U_j \varepsilon_{ijk}, \tag{1.7}$$

where $\underline{\boldsymbol{g}} = -g\underline{\boldsymbol{e_3}}$ is the acceleration induced by the weight on Earth whose norm g is assume uniform and equals to 9.81 $\mathrm{m\,s^{-2}}$, $\underline{\boldsymbol{\Omega}}$ is the Coriolis frequency at the latitude considered. Assuming that $\underline{\boldsymbol{e_1}}$ the west-east unitary vector, $\underline{\boldsymbol{e_2}}$ is the south-north one and $\underline{\boldsymbol{e_3}}$ the vertical one, we have $\underline{\boldsymbol{\Omega}} = \Omega\left(\cos(\phi)\underline{\boldsymbol{e_2}} + \sin(\phi)\underline{\boldsymbol{e_3}}\right)$ with $\Omega = \frac{2\pi}{\mathcal{T}_{\text{Earth}}} \simeq 7.210^{-5}\ \mathrm{s^{-1}}$ where $\mathcal{T}_{\text{Earth}} \simeq 86164$ s is the period of rotation of the Earth and ϕ the latitude. This choice of basis is a convention in the atmospheric study and will be referred as reference atmospheric basis. Furthermore, $\underline{\underline{\underline{\boldsymbol{\varepsilon}}}}$ is the third order Levi–Civita tensor enabling to write the Coriolis pseudo-forces in the Cartesian basis as $\Omega_k U_j \varepsilon_{ijk}\underline{\boldsymbol{e_i}} = \underline{\boldsymbol{\Omega}} \wedge \underline{\boldsymbol{U}}$ with:

$$\varepsilon_{ijk} = \begin{cases} 1 & \text{if } (i,j,k) = (1,2,3) \text{ or } (i,j,k) = (2,3,1) \text{ or } (i,j,k) = (3,1,2), \\ -1 & \text{if } (i,j,k) = (1,3,2) \text{ or } (i,j,k) = (2,1,3) \text{ or } (i,j,k) = (3,2,1), \\ 0 & \text{if } i = j \text{ or } i = k \text{ or } j = k. \end{cases} \tag{1.8}$$

Remark 1.2.2. Often only the term in $\Omega_3 = \Omega \sin(\phi)$ is considered in the momentum equation as, at high altitude, where this pseudo-force becomes preponderant, it is assumed that the flow is horizontal and the vertical velocity is neglected. It is then common in the atmospheric community to consider a Coriolis parameter $f^{\mathscr{C}}$ depending on the latitude defined as: $f^{\mathscr{C}} = 2\Omega \sin(\phi)$.

Remark 1.2.3. The axifugal pseudo-force $\underline{\boldsymbol{\Omega}} (\wedge \underline{\boldsymbol{\Omega}} \wedge \underline{\boldsymbol{x}})$ has not been presented here. If one wants to take it into account, it should be added to the gravitational acceleration $\underline{\boldsymbol{g}}$ which is defined by the plumb line experiment. In this case the gravitational acceleration should be seen as a local quantity which does not necessary point toward the centre of the Earth depending on the latitude. This pseudo-force will not be considered later on in this work.

Furthermore, the Cauchy tensor can be split between a reversible part and viscous and irreversible part such as:

$$\sigma_{ij} = -P\delta_{ij} + \tau_{ij}, \tag{1.9}$$

where $\underline{\underline{\boldsymbol{\tau}}}$ is the viscous shear tensor, P is the pressure, and δ_{ij} the Kronecker symbol equals to unity if $i = j$ and zero otherwise. We will consider only Newtonian flows, within which the viscous effects evolve linearly with the velocity gradient:

$$\tau_{ij} = 2\mu S_{ij} - \left(\frac{2}{3}\mu - \kappa\right)\frac{\partial U_k}{\partial x_k}\delta_{ij}, \tag{1.10}$$

where μ is the dynamic viscosity, κ the second viscosity and $\underline{\underline{\boldsymbol{S}}}$ the deformation rate tensor defined as:

$$S_{ij} = \frac{1}{2}\left(\frac{\partial U_i}{\partial x_j} + \frac{\partial U_j}{\partial x_i}\right). \tag{1.11}$$

Injecting Eqs. (1.6a), (1.7), (1.9) and (1.10) in Eq. (1.5c) we obtain the Navier–Stokes equation:

$$\rho\left(\frac{\partial U_i}{\partial t} + U_j\frac{\partial U_i}{\partial x_j}\right) = -\frac{\partial P}{\partial x_i} + \frac{\partial}{\partial x_j}\left(2\mu S_{ij} - \left(\frac{2}{3}\mu - \kappa\right)\frac{\partial U_j}{\partial x_j}\right) + \rho g_i - 2\rho\Omega_k U_j \varepsilon_{ijk}. \tag{1.12}$$

An assumption commonly made in fluid dynamics and first proposed by Stokes [1845], is to take $\kappa = 0$. This is rigorously true only for mono-atomic gases. However, the role of this viscosity becomes predominant only when considering compressibility effects such as wave dispersion or shock wave attenuation (interested reader may refer to Landau and Lifshitz [1987]). Such effects are out of the scope of the presented work and this assumption is conserved. Injecting the Stokes' assumption in the Navier–Stokes equation, it becomes:

$$\boxed{\rho\left(\frac{\partial U_i}{\partial t} + U_j\frac{\partial U_i}{\partial x_j}\right) = -\frac{\partial P}{\partial x_i} + \frac{\partial}{\partial x_k}\left(2\mu S_{ij} - \frac{2}{3}\mu\frac{\partial U_k}{\partial x_k}\right) + \rho g_i - 2\rho\Omega_k U_j \varepsilon_{ijk}.} \tag{1.13}$$

Energy: The specific total energy is the sum of the specific internal energy e, the specific kinetic energy $\frac{1}{2}\underline{\boldsymbol{U}} \cdot \underline{\boldsymbol{U}}$ and the specific potential energy gz. Multiplying the Navier–Stokes equation Eq. (1.13) by $\underline{\boldsymbol{U}}$ one can obtain the equation for the specific kinetic energy:

$$\rho \frac{\mathrm{d}\frac{1}{2}U_i U_i}{\mathrm{d}t} = \frac{\partial \sigma_{ij} U_i}{\partial x_j} - \sigma_{ij}\frac{\partial U_i}{\partial x_j} + \rho g_i U_i. \tag{1.14}$$

Injecting this equation and the continuity equation Eq. (1.6a) in the first law of thermodynamics Eq. (1.6c) we get:

$$\rho \frac{\partial e}{\partial t} + \rho U_j \frac{\partial e}{\partial x_j} = \sigma_{ij}\frac{\partial U_i}{\partial x_j} - \frac{\partial q_j}{\partial x_j} + \mathcal{S}_e. \tag{1.15}$$

One can model the specific heat flux transferred by conduction using the Fourier law [Fourier et al., 1822]. This model is quite similar to the hypothesis made for the viscous tensor assuming a linear relation between the temperature gradient and this flux transferred by molecular conduction:

$$\mathrm{div}(\underline{\boldsymbol{q}}) = \mathrm{div}(-\lambda \underline{\mathbf{grad}}\mathsf{T}), \tag{1.16}$$

with λ the thermal molecular conductivity of the flow, T its temperature. Finally, as the main goal of this study is to consider atmospheric flows, we will consider that the fluid treated is an ideal gas. Under this hypothesis, we consider that the gas molecules do not interact except for elastic rebounds taking place during molecular collisions. For ideal gas, the internal energy depends solely on the temperature as:

$$\mathrm{d}e = \mathrm{c}_v \mathrm{d}\mathsf{T}, \tag{1.17}$$

with $\mathrm{c}_v \simeq 717\,\mathrm{J\,K^{-1}\,kg^{-1}}$ the dry air heat capacity at constant volume. Thus, injecting Eqs. (1.9), (1.10) and (1.16) the first principle of thermodynamics can be written as a function of the temperature as:

$$\rho\left(\frac{\partial \mathrm{c}_v \mathsf{T}}{\partial t} + U_j \frac{\partial \mathrm{c}_v \mathsf{T}}{\partial x_j}\right) = -P\frac{\partial U_i}{\partial x_i} + \tau_{ij}\frac{\partial U_i}{\partial x_j} + \frac{\partial}{\partial x_j}\left(\lambda \frac{\partial \mathsf{T}}{\partial x_j}\right) + \mathcal{S}_e. \tag{1.18}$$

The term $\tau_{ij}\frac{\partial U_i}{\partial x_j}$ represents the production of energy by Joule effects. It is a source term as both components $\left(2\mu S_{ij} - \frac{2}{3}\mu\frac{\partial U_j}{\partial x_j}\delta_{ij}\right)\frac{\partial U_i}{\partial x_j}$ and $\kappa\left(\frac{\partial U_j}{\partial x_j}\right)^2$ are positive, provided that μ and κ are positive (the second term is here neglected). Using the continuity equation, we can replace the velocity divergence next to the pressure by the material derivative of density, after division by the density we obtain:

$$\frac{\partial \mathrm{c}_v \mathsf{T}}{\partial t} + U_j \frac{\partial \mathrm{c}_v \mathsf{T}}{\partial x_j} = \frac{P}{\rho^2}\frac{\mathrm{d}\rho}{\mathrm{d}t} + \frac{\tau_{ij}}{\rho}\frac{\partial U_i}{\partial x_j} + \frac{1}{\rho}\frac{\partial}{\partial x_j}\left(\lambda\frac{\partial \mathsf{T}}{\partial x_j}\right) + \frac{\mathcal{S}_e}{\rho}. \tag{1.19}$$

Injecting the ideal gas law:

$$P = \rho \mathsf{R}^{air}\mathsf{T}, \tag{1.20}$$

with $\mathsf{R}^{air} \simeq 287\,\mathrm{J\,K^{-1}\,kg^{-1}}$ the ideal gas constant of dry air, on the first RHS term of Eq. (1.19) we have:

$$\frac{P}{\rho^2}\frac{\mathrm{d}\rho}{\mathrm{d}t} = -P\frac{\mathrm{d}\frac{1}{\rho}}{\mathrm{d}t} = -P\frac{\mathrm{d}\frac{\mathsf{R}^{air}\mathsf{T}}{P}}{\mathrm{d}t} = -\mathsf{R}^{air}\frac{\mathrm{d}\mathsf{T}}{\mathrm{d}t} + \frac{\mathsf{R}^{air}\mathsf{T}}{P}\frac{\mathrm{d}P}{\mathrm{d}t}. \tag{1.21}$$

As we can consider the heat capacity constant, we get injecting this relation in Eq. (1.19)

$$(\mathrm{c}_v + \mathsf{R}^{air})\frac{\mathrm{d}\mathsf{T}}{\mathrm{d}t} = \frac{\mathsf{R}^{air}\mathsf{T}}{P}\frac{\mathrm{d}P}{\mathrm{d}t} + \frac{\tau_{ij}}{\rho}\frac{\partial U_i}{\partial x_j} + \frac{1}{\rho}\frac{\partial}{\partial x_j}\left(\lambda\frac{\partial \mathsf{T}}{\partial x_j}\right) + \frac{\mathcal{S}_e}{\rho}. \tag{1.22}$$

Using the Mayer's relation, we have for ideal gas $\mathrm{c}_p = \mathrm{c}_v + \mathsf{R}^{air}$ with $\mathrm{c}_p = 1004\ \mathrm{J\,K^{-1}\,kg^{-1}}$ the heat capacity at constant pressure of the dry air.

For an instant, let us consider the adiabatic atmosphere at rest. In such a situation only the first term of the RHS part of the equation remains. We have then:

$$\frac{1}{\mathsf{T}}\frac{\mathrm{d}\mathsf{T}}{\mathrm{d}t} = \frac{\mathsf{R}^{air}}{\mathrm{c}_p P}\frac{\mathrm{d}P}{\mathrm{d}t}. \tag{1.23}$$

This equation can be simply integrated between the reference state at the ground indexed with the subscript $_0$ and the value at a given height as:

$$\mathsf{T}_0 = \mathsf{T}\left(\frac{P_0}{P}\right)^{\frac{\mathsf{R}^{air}}{\mathrm{c}_p}} = \Theta, \tag{1.24}$$

where Θ is the potential temperature which remains constant over adiabatic and inviscid displacement in the atmosphere. As further detailed in Section 1.2.2.2, this quantity is commonly used in atmospheric studies as it is useful to easily characterise the thermal stability. Moreover, using the second law of thermodynamics for ideal gas, the potential temperature can be related to the entropy $\mathscr{s}$ as:

$$\mathsf{T}\frac{\mathrm{d}\mathscr{s}}{\mathrm{d}t} = \mathrm{c}_p\frac{\mathrm{d}\mathsf{T}}{\mathrm{d}t} - \frac{1}{\rho}\frac{\mathrm{d}P}{\mathrm{d}t}, \tag{1.25}$$

then:

$$\frac{\mathrm{d}\mathscr{s}}{\mathrm{d}t} = \mathrm{c}_p \underbrace{\frac{1}{\mathsf{T}}\left(\frac{P}{P_0}\right)^{\frac{\mathsf{R}^{air}}{\mathrm{c}_p}}}_{\Theta^{-1}} \underbrace{\left(\frac{P_0}{P}\right)^{\frac{\mathsf{R}^{air}}{\mathrm{c}_p}}\left(\frac{\mathrm{d}\mathsf{T}}{\mathrm{d}t} - \frac{\mathsf{R}^{air}\mathsf{T}}{\mathrm{c}_p P}\frac{\mathrm{d}P}{\mathrm{d}t}\right)}_{\frac{\mathrm{d}\Theta}{\mathrm{d}t}}. \tag{1.26}$$

It results that:

$$\frac{\mathrm{d}\mathscr{s}}{\mathrm{d}t} = \mathrm{c}_p\frac{\mathrm{d}\ln(\Theta)}{\mathrm{d}t}. \tag{1.27}$$

From the latter equation, it is clear that the potential temperature is a measure of the entropy. The former is then the thermodynamic quantity that we will follow. Its transport equation can be written as:

$$\rho\mathrm{c}_p\frac{\mathrm{d}\Theta}{\mathrm{d}t} = \left(\frac{P_0}{P}\right)^{\frac{\mathsf{R}^{air}}{\mathrm{c}_p}}\left(\tau_{ij}\frac{\partial U_i}{\partial x_j} + \frac{\partial}{\partial x_j}\left(\lambda\frac{\partial \mathsf{T}}{\partial x_j}\right) + \mathcal{S}_e\right) \tag{1.28a}$$

$$= \frac{\Theta}{\mathsf{T}}\left(\tau_{ij}\frac{\partial U_i}{\partial x_j} + \frac{\partial}{\partial x_j}\left(\lambda\frac{\partial \mathsf{T}}{\partial x_j}\right) + \mathcal{S}_e\right) \tag{1.28b}$$

Taking a closer look at the second RHS term we can notice that:

$$\frac{\Theta}{\mathsf{T}}\frac{\partial}{\partial x_j}\left(\lambda\frac{\partial \mathsf{T}}{\partial x_j}\right)=\frac{\partial}{\partial x_j}\left(\lambda\frac{\partial \Theta}{\partial x_j}\right)+\frac{1}{T}\frac{\partial}{\partial x_j}\left(\lambda\left(\Theta\frac{\partial \mathsf{T}}{\partial x_j}-\mathsf{T}\frac{\partial \Theta}{\partial x_j}\right)\right) \tag{1.29a}$$

with:

$$\frac{1}{T}\frac{\partial}{\partial x_j}\left(\lambda\left(\Theta\frac{\partial \mathsf{T}}{\partial x_j}-\mathsf{T}\frac{\partial \Theta}{\partial x_j}\right)\right)=\frac{1}{T}\frac{\partial}{\partial x_j}\left(\lambda\frac{\mathsf{T}^2\mathsf{R}^{air}}{P\mathrm{C}_p}\left(\frac{P_0}{P}\right)^{\frac{\mathsf{R}^{air}}{\mathrm{C}_p}}\frac{\partial P}{\partial x_j}\right) \tag{1.30a}$$

$$=\frac{1}{T}\frac{\partial}{\partial x_j}\left(\frac{\lambda\Theta}{\rho\mathrm{C}_p}\frac{\partial P}{\partial x_j}\right) \tag{1.30b}$$

Analysing the order of magnitude to quantify the relative effects of this contribution compared to the Laplacian of the potential temperature, we see that their relative weight scales approximately as:

$$\frac{\delta P}{\rho T\mathrm{C}_p}\simeq\frac{P-P_0}{P_0}\frac{\mathsf{R}^{air}}{\mathrm{C}_p}. \tag{1.31}$$

Considering flows within the lowest part of the atmosphere, this quantity remains small, thus one may neglect the second contribution in the diffusive term. The potential temperature equation can be simplified into:

$$\boxed{\rho\mathrm{C}_p\frac{\mathrm{d}\Theta}{\mathrm{d}t}=\frac{\Theta}{\mathsf{T}}\left(\tau_{ij}\frac{\partial U_i}{\partial x_j}+\mathcal{S}_e\right)+\frac{\partial}{\partial x_j}\left(\lambda\frac{\partial\Theta}{\partial x_j}\right).} \tag{1.32}$$

Remark 1.2.4. From now on, let us take the potential temperature to quantify the energy evolution of the system, this choice will be further discussed in Section 1.2.2.2. As we consider ideal gas, for smooth enough flow (i.e., in absence of shock) we would obtain a similar description resolving the specific total energy e^t, the specific internal energy e, the specific entropy $\mathscr{s}$ or the specific enthalpy $h=e+\frac{P}{\rho}$, which are in a general case (i.e. not for ideal gas) better description of the energetic state of the flow.

Incompressible Equation of Dynamics

Until now we have considered compressible flow, yet one may want to quantify the influence of the compressibility effects. The proper parameter to quantify these effects is the Mach number $Ma=\frac{U}{\mathscr{c}}$, where $\mathscr{c}$ is the sound celerity in the flow. The sound celerity defined as $\mathscr{c}=\sqrt{\frac{\partial P}{\partial\rho}|_{\mathscr{s}=cst}}$, with $\mathscr{s}$ the entropy, equals to $\sqrt{\frac{\gamma P}{\rho}}$ for ideal gas with $\gamma=\frac{\mathrm{C}_p}{\mathrm{C}_v}$ the capacity ratio equal to $\frac{7}{5}$ for diatomic gas such as the air. In atmospheric flows, this celerity is in general large compared to the flow velocity. Thus, the corresponding Mach number is sufficiently small to be able to consider such flows incompressible. This means that the dilatation rate and then the velocity divergence are null:

$$\boxed{\frac{\partial U_i}{\partial x_i}=0.} \tag{1.33}$$

This incompressibility hypothesis may be used on our set of equations to simplify it as:

$$\boxed{\begin{aligned}
\frac{\mathrm{d}\rho}{\mathrm{d}t} &= \frac{\partial \rho}{\partial t} + U_j \frac{\partial \rho}{\partial x_j} = 0, && (1.34a)\\
\rho\left(\frac{\partial U_i}{\partial t} + U_j \frac{\partial U_i}{\partial x_j}\right) &= -\frac{\partial P}{\partial x_i} + \frac{\partial}{\partial x_j}\left(\mu \frac{\partial U_i}{\partial x_j}\right) + \rho g_i - 2\rho \Omega_k U_j \varepsilon_{ijk}, && (1.34b)\\
\frac{\partial \Theta}{\partial t} + U_j \frac{\partial \Theta}{\partial x_j} &= \frac{\Theta}{\mathsf{T}}\left(\frac{\nu S^2}{\mathrm{C}_p} + \frac{\mathcal{S}_e}{\rho \mathrm{C}_p}\right) + \frac{1}{\rho \mathrm{C}_p}\frac{\partial}{\partial x_j}\left(\lambda \frac{\partial \Theta}{\partial x_j}\right), && (1.34c)
\end{aligned}}$$

with ν is the kinematic viscosity and $S^2 = 2S_{ij}S_{ij}$.

Boussinesq Approximation

Finally, a further approximation will be considered to estimate the effects of thermal dilatation on the flow density. Assuming that we remain sufficiently close to the reference stationary adiabatic atmosphere, with a Mach number sufficiently small, and with vertical displacement small compared to the height of the atmosphere, we can consider the Boussinesq approximation (see e.g. Spiegel and Veronis [1960]) . The latter one states that the variation of density can be neglected everywhere except in front of the gravitional term to be able to treat buoyancy effects. Furthermore, in agreement with the thermodynamic variables considered, it states that in this term the density is independent of the pressure and evolves linearly with the potential temperature. Thus, one can replace ρ by its reference value ρ_0 everywhere in Eqs 1.34, except in the buoyant terms which can be written $\rho_0(1-\beta_0(\Theta-\Theta_0))\underline{\boldsymbol{g}}$ where Θ_0 is the reference potential temperature at ground and $\beta_0 = \frac{1}{\rho_0}\frac{\partial \rho}{\partial \Theta}$ the thermal dilatation coefficient. For ideal gas the latter equals to Θ_0^{-1}.

Remark 1.2.5. Similar assumptions are also currently used to consider the influence of other physical quantities on the density. For example, if one wants to take into account the effects of the humidity in the air, it is current to introduce a similar dilation coefficient associated to the humidity $\beta_0^{\mathrm{hum}} = \frac{1}{\rho_0}\frac{\partial \rho}{\partial C^{\mathrm{hum}}}$ where C^{hum} is the concentration of water. The density is then treated as $\rho\underline{\boldsymbol{g}} = \rho_0(1+\beta_0^{\mathrm{hum}}(C^{\mathrm{hum}} - C_0^{\mathrm{hum}}) - \beta_0(\Theta-\Theta_0))\underline{\boldsymbol{g}}$. In the scope of oceanic flows, to treat thermohaline circulation one can consider the effect of the salinity instead of humidity in a similar manner (see e.g.Vallis [2017]).

Considering the Boussinesq assumption and still that the heat capacity variation is negligible, it is possible to rewrite the set of equations Eqs 1.34 as:

$$\boxed{\begin{aligned}
&\frac{\partial U_i}{\partial x_i} = 0, && (1.35a)\\
&\underbrace{\frac{\partial U_i}{\partial t}}_{1.a} + \underbrace{U_j \frac{\partial U_i}{\partial x_j}}_{1.b} = \underbrace{-2\Omega_k U_j \varepsilon_{ijk}}_{2.a} + \underbrace{g_i(1-\beta_0(\Theta-\Theta_0))}_{2.b} - \underbrace{\frac{1}{\rho_0}\frac{\partial P}{\partial x_i}}_{3.a} + \underbrace{\frac{\partial}{\partial x_j}\left(\nu \frac{\partial U_i}{\partial x_j}\right)}_{3.b.i}, && (1.35b)\\
&\underbrace{U_j \frac{\partial \Theta}{\partial t}}_{1.a} + \underbrace{U_j \frac{\partial \Theta}{\partial x_j}}_{1.b} = \underbrace{\frac{\Theta}{\mathsf{T}}\frac{\nu}{\mathrm{C}_p}S^2}_{3.b.ii} + \underbrace{\frac{\partial}{\partial x_j}\left(K_\Theta \frac{\partial \Theta}{\partial x_j}\right)}_{4} + \underbrace{\frac{\Theta}{\mathsf{T}}\frac{\mathcal{S}_e}{\rho \mathrm{C}_p}}_{5}, && (1.35c)
\end{aligned}}$$

where $K_\Theta = \frac{\lambda}{\rho \mathrm{C}_p}$ is the molecular thermal diffusivity.

Let us take an instant to summarise the physical phenomena at play and their effects in these equations:

1. The left-hand side (LHS) terms are the material derivatives of the quantities. They correspond to the temporal evolution of the flows and are composed of:
   1.a A first term induced by the local temporal variation of the flow,
   1.b A second one resulting from the advection by the velocity of the surrounding quantity in the volume considered.
2. We also have body forces affecting the flow in the bulk such as:
   2.a The Coriolis term even though rigorously speaking it is not a force. Indeed, it is an inertial effect triggered by the choice of the frame od reference. The latter is attached to the Earth and therefore is not an inertial frame of reference due to Earth rotation. It results that this term does not derive from any potential energy as highlighted by the fact it is written as a vector product of velocity. This is the reason why it does not affect the total specific energy nor the kinetic energy. In the case of atmospheric flows, this pseudo-force mainly yields to a rotation with the altitude of the horizontal velocity inducing the so-called Ekman spiral.
   2.b The buoyancy corresponding to the effects of the Earth gravitational attraction on the flow. It depends on the density of the flow which may be modified by thermal effects, resulting in the creation of a vertical displacement due to the Archimedes' principle. This physical phenomenon plays a fundamental role in atmospheric flows as further discussed in Section 1.2.2.2.
3. We also have surface effects arising from the divergence of the Cauchy stress tensor which can be decomposed between:
   3.a Its isotropic and reversible part which is the pressure gradient. This is a normal stress which can be understood, using the statistical kinetic theory, as an averaged description of the surface force resulting from molecular collisions at the microscopic scale. It is worth noticing that in the case of incompressible flow it does no longer appear in the temperature equation and then has no direct impact on this quantity. Considering horizontally stratified flows, the pressure gradient is in equilibrium with the buoyancy.
   3.b The second part of the Cauchy stress tensor corresponds to the viscous effects, which have two preponderant roles:
      3.b.i First, it plays a diffusive role for the momentum, as we can see in the Navier–Stokes equation Eq. (1.35b). In this equation it appears as a Laplacian term smoothing possible fluctuations.
      3.b.ii Second, it plays a dissipative role transforming kinetic energy into heat and then temperature. This effect can be seen through the presence of the dissipation function μS^2 which appears with positive sign in the potential temperature (and specific internal energy) equations and with a negative sign in the kinetic energy equation (in the term $-\sigma_{ij}\frac{\partial U_i}{\partial x_j}$ of Eq. (1.14)). In the general case, the energy produced by viscous dissipation is small compared by energy provided or absorbed by the ground due to the daily radiative cycle; it is thus commonly neglected. The physical ground of these assumptions will be further detailed in Paragraph 1.2.2.1.2.

4 As its name implies the thermal diffusivity plays a diffusive role for the temperature field.

5 This term is a source term of heat. In atmospheric flow, it is often associated to radiative effects (such as played by aerosol, carbon dioxides), to chemical reactions such as the exothermic production of ozone in the stratosphere, or to change of state of the water for example the production of cloud by condensation of humidity. These effects are out of the scope of the present work and will not be considered, so this term will be removed from now on.

Remark 1.2.6. Using a similar derivation as the one proposed here, one can present the incompressible transport equation for any passive scalar Ψ (e.g. a pollutant concentration) as:

$$\frac{\partial \Psi}{\partial t} + U_j \frac{\partial \Psi}{\partial x_j} = \frac{\partial}{\partial x_i}\left(\frac{\nu}{Sc}\frac{\partial \Psi}{\partial x_i}\right) + \frac{\mathcal{S}_\Psi}{\rho}, \tag{1.36}$$

where Sc is the Schmidt number corresponding to the ratio between the kinematic molecular viscosity and the scalar molecular diffusivity K_Ψ: $Sc = \frac{\nu}{K_\Psi}$. In addition, $\mathcal{S}_\Psi$ corresponds to either sink or source term caused for example by chemical reactions or nuclear disintegration. Furthermore, in this equation, the mass fluxes transported by molecular conduction have been modelled in a similar manner than the heat flux using the law proposed by Fick [1855]:

$$\mathrm{div}(\underline{\boldsymbol{q_\Psi}}) = -\mathrm{div}(\lambda_\Psi \underline{\mathbf{grad}}\Psi) + \mathcal{S}_\Psi, \tag{1.37}$$

with $\lambda_\Psi = \rho K_\Psi$ the scalar molecular conductivity

Let us briefly recall the main hypotheses considered to obtain these equations. We have first considered incompressible and expandable flows. The Boussinesq approximation is considered to treat the buoyancy terms.

1.2.1.2 Background on the Notion of Turbulence

In practice, as soon as we consider scales at which the viscous term is not large compared to the inertial one, instabilities and turbulence which is characterised by the presence of eddies and structures of different scales, appear. They may have a great impact on the dynamics of the flow as we can see in Figure 1.1. In order to quantify the relative importance of inertial and viscous effects, and then the possible presence of turbulent effects, we use the Reynolds number $Re = \frac{U^c L^c}{\nu}$ where U^c is the characteristic scale of velocity and L^c a characteristic length of the flow (see Reynolds [1895]).

When the latter is large, as it is the case in atmospheric flows turbulent eddies may appear. A few examples are briefly exposed here.

- As we can see in Figure 1.1A, even with a stationary incoming flow (from the upper right-hand corner) the perturbation caused by the presence of an obstacle (here the Canary Island) may result in the creation of a succession of very stable and large eddies whose rotating sense is inversed from one eddy to the following one. This succession of eddies after an obstacle is referred as the Von Kármán vortex street. It originates from the slowdown imposed by the obstacle creating instabilities in its wake. It is worth noting that after a wing profile, the opposite effect may appear. The acceleration of velocity may induce creation of eddies referred as anti Von Kármán vortex street.

(A) Von Kármán vortex street.

(B) Kelvin–Helmoltz instabilities.

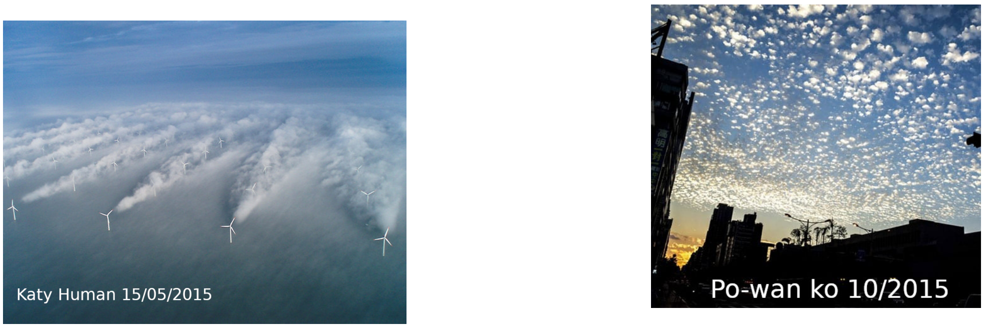

(C) Wake in a wind turbine farm.

(D) Alto-cumulus created by Rayleigh–Bénard convection.

Figure 1.1: Examples of atmospheric flows within which instabilities and turbulent effects are exhibited by their impacts on cloud formation and deformation.

- Furthermore, when the fluid velocity is not uniform in the vertical direction or at the interface between two non-miscible fluids with different densities, one can notice the creation of eddies due to Kelvin–Helmholtz instabilities as shown in Figure 1.1B. In this image, the flow is going from the right to the left and is slower on the lower part. The strong mean velocity gradients results in the creation of shear stress yielding to the production of vertical eddies. These vertical fluctuations of velocity are the origin of the wave-like cloud we can notice. Their formation is indeed a marker of the up-going eddies. The latter ones transport water vapor from the lower layer to the upper one which will condensate as the temperature diminishes with altitude.

- The situation in Figure 1.1C, results in a complex interplay of different phenomena. As we can see from the slight haze layer near the ocean, the atmosphere is almost at saturation. One can note that, behind the wind turbines, water condensation is triggered. Thanks to this condensation, the turbine wakes and the turbulent structures in their midst become visible. The processes governing the dynamics of clouds are complex (see e.g. Jacobson [2005]) and their analysis from a mere picture is difficult. One may assume that the turbulent eddies may play a mixing role in this process bringing humid air from the ocean surface up where it cools down and condensates. The dynamical effects played by the flow slow down and pressure variations may also play an important role. Yet, let us emphasise that this interpretation should be considered with great caution and a precise study should be considered if one wants to explain precisely the physics encountered in this situation.

- The last example presents the creation of alto-cumulus due to turbulent thermal effects in Figure 1.1D. In this case, the vertical eddies are created by buoyancy effects, induced by the presence of a strong temperature gradient. Hot stream of air elevates in altitude where it cools down increasing the air density until it dives anew. Here again, the presence of up-going eddies is marked by the creation of spot of cloud where these eddies bring water vapor which condensates.

Let us note that in these examples the presence of instabilities and turbulent eddies is highlighted by the creation or deformation of clouds due to the transport of water by these eddies. However, in the general case, the latter are not noticeable to the naked eye. The present subsection aims at describing the behaviour of turbulent eddies. First the physics of the small scale turbulence is briefly discussed considering the Kolmogorov theory in Paragraph 1.2.1.2.1. Then we will present the processes impacting the turbulence at the macroscopic scale considering Reynolds averaged equation in Paragraph 1.2.1.2.2. This presentation is not exhaustive and further information may be found in books focusing on turbulence such as Tennekes and Lumley [1972], Monin and Yaglom [1971, 1975], Pope [2000], Rodi [2000]

1.2.1.2.1 Kolmogorov Theory: a Description of the Small-Scale Turbulence

The goal of this paragraph is to provide background concerning the Kolmogorov theory of turbulence mainly focusing on small scales compared to the scales of the flow. It aims at putting emphasis on salient physical processes characteristic of turbulence and is therefore not an exhaustive description of the turbulence (for more information on Kolmogorov theory see e.g. Kolmogorov [1941, 1962], Monin and Yaglom [1971, Chapter 8] and Pope [2000, Chapter 6]).

Principle of the Energy Cascade

We will first discuss the process of transfer of energy within the different scales of turbulent structures. The idea of an energy cascade was first presented by Richardson [1922]. The overall idea is that turbulent kinetic energy (TKE) is produced at the larger scales, also referred as energy containing scales, by exchange of energy from the mean flow to the large eddies. The eddies created by this process being unstable, they tend to break creating smaller eddies which are sufficiently big for the viscous effects to be neglected. The newly formed eddies will also break creating even smaller eddies. This energy is then distributed from the larger eddies to the lower scales by successive breaking of eddies into smaller and smaller ones. As the transfer of energy continues, the size of the eddies diminishes until a scale where they are small enough for the molecular viscosity to dissipate this energy. This transfer of energy from large eddies, where it is produced, to the small ones where it is dissipated by a successive breaking of eddies is referred as the energy cascade. Let us note that, here, the word "eddy" has no rigorous definition and could be replaced by the words turbulent structure, turbulent motion, whirl or whorl. It is however characterised by a spatial scale ℓ, a velocity scale u_ℓ and a timescale $\mathcal{T}_\ell = \frac{\ell}{\mathrm{u}_\ell}$. This phenomenon was emblematically summarised by Richardson in a quite succinct yet poetic way as:

"Big whirls have little whirls
that feed on their velocity,
And little whirls have lesser whirls
and so on to viscosity ."

Kolmogorov later on gave theoretical background and quantification of this phenomenon in Kolmogorov [1941, 1962]. So as to simplify the description of the phenomenon, in this paragraph we will consider statistically stationary high Reynolds number flows without any thermal nor Coriolis effects. The first hypothesis of Kolmogorov states that at sufficiently high Reynolds number, sufficiently small turbulent eddies can be considered statistically isotropic. The flow anisotropy induced by the large scales is then lost by the successive exchange to smaller eddies as we go down the energy cascade. The behaviour at these scales being independent of the large scales, they are then universal for all high-Reynolds turbulent flows. In order to quantify such a behaviour, Kolmogorov presents two similarity hypotheses.

Kolmogorov Scales
The first one concerns the smaller scale of turbulence. It states that for sufficiently high Reynolds number, the statistics of the small-scale motions depend only on the viscosity ν and on the dissipation rate ϵ (i.e. the specific power at which the TKE is transformed in heat by the viscous effects). A scale depending on these parameters, referred as Kolmogorov scale and indexed with the subscript $_\eta$, can then be obtained by dimensional analysis as:

$$\ell_\eta = \left(\frac{\nu^3}{\epsilon}\right)^{\frac{1}{4}}, \tag{1.38a}$$

$$u_\eta = (\nu\epsilon)^{\frac{1}{4}}, \tag{1.38b}$$

$$\mathcal{T}_\eta = \left(\frac{\nu}{\epsilon}\right)^{1/2}. \tag{1.38c}$$

An important element is that this scale is the smallest turbulent scale and corresponds to a dissipative scale. This is attested by the corresponding Reynolds number which equals to one: $Re_\eta = \frac{u_\eta \ell_\eta}{\nu} = 1$.

Range of Turbulence
Now that we have a description of the diffusive processes at the lower scales, one may want to compare it to the larger scales producing the turbulent kinetic energy. The kinetic energy dissipated being in equilibrium with the production at the larger scales we have $\epsilon \simeq \frac{u_\mathcal{L}^3}{\mathcal{L}}$ where $u_\mathcal{L}$ and $\mathcal{L}$ are respectively the characteristic velocity and length of the large eddies. Injecting this equation in Eqs 1.38, we might have access to an estimation of the range of turbulent scales:

$$\frac{\ell_\eta}{\mathcal{L}} \simeq Re_\mathcal{L}^{-3/4}, \tag{1.39a}$$

$$\frac{u_\eta}{u_\mathcal{L}} \simeq Re_\mathcal{L}^{-\frac{1}{4}}, \tag{1.39b}$$

$$\frac{\mathcal{T}_\eta}{\mathcal{T}_\mathcal{L}} \simeq Re_\mathcal{L}^{-\frac{1}{2}}. \tag{1.39c}$$

It is then clear that all the scale ranges of turbulence increase with the Reynolds number $Re_\mathcal{L}$. The latter might be estimated based on the turbulent Reynolds number $Re_t = \frac{k^2}{\epsilon\nu}$ based on the velocity scale $\sqrt{k}$ and the length scale $\frac{k^{3/2}}{\epsilon}$ where k is the overall TKE. For atmospheric surface boundary layer flows, the latter is typically ten times smaller than Re: the Reynolds number based on the flow dimensions. Then the $Re_\mathcal{L}$ based on the larger scales is commonly around $10^6 - 10^7$ in such flows, triggering the existence of turbulence over a broad range of scales.

Remark 1.2.7.
If one wants to take into account the thermal effects, it is still possible to consider that the small eddy geometry is independent of the large scale and thus that their behaviour remains universal. Moreover, in this case, we shall also consider the kinetic energy produced by thermal effects in the dissipation rate $\epsilon \simeq \frac{\mathrm{u}_{\mathcal{L}}^3}{\mathcal{L}} + g\beta_0\delta\Theta u_{\mathcal{L}}$, we have then:

$$\frac{\ell_\eta}{\mathcal{L}} \simeq \left(\frac{g\beta_0\delta\Theta \mathrm{u}_{\mathcal{L}}\mathcal{L}^4}{\nu^3} + \frac{\mathrm{u}_{\mathcal{L}}^3\mathcal{L}^3}{\nu^3}\right)^{-\frac{1}{4}} = \left(\left(1 + \frac{g\beta_0\delta\Theta\mathcal{L}}{\mathrm{u}_{\mathcal{L}}^2}\right)\frac{\mathrm{u}_{\mathcal{L}}^3\mathcal{L}^3}{\nu^3}\right)^{-\frac{1}{4}} = \left((1+Ri)Re_{\mathcal{L}}^3\right)^{-\frac{1}{4}}, \tag{1.40a}$$

$$\frac{\mathrm{u}_\eta}{\mathrm{u}_{\mathcal{L}}} \simeq \left(\frac{g\beta_0\delta\Theta\nu}{\mathrm{u}_{\mathcal{L}}^3} + \frac{\nu}{\mathrm{u}_{\mathcal{L}}\mathcal{L}}\right)^{\frac{1}{4}} = \left(\left(1 + \frac{g\beta_0\delta\Theta\mathcal{L}}{\mathrm{u}_{\mathcal{L}}^2}\right)\frac{\nu}{\mathrm{u}_{\mathcal{L}}\mathcal{L}}\right)^{\frac{1}{4}} = \left(\frac{1+Ri}{Re_{\mathcal{L}}}\right)^{\frac{1}{4}}, \tag{1.40b}$$

$$\frac{\mathcal{T}_\eta}{\mathcal{T}_{\mathcal{L}}} \simeq \left(\frac{g\beta_0\delta\Theta\mathcal{L}^2}{\mathrm{u}_{\mathcal{L}}\nu} + \frac{\mathrm{u}_{\mathcal{L}}\mathcal{L}}{\nu}\right)^{-\frac{1}{2}} = \left(\left(1 + \frac{g\beta_0\delta\Theta\mathcal{L}}{\mathrm{u}_{\mathcal{L}}^2}\right)\frac{\mathrm{u}_{\mathcal{L}}\mathcal{L}}{\nu}\right)^{-\frac{1}{2}} = ((1+Ri)Re_{\mathcal{L}})^{-\frac{1}{2}}. \tag{1.40c}$$

Where $\frac{g\beta_0\delta\Theta\mathcal{L}}{\mathrm{u}_{\mathcal{L}}^2}$ is the Richardson number characterising the ratio between the buoyant and inertial effects. The spatial and temporal ranges of turbulence increase with the Reynolds and with the Richardson number when it is positive. This situation is then referred as thermally unstable. At the opposite, for negative values of the Richardson number, the situation is stable and the thermal effects damp the turbulent ones.

Inertial Sub-range

As the Reynolds number increases, so does the range of scales between the larger eddy $\mathcal{L}$ and the smaller ℓ_η. It is clear that for sufficiently high Reynolds number flows, one may insert an intermediate sub-range containing eddies of size ℓ such that $\mathcal{L} \gg \ell \gg \ell_\eta$. On the one hand, as these eddies are much smaller than the larger ones, they may be considered isotropic. On the other hand, they are much larger than the Kolmogorov scale, then their motion is not impacted by viscosity. The second hypothesis of similarity of Kolmogorov states that for sufficiently high Reynolds-number flows, there are eddies of scale ℓ such that $\mathcal{L} \gg \ell \gg \ell_\eta$ which have a universal and isotropic form that are uniquely determined by their size and the dissipation rate ϵ. For these eddies we can then construct velocity and timescales based on ϵ and ℓ such as:

$$\mathrm{u}_\ell = (\epsilon\ell)^{1/3} \simeq \mathrm{u}_{\mathcal{L}}\left(\frac{\ell}{\mathcal{L}}\right)^{1/3} \simeq \mathrm{u}_\eta\left(\frac{\ell}{\ell_\eta}\right)^{1/3}, \tag{1.41a}$$

$$\mathcal{T}_\ell = \left(\frac{\ell^2}{\epsilon}\right)^{1/3} \simeq \mathcal{T}_{\mathcal{L}}\left(\frac{\ell}{\mathcal{L}}\right)^{2/3} \simeq \mathcal{T}_\eta\left(\frac{\ell}{\ell_\eta}\right)^{2/3}. \tag{1.41b}$$

The effects taking place in these range being inertial, this range of eddies is referred as the inertial sub-range. Its main role is the transport of the turbulent kinetic energy from the large scales to the lower ones.

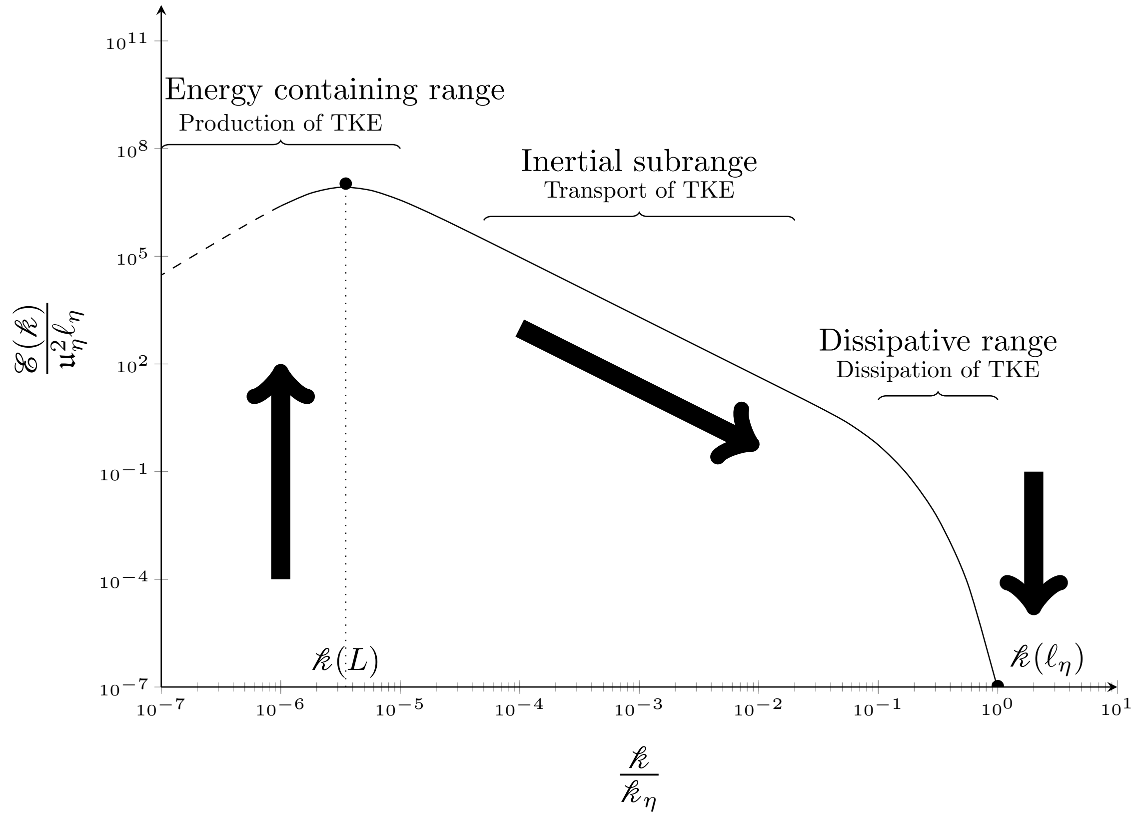

Figure 1.2: Scheme of the energy spectrum for high Reynolds number turbulence after Pope [2000].

Spectrum of Energy

Now that we have described the eddies at different scales, one may wonder how the turbulent kinetic energy is distributed among them. To this end, we will study the energy spectrum function $\mathscr{E}(\mathscr{k})$ which gives for each wavenumber $\mathscr{k} = \frac{2\pi}{\ell}$ the corresponding energy density. It is defined as follows:

$$k_{\mathscr{k}_a,\mathscr{k}_b} = \int_{\mathscr{k}_a}^{\mathscr{k}_b} \mathscr{E}(\mathscr{k})\mathrm{d}\mathscr{k}, \tag{1.42}$$

where $k_{\mathscr{k}_a,\mathscr{k}_b}$ is the kinetic energy contained in the eddies whose wavenumber is in the range $[\mathscr{k}_a, \mathscr{k}_b]$. As stated by the second Kolmogorov hypothesis, in the inertial sub-range, the turbulence is universally characterised by a function of ϵ and κ. By dimensional analysis we have then

$$\mathscr{E}(\kappa) = \mathrm{C}_{\mathscr{E}}^{SR}\epsilon^{2/3}\mathscr{k}^{-5/3}, \tag{1.43}$$

where $\mathrm{C}_{\mathscr{E}}^{SR}$ is a "universal" constant. This relation describing the evolution of the distribution of energy within the inertial sub-range is often referred as the "*five-third law*". It shows that as we go down the energy cascade the turbulent eddies tend to be less and less energetic. Thus, even-though this rule cannot be applied directly to the larger scales, it still highlights that the latter ones are the most energetic justifying the name of energy containing scales. A scheme of the spectrum of energy is presented in Figure 1.2, to summarise the description of the energy cascade.

Eulerian Structure Functions

Now that we have studied the role of each scale of turbulence and the distribution of energy within them, we will further investigate the corresponding spatial correlations. To do so, Kolmogorov [1941] proposed to study the second-order structure function $\underline{\underline{\boldsymbol{\mathscr{D}}}}_E$, which is the covariance of the velocity between a point $\underline{\boldsymbol{x}}$ and $\underline{\boldsymbol{x}} + \underline{\boldsymbol{\delta x}}$ using the Eulerian point of view:

$$\mathscr{D}_{E_{ij}}(\underline{\boldsymbol{x}}, \underline{\boldsymbol{\delta x}}) = \Big\langle (U_i(\underline{\boldsymbol{x}} + \underline{\boldsymbol{\delta x}}) - U_i(\underline{\boldsymbol{x}}))(U_j(\underline{\boldsymbol{x}} + \underline{\boldsymbol{\delta x}}) - U_j(\underline{\boldsymbol{x}}))\Big\rangle, \tag{1.44}$$

where the notation $\langle(.)\rangle$ is used for the ensemble average over a large number of samples. First, considering $\delta x = |\underline{\boldsymbol{\delta x}}| \ll \mathcal{L}$ the first Kolmogorov theory imposes a local isotropy which can be used to state that $\underline{\underline{\boldsymbol{\mathscr{D}}}}$ does not depend on $\underline{\boldsymbol{x}}$ but only on $\underline{\boldsymbol{\delta x}}$. Based on this property it can be written:

$$\mathscr{D}_{E_{ij}}(\underline{\boldsymbol{\delta x}}) = \mathscr{D}_{E_\perp}(\underline{\boldsymbol{\delta x}})\delta_{ij} + (\mathscr{D}_{E_\parallel}(\underline{\boldsymbol{\delta x}}) - \mathscr{D}_{E_\perp}(\underline{\boldsymbol{\delta x}}))\frac{\delta x_i \delta x_j}{\delta x^2}, \tag{1.45}$$

where $\mathscr{D}_{E_\perp}$ and $\mathscr{D}_{E_\parallel}$ are respectively the longitudinal and transverse structure functions. Considering $\underline{\boldsymbol{U}}(\underline{\boldsymbol{x}}) = U(\underline{\boldsymbol{x}})\underline{\boldsymbol{e}_\parallel}$, we can write $\underline{\underline{\boldsymbol{\mathscr{D}}}} = \mathscr{D}_{E_\parallel}\underline{\boldsymbol{e}_\parallel} \otimes \underline{\boldsymbol{e}_\parallel} + \mathscr{D}_{E_\perp}(\underline{\underline{\boldsymbol{1}}} - \underline{\boldsymbol{e}_\parallel} \otimes \underline{\boldsymbol{e}_\parallel})$. Thanks to the continuity equation we can express $\mathscr{D}_{E_\perp}$ as a function of $\mathscr{D}_{E_\parallel}$ as:

$$\mathscr{D}_{E_\perp}(\underline{\boldsymbol{\delta x}}) = \mathscr{D}_{E_\parallel}(\underline{\boldsymbol{\delta x}}) + \frac{\delta x_i}{2}\frac{\partial \mathscr{D}_{E_\parallel}(\underline{\boldsymbol{\delta x}})}{\partial \delta x_i}. \tag{1.46}$$

Then, considering small enough distance $|\delta x|$ so that the first hypothesis of Kolmogorov is valid, this structure function depends only on $\mathscr{D}_{E_\parallel}(\underline{\boldsymbol{\delta x}})$. Moreover, according to the first similarity hypothesis, for small enough distance $\underline{\boldsymbol{\delta x}}$, the latter one depends only on the distance δx, the dissipation rate ϵ and the viscosity ν:

$$\mathscr{D}_{E_\parallel}(\underline{\boldsymbol{\delta x}}, t) = \mathscr{D}_{E_\parallel}(\delta x) = \epsilon^{2/3}(\delta x)^{2/3}\mathscr{F}_{\mathscr{D}}\left(\frac{\delta x}{\ell_\eta}\right), \tag{1.47}$$

where $\mathscr{F}_{\mathscr{D}}(\frac{\delta x}{\ell_\eta})$ is a universal function. According to the second Kolmogorov similar hypothesis, in the inertial sub-range where the viscosity should not have any effect, this universal function should tend towards a constant $\mathrm{C}_{\mathscr{D}}$. We can then determine a fundamental law describing the spatial evolution of turbulence: the "*two-third law*" which is intrinsically bound to the "*five-third law*" and which states that for $\mathcal{L} \gg \delta x \gg \ell_\eta$, we have:

$$\mathscr{D}_{E_\parallel}(\delta x) = \mathrm{C}_{\mathscr{D}}\epsilon^{2/3}(\delta x)^{2/3}, \tag{1.48a}$$

$$\mathscr{D}_{E_\perp}(\delta x) = \frac{4}{3}\mathrm{C}_{\mathscr{D}}\epsilon^{2/3}(\delta x)^{2/3}. \tag{1.48b}$$

Lagrangian Auto-correlation Function and Characteristic Scale

Now that we have discussed how much a given eddy does evolve over a given distance, let us introduce the scale over which the turbulent motion as a whole remains coherent. First attempts to determine such integrated scales were proposed by Taylor [1922, 1935] and Von Karman and Howarth [1938] and were further described by Kolmogorov [1941, 1962]. For this purpose, let us consider a Lagrangian point of view and follow the eddies over time. Moreover, let us introduce the auto-correlation function of velocity $\mathscr{R}_L$ such as:

$$\mathscr{R}_L(\delta t) = \frac{\langle U(t^0)U(t^0 + \delta t)\rangle}{\langle U(t^0)^2\rangle}. \tag{1.49}$$

We have in the general case little information on this auto-correlation function. Its precise form does not play a major role in the case of diffusive regime for $\delta t \gg T_L$. However, for smaller timescale, for example to characterise the dispersion $\langle X^2\rangle(\delta t)$ with $\delta t \simeq T_L$, the form of $\mathscr{R}_L$ may have a significant impact. Some properties should be stated:

- The flow at the initial state is perfectly correlated with itself: $\mathscr{R}_L(0) = 1$.
- The auto-correlation cannot exceed its initial state where the flow is perfectly correlated: $|\mathscr{R}_L|(\delta t) < 1$ for any $\delta t > 0$.
- Near the initial state the first-order derivative is null, and the function is concave: $\left(\frac{\mathrm{d}\mathscr{R}_L}{\mathrm{d}t}\right)_{\delta t=0} = 0$, $\left(\frac{\mathrm{d}^2\mathscr{R}_L}{\mathrm{d}t^2}\right)_{\delta t=0} < 0$.
- After a time sufficiently long, the initial state will be forgotten $\mathscr{R}_L(t^\infty) = 0$.

We can then introduce an integral time T_L, referred as Lagrangian integral timescale or simply in this work as Lagrangian timescale, defined as:

$$T_L = \int_0^\infty \mathscr{R}_L(s)\mathrm{d}s, \tag{1.50}$$

which corresponds to the typical time scale over which the turbulence remains correlated to a previous state. A form commonly used to characterise the auto-correlation function is an exponential decrease $\exp\left(-\frac{\delta t}{T_L}\right)$. This function does not respect the condition to have a quadratic decrease near origin. However, away from this zone it seems to be an acceptable proposition as shown by Yeung and Pope [1989] and Squires and Eaton [1991].

Lagrangian Structure Functions

Finally, let us consider the evolution of the velocity differences using a Lagrangian point of view. The latter will play an important role in the derivation of Lagrangian stochastic models in Section 1.3.3. It can be written as:

$$\delta U(\underline{\boldsymbol{X}}^0, t, \delta t) = U(\underline{\boldsymbol{X}}(\underline{\boldsymbol{X}}^0, t+\delta t), t) - U(\underline{\boldsymbol{X}}^0, t) \tag{1.51}$$

Considering an increment of time δt smaller than the Lagrangian timescale T_L, $U(\underline{\boldsymbol{X}}(\underline{\boldsymbol{X}}^0, t+\delta t), t)$ remains somewhat close to $U(\underline{\boldsymbol{X}}^0, t)$. Therefore, in locally isotropic turbulence, for small enough increments of time $\delta t \ll \max(T_L, \frac{\mathcal{L}}{\mathrm{u}_{\mathcal{L}}})$, the difference of velocity $\delta U(\underline{\boldsymbol{X}}^0, t, \delta t)$ can be considered independent of the initial position $\underline{\boldsymbol{X}}^0$ and of the initial time t. Similarly, to the structure functions presented in a Eulerian scope, such a function can be introduced to estimate the evolution of velocity difference associated to a given fluid particle which then evolves in time as:

$$\mathscr{D}_{L_{ij}}(\delta t) = \Big\langle \delta U_i(\delta t)\delta U_j(\delta t)\Big\rangle. \tag{1.52}$$

Considering the first Kolmogorov and the first similarity condition hypotheses, for $\delta t \ll \min(T_L, \frac{\mathcal{L}}{\mathrm{u}_{\mathcal{L}}})$, the second-order Lagrangian structure function can be written as a function of δt, ϵ and ν as:

$$\mathscr{D}_{L_{ij}}(\delta t) = \epsilon\delta t\mathscr{F}_{\mathscr{D}_L}\left(\frac{\delta t}{\mathcal{T}_\eta}\right)\delta ij, \tag{1.53}$$

where $\mathscr{F}_{\mathscr{D}_L}$ is a universal function. Similarly, to the corresponding Eulerian one, it should tend towards a constant in the inertial sub-range where the viscous effects have no more impacts. Thus, using the second Kolmogorov similarity theory in the inertial range $\mathcal{T}_\eta \ll \delta t \ll \min(T_L, \frac{\mathcal{L}}{u_\mathcal{L}})$:

$$\mathscr{D}_{L_{ij}}(\delta t) = \mathrm{C}_0 \epsilon \delta t \delta_{ij}, \tag{1.54}$$

where C_0 is a universal constant.

Acceleration Auto-correlation

Furthermore, using a similar reasoning based on similarity theory, it is possible to show for the fluid particle acceleration A that in the inertial sub-range we have:

$$\langle A(t+\delta t)A(t)\rangle \simeq \frac{\epsilon}{\delta t}, \tag{1.55}$$

with at the origin:

$$\langle A^2\rangle \simeq \frac{\epsilon}{\mathcal{T}_\eta}. \tag{1.56}$$

Thus, the corresponding auto-correlation function evolves as:

$$\mathscr{R}_L^A(\delta t) = \frac{\langle A(t+\delta t)A(t)\rangle}{\langle A^2\rangle} \simeq \frac{\mathcal{T}_\eta}{\delta t}. \tag{1.57}$$

It results from this, that the integral timescale associated to the relaxation time of fluid particle acceleration is small compared to any timescale associated to the inertial sub-range. This property will also play an important role in the choice of modelling for the Lagrangian stochastic methods considered as presented in Section 1.3.3.

Remark 1.2.8. Let us note that when the Reynolds number is not sufficiently high the Kolmogorov theory is less valid as it is not always possible to separate clearly the large productive scales to the small dissipative ones. Furthermore, the presence of obstacles can also be a source of deviation to the Kolmogorov theory as they perturb the development of the energy cascade.

1.2.1.2.2 Characterisation of Large-Scale Turbulent Processes based on Reynolds Averaged Equations

In the previous paragraph, we have focused on the universal characteristics of the turbulence at small scales, in high Reynolds-number flows. However, Kolmogorov theory gives little information on the behaviour of the large scales of turbulence. In these scales the turbulent effects may be highly anisotropic depending on flow and geometric characteristics. These scales are often the most interesting from an engineering point of view. Indeed, as they contain most of the energy, they have a predominant impact on the mean flow but also of the mixing and transport at the large scales. The goal of this paragraph is to present the effects of turbulence on the flows and processes influencing the larger scales of turbulence.

Reynolds Averaging Operator

A first solution to extract more information on the large-scale behaviour is to consider a statistical description of the turbulence and to focus on the behaviour of the averaged quantities. To this end, Reynolds [1895] proposed to apply an averaging operator $\overline{(.)}$ referred as the Reynolds average on the Navier–Stokes equation. This operator is an ensemble average, where the same experiment is repeated a great number of times. Under ergodicity condition, it might be replaced by other averaging methods (e.g. temporal average for statistically stationary flows or spatial average for statistically uniform flows). It verifies for any field Φ, Ψ and any constant λ_1, λ_2 the following properties:

$$\text{Linearity:} \qquad \overline{\lambda_1\Phi + \lambda_2\Psi} = \lambda_1\overline{\Phi} + \lambda_2\overline{\Psi}, \tag{1.58a}$$

$$\text{Commutativity with partial derivation:} \qquad \overline{\frac{\partial\Psi}{\partial t}} = \frac{\partial\overline{\Psi}}{\partial t} \quad \text{and} \quad \overline{\frac{\partial\Psi}{\partial x_\alpha}} = \frac{\partial\overline{\Psi}}{\partial x_\alpha}, \tag{1.58b}$$

$$\text{Idempotence:} \qquad \overline{\left(\overline{\Psi}\right)} = \overline{\Psi}. \tag{1.58c}$$

This operator is then associated with the Reynolds decomposition:

$$\underbrace{\Psi}_{\text{Instantaneous field}} = \underbrace{\overline{\Psi}}_{\text{Averaged field}} + \underbrace{\psi}_{\text{Fluctuating field}} . \tag{1.59}$$

For any instantaneous uppercase fields Ψ or U, the lowercase fields respectively ψ or u will correspond to the fluctuations around their mean value. Exception to this rule is made for the fluctuation of temperature noted T' to avoid confusion with time and for the fluctuation of density noted ρ'. Because of the definition of the fluctuations and the properties of the operator, for any fluctuating field ψ we have:

$$\overline{\psi} = 0. \tag{1.60}$$

Let us highlight an important property of such decomposition. In the general case, the average of a product is not the product of the average:

$$\overline{\Phi\Psi} = \overline{\Phi}\;\overline{\Psi} + \overline{\phi\psi} \neq \overline{\Phi}\;\overline{\Psi}. \tag{1.61}$$

This relation plays a major role, since the advection term is not linear, it yields for incompressible flows to the decomposition:

$$\overline{\frac{\mathrm{d}\Psi}{\mathrm{d}t}} = \underbrace{\frac{\partial\overline{\Psi}}{\partial t} + \overline{U_i}\frac{\partial\overline{\Psi}}{\partial x_i}}_{\frac{D\overline{\Psi}}{Dt}\text{Material derivative advected by mean velocity}} + \underbrace{\frac{\partial\overline{u_i\psi}}{\partial x_i}}_{\text{Higher order terms}} , \tag{1.62}$$

considering compressible flows, a similar equation would be obtained replacing the second RHS term by $\overline{u_i\frac{\partial\psi}{\partial x_i}}$.

Remark 1.2.9. Let us note that other decomposition can be considered, e.g. large eddies simulation (LES) methods propose to use not an averaging operator but a spatial filtering one. The fields are then decomposed into large-resolved scales and small sub-grid scales which are modelled as further discussed in Section 1.3.1. In this case the set of equations obtained has a similar structure and the discussion remains pertinent keeping in mind the differences between averaged, resolved, fluctuating and sub-grid quantities. It is still worth saying that the spatial filtering used in LES methods are the results of a convolution and not of an average operator. Thus, in this case some of the properties stated in Eqs 1.58 may not be respected.

Averaged Equations

Now that we have defined the averaging operator used, we can apply it to instantaneous transport equations Eqs 1.35 to obtain the corresponding Reynolds averaged equations. As we only consider incompressible flows in this work, for simplicity reasons we will still consider the density uniform except in the buoyancy terms.

Continuity: It is straightforward to see that the zero divergence of velocity imposed by the incompressibility condition Eq. (1.33) is also respected by both the mean and fluctuating velocities

$$\operatorname{div}(\underline{\overline{\boldsymbol{U}}}) = 0, \tag{1.63a}$$

$$\operatorname{div}(\underline{\boldsymbol{u}}) = 0. \tag{1.63b}$$

Momentum: Applying the Reynolds average to the Navier–Stokes equation, Eq. (1.35b), we obtain the Reynolds averaged Navier–Stokes (RANS) equations. Under Boussinesq approximation, it states:

$$\frac{D\overline{U_i}}{Dt} = \frac{\partial \overline{U_i}}{\partial t} + \overline{U_j}\frac{\partial \overline{U_i}}{\partial x_j} = -\frac{1}{\rho}\frac{\partial \overline{P}}{\partial x_i} + g_i(1-\beta_0(\overline{\Theta}-\Theta_0)) - 2\Omega_k\overline{U_j}\varepsilon_{ijk} + \frac{\partial}{\partial x_j}\left(\nu\frac{\partial \overline{U_i}}{\partial x_j} - \mathcal{R}_{ij}\right). \tag{1.64}$$

We can see the presence of the term $\underline{\underline{\boldsymbol{\mathcal{R}}}} = \overline{u_i u_j}\,\underline{\boldsymbol{e_i}} \otimes \underline{\boldsymbol{e_j}}$ caused by the averaging of the non-linear inertial term. This tensor is called Reynolds tensor and corresponds to the averaged turbulent effects of the fluctuating velocities onto the mean one.

Pot. Temp.: Applying the averaging operator on the potential temperature equation Eq. (1.35c) we get:

$$\frac{D\overline{\Theta}}{Dt} = \frac{\partial \overline{\Theta}}{\partial t} + \overline{U_j}\frac{\partial \overline{\Theta}}{\partial x_j} = \frac{2\nu}{\mathsf{C}_p}\overline{\frac{\Theta}{\mathsf{T}}S_{ij}S_{ij}} + \frac{\partial}{\partial x_j}\left(K_\Theta\frac{\partial \overline{\Theta}}{\partial x_j} - \overline{u_j\theta}\right) + \frac{1}{\mathsf{C}_p}\overline{\left(\frac{\Theta}{\mathsf{T}}\frac{\mathcal{S}_e}{\rho}\right)}, \tag{1.65}$$

with $\overline{S_{ij}S_{ij}} = \overline{S_{ij}}\;\overline{S_{ij}} + \overline{s_{ij}s_{ij}}$, and $\overline{\underline{\boldsymbol{u}}\theta}$ the turbulent heat fluxes. The latter correspond to the averaged effects of fluctuating velocity and potential temperature onto the mean potential temperature. As indicated previously, both the production of potential temperature by viscosity and the source terms $\mathcal{S}_e$ are neglected and will not be treated hereafter.

Scalar: Similarly, for the transport of any passive scalar, averaging Eq. (1.36), we get:

$$\frac{D\overline{\Psi}}{Dt} = \frac{\partial \overline{\Psi}}{\partial t} + \overline{U_j}\frac{\partial \overline{\Psi}}{\partial x_j} = \frac{\partial}{\partial x_j}\left(\frac{\nu}{Sc}\frac{\partial \overline{\Psi}}{\partial x_j} - \overline{u_j\psi}\right) + \frac{\overline{\mathcal{S}_\Psi}}{\rho}, \tag{1.66}$$

where the turbulent scalar fluxes $\overline{\underline{\boldsymbol{u}}\psi}$ appear.

As we have detailed on equation Eq. (1.62), the averaging of advection by the mean velocity term introduces the divergence of a new higher order moment terms which has either to be modelled or transported. Thus, the averaging of a closed set of transport equations yields to a new set of equations which is not closed. This is often referred as the closure issue which is induced by turbulence. Before presenting methods to model these new second-order terms let us focus on their transport equations to describe a bit further the physical processes responsible of large-scale turbulence.

Reynolds Tensor

Let us note $\mathcal{NS}_i$ the equation of Navier–Stokes Eq. (1.35b) and $\overline{\mathcal{NS}_i}$ the Reynolds averaged Navier–Stokes equation Eq. (1.64) in the direction i. It is possible to derive the equation for the Reynolds tensor $\frac{D\underline{\underline{\boldsymbol{\mathcal{R}}}}}{Dt}$ as:

$$\frac{D\underline{\underline{\boldsymbol{\mathcal{R}}}}}{Dt} = \overline{\left(u_j\left(\mathcal{NS}_i - \overline{\mathcal{NS}_i}\right) + u_i\left(\mathcal{NS}_j - \overline{\mathcal{NS}_j}\right)\right)}\underline{\boldsymbol{e_i}} \otimes \underline{\boldsymbol{e_j}}. \tag{1.67}$$

Doing so, and assuming we consider an incompressible flow with a constant density except in the weight term, after rearrangement, the Reynolds tensor equation can be written:

$$\underbrace{\frac{D\underline{\underline{\boldsymbol{\mathcal{R}}}}}{Dt}}_{\text{Temp. evol.}} = \underbrace{\underline{\underline{\boldsymbol{\mathcal{P}}}}}_{\text{Production}} + \underbrace{\underline{\underline{\boldsymbol{\mathcal{G}}}}^{\ddagger}}_{\text{Buoyancy}} - \underbrace{\underline{\underline{\boldsymbol{\epsilon}}}^{\ddagger}}_{\text{Dissipation}} + \underbrace{\underline{\underline{\boldsymbol{\mathcal{C}}}}}_{\text{Coriolis}} + \underbrace{\underline{\underline{\boldsymbol{\Pi}}}^{\ddagger}}_{\text{Pressure-strain cor.}} + \underbrace{\underline{\underline{\boldsymbol{\mathcal{D}}}}^{\ddagger}}_{\text{Diffusion}}, \tag{1.68}$$

In this equation the terms have been regrouped in order to provide a description of the physical processes involved. Note that the terms with a superscript ‡, depend on quantities which are not transported. Thus, if one wants to transport the 2nd order moments, it would then be necessary either to add extra transport equations or to find correlation between the large-scale effects of this quantities and known quantities. The selection of such correlation corresponds to a choice of modelling discussed in Section 1.3.2. For now, let us focus on the physical processes whose imbalance is responsible for the temporal variation of the Reynolds tensor $\frac{D\overline{u_iu_j}}{D_t}$ on LHS of Eq. (1.68). The latter ones correspond to:

1. **Production of turbulence by shear stress $\underline{\underline{\boldsymbol{\mathcal{P}}}}$.** It stems from the transfer of momentum between the mean flow and the turbulent fluctuations:

   $$\mathcal{P}_{ij} = -\left(\overline{u_ku_i}\frac{\partial\overline{U_j}}{\partial x_k} + \overline{u_ku_j}\frac{\partial\overline{U_i}}{\partial x_k}\right). \tag{1.69}$$

   The interaction with the mean flow is characterised by the presence of the mean velocity gradient. When the flow is varying slowly, the turbulent shear stress and velocity gradient tend to align with one another, this term is then positive. It is still worth noticing that in the case of fast variation of the flow, the shear stress and the velocity gradient can be noticeably non-aligned. In such case, it is even possible for this term to be locally negative playing then a sink role.

2. **Source by buoyancy effects $\underline{\underline{\boldsymbol{\mathcal{G}}}}^{\ddagger}$.** It represents the effect of the weight force on turbulence expressed as:

   $$\mathcal{G}^{\ddagger}_{ij} = \frac{1}{\rho}\left(g_i\overline{u_j\rho'} + g_j\overline{u_i\rho'}\right), \tag{1.70}$$

   where $\rho' = \rho - \overline{\rho}$. The role played by this term depends on the stratification of the flow. When the density tends to increase with the height, the corresponding correlation $\overline{\rho'w}$ tends to be negative and this term behaves as a source term; we speak of thermally unstable case. In the opposite case where the density tends to decrease with the height, the correlation $\overline{\rho'w}$ tends to be positive resulting in a sink term. Let us note that in the general case, we need a relation to specify this term because of the unknown behaviour of $\overline{\rho'u_i}$. It is then necessary either to model this term or to transport it with an additional equation. Using a Boussinesq approximation this term can be written:

   $$\mathcal{G}_{ij} = -\beta\left(g_i\overline{u_j\theta} + g_j\overline{u_i\theta}\right), \tag{1.71}$$

   where the superscript ‡ may be removed when transporting the turbulent heat fluxes.

3. **Dissipation rate $\underline{\underline{\epsilon}}^{\ddagger}$.** This is the dissipative part of the viscous effects which tends to lower the turbulent fluctuations, as the diagonal terms are positive.

$$\epsilon^{\ddagger}_{ij} = 2\nu \overline{\frac{\partial u_i}{\partial x_k} \frac{\partial u_j}{\partial x_k}}. \tag{1.72}$$

   This dissipation takes place at smaller scales of turbulence and its behaviour has been further presented in Paragraph 1.2.1.2.1. A specific modelling of this quantity is also required.

4. **Redistribution of kinetic energy.** These terms have a zero trace. Thus, they do not have any impacts on the total TKE budget but only on its distribution in each direction. Two redistribution terms do appear in the Reynolds stress transport equations:

   (a) **Source by Coriolis effects $\underline{\underline{\mathscr{C}}}$.**

$$\mathscr{C}_{ij} = -2\mathit{\Omega}_l \left(\overline{u_i u_k} \varepsilon_{jkl} + \overline{u_j u_k} \varepsilon_{ikl} \right). \tag{1.73}$$

   Considering the effects of the Coriolis pseudo-force on the turbulence, the vertical fluctuations of velocity are of the same scale as the horizontal one. It is then necessary to consider both the horizontal and vertical components of $\underline{\boldsymbol{\Omega}}$. Let us specify each component of this tensor to describe its influence. Assuming that we are in the reference atmospheric basis ($\underline{\boldsymbol{e_1}}$ is the west-east unitary vector, $\underline{\boldsymbol{e_2}}$ the south-north vector and $\underline{\boldsymbol{e_3}}$ the local vertical direction), we have:

$$\begin{aligned}
\mathscr{C}_{11} &= -4\mathit{\Omega}(\sin(\phi)\overline{uv} - \cos(\phi)\overline{uw}), && (1.74a)\\
\mathscr{C}_{22} &= 4\mathit{\Omega}\sin(\phi)\overline{uv}, && (1.74b)\\
\mathscr{C}_{33} &= -4\mathit{\Omega}\cos(\phi)\overline{uw}, && (1.74c)\\
\mathscr{C}_{12} &= -2\mathit{\Omega}(\sin(\phi)(\overline{vv} - \overline{uu}) - \cos(\phi)\overline{vw}), && (1.74d)\\
\mathscr{C}_{23} &= -2\mathit{\Omega}(-\sin(\phi)\overline{uw} + \cos(\phi)\overline{uv}), && (1.74e)\\
\mathscr{C}_{13} &= -2\mathit{\Omega}(\sin(\phi)\overline{uw} + \cos(\phi)(\overline{uu} - \overline{ww})). && (1.74f)
\end{aligned}$$

   Summing up the tree first equations Eqs. (1.74a) to (1.74c), it is clear that the trace of this tensor is null. Let us note that this term is an isotropisation term. Let us place ourselves in the northern hemisphere, such that $\sin(\phi)$ and $\cos(\phi)$ are positive (similar results would occur in the southern one). Moreover, assuming $\overline{vv} > \overline{uu}$, Eq. (1.74d) triggers a reduction of $\overline{uv}$. This will induce a diminution of $\mathscr{C}_{22}$ through Eq. (1.74b) and then of $\overline{vv}$, whereas Eq. (1.74a) shows that $\mathscr{C}_{11}$ and then $\overline{uu}$, will tends to increase. Similarly, on Eq. (1.74f), assuming that $\overline{uu} > \overline{ww}$, we would have a decrease of $\overline{uw}$ and resulting in a decrease of $\mathscr{C}_{11}$ and in an increase of $\mathscr{C}_{33}$.

   (b) **Pressure-strain correlation $\underline{\underline{\boldsymbol{\Pi}}}^{\ddagger}$.** The second redistribution term is caused by the effects of the pressure fluctuation on the fluctuating velocity expressed as:

$$\Pi^{\ddagger}_{ij} = \overline{\frac{p}{\rho}\left(\frac{\partial u_i}{\partial x_j} + \frac{\partial u_j}{\partial x_i}\right)}. \tag{1.75}$$

   This is a large scale and averaged description of the process describing how the eddies transfer energy from one direction to the others. The breaking of large eddies into smaller ones results in fluctuations of pressure that tends to transfer the energy towards the other directions. This process is the reason why going down the Kolmogorov cascade the small eddies tend to forget the behaviour of the larger ones and become isotropic. In order to determine the behaviour of this term, let us focus on the behaviour of the fluctuating pressure p. One can obtain the Laplacian of the pressure fluctuation by taking the divergence of the difference between the Navier–Stokes equation and the Reynolds averaged Navier–Stokes equation. After rearrangement we get:

$$\frac{1}{\rho}\frac{\partial^2 p}{\partial x_i^2} = \underbrace{-\frac{\partial^2(u_i u_j - \overline{u_i u_j})}{\partial x_i \partial x_j} + \frac{\partial}{\partial x_i}\left(u_j \Omega_k \varepsilon_{ijk}\right)}_{\frac{1}{\rho}\mathrm{div}(\underline{\mathbf{grad}}(p))^{s,\ddagger}} \underbrace{-2\frac{\partial \overline{U_i}}{\partial x_j}\frac{\partial u_j}{\partial x_i}}_{\frac{1}{\rho}\mathrm{div}(\underline{\mathbf{grad}}(p))^{r,\ddagger}} + \underbrace{\frac{1}{\rho}\frac{\partial g_i \rho'}{\partial x_i}}_{\frac{1}{\rho}\mathrm{div}(\underline{\mathbf{grad}}(p))^{\mathcal{G},\ddagger}}, \tag{1.76}$$

where the Laplacian can be split into three terms that correspond respectively to a slow term $\mathrm{div}(\underline{\mathbf{grad}}(p))^{s,\ddagger}$, a rapid term $\mathrm{div}(\underline{\mathbf{grad}}(p))^{r,\ddagger}$ and a buoyant one $\mathrm{div}(\underline{\mathbf{grad}}(p))^{\mathcal{G},\ddagger}$. The former one is a slow process as it does not depend directly on the mean velocity but only on turbulent quantities whereas the second term depends explicitly on the mean velocity gradient. The latter one stems from buoyant effects. One can integrate the Laplacian of the pressure fluctuations to retrieve the pressure fluctuations and then the pressure-strain-correlations which depend on four terms:

$$\Pi_{ij}^{\ddagger} = \Pi_{ij}^{s,\ddagger} + \Pi_{ij}^{r,\ddagger} + \Pi_{ij}^{\mathcal{G},\ddagger} + \Pi_{ij}^{w,\ddagger}, \tag{1.77}$$

where $\Pi_{ij}^{w,\ddagger}$ is a wall echo term issued from this integration, caused be the presence of a wall on which pressure fluctuations are reflected.

5. **Diffusion $\underline{\underline{\boldsymbol{\mathcal{D}}}}$.** This term corresponds to the transport of the Reynolds tensor without dissipation and is due to three different processes:

$$\underline{\underline{\boldsymbol{\mathcal{D}}}}^{\ddagger} = \underline{\underline{\boldsymbol{\mathcal{D}}}}^{u^{\ddagger}} + \underline{\underline{\boldsymbol{\mathcal{D}}}}^{p^{\ddagger}} + \underline{\underline{\boldsymbol{\mathcal{D}}}}^{\nu}. \tag{1.78}$$

   (a) **The transport of Reynolds tensor by the fluctuations of velocity $\underline{\underline{\boldsymbol{\mathcal{D}}}}^{u^{\ddagger}}$** which stems from the averaging of the advection terms:

$$\mathcal{D}_{ij}^{u^{\ddagger}} = -\frac{\partial \overline{u_i u_j u_k}}{\partial x_k}. \tag{1.79}$$

   (b) **The transport of Reynolds tensor by the fluctuations of pressure $\underline{\underline{\boldsymbol{\mathcal{D}}}}^{p^{\ddagger}}$:**

$$\mathcal{D}_{ij}^{p^{\ddagger}} = -\frac{\partial}{\partial x_k}\left(\overline{\frac{p}{\rho}(u_i \delta_{jk} + u_j \delta_{ik})}\right). \tag{1.80}$$

   (c) **The transport of Reynolds tensor by the viscous transport $\underline{\underline{\boldsymbol{\mathcal{D}}}}^{\nu}$:**

$$\mathcal{D}_{ij}^{\nu} = \frac{\partial}{\partial x_k}\left(\nu \frac{\partial \overline{u_i u_j}}{\partial x_k}\right) \tag{1.81}$$

Turbulent Kinetic Energy
One may also consider the turbulent kinetic energy (TKE) defined as $k = \frac{1}{2}\mathrm{tr}(\underline{\underline{\boldsymbol{\mathcal{R}}}})$, whose equation is:

$$\underbrace{\frac{Dk}{Dt}}_{\text{Temp. evol.}} = \underbrace{\mathcal{P}}_{\text{Production}} + \underbrace{\mathcal{G}^{\ddagger}}_{\text{Buoyancy}} - \underbrace{\epsilon}_{\text{Dissipation}} \underbrace{+\mathcal{D}_k^{u^{\ddagger}} + \mathcal{D}_k^{p^{\ddagger}} + \mathcal{D}^{\nu}}_{\underline{\underline{\boldsymbol{\mathcal{D}}}}\text{: Diffusion}}, \tag{1.82}$$

with:

1. **the production by shear $\mathcal{P}$:**
$$\mathcal{P} = -\overline{u_k u_i}\frac{\partial \overline{U_i}}{\partial x_k}, \tag{1.83}$$
2. **the production or destruction by buoyancy effects $\mathcal{G}^{\ddagger}$:**
$$\mathcal{G}^{\ddagger} = \frac{1}{\rho} g_i \overline{u_i \rho'}, \tag{1.84}$$
Using a Boussinesq approximation this term can be written:
$$\mathcal{G} = -2 g_i \beta \overline{u_i \theta}, \tag{1.85}$$
where the superscript ‡ may be removed when transporting the turbulent heat fluxes.
3. **the dissipation by viscous effects ϵ:**
$$\epsilon = \nu \overline{\frac{\partial u_i}{\partial x_k}\frac{\partial u_i}{\partial x_k}}, \tag{1.86}$$
no superscript ‡ is used as the transport equation for this quantity will be further discussed here after.
4. **the diffusion by transport due to fluctuations of velocity $\mathcal{D}^{u,\ddagger}$:**
$$\mathcal{D}^{u,\ddagger} = -\frac{1}{2}\frac{\partial \overline{u_i u_i u_k}}{\partial x_k}, \tag{1.87}$$
5. **the diffusion by transport due to fluctuations of pressure $\mathcal{D}^{p,\ddagger}$:**
$$\mathcal{D}^{p,\ddagger} = -\frac{\partial}{\partial x_k}\left(\overline{\frac{p}{\rho} u_i \delta_{ik}}\right), \tag{1.88}$$
6. **the diffusion by viscous transport $\mathcal{D}^{\nu}$:**
$$\mathcal{D}^{\nu} = \frac{\partial}{\partial x_k}\left(\nu \frac{\partial k}{\partial x_k}\right), \tag{1.89}$$

whose terms arise directly from the stress tensor equation and correspond to similar processes.

Turbulent Kinetic Energy Dissipation Rate
Let us take an instant on the dissipation rate of kinetic energy, for which an "exact" transport equation can also be derived from Navier–Stokes equation after tedious manipulations (see e.g. Hanjalić and Launder [2022]). The transport equation of the TKE dissipation rate (often simply referred as the dissipation rate) can be written:

$$\underbrace{\frac{D\epsilon}{Dt}}_{\text{Temp. evol.}} = \underbrace{\mathcal{P}_{\epsilon}^{\ddagger}}_{\text{Production}} + \underbrace{\mathcal{G}_{\epsilon}^{\ddagger}}_{\text{Buoyancy}} + \underbrace{\mathscr{C}_{\epsilon}^{\ddagger}}_{\text{Coriolis}} - \underbrace{\epsilon_{\epsilon}^{\ddagger}}_{\text{Dissipation}} + \underbrace{\mathcal{D}_{\epsilon}^{\ddagger}}_{\text{Diffusion}}, \tag{1.90}$$

with:

1. **the production $\mathcal{P}_{\epsilon}$.** The latter can be decomposed into four terms:
$$\mathcal{P}_{\epsilon}^{\ddagger} = \underbrace{-2\nu\left(\overline{\frac{\partial u_i}{\partial x_j}\frac{\partial u_k}{\partial x_j}} + \overline{\frac{\partial u_j}{\partial x_i}\frac{\partial u_j}{\partial x_k}}\right)\frac{\partial \overline{U_i}}{\partial x_k}}_{\mathcal{P}_{\epsilon 1}^{\ddagger}+\mathcal{P}_{\epsilon 2}^{\ddagger}} \underbrace{-2\nu \overline{u_k \frac{\partial u_i}{\partial x_j}}\frac{\partial^2 \overline{U_i}}{\partial x_k \partial x_j}}_{\mathcal{P}_{\epsilon 3}^{\ddagger}} \underbrace{-2\nu \overline{\frac{\partial u_i}{\partial x_j}\frac{\partial u_i}{\partial x_k}\frac{\partial u_k}{\partial x_j}}}_{\mathcal{P}_{\epsilon 4}^{\ddagger}} \tag{1.91}$$

2. **the buoyant effects $\mathcal{G}_\epsilon^\ddagger$:**

$$\mathcal{G}_\epsilon^\ddagger = \frac{2\nu}{\rho} g_i \overline{\frac{\partial \rho'}{\partial x_k}\frac{\partial u_i}{\partial x_k}}, \tag{1.92}$$

   which gives under Boussinesq assumption:

$$\mathcal{G}_\epsilon^\ddagger = -2\nu\beta_0 g_i \overline{\frac{\partial \theta}{\partial x_k}\frac{\partial u_i}{\partial x_k}}, \tag{1.93}$$

3. **the Coriolis effects $\mathscr{C}_\epsilon^\ddagger$:**

$$\mathscr{C}_\epsilon^\ddagger = -2\epsilon_{ij}^\ddagger \varOmega_k \varepsilon_{ijk}, \tag{1.94}$$

   where the Levi–Civita tensor $\underline{\underline{\boldsymbol{\varepsilon}}}$ should not be confused with the dissipation rate tensor $\underline{\underline{\boldsymbol{\epsilon}}}^\ddagger$.

4. **the dissipation by viscous effects $\epsilon_\epsilon^\ddagger$:**

$$\epsilon_\epsilon^\ddagger = 2\nu^2 \overline{\frac{\partial^2 u_i}{\partial x_k \partial x_j}\,\frac{\partial^2 u_i}{\partial x_k \partial x_j}}, \tag{1.95}$$

5. **the diffusion $\mathcal{D}_\epsilon^\ddagger$:** it represents the transport due to three contributions:

$$\mathcal{D}_\epsilon^\ddagger = \mathcal{D}_\epsilon^{u,\ddagger} + \mathcal{D}_\epsilon^{p,\ddagger} + \mathcal{D}_\epsilon^{\nu,\ddagger}, \tag{1.96}$$

   with:

   - the diffusion by transport due to fluctuations of velocity $\mathcal{D}_\epsilon^{u,\ddagger}$:

$$\mathcal{D}_\epsilon^{u,\ddagger} = -\frac{\partial}{\partial x_k}\left(\nu \overline{u_k \frac{\partial u_i}{\partial x_j}\frac{\partial u_i}{\partial x_j}}\right), \tag{1.97}$$

   - **the diffusion by transport due to fluctuations of pressure $\mathcal{D}_\epsilon^{p,\ddagger}$:**

$$\mathcal{D}_\epsilon^{p,\ddagger} = -\frac{\partial}{\partial x_k}\left(-2\frac{\nu}{\rho}\overline{\frac{\partial p}{\partial x_i}\frac{\partial u_k}{\partial x_i}}\right), \tag{1.98}$$

   - **the diffusion by viscous transport $\mathcal{D}_\epsilon^{\nu}$:**

$$\mathcal{D}_\epsilon^{\nu} = \frac{\partial}{\partial x_k}\left(\nu \frac{\partial \epsilon}{\partial x_k}\right), \tag{1.99}$$

Due to the numerous double or triple correlations between gradients of instantaneous quantities, whose behaviour is difficult to determine, the proper physical description of each term is complex for the TKE dissipation rate. Yet, presenting the equation under this form, it has a similar structure than the transport equation of the TKE. A crude assumption is to consider that the physical processes involved are of similar nature. It is true that in this case, formally the effects of the Coriolis pseudo-force do appear here, yet the physical influence of this term may be minor in atmospheric flows. Indeed, the Coriolis effects mainly impacts the large scales structures as presented in Paragraph 1.2.2.1.2 whereas the dissipation rate mainly takes place on the smaller structures as discussed in Paragraph 1.2.1.2.1.

Thermal Heat Fluxes

As we have done for the Reynolds tensor, it is possible to derive the equation for the turbulent heat fluxes. Noting $Eq.\Theta$ the transport equation of the instantaneous temperature, Eq. (1.35c), we have:

$$\frac{D\overline{\underline{\boldsymbol{u}}\theta}}{Dt} = \overline{\theta\left(\mathcal{NS}_i - \overline{\mathcal{NS}_i}\right) + u_i\left(Eq.\Theta - \overline{Eq.\Theta}\right)}\underline{\boldsymbol{e_i}}. \tag{1.100}$$

This equation can be written as:

$$\underbrace{\frac{D\overline{\underline{\boldsymbol{u}}\theta}}{Dt}}_{\text{Temp. evol.}} = \underbrace{\underline{\boldsymbol{\mathcal{P}}}^{U}_{\Theta} + \underline{\boldsymbol{\mathcal{P}}}^{\Theta}_{\Theta}}_{\text{Inertial Production}} + \underbrace{\underline{\boldsymbol{\mathcal{G}}}^{\ddagger}_{\Theta}}_{\text{Buoyant Production}} + \underbrace{\underline{\boldsymbol{\mathscr{C}}}_{\Theta}}_{\text{Coriolis}} + \underbrace{\underline{\boldsymbol{\Pi}}^{\ddagger}_{\Theta}}_{\text{Scrambling}} - \underbrace{\underline{\boldsymbol{\epsilon}}^{\ddagger}_{\Theta}}_{\text{Dissipation}} + \underbrace{\underline{\boldsymbol{\mathcal{D}}}^{\ddagger}_{\Theta}}_{\text{Diffusion}}, \tag{1.101}$$

where similarly to the Reynolds tensor, the temporal evolution on the LHS is gouverned by the imbalance of the RHS triggered by:

1. **Production terms:**

   (a) **Production by inertial terms $\underline{\boldsymbol{\mathcal{P}}}_{\Theta}$.** Similarly to the production of Reynolds tensor, the latter ones come from the averaging of the inertial terms and are in general positive except potentially in fast varying flows. This term can be split into two contributions:

      i. Production of turbulent heat flux by the mean velocity gradient:

      $$\mathcal{P}^{U}_{\Theta i} = -\overline{u_k\theta}\frac{\partial\overline{U_i}}{\partial x_k}, \tag{1.102}$$

      ii. Production of turbulent heat flux by the mean temperature gradient:

      $$\mathcal{P}^{\Theta}_{\Theta i} = -\overline{u_i u_k}\frac{\partial\overline{\Theta}}{\partial x_k}. \tag{1.103}$$

   (b) **Production by buoyancy effects $\underline{\boldsymbol{\mathcal{G}}}^{\ddagger}_{\Theta}$.** As the density decreases with the temperature, we have $\overline{\theta\rho'} < 0$, thus for turbulent heat fluxes this quantity is always a positive term. In unstable case, as $w\theta$ is positive, this is a production term of normal fluxes. On the contrary for stable case, this term plays a damping role as $\overline{w\theta}$ is negative.

   $$\mathcal{G}^{\ddagger}_{\Theta i} = \frac{g_i}{\rho}\overline{\rho'\theta}, \tag{1.104}$$

   Using a Boussinesq approximation this term can be written:

   $$\mathcal{G}_{\Theta i} = -g_i\beta\overline{\theta^2}, \tag{1.105}$$

   where the superscript ‡ may be removed when transporting the potential temperature variance.

2. **Redistribution terms which are based on two processes:**

   (a) **Redistribution by Coriolis effects $\underline{\boldsymbol{\mathscr{C}}}_{\Theta}$:**

   $$\mathscr{C}_{\Theta i} = -2\Omega_k\overline{u_j\theta}\varepsilon_{ijk}. \tag{1.106}$$

In the reference atmospheric basis each component of this term becomes:

$$\begin{aligned}
\mathscr{C}_{\Theta_1} &= -2\varOmega\left(\overline{v\theta}\sin(\phi) - \overline{w\theta}\cos(\phi)\right), && (1.107a)\\
\mathscr{C}_{\Theta_2} &= \ 2\varOmega\overline{u\theta}\sin(\phi), && (1.107b)\\
\mathscr{C}_{\Theta_3} &= -2\varOmega\overline{u\theta}\cos(\phi). && (1.107c)\\
& && (1.107d)
\end{aligned}$$

Assuming that we are in the northern hemisphere (similar results are obtained in the southern one), if $\overline{w\theta}$ increases, it would result in an increase of $\overline{u\theta}$ through Eq. (1.107a), which would yield to a restoring effect on $\overline{w\theta}$ through Eq. (1.107c) and an increase on $\overline{vT'}$ through Eq. (1.107b). Thus, the Coriolis pseudo-forces tend to create isotropy between the normal and horizontal turbulent temperature fluxes. In the horizontal direction the behaviour is less straightforward, as the behaviour of $\overline{u\theta}$ and $\overline{v\theta}$ is not symmetric. Assuming an increase of $\overline{v\theta}$, the reacting effects of Coriolis pseudo-forces would be to increase $\overline{w\theta}$ but a decrease on both horizontal components. At the opposite, assuming an increase of $\overline{u\theta}$, the action of the Coriolis pseudo-forces would damp this increase but would also decrease the normal flux and increase $\overline{uv}$.

(b) **Redistribution through the scrambling term $\underline{\boldsymbol{\Pi}}^{\ddagger}_{\Theta}$:**

$$\Pi^{\ddagger}_{\Theta i} = \overline{\frac{p}{\rho}\frac{\partial\theta}{\partial x_i}}. \tag{1.108}$$

Similarly to the pressure-stress-correlation, this term plays a redistributive role. It is induced by the pressure fluctuations and it can also be decomposed into four contributions:

$$\Pi^{\ddagger}_{\Theta i} = \Pi^{s,\ddagger}_{\Theta i} + \Pi^{r,\ddagger}_{\Theta i} + \Pi^{\mathcal{G},\ddagger}_{\Theta i} + \Pi^{w,\ddagger}_{\Theta i}. \tag{1.109}$$

where $\Pi^{s,\ddagger}_{\Theta i}$ corresponds to the slow scrambling terms induced solely by turbulent quantities, whereas $\Pi^{r,\ddagger}_{\Theta i}$ is a rapid scrambling term interacting directly through the mean velocity and temperature gradients. In addition, $\Pi^{\mathcal{G}}_{\Theta i}$ represents the scramble induced by thermal effects and $\Pi^{w,\ddagger}_{\Theta i}$ the scrambling due to wall echo effects resulting from reflection of pressure fluctuations.

3. **Dissipation through molecular viscosity and diffusivity $\underline{\boldsymbol{\epsilon_\Theta}}^{\ddagger}$:**

$$\epsilon^{\ddagger}_{\Theta i} = (\nu + K_\Theta)\left(\overline{\frac{\partial u_i}{\partial x_j}\frac{\partial\theta}{\partial x_j}}\right). \tag{1.110}$$

This term has a similar structure than the dissipation term in the Reynolds tensor equation but is caused by both the viscosity and thermal diffusivity on the smaller scales of turbulence. Assuming high-Reynolds number turbulence, the latter ones can be considered isotropic. Yet, inverting the directions of our basis the sign of this term changes. However, for isotropic interactions, such a change of basis should not affect the behaviour of this term. Thus, one may assume that for high Reynolds number flows, this term is null.

4. **Diffusion $\underline{\boldsymbol{\mathcal{D}}}^{\ddagger}_{\Theta}$:** This diffusion is due to the transport without dissipation nor production by four different processes:

$$\underline{\boldsymbol{\mathcal{D}}}^{\ddagger}_{\Theta} = \underline{\boldsymbol{\mathcal{D}}}^{p,\ddagger}_{\Theta} + \underline{\boldsymbol{\mathcal{D}}}^{u,\ddagger}_{\Theta} + \underline{\boldsymbol{\mathcal{D}}}^{K_\Theta,\ddagger}_{\Theta} + \underline{\boldsymbol{\mathcal{D}}}^{\nu,\ddagger}_{\Theta}, \tag{1.111}$$

where the processes at stake are:

(a) **Diffusion by transport due to fluctuations of pressure** $\underline{\boldsymbol{\mathcal{D}}}_{\Theta}^{p,\ddagger}$

$$\mathcal{D}^{p,\ddagger}_{\Theta i} = -\frac{\partial}{\partial x_i}\left(\overline{\frac{p}{\rho}\theta}\right), \tag{1.112}$$

(b) **Diffusion by transport due to fluctuations of velocity** $\underline{\boldsymbol{\mathcal{D}}}_{\Theta}^{u,\ddagger}$

$$\mathcal{D}^{u,\ddagger}_{\Theta i} = -\frac{\partial \overline{u_i u_j \theta}}{\partial x_j}, \tag{1.113}$$

(c) **Diffusion by transport due to thermal diffusion** $\underline{\boldsymbol{\mathcal{D}}}_{\Theta}^{K_\Theta,\ddagger}$

$$\mathcal{D}^{K_\Theta,\ddagger}_{\Theta i} = \frac{\partial}{\partial x_j}\left(K_\Theta \overline{u_i \frac{\partial \theta}{\partial x_j}}\right), \tag{1.114}$$

(d) **Diffusion by viscous transport** $\underline{\boldsymbol{\mathcal{D}}}_{\Theta}^{\nu,\ddagger}$

$$\mathcal{D}^{\nu,\ddagger}_{\Theta i} = \frac{\partial}{\partial x_j}\left(\nu \overline{\theta \frac{\partial u_i}{\partial x_j}}\right). \tag{1.115}$$

Temperature Variance
Finally, one may consider the evolution of the temperature variance whose equation can be derived as:

$$\frac{D\overline{\theta^2}}{Dt} = \overline{2\theta\ (Eq.\Theta - \overline{Eq.\Theta})}. \tag{1.116}$$

We obtain:

$$\frac{D\overline{\theta^2}}{Dt} = \underbrace{\mathcal{P}_{\overline{\theta^2}}}_{\text{Production}} - \underbrace{\epsilon^{\ddagger}_{\overline{\theta^2}}}_{\text{Dissipation}} + \underbrace{\mathcal{D}_{\overline{\theta^2}}}_{\text{Diffusion}}. \tag{1.117}$$

The temporal evolution of the temperature variance is due to the imbalance of:

1. **Production by the mean temperature gradient** $\mathcal{P}_{\overline{\theta^2}}$:

$$\mathcal{P}_{\overline{\theta^2}} = -2\overline{u_i\theta}\frac{\partial \overline{\Theta}}{\partial x_i}, \tag{1.118}$$

2. **Dissipation by molecular diffusion** $\epsilon^{\ddagger}_{\overline{\theta^2}}$

$$\epsilon^{\ddagger}_{\overline{\theta^2}} = 2K_\Theta \overline{\frac{\partial \theta}{\partial x_i}\frac{\partial \theta}{\partial x_i}}, \tag{1.119}$$

3. **Diffusion terms by transport without production nor dissipation** $\mathcal{D}_{\overline{\theta^2}}$**.** It is composed of two terms:

$$\mathcal{D}^{\ddagger}_{\overline{\theta^2}} = \mathcal{D}^{u,\ddagger}_{\overline{\theta^2}} + \mathcal{D}^{K_\Theta}_{\overline{\theta^2}}, \tag{1.120}$$

   (a) **Diffusion by transport due to velocity fluctuations** $\mathcal{D}^{u,\ddagger}_{\overline{\theta^2}}$

$$\mathcal{D}^{u,\ddagger}_{\overline{\theta^2}} = -\frac{\partial \overline{u_i\theta^2}}{\partial x_i}, \tag{1.121}$$

(b) **Diffusion by transport due to thermal diffusion $\underline{\mathcal{D}}^{\nu}_{\Theta}$**

$$\mathcal{D}^{K_\Theta}_{\overline{\theta^2}} = \frac{\partial}{\partial x_i}\left(K_\Theta \frac{\partial \overline{\theta^2}}{\partial x_i}\right). \tag{1.122}$$

Remark 1.2.10. Note that due to the similar structure of the equations of transport of temperature, Eq. (1.35c), and of any scalar Ψ, Eq. (1.36), the scalar fluxes and variance would have structures similar to Eq. (1.101) and Eq. (1.117). The only difference might come from the absence of production of scalar by Joule effects (neglected here) and the slightly different shape of the source terms which are not considered here. Moreover, if the scalar is passive the buoyant effects are also absent. Furthermore, let us note that often the source terms associated to chemical reactions are highly non-linear. In such case we have $\overline{\mathcal{S}_\Psi(\Psi)} \neq \mathcal{S}_\Psi(\overline{\Psi})$, which can be stated as: the mean of the chemistry is not the chemistry of the mean. It would then be necessary to use a proper treatment of such averaged terms to retrieve physical behaviours (see Pope [1985, 2000] for more information).

1.2.2 Background on Atmospheric Flows for Pollutant Dispersion

The present subsection aims at briefly presenting the physics of atmospheric flows. This has been the subject of numerous books and interested reader may refer e.g. to Hanna et al. [1982], Stull [1988], Arya [1998, 1999], Jacobson [2005] for further information. It will mainly focus on the atmospheric boundary layer (ABL) which is the lowest part of the atmosphere directly influenced by ground effects and within which most of the pollutant dispersion produced near ground occurs. We can still note that pollutant dispersion above the ABL can be present, for example in case of volcanic eruptions or of plane induced pollutant dispersion. These situations will not be considered in this work.

1.2.2.1 Description of the Atmosphere

Let us first present an averaged description of the atmosphere using a characteristic timescale of observation long enough for the daily and yearly fluctuations to be smoothed.

1.2.2.1.1 Characterisation of the Different Zones in the Standard Atmosphere

The atmosphere in a broad sense corresponds to the region surrounding a planet within which a gas envelope exists. As we increase the altitude, the weight of the gas column above of point decreases and so does the pressure. As schematised in Figure 1.3, using the standard atmosphere described by the norm comity ISO/TC 20 [1975], the overall Earth atmosphere can be decomposed based on its mean temperature evolution as follows:

Troposphere: First, on the lower part of the atmosphere one can find the troposphere characterised by an averaged negative temperature gradient due to adiabatic dilatation of air with the altitude. Its height is about 11 km although it may vary from around 8 km at the poles to 18 km at the equator. Being the lowest zone of the atmosphere, it is the region within which the pressure is maximal. Therefore, it includes most of the air mass (around 90%). As it is the zone within which meteorological and dispersion phenomenon mainly takes place, this zone is the most interesting in the context of this work. The different layers composing it will be further discussed in Paragraph 1.2.2.1.2.

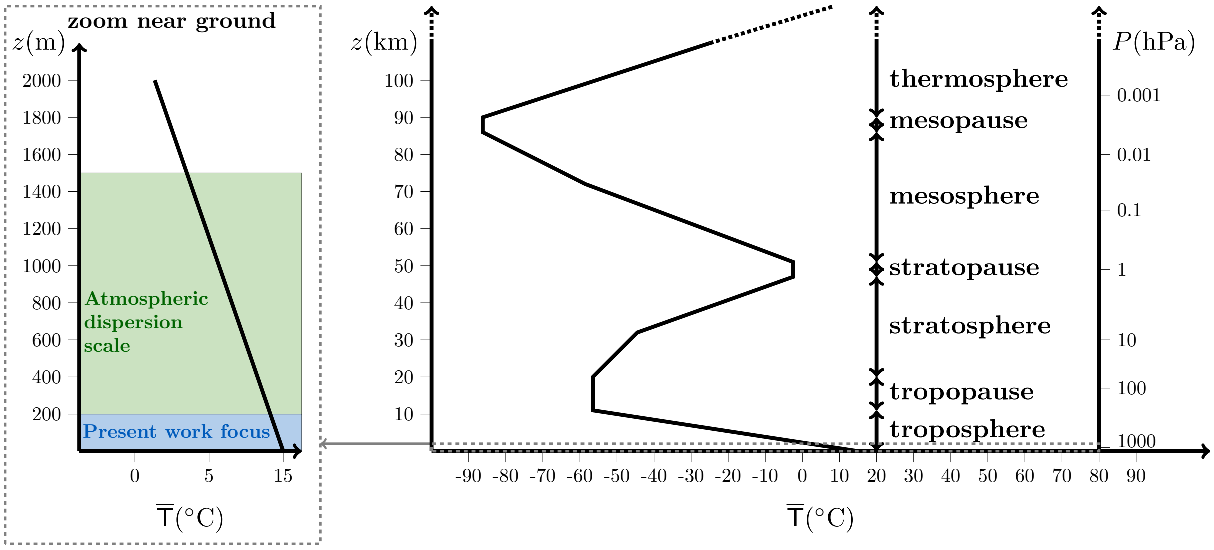

Figure 1.3: Schematic description of the standard atmosphere using comity ISO/TC 20 [1975] norm.

Tropopause: It corresponds to the buffer layer between the troposphere at 11 km and the stratosphere at 20 km. It is marked by a modification of the temperature gradient due to the apparition of exothermic reaction of dioxygen which is transformed into ozone through ultraviolet (UV) radiation absorption. In this zone, the thermal effects of adiabatic dilatation and ozone production somewhat compensate each other, and the temperature gradient can be considered null.

Stratophere: Above the tropopause, one can find the stratosphere where most of the ozone production takes place. Due to this exothermic reaction, the temperature gradient is positive in this zone which includes the so-called ozone layer. The stratosphere goes from 20 km up to 47 km.

Stratopause: This is a slight buffer zone between the stratosphere and the mesosphere going from 47 km to 51 km.

Mesosphere: It corresponds to the zone spanning from 51 to 86 km. In this zone the temperature is decreasing with the altitude. It corresponds to the lower part of the ionosphere characterised by the gas ionisation due to UV radiation.

Mesopause: It corresponds to the buffer layer from 86 to 95 km.

Thermosphere: This is the last layer of atmosphere before the exosphere and space; in this zone the pressure is very limited, and the gas really rarefied. It is characterised by the ionisation of the air and a positive gradient of temperature. Due to the scarce presence of atoms, it is difficult to properly describe the height of this zone, but it goes up to 350-800km.

1.2.2.1.2 Focus on the Dynamics of the Troposphere

As the dispersion mainly takes place in the troposphere, we will focus on the physical processes at stake in this zone. They are described by a multitude of phenomena whose spatial and temporal scales depend greatly: from the Kolmogorov scales for isotropic turbulence up to the planetary scale over decades or centuries for global warming. A scheme presenting example of atmospheric processes at different scales can be found in Figure 1.4.

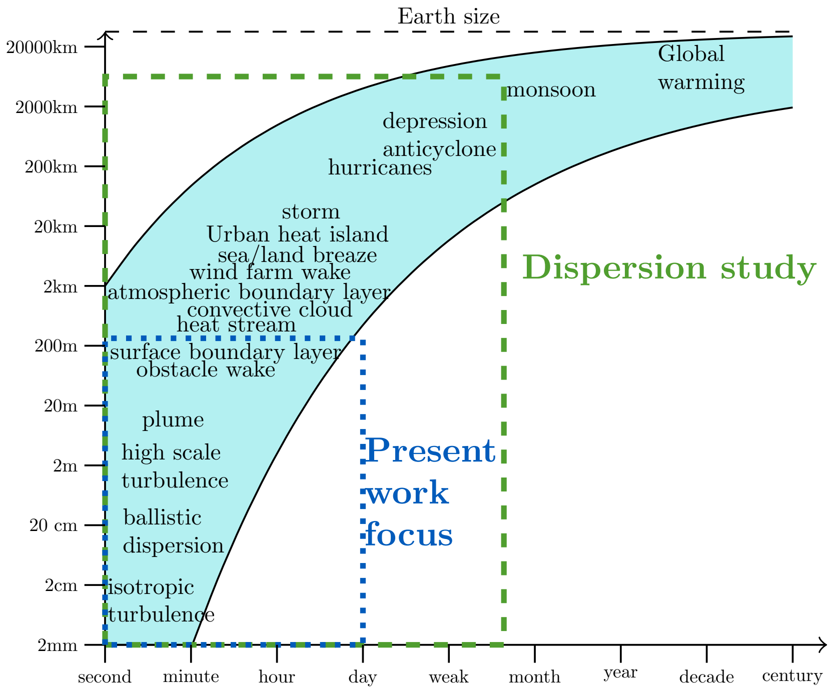

Figure 1.4: Description of physical phenomena at stake in the atmosphere with the corresponding spatial and temporal scale (after Stull [1988]). Note that on this scheme the spatial length scales provided can correspond either a vertical or horizontal scales.

Determination of the Preponderant Physical Effects in the Troposphere

Our goal is to present the different physical effects at stake in troposphere flows. A common method to compare the relative importance played by different physical effects at given scale is to compare their order of magnitude using adimensionised equations. To do so, we separate each quantity Ψ into a dimensionless varying part Ψ^+ whose scale remains close to unity and its characteristic order of magnitude Ψ^c. This operation should also be applied on the operator. We can consider a scale of velocity U^c, of length L^c typically the distance to the ground, of potential temperature increment $\delta\Theta^c$ due to buoyant effects. For Coriolis effects, the Coriolis parameter $f^{\mathscr{C}} = 2\Omega \sin \phi$ is used. The incompressible Navier–Stokes and potential temperature can then be decomposed as:

$$\frac{\rho(U^c)^2}{L^c}\frac{\mathrm{d}U_i^+}{\mathrm{d}t^+} = -\frac{\rho(U^c)^2}{L^c}\frac{\partial P^+}{\partial x_i^+} + \mu\frac{U^c}{(L^c)^2}\frac{\partial^2 U_i^+}{\partial x_j^+\partial x_j^+} + \rho g_i - \rho f^{\mathscr{C}} U^c \underline{\mathbf{1}}_k U_j^+ \varepsilon_{ijk}, \tag{1.123a}$$

$$\frac{\delta\Theta^c U^c}{L^c}\frac{\mathrm{d}\Theta^+}{\mathrm{d}t^+} = 2\frac{\nu(U^c)^2}{\mathrm{C}_p(L^c)^2}\frac{\Theta^+}{\mathsf{T}^+}S_{ij}^+\frac{\partial U_i^+}{\partial x_j^+} + \frac{K_\Theta\delta\Theta^c}{(L^c)^2}\frac{\partial^2\Theta^+}{\partial(x_j^+)^2}, \tag{1.123b}$$

where it has been chosen to consider a single scale to adimensionise the material derivative. Furthermore, we have considered for the order of magnitude of the pressure variation $\delta P^c \simeq \rho(U^c)^2$ based on energetic grounds coherent with Bernoulli's principle. Moreover, we will consider $\frac{\delta\rho}{\rho} \simeq \beta_0\delta\Theta^c$ in agreement with Boussinesq approximation to obtain the order of magnitude of buoyant effects. Now that we have decomposed Eqs 1.123, we can consider the corresponding dimensionless equations:

$$\frac{\mathrm{d}U_i^+}{\mathrm{d}t^+} = - \frac{\partial P^+}{\partial x_i^+} + \overbrace{\frac{\nu}{L^c U^c}}^{Re^{-1}} \frac{\partial^2 U_i^+}{\partial x_j^+ \partial x_j^+} - \overbrace{\frac{g\beta\delta\Theta^c L^c}{(U^c)^2}}^{Ri} \delta_{iz} - \overbrace{\frac{f^{\mathscr{C}} L^c}{U^c}}^{Ro^{-1}} \underline{\mathbf{1}}_k U_j^+ \varepsilon_{ijk}, \tag{1.124a}$$

$$\frac{\mathrm{d}\Theta^+}{\mathrm{d}t^+} = 2 \underbrace{\frac{\nu}{U^c L^c}}_{Re^{-1}} \underbrace{\frac{(U^c)^2}{\mathrm{c}_p \delta\Theta^c}}_{Ec} \frac{\Theta^+}{\mathsf{T}^+} S_{ij}^+ \frac{\partial U_i^+}{\partial x_j^+} + \underbrace{\frac{K_\Theta}{\nu}}_{Pr} \underbrace{\frac{\nu}{U^c L^c}}_{Re^{-1}} \frac{\partial^2 \Theta^+}{\partial (x_j^+)^2}. \tag{1.124b}$$

Let us notice that some dimensionless numbers appear. Each one characterises the relative influence of competitive processes. We can note the presence of the Reynolds number Re, already presented, corresponding to the competition between inertial and viscous effects; the Richardson number Ri being the ratio between buoyant and inertial effects; the Rossby number Ro being the ratio between inertial and Coriolis effects; the Eckert number Ec being the ratio between variation of enthalpy and variation of kinetic energy and finally the Prandtl number which is the ratio between molecular viscosity and thermal diffusivity. Except for the latter one which is mainly a fluid property with $Pr \simeq 0.707$ for air, the other dimensionless numbers depend on the flow. Thus, one can compare them to determine which effects are preponderant at different altitudes and which one can be neglected. So as to classify the relative impacts of the physical effects on different scales, let us see the evolution of this quantities as we move in the troposphere.

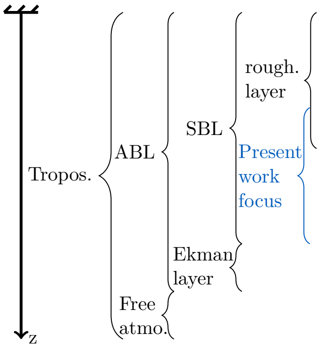

L^c	U^c	$\delta\Theta^c$	molecular dif. $\propto Re^{-1}$	buoyancy $\propto Ri$	Coriolis $\propto Ro^{-1}$	visc. therm. prod. $\propto Re^{-1}Ec$
0.01 m	0.1 - 1 $\mathrm{m\,s^{-1}}$	0.01 - 0.1 K	$10^{-3} - 10^{-2}$	$10^{-5} - 10^{-3}$	$10^{-5} - 10^{-6}$	$10^{-6} - 10^{-4}$
0.1 m	0.1 - 1 $\mathrm{m\,s^{-1}}$	0.01 - 0.1 K	$10^{-4} - 10^{-3}$	$10^{-3} - 10^{-2}$	$10^{-4} - 10^{-5}$	$10^{-7} - 10^{-5}$
1 m	1 $\mathrm{m\,s^{-1}}$	0.1 K	$10^{-6} - 10^{-5}$	$10^{-2} - 10^{-1}$	10^{-4}	10^{-7}
10 m	1 - 10 $\mathrm{m\,s^{-1}}$	0.1 - 1 K	$10^{-7} - 10^{-6}$	$10^{-2} - 10^{-1}$	10^{-4}	10^{-8}
100 m	10 $\mathrm{m\,s^{-1}}$	1 K	10^{-8}	10^{-1}	10^{-3}	10^{-9}
1000 m	10 $\mathrm{m\,s^{-1}}$	1-10 K	10^{-9}	1	10^{-2}	$10^{-9} - 10^{-10}$
10000 m	10 $\mathrm{m\,s^{-1}}$	10-100 K	10^{-10}	$10 - 100$	10^{-1}	$10^{10} - 10^{-11}$

Table 1.1: Comparison of the order of magnitude of the different physical processes at different heights in the troposphere. The layers and acronyms appearing on the left side are presented hereafter.

Evolution of the Ground induced Shear Stress in the Troposphere

As we can see in the Table 1.1, in the troposphere the main physical effects at stake are the inertia, the pressure, the buoyancy, and the Coriolis ones. In this table only the effects along the vertical scale are presented. With a view to have a rough idea of the evolution of the turbulence, let us also consider the typical phenomenon taking place in the horizontal direction. Let us assume that we have a stationary and uniform horizontal flow, with a long-range horizontal pressure gradient. The horizontal Navier–Stokes equations become:

$$-\frac{1}{\rho}\frac{\partial \overline{P}}{\partial x} + \Omega_k \overline{U_j} \varepsilon_{xjk} - \frac{\partial \overline{uw}}{\partial z} = 0, \tag{1.125a}$$

$$-\frac{1}{\rho}\frac{\partial \overline{P}}{\partial y} + \Omega_k \overline{U_j} \varepsilon_{yjk} - \frac{\partial \overline{vw}}{\partial z} = 0, \tag{1.125b}$$

The horizontal pressure gradient scale is typically around ten Pascals per thousand kilometres (i.e $10^{-5}\mathrm{Pa\,m^{-1}}$). Even though this value seems little, it should not be totally neglected as it is the source of the long-range horizontal flow. Our goal is here to present a crude description of the height over which the ground has a major role on the flow turbulence. As seen previously the Coriolis effects have a redistributive role on the Reynolds tensor but do not modify the overall TKE. In order to give a first crude description of the turbulent behaviour let us put these effects aside for the moment. Doing so we can define a single mean flow direction aligned with $\underline{\boldsymbol{e_1}}$. Moreover, we will make the crude assumption to consider $\frac{1}{\rho}\frac{\partial \overline{P}}{\partial x}$ is roughly constant close to the ground. Doing so, it is possible to exhibit a rough description of the ground induced turbulence evolution. Under these assumptions the turbulent shear stress $\overline{uw}$ may be integrated as:

$$\overline{uw} = -u_*^2 \left(1 - \frac{z}{L_{ABL}}\right) \tag{1.126}$$

with $u_* = \sqrt{\frac{\sigma_{\mathrm{wall}}}{\rho}}$ the friction velocity, σ_{wall} the shear stress at the wall (here the ground) and $L_{ABL} = \frac{\sigma_{\mathrm{wall}}}{\frac{\partial \overline{P}}{\partial x}}$ the length scale over which the shear stress produced at wall plays a preponderant effect.

Description of the Layers composing the Troposphere

The zone within which the ground effects play a primordial effect on the flow is the atmospheric boundary layer (ABL). Stull [1988] also characterised this zone by a timescale of response of the ground forcing of around one hour or less. Its characteristic height is roughly the kilometre and can be estimated using proposition of Zilitinkevich [1972]. Moreover, it evolves with the meteorological conditions. Indeed, it is lowered in the high-pressure anticyclonic zones due to downward flow from the upper regions. Similarly, it is elevated in the depression zones of low pressure where the flow tends to ascend. Let us emphasize that as the ABL is the most turbulent part of the atmosphere, it is then the zone within which most of the dispersion takes place. For this reason, we will give a special attention to this region which can be decomposed into multiple sub-layers:

Roughness Layer The lower part of the atmosphere is the roughness layer, within which the specific influence of given ground irregularities plays a preponderant role (see e.g., Stull [1988]). Indeed, in atmospheric flows, the ground is characterised by the presence of irregularities at different scales (grass, gravels, rocks, bushes, ears in fields, houses, trees, forests, cities, etc.). Each of these ground irregularities induces a local variation of the flow in a slight zone in its vicinity. In the case of atmospheric flows, it is not possible nor useful to explicitly describe the influence of each of these roughness elements. A part or the entire roughness layer is then modelled thank to averaged quantities such as the dynamical and thermal roughness height (z_0 and z_0^{Θ}) which aims at characterising the mean influence of the ground irregularities over the above flow. This parameterised near ground zone is referred as the unresolved basal layer (UBL) and always exists when describing atmospheric flows (see Rodean [1996]). The roughness layer depends on the local topography, but the UBL also depends on the choice of description followed. Indeed, its characteristic vertical size is a few times bigger than the irregularities which are not explicitly treated. Modelling dispersion at a continental scale the explicit description of buildings or cities will not be considered, thus the UBL order of magnitude is roughly the hundred metres. At the contrary, considering a lower scale description over tens of metres the explicit description of buildings would be necessary to retrieve proper local results. The order of magnitude of the UBL might then be lesser than the metre such as presented in Table 1.1. Let us note that, even-though this zone is not explicitly treated in atmospheric flows, roughness plays a major role on atmospheric flows. The modelling and parametrisation of these effects at different scales remain an important subject of study (see e.g. Kadivar et al. [2021]).

SBL The surface boundary layer (SBL) is defined as the zone near ground where the shear stress and vertical turbulent heat fluxes can be considered constant. There is no rigorous limit of this zone but commonly we consider that it corresponds to roughly the lowest 10% of the ABL. Within this zone the Coriolis effects and the long-range pressure gradient effects are commonly neglected. The present work focusses on this highly turbulent zone which plays a primordial role in the earlier state of pollutant dispersion. The flow within it will be further discussed in Section 1.2.2.3. Let us note that the rough layer can be seen as a part of the SBL, even though it has been chosen to introduce them separately.

Ekman Layer The region above the surface boundary layer is a buffer zone within which neither the shear produced by the ground, nor the Coriolis effects can be neglected. This region is called the Ekman layer or outer zone. Due to the Coriolis pseudo-force the direction of the wind rotates from the near ground flow direction to the upper wind direction over the height of this zone. This rotation of the mean flow with altitude is called the Ekman spiral. When increasing in altitude, it is directed rightward in the northern atmosphere and leftward in the southern one,. Moreover, the amplitude of this rotation might be over 30° to 45° but depends greatly on the location on Earth as the Coriolis effects are not uniform accross the globe.

Above the ABL, where the ground effects and the induced turbulence become negligible, the upper part of the troposphere is called the free atmosphere within which the vertical profiles are more uniform. In this region, the pressure gradient and Coriolis pseudo-force remain the only two physical effects at stake, so they tend to be at equilibrium. This results in a flow which tends to follow the isobars. The corresponding wind is called the geostrophic wind. Note that this is not true in the vicinity of the equator where the Coriolis pseudo-forces tend to disappear.

1.2.2.2 Influence of the Stability on the Dynamics and Dispersion

The depiction of the atmosphere presented in Section 1.2.2.1 is based on an averaged description of the mean flow over a period of time long enough to consider that the thermal fluctuations caused by ground forcing roughly cancel out. For this reason, we have mainly focused on the shear effects produced by the presence of the ground, yet a second primordial role played by the ground is a thermal one. During daytime, as the ground receives energy from the sun by radiation, it heats the lower parts of the atmosphere. At the opposite, at night, the ground cools down faster than the air and absorbs energy from the atmosphere. This thermal forcing, which fluctuates over the day and over the year, plays an important role in the dynamics of the ABL. Indeed, as the ground respectively heats or cools down the atmosphere, it modifies locally the temperature and the air density triggering buoyancy effects.

1.2.2.2.1 Adiabatic Displacement

To quantify the effects of these buoyancy effects, let us first consider the reference adiabatic dry atmosphere. It corresponds to an adiabatic flow of ideal gas in which the flow is purely horizontal and homogeneous in this direction. Moreover, the viscous dissipation and Coriolis effects in the vertical direction are neglected. The latter conditions are easily respected in the SBL. Finally, the atmosphere is assumed dry so that the effects played by humidity are not considered. Such effects are out of the scope of the present manuscript, even though it is expected that the work proposed within it can be extended to these flows without arising new major issues. The quantities associated to this reference state are referred with the subscript $_{ad}$ and are supposed to vary only along the vertical direction. The momentum equation then gives:

$$\frac{\mathrm{d}P_{ad}}{\mathrm{d}z} = -\rho_{ad} g. \tag{1.127}$$

Using the first law of thermodynamics written with the temperature Eq. (1.19), we get:

$$\frac{1}{\mathsf{T}_{ad}}\frac{\mathrm{d}\mathsf{T}_{ad}}{\mathrm{d}z} = \frac{\mathsf{R}^{air}}{\mathrm{c}_p P_{ad}}\frac{\mathrm{d}P_{ad}}{\mathrm{d}z}. \tag{1.128}$$

Injecting the first equation in the second and using the ideal gas law, we obtain the adiabatic temperature gradient:

$$\frac{\mathrm{d}\mathsf{T}_{ad}}{\mathrm{d}z} = -\frac{g}{\mathrm{c}_p}. \tag{1.129}$$

This corresponds to the evolution of temperature due solely to the dilatation effects, and then the temperature evolution in adiabatic atmosphere is linear. Using the ideal gas law to replace the density in the momentum equation and injecting the linear form of the temperature, we can easily integrate the pressure. Finally knowing both temperature and pressure it is possible to determine the evolution of the density in the adiabatic atmosphere. The thermodynamic quantities associated to the reference atmospheres can then be determined as:

$$\mathsf{T}_{ad}(z) = \mathsf{T}_0\left(1 - \frac{gz}{\mathrm{c}_p\mathsf{T}_0}\right), \tag{1.130a}$$

$$P_{ad}(z) = P_0\left(1 - \frac{gz}{\mathrm{c}_p\mathsf{T}_0}\right)^{\frac{\mathrm{c}_p}{\mathsf{R}^{air}}}, \tag{1.130b}$$

$$\rho_{ad}(z) = \rho_0\left(1 - \frac{gz}{\mathrm{c}_p\mathsf{T}_0}\right)^{\frac{\mathrm{c}_v}{\mathsf{R}^{air}}}, \tag{1.130c}$$

with P_0, T_0 and ρ_0 the constant reference value at the ground.

Remark 1.2.11. Note that, in this description, the state law used is the ideal gas law and not the Boussinesq approximation on the potential temperature. Using the latter approach, which is considered in this work, the potential temperature remaining constant over adiabatic displacement, the density remains constant. The corresponding set of equations is then:

$$\rho_{ad}^{\mathrm{Bous}_\Theta}(z) = \rho_0, \tag{1.131a}$$

$$P_{ad}^{\mathrm{Bous}_\Theta}(z) = P_0\left(1 - \frac{\rho_0 g z}{P_0}\right) = P_0\left(1 - \frac{gz}{\mathsf{R}^{air}\mathsf{T}_0}\right), \tag{1.131b}$$

$$\mathsf{T}_{ad}^{\mathrm{Bous}_\Theta}(z) = \mathsf{T}_0\left(\frac{P_{ad}^{\mathrm{Bous}_\Theta}(z)}{P_0}\right)^{\frac{\mathsf{R}^{air}}{c_p}} = \mathsf{T}_0\left(1 - \frac{gz}{\mathsf{R}^{air}\mathsf{T}_0}\right)^{\frac{\mathsf{R}^{air}}{c_p}}, \tag{1.131c}$$

where the thermodynamic quantities at ground (indexed with $_0$) still verify the perfect gas law. Considering that we limit ourselves to altitudes small compared to $\frac{\mathsf{R}^{air}\mathsf{T}_0}{g} \simeq 8.4$ km, we can make a Taylor expansion at the first order of Eq. (1.130b) and Eq. (1.131c) and we retrieve respectively Eq. (1.131b) and Eq. (1.130a). Thus, at the first order the Boussinesq approximation on the potential temperature enables to retrieve the proper temperature and pressure profiles describing the adiabatic atmosphere whereas the variation of density is not taken into account.

1.2.2.2.2 Presentation of the Notion of Stability

So as to quantify if the thermal stratification fuels or inhibits the vertical fluctuations which play a fundamental role in dispersion, one can compare the local temperature gradient with the adiabatic one. Indeed, a fluid particle at thermal equilibrium undergoing a vertical fluctuation of velocity would experience an adiabatic evolution of temperature over the corresponding displacement. Three situations, summed up in Figure 1.5, can be encountered:

Stable: If the temperature gradient of the atmosphere is less steep than the reference adiabatic atmosphere ($\frac{\partial \mathsf{T}}{\partial z} > \frac{\partial \mathsf{T}_{ad}}{\partial z}$), after a slight increase of height the particle would have a temperature lower than its surrounding yielding to downward buoyancy effects inhibiting the displacement as shown in Figure 1.5A. The situation being anti-symmetric if the particle goes downward the resulting buoyancy effects would be upward, also limiting the vertical displacements. This situation is referred as thermally stable.

Neutral: In the case where the temperature gradient is equivalent to the adiabatic one ($\frac{\partial \mathsf{T}}{\partial z} = \frac{\partial \mathsf{T}_{ad}}{\partial z}$), after displacement the fluid particle would still have a similar temperature compared to its surroundings. Thus, no reacting force would be triggered by the particle displacement. This situation is referred as thermally neutral.

Unstable: Finally in the case where the temperature gradient is steeper than the adiabatic one ($\frac{\partial \mathsf{T}}{\partial z} < \frac{\partial \mathsf{T}_{ad}}{\partial z}$), after an upward displacement the particles would have a temperature superior to its surrounding yielding to upward buoyancy effects fuelling the vertical displacement as schematised in Figure 1.5C. Similarly in case of downward displacement the buoyancy effects would increase the effects of the fluctuations, thus such cases are referred as thermally unstable.

As it can be cumbersome to compare the temperature gradient with the reference adiabatic one, it is common in the atmospheric community to consider not the temperature but the potential temperature $\Theta = \mathsf{T}\left(\frac{P_0}{P}\right)^{\frac{\mathsf{R}^{air}}{c_p}}$. This quantity presented in Paragraph 1.2.1.1.2 being directly correlated to the entropy, it remains constant in neutral, i.e. adiabatic situation and can be

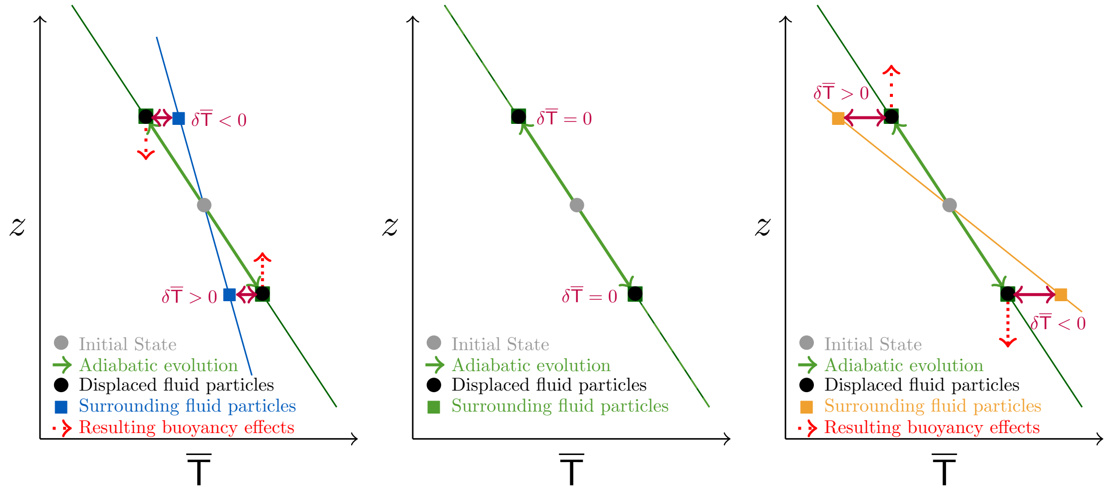

(A) Stable case. (B) Neutral case. (C) Unstable case.

Figure 1.5: Evolution of the response of the atmosphere to a small displacement of a fluid particle for different stability situations after Hanna et al. [1982].

used to define atmospheric stability with more ease. It corresponds to the temperature we would have in absence of adiabatic dilation. One can then establish the local stability situation simply by checking if the potential temperature increases or decreases as schematized in Figure 1.6.

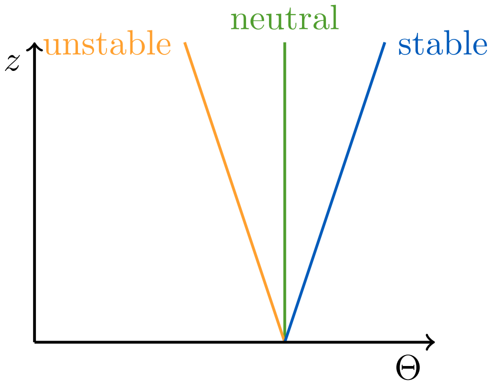

Figure 1.6: Vertical potential temperature profile for different stability situations.

1.2.2.2.3 Daily Cycle

The evolution of the stability within the ABL is strongly driven by a daily cycle. This cycle is illustrated in Figure 1.7 which corresponds to the energy scattered by the aerosol back to the grounds using a LIDAR measurement. The latter was obtained on June 3^{rd} 2010, using a Leosphere ALS 450 LIDAR at the SIRTA atmospheric observatory which at the time was in a rural to peri-urban area (see Haeffelin et al. [2005]). The corresponding data are freely available on sirta.ipsl.polytechnique.fr. The evolution of energy scattered back to the ground is representative of the distribution of aerosols in the atmosphere. Their dynamics may be used to characterise the turbulent effects and the evolution of the ABL.

At sunset, the sun starts to heat the ground through radiative processes. This results in a heating of the atmosphere by the lower part yielding to the development of a thermally unstable zone named the convective boundary layer or mixing layer. As underlined by its name, in this zone, the flow is mixed by turbulent transport triggered by buoyant effects. This can be seen in Figure 1.7, during daytime, where the particles are mixed in the ABL. As the convective boundary layer develops itself, it entrains above it the existing stable boundary layer issued from the previous night. This slight stable layer is referred as the entrainment zone which plays a capping effect. This slight stable layer makes the transition with the free atmosphere which also tends to be thermally stably stratified. This rupture of the potential temperature gradient is referred as capping inversion. It plays a fundamental role as it spatially limits the development of the turbulence by buoyancy in the convective boundary layer and maintains most of the pollutants within the ABL as we can see through the clear diminution of scattered energy after around 1.5 km.

Slightly before sunset, the radiative forcing on the ground is lowered and the convective boundary layer becomes neutrally stratified in a zone referred as residual boundary layer. Let us note that even though heavy aerosol tend to fall back due to their weight which is less compensated by the turbulence transport, the height of the ABL remains quite constant over the day-span. The latter one is spatially encapsulated between two stable layers. On the upper part the capping inversion subsists over the night and on the lower part a stable boundary layer is creating by cooling from the grounds. The destruction of the turbulence near ground can be observed noticing that the particles tend to fall back and accumulate in this zone. Let us note that the near ground flows within stable boundary layer are often quite calm, yet, during the night, it is common to see the development in altitude of wind whose velocity is greater than the geostrophic wind. Such effects, which will not be treated in this work, are referred as nocturnal jet. They are a source of mechanical turbulence whereas the thermal effects, in this situation, tends to dissipate the turbulence.

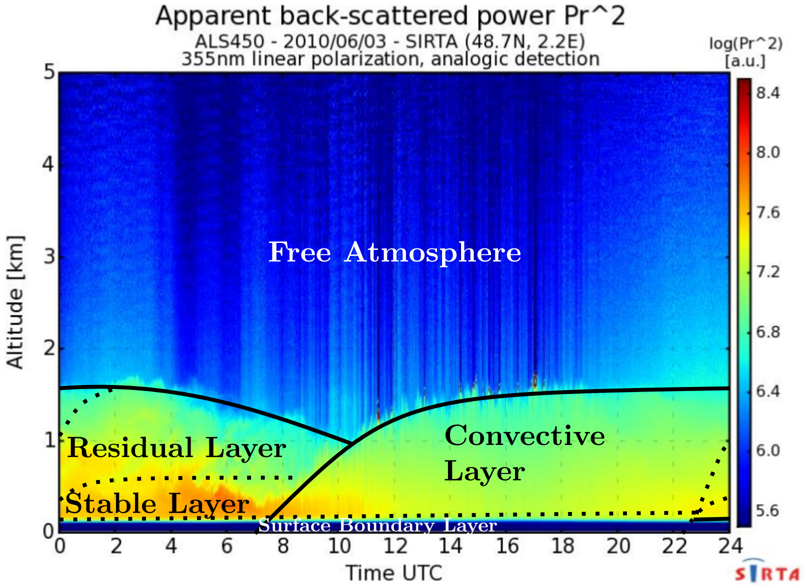

Figure 1.7: Scheme of the daily cycle of the atmospheric boundary condition made after Stull [1988] and based on apparent back scattered power measurement made at the SIRTA (see Haeffelin et al. [2005]).

1.2.2.2.4 Influence of the Stability on the Dispersion of Pollutants

Now that we have described the effects on the turbulence of the different stability situations encountered in the atmosphere, we will focus on its impact on the dispersion of pollutants (see e.g. Stull [1988], Arya [1999]). To this end, a few examples of characteristic type of dispersion will be briefly presented using images of smoke plumes. Let us note that the presence of smoke results from a fire and then a heat source triggering an initial rising of the plume which depends greatly on the nature and on the size of the source. The initial rising may be roughly estimated based on atmospheric and source characteristic (see e.g. Briggs [1965], Zonato et al. [1993], Fisher et al. [2001].

Coning in Neutral Case

The reference situation is the dispersion in neutral or near neutral atmosphere. It is the situation commonly encountered either in the residual layer, or in the case of strong winds. In such a case the thermal effect plays little role in the dynamics of the atmosphere and the dispersion in the horizontal and vertical direction are quite similar. Then assuming that we are far enough from the ground and the source the resulting plume shape is close to a cone. This situation is then sometimes referred as coning.

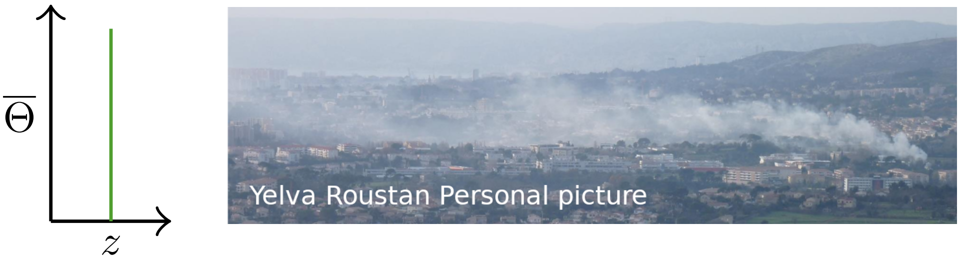

Figure 1.8: Example of coning dispersion on near neutral smoke plume.

Fanning in Stable Atmosphere

In the case of stable atmosphere, i.e. mainly during the end of the night and the start of the morning but also sometimes during the day in winter the turbulent eddies are destroyed by the buoyant effects. Thus, the turbulent dispersion is mitigated yielding to the creation of smaller but more concentrated plumes. Although through redistribution processes the attenuation of the vertical displacement also limits the horizontal fluctuations, the latter ones remain bigger, and the pollutants plumes mainly fan out in the horizontal direction. Such dispersion is then referred as fanning. Let us note in Figure 1.9, before this fanning out a first process is a rising of the plume caused by the heat produced at the fire source. After rising at a point where the potential temperature of the plume is at equilibrium with the local potential temperature of the atmosphere it tends to fan out. In the case of non-buoyant plumes, the fanning situation may be quite problematic as the pollutant would remain concentrated near ground in potentially inhabited areas.

Looping in convective atmosphere

In the case of a dispersion in a convective atmosphere, situation mainly encountered during hot afternoons, large eddies induced by the buoyancy effects are present. The latter ones play a preponderant role in the transport and dispersion of pollutants. They may be strong enough to explicitly impact the geometry of the plumes near its emission. Such a phenomenon referred as

Figure 1.9: Example fanning dispersion on stable smoke plume.

looping may be seen in Figure 1.10. In convective layer the dispersion is promoted yielding to the creation of broad plume within which the concentration is lowered.

Figure 1.10: Example of looping dispersion on unstable smoke plume.

Fumigation in Convective Atmosphere near Ground capped by a Stable Layer
This case can occur after sunset when the convective layer starts to build up and entrains the stable layer above it. It corresponds to the fumigation situation, illustrated in Figure 1.11, which is the worst-case scenario for safety issue in case of pollutant dispersion. Indeed, on the one hand, the pollutant is retained near ground due to the capping effects of the superior stable boundary layer. On the other hand, near ground the pollutants are well mixed by the convective layer and impact a broad zone of potentially inhabited areas.

Figure 1.11: Example of fumigation effects on a smoke plume in an atmosphere locally unstable near ground and stable above.

Lofting in Atmosphere Locally Stable near Ground overlooked by a Neutral Layer

Such as situation may be encountered at night, in early morning or in winter when the pollutants are emitted sufficiently high or with sufficient heat to reach the neutral residual layer. Such a case referred as lofting represents the counterpart of the fumigation situation as we can see in Figure 1.12. Indeed, in this situation, the ground is protected by the stable layer and the pollutant disperses only upward and horizontally with less local impacts on the population below.

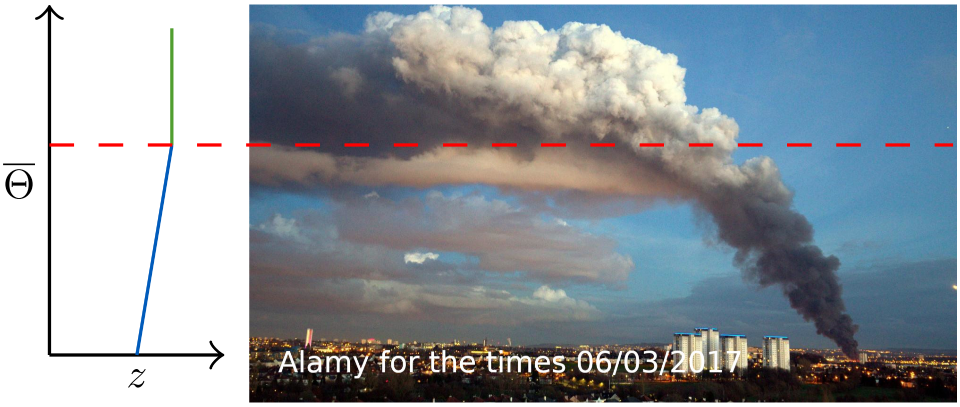

Figure 1.12: Example of lofting dispersion on a smoke plume in an atmosphere locally stable near ground and neutral above.

Remark 1.2.12. We have presented the behaviour of the dry atmosphere, note however that the presence of humidity may play an important role in both the stability situation and in the dispersion of pollutants. For example, regarding the stability effects, after sunset, the elevation of the stable layer caused by the production of a convective layer may trigger the creation of clouds. These clouds will promote the buoyancy effects as they will produce a cooling effect from the upper zone of the convective layer. Moreover, the presence of clouds may have a great impact on the radiative flux and on the thermal forcing. Regarding the dispersion of pollutant, the presence of humidity may also have a preponderant role as water droplet in suspension may absorb pollutant and rain may clean the atmosphere creating wet scavenging (see e.g. Sportisse [2007]). Such effects are out of the scope of the present work.

1.2.2.3 Focus on Surface-Boundary-Layer Flows using Similarity Theory

1.2.2.3.1 Treatment of the Neutral Surface Boundary Layer

In the SBL the Coriolis, viscous, horizontal pressure gradient may be neglected. Moreover, let us assume a stationary and horizontally homogeneous atmosphere. Under these hypotheses the Navier–Stokes equation is simplified into $\operatorname{div}(\overline{uw}) = \frac{\partial \overline{uw}}{\partial z} = 0$ with $\underline{\boldsymbol{e_1}}$ aligned with the wind direction. Then shear stress $\overline{uw} = -u_*^2$ imposed by the wind in the upper region is uniform until the surface. Let us first consider the neutral situation in which the buoyancy terms do not play any role. As suggested by Monin and Obukhov [1954], considering similarity theory, the evolution of the mean velocity between two points z_1 and z_2 can be obtained as:

$$\int_{z_1}^{z_2} \frac{\partial \overline{U}}{\partial z} \mathrm{d}z = \overline{U}(z_2) - \overline{U}(z_1) = \mathscr{F}_{\overline{U}}(u_*, z_1, z_2) = u_* f_{\overline{U}} \left(\frac{z_2}{z_1} \right), \tag{1.132}$$

where, $\mathscr{F}_{\overline{U}}$ and $\mathscr{f}_{\overline{U}}$ are universal functions. Let us consider a third altitude z_3, we have:

$$\overline{U}(z_3) - \overline{U}(z_1) = \overline{U}(z_3) - \overline{U}(z_2) + \overline{U}(z_2) - \overline{U}(z_1), \tag{1.133a}$$

$$u_* \mathscr{f}_{\overline{U}}\left(\frac{z_3}{z_1}\right) = u_* \left(\mathscr{f}_{\overline{U}}\left(\frac{z_3}{z_2}\right) + \mathscr{f}_{\overline{U}}\left(\frac{z_2}{z_1}\right)\right). \tag{1.133b}$$

This is true no matter the choice of z_1, z_2 and z_3 in the SBL. Thus, the universal function $\mathscr{f}_{\overline{U}}$ must respect the properties $\mathscr{f}_{\overline{U}}(x) + \mathscr{f}_{\overline{U}}(y) = \mathscr{f}_{\overline{U}}(xy)$. Only a class of function respects this condition which corresponds to the logarithmic functions. Then in the neutral SBL the mean velocity is logarithmic, this is the reason why it is often referred as the logarithmic zone. The coefficient in $\mathscr{f}_{\overline{U}}$ corresponds to the Von Kármán constant $\kappa \simeq 0.42$. We have then:

$$\frac{\partial \overline{U}}{\partial z} = \frac{u_*}{\kappa (z + z_0)}, \tag{1.134}$$

where z_0 is the roughness length which is an integrated parameter representing the effects of the ground roughness on the flow above the UBL. Considering rough surfaces, the mean velocity may be written as:

$$\overline{U}(z) = \frac{u_*}{\kappa} \ln\left(\frac{z + z_0}{z_0}\right). \tag{1.135}$$

1.2.2.3.2 Extension to Thermally Stratified Surface Boundary Layer using Monin–Obukhov Theory

Universal Profiles

We still assume a stationary and horizontally periodic flow, with a shear stress $\overline{uw} = -u_*^2$ uniform and imposed by the upper wind. We will now take into account the normal turbulent heat fluxes $\overline{w\theta}$ imposed by the ground forcing. For similar reasons than for the shear stress, the turbulent heat fluxes are also uniform, and one can introduce the friction potential temperature θ_* such as $\overline{w\theta} = -u_* \theta_*$ in the SBL. Thus, the flow quantities depend only on the altitude z, the buoyant term $-g\overline{w\theta} = g\beta_0 u_* \theta_*$, the shear stress u_*^2 and the dissipation rate as we can see for example in the TKE budget:

$$-\overline{uw}\frac{\partial \overline{U}}{\partial z} + g\beta\overline{w\theta} = \epsilon. \tag{1.136}$$

We have looking at the TKE budget:

$$\frac{\partial \overline{U}}{\partial z} = \frac{u_*}{\kappa z} \tilde{\mathscr{f}}_U \left(\frac{\epsilon}{g\beta\overline{w\theta}}\right). \tag{1.137}$$

Moreover, the dissipation rate is a variable depending on the shear stress, the buoyancy but also the altitude. It is thus possible to write:

$$\epsilon = \mathscr{F}_\epsilon\left(u_*, \kappa z, g\beta_0 u_* \theta_*\right) = \frac{u_*^3}{\kappa z} \mathscr{f}_\epsilon\left(\frac{\kappa g \beta_0 \theta_*}{u_*^2} z\right) = \frac{u_*^3}{\kappa z} \mathscr{f}_\epsilon\left(\frac{z}{L_{MO}}\right) = \frac{u_*^3}{\kappa z} \mathscr{f}_\epsilon\left(\zeta\right). \tag{1.138}$$

From this choice of parameters, a single dimensionless parameter $\zeta = \frac{1}{L_{MO}}$ with L_{MO} the Monin–Obukhov length scale first presented by Obukhov in 1948 (see Obukhov [1971]) and defined as:

$$L_{MO} = \frac{u_*^2}{\kappa g \beta_0 \theta_*}, \tag{1.139}$$

where the Von Kármán constant is kept by convention. This length scale is the ratio between the shear effects and the buoyant ones. It predicts the scale of altitude at which the buoyant effects become preponderant compared to the shear stress. Injecting Eq. (1.138) in Eq. (1.137), we get:

$$\frac{\partial \overline{U}}{\partial z} = \frac{u_*}{\kappa z}\varphi_m(\zeta), \tag{1.140a}$$

$$\overline{U} = \frac{u_*}{\kappa}\psi_m(L_{MO}, z, z_0), \tag{1.140b}$$

with φ_m the momentum universal function and $\psi_m(L_{MO}, z, z_0) = \int_{z_0}^{z} \frac{\varphi_m(\zeta)}{z} \mathrm{d}z$ its integrated form which are written as such by convention. Using these universal functions, the turbulent viscosity ν_t may be written:

$$\nu_t = -\frac{\overline{uw}}{\frac{\partial \overline{U}}{\partial z}} = \frac{u_* \kappa z}{\varphi_m}. \tag{1.141}$$

With a similar reasoning, one can determine that obtain a similar equation for the potential temperature:

$$-\frac{\partial \overline{\Theta}}{\partial z} = \frac{\theta_*}{\kappa z}\varphi_h(\zeta), \tag{1.142a}$$

$$\overline{\Theta} = \frac{\theta_*}{\kappa}\psi_h(L_{MO}, z, z_0), \tag{1.142b}$$

with φ_h the heat universal function and ψ_h the integrated formulation. The corresponding turbulent thermal diffusivity evolves then as:

$$K_{\Theta_t} = -\frac{\overline{w\theta}}{\frac{\partial \overline{\Theta}}{\partial z}} = \frac{u_* \kappa z}{\varphi_h}. \tag{1.143}$$

The two universal functions φ_m and φ_h can then be bound together by the turbulent Prandtl number as:

$$Pr_t = \frac{\nu_t}{K_{\Theta_t}} = \frac{\overline{uw}}{\frac{\partial \overline{U}}{\partial z}} \frac{\frac{\partial \overline{\Theta}}{\partial z}}{\overline{w\theta}} = \frac{\varphi_h}{\varphi_m}. \tag{1.144}$$

Note, that the knowledge of the first-order moments is not sufficient to properly characterise a flow. As for the mean flow, it is possible using similarity theory to derive universal functions for the second-order moments (see Monin and Yaglom [1971, Chapter 7.5]) depending only on ζ. The latter will be referred respectively as φ_k, $\varphi_{\langle uu \rangle}$, $\varphi_{\langle vv \rangle}$, $\varphi_{\langle ww \rangle}$, $\varphi_{\langle u\theta \rangle}$, $\varphi_{\langle \theta^2 \rangle}$ and are defined as corresponding second-order moment adimensionised by the proper combination of friction velocity and friction potential temperature.

Remark 1.2.13. Note that other dimensionless numbers are commonly encountered in atmospheric study. A first one is the flux Richardson number Ri_f characterising the relative effect of the buoyancy term and shear stress production in the TKE equation. It is defined as:

$$Ri_f = \frac{-\mathcal{G}}{\mathcal{P}} = \frac{g\beta\overline{w\theta}}{\overline{uw}\frac{\partial \overline{U}}{\partial z}} = \frac{g\beta u_*\theta_*}{\frac{u_*^3}{\kappa z}\varphi_m} = \frac{z}{L_{MO}\varphi_m} = \frac{\zeta}{\varphi_m}. \tag{1.145}$$

The gradient Richardson number Ri_g, which is a slightly different version of the flux Richardson number, is also commonly used to characterise the relative importance of the thermal effects. As its name suggests this number is based on the ratio of the gradients and is defined as:

$$Ri_g = g\beta\frac{\frac{\partial \overline{\Theta}}{\partial z}}{\left(\frac{\partial \overline{U}}{\partial z}\right)^2} = \underbrace{\frac{g\beta\kappa\theta_*}{u_*^2}}_{(L_{Mo})^{-1}}\frac{z}{\varphi_m}\frac{\varphi_h}{\varphi_m} = Ri_f Pr_t. \tag{1.146}$$

It corresponds to the product of the flux Richardson and the turbulent Prandtl numbers. In the SBL, the knowledge of both the momentum and heat universal functions is then equivalent to the knowledge of two dimensioneless number among the turbulent Prandtl number and the two Richardson numbers presented here.

Universal Functions Theoretical Evolution

We will briefly present the theoretical behaviour of these universal functions (for more information see Monin and Obukhov [1954], Monin and Yaglom [1971, Chapter 7]). As already stated, in convective situations, the development of large eddies due to buoyancy effects triggers mixing of both heat and momentum. Thus, velocity and temperature profiles are less steep than the profiles encountered in neutral situations. Similarly, in stable situations, the destruction of vertical eddies yields to a steeper temperature and velocity profiles. It is then clear that both the universal functions and the flux Richardson number increase with ζ. Moreover, let us note that we can write the stationary TKE budget at equilibrium as:

$$\mathcal{P} + \mathcal{G} = \mathcal{P}(1 - Ri_f) = \epsilon, \tag{1.147}$$

where both the production of TKE by shear and the dissipation are positive. For stationary flow at production-dissipation equilibrium the Richardson number is then upper bounded:

$$Ri_f < 1. \tag{1.148}$$

There is then an upper steady state limit of the flux Richardson number named the critical flux Richardson number Ri_f^{cr}. This condition is restrictive only for stable flows as the flux Richardson number is negative within unstable situations. In stable flows, the value of the Ri_f^{cr} is considered in the range $[0.2, 0.25]$ as demonstrated for example by Zilitinkevich et al. [2008], Zilitinkevich et al. [2010], Freire et al. [2019], and we will consider in this work $Ri_f^{cr} = 0.25$. Thus, in statistically stationary, horizontally uniform, stable SBL flows at production-dissipation equilibrium, the mean velocity gradient tends to become constant as we have $\varphi_m = \frac{\zeta}{Ri_f^{cr}}$. The mean velocity becomes then affine depending only on the Monin–Obukhov length scale. It results that the turbulence evolution tends to become independent of the height. Thus, the universal functions characterising the TKE, the Reynolds tensor diagonal terms but also the potential-temperature-variance and the horizontal fluxes all tend towards constant values see Monin and Yaglom [1971, Chapter 7.5].

One may also consider the convective limit situation which is the limit case when ζ tends negatively towards infinity. In this case, the asymptotic behaviour is a situation in which the production by shear can be considered null. This case corresponds to the physical state of the natural convection that can take place during a sunny day without any mean wind. First, a legitimate question is whether the Monin–Obukhov theory is still valid for extremely unstable situations. This raises the question whether the flow can be treated as statistically stationary and perfectly stratified in the horizontal direction. Indeed, the energy furnished by the thermal effects may stretch the turbulent eddies increasing their characteristic scale and the size of the ABL. From this growth of the ABL, it results that the latter can never reach a stationary state in convective situation. Yet, in the SBL, it is possible to consider that locally the situation is not impacted by the evolution of the upper part of the ABL which is far away. For convective cases, it is thus possible to consider that a stationary state can be reached not in the whole ABL but only locally in the SBL. Furthermore, the stretching of the turbulent eddies might destabilise the flow sufficiently to create convection cells in the inertial scale destroying the horizontal uniformity and creating structures similar to the ones encountered in Rayleigh–Bénard flows. Such structures may not be explicitly tackled using the Monin–Obukhov similarity theory and would be incorporated in the energy spectrum as large turbulent eddies. In this case the flow evolution does not depend explicitly on the shear stress but only on the thermal turbulence triggered by the convective fluxes $\frac{q}{\rho \mathrm{C}_p}$ imposed on the ground. Using similarity theory, we get:

$$\frac{\partial \overline{\Theta}}{\partial z} = \mathscr{F}_{\Theta}^{-\infty}\left(\kappa z, g\beta, \frac{q}{\rho \mathrm{C}_p}\right) = \frac{1}{\kappa z}\left(\frac{1}{\kappa z g \beta}\left(\frac{q}{\rho \mathrm{C}_p}\right)^2\right)^{\frac{1}{3}} \mathrm{C}_{\Theta}^{-\infty}. \tag{1.149}$$

Moreover, the heat being transported by turbulent heat fluxes, we have $\frac{q}{\rho \mathrm{C}_p} = -u_* \theta_*$ by definition of θ_*. Thus, we have:

$$\frac{\partial \overline{\Theta}}{\partial z} = \mathrm{C}_{\Theta}^{-\infty} \frac{\theta_*}{\kappa z}\left(\frac{-u_*^2}{\kappa g \beta \theta_* z}\right)^{\frac{1}{3}} = \frac{\theta_*}{\kappa z} \underbrace{\mathrm{C}_{\Theta}^{-\infty}\left(-\zeta\right)^{-\frac{1}{3}}}_{\varphi_h(\zeta)}. \tag{1.150}$$

Moreover, assuming that in the convective limit the turbulent Prandtl number converges towards a non-null constant $Pr_t^{-\infty}$ (this assumption will be further discussed in Section 5.1) we get:

$$\varphi_m(\zeta) \underset{\zeta \to -\infty}{\propto} (-\zeta)^{-\frac{1}{3}}, \tag{1.151}$$

where $\underset{\zeta \to -\infty}{\propto}$ means "ζ tending towards minus infinity, the LHS term tends to become proportional to". Thus, in the convective limits both the momentum and heat universal function decay with a power $-1/3$. Monin and Yaglom [1971, Chapter 7.5] showed that the resulting TKE will increase in all directions due to thermal forcing with a power $2/3$:

$$\varphi_k \underset{\zeta \to -\infty}{\propto} \varphi_{\langle uu \rangle} \underset{\zeta \to -\infty}{\propto} \varphi_{\langle vv \rangle} \underset{\zeta \to -\infty}{\propto} \varphi_{\langle ww \rangle} \underset{\zeta \to -\infty}{\propto} (-\zeta)^{2/3}, \tag{1.152}$$

whereas the temperature fluctuations will decrease by mixing with a power $-2/3$:

$$\varphi_{\langle \theta^2 \rangle} \underset{\zeta \to -\infty}{\propto} (-\zeta)^{2/3}. \tag{1.153}$$

Moreover, as the velocity tends to become uniform, the flow tends towards the true convection limit in which all the horizontal fluctuations become equivalent, yielding to:

$$\lim_{\zeta \to -\infty} \varphi_{\langle u\theta \rangle} = 0. \tag{1.154}$$

In addition, due to the velocity gradient evolution, we have a turbulent viscosity introduced in Eq. (1.141) which increases proportionally to $(-\zeta)^{4/3}$. Such an evolution of the turbulent viscosity associated with the TKE evolution induced that the diffusion of TKE tends towards a positive constant in the convective limit.

Literature Propositions of Universal Functions

Now that we have seen some theoretical features of the universal functions, one may want to have an explicit definition of these functions. The determination of these two universal functions has been subject to an intensive work (see e.g. Zilitinkevich and Chalikov [1968], Businger et al. [1971], Carl et al. [1973], Dyer [1974], Högström [1988], Hartogensis and De Bruin [2005], Chenge and Brutsaert [2005]) resulting in numerous propositions. Let us note that this list is far from being exhaustive (different other propositions may be found in Monin and Yaglom [1971, Chapter 7.4]. Some of them defined from Eqs 1.156 to Eqs 1.159 are plotted in Figure 1.13.

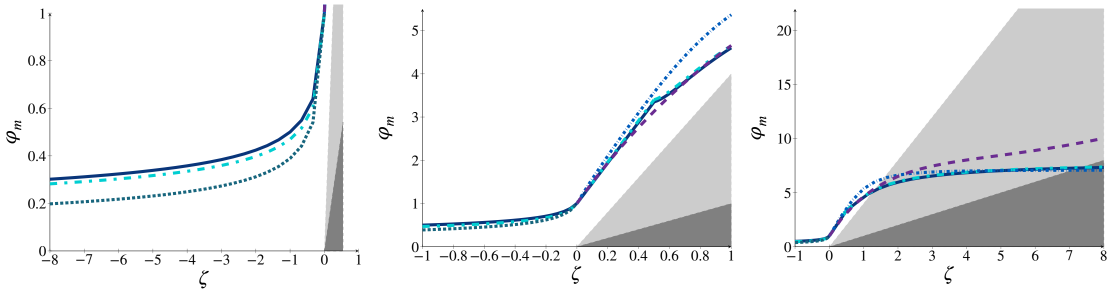

(A) Convective case.

(B) Near neutral case.

(C) Stable case.

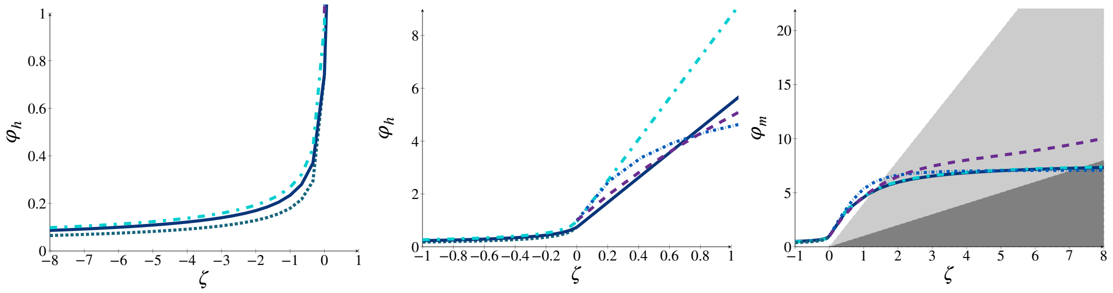

(D) Unstable case.

(E) Near neutral case.

(F) Stable case.

Figure 1.13: Example of literature universal functions: Businger et al. [1971] ▬, Carl et al. [1973] ▪▪▪▪▪, Högström [1988] ▬ ▪ ▪ , Chenge and Brutsaert [2005] ▪▫▪▫▪ ,Hartogensis and De Bruin [2005] ▬ ▬ . The light grey zone represents the area defined by $Ri_f > Ri_f^{cr}$ with $Ri_f^{cr} = 0.25$, and the dark grey one the area defined by $Ri_f > 1$, both these zones should be prohibited.

- Businger et al. [1971]:

$$\varphi_m(\zeta) = \begin{cases} (1-15\zeta)^{-1/4}, \ \zeta < 0, \\ 1 + 4.7\zeta, \ 0 \leq \zeta < 0.5, \\ 7.85 - \frac{4.25}{\zeta} + \frac{1}{\zeta^2}, \ 0.5 \leq \zeta < 10, \\ 0.7485\zeta, \ 10 \leq \zeta, \end{cases} \tag{1.155a}$$

$$\varphi_h(\zeta) = \begin{cases} 0.74\,(1-9\zeta)^{-1/2}, \ \zeta < 0, \\ 0.74 + 4.7\zeta, \ 0 \leq \zeta. \end{cases} \tag{1.155b}$$

- Carl et al. [1973]:

$$\varphi_m(\zeta) = (1-16\zeta)^{-1/3}\,,\ \zeta < 0, \tag{1.156a}$$

$$\varphi_h(\zeta) = 0.74\,(1-16\zeta)^{-1/2}\,,\ \zeta < 0. \tag{1.156b}$$

- Högström [1988] which is a revisited version of Businger et al. [1971]:

$$\varphi_m(\zeta) = \begin{cases} (1-19.3\zeta)^{-1/4}\,,\ \zeta < 0, \\ 1+4.8\zeta,\ 0 \le \zeta < 0.5, \\ 7.9 - \frac{4.25}{\zeta} + \frac{1}{\zeta^2},\ 0.5 \le \zeta < 10, \\ 0.7485\zeta,\ 10 \le \zeta, \end{cases} \tag{1.157a}$$

$$\varphi_h(\zeta) = \begin{cases} 0.95\,(1-11.6\zeta)^{-1/2}\,,\ \zeta < 0, \\ 0.95+7.8\zeta,\ 0 \le \zeta. \end{cases} \tag{1.157b}$$

- Hartogensis and De Bruin [2005]:

$$\varphi_m(\zeta) = 1+\zeta\left(a + b\exp(-d\zeta) - bd\left(\zeta - \frac{c}{d}\right)\exp(-d\zeta)\right),\ 0 \le \zeta, \tag{1.158a}$$

$$\varphi_h(\zeta) = 1+\zeta\left(a\left(1+\frac{2}{3}a\zeta\right)^{1/2} + b\exp(-d\zeta) - bd\left(\zeta - \frac{c}{d}\right)\exp(-d\zeta)\right),\ 0 \le \zeta, \tag{1.158b}$$

  with $a = 1, b = 2/3, c = 5, d = 0.35$.

- Chenge and Brutsaert [2005]:

$$\varphi_m(\zeta) = 1+a\left(\frac{\zeta + \zeta^b(1+\zeta^b)^{(1-b)/b}}{\zeta + (1+\zeta^b)^{1/b}}\right),\ 0 \le \zeta, \tag{1.159a}$$

$$\varphi_h(\zeta) = 1+c\left(\frac{\zeta + \zeta^d(1+\zeta^d)^{(1-d)/d}}{\zeta + (1+\zeta^d)^{1/d}}\right),\ 0 \le \zeta, \tag{1.159b}$$

  with $a = 1, b = 2/3, c = 5, d = 0.35$.

These functions are quite useful as they often provide inlet boundary condition to set up micro-scale numerical atmospheric simulations. Yet, these functions are not fully satisfactory for four main issues:

1. It is difficult to determine which proposition should be considered. Indeed, there is a multitude of propositions fitted on different experimental data and the selection of one profile instead of another one may be a tricky issue.
2. There is a lack of coherency with asymptotic theoretical results. Indeed, only Carl et al. [1973] proposes a function reaching the proper order of convergence in convective situation. Moreover, in stable situations, neither Businger et al. [1971] nor Högström [1988] nor Hartogensis and De Bruin [2005] nor Chenge and Brutsaert [2005] proposed universal functions respecting the condition $Ri_f < Ri_f^{cr}$ for all value of ζ.

3. There is a lack of information on the turbulent quantities. Indeed, only the information on the mean fields is provided. Yet, turbulent information at inlet may play a preponderant role over quite large distance in the flow.

4. Finally, there is lack of consistency with the turbulence model used. Indeed, these functions being fitted on experiments, they may not agree with the solution of the modelling selected on the SBL configuration. Thus, the profiles injected at inlet may not be maintained by the numerical solver in steady, horizontally uniform situations.

A method to determine universal functions for mean and turbulent quantities consistent with the modelling selected will be presented in Section 5.1.

1.2.2.3.3 Limitations of the Monin–Obukhov Theory

The present work will remain in the scope of Monin–Obukhov similarity theory. The present paragraph aims at putting emphasis on different limits of this theory.

Limitations due to the Altitude.

A first limitation of the Monin–Obukhov similarity theory is the altitude at which it is used. Indeed, the hypothesis considered are valid only in the SBL, where solely the grounds effects influence the flow leading to uniform shear and turbulent heat fluxes. However, as we increase the altitude Coriolis effects, large-scale horizontal pressure gradient and sink radiative terms should be considered (see Deardorff [1972]). For the purpose of extending the validity of the hypothesis made, it is thus necessary to take into account these effects and the resulting diminution of shear stress and normal turbulent flux with altitude. Some generalised theories have been proposed to tackle this issue and the interested reader may refer to Nieuwstadt [1984] or Gryning et al. [2007]. This extension of the physics considered may have a great impact on the pollutant dispersion, as we can see in Figure 1.14. In this case, the plume is first advected toward us and then in altitude its direction rotates toward the right which is in line with the effects of the Coriolis effects. Moreover, it is capped by a stable layer at an altitude z_i. In absence of further information, it is hard to assert if this capping corresponds to the upper part of the ABL or to entrainment zone above a developing convective layer.

Figure 1.14: Smoke plume capped by a stable layer (at the altitude z_i) and rotating rightward due to Coriolis effects in the Ekman layer.

Limitation due to a Lack Stationarity

A second pitfall that may arise is the difficulty to have a stationary situation. Indeed, the Monin–Obukhov cannot represent the vertical variation of stability appearing in the atmosphere due to the transient effects resulting from a temporal variation of thermal forcing. Such effects are encountered for example in the fumigation and lofting presented respectively in Figure 1.11 and Figure 1.12. In this case, it is thus limited near wall where the stability may be assumed uniform.

Moreover, in general compared to experimental laboratory results obtained in channel flows, atmospheric flows present low-frequency fluctuations which would modify the wind development. In the scope of atmospheric flow, these low-frequency fluctuations have been encapsulated as a part of the turbulent energy spectrum. It results that the model constant may have to be modified to take into account these effects as discussed further in Section 1.3.2. Moreover, the length scale over which the wind direction may be considered stationary limits the use of such assumption to local treatment over hundreds of meters. This issue is particularly present in the case of slow winds in which meanders, characterised by the fluctuations of the mean velocity direction, may occur, see (e.g. Anfossi et al. [2005] and Mortarini et al. [2013]).

Limitations due to Topography Effects

A final commonly encountered issue is the validity of the horizontal homogeneity. Indeed, multiple local effects may deviate the flow behaviour from the one predicted by Monin–Obukhov theory:

- The presence of obstacles may impact the behaviour of the flow. The effect of plants and forest canopies remains a complex and largely studied issue (see e.g. Brunet [2020], Finnigan [2021]). In urban context the presence of individual building and their accumulation also plays a fundamental role on the dynamics (see e.g. Rotach [1999], Barlow and Coceal [2009], Bahlali et al. [2019]).
- Near coast, the transition from water to the ground may induce a daily circulation referred as sea or land breeze depending on its provenance. Indeed, submitted to a given thermal forcing the evolution of water temperature is slower than the evolution of ground temperature due to the higher heat capacity of water. During daytime, the air is more heated above ground and tends to ascend more in this zone triggering a wind from the sea to compensate the local depression stemming from this upward air movement. This is the sea breeze. At the opposite, at night, the air is more cooled down on the ground yielding a to wind from the land towards the see: the land breeze.
- Similarly, convective effects may occur in presence of slope or mountains. During the day the slope being heated, an upward wind from the valley to the tops can arise. This convection driven wind is referred as anabatic. The opposite situation may append at night due to the cooling by the ground. It might result in a downward wind named katabatic wind.

1.3 Modelling Overview

Contents

Theoretically speaking, all the information describing the dynamics of a flow is contained within the instantaneous Navier–Stokes and potential temperature equations. However, the exact resolution of such a set of equations is in general impossible to reach due particularly but not only to the presence of turbulent effects. The goal of this section is to present Navier–Stokes based modelling approaches used to characterise flows in the context of high-Reynolds incompressible flows. This presentation will remain superficial to exhibit only the salient point of these approaches. It does not aim at being an exhaustive overview of the existing turbulent modelling which are object of multiple valuable books (see e.g. Launder and Spalding [1974], Pope [2000], Hanjalić and Launder [2022]). First, a classification of these methods is proposed in Section 1.3.1 and the level of description they can provide is briefly discussed. Then a particular attention is given to RANS and Lagrangian stochastic methods respectively in Section 1.3.2 and in Section 1.3.3, as these are the methods considered in the present work.

1.3.1 Classification of Navier–Stokes based Turbulence Modelling

A multitude of Navier–Stokes based turbulence modellings have been developed, with different levels of description. They can be regrouped into great classes of methods introduced here.

DNS: A first solution enabling to conserve all the information characterising a flow is to resolve directly the Navier–Stokes equation on all the scales of turbulence from the Kolmogorov scale to the larger ones. This provides information at a microscopic level. This method, referred as direct numerical simulation (DNS), is of major interest to provide strong information on theoretical case and a better understanding of the precise physical phenomena taking place within the turbulence. Indeed, it enables to explicitly describe all the turbulent structures and eddies in the flow and their interactions with one another. Even though difficulties to properly initialise all the scales of turbulence and to treat boundary condition (such as the walls which are often consider perfectly smooth until the lower scale) do exist, these methods can be regarded as reference numerical characterisation of the flow. However, as the range of turbulent scales resolved increases greatly with both the Reynolds Re (and potentially also the Richardson number Ri), their cost remains prohibitive for classical use and specially to treat atmospheric flows. For example, considering only inertial effects, to consider all the spatial scales, the mesh should at least contain $\frac{\mathcal{L}}{\ell_\eta}$ cells in each direction. As shown in Paragraph 1.2.1.2.1, a mesh containing $Re_{\mathcal{L}}^{9/4}$ cells would be needed. Moreover, to characterise all the turbulent timescales, the simulation should at least be made on $\frac{\mathcal{T}_{\mathcal{L}}}{\mathcal{T}_\eta} \simeq Re_{\mathcal{L}}^{1/2}$ iterations. This results in an increase of the computation time in $Re_{\mathcal{L}}^{11/4}$, which remains prohibitive even today for many engineering uses and especially in atmospheric flows.

LES: A first method to limit this numerical cost, named large eddies simulation (LES), is to resolve explicitly only the greatest scales which are commonly the one of most interest. This approach was first proposed for atmospheric simulation (see Smagorinsky [1963], Lilly [1966]) and then completed (see Deardorff [1971], Germano et al. [1991], Lilly [1992]) to provide a mesoscopic description of the flow. It is based on the fact that at large scales the anisotropy of turbulence is important, however, as we go down the energy cascade, the turbulence becomes more and more isotropic, and its behaviour is more and more universal. Thus, it proposes to resolve explicitly the large and very energetic eddies on a mesh whereas a statistical modelling of the smaller ones is provided. Classically the modelled turbulence referred as sub-grid turbulence aims at taking into account the transfers of energy and momentum towards the unresolved scales to provide an appropriate rate of TKE dissipation. To this end, a spatial filtering is considered to separate the resolved and the sub-grid turbulence. As the large structures play a preponderant role compared to the small ones in pollutant dispersions, their resolution enables to explicitly take into account this phenomenon. This approach although far more tractable than DNS, remains quite expensive numerically speaking. Indeed, so as to have a physical behaviour the simulation must be carried out along the three directions of space. Moreover, to have a physical behaviour, after inlet the resolved turbulence need a distance typically of the scale of a few auto-correlation lengths to develop itself properly. In order to tackle this constraint an intensive work has been done to recreate at best turbulent fluctuations at inlet (see e.g. Klein et al. [2003], Poletto et al. [2013]). Finally, it might be costly to select a spatial discretisation enabling to resolve a sufficient fraction of the total TKE, especially near obstacles where the sizes of the turbulent structures are restrained. A further discussion can be found e.g. in Pope [2000][Chapter 13].

RANS: A less time-consuming approach presented more in detail in Section 1.3.2, consists in modelling all scales of turbulence by separating the flow into an averaged and a fluctuating part. These approaches are referred as Reynolds averaged Navier–Stokes (RANS) and provide a macroscopic description of the flow. As introduced in Paragraph 1.2.1.2.2, this method relies on an application of an ensemble average operator on the Navier–Stokes equation as first presented by Reynolds [1895]. The modelling consists then in determining correlations between unknown averaged variables and the available ones to properly retrieve the large-scale statistical behaviour. As only information based on some transported statistical moments are computed the description of turbulence is coarser than the previous methods and depends on the choice of these averaged quantities. It is worth noticing that this macroscopic level of description is often sufficient from an engineering point of view. For this reason and because of its more attractive computation cost, this method remains the most commonly used for industrial context.

PDF: Stochastic methods, also referred to as probability density function (PDF) methods, are a class of methods in which the PDF associated to a given state vector, characterising the physical properties followed, is estimated in a weak sense through Monte Carlo averaging on a large number of stochastic particles as presented in the fundamental work of Pope [1985]. Such methods enable a mesoscale statistical description of the turbulence (see Minier [2016]) which is finer than RANS and coarser than LES. Commonly, a Lagrangian standpoint is considered as the latter enables to treat explicitly particle transport. These methods are then referred as Lagrangian stochastic methods or Lagrangian PDF methods (in this work, by simplicity we will also speak of PDF methods for these methods). They may be used to model single-phase flows as well as poly-disperse ones, as discussed at length in the important studies of Pope [2000] and Minier and Peirano [2001]. Stochastic processes are used to model the fast-varying processes which are not explicitly followed. In this work only one-particle methods are considered, from which one-point one-time Eulerian PDFs are derived, to estimate mean fields. The modelling of such approach has been mainly developed in the 1980s and 1990s, mostly by Pope and co-workers (see e.g. Haworth and Pope [1986], Pope and Chen [1990], Pope [1991, 1994a,b]) for single phase flow and later on by Minier and co-workers for poly-disperse one (see e.g. Minier and Pozorski [1997], Pozorski and Minier [1998], Minier and Peirano [2001], Minier et al. [2004], Minier [2015, 2016, 2021]). A main advantage of these methods is their capacity to treat without further modelling local source terms no matter how complex and non-linear they are. Such a property is of major interest to model reactive and/or poly-disperse flows. Indeed, due to non-linearity the averaged source terms might vary quite noticeably compared to the sources terms based on the averaged quantities. Let us note that, in one-point PDF methods, the information associated to the particles are local, it is thus not possible to derive spatial correlation such as the integral length scale or Eulerian structure functions. In order to do so, it is necessary to have non-local information using for example two points PDF methods (see Sabelfeld [2012]). The latter may be used on simple theoretical flows but are for now not tractable on industrial cases.

SPH: A second Lagrangian methods used to resolve the Navier–Stokes equation is the smoothed particle hydrodynamics (SPH). As stated in their name, these methods rely on a fully particular and grid free description of the flow. Each particle represents a given unit of fluid mass and interacts with the surrounding ones through the use of a spatial smoothing kernel. Each particle interacting only with the other particles in its kernel, the interaction forces between particles depend on the relative distance between the particles and on the shape selected for this kernel. For more information interested reader may refer e.g. to Violeau [2012]. The SPH methods are in their majority deterministic methods even though stochastic methods based on this approach have been proposed for example by Minier [2016].

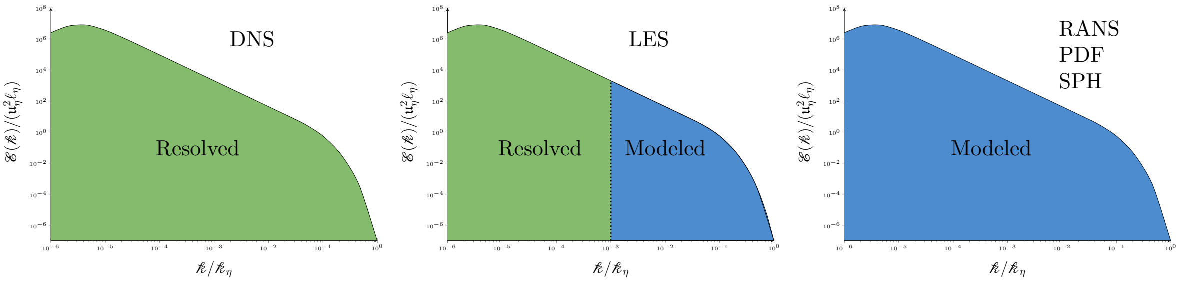

Figure 1.15: Comparison of the different turbulent methods related to the modelling of the turbulent energy spectrum.

Remark 1.3.1.

Gaus.: Although, strictly speaking, Gaussian methods do not provide any dynamical or thermal information on the flow itself, they are broadly used in the atmospheric community for dispersion of pollutants because of their relatively small computation cost especially when modelling the dispersion from few local sources. They are based on the analytical solution proposed by Roberts [1923] for stationary and uniform carrier flows. In this case the corresponding advection-diffusion equation reads:

$$\frac{\partial \langle C \rangle}{\partial t} + \langle U \rangle \frac{\partial \langle C \rangle}{\partial x} = K_{t\langle C \rangle, j} \frac{\partial^2 \langle C \rangle}{\partial x_i \partial x_i} \delta_{ij}, \tag{1.160}$$

where an injection rate Q is ensured imposed either by a scalar inlet or by a local source term. Furthermore, the molecular diffusivity is neglected, the mean advection-velocity $\langle U \rangle$ and the turbulent diffusivity $K_{t\langle C \rangle, \alpha} = -\frac{\langle u_\alpha c \rangle}{\frac{\partial \langle C \rangle}{\partial x_\alpha}}$ are considered uniform. Assuming that the advection is great compared to the diffusion terms the stationary solution is:

$$\langle C \rangle(x, y, z) = \frac{Q}{4\pi x \sqrt{K_{t\langle C \rangle, y} K_{t\langle C \rangle, z}}} \exp\left(-\frac{\langle U \rangle}{4x} \left(\frac{y^2}{K_{t\langle C \rangle, y}} + \frac{z^2}{K_{t\langle C \rangle, z}} \right) \right) \tag{1.161}$$

where the standard deviation of characterising the width of the plume $\tilde{\sigma}_{\langle C \rangle, \alpha}$ can identify as $\tilde{\sigma}_{\langle C \rangle, \alpha} = \sqrt{2 K_{t\langle C \rangle, \alpha} t} = \sqrt{2 K_{t\langle C \rangle, \alpha} \frac{x}{\langle U \rangle}}$. As we will see later in Section 2.3.1.1 such a relation is valid only in the diffusive regime far from the source. Moreover, specific correlations should be furnished to obtain proper formulations for these standard deviations. A currently used solution to relax the condition of uniformity in the mean wind direction is to to use Gaussian puff methods. In these methods, the position of the centre of the plume is tracked using a deterministic Lagrangian description and at each iteration a Gaussian puff is released to represent the dispersion around this mean location. Even though it is possible to take into account the presence of a flat ground using a second Gaussian dispersion symmetric compared to the grounds, these methods are misfitted to treat near source dispersion where the topography and presence of obstacles may have a primordial impact. Finally, all the turbulence being parameterised it corresponds clearly to a coarser description than the other methods presented. For more information the interested reader may refer e.g. to Stockie [2011] or to Leelóssy et al. [2018].

1.3.2 Introduction to Reynolds-Averaged Navier–Stokes Modelling

The goal of the present section is to discuss the methods used to model the turbulent effects in the context of RANS approaches. For this purpose, it is necessary to prescribe the behaviour of the Reynolds tensor $\underline{\underline{\boldsymbol{\mathcal{R}}}} = \overline{u_i u_j}\,\underline{\boldsymbol{e_i}} \otimes \underline{\boldsymbol{e_j}}$, and the turbulent heat fluxes $\overline{\underline{\boldsymbol{u}}\theta} = \overline{u_i\theta}\,\underline{\boldsymbol{e_i}}$ appearing respectively on the mean velocity and mean potential temperature equations. Two main classes of modelling can be considered: either to model directly these terms based on known variables or to transport them explicitly. The first approach is presented in Section 1.3.2.1 and corresponds to the eddy viscosity models (EVM) hypothesis in which the Reynolds tensor and turbulent heat fluxes are considered to have viscous-like effects. The second category presented in Section 1.3.2.2 corresponds to the second-order moment transport class of turbulent modelling.

1.3.2.1 Eddy Viscosity Models

Let us first focus only on the dynamics without considering thermal effects. A first description of the turbulence would be to consider that it plays a role similar to the viscosity i.e. diffusive and dissipative. Indeed, as briefly discussed in the examples presented in Section 1.2.1.2, the main effect of the large-scale turbulent fluctuations on the mean flow is to induce mixing and shear stress. Furthermore, in the RANS equation for the velocity Eq. (1.64) the Reynolds tensor appears indeed, in the divergence side-by-side with the viscosity. Such a description was first introduced by Boussinesq who proposed to write:

$$\overline{u_i u_j} = \frac{2}{3}k - \nu_t \overline{S_{ij}}, \tag{1.162}$$

where ν_t is called a turbulent viscosity. This hypothesis is referred as the Boussinesq hypothesis which is at the basis of the eddy viscosity model (EVM). Such models assume that the velocity gradient and the shear stress are aligned. Furthermore, it is worth noticing that unlike the molecular viscosity, which is mainly a fluid property, the turbulent viscosity is a flow property which can highly vary within it. The main question is then to determine how to model this turbulent viscosity. To this end, one may consider that the turbulent viscosity should be characterised by a length scale ℓ_t and velocity scale u_t, characteristics of the large-scale mean behaviour of turbulence and depending only on known or transported properties of the flow.

Remark 1.3.2. Note that the Boussinesq hypothesis presented here should not be confused with the Boussinesq approximation presented in Paragraph 1.2.1.1.2. The latter one does not concern the treatment of the Reynolds tensor but the treatment of buoyancy by providing a modelling of the thermal effects on density.

Algebraic Closures

A first proposition made was to consider algebraic solutions for these scales. Based on parietal flows, Prandtl [1925] proposed to take $u_t = \ell_t|\overline{S_{ij}}|$ and $\ell_t = \kappa z$ in the vicinity of the wall with z the wall distance and $\kappa = 0.42$ a constant referred as Von Kármán constant. Such a model has the main benefit to be simple and computationally cheap as no additional equation has to be considered. It provides moreover a quite accurate behaviour for simple wall bounded flows. However, a first drawback of this closure is that it is not universal as the constant characterising turbulent length scale is geometry and case dependent. Moreover, such models fail to characterise more complex flows (e.g. not simply sheared or complex geometries). For both these reasons algebraic closure is scarcely used.

First-Order Closures

A more currently used method consists in adding transported parameters characteristic of the flow. The natural choice to consider an averaged velocity scale of turbulence is $u_t = \sqrt{k}$. A transport equation is then considered for the kinetic energy; however, a length scale is still necessary. For this purpose, the reference choice is to take $\ell_t = \mathcal{C}_\mu \frac{k^{3/2}}{\epsilon}$. This results in the Prandtl-Kolmogorov formula $\nu_t = \mathcal{C}_\mu \frac{k^2}{\epsilon}$ where the two variables k and ϵ have to be transported. Without considering thermal effects, following Jones and Launder [1972], the corresponding high Reynolds incompressible transport equations are:

$$\frac{Dk}{Dt} = \underbrace{\frac{\partial}{\partial x_j}\left(\frac{\nu_t}{\sigma_k}\frac{\partial k}{\partial x_j}\right)}_{\mathcal{D}_k} + \underbrace{\nu_t S^2}_{\mathcal{P}} - \epsilon, \tag{1.163a}$$

$$\frac{D\epsilon}{Dt} = \underbrace{\frac{\partial}{\partial x_j}\left(\frac{\nu_t}{\sigma_\epsilon}\frac{\partial \epsilon}{\partial x_j}\right)}_{\mathcal{D}_k} + \underbrace{\frac{\epsilon}{k} C_{\epsilon 1}\nu_t S^2}_{\mathcal{P}_\epsilon} - \underbrace{C_{\epsilon 2}\frac{\epsilon^2}{k}}_{\epsilon_\epsilon}, \tag{1.163b}$$

with the different constants appearing in this equation summed up in Table 1.2.

$\mathcal{C}_\mu$	$C_{\epsilon 1}$	$C_{\epsilon 2}$	σ_k	σ_ϵ
0.09	1.442	1.92	1.0	1.3

Table 1.2: Standard $k - \epsilon$ constants from Launder and Spalding [1974].

Let us note that in the modelled TKE equation, Eq. (1.163a), the transport by fluctuations of pressure Eq. (1.88) and the viscous diffusion Eq. (1.89) are neglected. Moreover, the diffusion induced by velocity fluctuations Eq. (1.87) is modelled using a simple gradient diffusion hypothesis (SGDH) which states for any fields Ψ:

$$\overline{u_k\psi} = -\frac{\nu_t}{\sigma_\Psi}\frac{\partial\overline{\Psi}}{\partial x_k}. \tag{1.164}$$

Furthermore, let us notice that the dissipation rate equation is written in a way to mimic the structure of the TKE equation with the turbulent frequency $\widehat{\omega} = \frac{\epsilon}{k}$ as a pre-factor in front of the production and dissipation terms. Such an assumption remains relatively crude given the complexity of the exact equation presented from Eq. (1.90) to Eq. (1.99). Yet, the modelling of each correlation appearing in this equation would be too complex, cumbersome and costly to parameterise. In addition, for the thermal effects, a SGDH hypothesis is made. Doing so we obtain:

$$\frac{Dk}{Dt} = \underbrace{\frac{\partial}{\partial x_j}\left(\frac{\nu_t}{\sigma_k}\frac{\partial k}{\partial x_j}\right)}_{\mathcal{D}_k} + \underbrace{\nu_t S^2}_{\mathcal{P}} - \underbrace{g_i\frac{\nu_t}{\sigma_\rho}\frac{\partial\overline{\rho}}{\partial x_i}}_{\mathcal{G}} - \epsilon, \tag{1.165a}$$

$$\frac{D\epsilon}{Dt} = \underbrace{\frac{\partial}{\partial x_j}\left(\frac{\nu_t}{\sigma_\epsilon}\frac{\partial \epsilon}{\partial x_j}\right)}_{\mathcal{D}_k} + \underbrace{C_{\epsilon 1}\frac{\epsilon}{k}\nu_t S^2}_{\mathcal{P}_\epsilon} - \underbrace{\mathcal{C}_{\epsilon 3} g_i\frac{\epsilon}{k}\frac{\nu_t}{\sigma_\rho}\frac{\partial\overline{\rho}}{\partial x_i}}_{\mathcal{G}_\epsilon} - \underbrace{C_{\epsilon 2}\frac{\epsilon^2}{k}}_{\epsilon_\epsilon}, \tag{1.165b}$$

which can be rewritten using the Boussinesq approximation as:

$$\frac{Dk}{Dt} = \underbrace{\frac{\partial}{\partial x_j}\left(\frac{\nu_t}{\sigma_k}\frac{\partial k}{\partial x_j}\right)}_{\mathcal{D}_k} + \underbrace{\nu_t S^2}_{\mathcal{P}} + \underbrace{g_i\frac{\nu_t}{Pr_t^0}\beta_0\frac{\partial\overline{\Theta}}{\partial x_i}}_{\mathcal{G}} - \epsilon, \tag{1.166a}$$

$$\frac{D\epsilon}{Dt} = \underbrace{\frac{\partial}{\partial x_j}\left(\frac{\nu_t}{\sigma_\epsilon}\frac{\partial \epsilon}{\partial x_j}\right)}_{\mathcal{D}_k} + \underbrace{C_{\epsilon 1}\frac{\epsilon}{k}\nu_t S^2}_{\mathcal{P}_\epsilon} + \underbrace{\mathcal{C}_{\epsilon 3} g_i\frac{\epsilon}{k}\frac{\nu_t}{Pr_t^0}\beta_0\frac{\partial\overline{\Theta}}{\partial x_i}}_{\mathcal{G}_\epsilon} - \underbrace{C_{\epsilon 2}\frac{\epsilon^2}{k}}_{\epsilon_\epsilon}, \tag{1.166b}$$

with $\mathcal{C}_{\epsilon 3} = \mathcal{C}_{\epsilon 1}$, according to Lumley and Khajeh-Nouri [1975] and Pr_t^0 the turbulent Prandtl number considered constant. The value of the latter varies with buoyant effects and its near neutral value is in the range [0.6-0.9] (see Gibson and Launder [1978], Zilitinkevich et al. [2008], Srinivasan and Papavassiliou [2011], Kitamura et al. [2013]). Yet this value depends on the thermal evolution and even its near neutral value is still in debate and its determination is an active field of research (see e.g. Li [2019]). The value of the set of constants in Table 1.2 was fitted on channel flows. Other sets of constants taking into account the low frequency fluctuations of velocity occurring in atmospheric flow have been proposed e.g. by Panofsky et al. [1977], Detering and Etling [1985], Duynkerke [1988]. These alternative sets of constants are broadly used in the scope of atmospheric flows. Furthermore, numerous variants of the $k-\epsilon$ model exist such as the model developed by Spalart and Allmaras [1992] with only one transport equation for ν_t, the $k-\widehat{\omega}$ model presented by Wilcox [1988] where the second variable transported is the turbulent frequency $\widehat{\omega} = \frac{\epsilon}{k}$, or the turbulent timescale $k-\mathcal{T}_k$ model with $\mathcal{T}_k = \frac{k}{\epsilon}$ proposed by Speziale et al. [1992]. EVM tends to propose a quite good description of first-order moment when the fields are varying slowly enough but provide a quite poor description of the second-order moments. Furthermore, they tend to fail to predict proper results in the case of fast-varying flows where the assumption that the mean gradient and shear stress have sufficient time to align with one another is not valid (see Lumley and Khajeh-Nouri [1975]).

1.3.2.2 Second-Order Closures

A solution to improve the results especially in fast-varying fields is to transport explicitly the second-order moment instead of considering them only as diffusive terms. This idea is put forward by the fundamental work of Lumley and Khajeh-Nouri [1975] which states: "*There is thus an article of faith involved: if a crude assumption for second moments predicts first moments adequately, perhaps a crude assumption for third moments will predict second moments adequately*". Even though these methods give a richer physical description and were often used in theoretical atmospheric studies since the 70's (see e.g. Wyngaard and Coté [1974], Wyngaard et al. [1975], Wyngaard [1975], Launder [1975], Gibson and Launder [1978]); they are less used from an engineering point of view. This relatively little use of second-order models is mainly caused by two drawbacks. First the transport of 6 equations for the Reynolds tensor components instead of one for the TKE plus potentially the transport of 3 equations for turbulent heat fluxes instead of none trigger a significant increase of computation time. Furthermore, as the turbulence is not treated as a diffusive term but as a transport one, these methods induce realisability issues (i.e. the respect of the symmetric positive half-definite nature of the Reynolds tensor which is a physical constraint for this covariance matrix highlighted by Schumann [1977], Lumley [1979]). Moreover, for this reason, numerical stability and convergence issues should be tackled with even greater attention (see e.g. Norddine et al. [2023], Ferrand et al. [2023]). The goal of the present section is to describe the models used to close the transport equation of these second-order moments presented in Paragraph 1.2.1.2.2.

1.3.2.2.1 Direct Reynolds Stress Modelling

First, let us focus on the dynamics; the approaches consisting in transporting explicitly the Reynolds tensor are referred as Direct Reynolds Stress Modelling (DRSM). The terms indexed with the superscript ‡ in Paragraph 1.2.1.2.2 have to be modelled. The modelling of diffusion by fluctuation of pressure and velocity, but also the pressure-strain correlation, the dissipation rate and the buoyancy, are discussed in this section.

Diffusion by Fluctuation of Pressure and Velocity

Often the diffusion by fluctuation of pressure is neglected compared to the diffusion by velocity fluctuations. One can also consider that the modelling of the diffusion by pressure fluctuation is encompassed in the modelling of the diffusion by velocity fluctuation which is numerically speaking equivalent. The two most commonly used proposals will be presented here.

Shir: The first one is the Shir model (see Shir [1973]) which consists in applying a SGDH on the term of diffusion by velocity gradient as:

$$\mathcal{D}^u_{ij} = -\frac{\partial \overline{u_i u_j u_k}}{\partial x_k} \simeq \frac{\partial}{\partial x_k}\left(\mathcal{C}_S \frac{k^2}{\epsilon}\frac{\partial \overline{u_i u_j}}{\partial x_k}\right), \tag{1.167}$$

with $\mathcal{C}_S = 0.11$. Note that this closure assumes an alignment between the gradient of second-order gradient on the corresponding diffusion due to the SGDH hypothesis made.

Daly-Harlow: The second one is the Daly-Harlow model (see Daly and Harlow [1970]) which consists in applying a generalised gradient diffusion hypothesis (GGDH). It allows the gradient and the higher order term to be non-aligned corresponding then to physically richer description. It is written as:

$$\mathcal{D}^u_{ij} = -\frac{\partial \overline{u_i u_j u_k}}{\partial x_k} \simeq \frac{\partial}{\partial x_k}\left(\mathcal{C}_{DH}\overline{u_l u_k}\frac{k}{\epsilon}\frac{\partial \overline{u_i u_j}}{\partial x_l}\right), \tag{1.168}$$

with $\mathcal{C}_{DH} \simeq 0.22$

Let us note that both these models do not respect the symmetric nature of the third order moment $\overline{u_i u_j u_k}$. Other models are build to respect this constraint e.g. by Hanjalić and Launder [1972] or Mellor and Herring [1973] in their analysis of DRSM methods, but are not considered in this work. Indeed, as we are interested in the divergence of this third order tensor this issue is of lesser importance. In this work, focusing mainly on simple sheared flows the Shir model will be kept as it is numerically easier to treat and introduces less numerical errors.

Buoyancy Terms

Three kinds of closure can be easily used to close the buoyancy terms. We will assume that we place ourselves in the scope of Boussinesq approximation using the potential temperature.

SGDH: The first closure is the simplest one. It is similar to the treatment done in $k-\epsilon$ and consists in using a SGDH assumption on the turbulent heat fluxes.

$$\mathcal{G}_{ij} = \frac{1}{\rho}\left(g_i\overline{u_j\rho'} + g_j\overline{u_i\rho'}\right) \simeq \frac{\mathcal{C}_\mu}{Pr_t^0}\frac{k^2}{\epsilon}\beta_0\left(g_i\frac{\partial\overline{\Theta}}{\partial x_j} + g_j\frac{\partial\overline{\Theta}}{\partial x_i}\right) \tag{1.169}$$

GGDH: Similarly to the Daly-Harlow treatment for the diffusion, we can consider a generalised gradient diffusion hypothesis as here the Reynolds tensor is transported:

$$\mathcal{G}_{ij} = \frac{1}{\rho}\left(g_i\overline{u_j\rho'} + g_j\overline{u_i\rho'}\right) \simeq \beta_0\frac{3}{2}\frac{\mathcal{C}_\mu}{Pr_t^0}\frac{k}{\epsilon}\left(g_i\overline{u_j u_k}\frac{\partial\overline{\Theta}}{\partial x_k} + g_j\overline{u_i u_k}\frac{\partial\overline{\Theta}}{\partial x_k}\right) \tag{1.170}$$

DFM: The third solution is to keep this term without modelling adding a transport equation for the corresponding fluxes, this solution is referred as direct flux modelling (DFM). Using the Boussinesq approximation on the potential temperature and transporting explicitly the turbulent heat flux $\overline{\underline{\boldsymbol{u}}\theta}$, we have:

$$\mathcal{G}_{ij} = \frac{1}{\rho}\left(g_i\overline{u_j\rho'} + g_j\overline{u_i\rho'}\right) \simeq -g_i\beta_0\overline{u_j\theta} - g_j\beta_0\overline{u_i\theta} \tag{1.171}$$

The transport equation of $\overline{\underline{\boldsymbol{u}}\theta}$ having the same structure as Eq. (1.101), it is not closed. Its closure is discussed later in Paragraph 1.3.2.2.2.

Pressure-Strain Correlation

A main issue in the treatment of DRSM approach is the modelling of the pressure-strain correlation which plays a fundamental role in the redistribution of the kinetic energy among the spatial direction. The modelling of the slow, rapid and buoyant terms in the pressure-strain correlation will be presented. Limiting ourselves to the treatment of high Reynolds number flows, we will consider that we are sufficiently far from the wall so that the effects of pressure reflections on the latter are absorbed. The wall echo terms are then considered out of scope of the present work (for more information see e.g. Gibson and Launder [1978], Dehoux et al. [2011], Hanjalić and Launder [2022]).

Rotta: The first proposition made by Rotta [1951] was to consider only the slow term in the pressure-strain correlation as:

$$\Pi_{ij} = \overline{\frac{p}{\rho}\left(\frac{\partial u_i}{\partial x_j} + \frac{\partial u_j}{\partial x_i}\right)} \simeq \Pi_{ij}^s \simeq -\mathcal{C}_R \frac{\epsilon}{k}\left(\overline{u_i u_j} - \frac{2}{3} k \delta_{ij}\right) \tag{1.172}$$

with $\mathcal{C}_R = 4.15$.

LRR-IP: A second broadly used method is the LRR-IP model (Launder-Reece-Rodi isotropisation of production) derived by Launder et al. [1975] by adding a modelling term for the rapid pressure-strain correlation as an isotropisation of production term:

$$\Pi_{ij} = \overline{\frac{p}{\rho}\left(\frac{\partial u_i}{\partial x_j} + \frac{\partial u_j}{\partial x_i}\right)} \simeq -\mathcal{C}_R \frac{\epsilon}{k}\left(\overline{u_i u_j} - \frac{2}{3} k \delta_{ij}\right) - \mathcal{C}_{\mathcal{P}}\left(\mathcal{P}_{ij} - \frac{2}{3}\mathcal{P}\delta_{ij}\right) \tag{1.173}$$

with $\mathcal{C}_R = 1.8$ and $\mathcal{C}_{\mathcal{P}} = 0.6$. As a part of the redistribution process is carried out by the rapid term, the contribution of the slow one is diminished.

SSG: Finally, a more complex, non-linear and more commonly used model is the one developed by Speziale, Sarkar and Gatski (see Speziale et al. [1991]). The latter one is referred as SSG after the author names and is written as:

$$\underline{\underline{\boldsymbol{\Pi}}}^s \simeq -\mathcal{C}_1 \frac{\epsilon}{k}\underline{\underline{\boldsymbol{a}}} + C_1' \frac{\epsilon}{k^2}\left(\underline{\underline{\boldsymbol{a}}} \cdot \underline{\underline{\boldsymbol{a}}} - \frac{1}{3}\mathrm{tr}(\underline{\underline{\boldsymbol{a}}}^2)\underline{\underline{\boldsymbol{I}}}\right), \tag{1.174}$$

where $\underline{\underline{\boldsymbol{a}}}$ is the dimensionless anisotropy tensor defined as:

$$a_{ij} = \frac{\overline{u_i u_j}}{k} - \frac{2}{3}\delta_{ij}, \tag{1.175}$$

and $\underline{\underline{\boldsymbol{\Pi}}}^r$ is given by:

$$\begin{aligned} \underline{\underline{\boldsymbol{\Pi}}}^r \simeq & -\mathcal{C}_2' \frac{1}{k}\mathcal{P}\underline{\underline{\boldsymbol{a}}} + \left(\mathcal{C}_3 - \mathcal{C}_3'\sqrt{\mathrm{tr}(\underline{\underline{\boldsymbol{a}}}^2)}\right)k\underline{\underline{\boldsymbol{S}}} \\ & + \mathcal{C}_4\left(\underline{\underline{\boldsymbol{a}}} \cdot \underline{\underline{\boldsymbol{S}}} + \underline{\underline{\boldsymbol{S}}} \cdot \underline{\underline{\boldsymbol{a}}} - \frac{2}{3}\mathrm{tr}(\underline{\underline{\boldsymbol{a}}} \cdot \underline{\underline{\boldsymbol{S}}})\underline{\underline{\boldsymbol{I}}}\right) + \mathcal{C}_5 k\left(\underline{\underline{\boldsymbol{a}}} \cdot \underline{\underline{\boldsymbol{\omega}}} - \underline{\underline{\boldsymbol{\omega}}} \cdot \underline{\underline{\boldsymbol{a}}}\right), \end{aligned} \tag{1.176}$$

where $\underline{\underline{\boldsymbol{\omega}}} = \underline{\underline{\mathbf{grad}}}(\underline{\boldsymbol{u}}) - \underline{\underline{\boldsymbol{S}}}$ is the rotation tensor corresponding to the anti-symmetric part of the velocity gradient. The standard constants of this model are represented in Table 1.3.

$\mathcal{C}_1$	$\mathcal{C}_1'$	$\mathcal{C}_2'$	$\mathcal{C}_3$	$\mathcal{C}_3'$	$\mathcal{C}_4$	$\mathcal{C}_5$
1.7	-1.05	0.9	0.8	0.65	0.625	0.2

Table 1.3: SSG constants after Speziale et al. [1991].

Remark 1.3.3. Note that the effect of the Coriolis pseudo-force on the pressure-strain correlation is not presented here as it will not be considered in this study. Yet it is possible to take it into account by adding specific additional term in the slow pressure-strain component (see e.g. [Hanjalić and Launder, 2022, Chapter 4.5]).

$\underline{\underline{\boldsymbol{\Pi}}}^{\mathcal{G},}$: Quite similarly to the isotropisation by shear production of the LRR-IP model, Launder [1975] proposed to write the thermal contribution of the pressure-strain correlation as a term of isotropisation of the buoyancy:

$$\Pi_{ij}^{\mathcal{G},} \simeq \mathcal{C}_{\mathcal{G}}(\mathcal{G}_{ij} - \frac{2}{3}\mathcal{G}), \tag{1.177}$$

where we consider $\mathcal{C}_{\mathcal{G}} = 0.55$.

Dissipation

As discussed in Paragraph 1.2.1.2.1, the dissipation takes place in the lower scale of turbulence where the turbulence may be considered isotropic without memory of the large-scale turbulence. It is thus currently assumed that the dissipation term is isotropic:

$$\epsilon_{ij} = 2\nu\overline{\frac{\partial u_i}{\partial x_k}\frac{\partial u_j}{\partial x_k}} \simeq \frac{2}{3}\epsilon\delta ij \tag{1.178}$$

where the dissipation rate has to be transported. Let us note that models with non-isotropic dissipation do exist (see e.g.Rotta [1951]). This anisotropy is caused by the perturbation of the energy cascade. Its effects are noticeable mostly in the close vicinity of obstacles in a region where the Reynolds number can no longer be considered high enough for the viscous effects to be neglected. Such situations are out of the scope of the present work and will not be considered. The transport equation of the dissipation rate remains similar to the one used in the $k-\epsilon$ model. However, as the production is explicitly described, $\nu_t S^2$ is replaced by $\mathcal{P} = \frac{1}{2}\mathrm{tr}(\underline{\underline{\boldsymbol{\mathcal{P}}}})$ and $g_i \frac{\nu_t}{\sigma_\rho}\frac{\partial \overline{\rho}}{\partial x_i}$ by $\mathcal{G} = \frac{1}{2}\mathrm{tr}(\underline{\underline{\boldsymbol{\mathcal{G}}}})$ in coherence with the choice of closure made for $\underline{\underline{\boldsymbol{\mathcal{G}}}}$.

Potential Temperature Variance

In this equation, there is no redistribution term stemming from the pressure fluctuations as pressure does not appear in the potential temperature equation. Only the diffusion term and the dissipation term should be modelled. As previously, the former one can be modelled either using a SGDH methods or a GGDH one using the same constant as for the Reynolds tensor. Theoretically speaking, more physical information are provided by considering a transport equation on the dissipation of potential temperature variance $\epsilon_{\overline{\theta^2}}^{\ddagger}$ as advised by for example by Newman et al. [1981] or by Elghobashi and Launder [1983]. Yet, a commonly used assumption coherent with Kolmogorov theory is to consider the thermal and dynamical timescales proportional:

$$\frac{\mathcal{T}_k}{\mathcal{T}_{\overline{\theta^2}}} \simeq \frac{\epsilon_{\overline{\theta^2}}}{\overline{\theta^2}}\frac{k}{\epsilon} \simeq 2\mathcal{C}_\Theta, \tag{1.179}$$

where $\mathcal{C}_\Theta$ is a constant which may vary from one scalar to another and may also be flow dependent (see Rodi [2000], Hanjalić and Launder [2022]). The presence of a factor two will be justified in Paragraph 1.3.3.2.3. The value considered for this constant will be further discussed in Section 5.1.

1.3.2.2.2 Direct Flux Modelling

Similarly to the Reynolds tensor, some terms such as the diffusion, the scrambling and the buoyancy terms have to be modelled. However, let us notice that for symmetry reason it is possible to assume that the dissipation of this quantity is null, for high Reynolds number flows (see discussion in Paragraph 1.2.1.2.2).

Diffusion

As we consider only high Reynolds flows the diffusion by thermal diffusivity and viscosity will be neglected. Here again, the diffusion by fluctuations of pressure can be neglected or modelled with the diffusion by fluctuating velocity which is equivalent from a numerical point of view. The latter one can be model either using a Shir model or a Daly-Harlow one:

Shir: It consists in using a SGDH of the diffusion as:

$$\mathcal{D}_{\Theta_i} = -\frac{\partial \overline{u_i u_j \theta}}{\partial x_j} \simeq \frac{\partial}{\partial x_j}\left(\mathcal{C}_\theta^{\mathcal{D}} \frac{k^2}{\epsilon} \frac{\partial \overline{u_i \theta}}{\partial x_j}\right). \tag{1.180}$$

with $\mathcal{C}_\theta^{\mathcal{D}} = 0.31$.

Daly-Harlow: It consists in using a GGDH of the diffusion as:

$$\mathcal{D}_{\Theta_i} = -\frac{\partial \overline{u_i u_j \theta}}{\partial x_j} \simeq \frac{\partial}{\partial x_j}\left(\mathcal{C}_\theta^{\mathcal{D}} \overline{u_j u_k} \frac{k}{\epsilon} \frac{\partial \overline{u_i \theta}}{\partial x_k}\right). \tag{1.181}$$

with $\mathcal{C}_\theta^{\mathcal{D}} = 0.31$.

As for the Reynolds tensor, in this work, the Shir model will be considered to limit numerical error.

Production by Buoyancy

Using DFM models, it is current to transport also the variance of thermal quantities in our case the variance of potential temperature. Thus, the production of turbulent heat fluxes by buoyancy can simply be written under Boussinesq approximation as:

$$\mathcal{G}_{\Theta_i} = \frac{g_i}{\rho} \overline{\rho' \mathrm{T}'} \simeq g \beta_0 \overline{\theta^2} \delta_{iz}, \tag{1.182}$$

Scrambling

This term is quite similar to the pressure-correlation term and different models have been developed:

Monin Similarly to the assumption made by Rotta for the Reynolds tensor, Monin proposed to model the scrambling term considering only the slow term as:

$$\Pi_{\Theta_i} = \overline{\frac{p}{\rho} \frac{\partial \theta}{\partial x_i}} \simeq \Pi_{\Theta_i}^s \simeq -\mathcal{C}_{\theta 1} \frac{\epsilon}{k} \overline{u_i \theta}, \tag{1.183}$$

with $\mathcal{C}_{\theta 1} = 4.15$. This value will be discussed in Paragraph 5.1.1.3.3 when considering a Rotta-Monin modelling redistribution terms induced by the fluctuations of pressure.

Lin. model Launder [1975] proposed a modelling of the scrambling linear in the term appearing in the turbulent flux equations. It can be written as term such as:

$$\Pi_{\Theta_i} \simeq -\mathcal{C}_{\theta 1} \frac{\epsilon}{k} \overline{u_i \theta} - \mathcal{C}_{\theta 2} \mathcal{P}_{\Theta_i}^U - \mathcal{C}'_{\theta 2} \mathcal{P}_{\Theta_i}^\Theta - \mathcal{C}_{\theta 3} \mathcal{G}_{\Theta_i} \tag{1.184a}$$

$$\simeq -\mathcal{C}_{\theta 1} \frac{\epsilon}{k} \overline{u_i \theta} + \mathcal{C}_{\theta 2} \overline{u_j \theta} \frac{\partial \overline{U_i}}{\partial x_j} + \mathcal{C}'_{\theta 2} \overline{u_i u_j} \frac{\partial \overline{\Theta}}{\partial x_j} + \mathcal{C}_{\theta 3} g_i \beta_0 \overline{\theta^2}. \tag{1.184b}$$

This approach is coherent with the LRR-IP modelling also linear in the terms appearing in the Reynolds tensor equation. It results that together they correspond to a linear modelling of the pressure induced redistributive terms referred in this work as LRR-L model whose considered set of constants is provided in Table 1.4. Note that *a priori* $\mathcal{C}'_{\theta 2}$ should be null as the pressure term does not appear explicitly in the temperature equation.

$\mathcal{C}_R$	$\mathcal{C}_\mathcal{P}$	$\mathcal{C}_\mathcal{G}$	$\mathcal{C}_{\theta 1}$	$\mathcal{C}_{\theta 2}$	$\mathcal{C}'_{\theta 2}$	$\mathcal{C}'_{\theta 3}$	$\mathcal{C}_\Theta$
1.8	0.6	0.55	4.15	0.55	0.	0.5	0.625

Table 1.4: LRR-L (LRR-IP/isotropisation of the scrambling terms) constants considered see Saturne [2023].

Let us note that other models, for example non-linear ones, exist (see e.g. Kenjereš et al. [2005]) but will not be considered in this study.

Remark 1.3.4. If one wants to go closer to the wall, it is necessary to use model valid for low Reynolds number flows. In such models, it is necessary to take explicitly into account viscous and wall echo effects. To treat the latter ones, it is then necessary to use elliptic blending near the wall. The corresponding second-order methods are then referred as elliptic-blending Reynolds-stress model (EB-RSM) for the Reynolds tensor and elliptic-blending direct fluxes model (EB-DFM) which are out of the scope of the present work, interested reader may refer to Pope [2000], Dehoux [2012], Hanjalić and Launder [2022].

1.3.3 Presentation of the PDF Approach

This section presents a brief background on Lagrangian stochastic methods or PDF methods used to model turbulent flows. There is now a rather wide literature dedicated to presenting the PDF approach both for single-phase (see Pope [1985, 2000], Haworth [2010]) as well as for disperse two-phase flows (see Minier and Peirano [2001], Minier [2015, 2016]), so that only key points are recalled below.

As indicated by their name, these methods correspond to a statistical description which aims at modelling the PDF of a number of selected variables of interest for a given turbulent flow. The philosophy of Lagrangian stochastic methods is to transport explicitly the slow varying terms while considering a statistical treatment for the fast-varying processes treated as stochastic terms. To determine which process are fast-varying ones, one can assert if the value of their auto-correlation functions over the observation timescale is negligible. Using a Lagrangian formulation to model and simulate such flows means that we are tracking the evolution of a large number of numerical or notional stochastic particles in the computational domain. The instantaneous variables attached to these particles make up the particle state vector and each particle can then be seen as an independent realisation, or sample, of the corresponding PDF. We will first briefly introduce some mathematical features associated to these methods in Section 1.3.3.1. The modelling of turbulent flows using such methods is then presented in Section 1.3.3.2. Finally, an overview of their numerical implementation is put forward in Section 1.3.3.3.

1.3.3.1 Lagrangian Stochastic Mathematical Context

The present work aims at presenting salient mathematical elements necessary to understand the notions raised when considering Lagrangian stochastic methods. So as to avoid being mathematically too involved and to remain as brief as possible, no proof will be given to the point presented and some definitions will not be rigorously given using a mathematical formulation. The interested reader may refer to Arnold [1974] and to Øksendal [1995] for a precise mathematical description or to Gardiner [1985], Öttinger [1996], Sabelfeld [2012] for a more physics-oriented approach. Note that the points presented are present in the fundamental work of Pope [1985].

Diffusion Process

We aim at modelling the evolution of particles which will depend partly on deterministic terms and partly on stochastic terms stemming from the statistical treatment of fast-varying processes. Such differential equations composed of a deterministic part and stochastic process, i.e., a random variable evolving in time, are referred as stochastic differential equations (SDE). For reasons discussed at length in several works such as Pope [1985, 2000], Minier and Peirano [2001], Minier [2016], there are strong physical arguments, based on the Kolmogorov theory, to suggest to model the time evolution of the particle state vector by a general stochastic diffusion. As further addressed by Gardiner [1985] and Öttinger [1996], this means that the increments of the state vector $\underline{\boldsymbol{\mathcal{Z}}}(t)$ composed of all the transported instantaneous quantities, over a small time increments $\mathrm{d}t$ have the form:

$$\mathrm{d}\underline{\boldsymbol{\mathcal{Z}}} = \underbrace{\underline{\boldsymbol{\mathcal{A}}}\left(\underline{\boldsymbol{\mathcal{Z}}}(t), \langle \mathscr{F}\left(\underline{\boldsymbol{\mathcal{Z}}}(t)\right)\rangle; t\right)\mathrm{d}t}_{\text{Deterministic Part}} + \underbrace{\underline{\underline{\boldsymbol{\mathcal{B}}}}\left(\underline{\boldsymbol{\mathcal{Z}}}(t), \langle \mathscr{G}\left(\underline{\boldsymbol{\mathcal{Z}}}(t)\right)\rangle; t\right)\mathrm{d}\underline{\boldsymbol{\mathcal{W}}}}_{\text{Stochastic Part}}. \tag{1.185}$$

The RHS of Eq. (1.185) involves two terms having different physical meanings. On the one hand, the deterministic term in factor of the time increments is specified through the drift vector $\underline{\boldsymbol{\mathcal{A}}}$ which governs the linear-in-$\mathrm{d}t$ evolution of the conditional mean increments of $\mathrm{d}\underline{\boldsymbol{\mathcal{Z}}}$. On the other hand, the stochastic term in front of the independent Wiener process increments $\mathrm{d}\underline{\boldsymbol{\mathcal{W}}}$, which are presented hereafter, is specified through the diffusion matrix $\underline{\underline{\boldsymbol{\mathcal{B}}}}$ which characterises the linear-in-$\mathrm{d}t$ evolution of the conditional variances around these mean increments. In the drift vector and the diffusion matrix, a possible dependence on mean fields extracted from the PDF, manifested by the terms $\langle \mathscr{F}(\underline{\boldsymbol{\mathcal{Z}}}(t))\rangle$ and $\langle \mathscr{G}(\underline{\boldsymbol{\mathcal{Z}}}(t))\rangle$, is included, where $\langle (.)\rangle$ stands for the averaging operator. This dependence makes Eq. (1.185) a stochastic diffusion process of the McKean type (see Minier [2015, 2016]).

Remark 1.3.5. Note that although it is possible to develop methods in which instantaneous quantities associated to a particle interact explicitly with instantaneous properties associated to the surrounding particles, such methods are not considered here (see Minier [2016]). Indeed, it would require a Kernel function to determine how each particle is interacting with one another and would yield to a computation time in $O(N^2)$ where N is the number of particles. In order to lower this numerical cost, it is assumed that the particles are "weakly interacting" assuming a mean-field approximation. Particles do not interact directly with each other but only through mean fields or 'potential'. In the conceptual limit where an infinite number of particles is tackled or in the more numerically tractable limit where a large number of particles is simulated, one can consider that the particle-to-particle interactions tend towards zero. Thus, each particle is independent from one another. For more information on particle-method implementations and their interactions with a mesh see e.g. Hockney [1966].

Wiener Process

In Eq. (1.185), independent Wiener processes increments are present to model the evolution of the fast variable terms, which by definition are uncorrelated over the observation timescale considered. We will present briefly such processes; more information may be found in Gardiner [1985] or in Öttinger [1996]. The Wiener process belongs to the class of Markov processes which are memoryless random variables often compared to the drunkard march processes. Indeed, the next step or increment is independent of previous ones. Mathematically speaking this property is defined for any Markov process $\mathcal{M}$ by:

$$\mathscr{P}\left(\mathcal{M}^n = \mathscr{M}^n|_{\mathcal{M}^{n-1}=\mathscr{M}^{n-1},\dots,\mathcal{M}^1=\mathscr{M}^1,\mathcal{M}^0=\mathscr{M}^0}\right) = \mathscr{P}\left(\mathcal{M}^n = \mathscr{M}^n|_{\mathcal{M}^{n-1}=\mathscr{M}^{n-1}}\right), \tag{1.186}$$

with $\mathscr{M}^i$ the sample space value of the Markov process $\mathcal{M}^i$ at the time $t = t^i$, $\mathscr{P}\left(\mathcal{M}^n = \mathscr{M}^n\right)$ the probability for the Markov process $\mathcal{M}$ to have the value $\mathscr{M}^n$ at the time $t = t^n$ and $\mathscr{P}\left(\mathcal{M}^n = \mathscr{M}^n|_{\mathcal{M}^{n-1}=\mathscr{M}^{n-1},\dots,\mathcal{M}^1=\mathscr{M}^1,\mathcal{M}^0=\mathscr{M}^0}\right)$, the conditioned probability of $\mathcal{M}$ to have the value $\mathcal{M}^n$ at the time $t = t^n$ knowing the previous values of $\mathcal{M}$ at any previous time t^i. It results from this property that the increments of Markov process $\delta\mathcal{M}^n = \mathcal{M}^n - \mathcal{M}^{n-1}$ are independent of the previous states:

$$\mathscr{P}\left(\delta\mathcal{M}^n = \delta\mathscr{M}^n|_{\mathcal{M}^{n-1}=\mathscr{M}^{n-1},\dots,\mathcal{M}^1=\mathscr{M}^1,\mathcal{M}^0=\mathscr{M}^0}\right) = \mathscr{P}\left(\delta\mathcal{M}^n = \delta\mathscr{M}^n\right). \tag{1.187}$$

The Wiener process $\mathcal{W}$ is a Markov process with continuous trajectories and whose increments $\mathrm{d}\mathcal{W}$ over a small-time increment $\mathrm{d}t$ follow independent Gaussian centred distributions of variance $\mathrm{d}t$. It is selected to account for white-noise effects, as it is the only stochastic process with independent Gaussian increments and continuous trajectories. Yet, although continuous, Wiener process trajectories are highly erratic and even of infinite total variance in any interval (see the illustration in Figure 1.16), implying that they are nowhere differentiable so the classical integration rules cannot be applied. Yet, some useful properties may be considered:

1. Each increment is a Gaussian random variable: $\forall p > 0$ $\langle \mathrm{d}\mathcal{W}_j(t)^{2p+1}\rangle = 0$ for the odd moments, $\langle \mathrm{d}\mathcal{W}_j(t)^2\rangle = \mathrm{d}t$ and $\langle \mathrm{d}\mathcal{W}_j(t)^{2(p+1)}\rangle = o(\mathrm{d}t)$, for the even moments.
2. Increments over small time steps are stationary and independent, $\langle \mathrm{d}\mathcal{W}_j(t)\rangle = 0$, $\forall t$, and $\langle \mathrm{d}\mathcal{W}_j(t)\mathrm{d}\mathcal{W}_j(t')\rangle = 0$, with $t \neq t'$,
3. Trajectories are of unbounded variation in every finite interval.

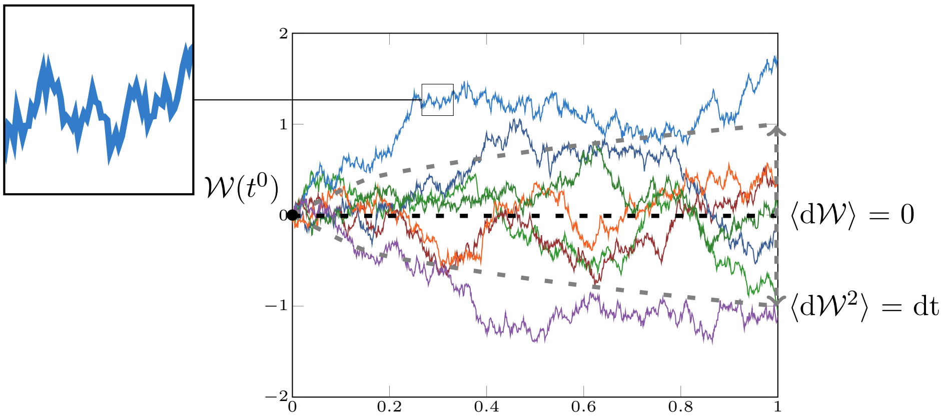

Figure 1.16: Some realisations of a conditional Wiener process, starting from 0 at time $t = 0$.

Duality of Lagrangian Stochastic Methods and PDF Methods

Note that the Lagrangian stochastic methods are often also referred as probability density functions (PDF) methods. For a stochastic process $\mathscr{Z}(t)$ the PDF $\mathscr{p}$ is defined as:

$$\mathscr{p}(\mathscr{X};t)\mathrm{d}\mathscr{X} = \mathscr{P}(\mathscr{X} \leq \mathscr{Z}(t) \leq \mathscr{X} + \mathrm{d}\mathscr{X}), \tag{1.188}$$

where $\mathscr{X}$ is the sample space value of the stochastic process $\mathscr{Z}$. There is a duality between the resolution of Lagrangian stochastic methods and the resolution of the corresponding PDF. It is, indeed, equivalent to resolve the diffusion processes associated to a large number of particles and to resolve the differential equation for the corresponding probability density function $\mathscr{p}_L$:

$$\frac{\partial \mathscr{p}_L}{\partial t} = -\frac{\partial}{\partial \mathscr{Z}_i}\Big(\mathcal{A}_i(\underline{\boldsymbol{\mathscr{Z}}}(t), \langle \mathscr{F}(\underline{\boldsymbol{\mathscr{Z}}}(t))\rangle; t)\ \mathscr{p}_L\Big) + \frac{1}{2}\frac{\partial^2}{\partial \mathscr{Z}_i \partial \mathscr{Z}_j}\left(\widetilde{\mathscr{D}}_{ij}\left(\underline{\boldsymbol{\mathscr{Z}}}(t), \langle \mathscr{G}(\underline{\boldsymbol{\mathscr{Z}}}(t))\rangle; t\right)\ \mathscr{p}_L\right) \tag{1.189}$$

with $\widetilde{\mathscr{D}}_{ij} = B_{il}B_{jl}$. In the case of the "trajectory point of view" where the particle trajectory is followed, each one of these trajectories represents an independent realisation of the stochastic process Eq. (1.185). Let us note that although the whole turbulence might be statistically described and modelled, Lagrangian stochastic methods enable to have access to the whole PDF and not only to some averaged moments. These methods are therefore physically richer than a RANS point of view.

Using Lagrangian stochastic methods, and considering a weak convergence, i.e. we do not consider single specific trajectories but only the statistics extracted from the set of particles, it is in general useful to consider the fine-grained pdf $\tilde{\mathscr{p}}_L$:

$$\tilde{\mathscr{p}}_L(\underline{\boldsymbol{\mathscr{X}}}; t) = \prod_{i=0}^{N_{\underline{\boldsymbol{\mathscr{Z}}}}} \tilde{\delta}(\mathscr{Z}_i(t) - \mathscr{X}_i), \tag{1.190}$$

with $N_{\underline{\boldsymbol{\mathscr{Z}}}}$ the size of $\underline{\boldsymbol{\mathscr{Z}}}$ and $\tilde{\delta}(\mathscr{Z}_i(t) - \mathscr{X}_i)$ the Dirac delta function which is non-null only on the interval $[0, \mathrm{d}\mathscr{X}_i]$ and whose integral equals to one. The estimation of the PDF referred $\mathscr{p}_L^{N_p}$ is often obtained using a Monte-Carlo methods through an ensemble averaged on N_p particles:

$$\mathscr{p}_L(\underline{\boldsymbol{\mathscr{X}}}; t) \simeq \mathscr{p}_L^{N_p}(\underline{\boldsymbol{\mathscr{X}}}; t) = \frac{1}{N_p}\sum_{i=1}^{N_p} \tilde{\mathscr{p}}_L^{(i)}(\underline{\boldsymbol{\mathscr{X}}}; t) = \frac{1}{N_p}\sum_{i=1}^{N_p}\left(\prod_{j=1}^{N_{\underline{\boldsymbol{\mathscr{Z}}}}} \tilde{\delta}\left(\mathscr{Z}_j^{(i)}(t) - \mathscr{X}_j\right)\right), \tag{1.191}$$

with N_p the number of particles used and $\mathscr{Z}_j^{(i)}(t)$ the of the j^{th} component of the stochastic process associated to the particle number i. This result would be exact using an infinite number of particles to estimate this PDF .

Relation between Eulerian and Lagrangian PDF

In the present PDF framework, we are basically handling a two-time one-particle Lagrangian PDF (each particle is treated independently, and its next step depends only on the previous one), from which a one-time one-point Eulerian PDF is derived, allowing moment equations to be extracted in a straightforward manner (see Pope [2000], Minier and Peirano [2001], Minier [2016]). This means that once a stochastic model is written, we obtain directly the corresponding expressions of the discrete Lagrangian $F_L^{N_p}$ and resulting Eulerian $F_E^{N_p}$ mass density functions

(MDF) through:

$$F_L^{N_p}(\underline{\boldsymbol{\mathscr{Z}}}\,;\,t) = \sum_{i=1}^{N_p} \delta m^{(i)} p_L^{(i)}(\underline{\boldsymbol{\mathscr{Z}}};t) \; = \sum_{i=1}^{N_p} \delta m^{(i)} \left(\prod_{j=0}^{N_{\underline{\boldsymbol{\mathcal{Z}}}}} \tilde{\delta}(\mathcal{Z}_j^{(i)}(t) - \mathscr{Z}_j) \right) , \tag{1.192}$$

$$F_E^{N_p}(\underline{\boldsymbol{\mathscr{Z}}}\,;\,t,\underline{\boldsymbol{x}}) = F_L^{N_p}(t\,;\,\underline{\boldsymbol{\mathcal{Y}}} = \underline{\boldsymbol{x}}, \underline{\boldsymbol{\mathscr{Z}}} \setminus \underline{\boldsymbol{\mathcal{Y}}}) \ , \tag{1.193}$$

where δm are the particle mass, $\underline{\boldsymbol{\mathcal{Y}}}_p$ is the sample space values corresponding to the random variables $\underline{\boldsymbol{X}}_p(t)$ and $\underline{\boldsymbol{\mathscr{Z}}} \setminus \underline{\boldsymbol{\mathcal{Y}}}$ is the sample space values corresponding to the random variables $\underline{\boldsymbol{\mathcal{Z}}}(t)$ excluding $\underline{\boldsymbol{X}}_p(t)$. It is then straightforward to derive the field values for the average $\langle \Psi \rangle(t,\underline{\boldsymbol{x}})$ of any particle variable $\Psi(t;\underline{\boldsymbol{\mathscr{Z}}})$,

$$\tilde{\alpha}(t,\underline{\boldsymbol{x}})\,\rho\langle \Psi \rangle(t,\underline{\boldsymbol{x}}) = \int \Psi(\underline{\boldsymbol{\mathscr{Z}}};t) F_E^{N_p}(\underline{\boldsymbol{\mathscr{Z}}} \setminus \underline{\boldsymbol{\mathcal{Y}}}; t, \underline{\boldsymbol{x}})\,\mathrm{d}\,(\underline{\boldsymbol{\mathscr{Z}}} \setminus \underline{\boldsymbol{\mathcal{Y}}}) \ , \tag{1.194}$$

where $\tilde{\alpha}(t,\underline{\boldsymbol{x}})$ is the mean particle volumetric fraction defined through a proper probabilistic normalisation constraint discussed in Minier and Peirano [2001] or in Peirano and Minier [2002]. In a numerical simulation, these theoretical expressions imply that, in a small volume around a given location $\underline{\boldsymbol{x}}$, mean values are estimated as the ensemble averages over the $N_p^{\boldsymbol{x}}$ particles present in that volume, or as Favre averages (or mass-weighted averages)

$$\langle \Psi \rangle(t,\underline{\boldsymbol{x}}) \simeq \frac{\displaystyle\sum_{i=1}^{N_p^{\boldsymbol{x}}} \delta m^{(i)} \Psi(\underline{\boldsymbol{\mathcal{Z}}}^{(i)}(t);t)}{\displaystyle\sum_{i=1}^{N_p^{\boldsymbol{x}}} \delta m^{(i)}} \ . \tag{1.195}$$

Stochastic Integral Definition

Let us note that although using a "PDF point of view" it is possible to write the temporal derivative, it should not be done using the "trajectory point of view". As we have seen the stochastic process $\underline{\boldsymbol{\mathcal{Z}}}(t)$ is not differentiable as the Wiener process is nowhere differentiable. It is true that sometimes the white noise function is defined as the time derivative of the Wiener process, yet this definition is not rigorous and should be avoided. It results that the stochastic equation should be written using an integrated formulation. A few words are in order to properly define the nature of the integrals considered when resolving such SDEs. To that effect, we consider a stochastic diffusion process for a particle state vector $\underline{\boldsymbol{\mathcal{Z}}} = (\mathcal{Z}_i)$ with the most general form Eq. (1.185). This formulation of the SDE is actually a short-hand notation for the proper mathematical expression, which is its integrated version:

$$\mathcal{Z}_i(t) = \mathcal{Z}_i(t^0) + \underbrace{\int_{t^0}^{t} \mathcal{A}_i\Big(\underline{\boldsymbol{\mathcal{Z}}}(s), \mathscr{F}(s,\underline{\boldsymbol{\mathcal{Z}}}(s)); s\Big)\,\mathrm{d}s}_{\text{Deterministic integral}} + \underbrace{\int_{t^0}^{t} \mathcal{B}_{ij}\Big(\underline{\boldsymbol{\mathcal{Z}}}(s), \mathscr{G}(s,\underline{\boldsymbol{\mathcal{Z}}}(s)); s\Big)\,\mathrm{d}\mathcal{W}_j(s)}_{\text{Stochastic integral}} \ . \tag{1.196}$$

On the first hand, the deterministic integral is defined in a classic Riemann sense, i.e using a partition with sub-intervals $[t^k\,;\,t^{k+1}]$, for $k = 1,\ldots,N$, of the interval $[t^0\,;\,t]$, it is defined as:

$$\int_{t^0}^{t} \mathcal{A}_i\Big(\underline{\boldsymbol{\mathcal{Z}}}(s), \mathscr{F}(s,\underline{\boldsymbol{\mathcal{Z}}}(s);s)\Big)\mathrm{d}s = \lim_{N\to+\infty} \sum_{k=0}^{N} \mathcal{A}_i\Big(\underline{\boldsymbol{\mathcal{Z}}}(\tau^k), \mathscr{F}(\tau^k,\underline{\boldsymbol{\mathcal{Z}}}(\tau^k)); \tau^k\Big)\,\Big(t^{k+1} - t^k\Big) \tag{1.197}$$

whose results is independent of the value of $\tau^k \in [t^k, t^{k+1}]$.

On the other hand, the second integration is performed with the stochastic variable and requires a strict mathematical treatment. Indeed, the previous definition can no longer be applied for the stochastic integrals due to the unbounded variation on all intervals. Thus, for the stochastic integral, the result obtained depends on the value considered for τ_k. We will consider Itô definition yielding to non-anticipating process taking $\tau^k = t^k$. Keeping the same partition as previously, the integral is defined by:

$$\int_{t0}^{t} \mathcal{B}_{ij}\left(\underline{\boldsymbol{\mathcal{Z}}}(s), \mathscr{G}(s, \underline{\boldsymbol{\mathcal{Z}}}(s)); s\right) \mathrm{d}\mathcal{W}_{s,j} = \text{ms-}\lim_{N\to\infty} \sum_{k=1}^{N} \mathcal{B}_{ij}\left(\underline{\boldsymbol{\mathcal{Z}}}(t^k), \mathscr{G}(t^k, \underline{\boldsymbol{\mathcal{Z}}}(t^k)); t^k\right) \left(\mathrm{d}\mathcal{W}_j(t^{k+1}) - \mathrm{d}\mathcal{W}_j(t^k)\right) , \tag{1.198}$$

where the limit must be understood as a limit in the mean-square sense (since a convergence trajectory by trajectory is not possible). The choice of this definition implies that the ordinary rules of differential calculus are no longer respected. Indeed, due to the presence of a stochastic term $\mathrm{d}\mathcal{W}$ scaling as $\sqrt{t}$, using Itô calculus, it is necessary to expand the differential to the second-order term. We have then for any smooth function $\Psi(\underline{\boldsymbol{\mathcal{Z}}}(t); t)$ (vector indexes and functional dependencies are left out here, for the sake of keeping simple notations)

$$\mathrm{d}\Psi(\underline{\boldsymbol{\mathcal{Z}}}(t); t) = \frac{\partial \Psi}{\partial t}(\underline{\boldsymbol{\mathcal{Z}}}(t); t)\mathrm{d}t + \frac{\partial \Psi}{\partial \mathcal{Z}_i}(\underline{\boldsymbol{\mathcal{Z}}}(t); t)\mathrm{d}\mathcal{Z}_i + \frac{1}{2}\frac{\partial^2 \Psi}{\partial \mathcal{Z}_i \partial \mathcal{Z}_j}(\underline{\boldsymbol{\mathcal{Z}}}(t); t)\widetilde{\mathscr{D}}_{ij}(\underline{\boldsymbol{\mathcal{Z}}}(t); t)\mathrm{d}t \tag{1.199}$$

This necessity to introduce new differential rules is offset by the respect of two fundamental properties. For any smooth-enough functions Φ and Ψ, zero mean property and the isometry properties states that:

$$\begin{cases} \left\langle \displaystyle\int_{t^0}^{t} \Phi(\underline{\boldsymbol{\mathcal{Z}}}(s))\mathrm{d}\mathcal{W}(s) \right\rangle & = 0 \; , \\ \left\langle \left(\displaystyle\int_{t^0}^{t^2} \Phi(\underline{\boldsymbol{\mathcal{Z}}}(u))\mathrm{d}\mathcal{W}(u)\right) \left(\displaystyle\int_{t^1}^{t^3} \Psi(\underline{\boldsymbol{\mathcal{Z}}}(v))\mathrm{d}\mathcal{W}(v)\right) \right\rangle & = \int_{t^1}^{t2} \langle \Phi(\underline{\boldsymbol{\mathcal{Z}}}(s))\Psi(\underline{\boldsymbol{\mathcal{Z}}}(s))\rangle \mathrm{d}s \; , \; t^0 \le t^1 \le t^2 \le t^3 \; . \end{cases} \tag{1.200}$$

A key consequence of the non-anticipation nature of the definition of the stochastic integrals is that the mean conditional increment of the stochastic process $\underline{\boldsymbol{\mathcal{Z}}}$ in Eq. (1.185) over a small time increment Δt is governed only by the drift term, which means that we have

$$\langle \Delta \mathcal{Z}_i \,|\, \underline{\boldsymbol{\mathcal{Z}}}(t^0) = \underline{\boldsymbol{\mathscr{Z}}}^0 \rangle \simeq \mathcal{A}_i(\underline{\boldsymbol{\mathscr{Z}}}^0, \mathscr{F}(t^0, \underline{\boldsymbol{\mathscr{Z}}}^0), t^0)\, \Delta t \; . \tag{1.201}$$

These relations play a central role in the development of the new algorithm in Chapter 2.

Remark 1.3.6. It is worth noticing that a second definition of the stochastic integral can be found in the literature. It corresponds to the Stratonovich interpretation denoted by $\circ$ in which the value τ_k corresponds to the middle point $0.5(t^k + t^{k+1})$.

$$\int_{t_0}^{t} \mathcal{B}_{ij}(\underline{\boldsymbol{\mathcal{Z}}}(s); s) \circ \mathrm{d}\mathcal{W}_j(s) \lim_{N\to+\infty} \sum_{i=0}^{n} \frac{1}{2}\left(\mathcal{B}_{ij}(\underline{\boldsymbol{\mathcal{Z}}}(t^k); t^k) + \mathcal{B}_{ij}(\underline{\boldsymbol{\mathcal{Z}}}(t^{k+1}); t^{k+1})\right)(\mathcal{W}(t^{k+1}) - \mathcal{W}(t^k)). \tag{1.202}$$

The main advantage of this definition is that the ordinary differential rules hold, however, the zero mean and isometry properties of Itô calculus Section 1.3.3.1 don't. It is important to keep in mind that the behaviour of stochastic integrals depending on the definition considered, the consistency of the model and the derivation of the numerical scheme used also depend on this definition. As presented for example by Arnold [1974] and Øksendal [1995]), there is an equivalence between the equation Eq. (1.203) written in the Stratonovich's sense:

$$\mathrm{d}\mathcal{Z}_i = \mathcal{A}_i \mathrm{d}t + \mathcal{B}_{ij} \circ \mathrm{d}\mathcal{W}_j . \tag{1.203}$$

and the following equation written in Itô's sense:

$$\mathrm{d}\mathcal{Z}_i = \left(\mathcal{A}_i + B_{kj} \frac{\partial \mathcal{B}_{ij}}{\partial z_k} \right) \mathrm{d}t + \mathcal{B}_{ij} \mathrm{d}\mathcal{W}_j . \tag{1.204}$$

1.3.3.2 Turbulent Flow Modelling using Lagrangian Stochastic Methods

Now that we have briefly described mathematical properties associated to Lagrangian stochastic methods, let us see how they can be applied on turbulent flows.

1.3.3.2.1 Presentation with Inertial Particles

Disperse turbulent two-phase flows involve discrete elements, or 'particles', transported by turbulent fluid flows. For the sake of simplicity, we first focus on particle dynamics while leaving out thermal effects, changes in the particle radius or mass, and particle collision effects. We consider the particle-attached variables making up the particle state-vector $\underline{\boldsymbol{\mathcal{Z}}}_p$. Here, the state vector is taken equal to $\underline{\boldsymbol{\mathcal{Z}}}_p = (\underline{\boldsymbol{X}}_p, \underline{\boldsymbol{U}}_p, \underline{\boldsymbol{U}}_s)$, with $\underline{\boldsymbol{X}}_p$ the particle position, $\underline{\boldsymbol{U}}_p$ its velocity and $\underline{\boldsymbol{U}}_s$ the velocity of the fluid seen. The system of SDEs is

$$\mathrm{d}X_{p,i} = U_{p,i}\, \mathrm{d}t \ , \tag{1.205a}$$

$$\mathrm{d}U_{p,i} = \left(\underbrace{\frac{U_{s,i} - U_{p,i}}{\tau_p}}_{\text{Drag}} + \underbrace{\frac{\rho_p - \rho}{\rho_p}\, g_i}_{\text{Gravity}} + \underbrace{\frac{\rho}{2\rho_p} (\mathrm{d}U_{s,i} - \mathrm{d}U_{p,i})}_{\text{Added mass}} + \underbrace{\frac{\rho}{\rho_p} \mathrm{d}U_{s,i}}_{\text{Pressure}} + \underbrace{\mathcal{F}_{p,i}}_{\text{Other forces}} \right) \mathrm{d}t \ , \tag{1.205b}$$

$$\mathrm{d}U_{s,i} = (\text{stochastic model}) \ . \tag{1.205c}$$

In Eqs 1.205, the velocity of the fluid seen $\underline{\boldsymbol{U}}_s$ is defined as the instantaneous fluid velocity sampled at the particle location, $\underline{\boldsymbol{U}}_s(t) = \underline{\boldsymbol{U}}(t, \underline{\boldsymbol{X}}_p(t))$ where $\underline{\boldsymbol{U}}(t, \underline{\boldsymbol{X}})$ is the fluid velocity field. Note that, for discrete particles in non-fully resolved turbulent flows, the velocity of the fluid seen cannot be obtained from the reduced information available on the fluid velocity field (typically, its first and second moments). This means that $\underline{\boldsymbol{U}}_s$ needs to be introduced as a separate particle-attached variable (see comprehensive discussions in Minier and Peirano [2001], Minier [2015, 2016]). On the right-hand side (RHS) of Eq. (1.205b) we have ρ and ρ_p respectively the fluid and particle densities. It is seen that $\underline{\boldsymbol{U}}_s$ enters the expression of different forces while the term $\mathcal{F}_p$ contains possible additional forces acting on discrete particles (such as electromagnetic or Basset forces). The drag force is expressed in terms of the particle relaxation timescale τ_p, defined as:

$$\tau_p = \frac{\rho_p}{\rho} \frac{4\, d_p}{3\, C_D |\, \underline{\boldsymbol{U}}_s - \underline{\boldsymbol{U}}_p \,|} \ , \tag{1.206}$$

with d_p the particle diameter and C_D the drag coefficient. This timescale represents the typical time over which particle velocities adjust to the local fluid velocity seen and is a measure of particle inertia. In the Stokes regime, valid when $Re_p \leq 1$ (with Re_p the particle Reynolds number defined by $Re_p = |\underline{\boldsymbol{U}}_r| d_p/\nu$, with $\underline{\boldsymbol{U}}_r = \underline{\boldsymbol{U}}_s - \underline{\boldsymbol{U}}_p$), the drag coefficient is $\mathrm{c}_D = 24/Re_p$. In that case, the particle relaxation timescale is given by the Stokes formula:

$$\mathcal{T}_p = \frac{\rho_p}{\rho} \frac{d_p^2}{18\nu_f}. \tag{1.207}$$

For general values of Re_p, the drag coefficient is obtained through empirical correlations such as proposed by Clift et al. [2005] or by Brennen [2005]

$$\mathrm{c}_D = \begin{cases} \dfrac{24}{Re_p}\left[1 + 0.15 Re_p^{0.687}\right] & \text{if } Re_p \leq 1000, \\ 0.44 & \text{if } Re_p \geq 1000. \end{cases} \tag{1.208}$$

In the general case, two limit situations are often encountered when dealing with flows containing physical particles. The first limit is the dense particle limit $\rho_p \gg \rho$ which enables to consider that the only forces acting on the particles are the drag and the gravity force. The second limit case encountered is the fluid particle limit encountered when the inertial relaxation times $\mathcal{T}_p$ tends towards zero. In this case, the equation Eq. (1.205b) imposes $\underline{\boldsymbol{U}}_s = \underline{\boldsymbol{U}}_p$ and one may consider only one velocity associated to the particles. We will place ourselves in this limit case for the following of this work.

Remark 1.3.7. Let us note that in the general case the external forces induce a mean drift between the discrete particles and the fluid around them. This results in separation of trajectories between fluid particles and discrete particles originally at the same location. This trajectory splitting triggers a decorrelation between the velocity seen at the new position of particles and the velocity of the fluid particles originated from the same point. This phenomenon is referred as crossing-trajectory effects. Because of this effect, when considering discrete particles, the modelling of the velocity seen differs from the modelling of fluid particles and requires a specific extension. Such effects and the corresponding extension of modelling are out of the scope of the present work, but the interested reader may refer to Pozorski and Minier [1998], Minier and Peirano [2001], Minier et al. [2004, 2014], Minier [2015].

1.3.3.2.2 Modelling of the Instantaneous Quantities Associated to the Particles

Choice of the State Vector

From now on, we will focus on the treatment of fluid particles. Moreover, the scope selected in this work is limited to high Reynolds number flows with an observation timescale δt which rely in the inertial sub-range ($\mathcal{T}_\eta \ll \delta t \lessapprox T_L$). Such a choice enables to have a proper description of local effects with a tractable cost for atmospheric flows. Because of the selected observation timescale, the acceleration can be treated as being a fast-varying variable according to Kolmogorov theory. Indeed, as discussed in Paragraph 1.2.1.2.1, the corresponding autocorrelation timescale is of the order of the Kolmogorov timescale. Moreover, as the observation timescale is smaller or of the same order than the velocity integral time, the latter will be treated as a stochastic process. This choice of description where the velocity is explicitly considered and modelled with a SDE corresponds to the Langevin point of view, first presented in the fundamental work on dispersion of Langevin [1908]. As we consider Lagrangian methods with a Langevin point of view, the particle state vector does include particle location and velocity as well as extra variables $\underline{\boldsymbol{Z}}'$ such as we have $\underline{\boldsymbol{\mathcal{Z}}} = (\underline{\boldsymbol{X}}, \underline{\boldsymbol{U}}, \underline{\boldsymbol{Z}}')$. Note that the statistical weight of a particle evolves with its mass and so the particle mass should be an explicit property associated to the state vector. However, in our case we will consider that all particles represent the same mass and that the latter one remains constant over particles trajectories. It is then not necessary to explicitly transport the particle mass and one can remove it from the particle state vector. For now, we will add the potential temperature in the state vector ($\mathscr{Z}' = \Theta$) to present its modelling. Note that Chapter 2 and Chapter 3 focusing on the dynamics, only the position and velocity will be treated ($\mathscr{Z}' = \emptyset$). In Chapter 4 a fictitious concentration is added in the state vector $\mathscr{Z}' = \widetilde{C}$ to treat concentration variance. It will be modelled similarly to the potential temperature considered in Chapter 5 to treat stability effects.

Remark 1.3.8. The selection of an observation timescale is a choice of the modeler. Methods where it is close to Kolmogorov scale do exist (see e.g. Reynolds [2003, 2004], Innocenti et al. [2020]). In this case the acceleration is not modelled as a fast-varying term but explicitly treated as a stochastic process. At the contrary, in the case where we consider an observation timescale great compared to the velocity timescale, it would be possible to treat the velocity as a fast-varying term and the position would be treated explicitly using a diffusion process. This corresponds to Einstein point of view named after its work on Brownian movement (see Einstein [1905]) where he first proposed a random-walk model.

Modelling of the Langevin Process

Once the state vector is defined, a diffusion process is fully characterised by the selection of the corresponding drift vector $\underline{\boldsymbol{\mathcal{A}}}$ and diffusion matrix $\underline{\underline{\underline{\boldsymbol{B}}}}$.

GLM For reasons exhaustively presented in numerous works (see Pope [1985], Haworth and Pope [1986], Pope [1994b, 2000], Minier and Pozorski [1997], Minier and Peirano [2001]), the instantaneous fluid velocity may be modelled using a Generalised Langevin Model (GLM) as:

$$\mathrm{d}U_i = -\frac{1}{\rho}\frac{\partial \langle P \rangle}{\partial x_i}\,\mathrm{d}t + (1-\beta_0(\Theta-\Theta_0))g_i\mathrm{d}t + G_{ij}\left(U_j - \langle U_j \rangle\right)\mathrm{d}t + \sqrt{\tilde{\mathcal{C}}_0 \epsilon \delta_{ij}}\,\mathrm{d}\mathcal{W}_j \ , \quad (1.209)$$

The RHS of Eq. (1.209) involves several mean field values, including the turbulent dissipation rate ϵ, the GLM relaxation tensor $\underline{\underline{\boldsymbol{G}}}$ the diffusion function $\tilde{\mathcal{C}}_0$. Even though the explicit dependency on the location has been removed for clarity issue, all these mean fields are to be evaluated locally in the vicinity of the particle. Note that this model is not closed as it requires to have a specification of the dissipation rate. Stand-alone methods within which the dissipation rate or turbulent frequency is added to the state vector and modelled with a stochastic process exist as studied by Pope [1985, 2000] but are not considered here. From now on, let us assume that the dissipation rate is provided by an external source. The first two RHS terms correspond respectively to the mean pressure gradient effects and buoyant effects treated with a Boussinesq approximation and are treated without further modelling. The two following terms encapsulate the choice of a specific GLM model which is entirely defined by the selection of a given value for the tensor $\underline{\underline{\boldsymbol{G}}}$ and the function $\tilde{\mathcal{C}}_0$. The latter may *a priori* depend on the Reynolds tensor, on the dissipation rate and on the mean velocity gradient but not on the mean velocity itself. Furthermore, $\tilde{\mathcal{C}}_0$ is a function which tends towards a constant $\mathcal{C}_0$ named the Kolmogorov constant for isotropic and uniform flows. Indeed, the shape of the diffusion matrix is derived in agreement with Kolmogorov [1941, 1962] theory, in order to retrieve the proper Lagrangian structure functions Eq. (1.52) for isotropic uniform turbulence:

$$\mathscr{D}_{ij}(\mathrm{d}t) = \langle (\mathrm{d}U_i \mathrm{d}U_j \rangle \simeq \widetilde{\mathscr{D}}_{ij}\mathrm{d}t = \mathcal{B}_{ik}\mathcal{B}_{jk}\mathrm{d}t = \mathcal{C}_0 \epsilon \delta_{ij}\mathrm{d}t \quad (1.210)$$

which is similar to the theoretical result presented in Eq. (1.54). The two modelled terms of Eq. (1.209) have a zero average and aim at modelling the redistribution and dissipation terms. As the trace of the redistribution term is null, we have:

$$G_{ik}\langle u_i u_k\rangle + \frac{3}{2}\tilde{\mathcal{C}}_0\epsilon = -\epsilon. \tag{1.211}$$

This equation stems from of transport equation of the second-order moments Eqs 1.221 associated to this model and presented hereafter. Decomposing the GLM tensor into its isotropic relaxation time and its anisotropic part as $\underline{\underline{\boldsymbol{G}}} = -T_L^{-1}\underline{\underline{\mathbf{1}}} + \underline{\underline{\boldsymbol{G}^*}}$, we get:

$$-2\frac{k}{T_L} + G^*_{ik}\langle u_i u_k\rangle + (1 + \frac{3}{2}\tilde{\mathcal{C}}_0)\epsilon = 0. \tag{1.212}$$

The respect of this relation enables to associate each GLM model to a consistent DRSM model as explained by Pope [1994b].

SLM In the present work, the evolution of the particle velocity is modelled with the simplified Langevin model (SLM) which, as indicated by its name, is the simplest formulation for a model belonging in the GLM class. It consists of taking the anisotropic part of the GLM tensor $\underline{\underline{\boldsymbol{G}^*}}$ null and $\tilde{\mathcal{C}}_0$ constant. The value of the latter is taken to 3.5 to obtain a proper production of TKE near the wall as proposed by Minier and Pozorski [1999]. In this model, it is assumed that the Lagrangian autocorrelation function $\mathscr{R}_L$ evolves exponentially as $\mathscr{R}_L(s) = \exp\left(-\frac{s}{T_L}\right)$, where the Lagrangian timescale modelling can be derived from Eq. (1.212) as:

$$T_L = \left(\frac{1}{\frac{1}{2} + \frac{3}{4}\mathcal{C}_0}\right)\frac{k}{\epsilon} = \frac{1}{\mathcal{C}_L}\frac{k}{\epsilon}\ , \tag{1.213}$$

The instantaneous velocity equation is then expressed as:

$$\mathrm{d}U_i = -\frac{1}{\rho}\frac{\partial\langle P\rangle}{\partial x_i}\,\mathrm{d}t + (1 - \beta_0(\Theta - \Theta_0))g_i\mathrm{d}t - \frac{U_i - \langle U_i\rangle}{T_L}\mathrm{d}t + \sqrt{\mathcal{C}_0\epsilon\delta_{ij}}\,\mathrm{d}\mathcal{W}_j\ . \tag{1.214}$$

The equation is the reference equation used throughout this work.

Remark 1.3.9. Note that a second approach is often used in atmospheric flow. The first one presented here was mainly developed by Pope and its co-workers. In this approach, the dynamics of the flow is explicitly resolved and simulated, based on physical modelling of its evolution. The second approach is derived from the work of Sawford [1986] and Thomson [1987]. It consists of transporting fluid particles on a flow whose statistics are known a priori. The assumed behaviour of the carrier flow is directly implemented in the drift vector and diffusion matrix. This second approach will not be used in the present work.

IEM Similarly to the SLM description followed for the dynamics, the interaction between the instantaneous properties will be treated using an interaction by exchange with the mean (IEM) model, also referred as linear mean square estimation (LMSE) model, written as:

$$\mathrm{d}\Theta = -\frac{(\Theta - \langle\Theta\rangle)}{\mathcal{T}_\Theta}\mathrm{d}t, \tag{1.215}$$

with a thermal relaxation timescale $\mathcal{T}_\Theta = \frac{k}{\mathcal{C}_\Theta\epsilon} = \frac{\mathcal{C}_L}{\mathcal{C}_\Theta}T_L$. The latter is then modelled to be proportional to the dynamical timescale in agreement with Kolmogorov theory and the treatment presented in the RANS approach (see Section 1.3.2). Moreover, in agreement with Taylor [1922]'s proposal for the velocity, we consider that the turbulent diffusion is high compared to the molecular one thus $\frac{K}{UL} = \frac{1}{PrRe} \ll 1$ and then $Pr \gg \frac{1}{Re}$ which is respected for high Reynolds number flows. The IEM model can be seen as a subclass of the Langevin models proposed by Pope [1985] where a diffusion term may be present. Numerous variants of these models have been proposed, e.g. by Cassiani et al. [2005] in the context of pollutant dispersion, or by Van Dop [1993], Bisignano and Devenish [2015] in the context of buoyant plumes. In the continuation of the work of Pope [1994b], Das and Durbin [2005] presented a modelling of this quantity as well as the instantaneous velocity which is consistent with a broader class of linear DRSM-DFM models. Let us note, that, in order to fulfil the necessity for the scalar to remain bounded, Valiño and Dopazo [1991] proposed a binomial Langevin model later on extended to the bounded Langevin model by Pozorski et al. [2003a]. Further proposals and comparisons between models can be found in the review article of Pozorski and Wacławczyk [2020]. For incompressible flows, methods taking into account explicit modelling of instantaneous pressure and internal energy have also been proposed (see Delarue and Pope [1997]).

Remark 1.3.10. Let us remark that the viscous effects are not explicitly present in the equations presented which are valid uniquely for high-Reynolds number flows. Lagrangian stochastic models developed for low-Reynolds number flows exist (see, e.g., Dreeben and Pope [1997a, 1998], Wacławczyk et al. [2004]) but will not be considered in this work. However, as models valid only for high-Reynolds number flows are used on wall-bounded flows, a specific treatment of the wall-boundary condition, presented in Paragraph 1.3.3.2.4, should be considered.

1.3.3.2.3 Averaged Equations derived from the Lagrangian Stochastic Modelling

It is common to observe first and second-order moments to characterise a flow. This description although being physically less rich than the knowledge of the whole PDF, can easily be obtained as a post-treatment of the particle trajectory using a Lagrangian stochastic approach. Now that we have described the class of PDF model selected let us put forward the transport equations for the moment deriving from this choice. We will consider, for this paragraph only, a general case using the GLM model for the dynamics and the IEM model for the temperature. The system of equations considered for the instantaneous quantities is:

$$\mathrm{d}X_i = U_i \mathrm{d}t, \tag{1.216a}$$

$$\mathrm{d}U_i = \left(-\frac{1}{\rho_r}\frac{\partial \langle P \rangle}{\partial x_i} + (1 - \beta_0(\Theta - \Theta_0)) g_i + G_{ij}(U_j - \langle U_j \rangle) \right) \mathrm{d}t + \sqrt{\tilde{\mathcal{C}}_0 \epsilon}\, \mathrm{d}\mathcal{W}_i, \tag{1.216b}$$

$$\mathrm{d}\Theta = -\frac{\Theta - \langle \Theta \rangle}{\mathcal{T}_\Theta} \mathrm{d}t. \tag{1.216c}$$

Remark 1.3.11. Let us keep in mind that in this work only the SLM-IEM model is used. The corresponding set of equations is then:

$$\mathrm{d}X_i = U_i \mathrm{d}t, \tag{1.217a}$$

$$\mathrm{d}U_i = \left(-\frac{1}{\rho_r}\frac{\partial \langle P \rangle}{\partial x_i} + (1 - \beta_0(\Theta - \Theta_0)) g_i - \frac{U_i - \langle U_i \rangle}{T_L} \right) \mathrm{d}t + \sqrt{\mathcal{C}_0 \epsilon}\, \mathrm{d}\mathcal{W}_i, \tag{1.217b}$$

$$\mathrm{d}\Theta = -\frac{\Theta - \langle \Theta \rangle}{\mathcal{T}_\Theta} \mathrm{d}t. \tag{1.217c}$$

Deriving the corresponding averaged equations from the GLM ones is straightforward simply by replacing G_{ij} by $-(T_L)^{-1}\delta_{ij}$ with T_L defined in Eq. (1.213) and $\tilde{\mathcal{C}}_0$ by $\mathcal{C}_0$.

Remark 1.3.12. A great advantage of Lagrangian stochastic methods is that it is straightforward to add instantaneous local source terms $\mathcal{S}_\Psi$ in Eqs 1.216. The corresponding instantaneous terms can be treated explicitly for each particle no matter how complex and how non-linear they are. The estimation of the statistics being a post processing step we can then easily derive the mean behaviour or this term $\langle \mathcal{S}_\Psi \rangle$, which can be different from the source term associated to the mean quantity $\mathcal{S}_{\langle \Psi \rangle}$. The latter property is of great interest to model non-linear source terms as commonly encountered in poly-dispersed flows (see Minier and Peirano [2001], Minier et al. [2014]) or in reactive flows (see Pope [1985]). Indeed, the mean chemistry may differ quite noticeably from the chemistry of the mean.

Mean Moment Equation

Let us first focus on the mean dynamics by averaging the instantaneous-velocity transport equation Eq. (1.216b) as:

$$\begin{aligned}
\langle \mathrm{d}U_i \rangle &= \left(\frac{\partial \langle U_i \rangle}{\partial t} + \langle U_k \rangle \frac{\partial \langle U_i \rangle}{\partial x_k} + \frac{\partial \langle u_k u_i \rangle}{\partial x_k} \right) \mathrm{d}t, && (1.218a)\\
&= \left(-\frac{1}{\rho_r} \frac{\partial \langle P \rangle}{\partial x_i} + (1 - \beta_0(\langle \Theta \rangle - \Theta_0)) g_i \right) \mathrm{d}t. && (1.218b)
\end{aligned}$$

Although this method differs from the RANS methods, it is clear that this equation is a high Reynolds number averaged Navier–Stokes equations with a similar structure than Eq. (1.64). Let us put emphasis on the fact that the instantaneous velocity being directly modelled, no further model is required for all the transport terms such as the Reynolds tensor. Indeed, the advection is treated exactly without further approximation.

Reynolds Tensor

Let us determine the transport equation for the Reynolds tensor. To this end, we need to estimate the transport equation of the fluctuating velocity. To that effect, let us first estimate the evolution of the averaged velocity:

$$\begin{aligned}
\mathrm{d}\langle U_i \rangle &= \left(\frac{\partial \langle U_i \rangle}{\partial t} + U_k \frac{\partial \langle U_i \rangle}{\partial x_k} \right) \mathrm{d}t, && (1.219a)\\
&= \langle \mathrm{d}U_i \rangle + \left(u_k \frac{\partial \langle U_i \rangle}{\partial x_k} - \frac{\partial \langle u_k u_i \rangle}{\partial x_k} \right) \mathrm{d}t, && (1.219b)\\
&= \left(-\frac{1}{\rho_r} \frac{\partial \langle P \rangle}{\partial x_i} + (1 - \beta_0(\langle \Theta \rangle - \Theta_0)) g_i + u_k \frac{\partial \langle U_i \rangle}{\partial x_k} - \frac{\partial \langle u_k u_i \rangle}{\partial x_k} \right) \mathrm{d}t. && (1.219c)
\end{aligned}$$

Knowing the transport equation of instantaneous and averaged velocity, we can exhibit the equation for the fluctuating velocity:

$$\begin{aligned}
\mathrm{d}u_i &= \mathrm{d}U_i - \mathrm{d}\langle U_i \rangle, && (1.220a)\\
&= \left(-u_k \frac{\partial \langle U_i \rangle}{\partial x_k} + \frac{\partial \langle u_k u_i \rangle}{\partial x_k} - \beta_0 \theta g_i + G_{ik}(U_k - \langle U_k \rangle) \right) \mathrm{d}t + \sqrt{\tilde{\mathcal{C}}_0 \epsilon}\, \mathrm{d}\mathcal{W}_i. && (1.220b)
\end{aligned}$$

We can then obtain the equation governing the second-order moments of the velocity using Itô calculus as:

$$\begin{aligned}
\langle \mathrm{d}u_i u_j \rangle &= \left(\frac{\partial \langle u_i u_j \rangle}{\partial t} + \langle U_k \rangle \frac{\partial \langle u_i u_j \rangle}{\partial x_k} + \frac{\partial \langle u_k u_i u_j \rangle}{\partial x_k} \right) \mathrm{d}t, && (1.221a) \\
&= \langle u_i \mathrm{d}u_j \rangle + \langle u_j \mathrm{d}u_i \rangle + \tilde{\mathcal{C}}_0 \epsilon \delta_{ij} \mathrm{d}t, && (1.221b) \\
&= \left(\underbrace{-\langle u_j u_k \rangle \frac{\partial \langle U_i \rangle}{\partial x_k} - \langle u_i u_k \rangle \frac{\partial \langle U_j \rangle}{\partial x_k}}_{\text{Production}} - \underbrace{\beta(\langle u_j \theta \rangle g_i + \langle u_i \theta \rangle g_j)}_{\text{Buoyancy}} + \underbrace{G_{ik} \langle u_j u_k \rangle + G_{jk} \langle u_i u_k \rangle + \tilde{\mathcal{C}}_0 \epsilon \delta_{ij}}_{\text{Dissipation and Redistribution}} \right) \mathrm{d}t. && (1.221c)
\end{aligned}$$

Note that the transport term being treated explicitly, the diffusion of the second-order moment by the fluctuations of velocity $-\frac{\partial \langle u_k u_i u_j \rangle}{\partial x_k}$ does not require any further modelling. On the contrary in the RANS approach a specific modelling is necessary for this term (e.g. a Shir or Daly-Harlow model). This is a first slight lack of consistency between RANS and PDF approach. Yet, apart from this issue each Lagrangian stochastic model is consistent with a given DRSM model which respects the condition:

$$G_{ik} \langle u_j u_k \rangle + G_{jk} \langle u_i u_k \rangle + \tilde{\mathcal{C}}_0 \epsilon \delta_{ij} = \Pi_{ij} - \epsilon_{ij}. \tag{1.222}$$

Taking the trace of this relation the redistribution term disappears and the relation Eq. (1.211) arises. This relation may be used to assert consistency with RANS models, e.g. it shows that the SLM model is consistent with the Rotta model presented Eq. (1.172) only if their respective constants satisfy:

$$\mathcal{C}_R = 1 + \frac{3}{2} \mathcal{C}_0 = 2 \mathcal{C}_L. \tag{1.223}$$

Potential Temperature

In a similar manner, let us focus on the evolution of the potential temperature. First, averaging the instantaneous potential temperature equation 1.216c we obtain:

$$\langle \mathrm{d}\Theta \rangle = \left(\frac{\partial \langle \Theta \rangle}{\partial t} + \langle U_k \rangle \frac{\partial \langle \Theta \rangle}{\partial x_k} + \frac{\partial \langle u_k \theta \rangle}{\partial x_k} \right) \mathrm{d}t = 0. \tag{1.224}$$

We can then determine the equation followed by the average temperature as:

$$\begin{aligned}
\mathrm{d}\langle \Theta \rangle &= \left(\frac{\partial \langle \Theta \rangle}{\partial t} + U_k \frac{\partial \langle \Theta \rangle}{\partial x_k} \right) \mathrm{d}t, && (1.225a) \\
&= \langle \mathrm{d}\Theta \rangle + \left(u_k \frac{\partial \langle \Theta \rangle}{\partial x_k} - \frac{\partial \langle u_k \theta \rangle}{\partial x_k} \right) \mathrm{d}t, && (1.225b) \\
&= \left(u_k \frac{\partial \langle \Theta \rangle}{\partial x_k} - \frac{\partial \langle u_k \theta \rangle}{\partial x_k} \right) \mathrm{d}t. && (1.225c)
\end{aligned}$$

From these two equations, we can exhibit the transport equation for the fluctuations of potential temperature:

$$\mathrm{d}\theta = -\left(\frac{\theta}{\mathcal{T}_\Theta} + u_k \frac{\partial \langle \Theta \rangle}{\partial x_k} - \frac{\partial \langle u_k \theta \rangle}{\partial x_k} \right) \mathrm{d}t. \tag{1.226}$$

Potential Temperature Variance

Based on the transport equation for the fluctuating potential temperature, it is possible to derive the equation for the corresponding variance as:

$$\begin{aligned}
\langle \mathrm{d}\theta^2 \rangle &= \left(\frac{\partial \langle \theta^2 \rangle}{\partial t} + \langle U_k \rangle \frac{\partial \langle \theta^2 \rangle}{\partial x_k} + \frac{\partial \langle u_k \, \theta^2 \rangle}{\partial x_k} \right) \mathrm{d}t, && (1.227a)\\
&= 2 \langle \theta \mathrm{d}\theta \rangle, && (1.227b)\\
&= \left(\underbrace{-2 \langle u_k \theta \rangle \frac{\partial \langle \Theta \rangle}{\partial x_k}}_{\text{Production}} - \underbrace{2 \frac{\langle \theta^2 \rangle}{\mathcal{T}_\Theta}}_{\text{Dissipation}} \right) \mathrm{d}t. && (1.227c)
\end{aligned}$$

The IEM model being based on the assumption of proportionality between dynamic and thermal turbulent timescale, the form of the dissipation rate for the potential temperature variance is coherent with the assumption presented in Paragraph 1.3.2.2.2 for RANS models. Furthermore, the time scale appearing in the dissipation term of Eqs 1.227 being $\mathcal{T}_{\langle \theta^2 \rangle} = \frac{\mathcal{T}_\Theta}{2}$, it justifies the presence of a factor 2 in Eq. (1.179).

Turbulent Heat Fluxes

Finally, having access to both fluctuating potential temperature and velocity equations, the turbulent heat flux equation can be derived as:

$$\begin{aligned}
\langle \mathrm{d}u_i \theta \rangle &= \left(\frac{\partial \langle u_i \theta \rangle}{\partial t} + \langle U_k \rangle \frac{\partial \langle u_i \theta \rangle}{\partial x_k} + \frac{\partial \langle u_k u_i \theta \rangle}{\partial x_k} \right) \mathrm{d}t, && (1.228a)\\
&= \langle u_i \mathrm{d}\theta \rangle + \langle \theta \mathrm{d}u_i \rangle, && (1.228b)\\
&= \left(\underbrace{-\langle u_k \theta \rangle \frac{\partial \langle U_i \rangle}{\partial x_k} - \langle u_i u_k \rangle \frac{\partial \langle \Theta \rangle}{\partial x_k}}_{\text{Production}} - \underbrace{\beta_0 \langle \theta^2 \rangle g_i}_{\text{Buoyancy}} + \underbrace{\langle u_k \theta \rangle (G_{ik} - \frac{\delta_{ik}}{\mathcal{T}_\Theta})}_{\text{Scrambling and Dissipation}} \right) \mathrm{d}t. && (1.228c)
\end{aligned}$$

It is worth noticing that the physical process at stake in the transport of turbulent flux being the same as the one impacting the Reynolds tensor and the thermal variance, the modelling of these three equations should not be independent. In the case of Lagrangian stochastic model, this dependency is straightforward as both the models on the dynamics and on the potential temperature appear through respectively the presence of G_{ik} and $\mathcal{T}_\Theta$. Considering only the slow redistribution term as assumed in the rest of this work, i.e. considering SLM/IEM modelling or equivalently Rotta/Monin modelling a new timescale $\mathcal{T}_{u\theta} = \frac{1}{\frac{1}{\mathcal{T}_L} + \frac{1}{\mathcal{T}_\Theta}} = \frac{1}{\mathcal{C}_{u\theta}} \frac{k}{\epsilon}$ with $\mathcal{C}_{u\theta} = \mathcal{C}_\Theta + \mathcal{C}_L$ arises. Different propositions have been made for $\mathcal{C}_\Theta$ or $\mathcal{C}_{u\theta}$ (see e.g. Pope [1994b], Rodi [2000], Dehoux et al. [2011]), and the value considered will be further discussed in Section 5.1. Thus, the SLM-IEM model is coherent with the Rotta-Monin model provided that:

$$\mathcal{C}_{\theta_1} = \mathcal{C}_\Theta + \mathcal{C}_L. \tag{1.229}$$

1.3.3.2.4 Wall-Boundary Conditions for Lagrangian Stochastic Methods

As the explicit treatment of molecular viscosity and diffusivity but also the wall echo terms are neglected, we have described a modelling valid only for high-Reynolds-number flows. Furthermore, we are interested in the description of parietal flows, the ground playing a major role in atmospheric flows. Yet, in the close vicinity of the wall the high Reynolds number assumption is not valid, and a specific treatment of this zone is necessary. Let us then take a moment to put emphasis on the treatment of the wall-boundary condition (WBC) (further information may be found in Dreeben and Pope [1997b] and Minier and Pozorski [1999].

To treat high-Reynolds-number parietal flows, the development of WBC in the spirit of the wall-function approach is important. Indeed, even though some Lagrangian stochastic models can simulate low-Reynolds-number flows (see e.g. Dreeben and Pope [1997a, 1998], Wacławczyk et al. [2004]), the highly inhomogeneous and anisotropic variations occurring in the viscous sub-layer require a costly refinement in this area and remain a challenging and time-consuming issue. Therefore, similarly to the wall-function treatment used in moment approaches, the WBC for particles aims at reproducing the behaviour of the turbulent SBL without considering explicitly the presence of this viscous sub-layer.

In classical FV formulations, wall functions are applied for the different mean fields at the centre of the first cell. The latter one must then be located within the fully turbulent SBL. In particle methods, the information is made up by instantaneous variables (e.g. instantaneous velocities) carried along particle trajectories whose location can be arbitrary close to the boundary of the domain. Thus, the boundary surface considered for particles should also be in a zone where the viscous effects can be neglected (i.e. above the UBL for atmospheric flows and in the logarithmic zone for thermally neutral one). To fulfil this condition, the boundary condition is then applied at a plane locally parallel to the physical wall but slightly shifted to a distance z^{pl}, as shown in Figure 1.17. The issue is to express what condition should be imposed on instantaneous particle-attached variables to obtain the correct resulting statistics which are representative of the physics of the high Reynolds number SBL.

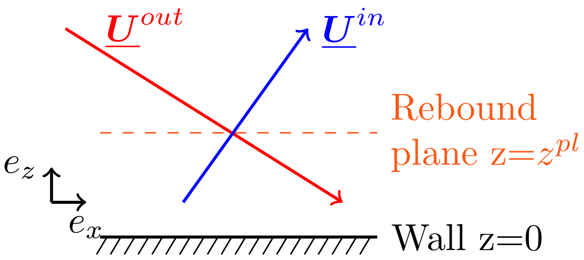

Figure 1.17: Illustration of the Lagrangian wall-boundary condition. The boundary condition is applied at a rebound plane shifted from the wall by a distance z^{pl}. For each particle crossing the rebound plane and leaving the domain a particle is reflected with properties estimated to respect statistical condition at the rebound plane (zero mean normal velocity, proper shear stress, ...).

Only fluid particles inside the domain, i.e. above the rebound plane on the scheme Figure 1.17, are simulated. Thus, for each fluid particle leaving the domain with instantaneous properties $\underline{\mathcal{Z}}^{out}$, a reflected mirror particle is injected with the instantaneous properties $\underline{\mathcal{Z}}^{in}$ as represented in Figure 1.17. In order to impose conditions on the statistics at the rebound plane $\langle f(\underline{\mathcal{Z}})\rangle^{pl}$ (for example non permeability of the wall, shear stress, scalar fluxes, ...), the instantaneous properties of the particles injected are chosen based on the corresponding values for the outgoing particles by considering requirements for the resulting fluxes at the rebound plane:

$$\langle f(\underline{\boldsymbol{\mathcal{Z}}})\rangle^{pl} = \frac{1}{2}\left(\langle f(\underline{\boldsymbol{\mathcal{Z}}})\rangle^{in} + \langle f(\underline{\boldsymbol{\mathcal{Z}}})\rangle^{out}\right). \tag{1.230}$$

Wall-Boundary Condition Applied for the Dynamics

First, in the SBL near the wall, the mean velocity normal to the wall is null: $\langle W\rangle^{pl} = 0$. This condition is necessary to ensure the non-permeability of the wall, thus avoiding spurious accumulation or depletion of fluid particles and then fluid mass in its vicinity. This can easily be respected by imposing this condition on each pair of leaving/entering particles. The normal velocity of the injected particle W^{in} is then the opposite of the normal velocity of the corresponding outgoing particle W^{out}:

$$W^{in} = -W^{out} \ , \tag{1.231}$$

from which it follows that specular reflection is applied to the particle distance to the wall (here the vertical coordinate Z):

$$Z^{in} = 2\, Z^{pl} - Z^{out} \ . \tag{1.232}$$

The condition on the streamwise velocity is less straightforward. Too often, a specular rebound is imposed with no specific condition for this variable. If this choice respects the necessity to keep the particles within the domain, it does not respect the physics considered. Indeed, this amounts to imposing a zero-gradient condition in the streamwise direction. This is clearly at variance with having a constant shear stress and with the physical exchange of momentum characteristic of the SBL. With the purpose of conserving this exchange of momentum and the gaussianity of the stochastic increments, Dreeben and Pope [1997b] and Minier and Pozorski [1999] proposed to estimate the injected streamwise velocity U^{in} as a linear function of U^{out} and W^{out}:

$$U^{in} = U^{out} + \alpha W^{out}. \tag{1.233}$$

The value α is then determined so that the correct shear stress at the plane is retrieved. This yields to:

$$\alpha = -2\frac{\langle uw\rangle(z^{pl})}{\langle w^2\rangle(z^{pl})}. \tag{1.234}$$

It is worth noting that a similar formulation is correct in the three directions replacing $\langle uw\rangle$ by $\underline{\underline{\boldsymbol{\mathcal{R}}}} \cdot \underline{\boldsymbol{n}}$ where $\underline{\boldsymbol{n}}$ is the vector normal to the face. Thus, the general form of the boundary condition imposed on the velocity is given in Eq. (1.235):

$$\underline{\boldsymbol{U}}^{in} = \underline{\boldsymbol{U}}^{out} - 2\frac{\underline{\underline{\boldsymbol{\mathcal{R}}}} \cdot \underline{\boldsymbol{n}}}{R_{nn}}\underline{\boldsymbol{U}}^{out} \cdot \underline{\boldsymbol{n}}. \tag{1.235}$$

This an-elastic rebound condition is considered as the reference one. It will be compared to the elastic or specular rebound and validated on both smooth and coarse walls in Section 3.1.2.

Remark 1.3.13. Let us highlight that rigorously speaking the statistics encountered in this paragraph are surface statistics $\langle (.) \rangle^{surf}$. The latter being conditioned on the crossing of a given surface, they differ from the volumetric ones considered until now are conditioned only by their location. Indeed, the particles crossing a surface are admittedly mainly particles in the vicinity of this surface but also preferentially particles with a greater displacement in the surface normal direction. As a result, the turbulent movements associated to the particles crossing the surface are greater than the ones associated to the particle in the vicinity of this surface and we have $\langle w^2 \rangle^{surf}(z^{pl}) > \langle w^2 \rangle(z^{pl})$. Yet as proven by Minier and Pozorski [1999], in the case of near Gaussian distribution of W we have $\langle w^2 \rangle^{surf}(z^{pl}) = 2\langle w^2 \rangle(z^{pl})$ and $\langle uw \rangle^{surf}(z^{pl}) = 2\langle uw \rangle(z^{pl})$ so that the results derived in this paragraph are valid considering either surface or volumetric statistics. This remark is also valid for the scalar WBC presented hereafter as for near Gaussian distribution of W we also have$\langle w\psi \rangle^{surf}(z^{pl}) = 2\langle w\psi \rangle(z^{pl})$.

Wall-Boundary Condition Applied for the Transport of Scalar

Transporting other instantaneous physical quantities such as the potential temperature or a pollutant concentration, it is also important to implement a proper boundary condition at the wall to properly treat the fluxes near the wall. Indeed, in non-neutral situations, the heat fluxes at the wall play a major role in the physics of the atmospheric surface boundary as further discussed in Section 5.2.1. Furthermore, for a pollutant whose near ground flux is known (e.g. due to known emissions or deposition rate) their proper representation is primordial to represent the pollutant transport and dispersion. Let us take a quantity Φ and assume a known value of the normal fluxes $\langle w\phi \rangle$, Similarly to the velocity one can write:

$$\Psi^{in} = \Psi^{out} + \alpha_\Psi W^{out}. \tag{1.236}$$

We have then:

$$\begin{aligned} \langle w\psi \rangle^{pl} =& \frac{1}{2}(\langle w\psi \rangle^{pl,in} + \langle w\phi \rangle^{pl,out}), \\ =& \frac{1}{2}\langle (\Psi^{out} - \Psi^{in} w^{out}) \rangle^{pl,out}, \\ =& -\frac{1}{2}\alpha_\Psi \langle w^{out} w^{out} \rangle^{pl,out}. \end{aligned} \tag{1.237}$$

We can then determine α_Ψ as:

$$\alpha_\Psi = -2\frac{\langle w\psi \rangle(z^{pl})}{\langle w^2 \rangle(z^{pl})}. \tag{1.238}$$

Reinjecting the result Eq. (1.238) in Eq. (1.236) we get:

$$\Phi^{in} = \Phi^{out} - 2\frac{\langle w\phi \rangle(z^{pl})}{\langle w^2 \rangle(z^{pl})} W^{out}. \tag{1.239}$$

This formulation was proposed for the real temperature by Pozorski et al. [2003b].

Remark 1.3.14. The an-elastic rebounds presented here are not necessarily limited to the treatment of the WBC. Indeed, it should be used in the general case where a homogeneous Neumann condition should be imposed on the normal fluxes. This is the case e.g. on the top of the domain when simulating SBL flows to maintain these fluxes in the whole domain.

1.3.3.3 Numerical Implementation of Particle Mesh Methods

Let us now focus on the numerical implementation of Lagrangian stochastic methods. To obtain numerical solutions of the SDEs considered, three issues need to be addressed:

1) How do we calculate the mean fields at particle positions?
2) How do we integrate in time the SDEs?
3) How do we extract statistics from the ensemble of particles?

These three points are related to three sources of error: the first one corresponds to the spatial discretisation error either due to an approximate expression of mean fields at particle locations or to estimation of ensemble statistics on too coarse averaging bins; the second one corresponds to the time error due to the integration scheme selected to update particle variables at discrete times; while the third one to the statistical error which is inherent in Monte Carlo methods. In a complete numerical formulation, these errors can impact each other and can even induce a fourth one referred to as the bias error. However, for reasons set forth below, this bias error is not present in the present context, and we can safely concentrate on the three ones mentioned above. Although relatively few studies have been devoted to their numerical analysis, these questions have been analysed in depth in at least two detailed investigations from Xu and Pope [1999] and Peirano et al. [2006], to which readers are referred to for further details.

Different mesh-less methods have been proposed to extract the mean fields entering Eqs 1.217 directly from the particle dynamics by resorting to a local kernel estimation centred around each particle position (see e.g. Hockney [1966]). However, particle-mesh methods also referred as grid-based methods, using an auxiliary grid to compute such statistics, have been broadly used for the great computational gain they enable. Note that, although not addressed in the present work, the introduction of an underlying mesh in the particle solver is also useful to simulate particle collision effects (see e.g. Schmidt and Rutland [2000], Sigurgeirsson et al. [2001]) when considering inertial particles. In particle-mesh methods, an additional step is necessary to resolve the first issue presented 1), as we first need to estimate the mean fields on the auxiliary grid. The algorithm followed can then be decomposed into four numerical steps: the estimation of the mean carrier fields on a mesh; the interpolation of these mean carrier fields from the mesh to the particle locations; the temporal integration of the instantaneous quantities associated to the particles; the estimation of the statistics extracted from the set of particles. The goal of the present section is to present the operator followed for each step and the associated error. A sketch of the overall formulation of the present hybrid method is shown in Figure 1.18 and is used to introduce the key aspects of the numerical steps to be addressed in later sections.

1.3.3.3.1 Estimation of the Mean Moments of the Carrier Flow on a Mesh

When dealing with fluid particles, a first possibility is to extract the mean fields directly from particle simulation. Such numerical formulations whether they are based on a mesh or not are called PDF stand-alone formulations. One of their interests is that they are consistent by construction while, on the other hand, the inherent statistical noise due to the use of a finite number of particles can induce a deterministic bias error highlighted by Xu and Pope [1999] and Peirano et al. [2006]. In the case where a stand-alone method is used with a particle-mesh formulation this step corresponds to the same as the estimation of the statistics from the particle set further discussed in Paragraph 1.3.3.3.4.

In the present work, we have chosen to adopt a hybrid formulation in which the fluid mean carrier fields are computed by a classical Navier–Stokes code with a turbulence model (typically a mesh-based solver using finite-volume techniques, referred to as the FV solver). They are then provided to the Lagrangian code (referred to as the particle solver) to be used in the particle evolution equations, cf. Eqs 1.217. A first advantage for doing so is that these mean fields are free from statistical noise (as they would be, should we use a stand-alone formulation), thereby avoiding a potential source of numerical bias. Another interest is that, since such hybrid formulations can be used to simulate disperse two-phase flows, we are resorting to a numerical formulation whose range of application encompasses also inertial particles. In that sense, the case of fluid particles considered in this work can still be regarded as the limit one (when particle inertia goes to zero) of a more general situation. On the other hand, since Lagrangian PDF models for fluid particles represent a turbulence model, we are dealing with a double description of a given turbulent flow raising immediately a consistency issue. At the numerical level, this implies that we have duplicate fields, where for example the mean velocity field is predicted by the FV solver but also by the particle one when first-order statistics are extracted from particle velocities. To prevent different predictions for the same physical quantity, it is necessary to ensure that these duplicate fields are identical when they correspond to the same physical variable. This consistency issue constitutes an important criterion to assess the validity of the overall formulation and, more specifically, to evaluate the numerical errors related to how particle statistics are simulated. In hybrid formulations, consistency at the discrete FV/particle level can only be achieved if the continuous moment/PDF description of a turbulent flow is also consistent. This point has been addressed in several works (see Pope [1994b, 2000], Chibbaro and Minier [2011]) but is worth repeating. It is also important to recall that, once particle velocities and potential temperatures are explicitly retained in the particle state vector as is the case here, then the turbulence model corresponding to such a PDF description is a DRSM-DFM type of model (for more details, see a specific discussion on this issue in Minier et al. [2014] or in [Minier, 2016, section 10.3]). Building on the well-established relations between generalised Langevin models and resulting second-order closures (interested reader are invited to refer to Pope [1994b, 2000], Haworth [2010]), this means that, if we retain the SLM-IEM in Eqs 1.217, a consistent hybrid formulation consists then in selecting a Rotta-Monin model in the moment description with constants respecting Eq. (1.223) and Eq. (1.229).

Remark 1.3.15. Note that in this case the FV methods can be treated has an external solver decoupled from the dynamics of the particles. Indeed, the latter one furnishes averaged quantities necessary to the particle solver, but the dynamics of the particles has no effects on the carrier fields. Such approaches are referred as one-way coupling. Considering inertial particles, they are valid only in the limit of dilute regime. In the general case, they require that the physics treated by the particle solver do not impact too much the carrier flow. Thus, for example thermal source terms created by chemical reaction treated within the particle solver should remain low. If the particle physics impacts noticeably the mean carrier flow, we should consider a two-way coupling within which particle solver also furnishes source terms representing the particle effects on the carrier flow to the FV solver (see e.g. Minier and Peirano [2001], Minier [2015], Innocenti et al. [2021]).

1.3.3.3.2 Interpolation of the Averaged Carrier Fields at the Position of the Particles

Since particles are distributed in the whole domain, they are generally not located at the positions where the mean carrier fields are estimated. It results that an interpolation step is necessary to determine the value of these mean fields at the particle locations. This introduces a deterministic spatial discretisation error $\mathcal{E}_{\Delta x}$ which depends on the mesh and on the specific interpolation scheme used. This numerical error has been recognised very early in particle simulations and has been the object of many studies over the years (see e.g. Xu and Pope [1999], Jenny et al. [2001], McDermott and Pope [2008], Viswanathan et al. [2011]). Note that this step requires to identify (at least) the cells in which particles are located so that there is a close connection between the interpolation step and particle tracking. When high-order interpolation schemes are developed, they are usually based on the mean fields in the cell where each particle is contained but also the mean fields in the neighbouring cells. However, for complex geometries or unstructured meshes, estimating the position of a particle in a mesh and the relative distance to neighbouring cells is a tedious and time-consuming task as highlighted by Löhner and Ambrosiano [1990]. For this reason, the interpolation scheme used is local, i.e., based only on the mean fields associated to the cell containing the particle. It is then possible to estimate the mean fields at the position of the particle using a Taylor expansion around the centre of this cell. Let us write $[\Psi]_m(\underline{\boldsymbol{X}})$ the $\mathsf{P_m}$ (i.e. piece-wise polynomial) interpolation at the order m of a given quantity Ψ at the location of the particle $\underline{\boldsymbol{X}}$ based on the value at the centre of the corresponding cell $\underline{\boldsymbol{X}}^c(\underline{\boldsymbol{X}})$. This $\mathsf{P_m}$ interpolation is defined as:

$$[\Psi]_m(\underline{\boldsymbol{X}}) = \sum_{|\alpha|\leq m} (\underline{\boldsymbol{\partial}^{\boldsymbol{\alpha}}}\Psi)(\underline{\boldsymbol{X}}^c)\frac{(\underline{\boldsymbol{X}}-\underline{\boldsymbol{X}}^c)^{\alpha}}{\alpha!}. \tag{1.240}$$

In this equation the multi-index notation is used starting at $\alpha = 0$. $(\underline{\boldsymbol{X}} - \underline{\boldsymbol{X}}^c)^m$ is the tensor of position at the order m. Similarly, $\underline{\boldsymbol{\partial}^{\boldsymbol{m}}}\Psi$ is the tensor of derivation at the order m. It corresponds to the value at the centre of the cell at the order 0, the gradient at the first order and the Hessian matrix at the second order, etc. For quantities varying in the three directions of space the number of derivative functions to compute increases quickly with the order of interpolation. For this reason, the interpolation first retained is the simplest possibility: the $\mathsf{P_0}$ (i.e. piece-wise constant) interpolation. In the latter we assign the same cell-centred mean values to all particles located within a cell. Such interpolation is coherent with the spirit of FV method where we consider the mean fields uniform within each cell. Based on the hybrid formulation followed, using this interpolation assumption and a SLM-IEM modelling, the particle equations Eqs 1.217, can be expressed as:

$$\begin{aligned}
\mathrm{d}X_i =& U_i\,\mathrm{d}t, && (1.241\text{a})\\
\mathrm{d}U_i =& \left(-\frac{1}{\rho}\left[\frac{\partial \overline{P}}{\partial x_i}\right]_0 (\underline{\boldsymbol{X}}(t);t) + (1-\beta_0(\Theta-\Theta_0))g_i - \frac{U_i - \left[\overline{U_i}\right]_0 (\underline{\boldsymbol{X}}(t);t)}{[T_L]_0\,(\underline{\boldsymbol{X}}(t);t)}\right)\mathrm{d}t && (1.241\text{b})\\
&+\sqrt{C_0\,[\epsilon]_0\,(\underline{\boldsymbol{X}}(t);t)\mathrm{d}\mathcal{W}_i}\ , \\
\mathrm{d}\Theta =& -\frac{\Theta - [\overline{\Theta}]_0(\underline{\boldsymbol{X}}(t);t)}{[\tau_\Theta]_0(\underline{\boldsymbol{X}}(t);t)}\mathrm{d}t. && (1.241\text{c})
\end{aligned}$$

where $[.]_0$ stands for the $\mathsf{P_0}$ interpolation and will be omitted in the following for the sake of clarity. While this implies discontinuous profiles of mean quantities when a particle moves across an interface between two adjacent cells, this drawback is offset by the simplicity of the numerical implementation and, in particular, by the fact that it remains valid and easy to apply even in the case of unstructured meshes (sometimes made up by several overlapping meshes) in complex geometries. The effects and errors introduced by such an interpolation on the dynamics of the particles will be further studied in Section 3.2 for neutral flows and in Section 5.2.2 for thermally stratified flows. Furthermore, considering finer interpolations methods would essentially be beneficial if they can be applied in the different cells crossed by particles during one time step. In that sense, the interpolation issue appears as complementary to the development of cell-to-cell integration schemes which will be developed in Chapter 2.

1.3.3.3.3 Temporal Integration of the Instantaneous Quantities Associated to the Particles

Once the mean fields at the position of the particles are estimated, the variables entering the particle state vector are updated by integrating their SDEs. In the present situation where $\underline{\boldsymbol{\mathcal{Z}}} = (\underline{\boldsymbol{X}}, \underline{\boldsymbol{U}}, \Theta)$, this amounts to integrate Eqs 1.217 over the selected time step Δt with a suitable numerical scheme. This time-integration step introduces a deterministic temporal discretisation error $\mathcal{E}_{\Delta t}$ which depends on the details of the integration scheme as well as on the time step Δt. The time integration scheme used in this study is the exponential scheme proposed by Minier et al. [2003b] and by Peirano et al. [2006]. Such a scheme is unconditionally stable, explicit, and exact for uniform fields. Note that the latter condition enables to avoid introducing a temporal error for the integration of a particle which remains within a cell when using a P_0 interpolation. Let us emphasise, that it enables to properly retrieve all asymptotic behaviours from fluid particles ($\Delta t \gg \mathcal{T}_p$) to inertial ones in diffusive to inertial regime. However, an exception should be highlighted. In the case where fluid particles are simulated in the diffusive regime ($\Delta t \gtrapprox T_L$) with a spatially varying Lagrangian timescale, a deterministic error appears as pointed out by Minier [2016]. Moreover, when the time step is large enough, particles can cross several cells leading to an interplay between spatial and time discretisation errors as studied in Chapter 2. This chapter focuses on the temporal integration scheme and the particle tracking algorithm and a more in length description of the numerical scheme used for both these aspects is given in Section 2.1.1.

1.3.3.3.4 Estimation of the Statistics Extracted from the Set of Particles

Once the particle-attached variables are updated, statistics can be extracted from the particle set using local Monte Carlo estimations or, in other words, locally-applied ensemble averaging. As mentioned above, in a hybrid formulation, particle statistics are not fed back into the governing SDEs and have, therefore, no direct influence on particle dynamics. Thus, the interpolation and averaging operators are here decoupled, and no further constraint appears. At the contrary using stand-alone PDF models based on a particle-mesh formulations, the interpolation scheme and how particle statistics are extracted appear as two adjoint operators (see Xu and Pope [1999], Peirano et al. [2006]). This results in the necessity to have a scheme to estimate the statistics of the same order or finer than the one used for the interpolation methods as presented by Hockney and Eastwood [1988].

In the context of hybrid formulation, the statistics derived from the set of particles constitute, nevertheless, the observables used to assess PDF models, since we are dealing with weak approaches (whereby only statistics obtained on a representative number of particles are relevant rather than individual particle properties). To extract these statistics, we consider a volumetric partition of the computational domain and treat each small volume as an averaging bin. This means that, once a number of particles are located in a given bin, these particles are regarded as equivalent samples of the same PDF (somewhat loosely associated to the barycentre of this small volume). Then, statistics of interest are derived by typical Monte Carlo estimations (or ensemble averaging over the particles in this bin). In the more general case of inertial particles or for specific applications, different statistical weights can be attached to particles, for example their mass when simulating poly-disperse two-phase flows. In the present study, we are dealing with fluid particles representing the same fixed amount of mass and all particles have therefore the same statistical weight, by which we simply apply ensemble averaging for the Monte Carlo estimations. It is important to be aware that this amounts to making a locally homogeneity hypothesis since we assume that, in each averaging bin, we can replace the true probabilistic expectation by spatial averaging over locally-present particles (see [Minier and Peirano, 2001, sections 6.4.4 and 8.2.8]). The limits of these hypotheses will be further discussed in Section 3.3

and in Section 5.2.3 respectively for neutral and thermally stratified flows. This averaging process corresponds to the nearest-grid-point (NGP) method also referred as particle-in-cell (PIC), which has the advantage of remaining local and robust even in complex partitions. This formulation is coherent with the aforementioned interpolation scheme which is also local. Similarly to the interpolation issue, higher-order methods, such as the cloud-in-cell methods which are linear or piece-wise quadratic, exist but cannot be easily applied for complex geometries or meshes (see Hockney [1966], Peirano et al. [2006]).

Also note that, for the definition of the volumetric partition used to extract statistics from particles, it is not mandatory to use the mesh considered in the FV approach. This is however a commonly made choice for three main practical reasons. First, it is more convenient to handle only one mesh, which makes the numerical implementation simpler since particles have to be tracked only in this mesh, thus limiting the computational cost. Second, a hypothesis made in the estimation of FV statistics of the mean fields is that the flow within each cell is statistically uniform. Then, when using P_0 interpolation of these fields to obtain mean field values at particle locations, it seems relevant to use the same volume elements in which these mean fields are regarded as constant (though, this point will be revisited in Section 3.2). Third, it is also practical to use same local volumes to monitor discrepancies between duplicated fields and to furnish source-terms to the FV solver when two-way coupling is used. Unless otherwise stated, only one division of the space is therefore considered in this study and the terms used to refer to the division of the domain are mesh and cells. Furthermore, the term “ensemble average” will refer in this study to the statistics derived from the particle set.

A few words on associated numerical errors are now in order. Since the number of particles used to calculate statistics is finite, Monte Carlo methods introduce a zero mean statistical error $\mathcal{E}_N$ which depends on the number of particles in each bin. For statistically stationary cases, we can then apply a time averaging method to reduce this statistical error (see Xu and Pope [1999], Muradoglu et al. [1999]). This means that, after a given time necessary to reach a statistically stationary state, the set of particles on which the statistics are extracted is increased at each iteration by accumulating the samples. Thus, after accumulating the particles during N^{it} iterations, the total number of samples used for the estimation of statistics is $N^p \times N^{it}$ with N^p the number of particles. This source of error is well known and will not be treated in this work. Finally, a non-zero averaged spatial error $\mathcal{E}_{\widetilde{\Delta_x}}$ can appear when computing the statistics on coarse bins in which mean quantities are not uniform as discussed by Viswanathan et al. [2011]. In our case, no smoothing step is applied, and the error is caused only by the spatial variation of these mean fields in a cell, as highlighted in Section 3.3.

The different steps involved in a hybrid formulation are indicated in Figure 1.18. In this sketch, two different types of averaging operators are used. On the left part, in the moment method, the RANS averaged values are obtained on the cells making up the mesh and are noted $\overline{(.)}$. On the right part, in the PDF method, the statistics are estimated using ensemble averaging noted $\langle(.)\rangle$ on averaging bins. If the cells and bins are identical, the duplicated fields corresponding to the same physical quantities (mean velocity, Reynolds tensor) that are computed twice with two different operators are then provided at the same points.

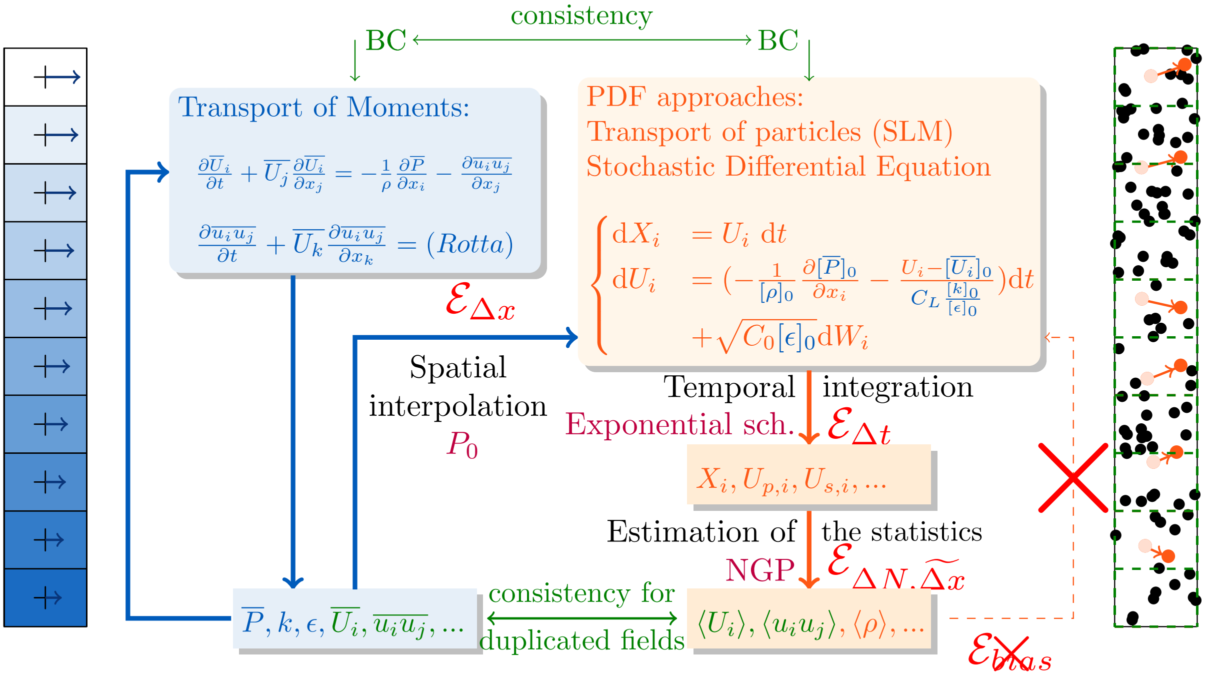

Figure 1.18: Summary of different steps followed by the hybrid FV/PDF methods and numerical methods considered at first (the interpolation scheme and the averaging methods are further discussed respectively in Section 3.2 and in Section 3.3).

Remark 1.3.16. Note that although they are not considered in the present work, methods in which stochastic particles are transported using LES fields exist. In this case, the stochastic modelling does not aim at modelling the whole turbulence but only the sub-grid turbulence and they provide access to the filtered-density-function (FDF). Such methods are referred as hybrid LES/FDF methods and have a structure close to the RANS/PDF methods. Therefore, a preponderant part of the information provided in this section remains somewhat pertinent keeping in mind the difference between FDF and PDF. The interested reader may refer to Minier [2015, 2016], Innocenti et al. [2016], Yang et al. [2021].

CHAPTER 2

A Time-Step-Robust Algorithm to Compute Particle Trajectories in 3-D Unstructured Meshes

Contents

This section is based on the published article of Balvet et al. [2023a] written in collaboration with J.P. Minier, C. Henry, Y. Roustan and M. Ferrand. Its purpose is to improve the temporal and the spatial accuracy of grid-based Lagrangian stochastic methods which is a major concern should such methods be used in a safety context. To do so, a time-step-robust cell-to-cell integration of particle trajectories in 3-D unstructured meshes is developed. The main idea is to dynamically update the mean fields used in the time integration of the set of SDEs considered by splitting, for each particle, the time step into sub-time steps, such that each of these sub-steps corresponds to particle cell residence times. This reduces the spatial discretisation error as a loss of accuracy can be observed when the mean fields, associated to a mesh, vary noticeably along the trajectory of the particle over a time step. Given the stochastic nature of the models, a key aspect is to derive estimations of the residence times that do not anticipate on the future of the Wiener process. To that effect, the new algorithm relies on a virtual particle, attached to each stochastic one, whose mean conditional behaviour provides free-of-statistical-bias predictions of residence times in each cell. This new method is consistently incorporated in a hybrid moment/PDF approach using an exponential integration scheme presented in Section 2.1.1.

This section is constructed as follows. First, the particle current integration-tracking algorithm, enabling to determine the cell associated to the particle along its trajectory in a 3-D unstructured mesh, is presented in Section 2.1. Then the new algorithm is presented in Section 2.2 and the drawings used for the estimations of the stochastic integrals are studied in Section 2.2.2. A particular attention is paid to ensure that the decomposition of each integration into multiple sub-integrations using adaptive time steps does not induce any statistical bias in Section 2.2.2.2. After this consistency checks, this new algorithm is validated on two representative test cases in Section 2.3. The first test aims at asserting that no statistical bias is introduced in the estimation of the stochastic integrals. To that effect, a point source dispersion in a statistically uniform flow is carried out in Section 2.3.1. Then, in order to ensure that the mean carrier fields at the particle locations are indeed properly dynamically updated, the particle dynamics in a non-uniform rotating flow is studied in Section 2.3.2.2.

2.1 Current Numerical Scheme for Particle Transport

Contents

Let us first present the method used to predict the evolution of the fluid particle properties. As the purpose of this work is to develop a time-splitting methods independently dividing the integration time based on each particle trajectory, we will focus on the particle dynamics. The state vector taken into account in this chapter is then simply constituted by the mean position and velocity: $\underline{\boldsymbol{\mathcal{Z}}} = (\underline{\boldsymbol{X}}, \underline{\boldsymbol{U}})$ and the corresponding set of SDEs is:

$$\mathrm{d}X_i = U_i \,\mathrm{d}t, \tag{2.1a}$$

$$\begin{aligned}\mathrm{d}U_i =& \left(-\frac{U_i}{[T_L]_0\,(\underline{\boldsymbol{X}}(t);t)} + \overbrace{\frac{\left[\overline{U_i}\right]_0 (\underline{\boldsymbol{X}}(t);t)}{[T_L]_0\,(\underline{\boldsymbol{X}}(t);t)} - \frac{1}{\rho}\left[\frac{\partial \overline{P}}{\partial x_i}\right]_0 (\underline{\boldsymbol{X}}(t);t)}^{[\mathcal{F}_i]_0(\underline{\boldsymbol{X}}(t);t)} \right)\mathrm{d}t \\ &+ \sqrt{\mathcal{C}_0\,[\epsilon]_0\,(\underline{\boldsymbol{X}}(t);t)}\mathrm{d}\mathcal{W}_i\ ,\end{aligned} \tag{2.1b}$$

where the specific deterministic forces are split between the relaxation term $-\frac{U_i}{T_L}$ playing a fundamental role in the development of the exponential temporal scheme used and the other terms gathered in $\mathcal{F}_i$ which could include additional forces. The extension to additional instantaneous quantities is straightforward and is set aside for the sake of clarity. Furthermore, also for clarity reason, the explicit notation of the interpolation method considered and the spatial and temporal dependencies will be set aside in the rest of the chapter. The presence of a numerical temporal scheme typically introduces the notion of a time step Δt for the integration of the particle equations of motion and discrete approximations of $\underline{\mathcal{Z}}$ at times $t^n = n\Delta t$, noted $\underline{\mathcal{Z}}^n$. These discrete approximations $\underline{\mathcal{Z}}^n$ are obtained by successive updates (i.e., computing $\underline{\mathcal{Z}}^{n+1}$ from $\underline{\mathcal{Z}}^n$), using an integrated form of the RHS of Eqs 2.1. In the frame of present hybrid methods, the current algorithm involves a two-step process:

- A time-integration scheme, which allows to obtain $\underline{\mathcal{Z}}^{n+1}$ from $\underline{\mathcal{Z}}^n$ using known values of the mean fields at particle location entering the SDEs in Eqs 2.1;
- A trajectory algorithm, which determines the location of each particle in the spatial domain. This second step is needed in hybrid FV/PDF approaches since we must know in which cell each particle is with respect to the mesh defined for the computation of the fluid phase. This information is necessary in order to update the values of the mean fields at each particle location for the next step of the time-integration process.

In the following, we briefly recall the details of the current algorithm used for each step.

2.1.1 Time-Integration Scheme to Predict the Particle State Vector

The numerical scheme used to integrate the SDEs, cf. Eqs 2.1, has been described in Peirano et al. [2006] and in Minier et al. [2003b], which provide comprehensive information on its derivation and main characteristics (see, in particular, the complete description of the different steps leading to its construction in Peirano et al. [2006]). Therefore, only the salient aspects are recalled here along with the resulting formulation.

Requirements

The time-integration scheme has been developed according to the following guidelines (more details can be found in Peirano et al. [2006] and in Minier et al. [2003b]):

- The numerical scheme is explicit (for simplicity reasons);
- The numerical scheme is unconditionally stable (this is of key interest when the time step cannot be reduced, as in hybrid methods, to respect potential stability criteria);
- The numerical scheme corresponds to the exact solution when the mean fields and timescales entering the modelled equations are constant;
- The numerical scheme should capture the correct physical behaviours in the limit cases when the time step becomes much larger than the physical timescales Peirano et al. [2006].

The main reason behind these requirements is that the time step used in hybrid FV-PDF formulations is generally the same for the fluid solver and for the particle solver. This is mandatory for unsteady flows, where fluid and particle properties must be obtained at the same time. Consequently, since the time step is usually imposed by the fluid solver (to properly compute the flow field on a given mesh), it cannot always be reduced/adapted for the particle solver (as could be done in PDF stand-alone approaches). In complex flows in which mean fluid velocities can drastically vary from one area to another one, this means that we do not control the number of cells that are crossed by particles during a time step. Furthermore, when the fluid timescales are also widely different, it is important to properly capture the diffusive limit rather than limiting the time step for the whole particle set as further studied by Peirano et al. [2006].

Chosen Scheme

The guiding principle underlying the present time-integration scheme is to express first the integrated form of the SDEs (using an assumption of constant properties) which leads directly to an exponential analytical form. In the general case, when mean fields and timescales are not constant but vary in space and time, the idea is to use Euler-like schemes by freezing their values at the beginning of the time step in the integrated form rather than in the SDEs (see a detailed description in Peirano et al. [2006]). Thanks to the formulation with exponential factors, unconditional stability is then automatically guaranteed. Although second-order schemes are quite possible using the same approach (see Peirano et al. [2006]), we limit ourselves to a first-order formulation in the following since our main concern is about the prediction of relevant mean fields in such schemes. Consequently, the resulting discrete numerical scheme for fluid particles writes:

$$\begin{aligned} X_i^{n+1} = X_i^n &+ U_i^n T_L^n \left(1 - \exp\left(-\frac{\Delta t}{T_L^n}\right)\right) + \mathcal{F}_i^n T_L^n \left(\Delta t - T_L^n \left(1 - \exp\left(-\frac{\Delta t}{T_L^n}\right)\right)\right) \\ &+ \underbrace{\sqrt{\frac{\mathcal{C}_0 \epsilon^n (T_L^n)^3}{2}} \frac{\left(1 - \exp\left(-\frac{\Delta t}{T_L^n}\right)\right)^2}{\sqrt{1 - \exp\left(-2\frac{\Delta t}{T_L^n}\right)}} \xi_i^U + \sqrt{\mathcal{C}_0 \epsilon^n (T_L^n)^2 \left(\Delta t - 2T_L^n \frac{1 - \exp\left(-\frac{\Delta t}{T_L^n}\right)}{1 + \exp\left(-\frac{\Delta t}{T_L^n}\right)}\right)} \xi_i^X}_{I_i^X(\Delta t)}, \end{aligned} \tag{2.2a}$$

$$U_i^{n+1} = U_i^n \exp\left(-\frac{\Delta t}{T_L^n}\right) + \mathcal{F}_i^n T_L^n \left(1 - \exp\left(-\frac{\Delta t}{T_L^n}\right)\right) + \underbrace{\sqrt{\mathcal{C}_0 \epsilon^n \frac{T_L^n}{2} \left(1 - \exp\left(-2\frac{\Delta t}{T_L^n}\right)\right)} \xi_i^U}_{I_i^U(\Delta t)}. \tag{2.2b}$$

The two terms ξ_i^X and ξ_i^U correspond to independent random numbers sampled in a normalised Gaussian distribution $\mathcal{N}(0,1)$. As indicated in Eqs 2.2, these random numbers intervene in the Choleski decomposition of the two correlated stochastic integrals, namely $I_i^U(\Delta t)$ and $I_i^X(\Delta t)$ (see descriptions in Peirano et al. [2006]).

As displayed in Figure 2.1, the time-integration scheme predicts the particle state vector at the next time step ($\underline{\boldsymbol{X}}^{n+1}, \underline{\boldsymbol{U}}^{n+1}$) using information on its values at the beginning of the time step ($\underline{\boldsymbol{X}}^n, \underline{\boldsymbol{U}}^n$) and local fluid characteristics at the position $\underline{\boldsymbol{X}}^n$.

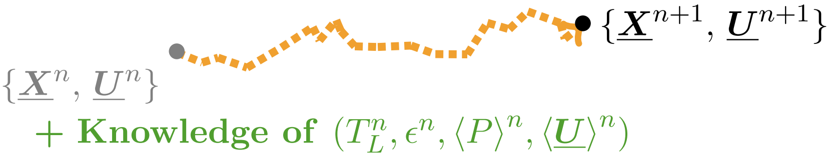

Figure 2.1: Sketch illustrating the time-integration with the current numerical scheme: the particle position X_i^{n+1} and velocity U_i^{n+1} at the next iteration are computed using information on the particle position and velocity at the previous iteration n as well as values of the fluid characteristics at the position X_i^n.

Remark 2.1.1. Let us note that no additional scalar Ψ is considered here. Yet in coherence with the exponential scheme developed for the dynamics, considering an IEM model for fluid particles the resulting numerical scheme would write:

$$\Psi^{n+1} = \Psi^n \exp\left(-\frac{\Delta t}{\mathcal{T}_\Psi^n}\right) + \overline{\Psi}^n \left(1 - \exp\left(-\frac{\Delta t}{\mathcal{T}_\Psi^n}\right)\right). \tag{2.3}$$

As no stochastic terms appear in the IEM model no stochastic draw appear in the previous equation. However due to the transport of the particles by stochastic velocity leading to a stochastic position this quantity Ψ would still be a random variable.

2.1.2 Trajectory Algorithm for Spatial Location

The time-integration scheme requires knowledge on the fluid mean fields at the particle position at a given time (e.g., fluid velocity, turbulent dissipation rate), which are known on a given mesh. As a result, the time-integration scheme has to be supplemented by a trajectory algorithm to locate each particle and assign the corresponding cell.

Assumptions
The trajectory algorithm has to satisfy the following requirements:

- First, since we resort to a NGP approach, the trajectory algorithm is expected to provide the cell in which each particle is located.
- Second, the trajectory algorithm has to be applicable in the case of generic 3-D unstructured meshes, with cells being star-shaped around their centre. This choice is motivated by the typical meshes used in the computation of the average flow-field.
- Third, the trajectory algorithm assumes a free-flight motion of particles during each time step. This means that, during each time step, particles are moving in a straight line from their initial position X_i^n to their final position X_i^{n+1}.

Chosen Algorithm
With respect to the previous requirements, we resort to an algorithm based on the successive neighbour searches. Such tracking algorithms determine the new cell inside which a particle is by using information only on its initial and final positions (see also Figure 2.2). The new cell is then determined by searching intersections between the trajectory vector (joining the initial and final position) and faces of the current cell. To do so, we rely on the algorithm proposed by

Möller and Trumbore [1997] which has been developed to determine the intersections between a vector and triangular sub-faces. This process is then repeated to check if the final position is in the new cell or if another face is crossed by the trajectory vector. The details and validation of this tracking algorithm are provided in Appendix 2.B.

Such tracking algorithms have been retained since they have been shown to be efficient for unstructured meshes (e.g., for Finite Difference approaches in Löhner and Ambrosiano [1990] or for Finite Volume approaches in Muradoglu and Pope [2002], Subramaniam and Haworth [2000]). Moreover, in the case of unstructured meshes, these tracking algorithms are more adequate than simple locating algorithms (which determine the location only using the information on the final position).

At this point, it is worth mentioning that additional conditions can be taken into account for each of the faces that are crossed during the tracking algorithm. In particular, when the crossed face corresponds to a physical boundary, specific boundary conditions can be added: for instance, particles can be removed from the simulation when reaching outlet boundaries while boundary conditions can be applied to wall surfaces (interested readers are referred to Dreeben and Pope [1997b], Minier and Pozorski [1999], Bahlali et al. [2020]). Similarly, specific conditions can be added to properly treat periodicity by translation and/or periodicity by rotation.

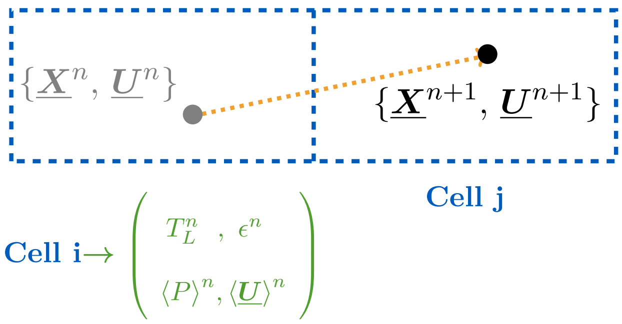

```
for time interval $n$ to $n+1$ do
    Integrate $\underline{\boldsymbol{X}}^{n+1}$
    Draw vector $\underline{\boldsymbol{\delta X}} = \underline{\boldsymbol{X}}^{n+1} - \underline{\boldsymbol{X}}^{n}$
    do
        Determine if $\underline{\boldsymbol{\delta X}}$ leaves the cell through a face
        Update the current cell
    while A face is crossed
    Track the final integrated position
end for
```

Figure 2.2: Current trajectory algorithm used after a single integration for the whole time step: the cell in which the particle resides at the end of the time step is tracked using a successive neighbour search algorithm.

2.2 A new Algorithm based on Cell-to-Cell Integration

Contents

In the context of present hybrid FV/PDF approaches, the P_0-interpolation (or piece-wise uniform interpolation) assumption for mean-field values means that the exponential scheme described in Section 2.1 is not only stable but provides an exact solution for the particle state vector as long as particles remain in the same cell they started from during the whole time step. However, in such hybrid formulations, the time step is often imposed by the mean fluid flow computation and cannot always be reduced so as to respect this criterion. This is especially encountered in disperse two-phase flow simulations with discrete particles having inertia that can range over several orders of magnitude, as indicated above. In the present work, we limit ourselves to fluid particles, but this general picture is an indication that we are faced with a situation where, during a given time step, a particle can cross several cells. The inherent assumption made in Euler schemes, and therefore also in the present exponential one, retains only mean-field values and timescales evaluated at the beginning of the time step, that is at the initial particle location. In non-uniform flows, with potential variations of mean flow field quantities, this implies that a spatial discretisation error is introduced, as illustrated in Figure 2.3.

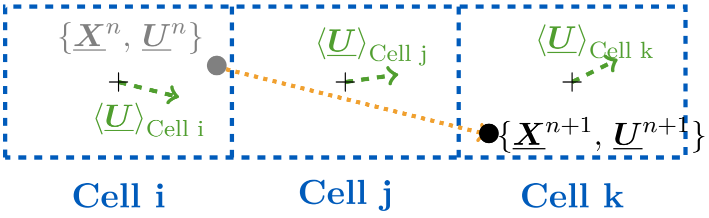

Figure 2.3: Sketch illustrating the issue with the current numerical scheme over large time steps in non-uniform flows: the particle can cross many cells in a single time step, meaning that the fluid characteristics (including velocities) in the intermediate cells are not taken into account in its trajectory.

Objectives

The aim of this chapter is to develop a new algorithm that remains accurate even for non-uniform flows in the case of large time steps when particles can cross several cells. For that purpose, we extend the numerical scheme described in Section 2.1 while keeping similar assumptions/requirements:

a) it should be explicit;

b) it should be unconditionally stable with respect to the time step;

c) it should be exact for constant flow mean fields (and thus within a given cell in line with the P_0 interpolation);

d) it should take into account spatial variations of flow mean fields encountered over large time steps.

2.2.1 Leading Principle: a Cell-to-Cell Integration for Large Time Steps

Principle

To improve the numerical accuracy in non-uniform flows and in the case of large time steps, the idea is to extend the present exponential scheme with a cell-to-cell integration. As illustrated in Figure 2.4, the leading principle consists in splitting the time step in several sub-iterations: the integration is stopped every time the particle exits a cell, such that each sub-iteration indexed by the superscript $^{[m]}$ corresponds to the motion of the particle within one cell. By doing so, it is straightforward to account for the change of flow characteristics every time a particle enters a new cell. Since we need to detect whenever a particle crosses an interface between two adjacent cells, the following two steps are applied for each sub-iteration: (1) a time-integration scheme and (2) a trajectory algorithm. When the time step is small enough for a particle to remain inside the same cell during a whole time step, the new scheme is the same as the one previously described.

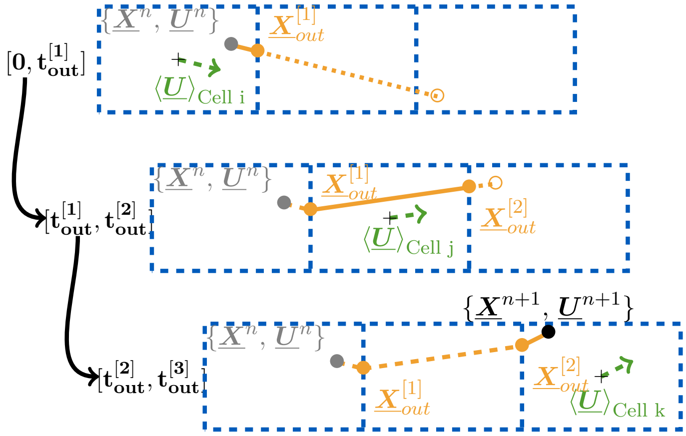

```
for time interval $n$ to $n+1$ do
    do
        Get relative intersection time $\eta^{[m+1]}$
        Integrate until the face
        Update cell and remaining time
        Increment sub-iteration $m$
    while A face is crossed
end for
```

Figure 2.4: Sketch illustrating the principle of a cell-to-cell integration for large time steps and the corresponding algorithm.

Additional Points

Compared to the two-step process described in Section 2.1, the new cell-to-cell integration brings out two additional questions:

- When does a particle exit a cell?
- Where does a particle exit a cell?

This means that the trajectory algorithm has to be modified since it only provides information on the new cell (simple tracking). The new trajectory algorithm should provide information on the exit time t_{out} and exit location $\underline{\boldsymbol{X}}_{\text{out}}$. These two additional pieces of information are indeed required to compute the motion of the particle during the remaining part of the time step. In fact, as displayed in Figure 2.4, the motion of the particle after crossing the face is given by a time-integration scheme starting at $\underline{\boldsymbol{X}}_{\text{out}}$ over the remaining time $\Delta t - t_{\text{out}}$. In that sense, the present algorithm draws on the cell-to-cell integration proposed by Popov et al. [2008] while extending it to respect the non-anticipating requirement for stochastic integrals in the Itô sense (this is discussed in the next paragraph).

The Key Issue of Non-Anticipating Estimations

Implementing the principle of the cell-to-cell algorithm may seem straightforward. A naive formulation would indeed consider that, starting from a particle position $\underline{\boldsymbol{X}}^n$ at time t^n, we apply the exponential scheme, cf. Eqs 2.2, to predict $\underline{\boldsymbol{X}}^{n+1}$ at time t^{n+1} and, then, use the trajectory algorithm to determine $\underline{\boldsymbol{X}}_{\text{out}}$ and the exit time of that cell t_{out} (see the top figure in Figure 2.4). However, whatever the geometrical method used to determine these quantities, it is clear that the resulting time t_{out} will depend on the random numbers $\underline{\boldsymbol{\xi}}$ which, in Eqs 2.2, represent the normalised increments of the Wiener process in the stochastic model, cf. Eqs 1.217. When combining the different diffusion coefficients obtained from each sub-iteration (for instance, the three sub-iterations depicted in Figure 2.4), the resulting diffusion coefficient will then be a function of the future of the Wiener process since the random numbers $\underline{\boldsymbol{\xi}}$ stand for the normalised values of $\underline{\boldsymbol{\mathcal{W}}}^{n+1} - \underline{\boldsymbol{\mathcal{W}}}^{n}$. In other words, the misleadingly simple approach will yield diffusion coefficients that anticipate on the future of the Wiener process. This is in direct violation of the very definition of the stochastic integrals in the Itô sense, thereby inducing spurious overall drift and diffusion numerical values (see a similar analysis in Minier et al. [2003a]).

Assumptions
Drawing on the aforementioned analysis, the new numerical scheme is designed so as to respect the following additional assumptions/constraints:

i) It should respect the non-anticipation rule with respect to the Wiener process;

ii) The trajectory algorithm is based on a neighbour search;

iii) The trajectory algorithm considers free-flight motion of particles within each sub-iteration.

2.2.2 Non-Anticipating Estimations of Intermediate Time Steps Using Virtual Partners

To obtain an estimate of the fraction of time spent by a particle in a given cell that remains independent of the future of the Wiener process entering the stochastic terms, a virtual partner is associated to each particle within each time step of the computation. This means that at the beginning of each time step $t = t^n$, this virtual partner starts from the same location as the real particle which is considered but moves in a deterministic manner (to be precised below) based only on the particle variables at time t^n and local mean-field values. The fraction of time spent by this virtual partner in the corresponding cell is therefore, by construction, free of any statistical dependence with the Wiener process driving the random terms and provides an estimate for the time spent by the real particle within that cell.

In the following, details about the algorithm are first provided in Section 2.2.2.1. The consistence of this algorithm with the current integration scheme is then demonstrated in Section 2.2.2.2.

2.2.2.1 Overview of the New Algorithm

As indicated, the new algorithm is based on a cell-to-cell integration for large time steps. This implies that each time iteration is split in a series of sub-iterations, each one corresponding to the motion of a particle in a given cell. As a result, the algorithm combines a number of successive time-integration and trajectory steps. During each time step, the virtual partners are used in the trajectory steps to determine the cell in which the particle is as well as to estimate the exit time and location.

In practice, the algorithm is composed of the following steps, which are depicted in Figure 2.5:

step-1 Based on the particle initial location $\underline{\boldsymbol{X}}^{[0]}$ and the knowledge of the fluid mean fields in that cell, a deterministic estimation of the particle position at the end of the time step Δt, noted $\widehat{\underline{\boldsymbol{X}}}^{[1]}$, is made. Note that the superscript $[m]$ means that it corresponds to the sub-iteration number m within the cell-to-cell integration. This is achieved by forcing the stochastic integrals to zero in the exponential time-integration scheme, which gives the following equation for $\widehat{\underline{\boldsymbol{X}}}^{[1]}$:

$$\widehat{\underline{\boldsymbol{X}}}^{[1]} = \underline{\boldsymbol{X}}^{[0]} + \underline{\boldsymbol{U}}^{[0]} T_L^{[0]} \left(1 - \exp\left(-\frac{\Delta t}{T_L^{[0]}}\right)\right) + \mathcal{F}_i^{[0]} T_L^{[0]} \left(\Delta t - T_L^{[0]} \left(1 - \exp\left(-\frac{\Delta t}{T_L^{[0]}}\right)\right)\right) . \tag{2.4}$$

It is important to note that $\widehat{\underline{\boldsymbol{X}}}^{[1]}$ corresponds to the mean conditional particle location at time Δt conditioned on the fact that its initial location is $\underline{\boldsymbol{X}}^{[0]}$, that is $\widehat{\underline{\boldsymbol{X}}}^{[1]} = \langle \underline{\boldsymbol{X}}(\Delta t) \,|\, \underline{\boldsymbol{X}}(0) = \underline{\boldsymbol{X}}^{[0]} \rangle$. Therefore, if we release a number of particles at $\underline{\boldsymbol{X}}^{[0]}$ at time

$t = 0$, $\widehat{\underline{\boldsymbol{X}}}^{[1]}$ represents the position of the centre of mass of the released cloud at time $t = \Delta t$.

step-2 Then, the trajectory algorithm based on a free-flight assumption is applied to determine if the particle leaves/remains in the cell. To avoid any anticipation issue, the trajectory algorithm is applied on the virtual partner and not on the real particle. The motion of the virtual partner is assumed to follow a straight line between the first location of the virtual partner (initialised at the particle position $\widetilde{\underline{\boldsymbol{X}}}^{[0]} = \underline{\boldsymbol{X}}^{[0]}$) and $\widehat{\underline{\boldsymbol{X}}}^{[1]}$. The trajectory algorithm is detailed in Appendix 2.B. Its outcome allows to distinguish between two cases:

- step-2a The virtual partner leaves the cell. In that case, the trajectory algorithm provides information on the face through which the virtual particle exits the cell but also on the exit time $\eta^{[1]}\Delta t$ (see the extension of the trajectory algorithm in Appendix 2.B). Thanks to the free-flight assumption, the exit location of this virtual partner, $\widetilde{\underline{\boldsymbol{X}}}^{1}$, is derived directly from the exit time. This case will activate a next sub-iteration to compute the motion of the particle during the remaining time (see Step-3a).
- step-2b The virtual partner remains in the cell. In that case, $\eta^{[1]} = 1$, and the position of the virtual partner at the end of the time step is equal to the first estimated position $\widetilde{\underline{\boldsymbol{X}}}^{[1]} = \widehat{\underline{\boldsymbol{X}}}^{[1]}$. This case will not activate a new sub-iteration and the cell-to-cell integration will be stopped (see Step-3b).

step-3 The position $\underline{\boldsymbol{X}}^{[1]}$ and velocity $\underline{\boldsymbol{U}}^{[1]}$ of the particle at the end of this sub-iteration are then computed using the full time-integration scheme, i.e., including the stochastic integrals (see Eqs 2.2). The only issue is to determine the amount of time that the particle has spent in the cell. From step-2, there are two possibilities:

- step-3a If the virtual partner exits the cell (step-2a), the elapsed time retained for the prediction of $(\underline{\boldsymbol{X}}^{[1]}, \underline{\boldsymbol{U}}^{[1]})$ is taken as being equal to the fraction of time computed for the virtual partner $\eta^{[1]}\Delta t$.

  Then, we have to pursue the computation of the particle motion during the remaining time $\Delta t^{[1]} = (1 - \eta^{[1]})\Delta t$. In the spirit of this cell-to-cell algorithm, this is achieved by repeating the previous three steps and updating the information required at each step (see sub-iterations 2 and 3 in Figure 2.5). In step-1 of the second sub-iteration, the mean conditional particle position $\widehat{\underline{\boldsymbol{X}}}^{[2]}$ at the end of the new time step $\Delta t^{[1]}$ is estimated starting from the particle position $\underline{\boldsymbol{X}}^{[1]}$ and particle velocity $\underline{\boldsymbol{U}}^{[1]}$. The mean fields required to estimate $\widehat{\underline{\boldsymbol{X}}}^{[2]}$ are now $(T_L(t, \widetilde{\underline{\boldsymbol{X}}}^{[1]}), \mathcal{F}_i(t, \widetilde{\underline{\boldsymbol{X}}}^{[1]}))$ taken in the cell in which the virtual partner is. Afterward, step-2 is applied to compute the trajectory of the virtual partner, assuming that it starts at the last exit location $\widetilde{\underline{\boldsymbol{X}}}^{[1]}$ and moves towards the estimated mean conditional position $\widehat{\underline{\boldsymbol{X}}}^{[2]}$. It is worth noting that the starting position is taken as the last exit location so that the trajectory of the virtual partner remains continuous. Subsequently, from the estimation of $\eta^{[2]}$ obtained in step-2, the position $\underline{\boldsymbol{X}}^{[2]}$ and velocity $\underline{\boldsymbol{U}}^{[2]}$ are computed in step-3 of this second sub-iteration.

  This three-step process is actually repeated until the virtual partner reaches a cell in which it remains for the whole remaining time step $\Delta t^{[m]}$ (recall that the superscript $[m]$ corresponds to the sub-iteration number m).
- step-3b If the virtual particle remains in the cell (step-2b), the elapsed time is actually equal to the remaining time step $\Delta t^{[m]}$ (i.e. $\eta^{[m]} = 1$). The position of the virtual partner

is equal to the last estimated position made in step-1 $\widetilde{\underline{\boldsymbol{X}}}^{[m]} = \widehat{\underline{\boldsymbol{X}}}^{[m]}$. In that case, the cell-to-cell iterative integration is stopped.

Final step When the virtual partner finally reaches a cell in which it remains for the remaining time, we obtain the particle position at the end of the whole time step $\underline{\boldsymbol{X}}(t + \Delta t)$. Yet, as can be seen in Figure 2.5, the particle might end up in a different cell than the virtual partner due to the stochastic terms. For that reason, we apply a last trajectory algorithm: we track the change of cell from the virtual partner last position $\widetilde{\underline{\boldsymbol{X}}}^{[m]}$ to the particle position $\underline{\boldsymbol{X}}(t + \Delta t)$. This last trajectory step ensures that the particle is associated to the correct cell inside which it resides at the end of the time step. This ensures that no error on the location is introduced for the next time step.

A few comments are in order. At first sight, it could be argued that the difference between the position of the virtual partner $\widetilde{\underline{\boldsymbol{X}}}^{[m]}$ and the position of the particle $\underline{\boldsymbol{X}}(t + \Delta t)$ at the last sub-iteration points to an error in the algorithm. However, it should be recalled that this difference is due to the stochastic terms that are taken into account when computing the particle position but not in the position of the virtual partner (which is fully deterministic). At this stage, it is worth emphasising that, within each time step of the computation, the role of the virtual partner is essentially to provide information on the time spent in each cell and to determine the neighbouring cells that a particle can cross during the time step, while ensuring that the anticipation issue is avoided. This further supports the choice of a tracking algorithm based on successive neighbour searches (see Section 2.1.2), since it naturally provides information on the successive cells crossed by a particle during a time step (contrary to simple localisation algorithms). At each sub-iteration of the algorithm, the increments of this virtual partner represent the mean conditional displacement and, in that sense, remain coherent with the underlying physical process modelled. Each virtual partner is therefore an auxiliary in the calculation of the (true) particle motion. Furthermore, we are basically interested in developing weak approximations, which means capturing particle dynamics in a statistical sense. As a result, what really matters is to obtain accurate estimations of statistics extracted from particle dynamics through Monte Carlo methods (e.g., average concentration, mean velocity), that is from an ensemble of particles. In other words, improvements in the prediction of individual particle variables (location as well as velocity) should always be assessed in a statistical sense. For that purpose, we now turn our attention to the resulting behaviour of such particle statistics in the rest of this work.

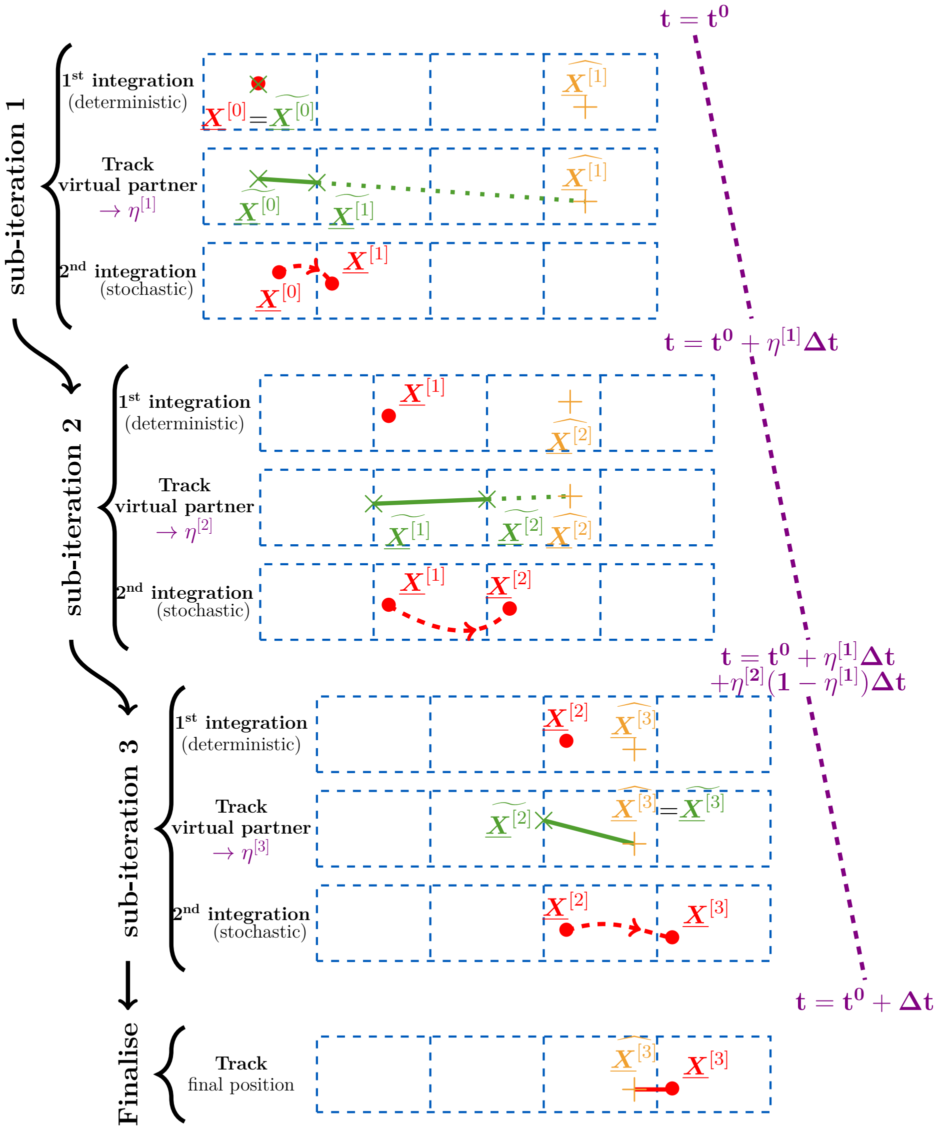

```
for time interval $n$ to $n+1$ do
    do
        (a) Integrate $\widehat{\underline{X}}^{[m+1]}$ from $\underline{X}^{[m]}$ with $I^{\mathcal{Z}} = 0$
        (b) Compute the exit point $\widetilde{\underline{X}}^{[m+1]}$ using the vector $\overline{\widetilde{\underline{X}}^{[m]}\widehat{\underline{X}}^{[m+1]}}$
            Compute the exit time $\eta^{[m+1]}dt^{[m]}$ with $\eta^{[m+1]} = \frac{|\overline{\widetilde{\underline{X}}^{[m]}\widetilde{\underline{X}}^{[m+1]}}|}{|\overline{\widetilde{\underline{X}}^{[m]}\widehat{\underline{X}}^{[m+1]}}|}$
        (c) Integrate $\underline{X}^{[m+1]}$ from $\underline{X}^{[m]}$ using the exit time $\eta^{[m+1]}\Delta t^{[m]}$ and random numbers $(\underline{\xi}^{\mathcal{Z}})^{[m+1]}$
        (d) Update cell, flow fields and remaining time $\Delta t^{[m+1]} = (1 - \eta^{[m+1]})\Delta t^{[m]}$
        Increment the sub-iteration $m$
    while (A face is crossed)
    Track the final integrated position
end for
```

Figure 2.5: Summary of the proposed algorithm.

2.2.2.2 Consistency Analysis of the Time Step Decomposition

Before considering proper validation test cases in Section 2.3, it is important to check that the new algorithm meets the criterion (c) set forth at the beginning of Section 2.2.

Verification Procedure

To that effect, we consider a situation where all mean fields and timescales are constant. In that case, we already know that the current numerical scheme, cf. Eqs 2.2 in which T_L, $\mathcal{F}_i$ and ϵ are now constant, provides the exact solution in the weak sense. We then consider the new algorithm and assume that one sub-iteration has taken place (the extension to several sub-iterations being immediate) at a time $\eta\Delta t$, implying that the particle state vector $\underline{\boldsymbol{\mathcal{Z}}}^{n+1}$ is now obtained from $\underline{\boldsymbol{\mathcal{Z}}}^{n}$ as the sum of two iterations (one over $\eta\Delta t$ and one over $(1-\eta)\Delta t$). The issue is then to check that, still in the weak sense, both predictions are identical.

In the following, we leave out the direction index i since this is basically a 1D formulation. Starting from a given particle state vector value $\underline{\boldsymbol{\mathcal{Z}}}^{n}$ at time t^n, predictions obtained in one iteration (i.e., the current algorithm) are indicated by the index $\{1\}$, while those obtained with two sub-iterations (i.e., the new algorithm) are indicated by the index $\{2\}$.

Predictions in one iteration are expressed directly by Eqs 2.2, which are rewritten here as:

$$(X^{n+1})^{\{1\}} = X^n + U^n T_L\left(1-\exp\left(-\frac{\Delta t}{T_L}\right)\right) + \mathcal{F}T_L\left(\Delta t - T_L\left(1-\exp\left(-\frac{\Delta t}{T_L}\right)\right)\right) + (I^X)^{\{1\}}(\Delta t)\ , \tag{2.5a}$$

$$(U^{n+1})^{\{1\}} = U^n\exp\left(-\frac{\Delta t}{T_L}\right) + \mathcal{F}T_L\left(1-\exp\left(-\frac{\Delta t}{T_L}\right)\right) + (I^U)^{\{1\}}(\Delta t). \tag{2.5b}$$

The two stochastic integrals are represented by the two correlated centred Gaussian random variables $(I^X)^{\{1\}}(\Delta t)$ and $(I^U)^{\{1\}}(\Delta t)$ which are fully determined by the matrix of their second-order moments Peirano et al. [2006]:

$$\left\langle \left((I^U)^{\{1\}}(\Delta t)\right)^2 \right\rangle = \mathcal{C}_0\epsilon\frac{T_L}{2}\left(1-\exp\left(-2\frac{\Delta t}{T_L}\right)\right)\ , \tag{2.6a}$$

$$\left\langle (I^U)^{\{1\}}(\Delta t)\,(I^X)^{\{1\}}(\Delta t) \right\rangle = \mathcal{C}_0\epsilon\frac{T_L^2}{2}\left(1-\exp\left(-\frac{\Delta t}{T_L}\right)\right)^2\ , \tag{2.6b}$$

$$\left\langle \left((I^X)^{\{1\}}(\Delta t)\right)^2 \right\rangle = \mathcal{C}_0\epsilon T_L^2\left(\Delta t - \frac{T_L}{2}\left(1-\exp\left(-\frac{\Delta t}{T_L}\right)\right)\left(3-\exp\left(-\frac{\Delta t}{T_L}\right)\right)\right)\ . \tag{2.6c}$$

In the case of two iterations, a first estimation of $\underline{\boldsymbol{\mathcal{Z}}}(\eta\Delta t)$ is made with Eqs 2.5 using the two correlated Gaussian random variables noted $(I^U)^{\{2\}}(\eta\Delta t)$ and $(I^X)^{\{2\}}(\eta\Delta t)$ and a second iteration is performed over the remaining time interval $(1-\eta)\Delta t$ to obtain the prediction of $\underline{\boldsymbol{\mathcal{Z}}}^{n+1}$ using two other correlated Gaussian random variables noted $(I^U)^{\{2\}}((1-\eta)\Delta t)$ and

$(I^X)^{\{2\}}((1-\eta)\Delta t)$. Note that $\Big((I^U)^{\{2\}}((1-\eta)\Delta t), (I^X)^{\{2\}}((1-\eta)\Delta t)\Big)$ are independent of $\Big((I^U)^{\{2\}}(\eta\Delta t), (I^X)^{\{2\}}(\eta\Delta t)\Big)$. Combining the two gives:

$$\begin{aligned}(X^{n+1})^{\{2\}} &= X^n + U^n T_L\left(1-\exp\left(-\frac{\Delta t}{T_L}\right)\right) + \mathcal{F}T_L\left(\Delta t - \exp\left(-\frac{\Delta t}{T_L}\right)\right) \qquad (2.7\text{a})\\ &+ \underbrace{(I^X)^{\{2\}}(\eta\Delta t) + (I^X)^{\{2\}}((1-\eta)\Delta t) + T_L (I^U)^{\{2\}}(\eta\Delta t)\left(1-\exp\left(-\frac{(1-\eta)\Delta t}{T_L}\right)\right)}_{(\widetilde{I}^X)^{\{2\}}(\eta,\Delta t)},\\ (U^{n+1})^{\{2\}} &= U^n \exp\left(-\frac{\Delta t}{T_L}\right) + \mathcal{F}T_L\left(1-\exp\left(-\frac{\Delta t}{T_L}\right)\right) \qquad (2.7\text{b})\\ &+ \underbrace{(I^U)^{\{2\}}(\eta\Delta t)\exp\left(-\frac{(1-\eta)\Delta t}{T_L}\right) + (I^U)^{\{2\}}((1-\eta)\Delta t)}_{(\widetilde{I}^U)^{\{2\}}(\eta,\Delta t)}.\end{aligned}$$

The variance of $(\widetilde{I}^U)^{\{2\}}(\eta,\Delta t)$ is easily calculated and is:

$$\left\langle \left((\widetilde{I}^U)^{\{2\}}(\eta,\Delta t)\right)^2 \right\rangle = \left\langle \left((I^U)^{\{2\}}(\eta\Delta t)\right)^2 \right\rangle \exp\left(-\frac{2(1-\eta)\Delta t}{T_L}\right) + \left\langle \left((I^U)^{\{2\}}((1-\eta)\Delta t)\right)^2 \right\rangle \qquad (2.8\text{a})$$

$$= \mathcal{C}_0\epsilon\frac{T_L}{2}\left(\left(1-\exp\left(-\frac{2\eta\Delta t}{T_L}\right)\right)\exp\left(-\frac{2(1-\eta)\Delta t}{T_L}\right) + 1 - \exp\left(-\frac{2(1-\eta)\Delta t}{T_L}\right)\right) \qquad (2.8\text{b})$$

$$= \mathcal{C}_0\epsilon\frac{T_L}{2}\left(1-\exp\left(-\frac{2\Delta t}{T_L}\right)\right) \qquad (2.8\text{c})$$

$$= \left\langle \left((I^U)^{\{1\}}(\Delta t)\right)^2 \right\rangle, \qquad (2.8\text{d})$$

where the last equality comes from. Eq. (2.6a). Similarly, the variance of $(\widetilde{I}^X)^{\{2\}}(\eta,\Delta t)$ is obtained as:

$$\begin{aligned}\left\langle \left((\widetilde{I}^X)^{\{2\}}(\eta,\Delta t)\right)^2 \right\rangle &= T_L^2\left(1-\exp\left(-\frac{(1-\eta)\Delta t}{T_L}\right)\right)^2 \left\langle \left((I^U)^{\{2\}}(\eta\Delta t)\right)^2 \right\rangle\\ &+2T_L\left(1-\exp\left(-\frac{(1-\eta)\Delta t}{T_L}\right)\right)\left\langle \left((I^X)^{\{2\}}(\eta\Delta t)(I^U)^{\{2\}}(\eta\Delta t)\right) \right\rangle \qquad (2.9)\\ &+\left\langle \left((I^X)^{\{2\}}(\eta\Delta t)\right)^2 \right\rangle + \left\langle \left((I^X)^{\{2\}}((1-\eta)\Delta t)\right)^2 \right\rangle,\end{aligned}$$

while the covariance is:

$$\begin{aligned}&\left\langle\left((\widetilde{I}^X)^{\{2\}}(\eta,\Delta t)(\widetilde{I}^U)^{\{2\}}(\eta,\Delta t)\right)\right\rangle = \\ &\qquad T_L\left(1-\exp\left(-\frac{(1-\eta)\Delta t}{T_L}\right)\right)\exp\left(-\frac{(1-\eta)\Delta t}{T_L}\right)\left\langle\left((I^U)^{\{2\}}(\eta\Delta t)\right)^2\right\rangle \\ &\qquad+\exp\left(-\frac{(1-\eta)\Delta t}{T_L}\right)\left\langle\left((I^X)^{\{2\}}(\eta\Delta t)(I^U)^{\{2\}}(\eta\Delta t)\right)\right\rangle \\ &\qquad+\left\langle\left((I^X)^{\{2\}}((1-\eta)\Delta t)(I^U)^{\{2\}}((1-\eta)\Delta t)\right)\right\rangle .\end{aligned}\tag{2.10}$$

The formulas in Eqs 2.6 can then be applied, using either $\eta\Delta t$ or $(1-\eta)\Delta t$ as the proper time interval, and injected in Section 2.2.2.2 and Eq. (2.10). Tedious but straightforward calculations show:

$$\left\langle\left((\widetilde{I}^X)^{\{2\}}(\eta,\Delta t)\right)^2\right\rangle = \left\langle\left((I^X)^{\{1\}}(\Delta t)\right)^2\right\rangle \tag{2.11a}$$

$$\left\langle\left((\widetilde{I}^X)^{\{2\}}(\eta,\Delta t)(\widetilde{I}^U)^{\{2\}}(\eta,\Delta t)\right)\right\rangle = \left\langle(I^U)^{\{1\}}(\Delta t)(I^X)^{\{1\}}(\Delta t)\right\rangle , \tag{2.11b}$$

which, with Eq. (2.8d), proves that $\left((\widetilde{I}^X)^{\{2\}}(\eta,\Delta t),(\widetilde{I}^U)^{\{2\}}(\eta,\Delta t)\right)$ is statistically equivalent to $\left((I^X)^{\{1\}}(\Delta t),(I^U)^{\{1\}}(\Delta t)\right)$ and, consequently, that Eqs 2.7 are identical to Eqs 2.5.

An Important Remark
These calculations remain valid even when η is a function of $\underline{\boldsymbol{\mathcal{Z}}}^n$ and of the mean fields and timescale (here $\mathcal{F}$ and T_L). However, it is worth emphasising that the fact that η is independent of the random variables representing the stochastic integrals is a crucial point in the above verification and that these properties would break down otherwise. Indeed, in this spurious case we would have:

$$\begin{aligned}&\left\langle\exp\left(-\frac{(1-\eta)\Delta t}{T_L}\right)(I^{\mathcal{Z}_1})^{\{2\}}(\eta\Delta t)(I^{\mathcal{Z}_2})^{\{2\}}(\eta\Delta t)\right\rangle \\ &\qquad\neq\left\langle\exp\left(-\frac{(1-\eta)\Delta t}{T_L}\right)\right\rangle\left\langle(I^{\mathcal{Z}_1})^{\{2\}}(\eta\Delta t)(I^{\mathcal{Z}_2})^{\{2\}}(\eta\Delta t)\right\rangle,\end{aligned}\tag{2.12}$$

with $\mathcal{Z}_1$ and $\mathcal{Z}_2$ either X or U and:

$$\left\langle\exp\left(-\frac{(1-\eta)\Delta t}{T_L}\right)\right\rangle\neq\exp\left(-\frac{(1-\eta)\Delta t}{T_L}\right). \tag{2.13}$$

This reflects the non-anticipation issue brought out repeatedly throughout this section. Having carried out this verification test case, we can now consider validation test cases.

Remark 2.2.1. In fact, it is specifically required for the estimation of the time step to be non-estimating. Nevertheless, respecting this constraint, it is possible to introduce an anticipating aspect in the stochastic drawings. Such a situation might be useful if the knowledge of final state of the stochastic processes is necessary *a priori*. It is however worth stating that any anticipation of the stochastic draw should be handled with great care and requires to introduce the notion of Brownian bridges. An extension of the algorithm presented here for these situations and based on Brownian bridges is proposed in Appendix 2.A.

2.3 Numerical Results

Contents

Having checked that all the criteria set forth at the beginning of Section 2.2 are met, the new algorithm is now validated. For that purpose, it has been implemented in the open source CFD solver code_saturne (see Archambeau et al. [2004]) and numerical results are compared to analytical ones in two situations:

- The first case consists in checking that statistics obtained from particle-attached variables by Monte-Carlo methods are in line with analytical expressions when all mean fields and timescales are constant (i.e. a uniform mean flow). This is done in Section 2.3.1 using a point source particle dispersion in a stationary homogeneous isotropic turbulent flow.
- The second case corresponds to a simple but challenging non-uniform flow involving curved streamlines, which allows to assess the accuracy of the new algorithm in complex situations where classical particle-tracking algorithms often encounter limitations (see Section 2.3.2).

2.3.1 Validation in a Uniform Flow

Drawing on the verification test case carried out in Section 2.2.2.2, the aim is twofold: first, to check that, with the new proposed time-splitting method, numerical results are exact when flow properties are constant in time and space; second, to bring out discrepancies induced when using an anticipation method even in such a simple case. To that end, the dispersion of particles released from a point source is analysed in a stationary homogeneous isotropic turbulent flow. This choice is motivated by the fact that, in such a context, analytical formulas can be derived as made e.g. by Minier et al. [2003b].

In the following, we start by describing the system considered, including physical aspects (e.g., flow characteristics), as well as numerical ones (e.g., spatial discretisation, time step) and theoretical results. Then, numerical results are validated with respect to these theoretical expressions.

2.3.1.1 System Considered: Point Source Dispersion in Homogeneous Isotropic Turbulence

Physical Aspects

The case studied consists of a point-source (fluid) particle dispersion in a stationary homogeneous isotropic turbulent flow. This means that the flow is uniform and stationary within the domain considered and that it is periodic in all directions. Here, we have imposed a velocity based on the turbulent dispersion $U_\alpha = \sqrt{\langle u_\alpha^2 \rangle} = 1\,\mathrm{m\,s^{-1}}$ and a Lagrangian timescale $T_L = 1\,\mathrm{s}$.

Numerical Aspects

Simulations were carried out using the CFD software code_saturne. The mean flow field is imposed taking into account an extra artificial forcing to maintain a constant level of energy within the system (see Pope [2000]). This leads to a flow field with a constant dissipation rate equal to $\epsilon = \frac{2}{\mathcal{C}_0} \frac{U_\alpha^2}{T_L}$ where the proper closure of T_L for homogeneous stationary flow is $T_L = 4k/(3\mathcal{C}_0\epsilon)$ (see Pope [2000], Minier and Peirano [2001]) with $k = 3/2U_\alpha^2$, and $\mathcal{C}_0$ the Kolomogorov constant in the diffusion coefficient of the Langevin model. Once fluid mean fields are obtained, 100 000 fluid particles are injected at the centre of the box. Their trajectories are computed using the new algorithm described in Section 2.2. The total size of the domain (box) is taken large enough so that the particles do not reach boundaries during each simulation.

Theoretical Aspects

As shown in Section 2.2.2.2, the algorithm is exact when all mean fields and timescales are constant. By resorting to Itô's calculus, it is then straightforward to derive analytical formulas for the variances $\langle X^2 \rangle$ and $\langle U^2 \rangle$ as well as for the covariance $\langle XU \rangle$ as a function of time, taking $t_0 = 0$ as the initial time when particles are released. From these analytical solutions, we can extract two limit cases: the ballistic (i.e., when $t \ll T_L$) and the diffusive one (i.e., when $t \gg T_L$). This was done in Minier et al. [2003b], yielding to the following limit expressions:

Ballistic limit case ($t \ll T_L$)

$$\langle X^2 \rangle \sim \mathcal{C}_0 \frac{\epsilon t^2 T_L}{2} = U_\alpha^2 t^2, \tag{2.14a}$$

$$\langle XU \rangle \sim \mathcal{C}_0 \epsilon t^2 = 2U_\alpha^2 \frac{t^2}{T_L}, \tag{2.14b}$$

$$\langle U^2 \rangle \sim \mathcal{C}_0 \epsilon t = 2U_\alpha^2 \frac{t}{T_L}. \tag{2.14c}$$

Diffusive limit case ($t \gg T_L$)

$$\langle X^2 \rangle \sim \mathcal{C}_0 \epsilon T_L^2 t = 2U_\alpha^2 T_L t, \tag{2.15a}$$

$$\langle XU \rangle \sim \frac{\mathcal{C}_0 \epsilon T_L^2}{2} = U_\alpha^2 T_L, \tag{2.15b}$$

$$\langle U^2 \rangle \sim \frac{\mathcal{C}_0 \epsilon T_L}{2} = U_\alpha^2. \tag{2.15c}$$

The asymptotic behaviour first presented by Taylor [1922] in its fundamental work on dispersion is well retrieved. It is worth mentioning that, in the diffusive regime, the only physically-relevant statistic is $\langle X^2 \rangle$ since the instantaneous particle velocity does not play a role anymore in the particle position evolution equation. This corresponds to the notion of fast-variable elimination (here U becomes a fast variable that can be eliminated), which is addressed extensively in standard textbook of Gardiner [1985] as well as in previous works both from the theoretical standpoint (see Minier and Peirano [2001], Minier [2016]) and the numerical one (see Peirano et al. [2006]). The constant value of the velocity second-order moment still retains its typical kinetic energy meaning (showing that we are actually dealing with particles in contact with a kind of thermostat) but the correlation $\langle XU \rangle$, which is less physically-meaningful, is also considered since both results are useful to discuss statistical noise in Monte Carlo estimations.

2.3.1.2 Validation

In the following, we check that numerical results are in agreement with analytical formulas regardless of the number of occurrences the time-splitting algorithm is called in two cases:

- A first set of simulations was performed with a focus on the ballistic regime. For that purpose, the time step was taken equal to $\Delta t = 0.05T_L$. Two spatial discretisations were considered: $\Delta x = U_\alpha \Delta t/50$ and $\Delta x = 10U_\alpha \Delta t$. These two grid sizes were carefully chosen so that first one (resp. the second one) corresponds to the case where the average particle displacement during one time step is much smaller (resp. much larger) than the grid size Δx. The simulations were run for a total time equal to $6T_L$.

Figures 2.6A-2.6C display the second-order moments as a function of the dimensionless time $t^* = t/T_L$, comparing results obtained with the new algorithm to analytical formulas. It can be seen that the outcomes of the new algorithm remain exact for both cases. This validates the new algorithm (which has been activated on average 50 times every time step in the case where $\Delta x = U_\alpha \Delta t/50$). Small differences between results obtained with the cell-to-cell algorithm and analytical values are simply related to statistical errors using Monte Carlo methods (due to a finite number of fluid particles), as discussed below.

As can be seen in Figs. 2.6D-2.6F, completely different results are obtained when using an anticipation method, such as the naive formulation outlined in Section 2.2.1. This is especially revealed by the strong dependence on the cell size, which indeed governs how often the time-splitting algorithm is applied. Whereas results remain roughly acceptable in the case of a large-enough cell size (meaning that the new algorithm is seldom called), numerical predictions quickly deteriorate when smaller cell sizes are considered (i.e. using $\Delta x = U_\alpha \Delta t/50$), therefore inducing severe errors.

- A second set of simulations was carried out in the diffusive limit case. For that purpose, the time step was taken equal to $\Delta t = 200 T_L$. To assess that numerical results are independent of the number of times the new algorithm is applied, two spatial discretisations were also considered: $\Delta x = U_\alpha \Delta t/20$ and $\Delta x = 2.5\ U_\alpha \Delta t$. The simulations were run for a total time equal to $24\,000\ T_L$.

  Figures 2.7A-2.7C display the evolution of the second-order moments as a function of time, indicating that the new algorithm provides accurate results regardless of the number of occurrences the time-splitting algorithm is used within a time step. In Figure 2.7A, it is seen that $\langle X^2 \rangle$ follows a linear evolution right from the outset, as it should be in the diffusive regime, and that the slope is properly reproduced when using non anticipating methods. This demonstrates that the particle dispersion coefficient is well captured. As mentioned above, it is interesting to consider the numerical predictions of $\langle U^2 \rangle$ in Fig. 2.7B and $\langle XU \rangle$ in Fig. 2.7C to bring out the statistical noise inherent to Monte Carlo methods. When considering $\langle U^2 \rangle$, the variance of the Monte Carlo estimator is constant in time since $\mathrm{Var}(U^2) = 2\,\langle U^2 \rangle^2$ and the 99% confidence interval is indicated by the two horizontal lines shown in Figs. 2.7B and 2.7E. However, for the correlation $\langle XU \rangle$, the variance of the estimator is a function of time since $\mathrm{Var}(XU)(t) = (\mathcal{C}_0 \epsilon)^2 T_L^4/2\,(1 + t/T_L)$ and the envelope lines limiting the 99% confidence interval are now increasing with time, as displayed in Figs. 2.7C and 2.7F. Note again that the resulting increasing level of noise for $\langle XU \rangle$ is a mere observable and has no feedback effect on the particle simulation.

  On the other hand, as can be seen in Fig. 2.7D, an anticipating method, such as the naive formulation outlined in Section 2.2.1, is unable to reproduce the correct dispersion coefficient, especially when the time-splitting algorithm is often called (in Fig. 2.7D, this corresponds to the case $\Delta x = U_\alpha \Delta t/20$ where 20 cells are crossed per iteration on average). For the sake of completeness, we also display $\langle U^2 \rangle$ in Fig. 2.7E and the correlation $\langle UX \rangle$ in Fig. 2.7F, which further confirms that an anticipation method yields results that fluctuate but around incorrect averages.

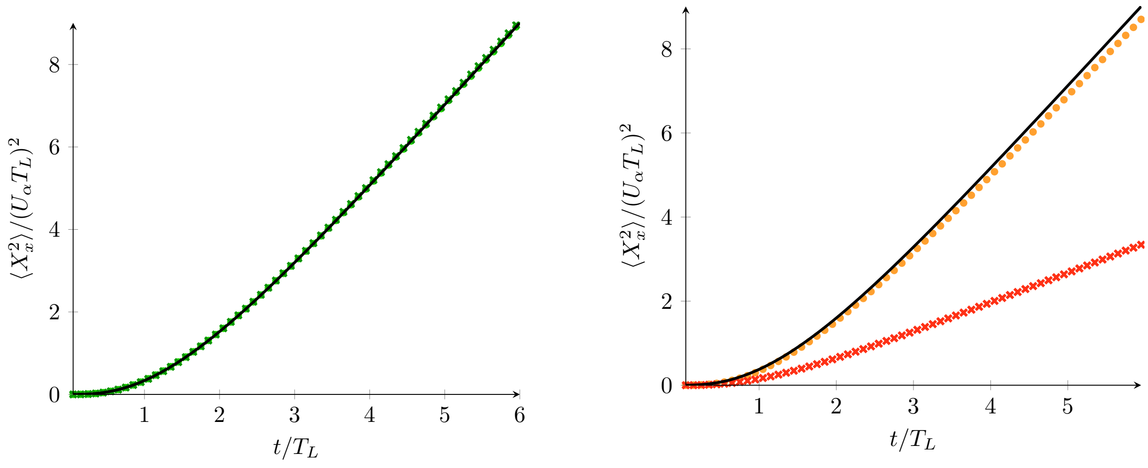

(A) $\langle XX \rangle$ using the proposed method.

(D) $\langle XX \rangle$ using an anticipating method.

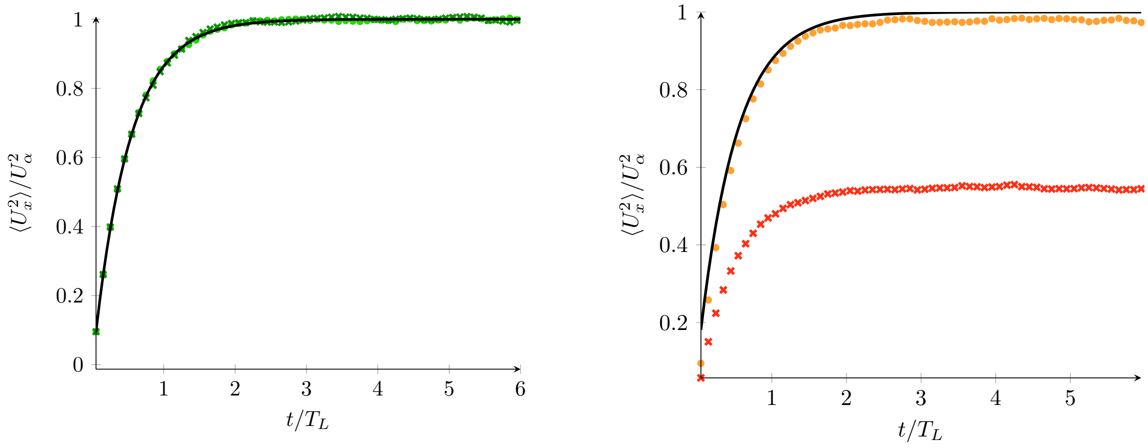

(B) $\langle UU \rangle$ using the proposed method.

(E) $\langle UU \rangle$ using an anticipating method.

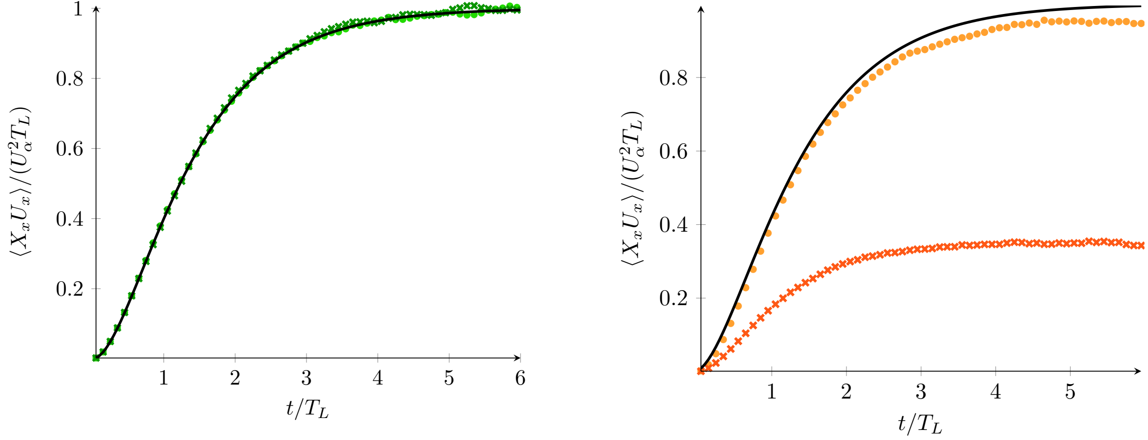

(C) $\langle XU \rangle$ using the proposed method.

(F) $\langle XU \rangle$ using an anticipating method.

Figure 2.6: Evolution of $\langle XX \rangle$, $\langle UU \rangle$, $\langle UX \rangle$ as a function of the dimensionless time in the ballistic limit case with a time step $\Delta t = 0.05 T_L$. Two spatial refinements are considered: × (resp. ●) corresponds to simulations with a cell size $\Delta x = U_\alpha \Delta t/50$ (resp. $10\ U_\alpha \Delta t$). On the left part, comparisons between the analytical solution (___) and numerical results obtained with the new algorithm are presented. On the right part, the results with a spurious anticipating method are plotted.

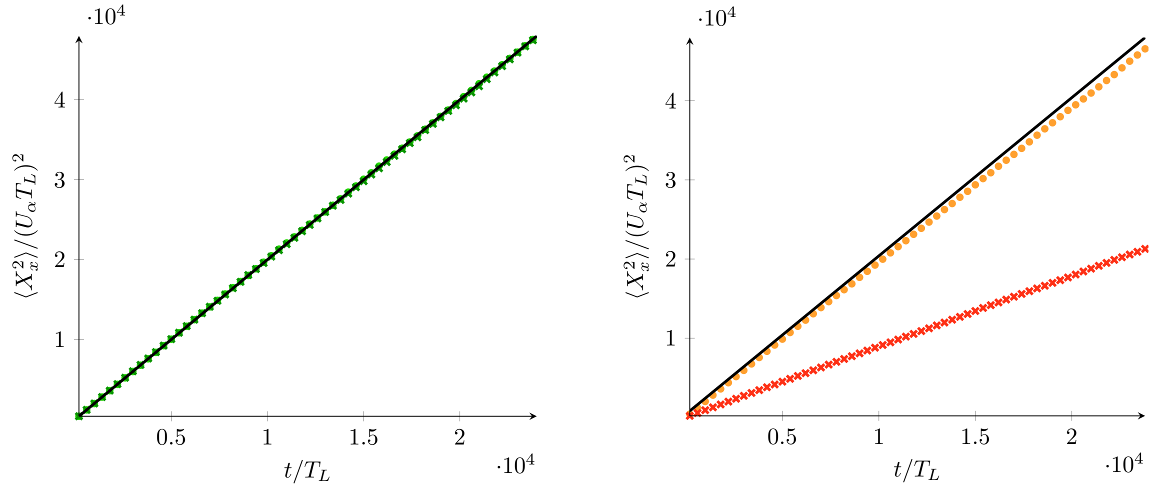

(A) $\langle XX\rangle$ using the proposed method.

(D) $\langle XX\rangle$ using an anticipating method.

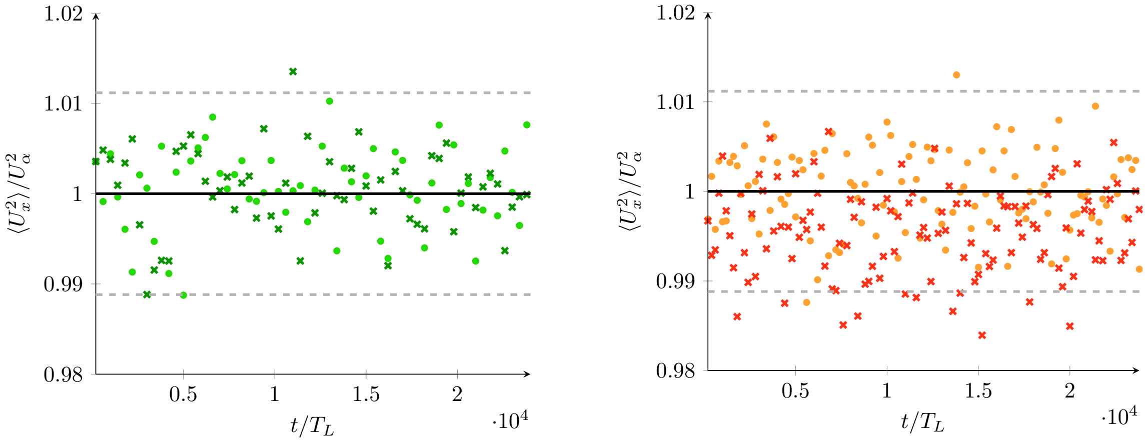

(B) $\langle UU\rangle$ using the proposed method.

(E) $\langle UU\rangle$ using an anticipating method.

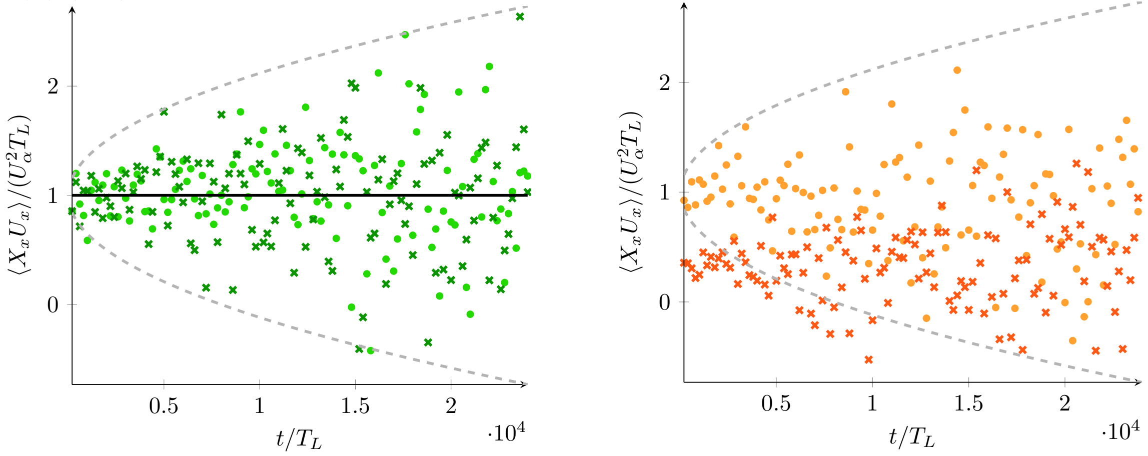

(C) $\langle XU\rangle$ using the proposed method.

(F) $\langle XU\rangle$ using an anticipating method.

Figure 2.7: Evolution of $\langle XX\rangle$, $\langle UU\rangle$, $\langle UX\rangle$ as a function of the dimensionless time in the diffusive limit case with a time step $\Delta t = 200T_L$. Two spatial refinements are considered: × (resp. •) corresponds to simulations with a cell size $\Delta x = U_\alpha\Delta t/20$ (resp. $2.5\ U_\alpha\Delta t$). On the left part, comparisons between the analytical solution (——) and numerical results obtained with the new algorithm are presented. On the right part, the results with a spurious anticipating method are plotted. The dashed lines (- - -) correspond to the envelop for the 99% confidence interval (analytical formula).

At this stage, it is worth emphasising that present results were obtained in a 1-D dispersion case. However, these results are directly generalised to 3-D dispersion cases since each direction is treated independently. Furthermore, similar behaviours were obtained using 3-D unstructured meshes instead of regular 1-D Cartesian meshes (details are provided in 2.B).

2.3.2 Validation in a Non-Uniform Flow

Having validated the new algorithm in a uniform flow, the idea is to validate the algorithm in the case of non-uniform flows. To that end, a laminar flow is considered so that the stochastic terms in the time-integration part of the algorithm are equal to zero. This ensures that the time-integration part is deterministic, hence allowing to check that the computed trajectory in non-uniform flows is exact. In addition, a cylindrical Couette flow has been chosen since it is one of the simplest non-uniform flows. In that case, each fluid particle is indeed expected to follow a purely circular motion around the centre of rotation of the cylinder.

In the following, we start by describing the system considered, including both physical aspects (e.g., geometry of the rotating cylinders, flow characteristics) and numerical aspects (e.g., spatial discretisation, time step). Then, the accuracy of the new trajectory algorithm is assessed. This validation is performed in two steps: first, we verify that the motion of a single particle actually follows a purely circular motion and, second, that statistics on particle concentration remain constant throughout the simulation time regardless of the time step used.

2.3.2.1 System Considered: a Laminar Cylindrical Couette Flow

Physical Parameters
The case studied here is a laminar cylindrical Couette flow. It consists of a fluid flow between two cylinders: the inner cylinder has a radius $r_{in} = 1\,\mathrm{m}$, rotating at a given angular velocity equal to $\omega_\theta(r_{in}) = 1\,\mathrm{s}^{-1}$, while the outer cylinder has a radius $r_{out} = 2\,\mathrm{m}$ and remains at rest. This means that the fluid is contained within the annulus of thickness $\delta r = 1\,\mathrm{m}$ that separates the two cylinders. The kinematic viscosity of the fluid is set to $1\,\mathrm{m}^2\mathrm{s}^{-1}$ so that the Reynolds number based on those quantities is equal to 1 (i.e., well within the laminar regime).

In this configuration, the fluid is flowing in a cylindrical motion. As a result, the velocity field is unidirectional and, written with the cylindrical coordinate $\underline{\boldsymbol{e_\eta}}$, is given by the analytical solution:

$$U = U_\theta(r) = \langle U_\theta \rangle(r) = \frac{r_{in}\omega_\theta(r_{in})}{\dfrac{r_{in}}{r_{out}} - \dfrac{r_{out}}{r_{in}}} \left(\frac{r}{r_{out}} - \frac{r_{out}}{r} \right) \tag{2.16}$$

where r is the distance from the rotating centre.

Numerical Parameters
The simulations are carried out using the CFD software code_saturne to solve the Navier–Stokes equation on a 360° polyhedral mesh: it comprises 360 cells in the azimuthal direction (i.e. the azimuthal discretisation angle is $\Delta\theta = 1°$) and 21 in the radial one. The simulations are run using a constant time step, whose value is taken between $0.055\,\mathrm{s}$ and $200\,\mathrm{s}$. This range of values has been chosen to assess the accuracy of the algorithm with respect to the time step, especially at large time steps where the average particle displacement is much greater than the grid size.

The tracking of fluid particles within this laminar cylindrical Couette flow is obtained by applying the algorithm described in Section 2.2. The Lagrangian integral time T_L has been set to $0\,\mathrm{s}$ to force a laminar flow (i.e., all stochastic integrals are equal to zero).

2.3.2.2 Accuracy of Numerical Results

The new algorithm is here validated by checking that, first, the trajectory of a single particle follows a purely cylindrical motion and, second, that the initial particle concentration along the radial direction is conserved in time. In the following, all results are plotted using a dimensionless time defined as $t^+ = t\,\omega_\theta(r_{in})/(\Delta\theta)$. This means that the dimensionless time step Δt^+ measures the ratio between the average particle displacement and the grid size (in the azimuthal direction) near the inner wall.

Results on a Single Particle Trajectory

The motion of a fluid particle in a laminar cylindrical Couette flow is expected to follow a purely circular trajectory. This means that each particle remains at a constant distance r from the rotating centre throughout the simulation. A simulation has been run for 400 iterations using a time step of 1.024 s. This means that the average particle displacement is equal to 55 times the grid size $\Delta\theta \times r_{in}$ near the inner cylinder and to 0.5 times the grid size $\Delta\theta \times r_{out}$ near the outer one.

Figure 2.8 displays the trajectory of two particles: one is initially located very close to the inner cylinder while the second one is initially located in the bulk. The trajectory (left-hand plot) clearly shows that the new algorithm does lead to a circular motion. These results confirm the accuracy of the new algorithm even for large values of the time step. This is further supported by the time-evolution of the radius r (right-hand plot). In fact, the results are not distinguishable from the theoretical expectations, even for the particle initially close to the inner cylinder (which has circled the cylinder close to 60 times by the end of the simulation).

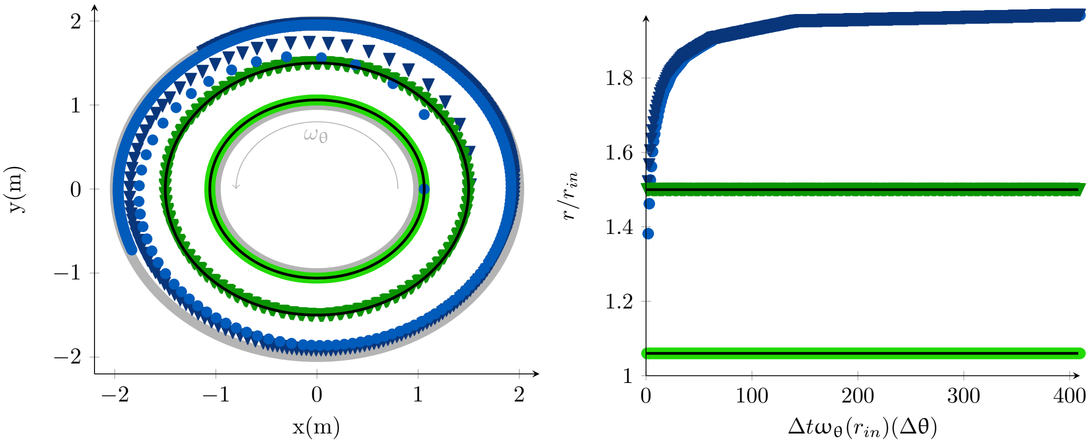

Figure 2.8: Trajectory of particles (left) and corresponding evolution of the radius r as a function of the time t (right) for a constant time step corresponding to $\Delta t^+ = 55$. Two particles are followed: one located initially in the vicinity of the wall (●) and one in the centre of the domain (▼). For each particle, the results obtained with the new algorithm (green) are in agreement with the expected trajectory (—) , while the results obtained with the reference scheme (blue) are flawed by integration error (leading to accumulation in the region near the outer cylinder).

Figure 2.8 also displays the results obtained with the reference algorithm, which does not account for cell-to-cell integration. It can be seen that the radius increases with time all the more when the time step increases. This is due to the error made when no cell-to-cell integration is made while using large time steps. The origin of the error is illustrated in Figure 2.9: the spatial discretisation and P_0 interpolation mean that each particle experiences a constant velocity within a cell. As a particle crosses a face, if the velocity is not updated immediately, the particle will move for the remainder of the time step with the velocity encountered in the previous cell. Since this previous fluid velocity is slightly shifted with respect to the radial direction in the current new cell, it induces an error without cell-to-cell integration which is directly proportional to the time step.

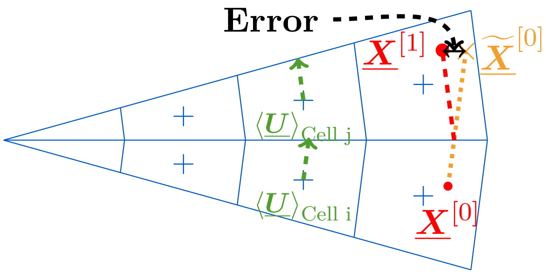

Figure 2.9: Scheme highlighting the origin of the numerical error in the algorithm without cell-to-cell integration. This error induces an accumulation of particles near the outer cylinder as time increases without cell-to-cell integration (see Figure 2.10).

Results on Particle Concentration

We focus now our attention on simulations in which a large number of fluid particles is tracked. In that case, the statistics of interest is the particle concentration along the radial direction. In fact, since each fluid particle follows a circular orbit, the particle concentration should remain constant throughout time. With this result in mind, we verify here that the particle concentration is homogeneous in space provided that fluid particles are homogeneously distributed in space initially.

Numerical simulations have been carried out with 200,000 fluid particles initially homogeneously distributed in space. The concentration is then analysed by computing the particle number concentration in each of the 21 cells along the radial direction. Figure 2.10 displays the evolution of the concentration, which has been normalised with the initial concentration, as a function of the distance r. It can be seen that, for a dimensionless time step equal to $\Delta t^{+} \simeq 5.5$, the concentration obtained remains constant in all the domain throughout the whole simulated time. Meanwhile, the results obtained with the reference algorithm (i.e., without cell-to-cell integration) show that particles tend to accumulate in the outer region, leading to an increasing concentration in the outer region with time (the stationary state at longer times will consist in having all particles located at the outer cylinder).

To further assess the accuracy of the new algorithm, the error between the numerical value and the theoretical value of the number concentration has been computed within each of the 21 regions. The average error over the whole domain and simulation time (here 41 s) is displayed in Figure 2.11 as a function of the dimensionless time step Δt^{+}. It confirms that the new algorithm provides accurate results regardless of the time step used, i.e., both when the average displacement is smaller or greater than the grid size. The small (constant) error with the new algorithm comes from the statistical noise due to Monte Carlo methods at initialisation. Indeed, due to the finite number of particles, the initial number of particle in each cell does not ensure exactly $c^{+} = 1$. Meanwhile, the results obtained without cell-to-cell integration clearly show an increasing numerical error with increasing time steps.

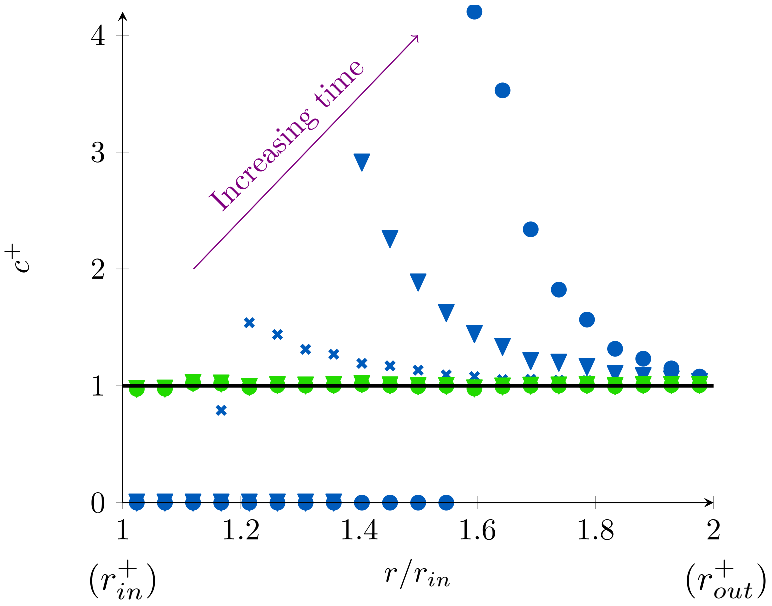

Figure 2.10: Evolution of the dimensionless concentration c^+ (concentration normalised by the initial concentration) as a function of the radius r. Results are displayed for various simulation times: t^+=275 (×), t^+=1100 (▼) and t^+=2200 (●). The time step is constant such that $\Delta t^+ \simeq 5.5$. The results obtained with the new algorithm (green) are in agreement with the analytical results (—) while the results obtained with the reference trajectory (blue) lead to an accumulation towards the outer cylinder which increases with time (arrow).

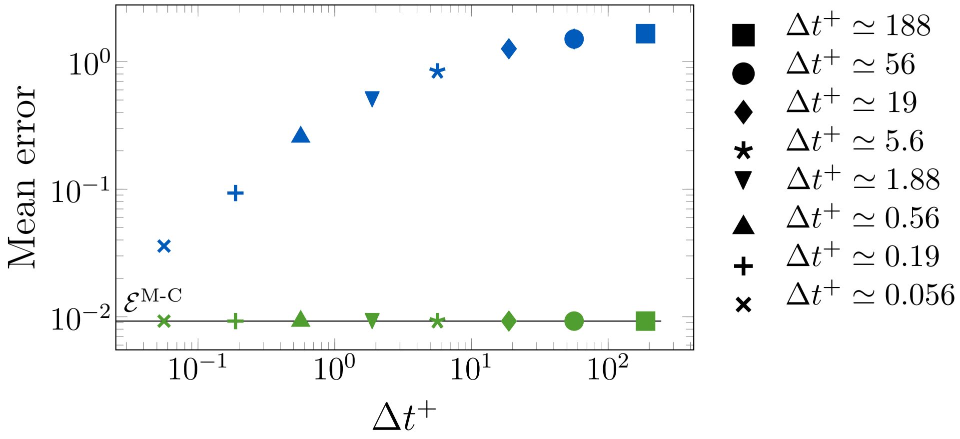

Figure 2.11: Convergence of the mean error on particle concentration computed at time t =41 s as a function of the time step, using the reference algorithm (blue) and the new cell-to-cell algorithm (green). Each pair of symbols corresponds to simulation carried out with the same given time step. These results confirm that the reference algorithm are impaired by integration error triggering an outward spurious drift (the error increases with increasing time steps) contrary to the new algorithm which remains accurate regardless of the time step (the constant non-zero error ε^{M-C} (—) is due to the statistical noise inherent to Monte Carlo methods).

Discussion on the computation cost

A short consideration regarding the processing cost induced by this algorithm is now in order. To support this discussion the averaged mean error is plotted against the computation time spent using one processor in Figure 2.12. It is evident that the sub-iterating process proposed increases the computation time for a given number of iteration (put forward by the use of a same symbol). Considering a very large number of iterations (points on the right of the plot), the splitting of the time step is seldom called. Therefore, the relative increase of computation time corresponding to a factor around 1.5 represents the computation cost related to the integration and trajectory steps associated to the auxiliary deterministic virtual partner. However, this increase can be offset by the necessity to run fewer iterations to obtain more accurate results. In fact, in the situation encountered here, where no particle is injected nor removed from the flow with stationary mean carrier fields, a single overall iteration is necessary. The new time-splitting method enables to reach the optimal time splitting with regard to the local CFL condition attached to each particle. While the particles in the vicinity of the inner ring are integrated over numerous small time steps, a large gain of processing time is achieved for the outer particles for which few integrations over large time steps are required due to their slow displacement on broad cells. In this sense, this algorithm enables to have a spatially adaptive time step depending on the dynamics of each particle. Furthermore, for large time steps as the number of sub-iteration tends to become proportional to the time steps, the overall computation time tends to stagnate. This can be seen on the points furthest to the left of Figure 2.12 where a limit computation time t^{opimal}_{comput} schematically represented arises. The latter is the minimum processing time necessary to properly treat the flow with respect to the local particle-attached CFL. In this example the time splitting algorithm proposed enables to gain both multiple scales of magnitude in accuracy and in processing times. This puts emphasis on the cell-to-cell integration efficiency and the gain it can provide for flows where the time step is limited by a CFL condition.

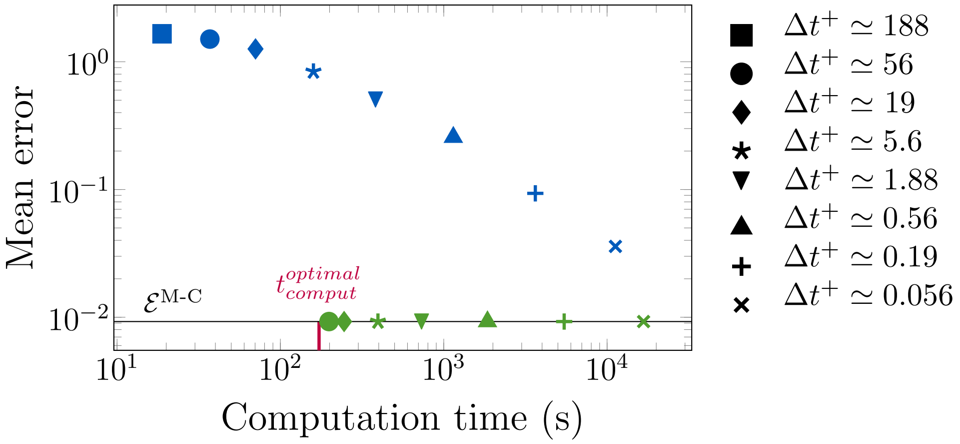

Figure 2.12: Convergence of the mean error on particle concentration computed at time t =41 s as a function of the computation time, using the reference algorithm (blue) and the new cell-to-cell algorithm (green). The different symbols correspond to different time steps used and correspond to the symbols used in Figure 2.11. Using the new algorithm, the error is independent of the time step and the computation time decreases with the increasing time step until a limit value t^{opimal}_{comput} reached when using a single integration optimally split for each particles.

2.4 Local Conclusions and Perspectives

In this chapter, we have developed a new cell-to-cell algorithm for particle tracking in the context of hybrid approaches that couple Lagrangian stochastic methods with mean-field ones. The cell-to-cell integration consists in dividing the time step into a number of sub-iterations, each one corresponding to the motion of a particle within one cell. This means that the motion of a particle is stopped each time it crosses a face and leaves a cell, at which point the mean fields are updated to compute particle displacement over the remainder of the time step. This decomposition allows naturally to account for changes in the mean fields every time a particle enters a new cell. Given the stochastic nature of the model, an additional constraint has to be satisfied: no anticipation should be made when estimating the residence time in each cell. Indeed, a naive formulation would consist in first predicting particle displacements over a time step and then try to deduce the residence times in the cells that have been crossed. Yet, this would yield estimations of these residence times that become functions of the future of the Wiener process driving the diffusion term, in direct violation of the very definition of the stochastic integral in the Itô sense. To avoid this pitfall, and the resulting spurious numerical drift and diffusion values it would entail, careful estimations based only on values at the beginning of each sub-time steps must be made. In the present algorithm, this is achieved by introducing the notion of a virtual partner whose motion is governed by mean conditional increments and which is used to provide free-of-statistical-bias estimation of the residence times in the different cells being crossed during one time step.

Drawing on these two notions (cell-to-cell integration and non-anticipation), the new algorithm is built on a three-step process. The first step consists in computing the deterministic estimation of the particle position at the end of the time step. Then, the trajectory algorithm based on a free-flight assumption is applied to determine if the particle leaves/remains in the cell. If it remains in the cell, the position and velocity of the particle at the end of the time step are computed. Otherwise, the trajectory algorithm provides information on the exit time and exit location. The whole three-step process is repeated again but starting from the last known exit location and for the remainder of the time step. This process is repeated until the particle reaches its final destination at the end of the time step Δt (i.e. it does remain in the cell).

A first analysis consists in checking that the new algorithm remains exact for constant mean fields. In the more general case of non-uniform flows, since the residence times are now only approximated, the time integration scheme cannot be regarded as exact but the overall scheme is guaranteed to respect the non-anticipating constraint and is shown to provide considerable improvements over the current algorithm for particle tracking in non-homogeneous flows. This is further demonstrated by considering numerical predictions in two test cases: particle dispersion in a uniform mean flow and particle dynamics in a non-uniform flow. These two cases have confirmed the improved accuracy of the new algorithm, even when large time steps are used.

At this point, it is worth emphasising that, although we have considered fluid particles and a simple Langevin model, the same method can be directly applied to dispersed turbulent two-phase flows, particles with additional quantities in the state vector, and, more generally, to similar stochastic dynamical models which require to track particles in complex geometries and meshes. Note that in the examples presented in Section 2.3 one concerns a laminar flow and the second one a high-Reynolds-number turbulent flow. However, the present methodology (i.e. the time-splitting algorithm) is not limited to these situations and can be applied to any flows regardless of the Reynolds number, provided that an adequate dynamical model and its corresponding numerical scheme are applied. Furthermore, this new algorithm paves the way towards the development of refined algorithms for such hybrid approaches that couple

Lagrangian methods with mean-field approaches. In this work, we have applied a cell-to-cell integration every time a particle enters a new cell. On the other hand, this time-splitting scheme could be applied only when mean fields differ significantly from one cell to another. Hence, a refined algorithm could be devised using test functions to quantify variations in the mean-field quantities along particle trajectories and apply this time-splitting method only when variations are larger than a given threshold.

Let us note that although this method improves the numerical robustness and accuracy associated to the temporal integration, in the context of dispersion of fluid particles in atmospheric flows a second issue associated to the integration scheme should still be tackled. Indeed, near wall the necessity to have a time step much lower than the Lagrangian timescale to avoid spurious downward effects is in general a condition harder to fulfil than the necessity for the particle to cross not too many cells over a time step. In order to be fully functional in such flows, the time splitting method developed here should be used with the extended integration scheme proposed by Minier [2016]. The development of the latter would enable to fully get rid of the constraint based on the value of the Lagrangian timescale. To that effect, a further study and validation on this extended scheme should be carried out.

Local Appendices

2.A An Anticipating Extension of the Methods using Brownian Bridges

In some methods, interactions such as collision between particles in diffusive regime are estimated using a stochastic approach knowing their initial and final positions (see e.g. Henry et al. [2014] Mohaupt et al. [2011]). An anticipated estimation of their positions before the cell-to-cell integration could be useful to determine if the particles interact during the whole time step and improve the treatment of those interactions. Such estimations might require anticipations of the draws for the Wiener process at the end of the time step and must be properly tackled to avoid spurious drifts.

In order to circumvent the drifts caused by mismanaged anticipations, a second idea is to make a first draw for the global time step and take it into account, in the draws used for the intermediate sub-iterations. A naive proposition could be to keep the value drawn for the global time step for each sub-iteration. However, this solution also implies statistical biases because by definition of Wiener processes, new increments of Wiener process have to be independent of the previous ones. It is thus necessary to be able to generate an intermediate path of the Wiener process knowing its value at the end of the time step. The goal of this section is to determine how to obtain such draws and their link with draws made for the global time step.

2.A.1 Presentation of Brownian Bridges

The case considered is a situation where the value of the Wiener process is fixed at both ends $\mathcal{W}(t_n)$ and $\mathcal{W}(t^{n+1})$ with $t^{n+1} = t^n + \Delta t$. Estimating an intermediate Gaussian trajectory between two known positions of a Wiener process, corresponds exactly to the situation of a Brownian bridge Glasserman [2013]. We can see some realisations of such Brownian bridges in Figure 2.A.1.

These Brownian bridges will then be used in this version of the algorithm. The corresponding drawings are briefly presented here. Let us take an intermediate time η fully independent of all drawings, the Brownian bridge $\mathcal{B}r$ is a random variable given by:

$$\mathcal{B}r(\eta) = \mathcal{W}(t^n + \eta\Delta t)|_{(\mathcal{W}(t^n), \mathcal{W}(t^n+\Delta t))} \sim \mathcal{N}(\mathcal{W}(t^n) + \eta(\mathcal{W}(t^n+\Delta t) - \mathcal{W}(t^n)), \eta(1-\eta)\Delta t) \quad (2.17)$$

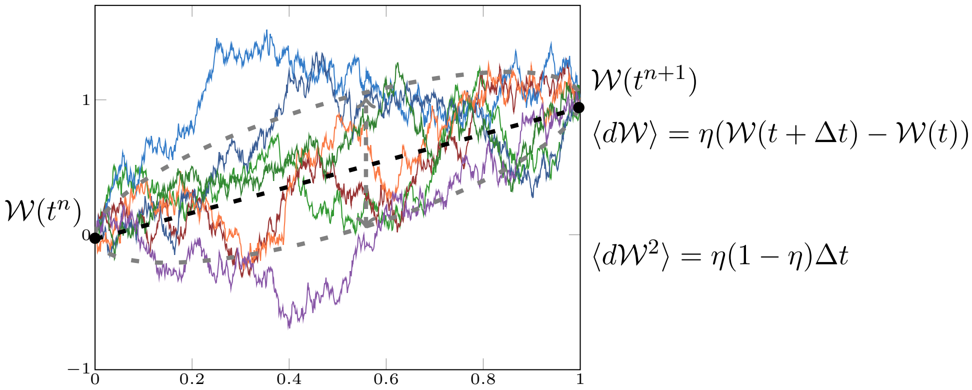

Figure 2.A.1: Some realisations of Gaussian trajectories using a Brownian Bridge.

It is worth noticing that its average value at a given time is the corresponding value on the segment between $\mathcal{W}(t^n + \Delta t)$ and $\mathcal{W}(t^n)$. The variance is defined as a quadratic function which is null at each intersection where the values are fixed. It is maximal at half the time step where we are the furthest from the restraining conditions. Thanks to this variable it is possible to have an estimation of the location of the Wiener process at any time between the two limits of the time step where the values are fixed.

2.A.2 Brownian Bridges based Draws used to Decompose the Time Step

First, we want to consider a decomposition of the time step into two sub-steps. The Wiener increment $\mathrm{d}\mathcal{W}_i^{\mathcal{Z}}(\Delta t)$ is then decomposed into two increments $\mathrm{d}\mathcal{W}_{1,i}^{\mathcal{Z}}(\eta\Delta t)$ and $\mathrm{d}\mathcal{W}_{2,i}^{\mathcal{Z}}((1-\eta)\Delta t)$ using an intermediate time $\eta\Delta t$. The sum of these two increments corresponds to the increment during the global time step.

$$\mathrm{d}\mathcal{W}_i^{\mathcal{Z}}(\Delta t) = \mathcal{W}_i^{\mathcal{Z}}(t^n + \Delta t) - \mathcal{W}_i^{\mathcal{Z}}(t^n) = \overbrace{\mathcal{W}_i^{\mathcal{Z}}(t^n + \Delta t) - B(\eta)}^{\mathrm{d}\mathcal{W}_{2,i}^{\mathcal{Z}}((1-\eta)\Delta t)} + \overbrace{B(\eta) - \mathcal{W}_i^{\mathcal{Z}}(t^n)}^{\mathrm{d}\mathcal{W}_{1,i}^{\mathcal{Z}}(\eta\Delta t)}. \tag{2.18}$$

We want to estimate the normalised draws corresponding to these two intermediate increments knowing that we have $\mathrm{d}\mathcal{W}^{\mathcal{Z}}(\Delta t)_i = \zeta_i^{\mathcal{Z}}\sqrt{\Delta t}$. Using the previous relation the two intermediate normalised draws $\zeta_{1,i}^{\mathcal{Z}}$ and $\zeta_{2,i}^{\mathcal{Z}}$ corresponding to $\mathrm{d}\mathcal{W}_{1,i}^{\mathcal{Z}}$ and $\mathrm{d}\mathcal{W}_{2,i}^{\mathcal{Z}}$ have to satisfy:

$$\zeta_i^{\mathcal{Z}}\sqrt{\Delta t} = \zeta_{1,i}^{\mathcal{Z}}\sqrt{\eta\Delta t} + \zeta_{2,i}^{\mathcal{Z}}\sqrt{(1-\eta)\Delta t}. \tag{2.19}$$

Dividing by the square root of the time step, we get:

$$\zeta_i^{\mathcal{Z}} = \zeta_{1,i}^{\mathcal{Z}}\sqrt{\eta} + \zeta_{2,i}^{\mathcal{Z}}\sqrt{(1-\eta)}. \tag{2.20}$$

Moreover, using the law proposed Eq. (2.17), we can determine an estimation of $\mathrm{d}\mathcal{W}_{1,i}^{\mathcal{Z}}(\eta\Delta t)$ using a new set of random variables $\chi_i^{\mathcal{Z}}$ which follow independent standard centred Gaussian distributions such as:

$$\mathrm{d}\mathcal{W}_{1,i}^{\mathcal{Z}}(\eta\Delta t) = \zeta_i^{\mathcal{Z}}\eta\sqrt{\Delta t} + \sqrt{\eta(1-\eta)\Delta t}\,\chi_i^{\mathcal{Z}}. \tag{2.21}$$

We can then compute the drawing to use for the first sub iteration.

$$\zeta_{1,i}^{\mathcal{Z}} = \zeta_i^{\mathcal{Z}}\sqrt{\eta} + \sqrt{1-\eta}\,\chi_i^{\mathcal{Z}}. \tag{2.22}$$

Knowing the value for the first draw, we can then determine, thanks to the relation described in Eq. (2.20), the corresponding draw for the remaining time which is:

$$\zeta^{\mathcal{Z}}_{2,i} = \sqrt{1-\eta}\zeta^{\mathcal{Z}}_{i} - \sqrt{\eta}\chi^{\mathcal{Z}}_{i}. \tag{2.23}$$

Once $\zeta^{\mathcal{Z}}_{i}$ and $\chi^{\mathcal{Z}}_{i}$ are drawn, the position of the intermediate value of the Wiener process $\mathcal{W}(\eta\Delta t)$ can be determined. It is worth noticing thatEq. (2.22) and Eq. (2.23) follow Gaussian distribution as a sum of similar Gaussian distributions. Moreover, $\zeta^{\mathcal{Z}}_{i}$ and $\chi^{\mathcal{Z}}_{i}$ following two independent standard centred Gaussian distributions, we have:

$$\langle\zeta^{\mathcal{Z}}_{1,i}\rangle = \langle\zeta^{\mathcal{Z}}_{2,i}\rangle = 0, \tag{2.24a}$$

$$\left\langle\left(\zeta^{\mathcal{Z}}_{1,i}\right)^2\right\rangle = \left\langle\left(\zeta^{\mathcal{Z}}_{2,i}\right)^2\right\rangle = 1, \tag{2.24b}$$

$$\langle\zeta^{\mathcal{Z}}_{1,i}\zeta^{\mathcal{Z}}_{2,i}\rangle = 0. \tag{2.24c}$$

The intermediate drawings respect well the condition imposed by their definition as dimensionless increments of Wiener processes Eq. (2.20) and follow independent standard centred Gaussian distributions. For a given sub-iteration $^{[m]}$ $(\zeta^{\mathcal{Z}}_{1,i})^{[m]}$ corresponds to the draw used for the integration until $\eta^{[m]}$, whereas $(\zeta^{\mathcal{Z}}_{2,i})^{[m]}$ corresponds to the remaining increment until $\mathcal{W}(t^{n+1})$. We have then $\zeta^{\mathcal{Z}}_{2,i})^{[m]} = (\zeta^{\mathcal{Z}}_{i})^{[m+1]}$.

2.A.3 Consistency Analysis of the Time Step Decomposition using Brownian Bridges

It is also important to ensure that this decomposition of the time step and the use of the two corresponding sub-time steps do not imply any statistical bias using the exponential scheme. Let us assume that we split an integration into two sub-integration as made in Section 2.2.2.2. The estimation of $(I^{\mathcal{Z}}_{i})^{\{2\}}(\eta\Delta t)$ and $(I^{\mathcal{Z}}_{i})^{\{2\}}((1-\eta)\Delta t)$ can be obtained similarly as previously simply by replacing the independent draws $(\zeta^{\mathcal{Z}}_{i})^{[1]}$ and $(\zeta^{\mathcal{Z}}_{i})^{[2]}$ by $(\zeta^{\mathcal{Z}}_{1,i})^{[1]}$ and $(\zeta^{\mathcal{Z}}_{2,i})^{[1]}$. The results found in Section 2.2.2.2 remain unchanged. The absence of statistical bias for a decomposition into two sub-iterations, remains correct providing that η is independent of the different stochastic draws. The latter ones being determined thanks to the independent draws $(\zeta^{\mathcal{Z}}_{i})^{[m]}$ and $(\chi^{\mathcal{Z}}_{i})^{[m]}$ the intersection time shall also be independent of any of these draws. The determination of the intersection time proposed in Section 2.2.2.2 remains valid. As previously, using a mathematical induction, it is possible to generalise this decomposition into any number of sub-steps without bias on the statistics.

A drawing method has been proposed to tackle without bias the anticipation of the value of the Wiener process thanks to the use of Brownian bridges. The sole modification, compared to the previous algorithm, is the necessity to initialise the global draw $(\zeta^{\mathcal{Z}}_{i})^{[0]}$ before the loop on the sub-iterations $(.)^{[m]}$, and to estimate not simply $\zeta^{\mathcal{Z}}_{[m],i}$ but $\zeta^{\mathcal{Z}}_{[m],1,i}$ as presented in Eq. (2.22). The draw $(\zeta^{\mathcal{Z}}_{2,i})^{[m]}$ corresponds to the new remaining draw for the rest of time step $(\zeta^{\mathcal{Z}}_{i})^[m]$. It will be used to determine the following draw $(\zeta^{\mathcal{Z}}_{1,i})^{[m+1]}$ used in the next iteration.

2.A.4 Verification using a Point Source Dispersion in a Maintained Uniform Isotropic Turbulent flow

The difference between this anticipating method using Brownian bridges and the standard non-anticipating time-splitting methods presented in Section 2.2 relies in the method to draw the Wiener processes appearing in the stochastic integrals. As in the non-uniform laminar test case studied in Section 2.3.2 the stochastic integrals are null, there is no difference between the reference time-splitting methods and the one presented in this appendix. In order to verify that the splitting of the time step using Brownian bridges does not induce bias in the estimation of the stochastic integral, a point source dispersion in a maintained uniform isotropic turbulent flow is considered. The same setup than in Section 2.3.1 is taken into account in Figure 2.A.2 and Figure 2.A.3. From these figures, it is clear that the Brownian bridges based anticipating methods presented here does not induce statistical bias on the estimation of the statistics. The interpretation of the results and the discussion on the statistical error provided in Section 2.3.1 given for the non-anticipating standard time splitting method are still valid and unchanged.

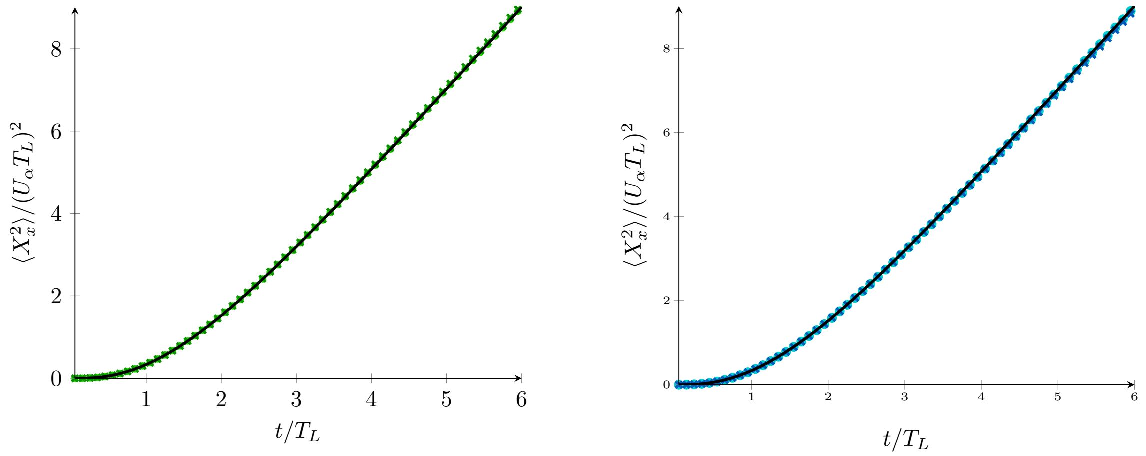

(A) $\langle XX\rangle$ using the standard non-anticipating time-splitting method.

(D) $\langle XX\rangle$ using the proper Brownian bridges based time-splitting method.

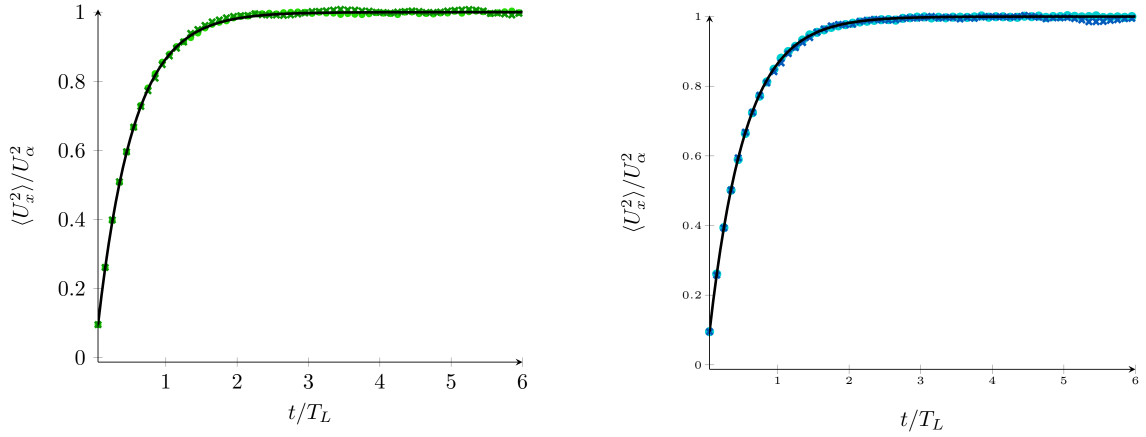

(B) $\langle UU\rangle$ using the standard non-anticipating time-splitting method.

(E) $\langle UU\rangle$ using using the proper Brownian bridges based time-splitting method.

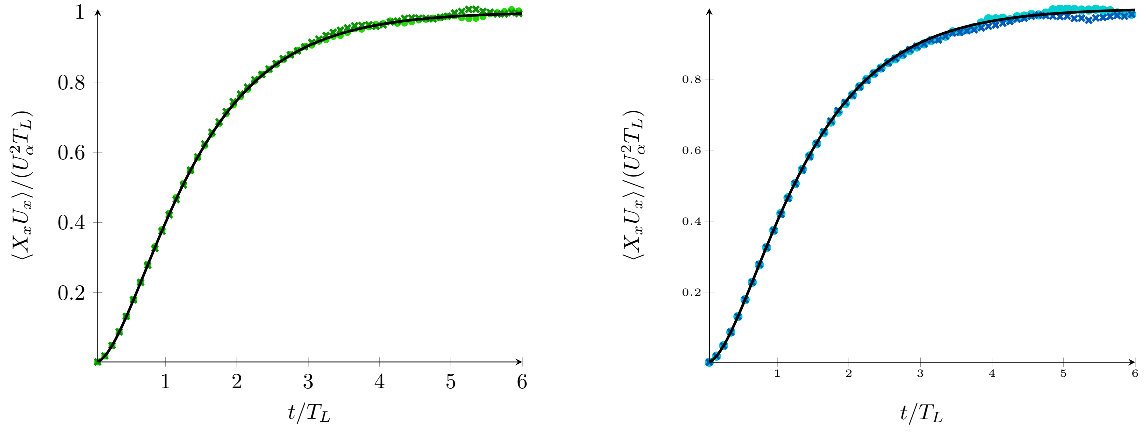

(C) $\langle XU\rangle$ using the standard non-anticipating time-splitting method.

(F) $\langle XU\rangle$ using using the proper Brownian bridges based time-splitting method.

Figure 2.A.2: Evolution of $\langle XX\rangle$, $\langle UU\rangle$, $\langle UX\rangle$ as a function of the dimensionless time in the ballistic limit case with a time step $\Delta t = 0.05T_L$. Two spatial refinements are considered: × (resp. •) corresponds to simulations with a cell size $\Delta x = U_\alpha \Delta t/50$ (resp. 10 $U_\alpha \Delta t$). On the left part, comparison between the analytical solution (—) and numerical results obtained with the standard time-splitting algorithm are presented. On the right part, the results obtained with the properly estimated anticipating methods based on Brownian bridges are plotted.

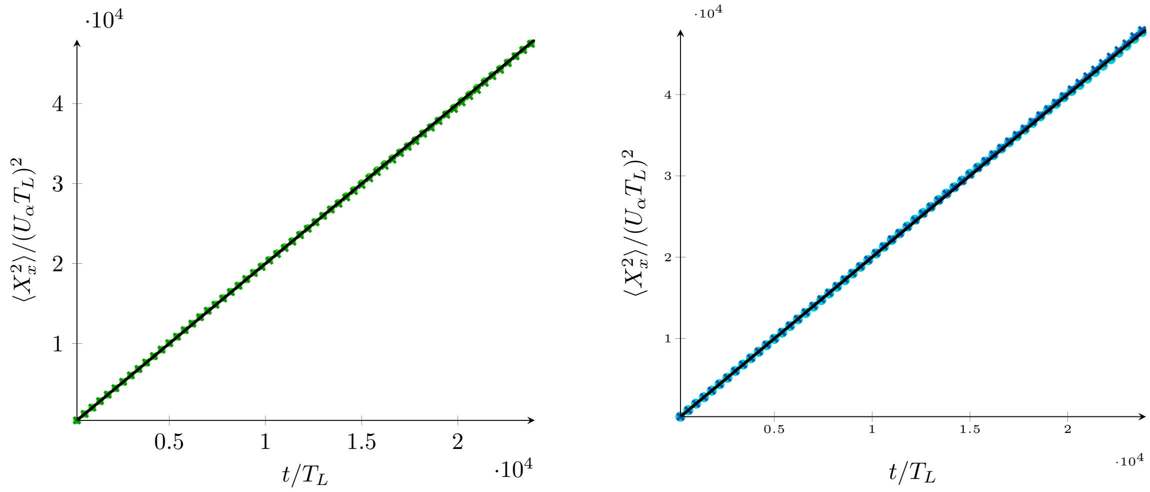

(A) $\langle XX \rangle$ using the standard non-anticipating time-splitting method.

(D) $\langle XX \rangle$ using the proper Brownian bridges based time-splitting method.

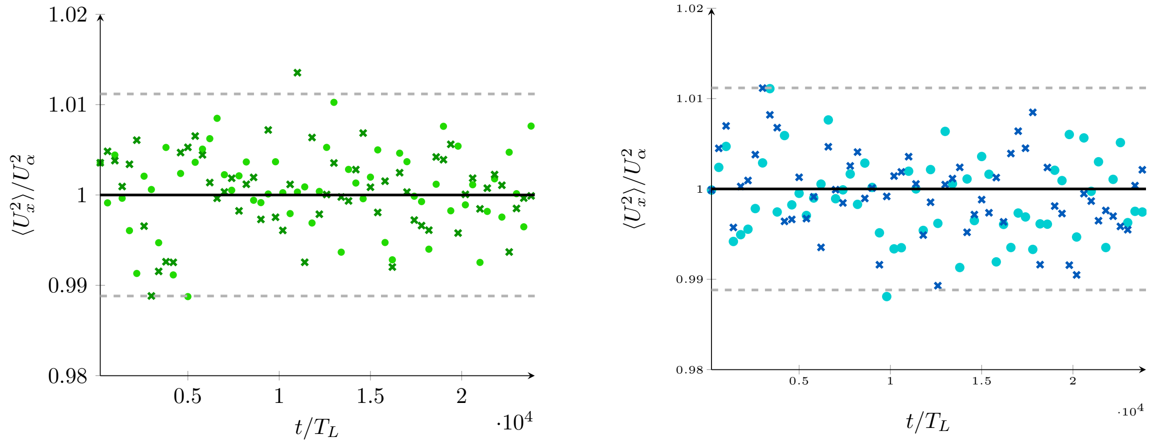

(B) $\langle UU \rangle$ using the standard non-anticipating time-splitting method.

(E) $\langle UU \rangle$ using the proper Brownian bridges based time-splitting method.

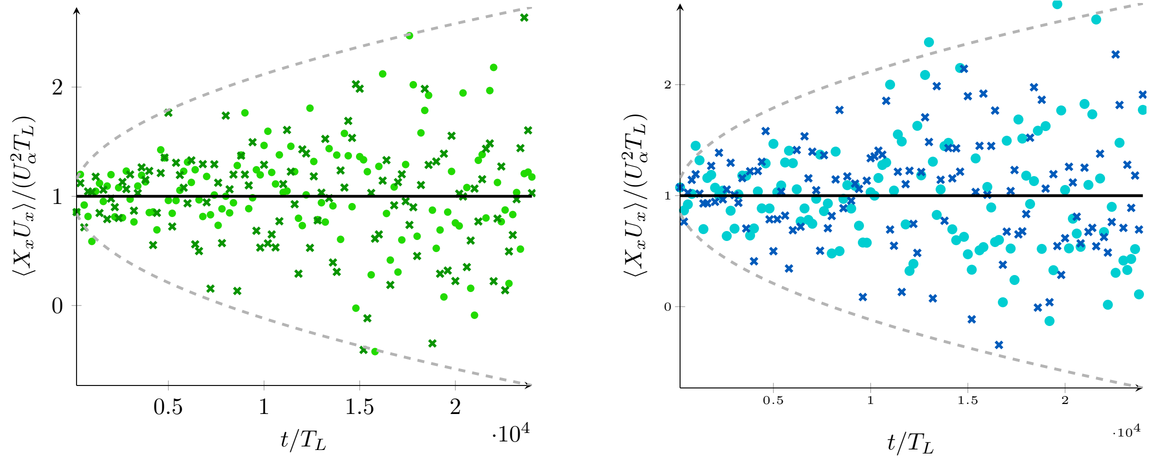

(C) $\langle XU \rangle$ using the standard non-anticipating time-splitting method.

(F) $\langle XU \rangle$ using the proper Brownian bridges based time-splitting method.

Figure 2.A.3: Evolution of $\langle XX \rangle$, $\langle UU \rangle$, $\langle UX \rangle$ as a function of the dimensionless time in the diffusive limit case with a time step $\Delta t = 200 T_L$. Two spatial refinements are considered: $\times$ (resp. $\bullet$) corresponds to simulations with a cell size $\Delta x = U_\alpha \Delta t/20$ (resp. $2.5\ U_\alpha \Delta t$). On the left part, comparison between the analytical solution (black line) and numerical results obtained with the standard time-splitting algorithm are presented. On the right part, the results obtained with the properly estimated anticipating methods based on Brownian bridges are plotted. The dashed lines correspond to the envelope for the 99% confidence interval (analytical formula).

2.B Details of the Particle Tracking Algorithm for 3-D Unstructured Meshes

This appendix presents the trajectory algorithm that is used in the present study. This algorithm is able to track the motion of particles even in 3-D fully unstructured meshes with warped faces. The tracking algorithm is first described, including the description of the original tracking algorithm with the detection of face-crossing events. Then, the algorithm is extended to compute the location and exit time when a particle crosses a face. Last, the algorithm is validated by comparing the numerical results obtained using various 3-D unstructured meshes in a simple non-uniform flow.

2.B.1 Principle of the neighbour search algorithm

The algorithm is based on a successive neighbour search. This means that the cell inside which a particle currently resides is determined by browsing through the neighbouring cells. Such algorithms require three pieces of information:

(a) The origin particle location $\underline{\boldsymbol{X}}_O = \underline{\boldsymbol{X}}^n$;

(b) The corresponding cell inside which it was initially;

(c) The destination particle location $\underline{\boldsymbol{X}}_D = \underline{\boldsymbol{X}}^{n+1}$ (as depicted in Figure 2.2).

The principle is then to determine if the particle leaves the current cell assuming a free-flight motion between point $\underline{\boldsymbol{X}}_O$ and $\underline{\boldsymbol{X}}_D$. This is performed by:

1. computing which faces of the current cell are intersected by the line $(\underline{\boldsymbol{X}}_O\underline{\boldsymbol{X}}_D)$;
2. checking if the intersection is on the straight-line vector $\underline{\boldsymbol{X}}_O\underline{\boldsymbol{X}}_D = \underline{\boldsymbol{X}}_D - \underline{\boldsymbol{X}}_O$.

The key issue is then to have a robust method to detect the intersection between a displacement vector and any face. It is of prime importance to prevent any particle from being permanently lost in the computational domain. For that reason, the method uses Boolean elementary tests which are reproducible from one cell to another so that it can handle pathological cases such as when the vector $\underline{\boldsymbol{X}}_O\underline{\boldsymbol{X}}_D$ crosses a face through one of its edges (to the machine precision).

2.B.1.1 Method to detect face-crossing events through warped-faces

The method to detect face-crossing events is based on the decomposition of each face into a set of triangular sub-faces (see also Figure 2.B.4). Each triangular sub-face is built using one of the oriented edges of the face (formed by two consecutive vertices $\underline{\boldsymbol{X}}_i$ and $\underline{\boldsymbol{X}}_j$) and the centre of gravity of the face $\underline{\boldsymbol{X}}_f$. This decomposition of faces ensures that each triangular sub-face treated is planar, hence making the method tractable even for warped meshes (i.e. with faces whose vertices do not belong to the same plane).

Once a face is decomposed into a set of triangular sub-faces, the intersection between a vector and each planar sub-face is detected using a kind of algorithm proposed by Möller and Trumbore [1997]. The principle is to project the vertices of each sub-face in the oriented plane orthogonal to the displacement vector $\underline{\boldsymbol{X}}_O\underline{\boldsymbol{X}}_D$ passing through $\underline{\boldsymbol{X}}_O$ noted $(\underline{\boldsymbol{X}}_O, \underline{\boldsymbol{X}}_O\underline{\boldsymbol{X}}_D^{\perp})$. Then, to compute if line $(\underline{\boldsymbol{X}}_O\underline{\boldsymbol{X}}_D)$ crosses a sub-face, we simply need to check if the point $\underline{\boldsymbol{X}}_O$ belongs to the triangle formed by the projection of the sub-face on this plane (as displayed in Figure 2.B.3, where the superscript $(.)^\dagger$ corresponds to the projection in the plane perpendicular to the displacement). For that purpose, we resort here to a series of three elementary Boolean tests, each one allowing to verify if the point $\underline{\boldsymbol{X}}_O$ is located on the "proper side" of a projected edge.

Elementary Boolean tests

For each of the three edges forming a projected sub-face (namely $\underline{\boldsymbol{X}}_f^\dagger \underline{\boldsymbol{X}}_i^\dagger$, $\underline{\boldsymbol{X}}_f^\dagger \underline{\boldsymbol{X}}_j^\dagger$ and $\underline{\boldsymbol{X}}_i^\dagger \underline{\boldsymbol{X}}_j^\dagger$), we have to verify whether the point $\underline{\boldsymbol{X}}_O$ is on the proper side of the projected edge. To that extent, we resort here to simple logical tests. For the sake of clarity, let's consider the case of an oriented edge connecting two points $\underline{\boldsymbol{X}}_\alpha \underline{\boldsymbol{X}}_\beta$ (where $_\alpha$ and $_\beta$ are the indexes of two vertexes of a sub-face) on the projection plane. In that case, the logical test $\mathscr{L}_{\alpha,\beta}^{\text{edge}}$ reads:

$$\mathscr{L}_{\alpha,\beta}^{\text{edge}} = \begin{cases} \mathit{true} & \text{if } (\underline{\boldsymbol{X}}_\alpha \underline{\boldsymbol{X}}_\beta \wedge \underline{\boldsymbol{X}}_\alpha \underline{\boldsymbol{X}}_O) \cdot \underline{\boldsymbol{X}}_O \underline{\boldsymbol{X}}_D > 0. \\ \mathit{false} & \text{otherwise.} \end{cases} \tag{2.25}$$

As displayed in Figure 2.B.1, this elementary Boolean test provides information on whether a point $\underline{\boldsymbol{X}}_O$ is in the half plane on the left (true) or on the right (false) of the projected line $(\underline{\boldsymbol{X}}_\alpha^\dagger \underline{\boldsymbol{X}}_\beta^\dagger)$. It is worth noticing that the inequality in this test being strict, the behavior on the oriented line is asymmetric. Indeed, if point $\underline{\boldsymbol{X}}_O$ belongs to this line at the machine precision, test $\mathscr{L}_{\alpha,\beta}^{\text{edge}}$ returns *false*. In other words, we arbitrarily consider that the line $(\underline{\boldsymbol{X}}_\alpha^\dagger \underline{\boldsymbol{X}}_\beta^\dagger)$ belongs to the closed right half plane and not to the open left one. As a result, the Boolean test $\mathscr{L}_{\alpha,\beta}^{\text{edge}} \bigcup \text{not}(\mathscr{L}_{\alpha,\beta}^{\text{edge}})$ is a partition of the domain. This means that the computation of $\mathscr{L}_{\alpha,\beta}^{\text{edge}}$ is reproducible for a given displacement vector $\underline{\boldsymbol{X}}_O \underline{\boldsymbol{X}}_D$ for two faces sharing the same edge[1] provided that the ordering of the vertices α and β is fixed. In the present work, we have imposed to sort the vertices in the following order: first $\underline{\boldsymbol{X}}_f$, then $\underline{\boldsymbol{X}}_i$ and finally $\underline{\boldsymbol{X}}_j$ (with $i < j$).

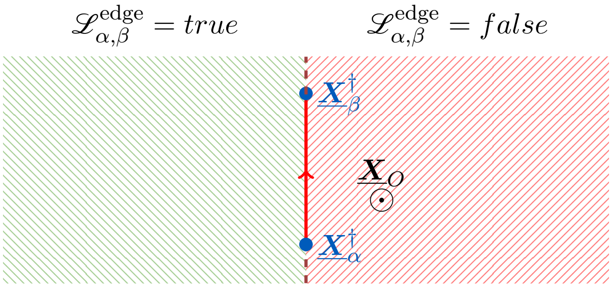

Figure 2.B.1: Sketch illustrating how the elementary boolean test $\mathscr{L}_{\alpha,\beta}^{\text{edge}}$ works: the point $(\underline{\boldsymbol{X}}_0$ can either be located on the left-hand side or on the right-hand side of the oriented line $(\underline{\boldsymbol{X}}_\alpha^\dagger \underline{\boldsymbol{X}}_\beta^\dagger)$. Here, the figure is seen from above the plane $(\underline{\boldsymbol{X}}_0, \underline{\boldsymbol{X}}_O \underline{\boldsymbol{X}}_D^\perp)$, meaning that the elementary Boolean test is *true* on the left-hand side of the figure. Note that the line belongs to the closed half-plane (i.e., *false* in red color).

Figure 2.B.1 also shows that this elementary Boolean test is not enough to determine if a point $\underline{\boldsymbol{X}}_O$ belongs to the projected triangle sub-face. In fact, a point can be located either on the right side or on the left side of the line depending on the orientation of the vector $\underline{\boldsymbol{X}}_i^\dagger \underline{\boldsymbol{X}}_j^\dagger$ but also on whether the point is above or below the plane. While the orientation of the vector is now fixed thanks to the sorted vertices introduced in the previous paragraph, we must introduce the notion of plane orientation to deal with the second issue. For that purpose, we rely on the orientation

---

[1] This is the case for instance for a sub-face seen from one cell or from the neighbouring one.

of the sub-face, and we introduce an additional logical test to know if the displacement vector $\underline{\boldsymbol{X}}_O\underline{\boldsymbol{X}}_D$ is aligned with the oriented sub-face. It returns true if they are aligned and false if they are not. This condition reads:

$$\mathscr{A}^{\text{face}}_{f,i,j} = \begin{cases} true & \text{if } (\underline{\boldsymbol{X}}_f\underline{\boldsymbol{X}}_i \wedge \underline{\boldsymbol{X}}_f\underline{\boldsymbol{X}}_j) \cdot \underline{\boldsymbol{X}}_O\underline{\boldsymbol{X}}_D > 0. \\ false & \text{otherwise.} \end{cases} \tag{2.26}$$

By combining both logical tests $\left(\mathscr{L}^{\text{edge}}_{i,j} \equiv \mathscr{A}^{\text{face}}_{f,i,j}\right)$ (where $\equiv$ means that both Boolean tests have the same value), we are able to determine on which side of the line $\underline{\boldsymbol{X}}^{\dagger}_i\underline{\boldsymbol{X}}^{\dagger}_j$ the particle lies with respect to the face orientation.

Combined elementary Boolean tests

To determine if the intersection point $\underline{\boldsymbol{X}}_i$ is within the projected face, we have then to combine these elementary logical tests together. As displayed in Figure 2.B.2, the intersection point belongs to the projected face if three conditions are met. These conditions depend on the orientation of the sub-face with respect to the displacement vector:

- When the displacement vector is aligned with the sub-face orientation (i.e., $\mathscr{A}^{\text{face}}_{f,i,j} = true$), the point is located to the left of each of the projected edges provided that we follow the sorted vertices (namely $\underline{\boldsymbol{X}}^{\dagger}_f\underline{\boldsymbol{X}}^{\dagger}_i$, $\underline{\boldsymbol{X}}^{\dagger}_i\underline{\boldsymbol{X}}^{\dagger}_j$ and $\underline{\boldsymbol{X}}^{\dagger}_j\underline{\boldsymbol{X}}^{\dagger}_f$). This means that the following three conditions have to be met: first, $\mathscr{L}^{\text{edge}}_{f,i} = true$; second, $\mathscr{L}^{\text{edge}}_{f,j} = false$ (due to its reverse orientation); third, $\mathscr{L}^{\text{edge}}_{i,j} = true$. This case is displayed in the LHS of Figure 2.B.2.
- When the displacement vector is not aligned with the sub-face orientation (i.e., $\mathscr{A}^{\text{face}}_{f,i,j} = false$), the point is located to the right of each of the projected edges provided that we follow the sorted vertices (namely $\underline{\boldsymbol{X}}^{\dagger}_f\underline{\boldsymbol{X}}^{\dagger}_i$, $\underline{\boldsymbol{X}}^{\dagger}_i\underline{\boldsymbol{X}}^{\dagger}_j$ and $\underline{\boldsymbol{X}}^{\dagger}_j\underline{\boldsymbol{X}}^{\dagger}_f$). This means that the following three conditions have to be met: first, $\mathscr{L}^{\text{edge}}_{f,i} = false$; second, $\mathscr{L}^{\text{edge}}_{f,j} = true$ (due to its reverse orientation); third, $\mathscr{L}^{\text{edge}}_{i,j} = false$. This case is displayed in the RHS of Figure 2.B.2.

To sum it up, the intersection point is inside a given sub-face if the following condition is respected:

$$\begin{aligned} & \left(\mathscr{L}^{\text{edge}}_{i,j} \equiv \mathscr{A}^{\text{face}}_{f,i,j}\right) \\ \text{and } & \left(\mathscr{L}^{\text{edge}}_{f,i} \equiv \mathscr{A}^{\text{face}}_{f,i,j}\right) \\ \text{and } & \left(\text{not}(\mathscr{L}^{\text{edge}}_{f,j}) \equiv \mathscr{A}^{\text{face}}_{f,i,j}\right) = true, \end{aligned} \tag{2.27}$$

where the symbol $\equiv$ corresponds to the operator “equivalent” (i.e., it is true if the two Boolean variables have the same value). This test is made for each sub-face. The algorithm is illustrated in Figure 2.B.3 (where the intersection point is on the right hand face).

In the case of warped faces, it is possible for a line ($\underline{\boldsymbol{X}}_O\underline{\boldsymbol{X}}_D$) to cross the same face several times. This is depicted in Figure 2.B.4. In that case, the algorithm monitors the number of times that the line ($\underline{\boldsymbol{X}}_O\underline{\boldsymbol{X}}_D$) crossed the face. If this number is even, it means that the particle remains in the current cell (it has left and reentered the cell). If this number is odd, it means that the particle leaves the cell through this face.

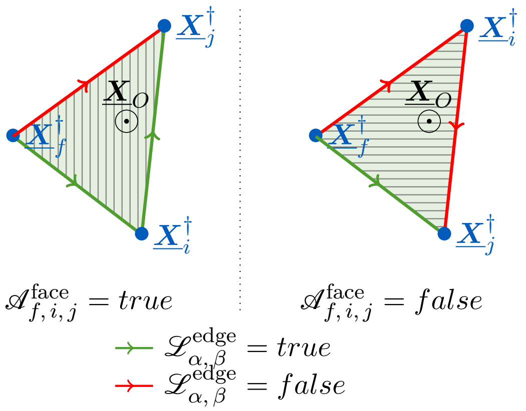

Figure 2.B.2: Sketch of the Boolean test for alignment $\mathscr{A}^{\text{face}}_{f,i,j}$. It determines if the displacement vector $\underline{\boldsymbol{X}}_O\underline{\boldsymbol{X}}_D$ is aligned with the oriented sub-face $\underline{\boldsymbol{X}}_f\underline{\boldsymbol{X}}_i\underline{\boldsymbol{X}}_j$ (and returns *true* in that case). The sketch shows the two possible cases: on the left-hand side, the displacement vector is aligned with the sub-face orientation; on the right-hand side, they are not aligned. In each case, the point $\underline{\boldsymbol{X}}_O$ lies within the projected sub-face if it is located on the proper side of all oriented edges (namely $\underline{\boldsymbol{X}}_f\underline{\boldsymbol{X}}_i$, $\underline{\boldsymbol{X}}_f\underline{\boldsymbol{X}}_j$ and $\underline{\boldsymbol{X}}_i\underline{\boldsymbol{X}}_j$, with $i < j$). The logical tests $\mathscr{L}^{\text{edge}}_{\alpha,\beta} = true$ are displayed according to their result (green $=$ *true* and red$=$*false*).

2.B.1.2 Method to estimate the intersection time and position

As mentioned in Section 2.2.2.1, the new algorithm not only requires information on the cell containing the particle but also on the intersection time and location. This means that the trajectory algorithm described previously must be extended to provide this information.

Having determined that the line $(\underline{\boldsymbol{X}}_O\underline{\boldsymbol{X}}_D)$ does cross a sub-face, the relative time $\eta = t_{\text{cross}}/\Delta t$ necessary to reach this sub-face can be estimated using the free-flight assumption. It gives:

$$\eta = \frac{\underline{\boldsymbol{X}}_O\underline{\boldsymbol{X}}_f \cdot (\underline{\boldsymbol{X}}_f\underline{\boldsymbol{X}}_i \wedge \underline{\boldsymbol{X}}_f\underline{\boldsymbol{X}}_j)}{\underline{\boldsymbol{X}}_O\underline{\boldsymbol{X}}_D \cdot (\underline{\boldsymbol{X}}_f\underline{\boldsymbol{X}}_i \wedge \underline{\boldsymbol{X}}_f\underline{\boldsymbol{X}}_j)}. \tag{2.28}$$

This equation is well-posed since we apply it only when we have previously determined that the line actually crosses the face. In fact, the value of η actually provides additional information. When η is negative, it means that the intersection point is an entrance point for the oriented axis $(\underline{\boldsymbol{X}}_O\underline{\boldsymbol{X}}_D)$. When η is positive, it means that the intersection point is an exit point. The number of sub-faces through which the oriented axis $(\underline{\boldsymbol{X}}_O\underline{\boldsymbol{X}}_D)$ enters (n_{in}) and leaves (n_{out}) is then counted. We then check if the particle is indeed in the correct cell thanks to these numbers. The particle is in the correct cell if the number of sub-faces through which the line $(\underline{\boldsymbol{X}}_O\underline{\boldsymbol{X}}_D)$ enters in the cell equals to the number of sub-faces through which it exits the cell and if both of these numbers are not zero (i.e., $n_{in} = n_{out} > 0$).

If the value of η defined in Eq. (2.28) is in the interval $\eta \in [0, 1[$, the particle does actually cross a face during the time step. The position of the particle at the intersection is then simply given using a simple linear interpolation (this linear interpolation is coherent with the assumption of free-flight motion):

$$\underline{\boldsymbol{X}}_I = \underline{\boldsymbol{X}}_O + \eta \times \underline{\boldsymbol{X}}_O\underline{\boldsymbol{X}}_D. \tag{2.29}$$

When a particle leaves a cell after crossing one face several times (as in wrapped faces), the exit time is considered equal to the largest value in the range $[0, 1[$ (i.e., the last exit time).

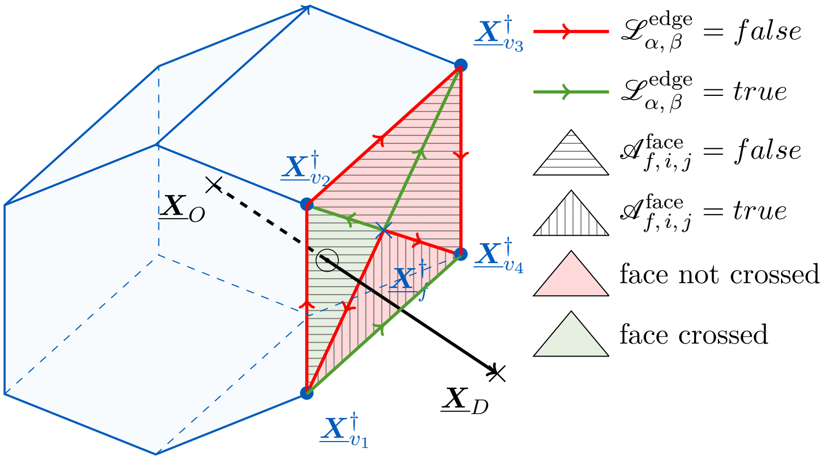

Figure 2.B.3: Sketch illustrating how the tracking algorithm determines if a particle displacement from $\underline{\boldsymbol{X}}_O$ to $\underline{\boldsymbol{X}}_D$ crosses a face. Here, the particle exits the cell through the face on the right. As a result, when the edges of this face are projected on the plane normal to the displacement vector (here with superscripts †), the various logical tests $\mathscr{L}^{\text{edge}}_{\alpha,\beta}$ and $\mathscr{A}^{\text{face}}_{f,i,j}$ confirm that one of the triangular sub-faces is detected as an exit face (green color) while the three other sub-faces are not (red color).

2.B.2 Validation on 3-D unstructured meshes

The trajectory algorithm has been tested using various meshes obtained from the FVCA6 benchmark test cases Eymard et al. [2011]. These meshes were selected to be representative of a range of different meshes, going from a regular Cartesian mesh to a highly distorted mesh with different refinements. The four meshes used here are displayed in Figure 2.B.5.

The case considered for validation actually corresponds to the uniform flow described in Section 2.3.1.1. It consists in a point source dispersion within homogeneous isotropic turbulence. To ensure that no particle is lost, the distance between the particles and the cell centre (point source) is tracked. In order to have a representative quantity independent of the mesh, the quantity followed is the dimensionless distance d^*. It is defined as $d^* = \frac{\|\underline{\boldsymbol{X}}_c - \underline{\boldsymbol{X}}_p\|}{\max\limits_{X\in\Omega_c}\|\underline{\boldsymbol{X}}_c - \underline{\boldsymbol{X}}\|}$ with $\underline{\boldsymbol{X}}_c$ the centre of gravity of the cell, $\underline{\boldsymbol{X}}_p$ the position of the particle and Ω_c the domain defined by the cell c. When particles are properly tracked, this distance is always smaller than 1. However, if one of the faces crossed by a particle were to be missed, the particle would be permanently lost since it could continue its motion without bound. [2] In such cases, the distance from the cell centre could diverge and become much greater than 1.

Results obtained with various meshes are compared using a timescale made dimensionless using the Lagrangian timescale $t^* = t/T_L$ (which is constant for all meshes considered). The results are displayed in Figure 2.B.6: we can see that, with 100 000 particles dispersed initially from the point source, the maximum distance to the cell centre converges towards 1 but remains always smaller than unity. This proves that the current algorithm is tractable even for 3-D unstructured meshes.

As in Section 2.3.1, we can also analyse the results obtained for the different second-order moments. We focus here on verifying that the results are consistent regardless of the mesh used using a given time step (the role of the time step has been detailed in Section 2.3.1). The results

---

[2] If the current cell associated to a particle is not correct, the algorithm would not detect other face-crossing events.

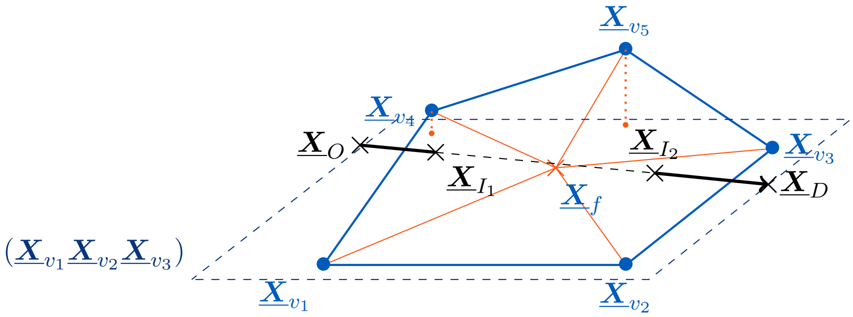

Figure 2.B.4: Sketch showing a particle displacement from $\underline{\boldsymbol{X}}_O$ to $\underline{\boldsymbol{X}}_D$ going through a warped face: it can be seen that the particle exits the cell through $\underline{\boldsymbol{X}}_{I_1}$ (which belongs to the sub-face ($\underline{\boldsymbol{X}}_f$, $\underline{\boldsymbol{X}}_{v_1}$, $\underline{\boldsymbol{X}}_{v_4}$) and re-enters the cell through $\underline{\boldsymbol{X}}_{I_2}$ (which belongs to the sub-face ($\underline{\boldsymbol{X}}_f$, $\underline{\boldsymbol{X}}_{v_2}$, $\underline{\boldsymbol{X}}_{v_3}$). This is naturally handled by the present algorithm which browses through all sub-faces and then counts the number of times a sub-face is crossed: a pair number means that it stays in the current cell while an odd number means that it exits the current cell.

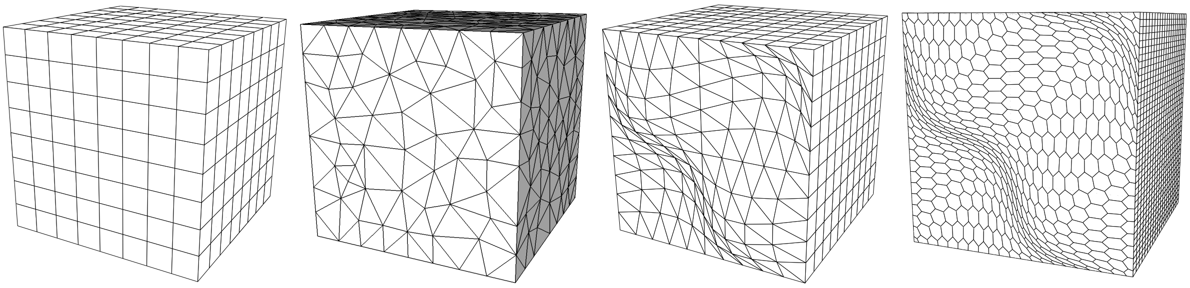

(A) Hexa mesh.

(B) Tetra mesh.

(C) PrT mesh.

(D) PrG mesh.

Figure 2.B.5: Type of mesh used in the present case, which span a range of possible configurations (from simple Cartesian mesh without wrapped faces to highly distorted meshes with wrapped faces.

are displayed in Figure 2.B.7: it can be seen that all numerical results match the analytical values regardless of the mesh used in such cases. This confirms the accuracy of the algorithm even when 3-D unstructured meshes are used. At this stage, it is also worth noting that 1-D simulation provide the same results as 3-D ones since each of the three directions can be treated independently of the other ones (this is actually a typical characteristic of homogeneous isotropic turbulence).

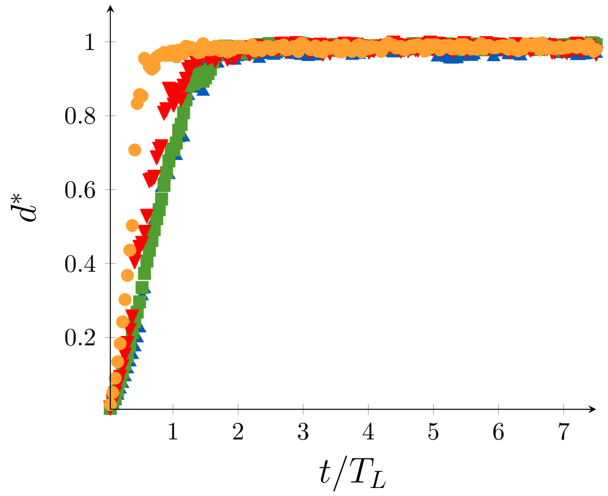

Figure 2.B.6: Maximum dimensionless distance between the particles and their centre of gravity using the Hexa mesh (■), the Tetra mesh (▲), the PrT mesh (▼) and the PrG mesh (●. All maximum dimensionless distances are smaller or equal to 1, meaning that the particles stay within the physical domain.)

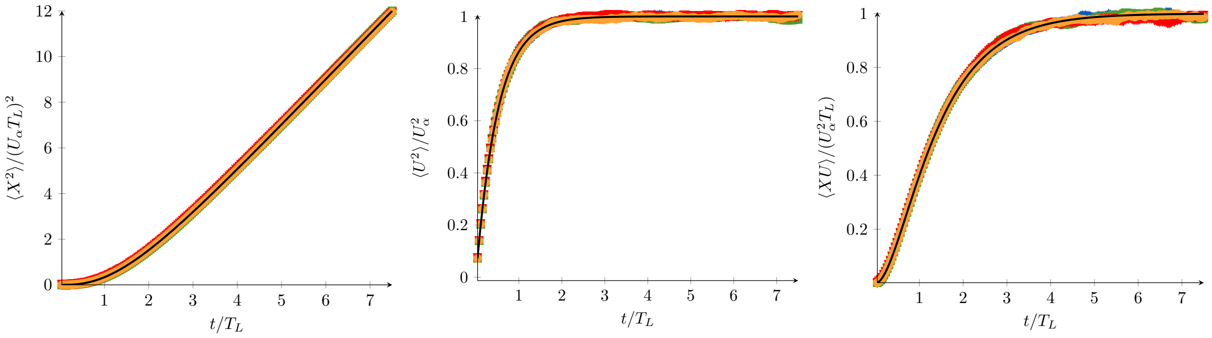

Figure 2.B.7: Evolution of $\langle XX\rangle$, $\langle UU\rangle$,$\langle XU\rangle$ for the point source dispersion in the ballistic limit case. Comparison between the analytical solution (black line) and numerical results obtained with the new algorithm for the various meshes. The numerical results are all in agreement with the analytical solution regardless of the mesh used.

CHAPTER 3

Analysis of Neutral Boundary Flows using Particles/Mesh PDF Methods

Contents

In the course of the development of Lagrangian stochastic models, two concerns have often surfaced. The first concern is related to the respect to the well-mixed condition which states that, for an incompressible flow, a uniform distribution of particles should remain so (interested reader may refer to Sawford [1986], Thomson [1987]). Indeed, since fluid particles represent the same fixed amount of mass, preserving a uniform concentration is equivalent to stating that the mass conservation equation should be satisfied. Actually, this issue was clarified very early by Pope [1985, 1987] and McInnes and Bracco [1992] and has been repeated in several works (see Minier and Peirano [2001], Minier et al. [2014]), where it was demonstrated that, as long as the mean pressure gradient is properly introduced in the particle velocity equation, the well-mixed criterion is automatically satisfied. This was revisited recently in the analysis of Bahlali et al. [2020] with a view towards atmospheric applications which confirmed previous conclusions. The second concern is related to the wall-boundary condition we should apply to ensure that the 'law of the wall' discussed in Pope [2000] is correctly reproduced by Lagrangian simulations. Contrary to the first concern, this point has received less attention (see an overview of existing attempts in Haworth [2010]) and is still the subject of some confusion as to the form and the physical meaning of the wall-boundary condition for fluid particles. In many applications, a simple elastic condition is applied at the wall boundary. Such a condition is clearly wrong for particle streamwise velocity components as it cancels the exchange of momentum occurring in the near-wall region, which is a key characteristic of the physics of wall boundary layers. On the other hand, an an-elastic wall boundary condition was proposed in earlier works by Dreeben and Pope [1997a] and Minier and Pozorski [1999], though its significance may not have yet been perceived for stochastic-particle-based simulations. The issue of what wall-boundary condition should be enforced in turbulent wall-bounded flows was addressed by Bahlali et al. [2020] who revealed that an elastic rebound condition leads to serious errors in the near-wall region and brought further validation for the an-elastic boundary condition. Yet, the analysis remained incomplete as to whether the correct profiles of the logarithmic region were really retrieved but was helpful to bring out a number of numerical issues concerning the interpolation of mean fields at particle positions and how particle statistics are to be calculated. In that sense, the present work is a follow-up of this first study and aims at clarifying the issues associated to the wall-boundary conditions needed in the spirit of the wall-function treatment of turbulent boundary layers, as well as bringing insights into the physical and numerical issues involved.

To address the above-mentioned issues, we analyse numerical outcomes in a neutral surface-boundary layer (SBL) flow. Since this configuration is the most classical way to describe near-ground atmospheric flows in the absence of thermal effects, it is of first importance for atmospheric applications. This is also a situation where the wall-boundary condition plays a key role. Furthermore, analytical solutions are available which allows to monitor numerical errors. Finally, this situation remains simple enough to allow in-depth numerical investigations to be performed, while conclusions remain applicable in more complex geometries since it is applied to describe locally a turbulent flow in the immediate vicinity of small wall-surface elements. In contrast to the first studies on the an-elastic wall-boundary condition of Dreeben and Pope [1997a] and Minier and Pozorski [1999] which were carried out using stand-alone simulations, present results were obtained using a hybrid finite-volume/particle (FV/particle) numerical method, corresponding to a hybrid Moments/PDF description of turbulent flows, and are therefore interesting to assess since they complement these first studies and provide additional support.

In short, the present work realised in collaboration with J.-P. Minier, Y. Roustan, M. Ferrand and published in Balvet et al. [2023b], has a three-fold objective:

(i) to present new numerical results to validate the an-elastic boundary condition and point out the shortcomings of the often applied elastic condition;

(ii) to investigate the numerical errors induced when interpolating mean fields at particle locations and propose local schemes to simulate particle dynamics;

(iii) to bring out statistical artefacts when extracting particle statistics in volumes where the local homogeneity assumption fails and to propose correction terms.

This chapter is organised as follows. First, detailed numerical results are presented in Section 3.1 to validate the an-elastic wall-boundary condition. The issues related to the interpolation of mean fields at particle locations are addressed in Section 3.2, while a careful investigation of potential artefacts in the statistical treatment of particle dynamics is carried out in Section 3.3. Conclusions are then given in Section 3.4.

3.1 Verification of the Wall-boundary Condition

Contents

The purpose of the present section is to revisit the reference wall-boundary condition (cf Paragraph 1.3.3.2.4) proposed by Dreeben and Pope [1998] and Minier and Pozorski [1999] to assess whether it properly represents the physics of the logarithmic zone and also to provide further numerical validation. To that effect, a turbulent 1-D infinite neutral SBL flow, which is characteristic of such situations, is considered. In Section 3.1.1, we first present the analytical results obtained using the SLM model, which serves as a reference in the verification process. We then highlight that the reference wall-boundary condition enables to simulate correctly the logarithmic zone, without any modification, for both smooth and rough walls. Finally, we show that the results obtained are independent of the position of the rebound plane within the logarithmic zone, which brings in new validation results compared to previous studies.

3.1.1 Surface-Boundary Layer

Leaving out thermal stratification and stability effects, the neutral SBL flow is the classical situation to model neutral near ground atmospheric flows. Furthermore, at high Reynolds-numbers and even in more complex situations, the flow in the vicinity of a small wall surface element can be described locally by such boundary layers. The situation considered here consists therefore in a 1-D incompressible and turbulent flow with a wall at the bottom, a constant shear stress condition at the top and periodicity in the two other directions. The flow is driven by the shear stress imposed at the top. We impose then $\overline{uw} = -u_*^2$ where u_* is the friction velocity defined as $u_* = \sqrt{\sigma_{\text{wall}}/\rho}$, with σ_{wall} the shear stress at the wall. In the Lagrangian scope, this is done by providing adequate mean carrier fields and by implementing an an-elastic boundary condition satisfying Eq. (1.235) on the top of the domain.

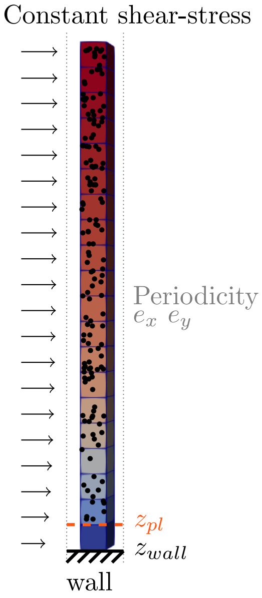

Figure 3.1: Scheme of the surface-boundary layer studied.

The high-Reynolds Navier-Stokes equation Eq. (3.1) governing the mean velocity can be extracted from Eq. (1.217b) as:

$$\frac{\langle \mathrm{d}\underline{\boldsymbol{U}}\rangle}{\mathrm{d}t} = \frac{\partial\langle\underline{\boldsymbol{U}}\rangle}{\partial t} + \underline{\mathbf{grad}}(\langle\underline{\boldsymbol{U}}\rangle)\cdot\langle\underline{\boldsymbol{U}}\rangle + \underline{\mathbf{div}}(\langle\underline{\boldsymbol{u}}\otimes\underline{\boldsymbol{u}}\rangle) = -\frac{1}{\rho}\underline{\mathbf{grad}}\langle P\rangle + \underline{\boldsymbol{g}}. \tag{3.1}$$

We consider a simple shear flow parallel to the wall, which depends only on the height: $\langle\underline{\boldsymbol{U}}\rangle = \langle U\rangle(z)\underline{\boldsymbol{e_x}}$. Moreover, the diffusion terms for the second-order moments are considered negligible. This results in a logarithmic boundary zone within which analytical solutions can be derived. The mean velocity profile is logarithmic and its value depends on the nature of the wall-boundary condition applied at the bottom and whose formulation for smooth or rough walls is:

$$\langle U\rangle = \begin{cases} u_*\left(\dfrac{1}{\kappa}\ln(\dfrac{zu_*}{\nu}) + C_{log}\right) & \text{for smooth walls,} \quad (3.2a) \\ \dfrac{u_*}{\kappa}\ln(\dfrac{z+z_0}{z_0}) & \text{for rough walls.} \quad (3.2b) \end{cases}$$

In these equations, κ is the Von Kármán constant equal to 0.42, ν is the kinematic viscosity, and C_{log} a constant equal to 5.2. Two characteristic heights appear. The first one is $\delta_\nu = \nu/u_*$ the viscous length scale, with respect to which we define the dimensionless height $z^+ = z/\delta_\nu = z\,u_*/\nu$ which characterises the flow within the logarithmic boundary condition. The second one is the roughness height z_0 characterising the effect of the wall roughness on the flow.

Using the SLM model and neglecting the effects of the third order terms, the equations governing the Reynolds tensor are simplified into Eqs 3.3:

$$\langle uu\rangle : \qquad 2\langle uw\rangle\frac{\partial\langle U\rangle}{\partial z} = -\frac{2\epsilon}{C_L}\frac{\langle uu\rangle}{k} + C_0\epsilon, \tag{3.3a}$$

$$\langle uw\rangle : \qquad \langle ww\rangle\frac{\partial\langle U\rangle}{\partial z} = -\frac{2\epsilon}{C_L}\frac{\langle uw\rangle}{k}, \tag{3.3b}$$

$$\langle vv\rangle : \qquad 0 = -\frac{2\epsilon}{C_L}\frac{\langle vv\rangle}{k} + C_0\epsilon, \tag{3.3c}$$

$$\langle ww\rangle : \qquad 0 = -\frac{2\epsilon}{C_L}\frac{\langle ww\rangle}{k} + C_0\epsilon. \tag{3.3d}$$

Resolving these equations shows that the second-order moments are constant in the domain with analytical values given by Eqs 3.4:

$$k = \frac{1+\frac{3}{2}C_0}{\sqrt{C_0}}u_*^2 \simeq 3.34u_*^2 \tag{3.4a}$$

$$\langle uu\rangle = \frac{C_0+2}{\sqrt{C_0}}u_*^2 \simeq 2.94u_*^2, \tag{3.4b}$$

$$\langle uw\rangle = -u_*^2, \tag{3.4c}$$

$$\langle vv\rangle = \langle ww\rangle = \sqrt{C_0}u_*^2 \simeq 1.87u_*^2, \tag{3.4d}$$

$$\langle uv\rangle = \langle vw\rangle = 0. \tag{3.4e}$$

3.1.2 Verification for Both Smooth and Rough Walls

We now verify that the physics of the SBL is well respected using the reference wall-boundary condition presented in Paragraph 1.3.3.2.4 for smooth as well as rough walls. Similar verification of the effects of the wall-boundary condition on smooth walls were proposed by Dreeben and Pope [1998] and Minier and Pozorski [1999] using a stand-alone approach, and by Bahlali et al. [2020] using a hybrid method. However, the case of rough walls, which is of major importance for atmospheric flows, was not considered. It is therefore interesting to extend the analysis to assess if the reference wall-boundary condition can also be applied for rough walls.

The simulations presented here were obtained with the numerical hybrid formulation introduced in Section 1.3.3.3. In this chapter, to focus on the analysis of the error introduced in the Lagrangian methods, analytic solutions described in Section 3.1.1 are used for the estimation of the mean carrier fields at the centre of the cells. The computations were carried out with the open-source CFD solver code_saturne (see Archambeau et al. [2004]) and a uniform mesh was used with $H/\Delta z = 100$, H and Δz being respectively the domain and the cell heights. The natural way to shift the rebound plane away of the physical location of the wall is to extract the Lagrangian domain from the FV one. This means that the FV mesh is also used for the Lagrangian method, but the boundary condition is set at a height z^{pl}. The particles are injected only above this plane as schematised in Figure 3.1. We consider the flow of air in a domain of height $H = 50\,\mathrm{m}$, with $u_* = 1\,\mathrm{m\,s^{-1}}$, thus with a Reynolds number $Re_* = H.u_*/\nu \simeq$

$3.35\ 10^6$. As indicated, the Lagrangian boundary condition is applied at a dimensionless height $z^{pl^+} = z^{pl}.u_*/\nu = 1.67.10^5$ in the logarithmic zone. The simulations were carried out with a time step sufficiently small compared to the lowest Lagrangian timescale seen by the particles and compared to the condition imposed by the CFL to neglect the temporal error discussed by Peirano et al. [2006]. Similarly, the number of particles is sufficiently high to consider that the statistical error is small compared to the spatial one. The main source of numerical error is the spatial discretisation, discussed in Sects. 3.2 and 3.3.

In the following, dimensionless quantities denoted with the superscript $^+$ are plotted as a function of the dimensionless height z/H (based on the height of the domain simulated). The mean velocity and Reynolds tensor are scaled with the friction velocity u_*, so that $\langle U\rangle^+ = \langle U\rangle/u_*$ and $\langle u_i u_j\rangle^+ = \langle u_i u_j\rangle/u_*^2$, while the mean concentration is normalised using the concentration $\langle C\rangle_H$ averaged all over the domain, giving $\langle C\rangle^+ = \langle C\rangle/\langle C\rangle_H$.

Two main criteria are considered: first, the respect of the well-mixed criterion and, second, the respect of the theoretical values of the first and second-order velocity moments, as prescribed in Section 3.1.1. The first condition states that, since particles represent a fixed unit of mass, their concentration must remain constant so as to ensure mass conservation and the validity of a Lagrangian stochastic approach (see Pope [1985]). In the present case, this means that we should conserve $\langle C\rangle^+ = 1$ everywhere across the domain. As will be seen below, this criterion is always respected here since the mean pressure gradient is properly introduced in the Langevin formulation. This point has been repeatedly addressed (e.g. by Minier et al. [2014] and Bahlali et al. [2020]) and is now well established. We therefore concentrate mostly on discussing the second criterion.

3.1.2.1 Verification on Smooth Walls

Results obtained using the reference wall-boundary condition and the specular one with a smooth wall are presented in Figure 3.2. As shown in Figure 3.2A, the concentration within the domain remains constant and the well-mixed criterion is respected, for both rebound conditions (the slight fluctuations are due to the inherent statistical noise of the Monte Carlo approach). This confirms that, once the mean pressure gradient is properly accounted for in the Langevin equation for particle velocities, there is no accumulation or depletion of particles even near the wall. This behaviour is not influenced by the details of the wall boundary condition applied to the particle streamwise velocity component and essentially reflects the specular reflection used for the particle vertical position. However, when we consider first- and second-order velocity moments, marked differences can be observed between the two boundary conditions. When the elastic rebound condition is used, a zero-gradient condition on the velocity is actually imposed, thus not respecting the shear stress which is the driving force in SBL flows. As the gradient of velocity tends towards zero, the velocity is overstated near the rebound plane as seen in Figure 3.2B. Without this gradient of velocity, the production terms in Eqs 3.3 tend to become null and this results in a tendency to have isotropic turbulence near the rebound plane. Such trends are clearly apparent in Figure 3.2C where the shear stress (on the left) goes to zero and the streamwise component of the Reynolds tensor (on the right) tends towards the normal component of the Reynolds tensor (on the middle). On the contrary, the reference an-elastic wall-boundary condition enables to properly maintain the shear stress across the whole SBL. This is evident in Figure 3.2C, where the components of the Reynolds tensor are effectively constant and in line with the values expected from Eqs 3.4. Note that we have also a proper profile of velocity in Figure 3.2B, i.e. linear on a semi-logarithmic scale.

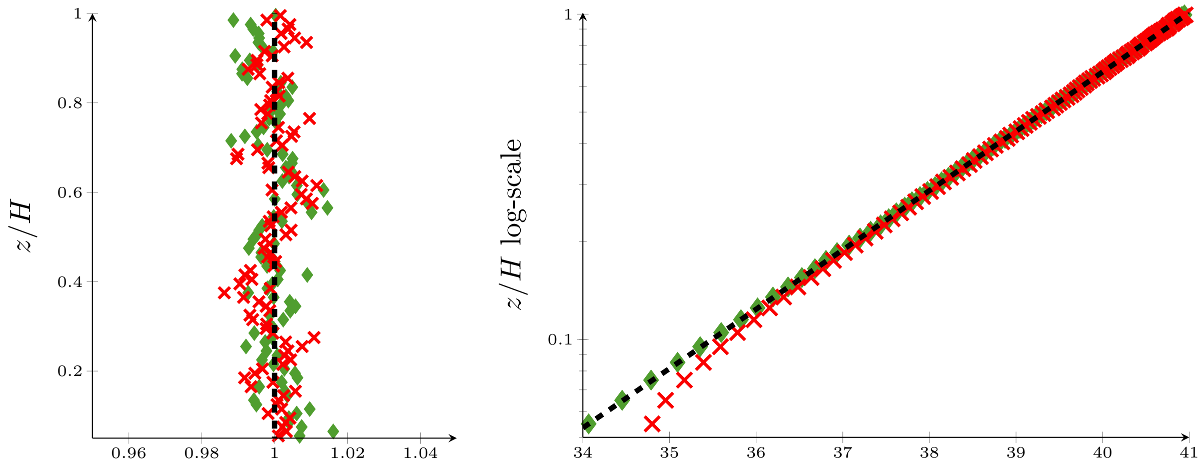

(A) Normalised concentration.

(B) Streamwise velocity.

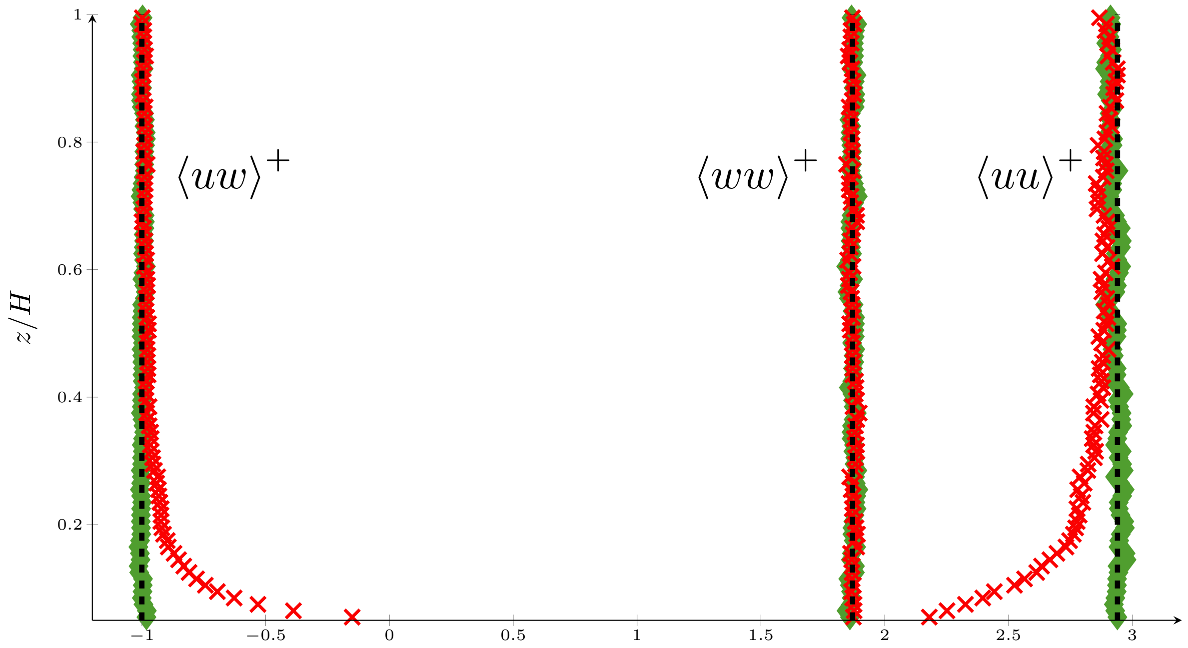

(C) Reynolds tensor.

Figure 3.2: Vertical profiles in the surface-boundary layer for smooth walls: the normalised concentration (A); the dimensionless mean streamwise velocity (B); and the four non null components of the dimensionless Reynolds tensor (C), (note that, since in the spanwise and normal direction the Reynolds tensor components are equal, only the latter one is plotted). Considering a smooth wall, two results corresponding to two distinct Lagrangian boundary conditions are compared: the reference an-elastic wall-boundary condition (◆) and the elastic wall-boundary condition (✕). Both respect the well-mixed criterion but only the reference wall-boundary condition enables to obtain correct mean velocity and Reynolds tensor profiles compared to the analytical solutions (▪▪▪).

3.1.2.2 Verification on Rough Walls

A similar analysis was performed with a rough wall instead of a smooth one. The roughness height considered is $z_0 = 0.1$ m. In the flow studied here, such a wall can indeed be considered as rough since $z_0^+ = z_0 u_*/\nu \sim 6.7\ 10^3 \gg 1$. It is important to realise that the dimensionless roughness height enters only the wall-function treatment of the moment approach (thus only in the FV solver) to obtain the correct mean velocity law according to Eq. (3.2b). Although this roughness height impacts the value of the mean velocity, it does not modify the shear stress which depends solely on the friction velocity u_* imposed by the upper flow. Therefore, since the boundary condition applied on the particles, cf. Eq. (1.235), is built to respect a condition not directly on the mean velocity but on the shear stress, it is unchanged regardless of whether we consider smooth or rough walls. This is demonstrated by the numerical results shown in Figure 3.3, which confirm that the boundary condition used in the Lagrangian stochastic method is still valid for rough walls. Given that the fully turbulent shear-stress evolution is alike with both smooth and rough walls, these results are quite similar to the ones obtained for smooth walls and the same interpretations can be made.

At this stage, it is worth repeating a word of caveat: too often, as recalled by Haworth [2010], a specular rebound is implemented to represent the effects of the wall for high-Reynolds-number flows. As demonstrated here, this condition does not respect the physics of the logarithmic zone and, in particular, the characteristic constant shear-stress profile. For this reason, it should be avoided and replaced by the reference an-elastic wall-boundary condition which, furthermore, is valid for both smooth and rough walls. The latter rebound condition is kept for the rest of this work.

3.1.3 Independence with Respect to z^{pl^+}

From now on, we mainly focus on the velocity second-order moments which are the most sensitive to potential sources of error. In the previous section, the height at which the boundary condition was implemented in the logarithmic zone was chosen somewhat arbitrarily. We now demonstrate that numerical outcomes are independent of the location at which the reference an-elastic wall-boundary condition is applied, as long as it is set in the logarithmic zone.

To this end, we consider that the rebound plane is implemented at different dimensionless heights z^{pl^+}. There are two ways to modify this value: either by modifying the nature of the flow through its Reynolds number, or by changing the geometrical height of the rebound plane. The results presented in Figure 3.4 are based on this second method but similar results would have been obtained by modifying the Reynolds number. For these simulations only, the Reynolds number characterising the flow is lowered to $Re_* = \frac{u_* H}{\nu} = 3348$. The plane is set on different height corresponding to $z^{pl^+} = 335$, $z^{pl^+} = 167$, $z^{pl^+} = 100$, and $z^{pl^+} = 67$. Then, as we can see in Figure 3.4, the results are independent of the choice made for the height of the rebound plane as long as it remains within the logarithmic zone. The only difference is that by lowering the physical position of the rebound plane we can have access to information closer to the wall.

To conclude, the numerical results presented in this section demonstrate the validity of the particle an-elastic wall boundary condition, Eq. (1.235), and provide additional support compared to previous studies. Two important results complete this validation process: first, this wall boundary condition can be used, without any modification, for smooth and rough walls; and second, the resulting profiles across the SBL are insensitive to the location of the rebound plane at which the an-elastic condition is applied provided that this rebound plane remains within the logarithmic region. Note that wall functions in the FV formulation usually

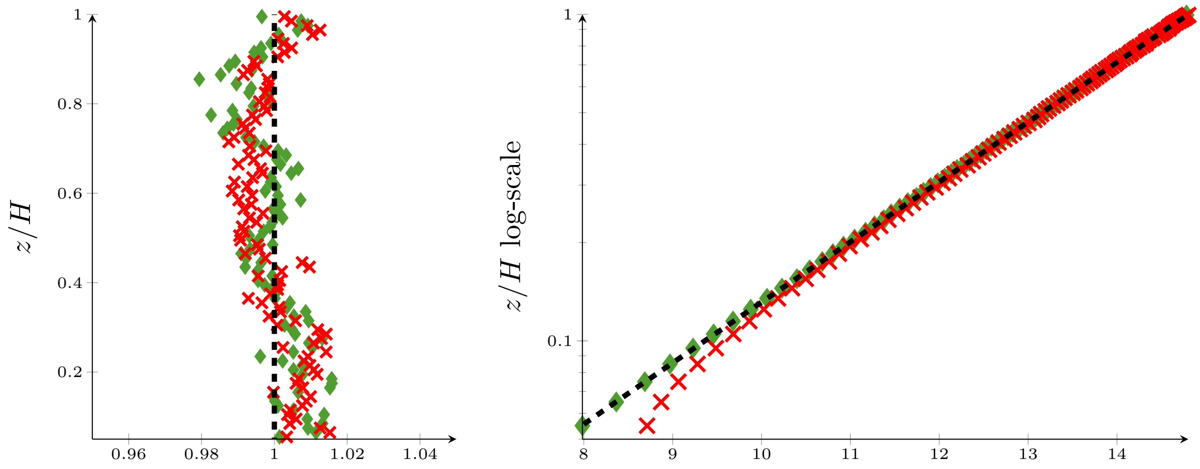

(A) Normalised concentration.

(B) Streamwise velocity.

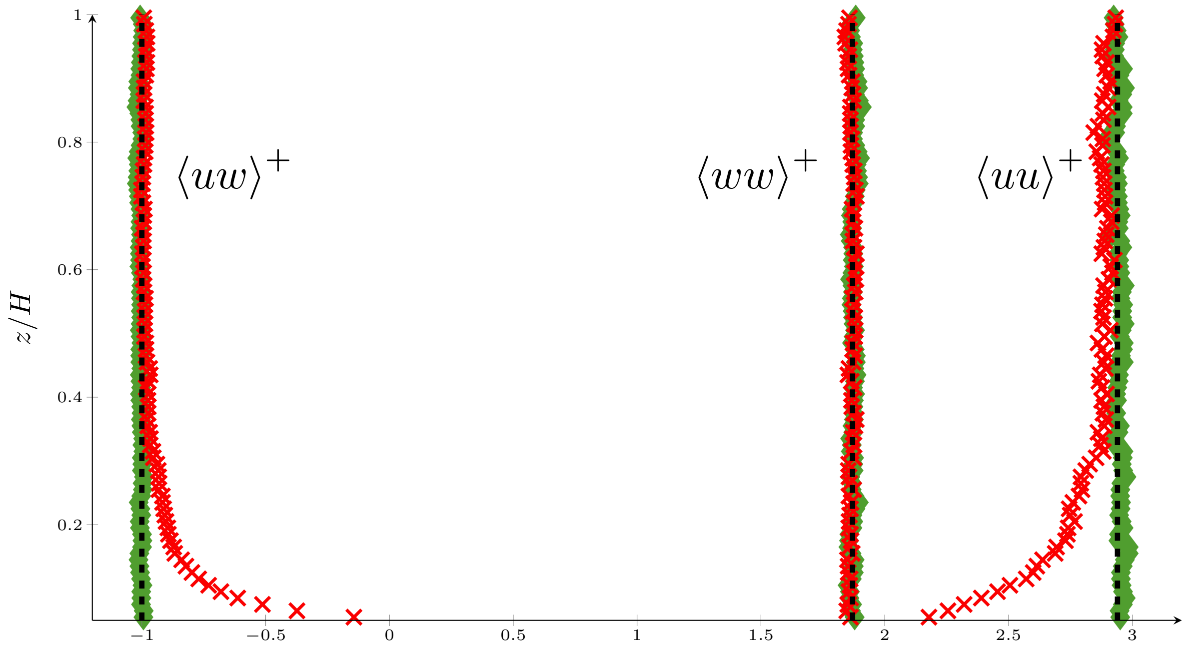

(C) Reynolds tensor.

Figure 3.3: Vertical profiles in the surface-boundary layer for rough walls: the normalised concentration (A); the dimensionless mean streamwise velocity (B); and the four non null components of the dimensionless Reynolds tensor (C) (note that in the spanwise and normal direction the Reynolds tensor components are equal, only the latter one is plotted). Considering a rough wall, two results corresponding to two distinct Lagrangian boundary conditions are compared: the reference an-elastic wall-boundary condition (◆) and the elastic wall-boundary condition (✖). Both respect the well-mixed criterion but only the reference wall-boundary condition enables to obtain correct mean velocity and Reynolds tensor profiles compared to the analytical solutions (▪▪▪).

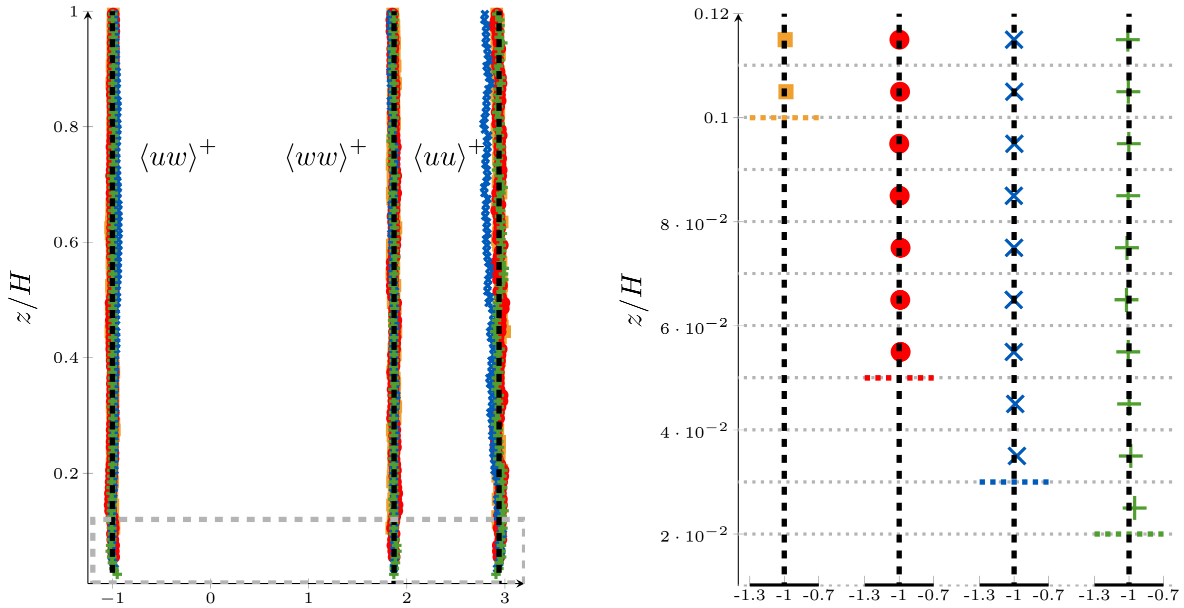

(A) Reynolds tensor
in the whole domain.

(B) $\langle uw\rangle^+$ near the wall
for each simulation.

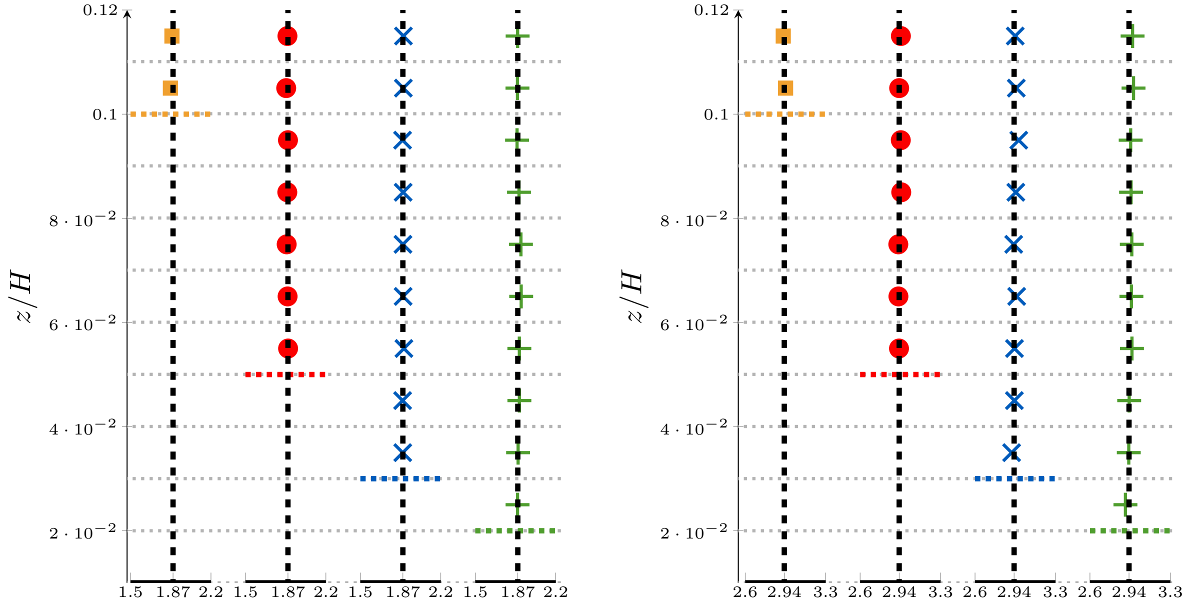

(C) $\langle ww\rangle^+$ near the wall
for each simulation.

(D) $\langle uu\rangle^+$ near the wall
for each simulation.

Figure 3.4: Vertical profiles of the four non null components of the dimensionless Reynolds tensor for different boundary condition implementation heights z^{pl^+} (note that in the spanwise and normal direction the Reynolds tensor components are equal, only the latter one is plotted). First the vertical profiles for all components are plotted all over the domain (A). Then for each component respectively $\langle uw\rangle$ (B), $\langle ww\rangle$ (C) and $\langle uu\rangle$ (D), a focus is set on the few cells near the wall and for each simulation the profiles are plotted side-by-side. The implementation height considered are: $z^{pl^+} = 335$ (🟧); $z^{pl^+} = 167$ (•); $z^{pl^+} = 100$ ×) and $z^{pl^+} = 67$ (+). The grey dashed box in the sub-figure (A) represents the zoomed zone near the wall. On the other sub-figures the grey dotted lines represent the FV cells and the coloured dotted lines the different boundary condition implemented. Note that the results are independent of the implementation height z^{pl^+}.

consider that the lower limit of the domain is shifted from the physical position of the wall by a distance, referred as z_0 for rough walls. One can then apply the PDF rebound plane directly on the boundary face of the FV mesh. This situation is considered from now on. Given the physical soundness of the present one-particle PDF model, we can turn our attention to the analysis of spatial numerical errors.

3.2 Interpolation of Mean Fields at Particle Positions

Contents

The purpose of this section is to introduce the issues related to the interpolation step. From now on, the fine FV mesh is made coarser to highlight the spatial numerical errors, we have then $H/\Delta z = 20$. The limit of the local uniformity hypothesis is first discussed in Section 3.2.1. In Section 3.2.2, we present improved interpolation methods as well as numerical results, after selecting which mean fields are best to interpolate.

3.2.1 Limitation of the Piece-wise Constant Interpolation Scheme

We start by bringing out the source of error that appears when using the local uniformity hypothesis for the interpolation of mean fields at particle locations in the vicinity of the wall.

To evaluate the local uniformity hypothesis, we can compare the first-order term in the Taylor expansion to the value at the centre of the cell $\underline{\boldsymbol{X}}^c$. For a variable Ψ, this local uniformity hypothesis requires that, everywhere in the local volume where the hypothesis is applied, we have:

$$|\underline{\mathbf{grad}}\Psi(\underline{\boldsymbol{X}}^c)||(X_i - X_i^c)| \ll \Psi(\underline{\boldsymbol{X}}^c). \tag{3.5}$$

In our case, given that the mesh is uniform, and that all the non-zero gradients increase as we get closer to the wall, the condition has just to be fulfilled at the rebound plane. For example, this condition for the Lagrangian timescale at the rebound plane implies that:

$$\frac{2\kappa}{\sqrt{\mathcal{C}_0}u_*}0.5\Delta z \ll \frac{2\kappa}{\sqrt{\mathcal{C}_0}u_*}(0.5\Delta z + z^{pl}). \tag{3.6}$$

If we want to implement the rebound plane at the same location as the FV parietal law, i.e by setting $z^{pl} = z_0$, the latter condition cannot be respected. Indeed, a hypothesis underlying the use of such parietal laws is to observe spatial scales larger than the shift implied by this parietal law. Therefore, we should have $2z_0/\Delta z \ll 1$. This means that the condition Eq. (3.6) and the uniformity hypothesis are not respected.

Furthermore, when considering uniform mean fields within a cell, the local variations of statistics and their mean gradients result from the presence of particles coming from nearby cells. The latter ones "keep in memory" the mean field encountered previously during a time which is of the order of the Lagrangian timescale defined in Eq. (1.213). Therefore, if the particle residence time in a given cell is larger than the local value of the Lagrangian timescale, the dynamics is mostly governed by the uniform fields within this cell, regardless of what happens in the surrounding ones and without any noticeable effects of the mean gradients. Since the mean velocity gradient is the source of the production terms in Eqs 3.3, under these conditions, the estimated kinetic energy of the particles would then tend towards the case of a uniform isotropic maintained turbulence (this issue is further discussed in Appendix 3.A). At the opposite, when Lagrangian timescales are small, near the interfaces between two cells, the step in the mean fields has to be bridged quickly, thus over a small distance. This yields locally to an overstatement of the estimated mean velocity gradient and of the estimated shear stress and streamwise component of the Reynolds tensor. Such spurious effects are illustrated in Figure 3.5.

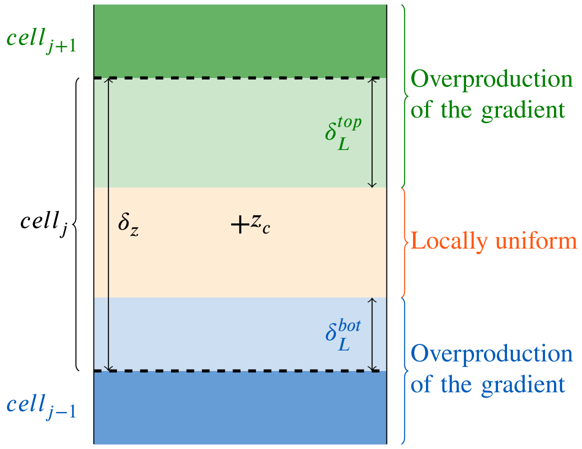

Figure 3.5: Illustration of the spurious evolution of the statistics within a cell when a piece-wise constant interpolation is used in a zone where the turbulent length scale δ_L is small compared to the cell size Δz. This situation occurs near the wall. In this case the turbulent mixing is not sufficient leading to an overestimation of the gradient and production term at the faces and an underestimation of these quantities at the centre of the cells.

Using a P_0 interpolation method, for this 'mixing effect' to properly take place, it is thus necessary to ensure that there is no zone where particle dynamics is governed only by the uniform fields assumed in the current cell in which they are located. In order to do so, one may assert that the characteristic vertical turbulence length scale $\delta_L = \sqrt{\langle ww \rangle} T_L$ (the distance over which a particle "keeps memory" of carrier fields from other cells) must be large compared to the size of the cells. In this situation the evolution of δ_L is governed by:

$$\delta_L(z) \simeq \sqrt{\langle ww \rangle} T_L = \mathcal{C}_0^{\frac{1}{4}} u_* \frac{2\kappa}{\sqrt{\mathcal{C}_0} u_*} z \simeq 0.61 z. \tag{3.7}$$

The respect of the condition Eq. (3.8) can give us a criterion to consider if a mesh is sufficiently fine. In SBL flows, it is sufficient to respect this condition at the rebound plane:

$$\delta_L \simeq 0.61(0.5\Delta z + z^{pl}) > \Delta z. \tag{3.8}$$

Once again, if we impose $z^{pl} = z_0$, this condition is not satisfied. Thus, using a P_0 interpolation scheme, at the centre of the cells in the immediate vicinity of the wall-boundary condition, we expect to find a zone in which particles see only the uniform properties associated to this cell. The corresponding errors are further highlighted in Appendix 3.A and solutions to limit them are discussed in Section 3.2.2.

3.2.2 Improved Interpolation Methods

We have seen in Section 3.2.1 that, near the wall and especially if we set the rebound plane at the FV wall boundary, the P_0 interpolation is not valid anymore and does not enable to properly recreate the particle-based mean velocity gradient and the production terms. Improved interpolation methods are thus needed. It is however useful to select first which mean fields are to be interpolated before addressing how this can be achieved.

3.2.2.1 Selection of the Mean Fields to Interpolate

To select the fields to be interpolated, we can think of the mean fields appearing in the evolution of the moment of interest, cf. Eq. (3.1) and Eqs 3.3. This corresponds to the mean velocity and its gradient, the mean pressure gradient, the Reynolds tensor and the dissipation rate. On the one hand the variations of density, pressure gradient, and Reynolds tensor must be small compared to their value at the centre of the cells. This is especially true in the case of neutral SBLs where these quantities should be constant. On the other hand, near the wall, the dissipation rate and the mean velocity gradient become very large. Thus, for these fields, we can no longer estimate that only the first term in the Taylor expansion is dominant. For the mean velocity, this would result in a poor estimation of the production term and the Reynolds tensor as the ensemble-averaged velocity gradient is not handled very well near the wall with a P_0 interpolation. In consequence, a finer reconstruction method is needed for the mean velocity, which is to be retained as a mean field to interpolate. For similar reasons, a finer description should also be considered for the evolution of a turbulent quantity associated to the dissipation rate. The issue is then to select which turbulent scales is best to consider from a numerical standpoint. In that sense, the turbulent dissipation rate is not the best candidate due to its hyperbolic variation. Near the wall, it is more convenient to consider the turbulent timescale $\mathcal{T}_k = k/\epsilon$ which is far smoother than the turbulent dissipation rate and does not have any singular point as discussed by Speziale et al. [1992]. In particular, within the logarithmic zone, $\mathcal{T}_k$ evolves linearly with the distance to the wall whereas ϵ evolves with the inverse of this distance. Numerically, the Lagrangian timescale appears therefore as the relevant turbulent variable to interpolate. In the spirit of $k - \mathcal{T}_k$ models, $\mathcal{T}_k$ is then chosen to reconstruct the Lagrangian timescale and to use this quantity instead of the dissipation rate. Note that this amounts to using a $R_{ij} - T_L$ formulation instead of a $R_{ij} - \epsilon$ one. Other quantities such as the turbulent Reynolds number $Re_t = \frac{k^2}{\epsilon}$ as proposed by Zhang et al. [2020] may be promising candidate for similar reasons than $\mathcal{T}_k$ but are not considered in this work. It is also worth noticing that the selection of the fields to interpolate more precisely depends on the physics considered and the variables retained in the state vector. For example, when considering the transport of a scalar Ψ, if we are interested in its variance or in its turbulent fluxes, the treatment of the scalar gradient in the corresponding production term requires a precise interpolation of the mean field $\langle \Psi \rangle$.

3.2.2.2 Interpolation Methods

To select interpolation methods, we first require that they respect three conditions. More precisely, a proper interpolation method should:

Cond. i be local, so as to be easily implemented in complex geometries and within non-homogeneous meshes (this is in line with the NGP interpolation considered);

Cond. ii provide an improved description of the mean velocity and Lagrangian timescale fields compared to the case of a uniform interpolation near the wall, so as to avoid the pitfalls presented previously;

Cond. iii respect key physical equilibrium near the wall, in particular to ensure that the production-dissipation balance is still satisfied.

To highlight the relative importance of the two last conditions, four interpolation methods of the mean fields at the position of the particles are now introduced. They are:

Interp. 1 P_0 interpolation on the mean velocity and Lagrangian timescale fields.

This first interpolation is the one used previously. It does not respect the conditions Cond. ii and Cond. iii. It should yield to the spurious effects specified in Section 3.2.1, illustrated in Figure 3.5 and plotted in Appendix 3.A in Figure 3.A.1.

Interp. 2 P_1 interpolation on the mean velocity and Lagrangian timescale.

This interpolation is the simplest and most natural one when accounting for the necessity to improve the interpolation for these two fields (see Cond. ii). This is especially true for the Lagrangian timescale for which such an interpolation method enables to retrieve the analytical profile near the wall. However, within a cell, this method is not consistent with the condition Cond. iii for the production-dissipation balance governing the dynamics of the SBL. Indeed, as the mean velocity field is linearly interpolated, its gradient is considered constant within a cell which means that the production term and the Lagrangian timescale should also be piece-wise constant.

Interp. 3 P_1 interpolation on the mean velocity field and P_0 interpolation on the Lagrangian timescale field.

Although less accurate than the previous one, this interpolation respects the condition Cond. iii and the production-dissipation balance. However, it does not respect the condition Cond. ii; as seen with Eq. (3.6), the local uniformity hypothesis for the Lagrangian timescale does not hold at the wall.

Interp. 4 A logarithmic interpolation of the mean velocity field with a linear interpolation of the Lagrangian timescale field within wall cells and the interpolation Interp. 3 everywhere else.

This interpolation is proposed in the spirit of the wall-function treatment to retrieve both conditions Cond. ii and Cond. iii. Indeed, to respect the condition Cond. ii and especially the analytical profile near the wall, a linear interpolation should be used for the Lagrangian timescale. Then, to respect the production-dissipation balance condition Cond. iii, this choice of interpolation for the Lagrangian timescale requires to select a logarithmic interpolation for the mean velocity. Such an interpolation hypothesis is less justified in the whole domain and, moreover, it requires to have access to the relative position between a particle and the wall everywhere. Thus, to remain local and respect the condition Cond. i, this interpolation is applied only in the cell in which the wall boundary condition is applied. In these near-wall cells, the assumption of a locally developed logarithmic layer is indeed consistent with the wall-function treatment used for the carrier flow. In the case where a cell is in contact with several wall-boundary conditions, we can consider only the interactions with the closest one to the particle. To do so, only the normal distance to the corresponding face and the shear stress associated to this face are necessary. Outside the immediate near-wall cells, it is necessary to consider another interpolation scheme. The one kept is the third one (i.e. Interp. 3) as it respects all the three conditions outside the close vicinity of the wall.

In the present work, we restrict ourselves to these simple and local interpolation schemes even though more advanced and accurate interpolation methods exist (see Subramaniam and Haworth [2000], Jenny et al. [2001], McDermott and Pope [2008], Viswanathan et al. [2011]). If one wishes to use such extended schemes, three main issues should however be carefully addressed:

- The consistency between the reconstruction of the production and dissipation terms (Cond. iii) should be assessed. Indeed, the error induced by inconsistent reconstructions can offset the gain of accuracy in the interpolation of mean fields, as shown in Figure 3.6;
- The implementation of such methods on 3-D unstructured meshes can turn into a daunting task;
- Within the scope of self-contained or stand-alone methods, the modification of the interpolation scheme is not as straightforward and cannot be applied as such. Indeed, in this context, the averaging scheme used to obtain the statistics issued from the particles must be of same or higher order than the interpolation scheme used to interpolate the mean moments at the position of the particles (see Hockney [1966]). An analysis on the averaging scheme considered would then be a prerequisite and the local NGP method used should certainly be modified.

For these reasons, such more complex schemes are not considered in the present work.

3.2.2.3 Numerical Results

In order to compare the interpolations proposed above, a SBL is simulated as previously. The simulations were carried out considering a 20 cells mesh for the finite volume calculation. A rough wall-boundary condition is implemented with a roughness height of 0.1 m. The rebound plane is set on the same level than the FV wall-boundary condition, i.e. at a dimensionless height of $z_0^+ = 6.7\ 10^4$. Since the zone of interest is near the rebound plane, we focus on the flow obtained within the first few cells of the FV mesh. To access the spatial evolution of the extracted statistics within each FV cell in order to assess the errors induced by the different interpolation schemes, a specific treatment is applied to the statistics plotted in Figure 3.6. The ensemble statistics are first estimated on a spatial partition of the domain 100 times finer than the FV mesh. They are then spatially averaged over ten bins, which means that in each FV cell 10 points are plotted. By doing so, we remove the spatial error introduced by the estimation of the statistics on statistically non-uniform averaging bins. This error is discussed later in Section 3.3.

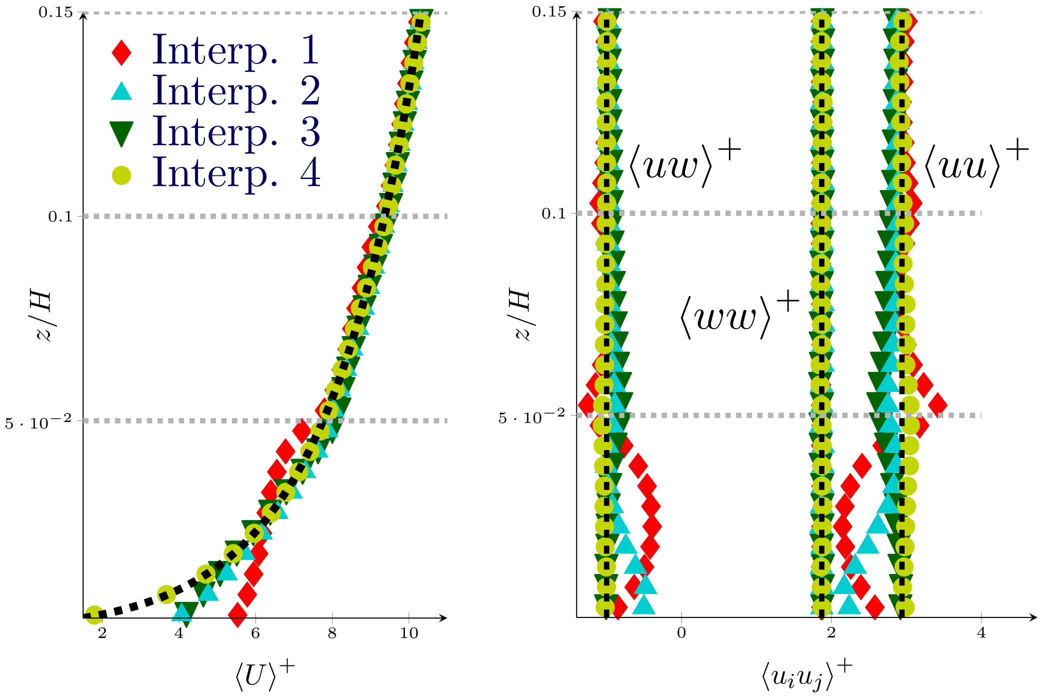

(A) Dimensionless streamwise velocity.

(B) Dimensionless Reynolds tensor.

Figure 3.6: Vertical profiles of the dimensionless mean streamwise velocity (A), the four non null components of the dimensionless Reynolds tensor (B) in the few cells near the wall (note that in the spanwise and normal direction the Reynolds tensor components are equal, only the latter one is plotted). The results obtained with four interpolation methods are compared: Interp. 1, which is a piece-wise constant interpolation for all mean fields(♦); Interp. 2, which is a piece-wise linear interpolation for both mean velocity and mean Lagrangian timescale fields (▲); Interp. 3, which is a piece-wise linear interpolation for the mean velocity field and piece-wise constant interpolation for the mean Lagrangian timescale field (▼); Interp. 4, which is a logarithmic interpolation for the mean velocity field and piece-wise linear interpolation for the mean Lagrangian timescale field in the cell at wall and similar to the previous interpolation otherwise (●). These statistics are compared to the analytical solution (▪▪▪). Note that a specific statistical treatment has been made to avoid the statistical error discussed on Section 3.3.

When using the P_0 interpolation on all mean fields, we observe, as expected, a spurious behaviour near the wall with a uniform flow tending to appear at the centre of the first cell and overestimated fluctuations near the cell interfaces. This can be noticed by the erroneous S-shaped profile of the mean velocity within the first cell in Figure 3.6A. This is also quite noticeable in Figure 3.6B for the estimations of the second-order moments. Indeed, the streamwise components tend towards the values corresponding to a uniform maintained isotropic turbulence in the centre of the first cell while they are overpredicted at the interfaces due to overestimated gradient of the mean velocity in these areas. Those effects are well diminished by using a P_1 interpolation on the velocity.

However, since such P_1 reconstructions are in general discontinuous, we can see an error on the second-order moments between the first and second cells due to the step of the mean velocity field at the cell interface. Having a more continuous profile for the Lagrangian timescale, the numerical discontinuity for the mean moments is better handled with Interp. 2 than with Interp. 3, as we can see at the interface between the two first cells. Yet, near the rebound plane, an underestimation of the shear stress is noticeable at the wall using Interp. 2 but not using Interp. 3. Interp. 2 does not respect Cond. iii for the production-dissipation balance, due to the P_1 interpolation of the Lagrangian timescales. Indeed, since the velocity gradient and the production term are considered as uniform, the linear decrease of the Lagrangian timescale characterising the turbulent structures lifetimes is not compensated. Near the wall, this results in a spurious decrease of the shear stress and streamwise component of the Reynolds tensor. Across the first cell, the consistency in the production-dissipation equilibrium, cf. Cond. iii, seems to play a key role compared to the accuracy in the description of the Lagrangian timescale Cond. ii. Then, Interp. 3 yields almost perfect predictions for the second-order moment. However, near the rebound plane, there is still a noticeable discrepancy between the results obtained respectively with a linear and with a logarithmic interpolation. Finally, Interp. 4, relying on an analytical interpolation in the first cell, seems to reproduce the exact solution for both mean velocity and Reynolds tensor. It is thus the one proposed when we can ensure that, everywhere in each point of the wall cells, the linearly interpolated Lagrangian timescale field is sufficiently large to use the SLM model developed for high Reynolds number flows.

To conclude, in the vicinity of the wall a description finer than P_0 is necessary to properly recreate the mean velocity gradient and the production terms. It is emphasised that the consistency between the interpolation of the mean velocity and the Lagrangian timescale plays an essential role. To fulfil these conditions, the mixed interpolation method, namely Interp. 4, is proposed. In the spirit of a wall-function treatment, analytic interpolations of the mean velocity and Lagrangian timescale at particle positions are used in the cells in the immediate vicinity of the wall. Further from the wall, the simpler interpolation method, Interp. 3, which consists in a piece-wise linear interpolation of mean velocity field and piece-wise constant interpolation of the Lagrangian timescale is used to respect the production-dissipation equilibrium. In order to obtain these results, a spatial average has been applied to remove spurious statistical artefacts that are studied in Section 3.3.

3.3 Analysis of Statistical Bias Induced by Local Spatial Averaging

Contents

As described in Section 1.3.3.3, either at the end of each iteration or in a post-treatment step, statistics extracted from a set of particles are estimated on a given partition of the space. For fluid particle simulations based on hybrid methods, it is worth recalling that statistics derived from the set of particles do not enter the particle evolution equations. These statistics are, however, observables used to assess particle dynamics. It is therefore of key importance to ensure that they are not biased by statistical artefacts that would result in misleading interpretations.

In that sense, the main purpose of this section is to focus on the potential numerical errors appearing when estimating statistics by local averaging.

As specified in Paragraph 1.3.3.3.4, these errors are of two kinds. On the one hand, there is the inherent zero-average statistical noise due to Monte Carlo estimations using a finite number of particles. This well-known error converges with the square root of the number of particles and is not further discussed in the following. On the other hand, a second source of error is caused by spatial discretisation when statistics are obtained over particles within small averaging bins. If the hypothesis of local homogeneity is not respected within these averaging bins, spatial errors can appear in the estimations of the covariances as demonstrated in Section 3.3.1. To limit this source of error, the straightforward solution is to estimate statistics on finer bins. If the same statistics are needed on coarser bins, one may simply spatially average them in the spirit of multi-grid methods. However, this refinement process introduces multiple spatial divisions of the domain which are inconvenient for particle tracking and more time consuming. To avoid such statistical artefacts while keeping the original coarse bins, a new approach is developed in Section 3.3.2 which consists in correcting statistics. These new correction terms are based on an assumption about the profiles of the first-order statistics within the averaging bins. Unless otherwise stated, from now on, the mean moments of the carrier flow are analytically interpolated at the position of the particles in the whole domain. This is done to focus on the error impacting the statistics without interference from issues associated to the determination of the mean moments of the carrier flow or their interpolations.

3.3.1 Effect of the Non-Uniformity in the Averaging Bins on the Statistics

The goal in this section is to identify and quantify the source of spatial numerical error which can affect the estimation of statistics in averaging bins when the hypothesis of homogeneity, upon which probabilistic averages are replaced by spatial ones, breaks down.

3.3.1.1 Effect of the Non-Uniformity within the Averaging bins on the Estimator of the Moments

For any quantity Ψ, its averaged value at a position $\underline{\boldsymbol{X}}$ noted $\langle\Psi\rangle(\underline{\boldsymbol{X}})$ is approximated by the estimator of the mean noted $\langle\Psi\rangle_\Omega$. This estimator corresponds to the ensemble average over all the particles located within a given averaging volume Ω around the position $\underline{\boldsymbol{X}}$. It converges towards the true statistic, which is the element of interest, when the averaging volume tends towards zero and the number of samples tends towards infinity, i.e. $\langle\Psi\rangle(\underline{\boldsymbol{X}}) = \underset{\substack{\Omega\to 0\\ n_\Omega\to\infty}}{lim} \langle\Psi\rangle_\Omega$

We might wonder if $\langle\Psi\rangle_\Omega$ effectively represents the spatial average of the mean $(\frac{1}{\Omega}\int_\Omega \langle\Psi\rangle(\underline{\boldsymbol{X}})\mathrm{d}\Omega)$ even when $\langle\Psi\rangle(\underline{\boldsymbol{X}})$ is not uniform in this volume Ω. For this purpose, let us consider a coarse averaging bin Ω containing particles uniformly distributed but in which mean moments vary (which means that the hypothesis of local homogeneity is not satisfied). Let us split this coarse volume Ω in a sufficiently high number of smaller sub-volumes ω so that statistics can be regarded as uniform within each of these sub-volumes. A scheme of such a splitting in the vertical direction is represented in Figure 3.7. Note that for the sake of simplicity and clarity we consider that the mean flow varies only in one direction where the refinement is applied. Indeed, the present methodology does not depend on the number of dimensions of the problem and can easily be generalised in 3-D so that it is sufficient to discuss the 1-D situation.

We assume that the number of particles n_ω within each sub-volume ω is sufficiently large to consider that the ensemble average does not suffer from statistical error. After obtaining the statistics issued from the set of particles on each of the sub-volumes, we can take the spatial average of those statistics over all the sub-volumes composing Ω as shown in Figure 3.7. Under the hypothesis considered we have $\langle\Psi\rangle_\omega = \langle\Psi\rangle(\underline{\boldsymbol{X}})$ and thus $\frac{1}{\Omega}\int_\Omega \langle\Psi\rangle(\underline{\boldsymbol{X}})\mathrm{d}\Omega = \sum_{\omega\in\Omega}\frac{n_\omega}{n_\Omega}\langle\Psi\rangle_\omega$. For the estimator of the mean on the coarsest volume we have:

$$\langle\Psi\rangle_\Omega = \frac{1}{n_\Omega}\sum_{p\in\Omega}\Psi^p = \sum_{\omega\in\Omega}\frac{n_\omega}{n_\Omega}\underbrace{\left(\frac{1}{n_\omega}\sum_{p\in\omega}\Psi^p\right)}_{\langle\Psi\rangle_\omega} = \frac{1}{\Omega}\int_\Omega \langle\Psi\rangle(\underline{\boldsymbol{X}})\mathrm{d}\Omega \tag{3.9}$$

Thus, there is no spatial artefact on the estimation of the mean quantities even if the flow is not uniform inside a given averaging bin.

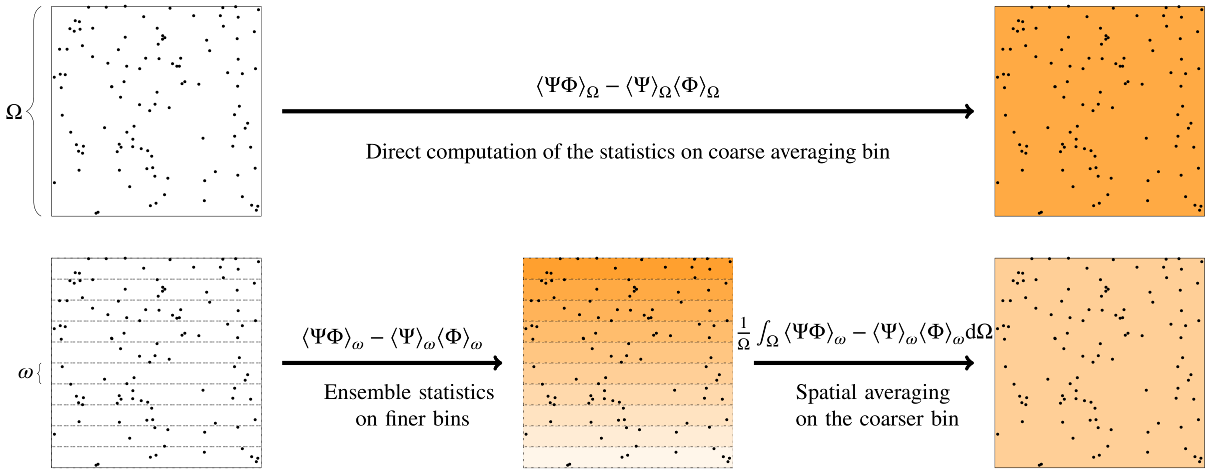

Figure 3.7: Illustration of the error appearing during the statistic estimation step due to the lack of uniformity of the mean fields within the averaging bins. In the upper part, the covariances are estimated directly on the coarse bin Ω and are affected by numerical error. In the lower part, the refinement method used to limit this error is depicted. First, statistics are estimated on more refined bins ω and are then spatially averaged to obtain the results on the coarser bin Ω. The refinement is made only in one direction as we consider a 1-D validation case. Note that only the estimation of the covariances are affected by this deterministic spatial errors .

We also want to check if the covariance estimator is unbiased, i.e. if the estimation of the covariance obtained on the whole volume is the same as the spatial average of the true covariance. We have then for two quantities Ψ and Φ:

$$\begin{aligned}\underbrace{\langle\Psi\Phi\rangle_\Omega - \langle\Psi\rangle_\Omega\langle\Phi\rangle_\Omega}_{\text{Estimator of the covariance}} &= \sum_{\omega\in\Omega}\frac{n_\omega}{n_\Omega}\underbrace{\left(\frac{1}{n_\omega}\sum_{p\in\omega}\Psi^p\Phi^p\right)}_{\langle\Psi\Phi\rangle_\omega} - \langle\Psi\rangle_\Omega\langle\Phi\rangle_\Omega \\ &= \underbrace{\frac{1}{\Omega}\int_\Omega \langle\Psi\Phi\rangle - \langle\Psi\rangle\langle\Phi\rangle\mathrm{d}\Omega}_{\text{True covariance of interest}} + \underbrace{\frac{1}{\Omega}\int_\Omega \langle\Psi\rangle\langle\Phi\rangle\mathrm{d}\Omega - \langle\Psi\rangle_\Omega\langle\Phi\rangle_\Omega}_{\text{Bias: Spatial covariance of the mean fields}}\end{aligned} \tag{3.10}$$

It follows that, when the first-order moments vary across the coarse averaging bin Ω, the estimator of the covariances extracted directly from the whole set of particles (on the LHS of Eq. (3.10)) differs from the spatial average of the true covariances (the first term in the RHS term). This is emphasised by the presence of the spatial covariance of the first-order moments within the coarse volume (the second RHS term) which is a spatial artefact caused by the non-respect of the local homogeneity hypothesis within the averaging bins. It is clear that similar issues would occur for higher order moments. Yet, in this study, we limit ourselves to the estimation of covariance as higher order statistics are less used as observable.

To conclude, even for correct particle dynamics, an error can impact some covariance estimators. The estimators which are biased are the ones whose corresponding first-order moments vary within the averaging bins.

3.3.1.2 Convergence of the Spatial Error on the Estimator of the Covariance

In this subsection, we estimate the magnitude of the deterministic bias introduced in Eq. (3.10). Since it is due to the spatial variation of mean velocity within the averaging bins, it is clear that this error depends on both the profiles of mean statistics ($\langle\Psi\rangle$, $\langle\Phi\rangle$) as well as on the size of these averaging bins. In the situation studied, as the flow is uni-axial, taking Ψ and Φ as the components of velocity, an error appears only if $\Psi = \Phi = U$. Since the spatial variance of the mean streamwise velocity is positive, if the averaging bins are too coarse, the streamwise component of the Reynolds tensor is overestimated. Far from the wall, the velocity gradient is small and thus the spatial averaging bias remains low. However, as we go closer to the wall where the velocity gradient increases drastically this error becomes more important. For given particle dynamics with an analytical interpolation of the mean carrier fields at the position of the particles, this effect is demonstrated in Figure 3.8. This source of error can be preponderant, for example in this case without refinement, when the bias is of the same magnitude as the covariance itself and when the estimated covariance is twice higher than expected. It is also clear that this error converges to zero when the averaging bins are refined. Note that, since we consider a 1-D problem the refinement is made uniformly only in the direction of interest as schematised Figure 3.7.

To circumvent the overestimation of covariances seen in Section 3.3.1, we can first estimate statistics on a sufficiently fine partition of the domain. Once statistics are estimated on this refined partition, we can spatially average them on the coarser partition of the domain as illustrated in Figure 3.7 in one dimension. With this method, the evolution of the relative error on the streamwise component of the Reynolds tensor within the first coarse FV cell (Ω) near the wall is plotted in Figure 3.9 using different refinement for the intermediate finer averaging bins (ω). The coloured points correspond to the errors after averaging the profiles Figure 3.8 in the first cell. Two zones can be identified: a first one below a refinement factor (ratio between the cell size Ω and the bin size ω) of 30 where the error converges with an order 3/2; and a second one above the refinement factor of 30 which appears as a plateau region where the other sources of numerical errors presented in Section 1.3.3.3 become preponderant (in this second zone, we can then consider the averaging bins to be small enough).

Such a method is applicable even for highly 3-D unstructured meshes. Indeed, each volume can always be split into sub-pyramidal volumes based on one of the faces of the original volume and on its centre of gravity. This step can be repeated to have a mesh as refined as wanted. However, tracking particles into such a finer mesh could be time consuming. Yet, in the scope of hybrid methods, the statistics issued from the set of particles do not impact their dynamics. Thus, this could be done only once as a post-processing step, so as to limit the increase of computation time. Even so, an important issue at stake is to be able to determine a criterion to ensure that the averaging bin is small enough. This criterion should provide the relative importance of this source of error compared to the other ones stated in Section 1.3.3.3. However, criteria to

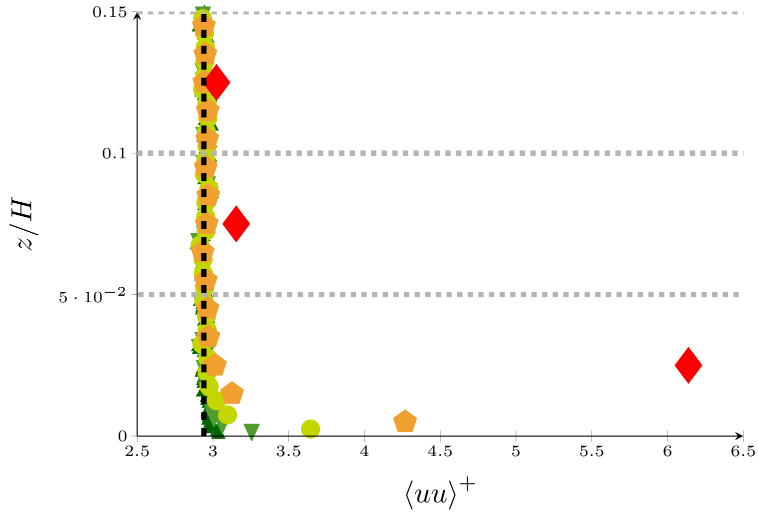

Figure 3.8: Vertical profiles of the statistical estimator of the streamwise component of the Reynolds tensor in the vicinity of the wall using different spatial bins for the local averaging. Compared to the FV cells (indicated by the grey dotted lines), the bins are respectively: of the same size (♦); 5 times finer (⬟); 10 times finer (●); 20 times finer (▼); 50 times finer (▲). Note that these observed statistical estimators are extracted from the same particle set, i.e. they correspond to identical particle dynamics.

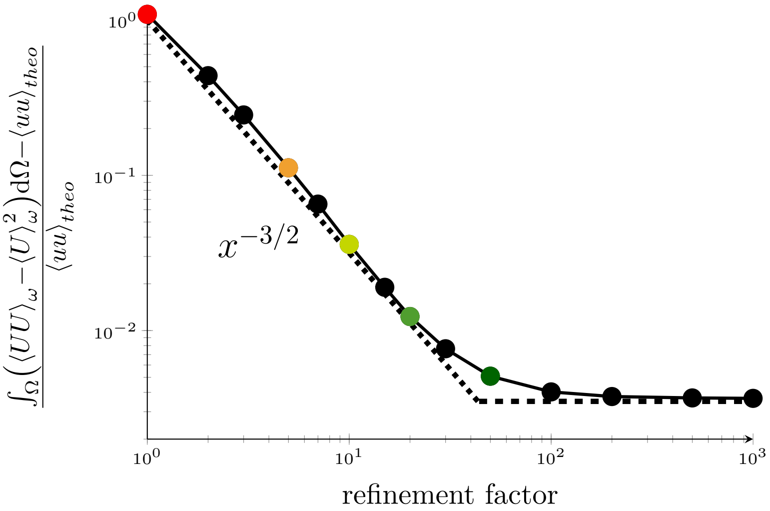

Figure 3.9: Evolution of the error on the estimator of the streamwise component of the Reynolds tensor in the first FV cell with the refinement factor. The refinement factor corresponds to the ratio between the size of the FV cell Ω and the size of the averaging bins ω used to estimate the intermediate statistics at first. These statistics are then spatially averaged on the FV cell. It is observed that the error first converges with a rate $x^{-3/2}$ (····) as long as the spatial error on the statistics is the main source of error (until a refinement factor around 30). Then the level of error due to the statistical noise of the Monte Carlo methods on a finite number of particles is reached and this error stagnates on a plateau (- - -). Each coloured dot represents the error obtained after a spatial average of the corresponding profile in Figure 3.8 within the first cell. Note that these observed statistical estimators are extracted from the same particle set, i.e. they correspond to the identical particle dynamics.

quantify *a priori* these other sources of error do not exist in the general case. It is still possible to resort to an iterative process to determine if the averaging bins are small enough. At each iteration, the previous averaging partition of the domain is refined and the results on the new averaging partitions are compared with the results on the previous one. Once these results are similar the averaging bins can be considered small enough.

3.3.2 Proposition of Correction of the Statistics on the Finite-volume Mesh Assuming Profile of the First-Order Statistics within the Averaging Bins

To avoid iterative refinement processes and having to deal with multiple space divisions, a second idea is to directly estimate the covariance of mean moments on the coarse averaging bins Ω (e.g. the FV cells) and propose correction terms to compensate the bias appearing in Eq. (3.10). To do so, we need to reconstruct the fields corresponding to the mean quantities $\langle\Psi\rangle$ and $\langle\Phi\rangle$ in the domain based on the knowledge of their values at the cell centres. These reconstructed profiles are noted $\mathfrak{R}_{\langle\Psi\rangle}(\underline{\boldsymbol{X}})$ and $\mathfrak{R}_{\langle\Phi\rangle}(\underline{\boldsymbol{X}})$, respectively, and depend on the position as well as on statistics estimated within the corresponding averaging bin Ω. We can then write the corrective term of the covariance estimator $Cor_{\Omega}^{\triangleright}\left(\mathfrak{R}_{\langle\Psi\rangle},\mathfrak{R}_{\langle\Phi\rangle}\right)$ as the spatial covariance of the reconstructed mean fields:

$$
\begin{aligned}
Cor_{\Omega}^{\triangleright}\left(\mathfrak{R}_{\langle\Psi\rangle},\mathfrak{R}_{\langle\Phi\rangle}\right) = {} & \frac{1}{\Omega}\int_{\Omega}\mathfrak{R}_{\langle\Psi\rangle}(\langle\underline{\boldsymbol{X}}\rangle)\mathfrak{R}_{\langle\Phi\rangle}\left(\langle\underline{\boldsymbol{X}}\rangle\right)\mathrm{d}\Omega \\
& -\frac{1}{\Omega}\int_{\Omega}\mathfrak{R}_{\langle\Phi\rangle}\left(\langle\underline{\boldsymbol{X}}\rangle\right)\mathrm{d}\Omega\frac{1}{\Omega}\int_{\Omega}\mathfrak{R}_{\langle\Phi\rangle}\left(\langle\underline{\boldsymbol{X}}\rangle\right)\mathrm{d}\Omega.
\end{aligned}
$$

This value is expected to be close to the spatial bias which is the true spatial covariance of the mean fields. Assuming that particles are uniformly distributed within the averaging bins, one may use an ensemble average over the particles located in each bin ($\langle(.)\rangle_{\Omega}$) to estimate the spatial statistics. We have then:

$$
Cor_{\Omega}^{\triangleright}\left(\mathfrak{R}_{\langle\Psi\rangle},\mathfrak{R}_{\langle\Phi\rangle}\right) \simeq \langle\mathfrak{R}_{\langle\Psi\rangle}(\langle\underline{\boldsymbol{X}}\rangle)\mathfrak{R}_{\langle\Phi\rangle}\left(\langle\underline{\boldsymbol{X}}\rangle\right)\rangle_{\Omega} - \langle\mathfrak{R}_{\langle\Phi\rangle}\left(\langle\underline{\boldsymbol{X}}\rangle\right)\rangle_{\Omega}\langle\mathfrak{R}_{\langle\Phi\rangle}\left(\langle\underline{\boldsymbol{X}}\rangle\right)\rangle_{\Omega}. \tag{3.11}
$$

At this stage, the issue is then to come up with proposals on how to reconstruct the fields corresponding to the mean moments (i.e. $\mathfrak{R}_{\langle\Psi\rangle}(\underline{\boldsymbol{X}})$) within the averaging bins.

3.3.2.1 Proposition of Correction terms

In the following, three reconstruction methods are proposed. They correspond to:

Reconst. unif $\mathfrak{R}_{\langle\Psi\rangle}^{unif}(\underline{\boldsymbol{X}}) = \langle\Psi\rangle_{\Omega}\forall\underline{\boldsymbol{X}} \in \Omega$: no variation of the first-order statistics within the averaging bins.

The simplest idea is to consider the mean moment constant within the averaging bin and thus the correction $Cor_{\Omega}^{\triangleright}\left(\mathfrak{R}_{\langle\Psi\rangle}^{unif},\mathfrak{R}_{\langle\Phi\rangle}\right)$ is null. This is not coherent with the necessity to use finer interpolation, as discussed in Section 3.2.2. Moreover, as we can derive from Figure 3.6A, even a P_0 interpolation of the mean carrier flow does not result in a homogeneous evolution for the corresponding moment within a bin due to the mixing process discussed in Section 3.2.1. Finer descriptions for this evolution should then be considered.

Reconst. lin $\mathfrak{R}^{lin}_{\langle\Psi\rangle}$: linear variation of the first-order statistics within the averaging bins.

In the general case, one could use a Taylor expansion to estimate the evolution of the flow within a bin. The estimation of the profile for a quantity $\langle\Psi\rangle$ would then require to know the value of its gradient: $\underline{\mathbf{grad}}_\Omega\langle\Psi\rangle$. We have to extract the corresponding mean gradient from the set of particles. Assuming a local uniformity of the spatial distribution of the particles in the bin, it is here proposed to estimate this quantity using the covariance of Ψ and the position $\underline{\boldsymbol{X}}$ and the covariance of the position as:

$$\underline{\mathbf{grad}}_\Omega\langle\Psi\rangle \simeq \widetilde{\underline{\mathbf{grad}}}_\Omega\langle\Psi\rangle = \underbrace{\left(\langle\Psi\underline{\boldsymbol{X}}\rangle_\Omega - \langle\Psi\rangle_\Omega\langle\underline{\boldsymbol{X}}\rangle_\Omega\right)}_{\langle\psi\underline{\boldsymbol{x}}\rangle_\Omega}\cdot\underbrace{\left(\langle\underline{\boldsymbol{X}}\otimes\underline{\boldsymbol{X}}\rangle_\Omega - \langle\underline{\boldsymbol{X}}\rangle_\Omega\otimes\langle\underline{\boldsymbol{X}}\rangle_\Omega\right)^{-1}}_{\left(\langle\underline{\boldsymbol{x}}\otimes\underline{\boldsymbol{x}}\rangle_\Omega\right)^{-1}}, \tag{3.12}$$

with $\underline{\boldsymbol{x}}$ the distance to the local barycentre associated to the particle, i.e. $\underline{\boldsymbol{x}} = (\underline{\boldsymbol{X}} - \langle\underline{\boldsymbol{X}}\rangle)$. The covariance of the position can be reversed since it is a symmetric definite positive tensor provided that the variance of the diagonal term is non zero. The latter condition is respected as long as there are at least 3 non coplanar particles within the averaging bin. With this estimated mean gradient $\widetilde{\underline{\mathbf{grad}}}_\Omega\langle\Psi\rangle$, an estimated reconstruction of the mean profiles of $\langle\Psi\rangle$ within the bin can be built as:

$$\mathfrak{R}^{lin}_{\langle\Psi\rangle}(\underline{\boldsymbol{X}}) = \langle\Psi\rangle_\Omega + \widetilde{\underline{\mathbf{grad}}}_\Omega\langle\Psi\rangle\cdot\underline{\boldsymbol{x}}. \tag{3.13}$$

It is then possible to estimate the correction $Cor^{\triangleright}_{\Omega}\left(\mathfrak{R}^{lin}_{\langle\Psi\rangle}, \mathfrak{R}^{lin}_{\langle\Phi\rangle}\right)$ as:

$$Cor^{\triangleright}_{\Omega}\left(\mathfrak{R}^{lin}_{\langle\Psi\rangle}, \mathfrak{R}^{lin}_{\langle\Phi\rangle}\right) = \left(\widetilde{\underline{\mathbf{grad}}}_\Omega\langle\Psi\rangle\otimes\widetilde{\underline{\mathbf{grad}}}_\Omega\langle\Phi\rangle\right) : \langle\underline{\boldsymbol{x}}\otimes\underline{\boldsymbol{x}}\rangle_\Omega. \tag{3.14}$$

Reconst. log $\mathfrak{R}^{log}_{\langle\Psi\rangle}$: logarithmic variation of the first-order statistics within the averaging bins

Near the wall and within a SBL it is reasonable to suppose that the mean velocity follows a logarithmic profile. In order to use such a reconstruction method, we need the shear velocity $\tilde{u}_*$. One may assume that the shear stress is constant in such zone and estimate it as:

$$\tilde{u}_* = \sqrt{|\langle u_\tau u_n\rangle_\Omega|} \tag{3.15}$$

where u_τ and u_n are respectively the fluctuations of the velocity components along the streamwise and normal directions. The covariance $\langle u_\tau u_n\rangle$ should not be affected by the spatial averaging error since, near wall, the normal mean velocity should be null: $\langle U_n\rangle = 0$. In the general case for a quantity Ψ one may want to estimate the corresponding value $\tilde{\psi}_*$ defined as:

$$\tilde{\psi}_* = \frac{-\langle\psi u_n\rangle_\Omega}{\sqrt{|\langle u_\tau u_n\rangle_\Omega|}} \tag{3.16}$$

Based on this value, for rough walls, one can estimate $\mathfrak{R}^{log}_{\langle\Psi\rangle}(\underline{\boldsymbol{X}})$ as:

$$\mathfrak{R}^{log}_{\langle\Psi\rangle}(\underline{\boldsymbol{X}}) = \langle\Psi\rangle_\Omega + \frac{\tilde{\psi}_*}{\kappa}\left(\ln\left(d_{wall}\right) - \langle\ln\left(d_{wall}\right)\rangle_\Omega\right), \tag{3.17}$$

where d_{wall} is the distance of the particle to the wall, typically for rough wall one may consider $d_{wall} = X_n + z_0$. Thus, for the mean streamwise velocity, the corresponding spurious spatial covariance can be estimated as:

$$Cor_{\Omega}^{\triangleright}\left(\mathfrak{R}^{log}_{\langle\Psi\rangle}, \mathfrak{R}^{log}_{\langle\Phi\rangle}\right) = \frac{\tilde{\psi}_*\tilde{\phi}_*}{\kappa^2}\left(\left\langle \ln\left(d_{wall}^2\right)\right\rangle_{\Omega} - \left\langle \ln\left(d_{wall}\right)\right\rangle_{\Omega}^2\right).$$

Let us remark that Eq. (3.11) allows the reconstruction methods for $\langle\Psi\rangle$ and $\langle\Phi\rangle$ to differ. For example, one may estimate:

$$Cor_{\Omega}^{\triangleright}\left(\mathfrak{R}^{lin}_{\langle\Psi\rangle}, \mathfrak{R}^{log}_{\langle\Phi\rangle}\right) = \frac{\tilde{\phi}_*\widetilde{\underline{\mathbf{grad}}}_{\Omega}\langle\Psi\rangle}{\kappa}\left\langle \underline{\boldsymbol{x}} \ln\left(d_{wall}\right)\right\rangle_{\Omega} \tag{3.18}$$

3.3.2.2 Numerical Results

To investigate the effects of the proposed correction terms in conjunction with the interpolation methods, numerical results were obtained in the SBL case. Two sets of results are presented in Figure 3.10 corresponding to two slightly different particle dynamics: in Figure 3.10A, the mean field values at particle locations were obtained from an analytical interpolation in the whole flow (i.e. similar to the one used in the first cell using the Interp. 4 scheme), whereas in Figure 3.10B a linear interpolation method (the Interp. 3 scheme) was used to simulate particle dynamics. In each situation, the three different reconstruction methods for the statistical operator are then applied. It is worth stressing that, in each case, these three reconstructions correspond to the same particle dynamics.

It is seen that, in both situations, the three statistical reconstruction methods differ mostly in the first cell near the wall which, with the coarse mesh used in the simulations, is indeed where the discrepancy between the linear and logarithmic evolutions is significant (see Figure 3.6A). In Figure 3.10A, the linear reconstruction clearly underestimates the variation of the mean velocity within the cell and the corresponding correction term (Reconst. lin) is too small. On the other hand, the correction term based on the logarithmic profile (Reconst. log) enables to perfectly correct the source of error presented in Section 3.3.1. In Figure 3.10B, the logarithmic assumption (Reconst. log) strongly overestimates the variation of the mean velocity whereas the linear assumption (Reconst. lin) gives now much better results. Therefore, these results show clearly that the interpolation of the mean fields at particle positions presented in Section 3.2.2 and the reconstruction of these mean fields used in the corrected estimator presented in Section 3.3.2 must be consistent.

These conclusions are supported by additional results obtained with another interpolation method, namely Interp. 4 (see Section 3.2.2) which consists in a mixed interpolation scheme based on a logarithmic profile in the first cell near the wall and a linear profile otherwise. Results are presented in Figure 3.11 where it is seen that nearly perfect predictions are obtained when a coherent reconstruction method is used to correct statistical estimators, i.e. using the logarithmic reconstruction in the first cell near the wall and the linear one elsewhere. Note that the requirement to have consistent methods between what appears as two adjoint operators, the interpolation method (i.e. going from the mesh to the particles) on the one hand and the one used to extract statistics (i.e. going from the particles to the mesh) on the other hand, is in line with the analysis set forth in Peirano et al. [2006] about similar concerns.

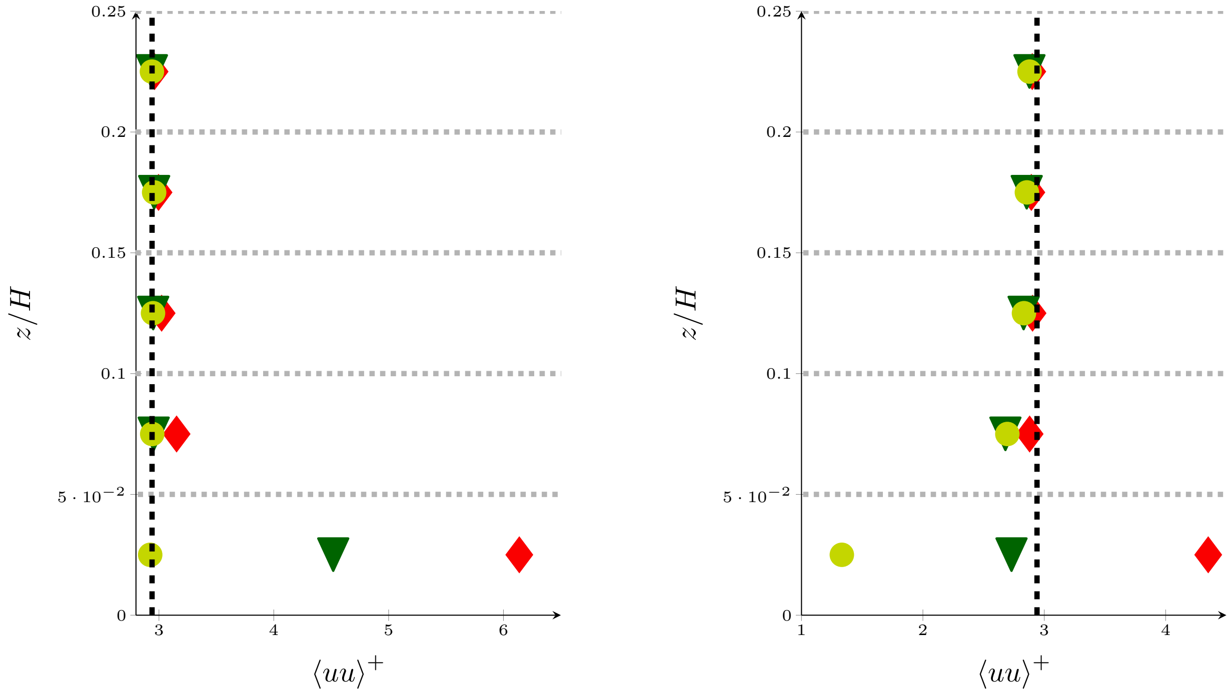

(A) logarithmic interpolation.

(B) Interp. 3: linear interpolation.

Figure 3.10: Vertical profiles of the statistical estimators of the streamwise component of the Reynolds tensor in the vicinity of the wall for different interpolation-reconstruction combinations compared to the analytical solution (▪▪▪). The three reconstruction methods described in Section 3.3.2, corresponding to three assumptions on how the ensemble mean velocity field varies in averaging bins, are compared: Reconst. unif, assuming a piece-wise constant profile (♦); Reconst. lin, assuming a piece-wise linear profile (▼); Reconst. log, assuming a logarithmic profile (●). The two sub-figures correspond to two different particle dynamics on which these correction terms are tested. In sub-figure (A), particles were simulated using the logarithmic interpolation of the mean velocity field at their positions. In that case, the linear reconstruction (Reconst. lin) works better than having no correction (Reconst. unif) but is not sufficient, whereas the logarithmic reconstruction (Reconst. log) corrects nearly perfectly the statistical estimation. In sub-figure (B), particles were simulated using the piece-wise linear interpolation of the mean velocity field at their positions. In this case, the logarithmic reconstruction (Reconst. log) overestimates the correction needed, whereas the linear reconstruction (Reconst. lin) provides now a fairly good correction of the results obtained with no reconstruction (i.e. with Reconst. unif).

3.4 Local Conclusions and Perspectives

In this chapter, a detailed analysis to evaluate how SBLs are predicted by a one-particle PDF model was carried out. This analysis was performed with two main objectives in mind.

The first main objective was to assess the validity of the wall boundary condition developed by Dreeben and Pope [1997a] and Minier and Pozorski [1999] in the spirit of the wall-function treatment of the near-wall region. On the one hand, pursuing the analysis proposed by Bahlali et al. [2020] for hybrid methods, we have shown that this reference an-elastic wall-boundary condition allows to correctly reproduce the characteristic mean-field profiles of SBLs, by which

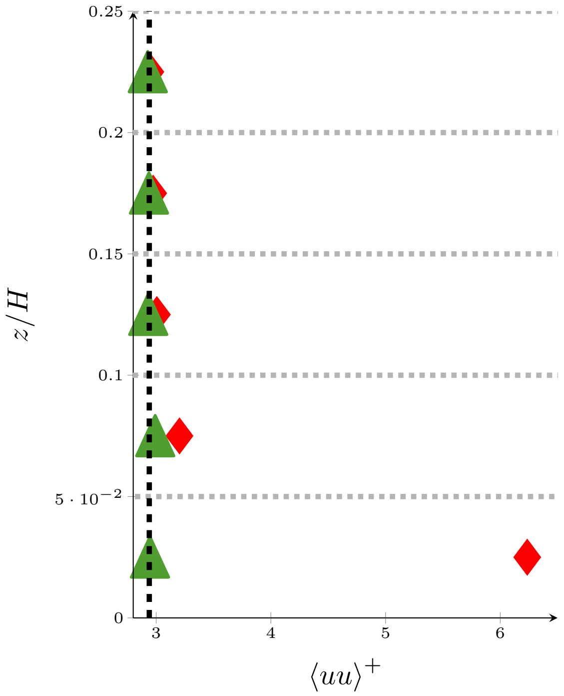

Figure 3.11: Vertical profiles of the statistical estimators of the streamwise component of the Reynolds tensor in the vicinity of the wall when using the method Interp. 4 to interpolate the mean carrier fields at particle locations. Two results corresponding to two corrections of the statistics are compared with the analytical ones (▪▪▪): Reconst. unif (♦); and, a correction coherent with the interpolation methods considered, i.e. a logarithmic reconstruction of the ensemble mean velocity $\mathfrak{R}^{log}_{\langle U \rangle}$ in the first cell near the wall and a piece-wise linear reconstruction $\mathfrak{R}^{log}_{\langle U \rangle}$ otherwise (▲).

we can say that the physics of such layers is indeed well captured. On the other hand, it was demonstrated that applying a specular rebound as the wall boundary condition yields non-physical results and serious discrepancies near the wall. Compared to previous studies, additional results have been obtained. Since the reference an-elastic wall-boundary condition is built so as to reproduce the shear stress within the logarithmic zone, the results put forward in Section 3.1.2 prove that this condition can be applied, without any modification, for both rough and smooth walls. Another key result is that the height at which the rebound plane is implemented can be chosen arbitrarily in the logarithmic zone without impacting the statistics extracted, as demonstrated by the numerical results presented in Section 3.1.3. It is important to note that the formulation of the reference an-elastic wall boundary condition does not depend on the specific details of the Langevin model retained to simulate the velocity of fluid particles. In that sense, present results and conclusions, obtained with a SLM modelling, are nevertheless valid and applicable to general PDF models based on particle locations and velocities.

The second main objective was to investigate spatial numerical errors in the context of hybrid FV/PDF formulations and corresponding Monte Carlo particle/mesh methods. In such hybrid simulations, it is useful to distinguish two sources of spatial errors, depending on whether they influence particle dynamics or not. The first source of spatial error is caused by the interpolation of mean fields at particle positions. These interpolated mean field values enter the Langevin equation that models the evolution of particle velocities and, therefore, directly affect particle dynamics. The results put forward in Section 3.2.2 show that, to properly reproduce the local mean gradients and production terms, it is important to have a non-uniform interpolation of the mean velocity field. Furthermore, these results also illustrate a new approach introduced in the present numerical formulation, which consists in interpolating the Lagrangian timescale along with the fluid mean velocity. Numerical results indicate that the interpolation of the Lagrangian timescale should be coherent with the one used for the mean velocity so as to satisfy the production-dissipation balance at the numerical level. To fulfil these conditions, a local interpolation method has been proposed with a specific treatment in the wall cells in the spirit the wall functions. This interpolation method is based on the assumption of an established SBL within wall cells and can be easily implemented on complex meshes. The second source of spatial error arise when particle statistics are derived by performing local Monte Carlo estimations in small volumes around a given point. In the context of hybrid FV/PDF methods, statistics for fluid particles are not used in the Langevin evolution equation, which means that they do not affect particle dynamics. These statistics are then mere observables, but it is important to bring out potential spurious effects to avoid misleading interpretations of particle dynamics. Such statistical artefacts are linked to the breakdown of the underlying assumption of local homogeneity upon which these spatial averaging is based. Indeed, as shown in Section 3.3.1, when first-order statistics are not uniform within the averaging bin, spurious artefacts appear in the estimation of the corresponding covariances. To lower such effects, a first solution consists in introducing finer averaging bins. In practice, this means that we are handling two meshes, one for the fluid mean field computation in the FV solver and one to extract particle statistics in the PDF solver. In complex geometries, tracking particles in such duplicate partitions of space (or meshes) can quickly become cumbersome. To keep only one space decomposition while avoiding these potential artefacts when deriving particle statistics, new correction methods have been developed. Based on an assumed reconstruction of profiles of the first-order statistics within the averaging volume, it is shown in Section 3.3.2 that these statistical artefacts can indeed be almost perfectly corrected. To achieve this, it is important that the interpolation scheme and the reconstruction assumed in this correction be coherent. Using this method, the statistics can then be estimated directly on the same mesh than the one used for the interpolation step.

This study has mainly focused on hybrid FV/PDF formulations. However, they can be extended to stand-alone methods, with the difference that the second source of spatial numerical error would also affect particle dynamics. Indeed, in stand-alone methods, the statistic extracted from the set of particles are reinjected in the dynamics creating a bias error. Furthermore, only the dynamic aspect of the flow with a very simple state vector $\underline{\boldsymbol{Z}} = (\underline{\boldsymbol{X}}, \underline{\boldsymbol{U}})$ has been taken into account in the present work. It is worth noticing that considering more complex physics, transporting additional fields such as passive or active scalars, similar reasoning should be applied for the choice of the wall-boundary condition, interpolation scheme and averaging methods for the turbulent fluxes and variances of interest. This issue is explicitly tackled for the potential temperature in Section 5.2 to extend the present analysis to thermally stratified SBL flows.

Local Appendix

3.A Complement on the Error Induced by Piece-wise Constant Interpolation

Contents

The goal in the present appendix is to further discuss the influence of the interpolation methods considered on the particle dynamics. The errors occurring when using a piece-wise constant interpolation near the wall are emphasised.

Injecting the interpolated mean carrier fields at the position of the particle in the modelling of the increments of velocity Eq. (1.217b), the SLM model becomes:

$$\mathrm{d}\underline{\boldsymbol{U}} = -\frac{1}{[\overline{\rho}]}[\underline{\mathbf{grad}\overline{P}}]\,(\underline{\boldsymbol{X}}(t);t)\,\mathrm{d}t - \frac{\underline{\boldsymbol{U}} - [\underline{\overline{\boldsymbol{U}}}](\underline{\boldsymbol{X}}(t);t)}{[\overline{T_L}](\underline{\boldsymbol{X}}(t);t)}\mathrm{d}t + \sqrt{C_L C_0 \frac{[\overline{k}](\underline{\boldsymbol{X}}(t);t)}{[\overline{T_L}](\underline{\boldsymbol{X}}(t);t)} T_L(\underline{\boldsymbol{X}}(t);t)}\,\mathrm{d}\underline{\boldsymbol{W}}\ , \tag{3.19}$$

where for any carrier field Ψ, $\overline{\Psi}$ denotes the averaged value extracted from the finite volume approach and $[\overline{\Psi}](\underline{\boldsymbol{X}}(t);t)$ its interpolation at the position of the particle $\underline{\boldsymbol{X}}(t)$ at the instant t. For the sake of clarity the term $(\underline{\boldsymbol{X}}(t);t)$ will be discarded from now on, yet it is important to keep in mind that generally these interpolated values are space and time dependent. The corresponding equation for the first-order statistics is:

$$\frac{\partial\langle U_i\rangle}{\partial t} + \langle U_k\rangle\frac{\partial\langle U_i\rangle}{\partial x_k} + \frac{\partial\langle u_k u_i\rangle}{\partial x_k} = -\frac{1}{\rho_r}\frac{\partial\overline{P}}{\partial x_i} - \frac{\langle U_i\rangle - [\overline{U_i}]}{[\overline{T_L}]}. \tag{3.20}$$

An additional relaxation term between the mean velocity extracted from the set of particles and the interpolation of the mean carrier flow at this position appears. For the streamwise mean velocity the equation Eq. (3.20) becomes:

$$\frac{\partial\langle uw\rangle}{\partial z} = -\frac{\langle U\rangle - [\overline{U}]}{[\overline{T_L}]}. \tag{3.21}$$

Thus, if the mean velocity associated to the particles ($\langle U\rangle$) differs from the local interpolation of the mean carrier velocity fields at this position ($\overline{U}$), the local shear stress associated to the particle will not remain uniform. This effect is strengthened when approaching the wall where the Lagrangian timescale becomes small. From this equation one can obtain the equation for the particle-averaged velocity:

$$\langle U\rangle = [\overline{U}] - \frac{\partial\langle uw\rangle}{\partial z}[\overline{T_L}]. \tag{3.22}$$

In a zone where the interpolated mean carrier velocity field is differentiable, we can write:

$$\frac{\partial\langle U\rangle}{\partial z} = \frac{\partial[\overline{U}]}{\partial z} - \frac{\partial^2\langle uw\rangle}{\partial z^2}[\overline{T_L}] - \frac{\partial\langle uw\rangle}{\partial z}\frac{\partial[\overline{T_L}]}{\partial z}. \tag{3.23}$$

Supposing piece-wise uniform interpolation denoted ($[.]_0$), away from the faces of the cells, the gradients of the interpolated mean carrier fields are well defined and are null. We get :

$$\frac{\partial\langle U\rangle}{\partial z} = -\frac{\partial^2\langle uw\rangle}{\partial z^2}[\overline{T_L}]_0. \tag{3.24}$$

The derivation of the Reynolds tensor remains formally unchanged, however the shear stress being now non uniform we will also consider the turbulent diffusion terms in the equation:

$$\frac{\partial\langle u_i u_j w\rangle}{\partial z} = -\delta_{xj}\langle u_i w\rangle\frac{\partial\langle U\rangle}{\partial z} - \delta_{ix}\langle u_j w\rangle\frac{\partial\langle U\rangle}{\partial z} - \frac{2\langle u_i u_j\rangle}{T_L} + C_0 C_L\frac{k}{T_L}\delta_{ij}. \tag{3.25}$$

Injecting the mean velocity gradient Eq. (3.24) in the shear stress equation, we have:

$$\frac{\partial\langle uww\rangle}{\partial z} = \langle ww\rangle\frac{\partial^2\langle uw\rangle}{\partial z^2}[\overline{T_L}]_0 - 2\frac{\langle uw\rangle}{[\overline{T_L}]_0}, \tag{3.26a}$$

$$\langle uw\rangle = -\frac{[\overline{T_L}]_0}{2}\frac{\partial\langle uww\rangle}{\partial z} + \langle ww\rangle\frac{\partial^2\langle uw\rangle}{\partial z^2}\frac{\left([\overline{T_L}]_0\right)^2}{2}. \tag{3.26b}$$

Injecting the mean velocity gradient Eq. (3.24) and the shear stress Eq. (3.26b) in the streamwise component of the Reynolds tensor equation we get:

$$\frac{\partial\langle uuw\rangle}{\partial z} = \left(-[\overline{T_L}]_0\frac{\partial\langle uww\rangle}{\partial z} + \langle ww\rangle\frac{\partial^2\langle uw\rangle}{\partial z^2}\left([\overline{T_L}]_0\right)^2\right)\left(\frac{\partial^2\langle uw\rangle}{\partial z^2}[\overline{T_L}]_0\right) - 2\frac{\langle uu\rangle}{[\overline{T_L}]_0} + C_L C_0\frac{[\overline{k}]_0}{[\overline{T_L}]_0}, \tag{3.27a}$$

$$\langle uu\rangle = \underbrace{\frac{C_L C_0[\overline{k}]_0}{2}}_{\langle ww\rangle=\langle vv\rangle=\frac{2}{3}k^{iso}} - \frac{[\overline{T_L}]_0}{2}\frac{\partial\langle uuw\rangle}{\partial z} + \frac{\left([\overline{T_L}]_0\right)^2}{2}\frac{\partial^2\langle uw\rangle}{\partial z^2}\left(-\frac{\partial\langle uww\rangle}{\partial z} + \langle ww\rangle\frac{\partial^2\langle uw\rangle}{\partial z^2}[\overline{T_L}]_0\right). \tag{3.27b}$$

Assuming that we are going close to the wall where the Lagrangian timescale tends towards zero the equations Eq. (3.24), Eq. (3.26b), Eq. (3.27b) imply that the particle-averaged velocity gradient and the shear stress tend towards zero whereas the streamwise component of the Reynolds tensor tends towards the normal component of the Reynolds tensor i.e. the one obtained for maintained isotropic turbulence. This spurious behaviour is schematised on Figure 3.5 and demonstrated in Figure 3.A.1.

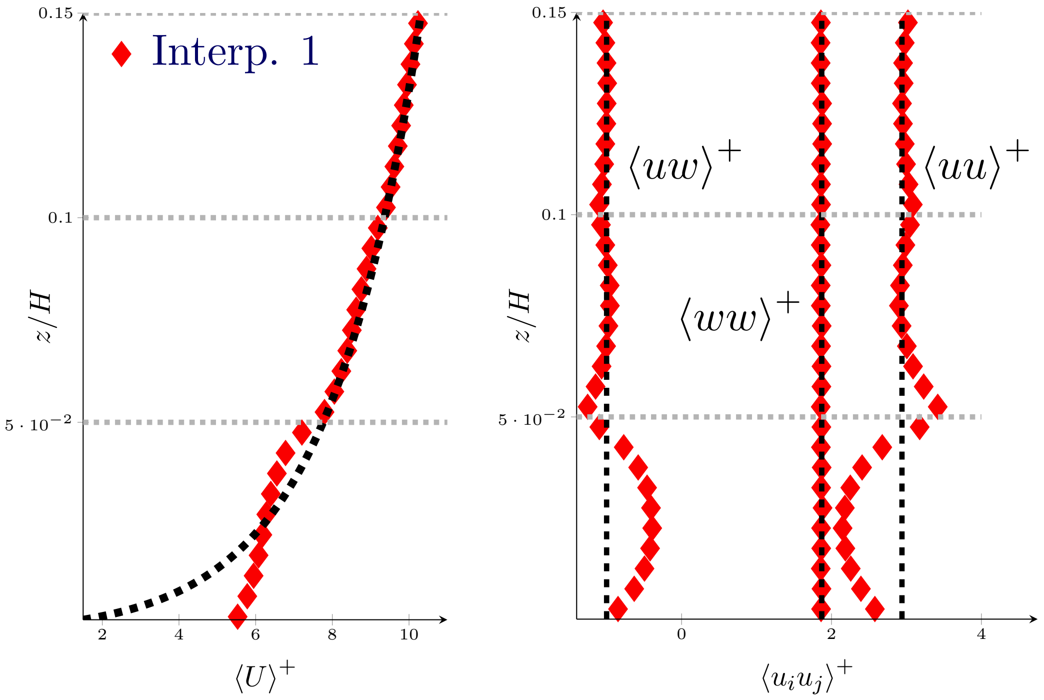

(A) Dimensionless streamwise velocity.

(B) Dimensionless Reynolds tensor.

Figure 3.A.1: Vertical profiles of the dimensionless mean streamwise velocity (A), the four non null components of the dimensionless Reynolds tensor (B) in the few cells near the wall near the wall using a piece-wise uniform interpolation scheme Interp. 1(♦) (note that in the spanwise and normal direction the Reynolds tensor components are equal, only the latter one is plotted). These statistics are compared with analytical solution (▪▪▪). In each cell of the FV simulation (whose faces are schematised by the grey dotted lines) the statistics are first estimated into 100 finer bins. The results plotted are an agglomeration of these statistics based on a spatial average over ten bins.

CHAPTER 4

Linear Source Dispersion in a Neutrally Stratified Channel Flow

Contents

The goal of this chapter is to describe the dispersion of passive non-reactive pollutants in neutrally stratified flows. To this end, we will study a case of linear source dispersion based on experimental setup of Gamel [2015]. To limit the computational cost of this approach, only the flow issued from the linear source will be simulated using particles. As the flow rate of pollutant is very small compared to the total flow rate, this would enable a large limitation of the computational cost. First, we will introduce in Section 4.1 the method used in the context of hybrid moment/PDF approaches to derive averaged statistics associated to the whole flow from statistics associated to a particle set conditioned on its injection location. Then two cases of linear source dispersion issued from Gamel [2015] work will be studied with both a RANS approach and a hybrid RANS/PDF method. The simulation results will be compared to experimental data. The first case, presented in Section 4.2, is a dispersion of pollutant injected at the ground in an unobstructed 2D channel flow. Finally, a more complex setup will be put forward in Section 4.3 where pollutant is injected at the ground in the wake of an infinite isolated obstacle.

4.1 Modelling of Pollutant Plumes with Hybrid Moment/PDF Methods

Contents

4.1.1 Leading Approach

We will first focus on the treatment of such dispersion from a hybrid moment/PDF point of view. As we consider a neutral situation here again the potential temperature is not considered. For the dynamics, we still consider the SLM model. Two approaches might be followed to treat the evolution of the pollutant dispersion.

- The first one consists of a description of the whole flow by simulating both the flow issued from the source of pollutant and the flow issued from other inlets referred as background flow. Doing so, we can consider the micro-mixing between the particles issued from the pollutant source and the background particles issued from other inlets. Thus, similarly to the treatment presented for the temperature in Paragraph 1.3.3.2.2, the evolution of the instantaneous concentration of pollutant in each particle can be treated with an IEM model: $\mathrm{d}C = \frac{C - \langle C \rangle}{\mathcal{T}_c}$ with $\mathcal{T}_C$ a characteristic exchange time defined as $\mathcal{T}_C = \frac{k}{C_C \epsilon}$. Doing so, the mass of pollutant may migrate from source issued particles to background particles. Yet, the flow rate issued from a leak of pollutant is in general negligible compared to the whole flow rate. The mass of fluid issued from the source, whose explicit treatment is necessary to obtain a proper description of the dispersion, is then negligible compared to the background particles mass. It would thus be required to use a very large number of particles to simulate this background flow. The explicit treatment of the later one in a Lagrangian stochastic context therefore provides little information compared to the corresponding increase of computational cost. This is the reason why such formulations, where both particles issued from the source and from the background flow are simulated, are in general too costly for industrial setups.

- In order to drastically reduce this cost, a second idea, considered here, is to focus only on the description of the particles issued from the source of pollutants without explicitly computing the background ones. Doing so the micro-mixing, which is responsible for the exchange of pollutant mass between source issued particles and the rest of the flow, becomes difficult to treat. Indeed, so as to conserve the mass of pollutant, the mass lost by the particles issued from the source of pollutant should be added somewhere else. To decorrelate the pollutant mass in the particles issued from the source and from the background particles, it is then necessary to neglect the micro-mixing as proposed by Pope [2000]. This hypothesis states that the mass of pollutant δm^P in a particle remains constant over its trajectory: $\mathrm{d}\delta m^P = 0$. It is thus not necessary to explicitly add the concentration or mass of pollutant in the state vector as it remains a constant property which has not to be transported. This assumption is in line with the hypothesis made by Taylor [1922] stating that at high Reynolds number the transport of scalar by molecular induced micro-mixing is negligible compared to the turbulent transport and the advection by the mean flow. However, for the scalar variance the micro-mixing effects play a first-order role as indicated by Pope [2000][Chapter 12.4] and cannot be neglected should we be interested in this quantity. Furthermore, looking only at the statistics associated to pollutant concentration and assuming a zero micro-mixing hypothesis, it is equivalent to consider explicitly or not the background particles.

4.1.2 Estimation of the Flow Statistics from Conditioned Statistics

Presentation of the Statistics Obtained on Different Set of Particles

An important issue remains that the statistics issued from a set of particles conditioned by their original location cannot be directly used to describe the whole flow. Let us assume that the latter is described with a Lagrangian stochastic methods using a set of particles $\mathbb{P}^T$ containing n^T particles. This set may be split into two sub-sets $\mathbb{P}^S$ and $\mathbb{P}^B$ composed respectively of the n^S particles issued from the source and the n^B background ones (which are not simulated in our case). For any quantity Ψ it is then possible to consider different averaging operators depending on the set of particles considered:

$$\langle \Psi \rangle^S = \frac{1}{M^S} \sum_{i^S \in \mathbb{P}^S} \delta m^{(i^S)} \Psi^{(i^S)}, \tag{4.1a}$$

$$\langle \Psi \rangle^B = \frac{1}{M^B} \sum_{i^B \in \mathbb{P}^B} \delta m^{(i^B)} \Psi^{(i^B)}, \tag{4.1b}$$

$$\langle \Psi \rangle = \frac{1}{M^T} \sum_{i \in \mathbb{P}^T} \delta m^{(i)} \Psi^{(i)}. \tag{4.1c}$$

where $\delta m^{(i)}$ corresponds to the mass of the particle i, M^T, M^S and M^B represent the total mass of the particles respectively of the whole set, of particles issued from the source and of background particles. We have then $M^T = M^S + M^B$ and $M^B \gg M^S$. In the case considered, only the particles of the sub-set $\mathbb{P}^S$ issued from the source are simulated and then we have a direct access only to the conditioned statistics $\langle (.) \rangle^S$. Because of this condition on the statistics, no averaged field estimated with this approach represents a duplicated field of any carrier field provided by the FV solver. The goal of this section is to present how to derive mean quantities associated to the whole flow (i.e. based on the whole set $\mathbb{P}^T$) knowing only the conditioned statistics associated to the subset $\mathbb{P}^S$.

Estimation of the Mean Pollutant Concentration

The mean concentration of pollutant in a volume Ω is defined by $\langle C\rangle_\Omega = \frac{M_\Omega^P}{\Omega}$, with M_Ω^P the mass of pollutant in the volume Ω. It is then direct to define the concentration in a particle i as $C^{(i)} = \frac{\delta m^{P,(i)}}{\omega^{(i)}}$ with $\omega^{(i)}$ its representative volume. It is assumed that the pollutant is a passive scalar and then $\rho^P = \rho$, we have then $C^{(i)} = \rho\frac{\delta m^{P,(i)}}{\delta m^{(i)}}$ and:

$$\langle C\rangle_\Omega = \frac{1}{M_\Omega^T}\sum_{i\in\mathbb{P}_\Omega^T}\delta m^{(i)}C^{(i)} = \frac{1}{\Omega}\sum_{i\in\mathbb{P}_\Omega^T}\delta m^{P,(i)}, \tag{4.2}$$

with M_Ω^T the total mass of fluid in the volume Ω. This average on the whole set of particles can be split between the two sets $\mathbb{P}_\Omega^S$ and $\mathbb{P}_\Omega^B$ as:

$$\langle C\rangle_\Omega = \frac{1}{M_\Omega^T}\left(\sum_{i^S\in\mathbb{P}_\Omega^S}\delta m^{(i^S)}C^{(i^S)} + \sum_{i^B\in\mathbb{P}_\Omega^B}\delta m^{(i^B)}C^{(i^B)}\right) = \frac{1}{\Omega}\left(\sum_{i^S\in\mathbb{P}_\Omega^S}\delta m^{P,(i^S)} + \underbrace{\sum_{i^B\in\mathbb{P}_\Omega^B}\delta m^{P,(i^B)}}_{=0}\right). \tag{4.3}$$

Background particles, originating from location far upstream the pollutant source, have initially no trace of pollutant. Moreover, neglecting the micro-mixing, the mass of pollutant remains constant over each particle trajectory. Thus, these background particles keep a concentration of pollutant null everywhere even downstream the pollutant source. Note that in the case where there is pollutant in the background, this background concentration should simply be added. One can also assume that in the general case, the concentration simulated represents the excess of pollutant compared to the background. We have thus simply:

$$\langle C\rangle_\Omega = \frac{1}{\Omega}\sum_{i^S\in\mathbb{P}_\Omega^S}\delta m^{P,(i^S)} = \frac{M_\Omega^P}{\Omega} = C_{inj}\frac{M_\Omega^S}{M_\Omega^T}, \tag{4.4}$$

with C_{inj}, the pollutant concentration at injection.

Estimation of the Turbulent Scalar Fluxes

Once we have estimated the mean concentration, we can take an interest in the scalar fluxes $\langle \underline{\boldsymbol{uc}}\rangle$ noting:

$$\langle \underline{\boldsymbol{u}}c\rangle = \langle \underline{\boldsymbol{U}}C\rangle - \langle \underline{\boldsymbol{U}}\rangle\langle C\rangle. \tag{4.5}$$

As the whole flow is not simulated within the Lagrangian solver, it is not possible to directly have access to the mean velocity $\langle \underline{\boldsymbol{U}}\rangle$. Yet, in the scope of hybrids moment/PDF methods, we can use the mean velocity provided by the FV solver $\overline{\underline{\boldsymbol{U}}}$ and the relation between duplicated fields: $\langle \underline{\boldsymbol{U}}\rangle = \overline{\underline{\boldsymbol{U}}}$. Rigorously speaking, we should ensure the consistency between RANS and PDF models to use such a relation. However, as presented in Section 4.2.3 and in Section 4.3.3, it can still be used with non-consistent models, keeping in mind this potential source of error. The mean flow velocity being provided by the FV solver and the determination of $\langle C\rangle$ being already treated in Eq. (4.4), we should then focus on the estimation of $\langle \underline{\boldsymbol{U}}C\rangle$. In a volume Ω we have:

$$\langle \underline{\boldsymbol{U}} C\rangle_\Omega = \frac{1}{M_\Omega^T}\left(\sum_{i\in\mathbb{P}_\Omega^T}\delta m^{(i)}\underline{\boldsymbol{U}}^{(i)}C^{(i)}\right) = \frac{1}{M_\Omega^T}\left(\sum_{i^S\in\mathbb{P}_\Omega^S}\delta m^{(i^S)}\underline{\boldsymbol{U}}^{(i^S)}C^{(i^S)} + \underbrace{\sum_{i^B\in\mathbb{P}_\Omega^B}\delta m^{(i^B)}\underline{\boldsymbol{U}}^{(i^B)}C^{(i^B)}}_{=0}\right) \tag{4.6}$$

For reason similar to the mean concentration, the second sum is null, and we have simply:

$$\langle \underline{\boldsymbol{u}} c\rangle_\Omega = \frac{1}{\Omega}\left(\sum_{i^S\in\mathbb{P}_\Omega^S}\delta m^{P,(i^S)}(\underline{\boldsymbol{U}}^{(i^S)} - \overline{\underline{\boldsymbol{U}}})\right) \tag{4.7}$$

Assuming that all particles have the same statistical weight and initial concentration, they represent the same unit of fluid and pollutant mass. We can then extract the particle mass from the sum, and the previous equation can be simplified into:

$$\langle \underline{\boldsymbol{u}} c\rangle = \langle C\rangle(\langle \underline{\boldsymbol{U}}\rangle^S - \overline{\underline{\boldsymbol{U}}}), \tag{4.8}$$

with $\langle \underline{\boldsymbol{U}}\rangle^S$ defined based on Eq. (4.1a). From this equation, it is clear that the averaged fields provided by both approaches are not duplicated fields. Indeed, the difference between both mean velocity $\langle \underline{\boldsymbol{U}}\rangle^S$ and $\overline{\underline{\boldsymbol{U}}}$ is directly proportional to the turbulent scalar fluxes.

Estimation of the Concentration Variance using a Volumetric Particle Approach
As each particle represents the statistical behaviour of a given mass of fluids, the concentration in each particle remains constant. The reasoning followed for the turbulent fluxes, based on zero micro-mixing hypothesis, does not hold for variance estimation as recalled by Pope [2000][Chapter 12.4]. Indeed, following the same logic as previously, we would obtain:

$$\langle cc\rangle_\Omega = \frac{1}{\Omega}\left(\sum_{i^S\in\mathbb{P}_\Omega^S}\delta m^{P,(i^S)}(C^{(i^S)} - \langle C\rangle_\Omega)\right) \tag{4.9}$$

Assuming that at the source all the particles are injected with the same concentration C_{inj} we would have:

$$\langle cc\rangle_\Omega = \langle C\rangle_\Omega(C_{inj} - \langle C\rangle_\Omega), \tag{4.10}$$

with the concentration at injection C_{inj} which is great compared to $\langle C\rangle_\Omega$ as soon as we move away from the injection. This estimation $\langle cc\rangle \simeq \langle C\rangle C_{inj}$ is a gross overestimation of the physics as highlighted later on in Figure 4.16A. This might well be understood looking at the corresponding transport equation similar to Eqs 1.227, where the dissipative term is null in absence of micro-mixing. Thus, there is no term to balance the production term.

To improve this result, Cassiani [2013] proposed the so called volumetric particle approach. The key idea is that each numerical particle does not represent the statistical description of physical domain containing a given mass of fluid δm but a given mass of pollutant δm^P. It is then possible to take into account the micro-mixing within a particle without loss of pollutant mass by increasing particle size. In this scope, the conservation of the mass of pollutant over the trajectory $\frac{\mathrm{d}m^{(i),P}}{\mathrm{d}t} = 0$ does not ensure the conservation of the total mass in the particles which increases as the pollutant dilutes itself. This interpretation is not fully satisfactory as the modification of the particle total mass with dilution implies the absorption of mass from the background flow (with different dynamics). The latter would have an impact on the particle dynamics which is not tackled. First, we have no control on the evolution of the particle total mass δm. The physical domain represented by the particle volume might become too big to consider the instantaneous quantities associated to the state vector and the mean carrier flow uniform within it. Moreover, the impact of the added background mass on the particle instantaneous velocity and trajectory is not straightforward and would require a specific modelling.

One may prefer an interpretation where the particle mass remains constant so there is no impact on the particle dynamics. In this case, we also consider a dummy volume $\delta\widetilde{\omega}$ to take into account micro-mixing. The latter represents the volume over which the particle may have exchanged mass by micro-mixing processes assuming all the pollutant mass would have remained in the close vicinity of the simulated particle as schematised in Figure 4.1). This quantity will be used only to estimate concentration variance. It is then possible to introduce for each particle the corresponding concentration $\widetilde{C} = \frac{\delta m^P}{\delta\widetilde{\omega}}$ which will decrease over particle trajectory by micro-mixing induced dilution.

The mean value associated to $\widetilde{C}$ can be estimated as:

$$\langle\widetilde{C}\rangle = \frac{1}{M_\Omega^T}\sum_{i^S\in\mathbb{P}_\Omega^T}\delta\widetilde{m}^{(i^S)}\widetilde{C}^{(i^S)} = \frac{1}{\Omega}\sum_{i^S\in\mathbb{P}_\Omega^T}\delta m^{P,(i^S)} = \langle C\rangle_\Omega, \tag{4.11}$$

with $\delta\widetilde{m} = \rho\delta\widetilde{\omega}$, the mass of fluid within the dummy volume $\delta\widetilde{\omega}$.

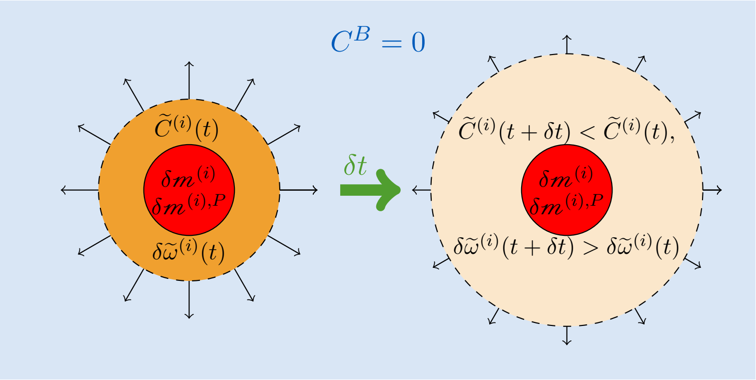

Figure 4.1: Scheme representing the leading idea of the volumetric particle approach proposed by Cassiani [2013]. The red circles represent the i^{th} simulated particle with constant masses $\delta m^{(i)}$ and $\delta m^{(i),P}$. The encompassing orange ones represent the dummy volume $\delta\widetilde{\omega}^{(i)}$ interacting by micro-mixing.

The corresponding second-order moment is then:

$$\langle\widetilde{c}\widetilde{c}\rangle_\Omega = \frac{1}{M_\Omega^T}\left(\sum_{i^S\in\mathbb{P}_\Omega^S}\delta\widetilde{m}^{(i^S)}\left(\widetilde{C}^{(i^S)}\right)^2\right) - \langle C\rangle^2 = \frac{1}{\Omega}\left(\sum_{i^S\in\mathbb{P}_\Omega^S}\delta m^{P,(i^S)}(\widetilde{C}^{(i^S)} - \langle C\rangle_\Omega)\right) \tag{4.12}$$

This equation is somewhat similar to Eq. (4.9), yet, the dummy volume $\delta\widetilde{\omega}$ being a variable growing by micro-mixing, $\widetilde{C}$ is smaller than C_{inj} leading to more physical results as shown later on in Figure 4.16B. Thus, one can add one of these two quantities to the state vector to consider micro-mixing effects on the second-order moments, (it is not necessary to add both as they are univocally related by the pollutant mass associated to the particle which remains constant). Considering a state vector $\mathcal{Z} = (\underline{\boldsymbol{X}}, \underline{\boldsymbol{U}}, \widetilde{C})$ it is then possible to use an IEM model for the concentration based on the dummy volume $\delta\widetilde{\omega}$:

$$\mathrm{d}\widetilde{C} = \frac{\widetilde{C} - \langle C \rangle}{\tau_C}. \tag{4.13}$$

Considering volumetric particle approach, it is important to ensure that the sum of the fictitious mass $\delta\widetilde{m}$ of the particles in a domain Ω shall be upper bounded by the total mass of fluid in this domain.

$$\frac{1}{M_\Omega^T} \sum_{i \in \mathbb{P}_\Omega^T} \delta\widetilde{m}^{(i)} < 1 \tag{4.14}$$

In practice nothing ensures that this constraint is respected. It is necessary to clip the particle $\widetilde{C}$ so the sum of fictitious mass $\delta\widetilde{m}$ in a volume Ω remains smaller than the overall mass M_Ω^T within this volume . Furthermore, the assumption stating that the micro-mixing occurs only in a unit of volume encompassing the simulated particle and following it in its trajectory remains a crude assumption. The results obtained with this choice of modelling will differ from the results where micro-mixing would be taken into account explicitly by transporting background particles. Indeed, in the latter situation, the pollutant mass being distributed by micro-mixing between particles issued from the source and the background ones, it can diverge from the trajectory of the source issued particles.

Remark 4.1.1. Note that the statistics were derived in the general case of mass weighted statistics. It is straightforward to see that such statistics are consistent with Favre averaging. Little attention has been given to the estimation of mean density of the flow $\langle \rho \rangle$ as we consider in this chapter a flow in which it is assumed constant. In general, transporting fluid particles or inertial ones in a sufficiently dilute regime, one may simply use the value $\overline{\rho}$ furnished by the FV solver without specific treatment. Furthermore, for the simulation presented in this work, all the particles are statistically equivalent. Therefore, they all represent the same unit of fluid mass δm with the same initial concentration C_{inj}, thus also the same unit of pollutant mass δm^P. In this situation, one can simply replace the mass weighted averages by ensemble averages on the number of particles as presented in Eq. (4.8).

4.2 Dispersion near Ground in an Unobstructed Channel Flow

Contents

The first test case considered is a statistically stationary turbulent linear emission of pollutant in an unobstructed 1 m high channel flow based on the work of Gamel [2015]. A 1 cm large pollutant injection is located at the ground in an almost fully developed channel flow as schematised in Figure 4.2 with the boundary conditions in purple. Experimentally the pollutant used is the ethane which can be considered a good passive tracer as its density is the same as the air. Moreover, it does not react with air and does not deposit. Furthermore, the 600 $\mathrm{L\,h^{-1}}$ flow rate at injection Q_{inj}/ρ is sufficiently small to prevent any perturbation of the overall flow. Indeed, given the linear source dimension, the injection velocity induced is around 0.0238 $\mathrm{m\,s^{-1}}$. The inlet is located at 1 m upstream the pollutant injection and the injected profiles are based on interpolation of the first experimental data available. The lower boundary condition is a rough wall whose roughness height z_0 will be further discussed in Section 4.2.2.1. Experimentally, square wooden wands whose size are $l_{rough} \times l_{rough} \times L_Y$ with l_{rough} 15 mm are placed every 45 mm from one to another to create such rough walls. Due to these roughness elements, present only on the lower part of the channel, the flow is not symmetric in the vertical direction. The flow over the whole channel height is then simulated with a smooth wall on the upper part. As a linear point source dispersion is presented, one may assume that the flow is periodic in the spanwise direction and consider only a 2-D flow. Experimentally, this assumption may be challenge due to the finite size of the channel flow in the spanwise direction which equals to $L_y = 0.7$ m and will be further discussed in Section 4.2.1.1. It has however been asserted that, around the half-plane cutting the channel flow in the spanwise direction, the streamwise velocity and Reynolds tensor gradients in this direction are relatively small. So, such a 2-D simulations are coherent if we compare simulation results to experimental data taken on this mid-channel plane.

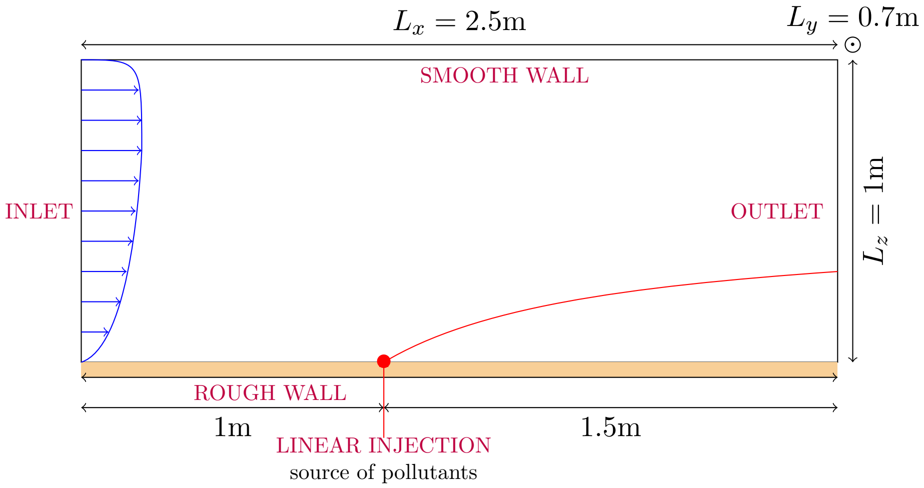

Figure 4.2: Description of the domain studied in the case of linear source dispersion in an unobstructed channel flow.

4.2.1 Analysis and Discussion about the Experimental Setup and Data

4.2.1.1 Discussion about Potential 3-D Effects

Considering the aspect ratio of the channel flow considered, it is likely that secondary flows orthogonal to the mean flow do exist (see e.g. Melling and Whitelaw [1976], Akihiro Tominaga and Nakagawa [1989], Demuren and Rodi [1984]). Some signals may be in line with this assumption such as the presence of non-negligible vertical mean velocities and an overestimation of the overall mean scalar flux respectively discussed in Paragraph 4.2.1.1.1 and in Paragraph 4.2.1.1.2.

4.2.1.1.1 Discussion about Spurious Vertical Mean Flows

In the experimental setup, one can note the presence of a quite surprising downward vertical mean velocity in Figure 4.3. In this figure, the mean normal velocity is adimensionised by the turbulent scale of normal velocity $\sqrt{\overline{ww}}$ to see the potential relative effects of the induced advection compared to the normal dispersion. The red arrow magnitude equals to 1, thus this spurious mean velocity evolves from almost zero near wall to a value similar to the normal turbulent velocity scale $\sqrt{\overline{ww}}$.

For fully developed 2-D channel flows, the normal velocity should be null to conserve the mass continuity. Furthermore, in the case of a developing 2-D channel flow, it is true that a mean normal velocity may appear near wall. Yet, the expected direction would be upward to compensate the slowing down of velocity at the ground and to maintain the mass continuity. The experimental results although potentially coherent at the ground are not in the bulk. If this spurious vertical mean velocity reflects physical effects and not a measurement error, it might result in a non-negligible effect on the pollutant dispersion pushing the pollutant back to the wall.

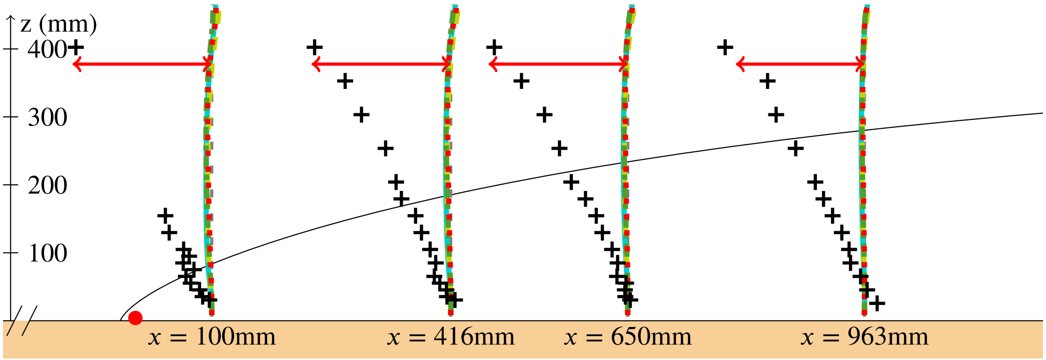

Figure 4.3: Mean normal velocity adimensionised by the standard deviation of normal velocity downstream the pollutant source for different turbulence model. The results using four turbulent models: $k-\epsilon$ (⋯⋯); SSG (——); Rotta (-·-·) ; LRR-IP (— —) are compared to Gamel [2015] experimental data. The red arrow represents of magnitude of 1. The plume shape presented is estimated based on experimental data.

Let us first ask ourselves if this error is not an experimental error due to a misalignment between the hot wire anemometer directions and the flow directions. First, let us note that this error is not randomly distributed as one may assume for such a misalignment error. Yet, it is possible that the experimental setup induces a systematic misalignment between the flow and measured direction e.g., in the case where the arm holding the anemometer is not perfectly vertical. In this case we would then have:

$$\overline{U}^{measured} = \overline{U}\cos\theta + \overline{W}\sin\theta, \tag{4.15a}$$

$$\overline{W}^{measured} = \overline{W}\cos\theta - \overline{U}\sin\theta, \tag{4.15b}$$

with $\overline{U}^{measured}$ and $\overline{W}^{measured}$ the measured velocities rotated from the mean velocity by an angle θ. A constant value for this angle may testimony for a systematic misalignment of the hot wire anemometer. Assuming $\overline{W} \ll \overline{U}$, one may attest this assumption by plotting $-\frac{\overline{W}^{measured}}{\overline{U}^{measured}} \simeq \tan\theta$ as done in Figure 4.4. In this figure, one may see that the value of θ increases in a similar manner on all plots with the altitude from 0° to around 2.3°. This tends to give credit to the interpretation stating that this mean downward velocity measured is triggered by a physical flow property. The latter could be caused by the presence of secondary flow structures in the direction orthogonal to the mean flow. Such structures are induced by turbulent effects resulting from the relatively close presence of the wall in the spanwise direction (at a distance $0.5L_y = 0.35L_z = 0.35$ m). In this case, such structures which are not taken into account in these 2-D simulations may have an explicit effect on the pollutant dispersion. Indeed, locally near the median plane considered, the resulting downward flow would oppose the normal dispersion.

4.2.1.1.2 Discussion concerning the Total Scalar Fluxes

A second element in line with the potential presence of 3-D effects is the value of the total mean scalar flux integrated over the height of the channel flow. The latter is based on the value measured at the centre of the channel flow. In Figure 4.5, an estimation of the total mean flux integrated over the whole height scaled by the mean surface flux $\langle UC\rangle_*^{tot} = L_y/(Q^{inj})\int_0^{L_z}\langle UC\rangle\mathrm{d}z$ at different distance downstream to the source is presented. In the purpose of accessing this value, an assumption has been made to estimate the mean flux below the first data available. It has first been considered that the concentration remains uniform in this region, moreover a linear decrease has been considered for the mean velocity and horizontal

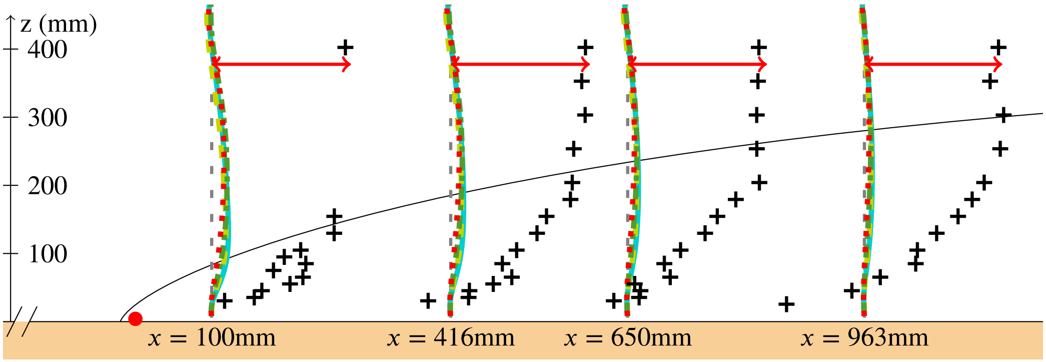

Figure 4.4: Esimation of $\tan\theta$ downstream the pollutant source for different turbulence model. The results using four turbulent models: $k-\epsilon$ (····); SSG (▬); Rotta (-·-·) ; LRR-IP (- -) are compared to Gamel [2015] experimental data. The red arrow represents of magnitude of 0.04 corresponding to an angle of around 2.3°. The plume shape presented is estimated based on experimental data.

scalar fluxes. Let us note that the presence of roughness elements represented by periodic wands may induce a deviation from this assumption. Indeed no flux might traverse them when they are present and recirculation zone might exist in between. For this reason, both the total mean fluxes with this estimated mean flux below first data and without it are plotted. As expected, the flow below the first available data has a greater impact in the vicinity of the source. Considering this estimation of the fluxes below the first data available, it is clear that the overall fluxes in the centre of the domain are overestimated compared to the 2-D periodic situation. Such an excess of pollutant might be caused by a poor injection of pollutant at the source but also by turbulent induced secondary flows. In the plane orthogonal to the mean flow direction, such secondary flows might contribute to transport pollutant from the slow near wall region (lateral ones) towards the centre of the domain. For this reason, it is considered for the rest of the section that the mean concentration, turbulent scalar fluxes, and scalar deviation should be re-scaled by the local value of $\langle UC \rangle_*^{tot}$ to be coherent with the 2-D simulations considered. A further study with 3-D simulations should be carried out to assert the basis of this assumption.

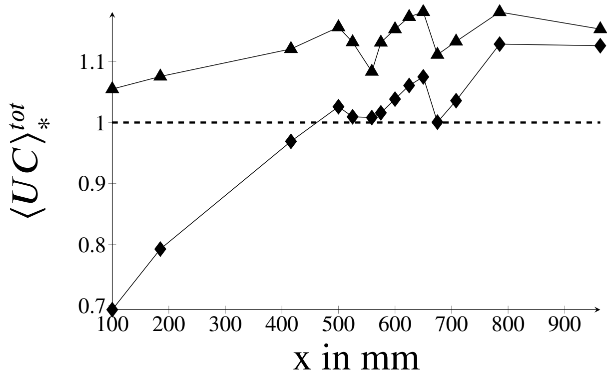

Figure 4.5: Estimation of the adimensionised total scalar flux integrated over the height from Gamel [2015] data in an unobstructed channel flow. A plot with an estimation of the scalar flux below first available data (◆—◆) is compared to the results without this extrapolated flux (▲—▲) and to the expected flux (- - -).

Remark 4.2.1. Let us note that the transport by turbulent scalar fluxes in the streamwise direction opposes the transport by the mean velocity and is not negligible especially near the source as shown in Figure 4.6. In this figure, the ratio between the fluxes transported by turbulent fluctuations integrated over the height $\langle uc\rangle_*^{tot} = L_y/(Q^{inj}) \int_0^{L_z} \langle uc\rangle \mathrm{d}z$ and the total scalar fluxes $\langle UC\rangle_*^{tot}$ is presented. The transport by turbulent fluctuation reaches in norm from 10% to 30% of the total transport depending on the distance to the source. As we move further away from the source, the mean concentration horizontal gradient tends to plummet and so does the streamwise turbulent transport.

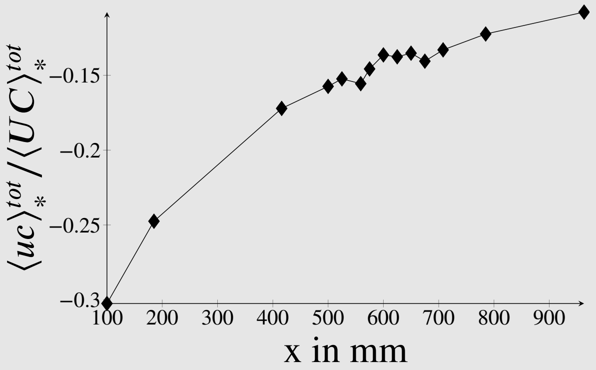

Figure 4.6: Estimation of the scalar flux transported by turbulent fluctuations integrated over the height and adimensionised by the total scalar flux integrated over the height from Gamel [2015] data in an unobstructed channel flow.

4.2.1.2 Estimation of the Friction Velocity and the Roughness Height

In the generic case, developed rough channel flows are fully characterised by the knowledge of three quantities: the dimensions of the channel, which are known, the friction velocity u_* resulting from the pressure gradient imposed by the pump and the roughness height z_0 modelling the influence of roughness elements on the flow.

In our case, where the carrier flow inlet is imposed through interpolated experimental results, only the knowledge of this second parameter is necessary. Yet, the values of both the friction velocity and the roughness height should be extracted in a coherent manner from the experimental mean velocity and shear stress profiles. Assuming that the channel flow is almost developed, the latter should remain constant in the streamwise direction, so we can use a spatial average over all the experimental profiles to obtain our reference profiles shown in Figure 4.7. Based on these profiles, different assumptions may be made to estimate u_* and z_0. Three assumptions will be considered:

(i) First, as proposed by Gamel [2015], one can determine the friction velocity from the shear stress profile assuming a constant value near wall as:

$$u_* = \sqrt{\overline{uw}}(z^{log}) \simeq 0.37 \text{ m s}^{-1}. \tag{4.16}$$

with z^{log} an altitude in the near-logarithmic zone going approximately from $0.1\delta_{U_{max}}$ up to $0.3\delta_{U_{max}}$, and $\delta_{U_{max}} \simeq 0.55$ m the surface layer height defined as the height where the velocity equals to 99% of its maximal value. Note that this value, highlighted in Figure 4.7B by the green dash-dotted line, is bigger than the value proposed by Gamel. A main drawback of this method to estimate the friction velocity is that it seems to

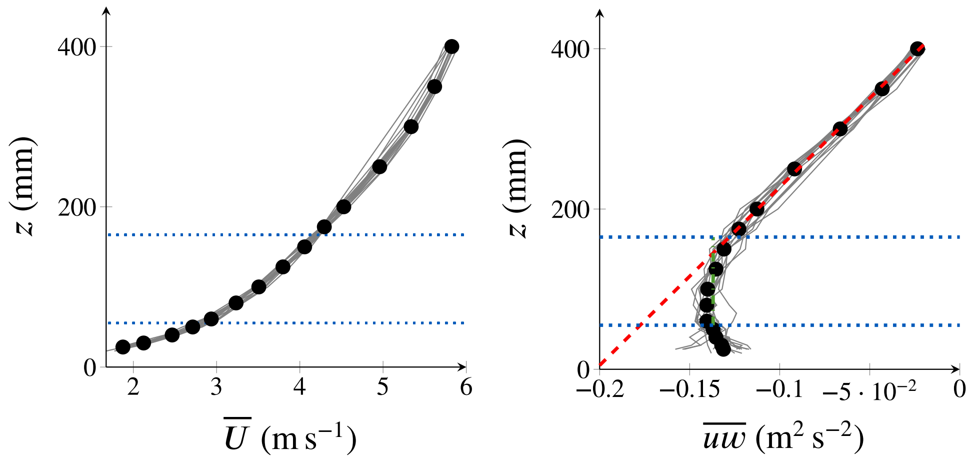

(A) Streamwise mean velocity $\overline{U}$.

(B) Turbulent shear stress $\overline{uw}$.

Figure 4.7: Gamel [2015] experimental data used to estimate the mean friction velocity u_* and roughness height z_0. The grey solid lines (——) correspond to the different experimental profiles and the dots (●) represent the corresponding mean value after average on all profiles. In Figure 4.7B, the green dash-dotted line (-·-·) and the red dashed lines (- -) represents respectively the estimation of the shear stress under constant assumption (i) and linear assumption (ii). The blue dotted lines (······) represent the limit in which the shear stress is considered almost uniform and the velocity nearly logarithmic.

understate its value. Indeed, according to Gamel, with this value we get $\frac{k}{u_*^2}\frac{1}{\sqrt{\mathcal{C}_\mu}} \simeq 4$, thus $\mathcal{C}_\mu \simeq 0.063$. This value is lower than the expected value of 0.09 proposed by Launder and Spalding [1974] (see Table 1.2) and which was also experimentally fitted on channel flows. One may wonder if this is caused by the experimental setups used, notably the hot wire anemometer, which might have difficulty to measure the vertical velocity fluctuations in the vicinity of the wall.

In any case, for a given friction velocity, it is possible to determine the roughness height yielding to the best description of the experimental mean velocity profile. Indeed, assuming that the mean velocity profile should be close to a logarithmic profile in the zone close to the wall but sufficiently far from the roughness elements to avoid induced local effects (i.e. in the zone $0.1\delta_{U_{max}} < z < 0.3\delta_{U_{max}}$). In such a zone, based on analytical profile assumed for rough logarithmic flows presented in Eq. (3.2b), the roughness height can be estimated as:

$$z_0 = \frac{z}{\exp\frac{\overline{U(z)}}{u_*} - 1}. \tag{4.17}$$

As shown in Figure 4.8, based on the friction velocity presented in Eq. (4.16), a first value of the roughness height $z_0 \simeq 1.95$ mm can then be estimated.

(ii) The second hypothesis consists in assuming a linear interpolation of the shear stress based on the slope above $z = 0.3\delta_{U_{max}}$. Indeed, although it is expected for the turbulent shear stress to decrease near the wall, theoretically the total shear stress profile is linear in channel flows because of viscous effects. Doing so, we retrieve $u_* \simeq 0.45$ m s^{-1} (see red dashed line in Figure 4.7B). With this new value of u_*, using Eq. (4.17) we determine that we have $z_0 \simeq 3.92$ mm as shown in Figure 4.8. Considering this value of u_*, the TKE is underproduced as we have $\mathcal{C}_\mu = \frac{u_*^4}{k^2} \simeq 0.13$.

(iii) The third assumption is a brute force method based uniquely on the mean velocity profile. It consists in testing all the (u_*, z_0) combinations and in keeping only the one minimising the mean square-root error between the corresponding logarithmic profile and the experimental values in the range of altitude between $\delta_{U_{max}}$ and $3\delta_{U_{max}}$. Using this method, we find: $u_* \simeq 0.55$ m s^{-1} and $z_0 \simeq 7.32$ mm.

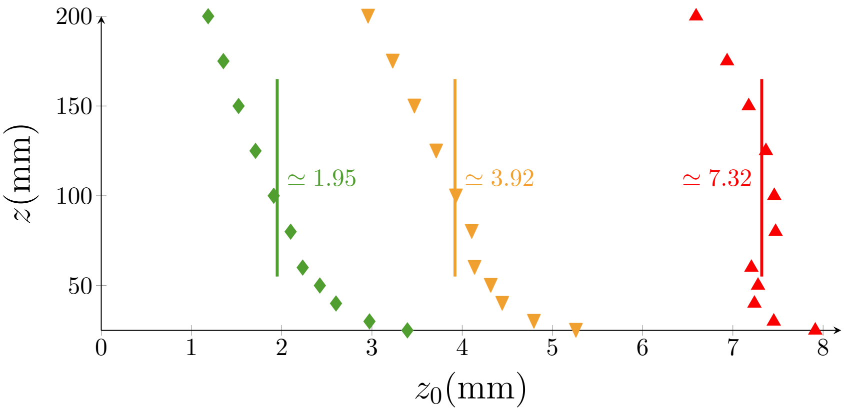

Figure 4.8: Estimation of the roughness height using Eq. (4.17), for different values of friction velocity: (◆) $u_* = 0.37$ m s^{-1} using constant shear assumption (i); (▼) $u_* = 0.45$ m s^{-1} using linear shear assumption (ii) and (▲) $u_* = 0.55$ m s^{-1} using the assumption (iii) based only on the mean velocity profiles.

4.2.2 Results using a Moment Approach

First the mean carrier flow dynamics is studied using the Eulerian moment approach. The latter dynamics is a key element in the dispersion of pollutants both considering a Lagrangian and Eulerian point of view. The dispersion results obtained with Eulerian approaches will then be discussed to have a comparison point with the Lagrangian results obtained. After a temporal and spatial convergence study on the dynamics, it has been chosen to consider a time step of 5.10^{-4}s; a spatial discretisation of 5 mm near source in the streamwise direction and 5 mm in the normal direction with an expansion factor of 1.05 as shown in Figure 4.9.

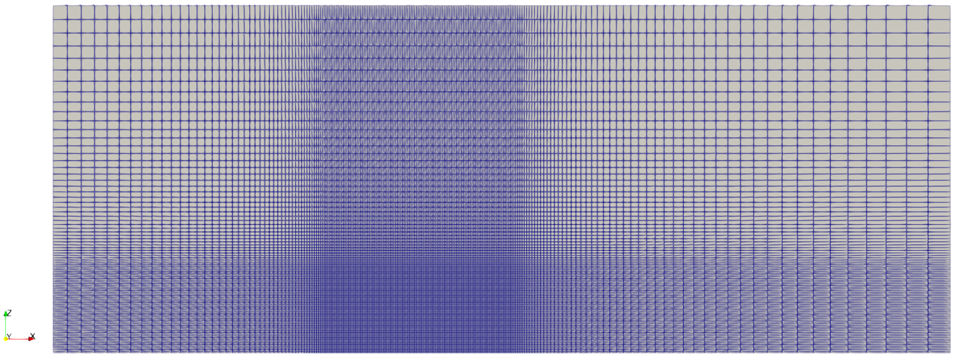

Figure 4.9: Reference mesh used to treat dispersion of pollutants in an unobstructed channel flow considering a rough wall-modelled description.

4.2.2.1 Treatment of the Wall Roughness

In an effort to characterise the carrier flow dynamics, we will first discuss the roughness treatment. We will simulate the flow using a Rotta model, with the three different roughness heights proposed in Section 4.2.1.2. In order to have a further comparison element, we will also simulate explicitly the roughness elements removing the corresponding cells from the mesh and considering a smooth wall as presented in Figure 4.10.

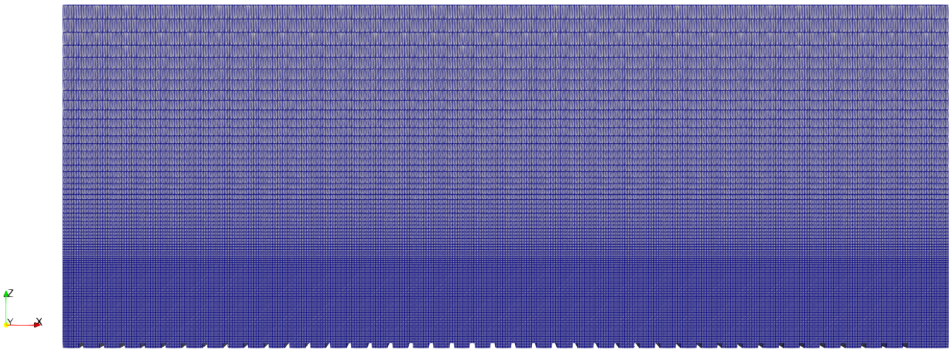

Figure 4.10: Mesh used to treat dispersion of pollutants in an unobstructed channel flow with an explicit description of the roughness elements.

The results for each of the roughness treatments considered are plotted in Figure 4.11. First, let us note that above 2 or 3 l_{rough} i.e. 30 to 45 mm, the mean velocity profile obtained using an explicit description of the roughness elements is relatively close to the one obtained with modelled roughness. In the former case, below this zone, the flow varies much in the streamwise position, and depends explicitly on the relative location of the profile to the surrounding wands. Furthermore, looking at the shear stress, we can note that the flat behaviour experimentally obtained is well retrieved when considering explicitly the roughness elements. This highlights that the flat shape experimentally obtained is not the result of a measurement error near wall. This shape might be caused by the creation of periodic structures such as recirculation zones in between successive wooden wands. The near ground behaviour is less accurately described using a roughness modelling which cannot take into account such periodic recirculation zones (see e.g. the discussion about k-type roughness and d-type roughness in Kadivar et al. [2021]). Looking at the kinetic energy distribution, using the explicit treatment of the roughness elements, the kinetic energy in the streamwise direction is underestimated whereas it is overestimated in the normal direction. This is due to the isotropic modelling of the pressure-strain correlation considered providing too much energy in the direction orthogonal to the flow and too little in the flow direction.

Let us now compare the results obtained with modelled roughness. Focusing on the mean velocity Figure 4.11A, we can see that the mean velocity near wall decreases with the increasing roughness height value. This results from the fact that the roughness tends to promote the transfer of energy from the mean flow towards the turbulent one. The best results on the mean velocity are obtained with the highest roughness $z_0 = 7.32$ mm. Such a behaviour is expected as this roughness height was fitted solely to retrieve a proper evolution of this mean quantity based through the assumption (iii).

However, the description of the turbulent behaviour characterised by the Reynolds tensor, presented from Figure 4.11B to Figure 4.11D, is less straightforward. First it is clear that the higher roughness corresponds to a greater level of TKE. Looking at the TKE in the streamwise direction in Figure 4.11C, better results are retrieved with the greater roughness height. Yet,

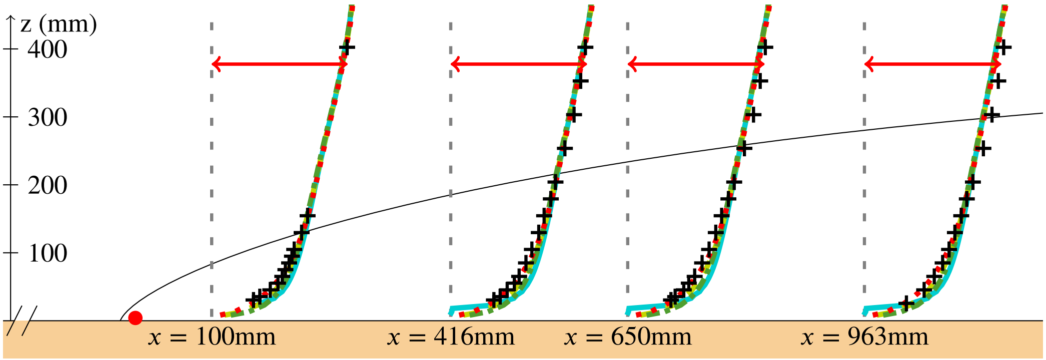

(A) Streamwise mean velocity $\overline{U}$. The red arrow represents of a magnitude of 5.8 $\mathrm{m\,s^{-1}}$.

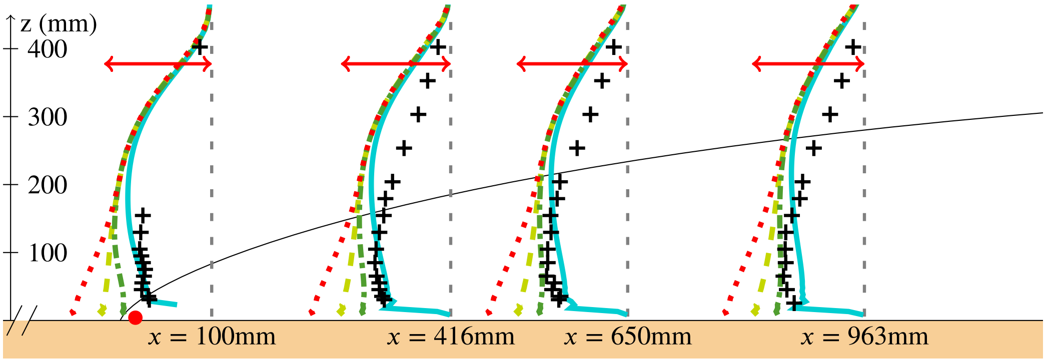

(B) Shear stress $\overline{uw}$. The red arrow represents of a magnitude of -0.3 $\mathrm{m^2\,s^{-2}}$.

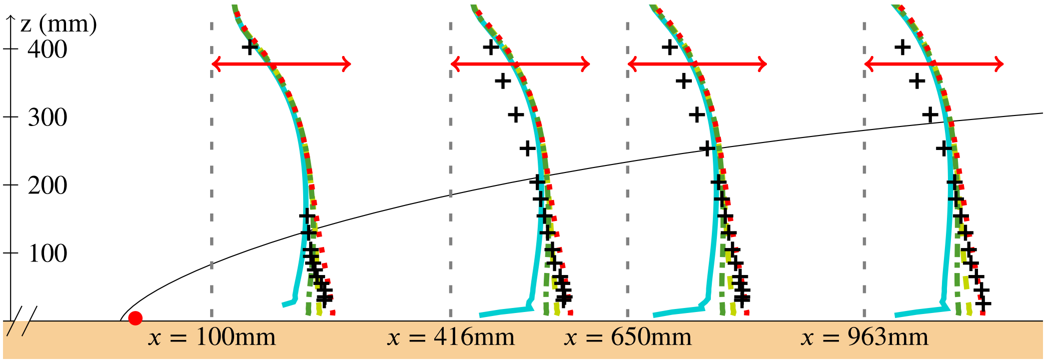

(C) Streamwise velocity standard deviation $\sqrt{\overline{uu}}$. The red arrow represents of a magnitude of 1 $\mathrm{m\,s^{-1}}$.

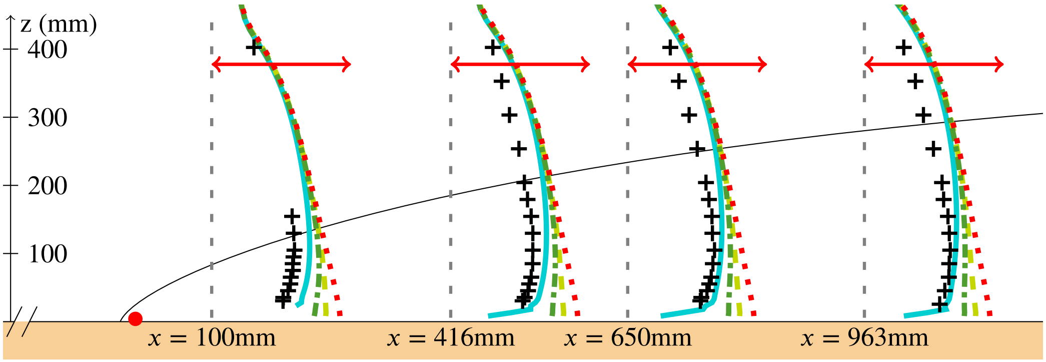

(D) Normal velocity standard deviation $\sqrt{\overline{ww}}$. The red arrow represents of a magnitude of 0.75 $\mathrm{m\,s^{-1}}$.

Figure 4.11: Profiles of the RANS modelled dynamic properties downstream the pollutant source for different treatments of the wall roughness. Experimental data of Gamel [2015] (+) are compared to four simulations: a first one considering an explicit treatment of the roughness elements with smooth walls (——) and three modelled roughness with different roughness height respectively $z_0 = 1.95$ mm (-·-·-); $z_0 = 3.92$ mm (– –) and $z_0 = 7.32$ mm (····). On each plot, the red arrow represents the same physical magnitude. The plume shape plotted is estimated based on experimental mean concentration profiles.

with this value both the shear stress and the normal component of the Reynolds tensor are overestimated, and better results are obtained with smaller roughness heights as we can see respectively in Figure 4.11B and Figure 4.11D. Let us note that, physically, the fluctuations of velocity in the normal direction play a preponderant role in the turbulent dispersion of pollutant as we have $\mathrm{div}(\overline{\boldsymbol{uc}}) \simeq \frac{\partial \overline{wc}}{\partial z}$. This preponderant importance of the normal component of the Reynolds tensor can be asserted considering a GGDH modelling of the normal scalar fluxes. The concentration gradient being mostly vertical, we would have $\overline{wc} \simeq \frac{3}{2} \frac{\mathcal{C}_\mu}{Sc_t} \frac{k}{\epsilon} \overline{ww} \frac{\partial \overline{C}}{\partial z}$. Furthermore, explicitly transporting the normal turbulent scalar fluxes $\overline{wc}$ with a DFM approach, we can note that $\overline{ww}$ appears in the production term of the normal scalar fluxes.

For all the roughness and simulations carried out too much energy is provided. This is probably caused by an overestimation of the energy injected at the inlet for which experimental data were not available over all the height of the domain. This excess of energy results in an overflow of TKE when selecting a high roughness height or in an overflow of kinetic energy associated to the mean flow when considering lower roughness heights. In both case this energy surplus will have an impact on the dispersion of pollutant and will induce an underestimation of its concentration. Indeed, an overestimated mean velocity will trigger an overestimation of the advection cleaning up the air too fast. Similarly, an overproduction of the TKE will prompt an overestimation of the normal turbulent transport towards high velocity zone also resulting in a too fast pollutant evacuation.

So as to have a first idea of the impact of the dynamics on the pollutant dispersion, let us simulate it using a RANS modelling. The mean concentration and its standard deviation are plotted in Figure 4.12 obtained using a SGDH model. This model providing an isotropic turbulent viscosity is physically less rich than GGDH or DFM approaches but has the advantage of numerical robustness and is also applicable using EVM methods to model turbulence as proposed hereafter. Furthermore, in this chapter the concentration will be normalised by the injection rate such that the mean concentration and its standard deviation are given in atmospheric transfer coefficient (ATC) whose dimension is $\mathrm{m}^{-3}\mathrm{s}$.

Looking at Figure 4.12, all fluctuations of concentration are overestimated compared to the experimental data. Focusing on the mean concentration in Figure 4.12A, better results are still obtained with an explicit treatment of the roughness elements. In this case, in absence of roughness element, in the first few cells near wall the concentration profile is almost uniform. Such a shape might characterise the presence of recirculating zones trapping the pollutant and mixing it in their midst. Yet, in this case, keeping in mind the assumption made during the rescaling, this effect yields to an increase of pollutant concentration near wall which seems to be stronger than experimentally encountered. The specific structures associated to this topography may induce a non-negligible effect on the pollutant dispersion. Modelling these roughness elements, smoother profiles are obtained. In this case, the shape of the plume flattens with the increasing roughness height. This is due to two combined effects. First, as the roughness height increases, the mean velocity decreases and so does the advection. This provides more time for the plume to develop itself in the normal direction. Secondly, in neutral surface boundary flows, close to the situation encountered here, the turbulent viscosity grows proportionally to $u_* \kappa (z + z_0)$ with u_* also growing with the roughness height as displayed in Section 4.2.1.2. With the rescaling hypothesis considered, the mean concentration profiles seem then to be better captured considering the lowest roughness height associated to a constant shear assumption (i). This case also corresponds to the situation where the dispersion plays a lesser role compared to the advection as more energy is included in the mean velocity and less in the TKE. Looking at the concentration standard deviation in Figure 4.12B the explicit treatment of the roughness element results in a bigger overestimation of this quantity whereas the roughness height seems to have little effect.

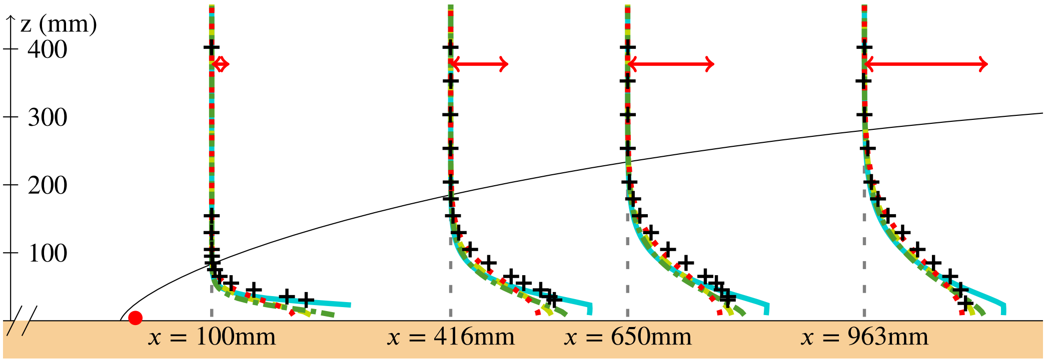

(A) Mean concentration $\frac{\overline{C}}{Q_{inj}}$. The red arrow represents an ATC magnitude of 0.6 $\mathrm{m}^{-3}\,\mathrm{s}$.

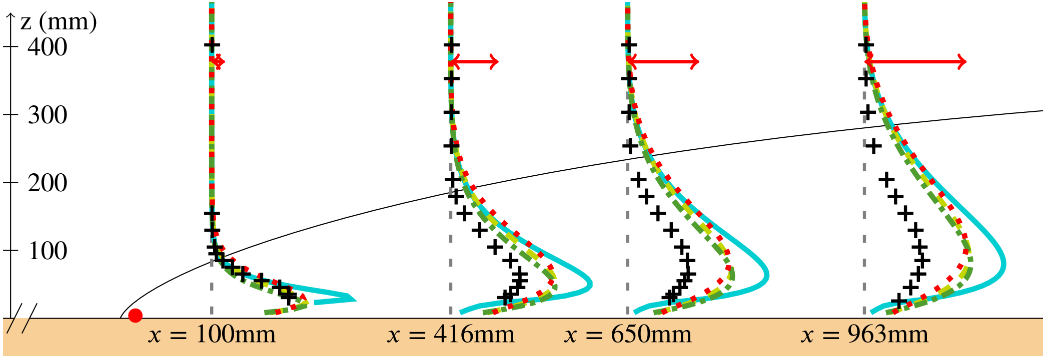

(B) Concentration standard deviation $\frac{\sqrt{\overline{cc}}}{Q_{inj}}$. The red arrow represents an ATC magnitude of 0.45 $\mathrm{m}^{-3}\,\mathrm{s}$.

Figure 4.12: Profiles characterising the RANS modelled pollutant dispersion downstream the pollutant source for different treatments of the wall roughness. Experimental data of Gamel [2015] (+) are compared to four simulations: a first one considering an explicit treatment of the roughness elements with smooth walls (—) and three modelled roughness with different roughness height respectively $z_0 = 1.95$ mm (-·-); $z_0 = 3.92$ mm (– –) and $z_0 = 7.32$ mm (····). On each plot, the red arrow represents the same physical magnitude. The plume shape plotted is estimated based on experimental mean concentration profiles.

4.2.2.2 Comparison with Different Models for the Turbulence

One may wonder, if the errors noticed in the previous simulations are due to the choice of the turbulent model. In Figure 4.13, an EVM model: the $k - \epsilon$ model, and 3 DRSM models: the Rotta, the LRR-IP, and the SSG models are considered. These different models have been briefly presented in Section 1.3.2. For the pollutant dispersion, a SGDH model is still considered with a roughness height of 1.95 mm.

As we can see in Figure 4.14A, the different models being often fitted on channel flow there is little difference on the mean velocity between the different results. Using the $k - \epsilon$ model, the Reynolds tensor is post-treated based on the Boussinesq assumption presented Eq. (1.162). As shown in Figure 4.14B and in Figure 4.14C, using this model, the isotropic distribution of energy in the different directions is not in accord with the physics at stake. Yet, the overall level TKE seems to be similar to the one obtained with DRSM methods. It can be noted that the SSG model provides the best description of the Reynolds tensor. Indeed, using this model, the anisotropy of the pressure-strain correlation in the three spatial directions is tackled. In contrast, only the anistropy between the orthogonal and streamwise components of the pressure-strain correlation (without difference between normal and spanwise components) is taken into account considering a LRR-IP model and the redistribution is assumed isotropic with a Rotta modelling. In any case, as previously stated the overall level of TKE is overestimated.

Looking on the pollutant dispersion in Figure 4.13, one may see that these differences have little impact on the dispersion of pollutants due to the isotropic assumptions considered within the SGDH formulation. Yet slightly better results are obtained with more advanced model such as the SSG. Moreover, the SLM model being fuelled only with the pressure gradient, the TKE and the dissipation rate, the influence of the relative distribution of TKE might have little impact as a carrier flow for the Lagrangian stochastic methods.

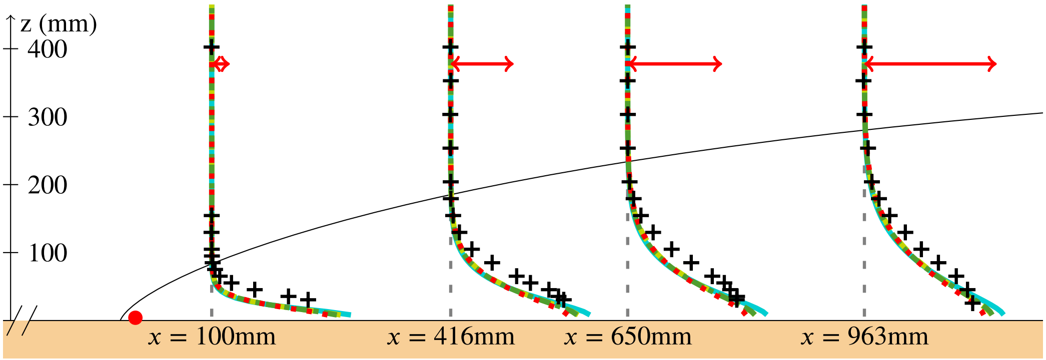

(A) Mean concentration $\frac{\overline{C}}{Q_{inj}}$. The red arrow represents an ATC magnitude of 0.6 m^{-3} s.

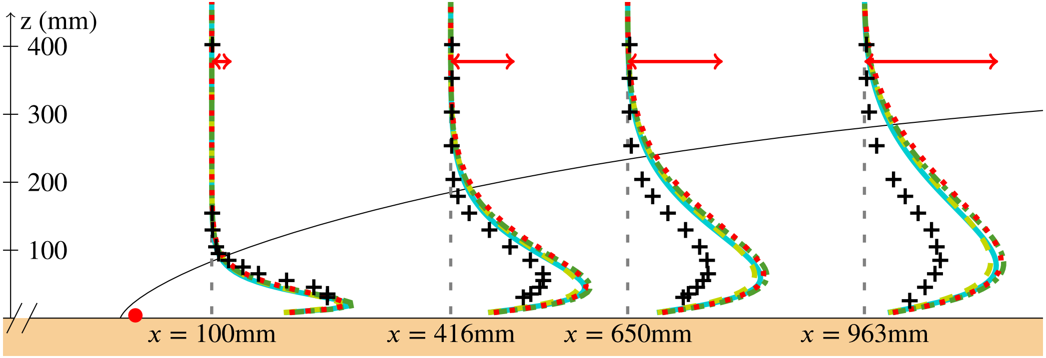

(B) Concentration standard deviation $\frac{\sqrt{\overline{cc}}}{Q_{inj}}$. The red arrow represents an ATC magnitude of 0.45 m^{-3} s.

Figure 4.13: Profiles characterising the RANS modelled pollutant dispersion downstream the pollutant source for different turbulence modelling. The results using four turbulent models: $k-\epsilon$ (....); SSG (——); Rotta (-.-.-) ; LRR-IP (– –) are compared to Gamel [2015] experimental data. On each plot, the red arrow represents the same physical magnitude. The plume shape plotted is estimated based on experimental mean concentration profiles.

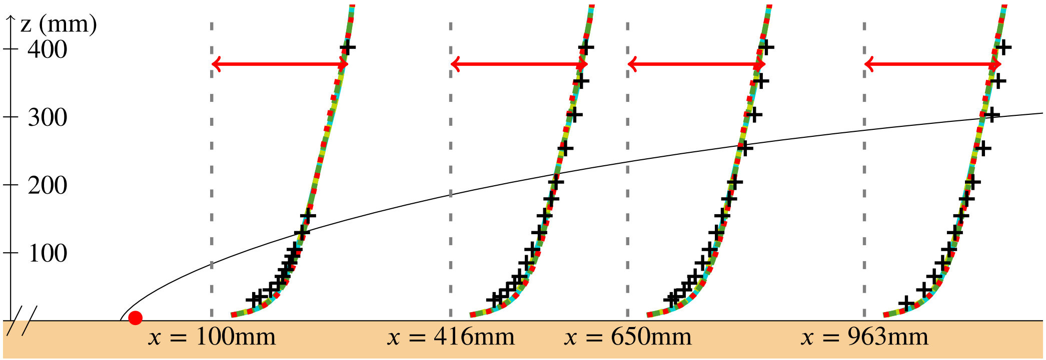

(A) Mean streamwise velocity profile $\overline{U}$. The red arrow represents of a magnitude of 5.8 $\mathrm{m\,s^{-1}}$.

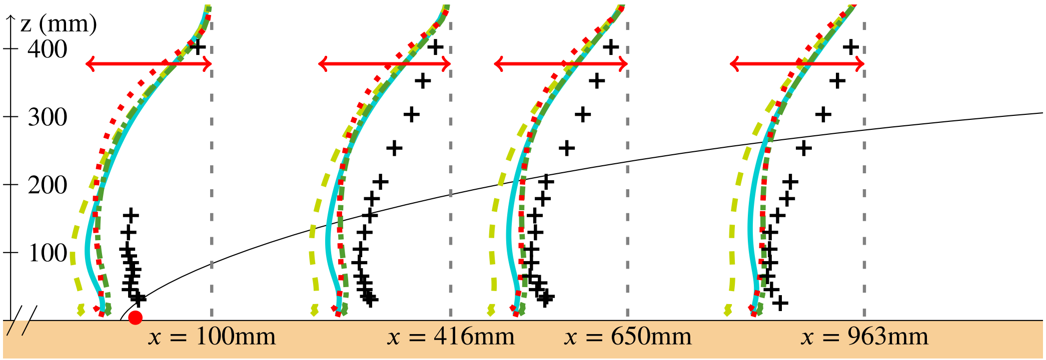

(B) Shear stress $\overline{uw}$. The red arrow represents of a magnitude of -0.2 $\mathrm{m^2\,s^{-2}}$.

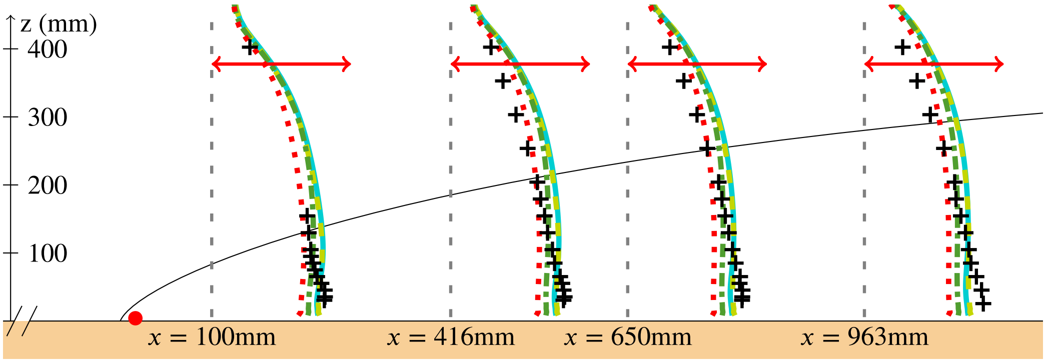

(C) Streamwise velocity standard deviation $\sqrt{\overline{uu}}$.The red arrow represents of a magnitude of 1 $\mathrm{m\,s^{-1}}$.

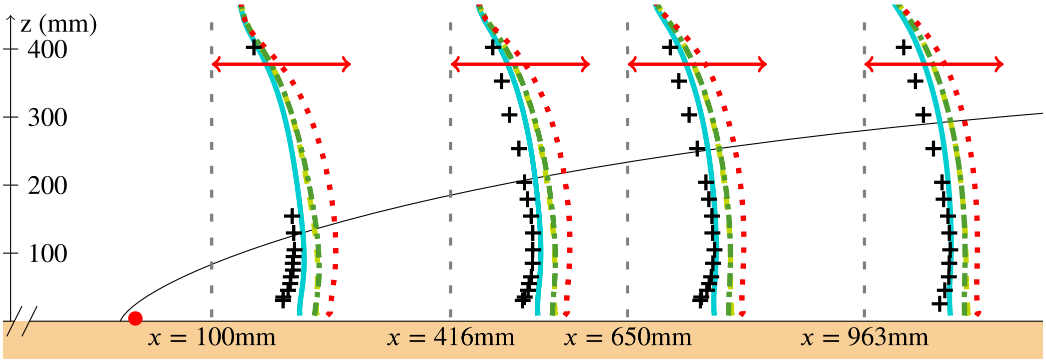

(D) Normal velocity standard deviation $\sqrt{\overline{ww}}$. The red arrow represents of a magnitude of 0.75 $\mathrm{m\,s^{-1}}$.

Figure 4.14: Dynamical profiles downstream the pollutant source for different turbulent models. The results using four turbulence models: $k - \epsilon$ (····); SSG (——); Rotta (-·-·) ; LRR-IP (– –) are compared to Gamel [2015] experimental data. On each plot, the red arrow represents the same physical magnitude. The plume shape presented is estimated based on experimental data.

4.2.3 Results using a Hybrid Moment/PDF Approach

We will now continue this dispersion study with a hybrid moment/PDF approach. Except if otherwise stated, the results presented in this section will be obtained using a piece-wise linear interpolation of mean velocity field, the an-elastic wall boundary condition studied in Chapter 3 and injecting 100000 particles per second to represent the flow issued from the source of pollutants.

4.2.3.1 Treatment of the Wall Roughness

First, let us see the influence of the wall treatment on the dispersion of pollutants. The mesh and time step are conserved unchanged compared to the RANS simulations. It is clear, looking at the mean concentration, that these simulations are too diffusive even compared to their Eulerian counterparts. Indeed, focusing on the core of the plume near wall the mean concentration in Figure 4.15A is underestimated, whereas it tends to be overestimated on the border of the plume. Furthermore, even though it provides slightly better results, the explicit treatment of the roughness element seems to play a lesser role compared to the moment simulations Section 4.2.2.1. The normal scalar flux which is the only source of scalar transport in the normal direction, although too diffuse, is relatively quite well captured near the ground as shown in Figure 4.15C. Yet, it is overestimated after its peak value. These profiles for the normal fluxes associated to the underestimation of the concentration near wall testimony for an overshoot of vertical velocity associated to the particles. This might be explained partly by two elements. On the one hand, the total level of TKE is overestimated compared to the experimental flow yielding to an excess in the overall turbulent dispersion. On the other hand, the isotropic Lagrangian timescale and production of turbulent fluctuations assumed in the SLM model also results in an overestimation of the TKE ratio in the normal direction. This issue is further discussed in Section 4.2.3.5. Yet, the impact of these issues on the Lagrangian stochastic side is surprising in comparison with the results obtained with a SGDH modelling of the dispersion. Indeed, in this case also overly turbulent mean carrier fields are provided. Moreover, the isotropic turbulent diffusion and TKE distribution considered are expected to yield to an even more diffusive situation in the normal direction. Further information on the dissipation rate empirically encountered might shed light on the reason of such a behaviour.

Furthermore, it is possible, for the Lagrangian stochastic methods, to be more sensitive to the lack of structures associated to secondary flows potentially experimentally encountered. Yet, such effects should remain weak.

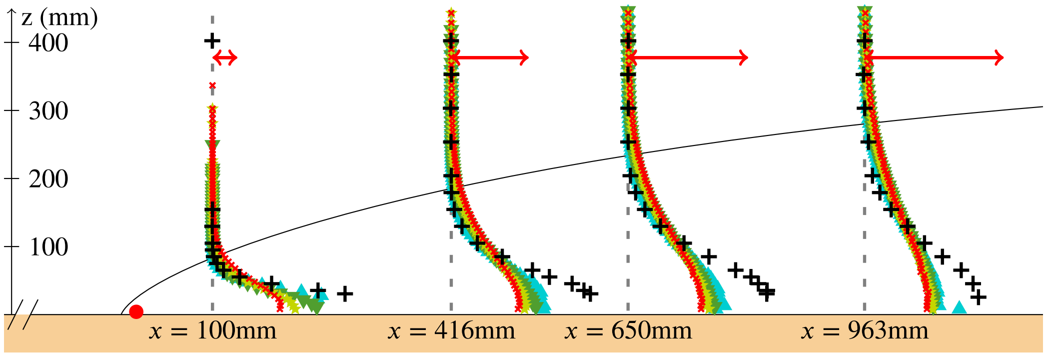

(A) Mean concentration $\frac{\langle C \rangle}{Q_{inj}}$. The red arrow represents an ATC magnitude of 0.6 m^{-3} s.

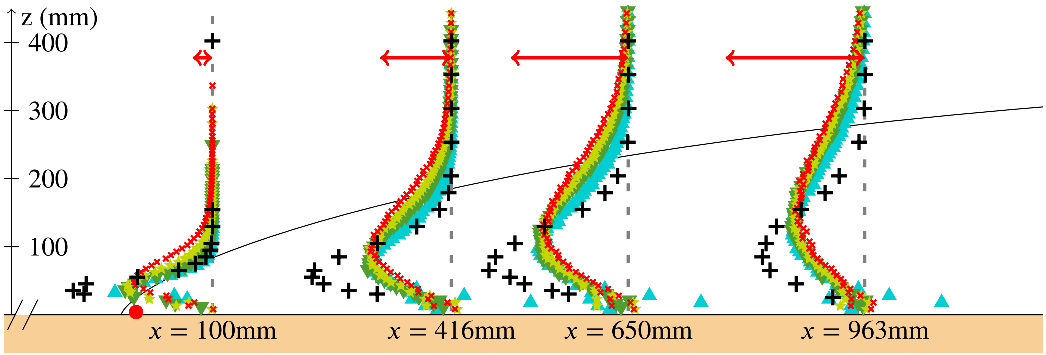

(B) Streamwise turbulent scalar fluxes $\frac{\langle uc \rangle}{Q_{inj}}$. The red arrow represents a magnitude of -0.15 m^{-2}.

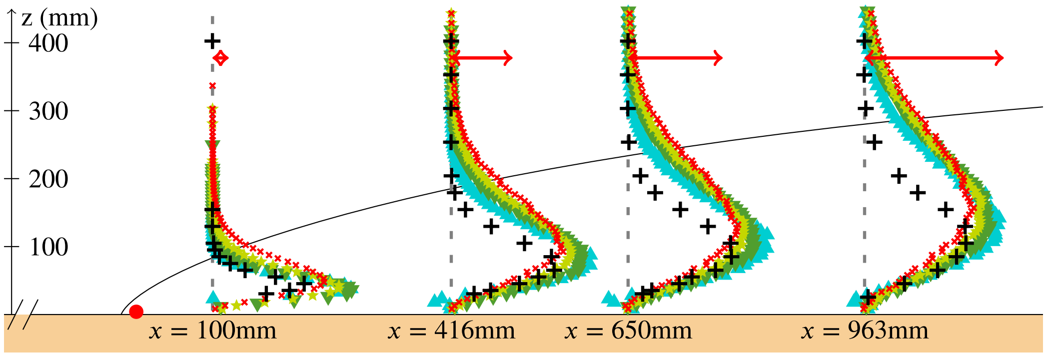

(C) Normal turbulent scalar fluxes $\frac{\langle wc \rangle}{Q_{inj}}$. The red arrow represents a magnitude of 0.06 m^{-2}.

Figure 4.15: Profiles characterising the PDF modelled pollutant dispersion downstream the pollutant source for different treatments of the wall roughness. Experimental data of Gamel [2015] (+) are compared to four simulations: a first one considering an explicit treatment of the roughness elements with smooth walls (▲) and three modelled roughness with different roughness height respectively $z_0 = 1.95$ mm (▼); $z_0 = 3.92$ mm (★) and $z_0 = 7.32$ mm (✖). On each plot, the red arrow represents the same physical magnitude. The plume shape plotted is estimated based on experimental mean concentration profiles.

4.2.3.2 Estimation of Concentration Fluctuations

Let us take a look at the fluctuations of concentrations. As we can see in Figure 4.16A, estimating it directly in absence of micro-mixing as proposed in Eq. (4.9), results in a crude overestimation. Yet, considering a volumetric particle approach proposed by Cassiani [2013] with a constant $\mathcal{C}_C = \mathcal{C}_L$, the shape of the concentration standard deviation in Figure 4.16B, remains too diffusive but the proper order of magnitude is obtained. This choice of constant was made to impose a turbulent Schmidt number of one, i.e., to enforce that the concentration diffuses in a similar manner than the momentum. Other propositions do exist in the literature, Pope [1994b] proposed a value of 1 in the generic case where all the flow is explicitly simulated. Furthermore, similarly to the temperature and as proposed by Launder [1975], Rodi [2000], we could take $\mathcal{C}_C \simeq 0.625$. These different values are tested using modelled roughness with a roughness height $z_0 = 1.95$ mm. As we can notice in Figure 4.17, the concentration fluctuations are highly dependent on the relaxation timescale considered for the micro-mixing. Indeed, both $\mathcal{C}_C = 1$ and $\mathcal{C}_C = 0.625$ induce a micro-mixing too slow which results in an overestimation of the concentration standard deviation. At the contrary, the global shape of the latter is properly captured using $\mathcal{C}_C \simeq \mathcal{C}_L = 3.125$.

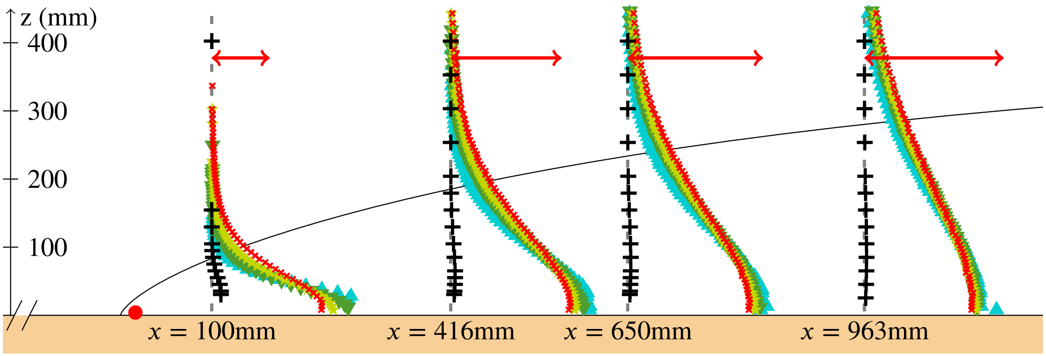

(A) Concentration standard deviation $\frac{\sqrt{\langle cc \rangle}}{Q_{inj}}$ based on the spurious estimation Eq. (4.9). The red arrow represents an ATC magnitude of 16.5 $\mathrm{m}^{-3}\,\mathrm{s}$.

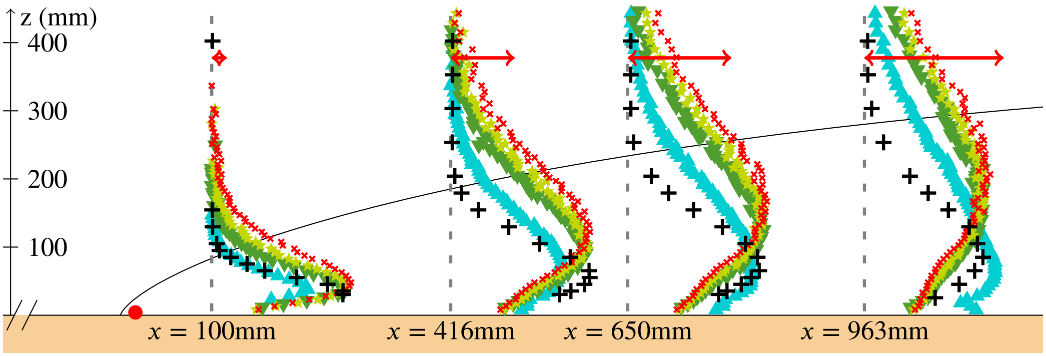

(B) Concentration standard deviation $\frac{\sqrt{\langle \widetilde{cc} \rangle}}{Q_{inj}}$ based on the volumetric particle approach estimation Eq. (4.12). The red arrow represents an ATC magnitude of 0.3 $\mathrm{m}^{-3}\,\mathrm{s}$.

Figure 4.16: Concentration standard deviation profiles downstream the pollutant source estimated with PDF model for different treatments of the wall roughness. Experimental data of Gamel [2015] (+) are compared to four simulations: a first one considering an explicit treatment of the roughness elements with smooth walls (▲) and three modelled roughness with different roughness height respectively $z_0 = 1.95$ mm (▼); $z_0 = 3.92$ mm (★) and $z_0 = 7.32$ mm (✖).

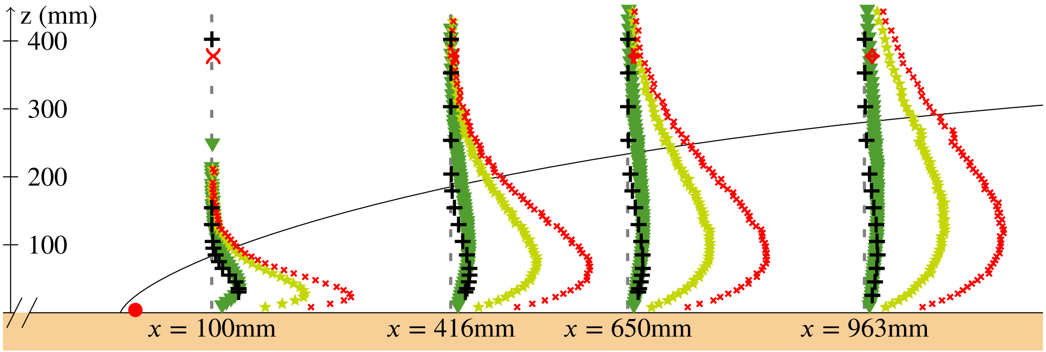

Figure 4.17: Concentration standard deviation profiles downstream the pollutant source estimated with Eq. (4.12) for different IEM constants. The experimental data of Gamel [2015] (+) are compared to Lagrangian stochastic simulations with $\mathcal{C}_C = 0.625$ (✖), $\mathcal{C}_C = 1$ (★), and $\mathcal{C}_C = \mathcal{C}_L = 3.125$ (▼). The red arrow represents an ATC magnitude $\frac{\sqrt{\langle cc \rangle}}{Q_{inj}} = 0.3$ m^{-3} s.

4.2.3.3 Influence of the Modelling selected for the Mean Carrier Flow

To measure the effects of the mean carrier flow modelling, simulations using the four models treated in Section 4.2.2.2 are presented in Figure 4.18. Due to the simplicity of the flow, which is often used to fit the model constants, most of the difference between the mean carrier fluid models relies in the anisotropy of the Reynolds tensor. Yet, as presented in Paragraph 1.3.3.2.2, the SLM solver does not explicitly take into account these elements and considers mainly the mean velocity and total TKE budget (the pressure gradient and dissipation rate are also required but no experimental data are available for these quantities). It results from this, that no matter the model considered for the mean carrier fields, little effects can be seen on the particle dispersion in Section 4.2.2.2.

Focusing on the streamwise turbulent scalar fluxes, let us however remark that, at the wall, a spurious behaviour may be noticed when using non-consistent models. The latter is due to the treatment of the wall boundary condition presented in Paragraph 1.3.3.2.4 which depends explicitly on the Reynolds tensor anisotropy. Indeed, its impact on the streamwise velocity, highlighted in Eq. (1.235), is directly proportional to the ratio between the Reynolds tensor normal component and the shear stress. An overestimation of this ratio compared to the SLM model, as encountered using a SSG or a LRR-IP model triggers an overestimated slow down. This induces an underestimation of the mean velocity and then also of the streamwise turbulent scalar flows. At the opposite, when using a $k - \epsilon$ model, the shear stress to normal Reynolds component is lower, yielding to an overestimation of the streamwise velocity and turbulent scalar fluxes.

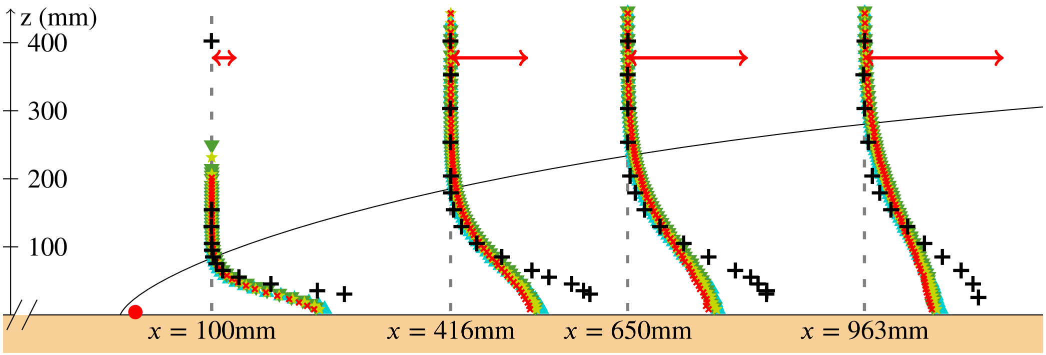

(A) Mean concentration $\frac{\langle C \rangle}{Q_{inj}}$. The red arrow represents an ATC magnitude of 0.6 $\mathrm{m}^{-3}\,\mathrm{s}$.

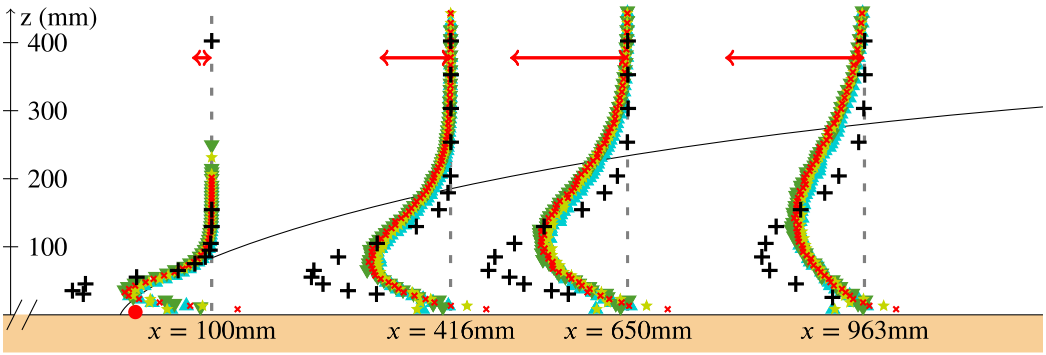

(B) Streamwise turbulent scalar fluxes $\frac{\langle uc \rangle}{Q_{inj}}$. The red arrow represents a magnitude of $-0.15\ \mathrm{m}^{-2}$.

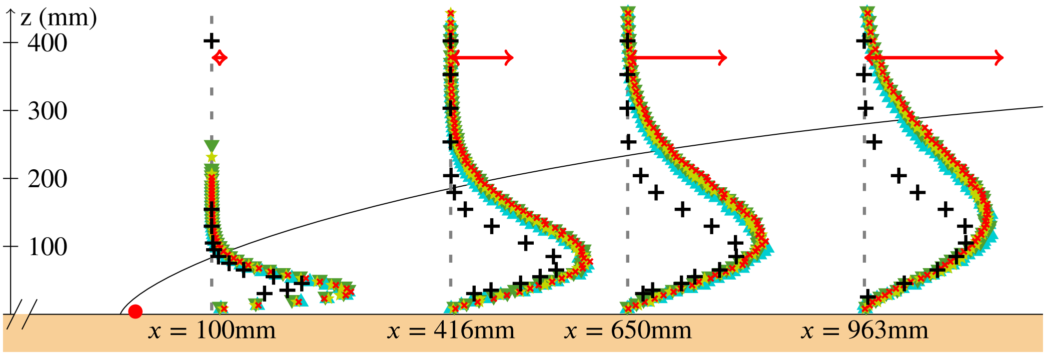

(C) Normal turbulent scalar fluxes $\frac{\langle wc \rangle}{Q_{inj}}$. The red arrow represents a magnitude 0.06 m^{-2}.

Figure 4.18: Profiles characterising the PDF modelled pollutant dispersion downstream the pollutant source. The results using four turbulent models for the carrier fields: $k-\epsilon$ (✖); SSG (▲) ; Rotta (▼); LRR-IP (★) are compared to Gamel [2015] experimental data.

4.2.3.4 Influence of the Spatial Interpolation and Wall Boundary Condition

Let us study the effects of the near wall treatment presented in Chapter 3, on the pollutant dispersion. To this end, five simulations are carried out in Figure 4.19 and in Figure 4.20 considering the same mean carrier flow obtained with a Rotta model and a roughness height $z_0 = 1.95$ mm.

- The first simulation plotted is a spurious situation, where an elastic wall boundary condition is used with a piece-wise uniform interpolation for the mean velocity field.
- In order to see the influence of the interpolation scheme, the previous simulation may be compared to this situation where an elastic rebound is also considered but with a piece-wise linear interpolation of the mean velocity field.
- To see the influence of the boundary condition, as previously, a piece-wise linear interpolation of the mean velocity field is considered with the proper an-elastic boundary condition.
- So as to better take into account the dynamics near wall and especially near injection, a logarithmic interpolation of the mean velocity field is proposed in the wall cells. In order to be coherent with the production dissipation equilibrium a piece-wise linear interpolation of the Lagrangian timescale is provided. In the rest of the domain a piece-wise linear interpolation of the mean velocity fields and a piece wise uniform interpolation of the Lagrangian timescale is used. In this case, the wall boundary condition is the proper an-elastic rebounds.
- Finally, with a view to discussing the error that may arise when considering a linear interpolation of the Lagrangian timescale, a situation similar to the previous one is considered with a piece-wise uniform interpolation of the Lagrangian timescale in the whole domain.

The results presented in Chapter 3 for the particles dynamics, are noticeable. Let us keep in mind that on these plots the dynamics of the flow issued from the source (simulations) is expected to differ from the dynamics of the whole flow (measurements). The experimental data are then here only to recall the flow behaviour but should not be compared directly to simulation results. Looking at both the shear stress and horizontal component of the TKE, the piece-wise interpolation of the mean velocity fields with elastic rebounds underestimates this value compared to the one using the an-elastic wall boundary condition. Although less noticeable, it is worth noticing that the mean velocity is also slightly overestimated due to the use of the elastic rebounds. Similarly, comparing both simulations with elastic boundary conditions, the choice of a piece-wise uniform velocity interpolation near wall results in a further underestimation of the shear stress and the kinetic energy in the streamwise direction, but also and less noticeably an overestimation of the mean velocity. Furthermore, considering the logarithmic interpolations near wall little modification of the streamwise component of the Reynolds tensor arise, yet an inflection of the shear tress appears when considering a linear interpolation of the Lagrangian timescale in wall cells. The error appearing with this interpolation will be further discussed hereafter.

The influences of the interpolation methods and wall boundary condition are also noticeable on the pollutant associated statistics. These impacts on the mean concentration remains small as we can see in Figure 4.20A, except when a piece-wise linear interpolation of the Lagrangian timescale is provided. In this case, an overestimation of the concentration in the wall cell is

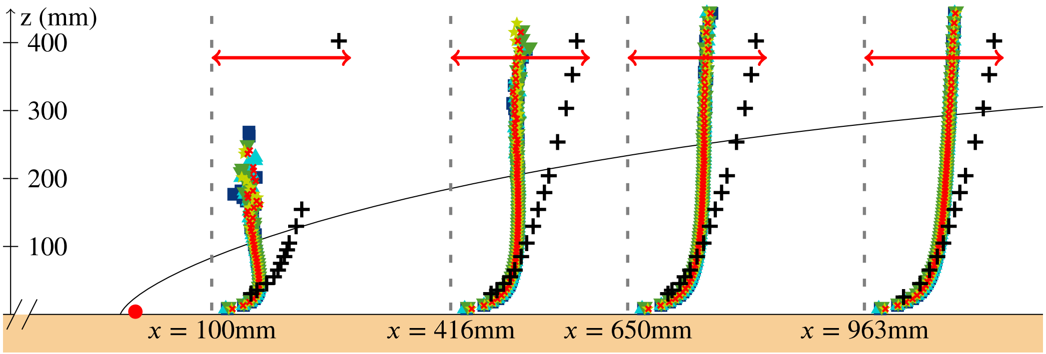

(A) Mean streamwise velocity $\langle U \rangle^S(z)$. The red arrow represents a magnitude of 5.8 $\mathrm{m\,s^{-1}}$.

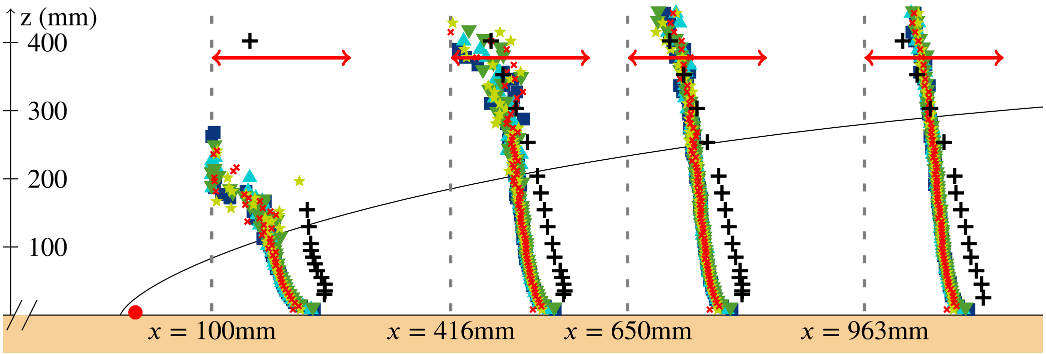

(B) Streamwise velocity standard deviation $\langle uu \rangle^S(z)$. The red arrow represents a magnitude of 1 $\mathrm{m\,s^{-1}}$.

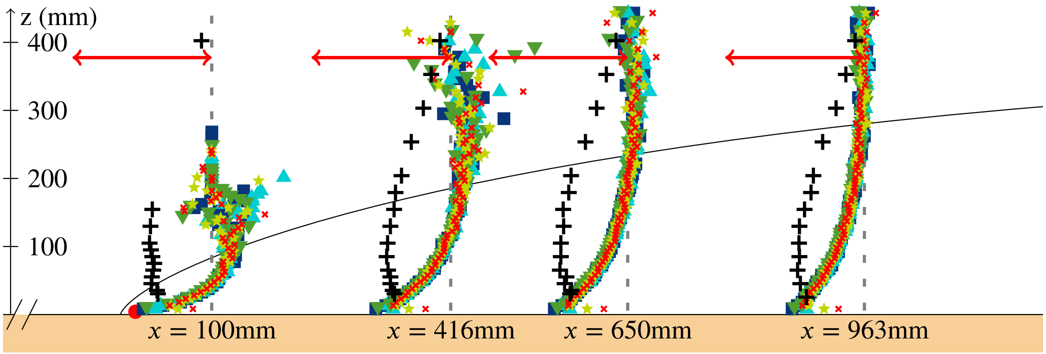

(C) Shear stress $\langle uw \rangle^S(z)$. The red arrow represents a magnitude of -0.3 $\mathrm{m^2\,s^{-2}}$.

Figure 4.19: Profiles characterising the PDF modelled pollutant dynamics downstream the pollutant source for different interpolation methods and wall boundary conditions. The experimental data of Gamel [2015] (+) are compared to Lagrangian stochastic simulations using respectively an elastic rebound with a P_0 velocity interpolation (✖); an elastic rebound with a P_1 velocity interpolation (★); an an-elastic rebound with a P_1 velocity interpolation (▼); an an-elastic rebound with an interpolation locally logarithmic on velocity and either a linear interpolation on Lagrangian timescale (▲) or an uniform one (■). On each plot, the red arrow represents the same physical magnitude. The plume shape plotted is estimated based on experimental mean concentration profiles.

clearly noticeable. Yet, looking at the streamwise turbulent fluxes, on can see that the poor choice of the interpolation scheme or of the wall boundary condition results in non negligible error near wall.

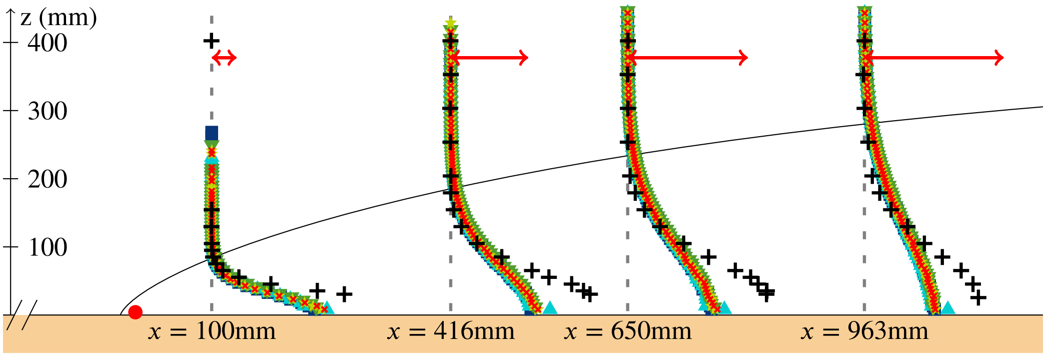

(A) Mean concentration $\frac{\langle C\rangle}{Q_{inj}}$. The red arrow represents an ATC magnitude of 0.6 $\mathrm{m}^{-3}\,\mathrm{s}$

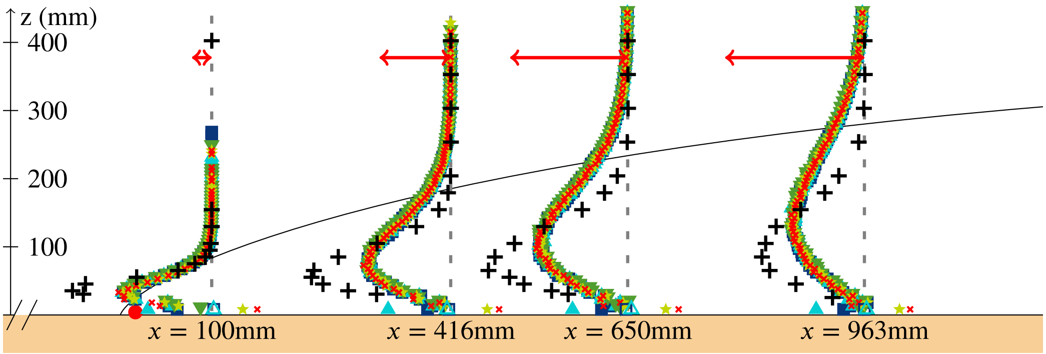

(B) Streamwise turbulent scalar fluxes $\frac{\langle uc\rangle}{Q_{inj}}$. The red arrow represents a magnitude $-0.15\ \mathrm{m}^{-2}$

Figure 4.20: Profiles characterising the PDF modelled pollutant dispersion downstream the pollutant source for different interpolation methods and wall boundary conditions. The experimental data of Gamel [2015] (+) are compared to Lagrangian stochastic simulations using respectively an elastic rebound with a P_0 velocity interpolation (✖); an elastic rebound with a P_1 velocity interpolation (★); an an-elastic rebound with a P_1 velocity interpolation (▼) and an an-elastic rebound with an interpolation locally logarithmic on velocity and either a linear interpolation on Lagrangian timescale (▲) or an uniform one (■). Note that for the two latter interpolation methods unfilled markers (△) and (□) are present in the wall cells of Figure 4.20B. They correspond to corrected estimation of the horizontal scalar fluxes taking into account the logarithmic profile of the carrier velocity in these cells. On each plot, the red arrow represents the same physical magnitude. The plume shape plotted is estimated based on experimental mean concentration profiles.

Let us now focus on the error introduced using the logarithmic interpolation. Two sources of error may be segregated. The first one, impacting the horizontal scalar flux, is a post-treatment error impairing only the estimation of the statistics. Indeed, the horizontal scalar flux is proportional to $\langle U\rangle^S - \langle U\rangle$. In the bulk of the flow, it has been assumed that we have $\langle U\rangle \simeq \overline{U}$, yet in wall cells this assumption is not respected as a logarithmic interpolation of the carrier mean velocity is imposed. The corresponding mean value may differ from the one provided by the FV solver. We should then consider in the first cell a mean value of $\langle U\rangle$ coherent with the logarithmic interpolation. For Cartesian cells, the latter may be written:

$$\langle U \rangle = \frac{\sqrt{-\langle uw \rangle}}{\kappa \delta z} \left((\delta z + z_0) \ln \left(\frac{\delta z + z_0}{z_0} \right) - \delta z \right), \tag{4.18}$$

with δz the height of the first cell. Doing so, we retrieve proper results in the first cell. Note that, as shown in Figure 4.20B, this issue does not arise with linear interpolation because such an interpolation does not modify the mean integrated value in the cell. The second source of error impacts mostly the vertical transport of the particle and then the shear stress but also the concentration. It appears only when a piece-wise linear modelling of the Lagrangian timescale is tackled. In this case, particles might be located too deep in the boundary layer to use a model developed for high Reynolds number flows. Indeed, the Lagrangian timescale near wall converges towards a value which might be small compared to the value stored at the centre of the cells. Therefore, it is possible for the particles to remain trapped near wall. In order to be able to properly treat such zones, it would be necessary to consider models valid for low Reynolds number where the viscous diffusion by Brownian processes is explicitly treated with additional stochastic terms (see e.g. Dreeben and Pope [1997a, 1998], Wacławczyk et al. [2004]). Moreover, for now the Lagrangian timescale is simply clipped by its analytical value at the altitude z_0. It is then possible, in wall cells, to have zones in which the Lagrangian timescale interpolated is locally uniform at this too small value. An improvement of this method would be to overwrite the Lagrangian timescale gradient in wall cells to avoid such clipping. For these reasons, this interpolation will not be used later on.

4.2.3.5 Effects of the PDF Modelling Selected

In order to characterise. the effects of the modelling selected in the scope of Lagrangian methods, the results obtained with different toy models are presented in Figure 4.21. These toy models aim at mimicking the distribution of kinetic energy obtained with known moment approach models. They are derived to be valid only in the specific case of stationary, and horizontally uniform neutral surface boundary flows which are assumed close to the flow encountered in this situation. To this end, anisotropic Lagrangian timescales are specified as presented in Appendix 4.A. Furthermore, so as to mitigate the error induced by the estimation of the mean carrier fields, the largest roughness height is considered to obtain the best estimation of the mean velocity. Moreover, the level of TKE is reduced by 25% corresponding approximately to the TKE overshoot of the FV simulation. This is a crude assumption as the experimental data used do not contain any information about the spanwise turbulent kinetic energy nor the dissipation rate kept unchanged. In this case, the TKE in the close vicinity of the wall remains somewhat superior to the one estimated experimentally due to the difference of slopes between FV results and experimental ones. First, for all models considered, this crude corrections of the mean carrier flows enable to achieve much better results. This might serve as a reminder that the results of hybrid moment/PDF simulations greatly depend on the quality of the mean carrier fields provided by the FV approach.

Doing so, one can see that the modelling selected within the Lagrangian method has an impact on the plume description. Indeed, the SLM model, which is consistent with Rotta modelling, assumes an isotropic shape for the pressure-strain correlation. This is not representative of the physics near wall where more TKE is redistributed towards the streamwise components. Mimicking modelling taking into account this anisotropic redistribution such as the LRR-IP or the SSG models, less kinetic energy is furnished to the normal fluctuation yielding to less diffuse plume, as we can see on the mean concentration in Figure 4.21A. This is more noticeable looking at the turbulent scalar fluxes in Figure 4.21B and Figure 4.21C especially when mimicking the SSG model which better represents the TKE distribution. Indeed, as the concentration near wall and the turbulent fluctuations of velocity in the streamwise direction increase, better results are obtained on the streamwise turbulent scalar fluxes. Looking at the vertical turbulent scalar fluxes, the decrease of TKE in this direction is compensated by an increase of concentration. This enables to properly capture the normal fluxes which almost perfectly fit the experimental data mimicking the SSG model avoid the overly diffusive tail otherwise present. Assuming a isotropic distribution of the TKE, which is somewhat similar to the assumption made in SGDH methods, poor overly diffusive results are obtained.

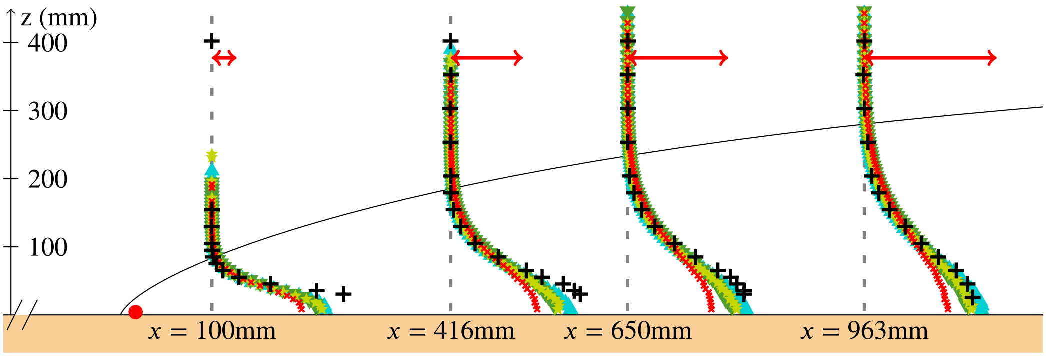

(A) Mean concentration $\frac{\langle C\rangle}{Q_{inj}}$. The red arrow represents an ATC magnitude of 0.6 m^{-3} s.

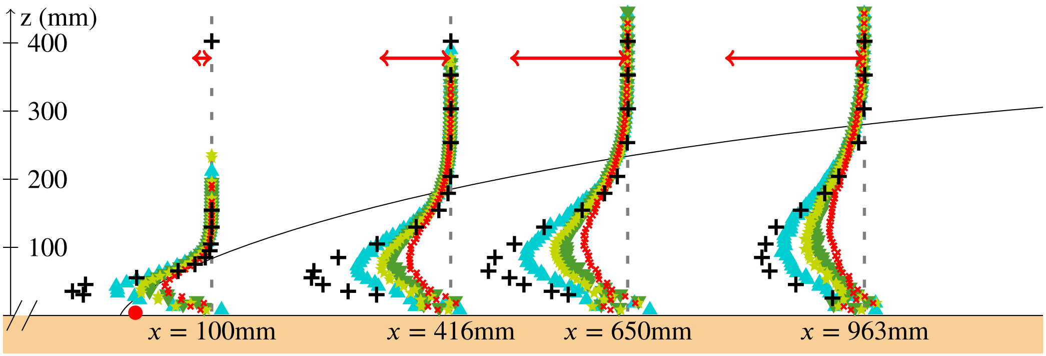

(B) Streamwise turbulent scalar fluxes $\frac{\langle uc\rangle}{Q_{inj}}$. The red arrow represents a magnitude of -0.15 m^{-2}.

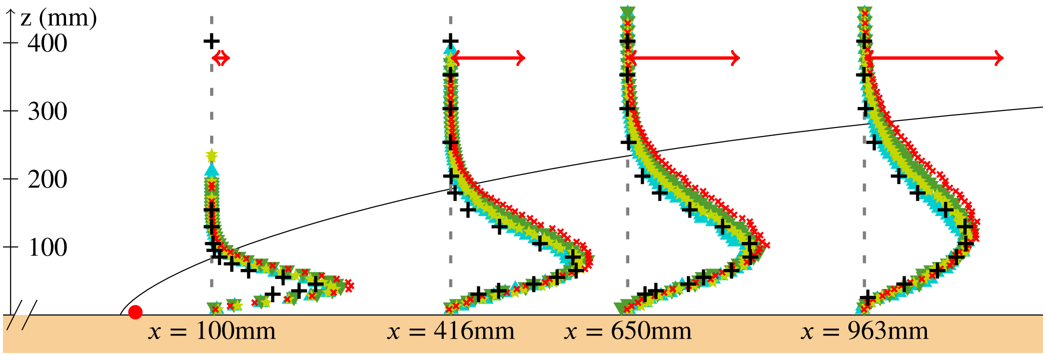

(C) Normal turbulent scalar fluxes $\frac{\langle wc\rangle}{Q_{inj}}$. The red arrow represents a magnitude 0.06 m^{-2}.

Figure 4.21: Profiles characterising the PDF modelled pollutant dispersion downstream the pollutant source using different toy models within the particle solver. The results mimicking respectively: $k-\epsilon$ (✖); SSG (▲) ; Rotta (▼); LRR-IP (★) TKE distributions are compared to Gamel [2015] experimental data. On each plot, the red arrow represents the same physical magnitude. The plume shape plotted is estimated based on experimental mean concentration profiles.

4.3 Linear-Source Dispersion near Ground in the Wake of an Isolated Obstacle

Contents

We will now focus on a slightly more complex situation: a statistically stationary turbulent linear-source dispersion in the wake of an infinite isolated obstacle of height $H = 0.1$ m. It is still based on the experimental study of Gamel [2015] made in a channel flow and our results will be compared to these data. As the obstacle is considered infinite in the spanwise direction and the source is linear, one may consider a 2-D flow. Here again the potential effects of structures orthogonal to the streamwise direction are not considered but are quickly discussed in Section 4.3.1.

The domain is schematised in Figure 4.22, with the boundary conditions (in purple) and the main flow characteristics. A $0.1H$ large linear source of pollutants (red dot) is placed at a distance H in the wake of a square obstacle of length H within its recirculation zone (in blue). The injected flow rate at the pollutant source Q_{inj}/ρ is still 600 $\mathrm{L\,h^{-1}}$, resulting in an injection velocity of 0.0238 $\mathrm{m\,s^{-1}}$. The latter remains sufficiently small, so it does not perturb the overall flow dynamics which is imposed by the free-of-pollutant flow injected upstream (also in blue) The main aim is to study the dispersion of the pollutants downstream the obstacle (the corresponding plume is schematised by the red line).

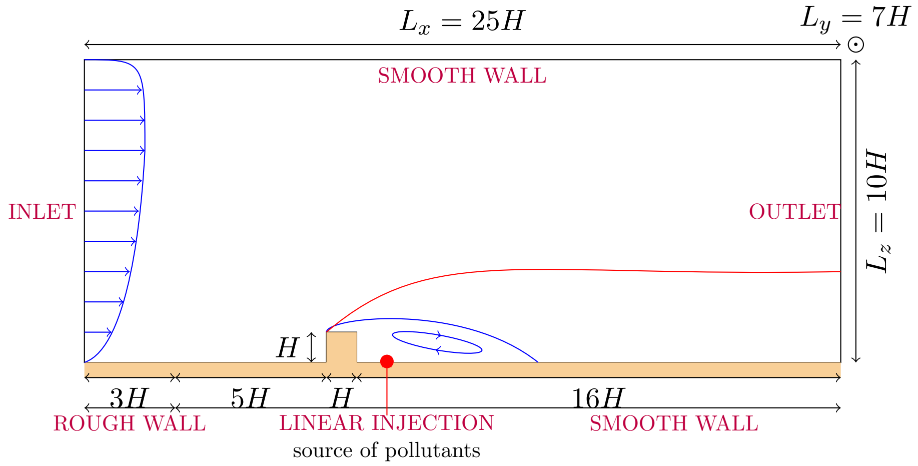

Figure 4.22: Description of the domain studied to study the linear source dispersion in the wake of an infinite isolated obstacle.

The inlet condition is provided by interpolation of the simulation results carried out in Section 4.2, with a Rotta model and a roughness height $z_0 = 1.92$ mm. The 2-D geometry consists in a rectangular domain of $25H \times 10H$ in which the obstacle has been introduced by removing the corresponding cells. The domain dimensions respect the recommendations of Franke et al. [2007] provided to treat dispersion around obstacles. Indeed, in the streamwise direction, we have an upstream region of $8H$ bigger than the advised limit value of $5H$. In coherence with the experimental setup, a rough wall is kept over a distance of $3H$ downstream the inlet with $z_0 = 1.92$ mm, and the wall over the remaining $5H$ upstream the obstacle is assumed smooth. The wake region is $16H$ long which is also longer than the recommended

$15H$. Furthermore, in the spanwise and normal direction, the dimension of the experimental channel flow are kept i.e., respectively $7H$ and $10H$. The latter dimension is bigger than the $6H$ above the obstacle recommended to avoid spurious acceleration effects. The mesh considered is uniform and its cell dimension is $l_c \times l_c \times L_y$. As the flow is 2-D, only one cell is considered in the spanwise direction. In the plane perpendicular to this direction the domain surface is 249 H^2. The number of cells is then $249H^2/l_c^2$. Given that the source of pollutant is $0.1H$ large, to properly characterise this zone, we will take a cell length l_c such as $0.1H$ is a multiple of l_c i.e. $0.1H = n\ l_c$ with n the number of cells above the injection zone. We consider that the injection zone is two cells large (n=2): $l_c = H/20 = 0.005$ m. The mesh considered is then composed of $249 \times 20 \times 20 = 96.000$ cells as shown in Figure 4.23.

Figure 4.23: Reference mesh used to treat pollutant dispersion in the wake of an isolated obstacle.

Such a mesh may not be totally converged, however considering finer meshes the dimensionless heights to the wall $z^+ = zu_*/\nu$ would become too small for the high-Reynolds methods considered to be valid as we can see looking at the dimensionless height z^+ at the ground in Figure 4.24. Indeed, the lowest part of the logarithmic zone is described by a zone where z^+ is somewhere around 30 to 50.

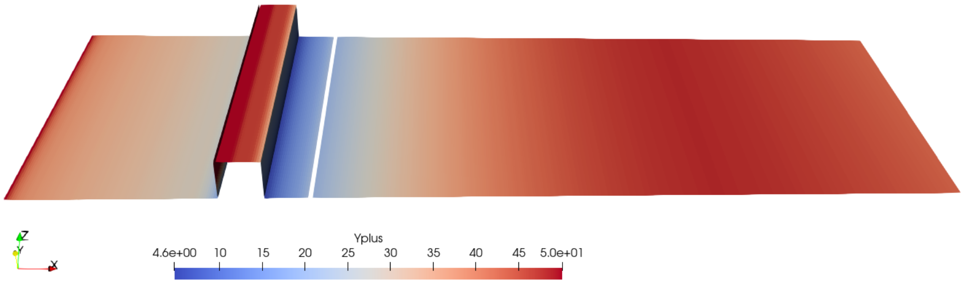

Figure 4.24: Dimensionless height z^+ near the obstacle for 5 mm high wall cells.

4.3.1 Discussion on the Experimental Data

Also, in this case, spurious mean normal velocities seem to be present on the experimental data as we can see in Figure 4.25. Indeed, the latter ones are always negative even in the region close to the obstacle and slightly above it. In such an area it is expected to find an upward velocity with an increase of streamwise velocity due to the continuity condition as the flow is blocked by the obstacle. As in the unobstructed flow, such a downward velocity may testify for the presence of measurement error or of secondary structures orthogonal to the main flow direction. The latter ones may be caused by the presence of the channel flow wall nearby in the spanwise direction. In the wake of an obstacle, the normal velocity varies with the distance to the obstacle and cannot be neglected. Thus, in this case, the study of a potential misalignment angle θ is not carried out.

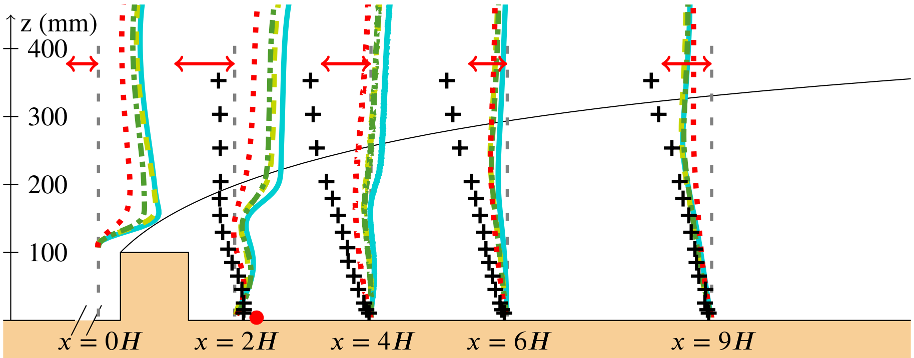

Figure 4.25: Profiles of the RANS modelled normal mean velocity adimensioned by the normal turbulent velocity scale $\sqrt{\overline{ww}}$ downstream the obstacle. The results using four turbulent models: $k - \epsilon$ (····); SSG (——); Rotta (-·-·-) ; LRR-IP (— —) are compared to Gamel [2015] experimental data. The red arrow represents a physical magnitude of 1. The plume shape plotted is estimated based on experimental mean concentration profiles.

Moreover, as previously looking at the integrated flux over the height in Figure 4.26, we can note the presence of an overestimation of the total fluxes especially near the injection point in the recirculation zone. In this situation, the fluxes below the first values are almost null. Here again we will rescale the mean concentration, turbulent scalar fluxes and concentration deviation using these $\langle UC \rangle_*^{tot}$.

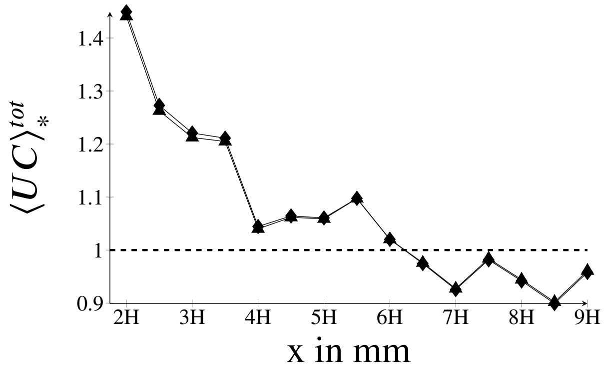

Figure 4.26: Estimation of the adimensionised total scalar flux integrated over the height from Gamel [2015] data when considering dispersion in the wake of an isolated obstacle. A plot with an estimation of the scalar flux below first available data (◆—◆) is compared to the results without this added flux (▲—▲) and to the expected flux (- - -).

4.3.2 Results using the Moment Approach

First, we focus on the dynamics of the mean carrier flow after the obstacle. The results using four different closures of the turbulence are compared: one EVM and three 2^{nd} order DRSM methods. As previously, the models compared are respectively the $k-\epsilon$, Rotta, LRR-IP and SSG models. It is worth noticing that surprisingly the best results are obtained for the $k-\epsilon$ model which fits the experimental dynamics with more accuracy, as we can see in Figure 4.28. The latter tends to properly retrieve the end of recirculating zone at around $6H$ whereas the three DRSM models tends to estimate a distance of $9H$. Moreover, both within and out the recirculating zone the $k-\epsilon$ model provides better mean velocity and Reynolds tensor profiles. The three DRSM models tend to underestimate the overall energy associated to both the mean and turbulent flows.

As the $k-\epsilon$ model better reproduces the flow dynamics, it is expected that the best results for the pollutant mean concentration are also obtained using this closure as one can see respectively in Figure 4.27. It is yet noticeable that the near wall dispersion is less accurate using this EVM based carrier flow. Considering DRSM methods the pollutant is less diffused and more transported by the mean flow, so more concentration reaches the top of the obstacle and are transported from there. This is also noticeable on the concentration standard deviation which remains closer the experimental data whereas the $k-\epsilon$ tends to overestimate this value.

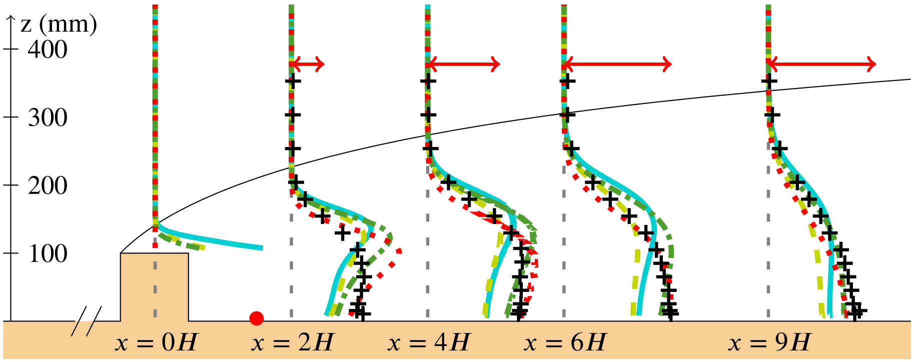

(A) Mean concentration $\frac{\overline{C}}{Q_{inj}}$. The red arrow represents an ATC magnitude of 0.45 $\mathrm{m}^{-3}\,\mathrm{s}$.

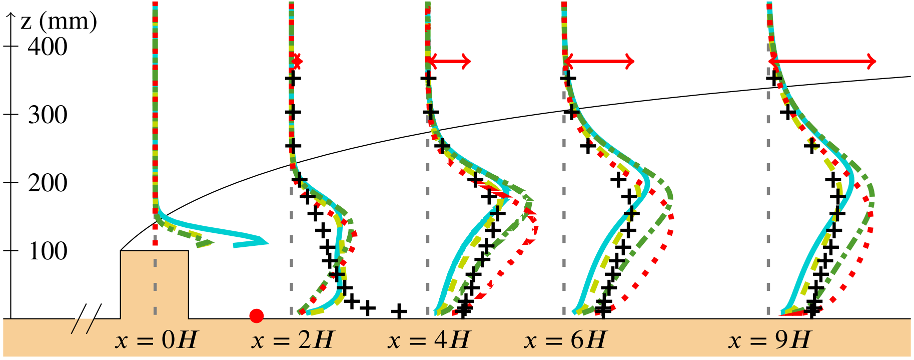

(B) Concentration standard deviation $\frac{\overline{cc}}{Q_{inj}}$. The red arrow represents an ATC magnitude of 0.24 $\mathrm{m}^{-3}\,\mathrm{s}$.

Figure 4.27: Profiles characterising the RANS modelled pollutant dispersion downstream the obstacle. The results using four turbulence models: $k-\epsilon$ (····); SSG (——); Rotta (-·-·); LRR-IP (– –) are compared to Gamel [2015] experimental data.

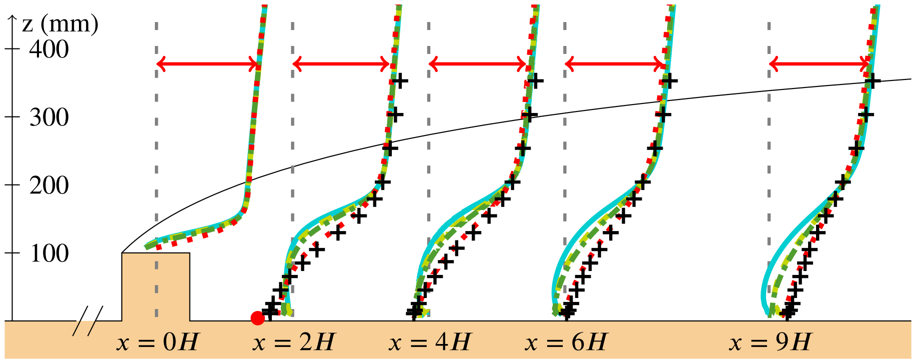

(A) Streamwise mean velocity $\overline{U}$. The red arrow represents a magnitude of 5.8 $\mathrm{m\,s^{-1}}$.

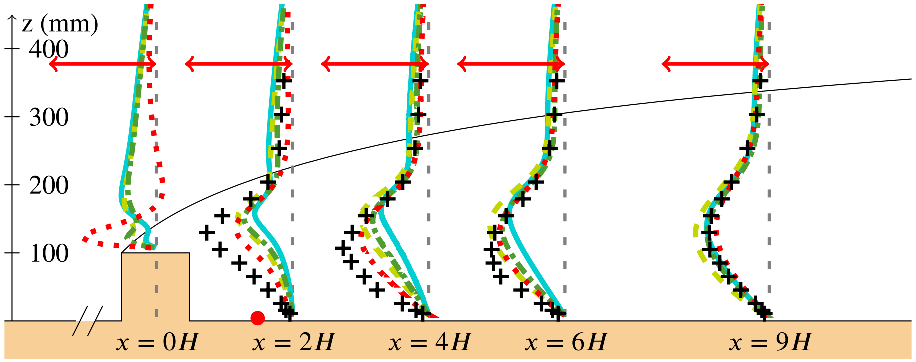

(B) Shear stress $\overline{uw}$. The red arrow represents a magnitude of -1 $\mathrm{m^2\,s^{-2}}$.

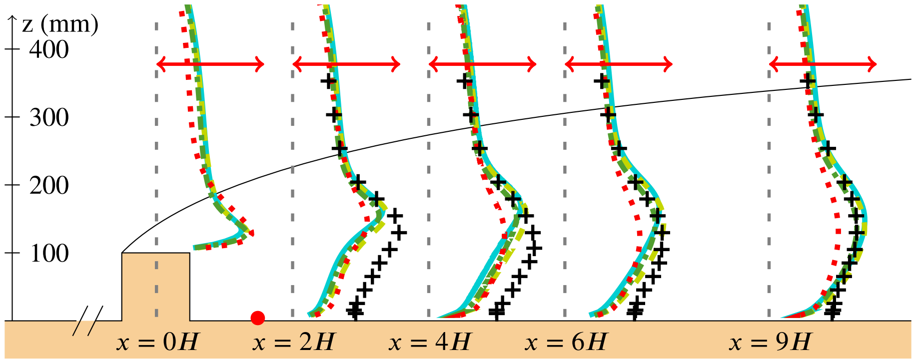

(C) Streamwise velocity standard deviation $\sqrt{\overline{uu}}$. The red arrow represents a magnitude of 1.5 $\mathrm{m\,s^{-1}}$.

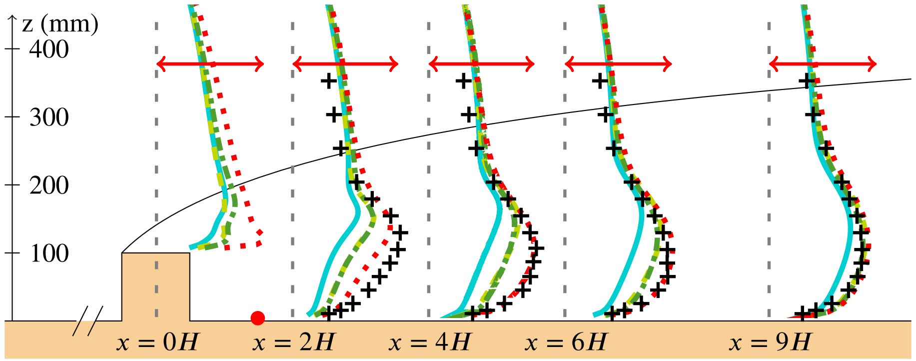

(D) Normal velocity standard deviation $\sqrt{\overline{ww}}$. The red arrow represents a magnitude of 1.1 $\mathrm{m\,s^{-1}}$.

Figure 4.28: Profiles of the RANS modelled dynamic properties downstream the obstacle. The results using four turbulent models: $k-\epsilon$ (⋯); SSG (—); Rotta (-·-·) ; LRR-IP (– –) are compared to Gamel [2015] experimental data.

4.3.3 Results using the Moment/PDF Approach

SLM based Lagrangian stochastic simulations using the four models presented in Section 4.3.2 for the mean carrier flow are compared. as we can see in Figure 4.29A, a spurious effect still exists within the wall cells where the mean concentration is overestimated. The best results are obtained using the mean carrier fields issued from the $k - \epsilon$ simulation which provides the best description of the flow dynamics. This highlights that the error arising from the lack of consistency between this first-order model is small compared to the benefit of a more accurate description of the mean carrier flow. The results obtained with the Lagrangian stochastic methods seem adequately capture the dynamics of the pollutant plume. Moreover, the scalar fluxes are fairly well retrieved as demonstrated in Figure 4.29B and Figure 4.29C respectively for $\langle uc \rangle$ and $\langle wc \rangle$. Yet, although the order of magnitude of the concentration standard deviation seems to be correct, a strong overestimation of its value is still obtained using the volumetric particle approach as shown Figure 4.29D.

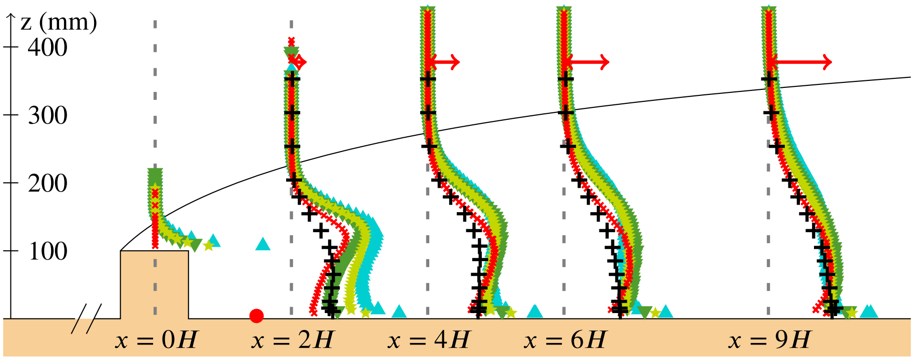

(A) Mean concentration $\frac{\langle C\rangle}{Q_{inj}}$. The red arrow represents an ATC magnitude of 0.36 $\mathrm{m}^{-3}\,\mathrm{s}$.

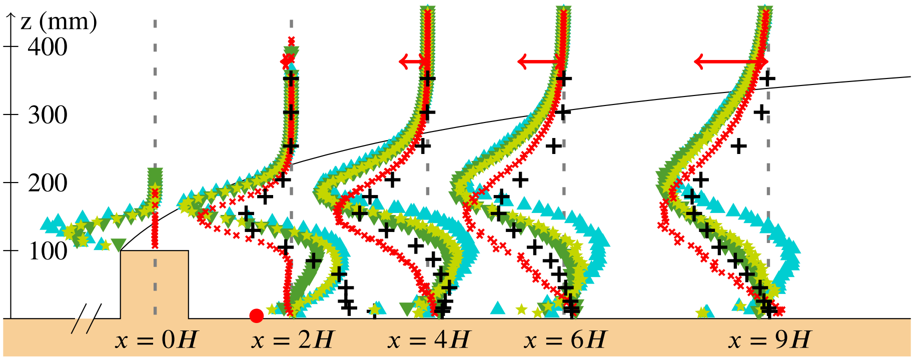

(B) Streamwise turbulent scalar fluxes $\frac{\langle uc\rangle}{Q_{inj}}$. The red arrow represents a magnitude of -0.075 m^{-2}.

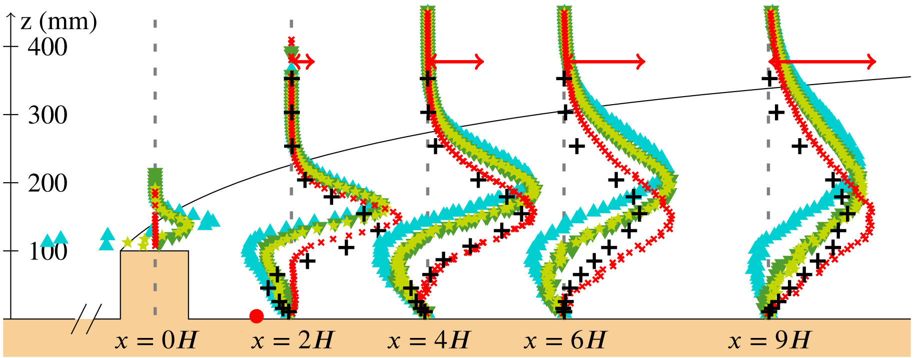

(C) Normal turbulent scalar fluxes $\frac{\langle wc\rangle}{Q_{inj}}$. The red arrow represents a magnitude of -0.072 m^{-2}.

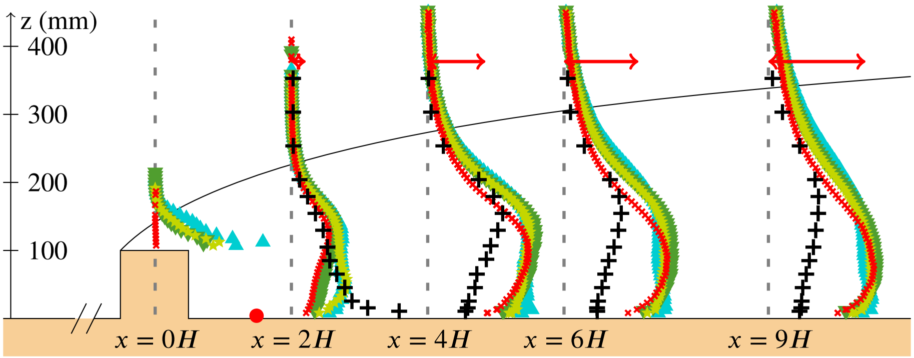

(D) Concentration standard deviation $\frac{\sqrt{\langle \widetilde{cc}\rangle}}{Q_{inj}}$ estimated with Eq. (4.12). The red arrow represents a magnitude of -0.02 $\mathrm{m}^{-3}\mathrm{s}$.

Figure 4.29: Profiles characterising the PDF modelled pollutant dispersion downstream the pollutant source. The results using four turbulent models for the carrier fields are compared: $k-\epsilon$ (✖); SSG (▲) ; Rotta (▼); LRR-IP (★) are compared to Gamel [2015] experimental data. On each plot, the red arrow represents the same physical magnitude. The plume shape plotted is estimated based on experimental mean concentration profiles.

4.4 Local Conclusions and Perspectives

The description of the dispersion of pollutant downstream a linear source can be made using a hybrid moment/PDF method by simulating solely the particles issued from the source of pollutant. Using such a description, the mean concentration but also scalar fluxes can be directly derived and represent a relatively good description of the plume physics. Even though it is not possible to directly have access to the concentration fluctuations considering a zero-micro mixing assumption, an acceptable yet overestimated value of the scalar variance may be reached using a volumetric particle approach developed by Cassiani [2013] with an adequate relaxation timescale. In the scope of SLM-IEM modelling, so as to consider a turbulent Schmidt number of one it is then advised to consider the same timescale for the velocity and concentration (i.e. taking $T_L = \mathcal{T}_C$ and thus $\mathcal{C}_C = \mathcal{C}_L$).

The preponderant element to characterise the pollutant dispersion remains the capacity to properly treat the dynamics of the carrier flow. For this purpose, the proper treatment of the roughness and choice of an adequate turbulence modelling are of primordial importance. As seen in Section 4.3.3, the error induced by the non-consistency between PDF and moment solver may be negligible compared to the benefit provided by a better description of the mean carrier flow. Furthermore, using toy model, it has been demonstrated that the modelling selected within the PDF methods have a significant effect on the simulated dispersion. This advocates for the implementation of more complex GLM models which are expected to propose a better physical description near wall. In addition, as presented in Section 4.2.3.4, the proper choice of an interpolation method and a wall boundary condition, are not totally negligible in the vicinity of the wall. However, at this scale, the corresponding errors remain of lesser importance compared to the error induced by a poor description of the mean carrier flow or by a poor Lagrangian modelling. Furthermore, an error on the concentration within the wall cell may be noticed when going too close to the wall. A potential source of error may be the necessity to explicitly treat the diffusion by Brownian movement to consider viscous effects in this zone. Without this Brownian movement, the particles may be trapped for too long in this zone. A comparison with Lagrangian stochastic models valid for low Reynolds number flow may be of great interest to determine if we have indeed reached the limit of validity of the SLM model developed for high Reynolds number flows.

Finally, let us note the presence in the experimental data of a downward mean velocity. Given the nature of this flow, the latter are not physical considering a spanwise periodic flow. In order to assert if this normal velocity results from measurement error or from physical secondary flow orthogonal to the mean flow, a further 3-D study may be carried out. These potential 3-D effects might be the cause the error observed on the estimation of the total mean scalar fluxes based only on the value at the centre of the channel. Such 3-D simulations may then be used to quantify influence of potential secondary flows on the pollutant dispersion.

Local Appendix

4.A Description of the Class of Toy Models used to Discuss PDF Model Sensibility

The goal of the present section is to present the derivation of a class of simple Lagrangian toy models used in Section 4.2.3.5. The latter ones aim at mimicking the TKE distribution of different RANS model in the case of stationary horizontally uniform neutral surface-boundary layer flows. In order to do so, the conditions to fulfil are:

$$\text{Balance of production and dissipation:} \qquad \mathcal{P} = \epsilon = \frac{k}{\mathcal{T}_k}, \tag{4.19a}$$

$$\text{Production and kinetic energy:} \qquad k = -\frac{1}{\sqrt{\mathcal{C}_\mu}}\langle uw \rangle, \tag{4.19b}$$

$$\text{Proportion in each direction :} \qquad \mathscr{r}_\alpha = \frac{\langle u_\alpha u_\alpha \rangle}{k}, \tag{4.19c}$$

where the considered distributions of TKE $\mathscr{r}_\alpha$ are given in Table 4.A.1.

	$k-\epsilon$ std.	Rotta ($\mathcal{C}_R = 3.5$)	LRR-IP ($\mathcal{C}_R = 1.8, \mathcal{C}_\mathcal{P} = 0.6$)	SSG std. (see Table 1.3)
$\mathscr{r}_x$	$\frac{2}{3}$	0.88	0.96	1.07
$\mathscr{r}_y$	$\frac{2}{3}$	0.56	0.52	0.52
$\mathscr{r}_z$	$\frac{2}{3}$	0.56	0.52	0.41

Table 4.A.1: Distribution of kinetic energy of a few RANS models.

The simplest GLM model enabling to have a non-isotropic redistribution is to consider a diagonal matrix $\underline{\underline{\boldsymbol{G}}}$ with integral time-scale $T_{L,\alpha} = \frac{\mathcal{T}_k}{\tilde{\lambda}_\alpha} = \frac{k}{\tilde{\lambda}_\alpha \epsilon}$ depending on the direction. A great interest for the integration of such models is that each direction can still be considered independent, thus, the temporal scheme currently used can be used without modification. The instantaneous velocity equation can be written:

$$\mathrm{d}U_\alpha = \left(-\frac{1}{\rho}\frac{\partial\langle P\rangle}{\partial x_\alpha} - \widetilde{\lambda}_\alpha \frac{U_\alpha - \langle U_\alpha\rangle}{\mathcal{T}_k}\right)\mathrm{d}t + \sqrt{\mathcal{C}_0\frac{k}{\mathcal{T}_k}}\mathrm{d}W_\alpha. \tag{4.20}$$

The three conditions imposed on Eqs 4.19 will be useful to fix the four parameters of these models: the three $\widetilde{\lambda}_\alpha$ and $\mathcal{C}_0$. Such a modification of model will not appear on the mean velocity equation and the equation for the Reynolds tensor becomes:

$$\begin{aligned}\langle\frac{du_\alpha u_\beta}{dt}\rangle =& \frac{\partial\langle u_\alpha u_\beta\rangle}{\partial t} + \langle U_k\rangle\frac{\partial\langle u_\alpha u_\beta\rangle}{\partial x_k} + (\langle u_\alpha u_k\rangle\frac{\partial\langle U_\beta\rangle}{\partial x_k} + \langle u_\beta u_k\rangle\frac{\partial\langle U_\alpha\rangle}{\partial x_k}) + \frac{\partial\langle u_\alpha u_\beta u_k\rangle}{\partial x_k},\\ =& -(\widetilde{\lambda}_\alpha + \widetilde{\lambda}_\beta)\frac{\langle u_\alpha u_\beta\rangle}{\mathcal{T}_k} + \mathcal{C}_0\frac{k}{\mathcal{T}_k}\delta_{\alpha\beta}.\end{aligned} \tag{4.21}$$

For a surface boundary layer, it can be simplified into:

$$(\langle u_\alpha w\rangle\frac{\partial\langle U\rangle}{\partial z}\delta_{x\beta} + \langle u_\beta w\rangle\frac{\partial\langle U\rangle}{\partial z})\delta_{x\alpha} + (\widetilde{\lambda}_\alpha + \widetilde{\lambda}_\beta)\frac{\langle u_\alpha u_\beta\rangle}{\mathcal{T}_k} = \mathcal{C}_0\frac{k}{\mathcal{T}_k}\delta_{\alpha\beta}. \tag{4.22}$$

which component by component reads:

$$\text{for } \langle u^2\rangle\text{:} \qquad \widetilde{\lambda}_x\langle u^2\rangle = -\langle uw\rangle\frac{\partial\langle U\rangle}{\partial z}\mathcal{T}_k + \frac{\mathcal{C}_0}{2}k, \tag{4.23a}$$

$$\text{for } \langle v^2\rangle\text{:} \qquad \widetilde{\lambda}_y\langle v^2\rangle = \frac{\mathcal{C}_0}{2}k, \tag{4.23b}$$

$$\text{for } \langle w^2\rangle\text{:} \qquad \widetilde{\lambda}_z\langle w^2\rangle = \frac{\mathcal{C}_0}{2}k, \tag{4.23c}$$

$$\text{for } \langle uw\rangle\text{:} \qquad -(\widetilde{\lambda}_x + \widetilde{\lambda}_z)\langle uw\rangle = \langle w^2\rangle\frac{\partial\langle U\rangle}{\partial z}\mathcal{T}_k, \tag{4.23d}$$

$$\text{for } \langle uv\rangle\text{:} \qquad \langle uv\rangle = 0, \tag{4.23e}$$

$$\text{for } \langle vw\rangle\text{:} \qquad \langle vw\rangle = 0. \tag{4.23f}$$

From Eq. (4.23a), in order to ensure the balance of the production and conservation Eq. (4.19a) we have then to ensure that we have:

$$-\langle uw\rangle\frac{\partial\langle U\rangle}{\partial z} = -\frac{\mathcal{C}_0}{2}\frac{k}{\mathcal{T}_k} + \widetilde{\lambda}_x\frac{\langle u^2\rangle}{\mathcal{T}_k} = \frac{k}{\mathcal{T}_k}. \tag{4.24}$$

Injecting the condition on the distribution of the streamwise energy Eq. (4.19c), we have then:

$$\widetilde{\lambda}_x = \frac{\mathcal{C}_0 + 2}{2\mathscr{r}_x}. \tag{4.25}$$

From Eq. (4.23c) the condition Eq. (4.19c) directly gives:

$$\widetilde{\lambda}_z = \frac{\mathcal{C}_0}{2\mathscr{r}_z}. \tag{4.26}$$

From the definition of the kinetic energy $k = \frac{\langle u_\alpha u_\alpha\rangle}{2}$ and the condition on the distribution of the kinetic energy Eq. (4.19c) we have:

$$\mathscr{r}_y = 2 - \mathscr{r}_x - \mathscr{r}_z. \tag{4.27}$$

Injecting this result in Eq. (4.23b), we obtain:

$$\widetilde{\lambda}_y = \frac{\mathcal{C}_0}{2(2 - \mathscr{r}_x - \mathscr{r}_z)}. \tag{4.28}$$

Finally, multiplying the Eq. (4.23d) by $\langle uw \rangle$ we have:

$$-(\widetilde{\lambda}_x + \widetilde{\lambda}_z)\langle uw \rangle^2 = \langle w^2 \rangle \langle uw \rangle \frac{\partial \langle U \rangle}{\partial z} \mathcal{T}_k = -\mathscr{r}_z k^2, \tag{4.29a}$$

$$k^2 = -\frac{\widetilde{\lambda}_x + \widetilde{\lambda}_z}{\mathscr{r}_z} \langle uw \rangle^2. \tag{4.29b}$$

Injecting this result in the condition Eq. (4.19b) and developing the coefficient $\widetilde{\lambda}_x$ and $\widetilde{\lambda}_z$ we get:

$$\frac{1}{\mathcal{C}_\mu} = \frac{\widetilde{\lambda}_x + \widetilde{\lambda}_z}{\mathscr{r}_z} = \frac{1}{\mathscr{r}_z}\left(\frac{\mathcal{C}_0 + 2}{2\mathscr{r}_x} + \frac{\mathcal{C}_0}{2\mathscr{r}_z}\right), \tag{4.30a}$$

$$\mathcal{C}_0 = 2\mathscr{r}_z \frac{\mathscr{r}_z \mathscr{r}_x - \mathcal{C}_\mu}{\mathcal{C}_\mu(\mathscr{r}_z + \mathscr{r}_x)}. \tag{4.30b}$$

Considering, the TKE distribution of Table 4.A.1 the coefficient associated to each toy model considered are presented in Table 4.A.2. By construction of the model, if one wants to mimic the Rotta model the SLM modelling is retrieved.

	$k - \epsilon$ std.	Rotta $(\mathcal{C}_R = 3.5)$	LRR-IP $(\mathcal{C}_R = 1.8, \mathcal{C}_\mathcal{P} = 0.6)$	SSG std. (see Table 1.3)
$\mathcal{C}_0$	3.96	3.5	3.21	2.16
$\widetilde{\lambda}_x$	4.47	3.125	2.71	1.94
$\widetilde{\lambda}_y$	2.97	3.125	3.9	2.63
$\widetilde{\lambda}_z$	2.97	3.125	3.09	2.08

Table 4.A.2: Value of the toy model constants for different mimicked RANS models.

CHAPTER 5

Treatment of the Thermally Stratified Atmospheric Surface-Boundary Layer

Contents

As presented in Paragraph 1.2.2.3.2, in order to take into account the effects of the potential temperature stratification on near ground atmospheric flows, one can consider the Monin–Obukhov similarity theory. In the scope of this theory, all mean and turbulent quantities in the surface-boundary layer (SBL) may be derived based on so called “universal functions”. In the literature many propositions have been made to determine such functions for the mean velocity and mean potential temperature (see e.g. Businger et al. [1971], Carl et al. [1973], Högström [1988], Chenge and Brutsaert [2005], Hartogensis and De Bruin [2005]). However, the selection of a specific proposition may be tricky and not fully satisfactory for multiple reasons. First, on theoretical grounds, many propositions do not respect the stable or convective asymptotic behaviour derived from the Monin–Obukhov similarity theory. Moreover, they do provide information only on the mean first-order moments and are therefore not sufficient to characterise the flows as no information on the turbulent quantities is provided. Finally, these functions are experimentally fitted and may not agree with the turbulence model considered in numerical simulations. Due to this issue, the selected universal functions, often used as inlet profiles for micro-scale flows, are not solution of the numerical solver in statistically stationary and horizontally uniform condition, yielding to the impossibility to maintain the injected profiles.

To avoid these difficulties, the main goal of Section 5.1 is to present a method to evaluate model-consistent universal functions. In this scope, we aim at estimating the solutions of the numerical solver to use them as universal functions. This method has been applied for a range of second-order RANS models with a linear modelling of the pressure-strain correlation and scrambling terms. The solution of algebraic equations consistent with the model selected are derived in Section 5.1.1. This step enables to provide universal functions for all mean and turbulent quantities except the mean velocity. Moreover, all these universal functions depend solely on this universal function associated with the mean velocity, which has still to be exhibited. To do so, an iterative resolution of the dissipation rate equation is carried out. A solution in agreement with the theoretical asymptotic solution is then obtained in Section 5.1.2 and verified in Section 5.1.3.

In addition, an extension of the spatial numerical treatment, presented in Chapter 3, is then provided to treat thermally stratified wall flow in Section 5.2. It is first highlighted, in Section 5.2.1, that a proper treatment of the wall boundary condition for the potential temperature is necessary to retrieve the physical evolution of thermal quantities in stratified SBL. Moreover, it is necessary to avoid errors on the well-mixed criterion tarnishing the concentration profiles. Afterwards, similarly to the mean velocity and Lagrangian timescale fields, the necessity to consider a proper interpolation scheme for the thermal properties is presented in Section 5.2.2. Then, the error arising when estimating second-order moments on too coarse averaging bins is put forward for stratified flows in Section 5.2.3.

Finally, the effects of the thermal stratification on the pollutant dispersion will be highlighted in Section 5.3 with both moment and Lagrangian stochastic methods. It is shown that the plume shape does not depend on the wind velocity but solely on the thermal stratification of the atmosphere as presented by Monin [1959]. Moreover, in the Lagrangian standpoint, the impacts of the proper thermal modelling are emphasised.

5.1 Derivation of Universal Functions Coherent with the Selected Turbulent Closure

Contents

The goal of the present section is to fully characterise the stratified SBL flows simulated with a given modelling of the turbulence. This issue is of particular interest to provide pertinent inlet condition for micro-scale atmospheric simulation when no wind data are available. We will place ourselves in the scope of the Monin–Obukhov similarity theory presented in Paragraph 1.2.2.3.2. This theory provides the dependence between physical quantities but not the explicit shape of these dependencies characterised by universal functions. As aforementioned and further discussed in Paragraph 1.2.2.3.2, selecting experimentally fitted universal functions of the literature results in an incoherence between profiles injected at inlet and the solution of the numerical solver. As a way to avoid these pitfalls, in the continuation of the work proposed by Gibson and Launder [1978], this section aims at deriving solutions consistent with the modelling selected and the numerical solutions. Indeed, the modelled set of equations considered to describe the flow is closed and therefore it is possible to derive the universal function by resolving it. We will consider a DRSM-DFM approach in which this set of equations is composed of 15 modelled equations (i.e. 3 equations for mean velocity, 1 equation for mean potential temperature, 6 equations for Reynolds tensor equation, 3 equations for the turbulent heat fluxes, 1 equation for the potential temperature variance and 1 equation for the TKE dissipation rate), yet the approach presented here remains valid for other choice of modelling as shown in Appendix 5.A.

5.1.1 Derivation of Universal Functions for the Second-Order Turbulent Quantities

To have a proper description of the turbulence, which plays a fundamental role in the treatment of pollutant dispersion, we will first focus on the second-order turbulent quantities. To do so, we will start by presenting the theoretical assumption considered. Then the derivation of the corresponding algebraic model on the Reynolds tensor and the scalar fluxes is detailed.

5.1.1.1 Hypothesis Considered

Let us first introduce the assumptions considered. We remain in the SBL, sufficiently high for the viscous effects to be negligible but sufficiently close to the ground to also neglect the long-distance pressure gradient and Coriolis effects. The situation considered is then a horizontally uniform and statistically stationary flow. It is vertically stratified due to the shear stress imposed by the upper region wind and the thermal forcing imposed at the ground assumed flat and horizontal. In this context, as discussed in Section 1.2.2.3, the mean velocity and potential temperature equations simplify respectively into $\frac{\partial \langle uw \rangle}{\partial z} = 0$ and $\frac{\partial \langle w\theta \rangle}{\partial z} = 0$, with $\underline{\boldsymbol{e_1}}$ aligned with the flow mean direction and $\underline{\boldsymbol{e_3}}$ aligned with the vertical. Thus, the shear stress $\langle uw \rangle = -u_*^2$, and the vertical turbulent heat flux $\frac{q_{heat}}{\rho C_p} = \langle w\theta \rangle = -u_*\theta_*$ are constant properties. We can then focus on the treatment of turbulent quantities.

5.1.1.1.1 Reynolds Tensor and Turbulent Scalar Fluxes Modelling

In coherence with the high Reynolds number limit considered, the dissipation tensor in Reynolds tensor equation is considered isotropic: $\underline{\underline{\boldsymbol{\epsilon}}} = \frac{2}{3}\epsilon\underline{\underline{\mathbf{1}}}$ whereas the dissipation of turbulent scalar fluxes is null: $\underline{\boldsymbol{\epsilon_\theta}} = 0\underline{\mathbf{1}}$ (see discussion in Paragraph 1.2.1.2.2). Furthermore, for the pressure-strain correlation $\underline{\underline{\mathbf{\Pi}}}$ and scrambling term $\underline{\mathbf{\Pi_\theta}}$ introduced respectively on Eq. (1.75) and Eq. (1.108), we limit ourselves to models in which they are treated as linear functions of the turbulent quantities available:

$$\Pi_{ij} = \underbrace{-\mathcal{C}_R\epsilon\left(\frac{\langle u_i u_j \rangle}{k} - \frac{2}{3}\delta_{ij}\right)}_{\Pi_{ij}^s} \underbrace{+2C_k k S_{ij} - \mathcal{C}_{\mathcal{P}}\left(\mathcal{P}_{ij} - \frac{2}{3}\mathcal{P}\delta_{ij}\right)}_{\Pi_{ij}^r} \underbrace{-\mathcal{C}_{\mathcal{G}}\left(\mathcal{G}_{ij} - \frac{2}{3}\mathcal{G}\delta_{ij}\right)}_{\Pi_{ij}^{\mathcal{G}}}, \tag{5.1}$$

$$\Pi_{\theta,i} = \underbrace{-\mathcal{C}_{\theta_1}\frac{\epsilon}{k}\langle u_i\theta \rangle}_{\Pi_{\theta,i}^s} - \underbrace{\mathcal{C}_{\theta_2}\mathcal{P}_{\theta,i}^U - \mathcal{C}_{\theta_2'}\mathcal{P}_{\theta,i}^\Theta}_{\Pi_{\theta,i}^r} - \underbrace{\mathcal{C}_{\theta_3}\mathcal{G}_{\theta,i}}_{\Pi_{\theta,i}^{\mathcal{G}}}, \tag{5.2}$$

with S_{ij} the deformation rate tensor $S_{ij} = \frac{1}{2}\left(\frac{\partial\langle U\rangle_i}{\partial x_j} + \frac{\partial\langle U\rangle_j}{\partial x_i}\right)$ which only has one component in the case studied $S_{xz} = \frac{1}{2}\frac{\partial\langle U\rangle}{\partial z}$. Moreover, in these equations the superscript ^{s} refers to slow terms depending on the turbulent properties but not directly on the first-order-moment gradients. The superscript ^{r} characterises rapid redistribution terms within which the first-order-moment gradients have a direct impact. Finally, the last term with the superscript $^{\mathcal{G}}$ represents the redistribution induced by the buoyant effects. It is worth noticing that the redistributing mechanism for the Reynolds tensor, the thermal variance and the turbulent heat fluxes results from similar physical processes. The choice of modelling for the corresponding terms is thus not independent from each other Pope [1994b]. The class of model selected does not encompasses non-linear treatment of fluctuating pressure induced redistribution terms. Then, for example the SSG model for the Reynolds tensor (see Speziale et al. [1991]) or the methods proposed by Kenjereš et al. [2005] for the turbulent heat fluxes remain out of the scope of the present study.

5.1.1.1.2 Weak Equilibrium Assumption

With an aim to exhibit a proper algebraic model describing the flow, which aims at being local, we place ourselves under the weak equilibrium assumption which is a common assumption within SBL flows (see e.g., Launder [1975], Gibson and Launder [1978], Rodi [2000], Pope [2000], Ferrand and Violeau [2012]). This hypothesis states for the Reynolds tensor:

$$k\left(\frac{D\frac{\langle u_i u_j\rangle}{k}}{Dt} - \mathcal{D}_{\frac{\langle u_i u_j\rangle}{k}}\right) = 0, \tag{5.3}$$

i.e.,

$$\frac{D\langle u_i u_j\rangle}{Dt} - \mathcal{D}_{\langle u_i u_j\rangle} = \frac{\langle u_i u_j\rangle}{k}\left(\frac{Dk}{Dt} - \mathcal{D}_k\right), \tag{5.4a}$$

$$= \frac{\langle u_i u_j\rangle}{k}\left(\mathcal{P} + \mathcal{G} - \epsilon\right). \tag{5.4b}$$

Similarly, to this hypothesis made on the dynamics, we also consider the weak equilibrium assumption for the turbulent heat fluxes:

$$\sqrt{\langle\theta^2\rangle k}\left(\frac{D\frac{\langle u_i\theta\rangle}{\sqrt{\langle\theta^2\rangle k}}}{Dt} - \mathcal{D}_{\frac{\langle u_i\theta\rangle}{\sqrt{\langle\theta^2\rangle k}}}\right) = 0. \tag{5.5}$$

We have then:

$$\frac{D\langle u_i\theta\rangle}{Dt} - \mathcal{D}_{\langle u_i\theta\rangle} = \frac{\langle u_i\theta\rangle}{\sqrt{\langle\theta^2\rangle k}}\left(\frac{D\sqrt{\langle\theta^2\rangle k}}{Dt} - \mathcal{D}_{\sqrt{\langle\theta^2\rangle k}}\right), \tag{5.6a}$$

$$= \frac{1}{2}\left(\frac{\langle u_i\theta\rangle}{\langle\theta^2\rangle}\left(\frac{D\langle\theta^2\rangle}{Dt} - \mathcal{D}_{\langle\theta^2\rangle}\right) + \frac{\langle u_i\theta\rangle}{k}\left(\frac{Dk}{Dt} - \mathcal{D}_k\right)\right), \tag{5.6b}$$

$$= \frac{\langle u_i\theta\rangle}{2}\left(\frac{\mathcal{P}_{\langle\theta^2\rangle} - \epsilon_{\langle\theta^2\rangle}}{\langle\theta^2\rangle} + \frac{\mathcal{P} + \mathcal{G} - \epsilon}{k}\right). \tag{5.6c}$$

5.1.1.1.3 Production-Dissipation Equilibrium Assumption

Furthermore, a more constraining equilibrium assumption is made for the kinetic energy and the thermal variations. An equilibrium between their production and dissipation is assumed. This is also a classical assumption within the SBL which states:

$$\mathcal{P} + \mathcal{G} = \epsilon, \tag{5.7a}$$

$$\mathcal{P}_{\langle\theta^2\rangle} = \epsilon_{\langle\theta^2\rangle}. \tag{5.7b}$$

This condition imposes that the LHS terms (i.e., the difference between temporal evolution and diffusion) in Eqs 5.4 and Eqs 5.6 are null. Assuming a statistically stationary and horizontally homogeneous flow, the temporal evolution is strictly null, so this assumption corresponds to neglecting the diffusive term on the kinetic energy and on the potential temperature variance. The limit of this hypothesis will be discussed in Paragraph 5.1.3.2.2. It should be noted that, combined with the weak equilibrium hypothesis, this results in the temporal evolution and diffusive terms of the Reynolds tensor and turbulent heat fluxes also being neglected.

Furthermore, under production dissipation equilibrium, it is possible to exhibit a relation between the dissipation rate and the flux Richardson number or the momentum universal function such as:

$$\epsilon = \mathcal{P}\left(1 - Ri_f\right) = \frac{u_*^3}{\kappa z}\left(\varphi_m - \zeta\right) = \frac{u_*^3}{\kappa L_{MO}} \frac{1 - Ri_f}{Ri_f}. \tag{5.8}$$

with the flux Richardson number $Ri_f = -\frac{\mathcal{G}}{\mathcal{P}} = \frac{\zeta}{\varphi_m}$ (see Paragraph 1.2.2.3.2). Furthermore, let us recall that in this situation, we can express the ratio of the production terms over the dissipation rate as a function of the flux Richardson number:

$$\frac{\mathcal{P}}{\epsilon} = \frac{1}{1 - Ri_f}, \tag{5.9a}$$

$$\frac{\mathcal{G}}{\epsilon} = -\frac{Ri_f}{1 - Ri_f}. \tag{5.9b}$$

5.1.1.1.4 Proportionality between Dynamical and Thermal Turbulent Timescale

Moreover, according to Kolmogorov [1941, 1962] theory, we assume that the thermal and turbulence relaxation times are proportional with a factor $\mathcal{C}_\Theta$ constant, given that they are caused by the same physical phenomenon i.e.:

$$\mathcal{C}_\Theta = \frac{\mathcal{T}_k}{\mathcal{T}_\Theta} = \frac{k}{\epsilon} \frac{\epsilon_{\langle\theta^2\rangle}}{2\langle\theta^2\rangle}. \tag{5.10}$$

The equation of $\langle\theta^2\rangle$ Eq. (1.117) under equilibrium assumption can be written:

$$\begin{aligned}
\langle\theta^2\rangle &= \frac{k}{\epsilon}\frac{\epsilon_{\langle\theta^2\rangle}}{2\mathcal{C}_\Theta} = \frac{k}{\epsilon}\frac{\mathcal{P}_{\langle\theta^2\rangle}}{2\mathcal{C}_\Theta}, && (5.11a)\\
&= \frac{k}{\mathcal{C}_\Theta\left(1-Ri_f\right)}\frac{\langle w\theta\rangle\frac{\partial\langle\Theta\rangle}{\partial z}}{\langle uw\rangle\frac{\partial\langle U\rangle}{\partial z}}, && (5.11b)\\
&= \frac{\theta_*^2}{\mathcal{C}_\Theta\left(1-Ri_f\right)}\frac{k}{u_*^2}Pr_t. && (5.11c)
\end{aligned}$$

The question raising is how to set the constant $\mathcal{C}_\Theta$. The derivation of this value to capture the proper turbulent Prandtl number near-neutral situations is presented later in Paragraph 5.1.1.3.3 in the scope of Rotta–Monin model. In the following, the algebraic solutions corresponding to different models will be plotted. First the fully linear LRR-L model proposed by Launder [1975] is plotted with the constants introduced in Table 1.4. The two other models correspond to Rotta–Monin models with respectively $\mathcal{C}_R = 6.25$; $\mathcal{C}_\Theta = 1.875$ and $\mathcal{C}_R = 19$; $\mathcal{C}_\Theta = 5.7$. The two $\mathcal{C}_R$ constants correspond to the value necessary to retrieve the proper production of TKE in neutral situation respectively according to Launder and Spalding [1974] fitted on channel flow or to Duynkerke [1988] fitted on atmospheric flows. The value of $\mathcal{C}_\Theta$ is then obtained in coherence this choice to obtain turbulent Prandtl number of 0.8 in near-neutral flows (see Zilitinkevich et al. [2008], Zilitinkevich et al. [2010], Freire et al. [2019]) as presented later on in Paragraph 5.1.1.3.3.

5.1.1.2 Derivation of Algebraic Model Consistent Universal Functions for the Reynolds Tensor

As a way to determine the appropriate universal functions that are consistent with the chosen model, we will derive the solutions for the corresponding the algebraic model. Only the results obtained using a DRSM-DFM closure which is a second-order closure on both the dynamics and the temperature are presented here. The results obtained using lower order methods are derived in Appendix 5.A.

First considering the Reynolds tensor, one aims at obtaining the equation driving the dynamic aspect of turbulence. The transport equation for the Reynolds tensor is recalled here:

$$\frac{D\langle u_iu_j\rangle}{Dt} - \mathcal{D}_{\langle u_iu_j\rangle} = \underbrace{-\langle u_iu_k\rangle\frac{\partial\langle U_j\rangle}{\partial x_k} - \langle u_ju_k\rangle\frac{\partial\langle U_i\rangle}{\partial x_k}}_{\mathcal{P}_{ij}}\,\underbrace{-g_i\beta_0\langle u_j\theta\rangle - g_j\beta_0\langle u_i\theta\rangle}_{\mathcal{G}_{ij}} + \Pi_{ij} - \epsilon_{ij}. \quad (5.12)$$

Injecting Eq. (5.1) in Eq. (5.12) the modelled transport equation is:

$$\begin{aligned}
\frac{D\langle u_iu_j\rangle}{Dt} - \mathcal{D}_{\langle u_iu_j\rangle} = &-\mathcal{C}_R\epsilon\frac{\langle u_iu_j\rangle}{k} + \frac{2}{3}\left(\mathcal{P}+\mathcal{G}-\epsilon+C_R\epsilon\right)\delta_{ij} + 2C_kkS_{ij},\\
&+\left(1-\mathcal{C}_\mathcal{P}\right)\left(\mathcal{P}_{ij}-\frac{2}{3}\mathcal{P}\delta_{ij}\right) + \left(1-\mathcal{C}_\mathcal{G}\right)\left(\mathcal{G}_{ij}-\frac{2}{3}\mathcal{G}\delta_{ij}\right).
\end{aligned} \quad (5.13)$$

With the two equilibrium assumptions considered the LHS terms are null and the production dissipation-equilibrium ensures that $\mathcal{P}+\mathcal{G}-\epsilon = 0$. Thus, an algebraic model can be derived as:

$$\frac{\langle u_i u_j\rangle}{k} = \frac{2}{3}\delta_{ij} + 2\frac{C_k}{C_R}\frac{kS_{ij}}{\epsilon} + \frac{(1-\mathcal{C}_{\mathcal{P}})}{\mathcal{C}_R}\frac{\mathcal{P}}{\epsilon}\frac{\left(\mathcal{P}_{ij} - \frac{2}{3}\mathcal{P}\delta_{ij}\right)}{\mathcal{P}} + \frac{(1-\mathcal{C}_{\mathcal{G}})}{\mathcal{C}_R}\frac{\mathcal{G}}{\epsilon}\frac{\left(\mathcal{G}_{ij} - \frac{2}{3}\mathcal{G}\delta_{ij}\right)}{\mathcal{G}}. \tag{5.14}$$

Under equilibrium assumption, the production by dissipation ratios are given by Eqs 5.9. Injecting these equations in the previous one, we can write:

$$\begin{aligned}\frac{\langle u_i u_j\rangle}{k} =& \frac{1}{(1-Ri_f)}\left(\left(\frac{2}{3}\delta_{ij} + 2\frac{C_k}{C_R}\frac{k}{u_*^2}\frac{\kappa z S_{ij}}{u_*\varphi_m} + \frac{(1-\mathcal{C}_{\mathcal{P}})}{\mathcal{C}_R}\frac{\left(\mathcal{P}_{ij} - \frac{2}{3}\mathcal{P}\delta_{ij}\right)}{\mathcal{P}}\right)\right.\\ &\left. - Ri_f\left(\frac{2}{3}\delta_{ij} + \frac{(1-\mathcal{C}_{\mathcal{G}})}{\mathcal{C}_R}\frac{\left(\mathcal{G}_{ij} - \frac{2}{3}\mathcal{G}\delta_{ij}\right)}{\mathcal{G}}\right)\right).\end{aligned} \tag{5.15}$$

Component by component this equation reads:

$$\frac{\langle uu\rangle}{k} = \frac{1}{(1-Ri_f)}\left(\frac{2}{3}\frac{\mathcal{C}_R + 2(1-\mathcal{C}_{\mathcal{P}})}{\mathcal{C}_R} - Ri_f\frac{2}{3}\frac{\mathcal{C}_R - (1-\mathcal{C}_{\mathcal{G}})}{\mathcal{C}_R}\right), \tag{5.16a}$$

$$\frac{\langle vv\rangle}{k} = \frac{1}{(1-Ri_f)}\left(\frac{2}{3}\frac{\mathcal{C}_R - 1 + \mathcal{C}_{\mathcal{P}}}{\mathcal{C}_R} - Ri_f\frac{2}{3}\frac{\mathcal{C}_R - (1-\mathcal{C}_{\mathcal{G}})}{\mathcal{C}_R}\right), \tag{5.16b}$$

$$\frac{\langle ww\rangle}{k} = \frac{1}{(1-Ri_f)}\left(\frac{2}{3}\frac{\mathcal{C}_R - 1 + \mathcal{C}_{\mathcal{P}}}{\mathcal{C}_R} - Ri_f\frac{2}{3}\frac{\mathcal{C}_R + 2(1-\mathcal{C}_{\mathcal{G}})}{\mathcal{C}_R}\right), \tag{5.16c}$$

$$\frac{\langle uv\rangle}{k} = 0, \tag{5.16d}$$

$$\frac{\langle vw\rangle}{k} = -Ri_f\frac{(1-\mathcal{C}_{\mathcal{G}})\frac{\langle v\theta\rangle}{\langle w\theta\rangle}}{\mathcal{C}_R\,(1-Ri_f)}, \tag{5.16e}$$

$$\frac{\langle uw\rangle}{k} = \frac{1}{(1-Ri_f)}\left(-\frac{C_k}{C_R}\frac{k}{\langle uw\rangle} + \frac{(1-\mathcal{C}_{\mathcal{P}})}{\mathcal{C}_R}\frac{\langle ww\rangle}{\langle uw\rangle} - Ri_f\frac{1-\mathcal{C}_{\mathcal{G}}}{\mathcal{C}_R}, \frac{\langle u\theta\rangle}{\langle w\theta\rangle}\right). \tag{5.16f}$$

It is worth noticing from the diagonal terms Eq. (5.16a) to Eq. (5.16c) that for a given model of the class selected and a known flux Richardson number the distribution of turbulent kinetic energy might be determined. To simplify the notation and the comprehension, the equation of the diagonal Reynolds tensor components can be written:

$$\frac{\langle uu\rangle}{k} = \frac{1}{(1-Ri_f)}\underbrace{\frac{2}{3}\frac{\mathcal{C}_R + 2(1-\mathcal{C}_{\mathcal{P}})}{\mathcal{C}_R}}_{\lambda_x}\left(1 - Ri_f\underbrace{\frac{\mathcal{C}_R - (1-\mathcal{C}_{\mathcal{G}})}{\mathcal{C}_R + 2(1-\mathcal{C}_{\mathcal{P}})}}_{\mu_x<1}\right) = \lambda_x\frac{1-\mu_x Ri_f}{(1-Ri_f)}, \tag{5.17a}$$

$$\frac{\langle vv\rangle}{k} = \frac{1}{(1-Ri_f)}\underbrace{\frac{2}{3}\frac{\mathcal{C}_R - (1-\mathcal{C}_{\mathcal{P}})}{\mathcal{C}_R}}_{\lambda}\left(1 - Ri_f\underbrace{\frac{\mathcal{C}_R - (1-\mathcal{C}_{\mathcal{G}})}{\mathcal{C}_R - (1-\mathcal{C}_{\mathcal{P}})}}_{\mu_y\sim 1}\right) = \lambda\frac{1-\mu_y Ri_f}{(1-Ri_f)}, \tag{5.17b}$$

$$\frac{\langle ww\rangle}{k} = \frac{1}{(1-Ri_f)}\underbrace{\frac{2}{3}\frac{\mathcal{C}_R - (1-\mathcal{C}_{\mathcal{P}})}{\mathcal{C}_R}}_{\lambda}\left(1 - Ri_f\underbrace{\frac{\mathcal{C}_R + 2(1-\mathcal{C}_{\mathcal{G}})}{\mathcal{C}_R - (1-\mathcal{C}_{\mathcal{P}})}}_{\mu>1}\right) = \lambda\frac{1-\mu Ri_f}{(1-Ri_f)}. \tag{5.17c}$$

In order to have a physical behaviour, a few conditions should be respected by these new constants:

- First, it is necessary to ensure that in neutral situations the TKE distribution is well reproduced and is independent of the modelling selected for the thermal quantities. To this end, one may consider the constants λ_x and λ which represent, for neutral flows, the proportion of TKE respectively in the streamwise direction and in the other directions. These constants should then be positive, which is well respected for $\mathcal{C}_{\mathcal{P}}$ in the range $[0-1]$, and $\mathcal{C}_R > 1$.
- One may then consider the deviation from the neutral state due to thermal effects by comparing the constants μ, μ_x,μ_y to unity.
  - In the normal direction: μ is greater than unity, indicating that the normal component of the Reynolds tensor is decreasing with the flux Richardson number. This condition reflects the fact that for unstable cases the convective effects produce kinetic energy in this direction, whereas they destruct it for stable situations as we can see in Figure 5.1A.
  - In the spanwise direction: the constant μ_y is almost one. The proportion of kinetic energy in this direction does not strongly depend on the stability as evidenced in Figure 5.1B). Indeed, the redistribution of energy is quite similar whether it is produced by the shear stress or by thermal effects. This is emphasised by the value of the constants $\mathcal{C}_{\mathcal{P}}$ and $\mathcal{C}_{\mathcal{G}}$ which are somewhat similar.
  - In the streamwise direction: the constant is below one, highlighting that the proportion of kinetic energy in this direction increases with the stability. In fact, given that the proportion of kinetic energy in the spanwise direction is almost constant, it compensates almost completely for the evolution of kinetic energy ratio in the normal direction as illustrated Figure 5.1C.
- Finally, it is essential to ensure that the diagonal terms of the Reynolds tensor describing the kinetic energy in each direction remain positive. This requires ensuring that the constants μ, μ_y, and μ_x are smaller than $1/Ri_f^{cr}$. In practice, we have $\mu > \mu_y > \mu_x$, so respecting this constraint only along the vertical direction is sufficient.

Remark that, as presented in Eqs 5.17, the relative distribution of kinetic energy in each direction is uniform in stratified flows in the stable limit situation ($Ri_f \to Ri_f^{cr}$) at all heights, but also in the convective limit ($Ri_f \to -\infty$). However, this is not the case outside these limit situations. In fact, local thermal effects, which either kill or produce normal fluctuations, modify the weight of the corresponding component, which is compensated for by the other. As a result, this distribution varies with altitude and the weak equilibrium assumption on the Reynolds tensor Eqs 5.4 is not perfectly verified in such flows. This is a first limitation of the algebraic methods presented here.

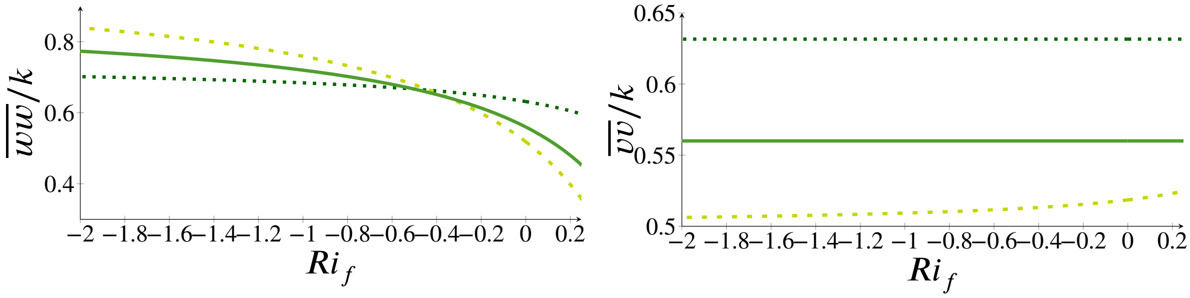

(A) $\langle ww\rangle/k$

(B) $\langle vv\rangle/k$

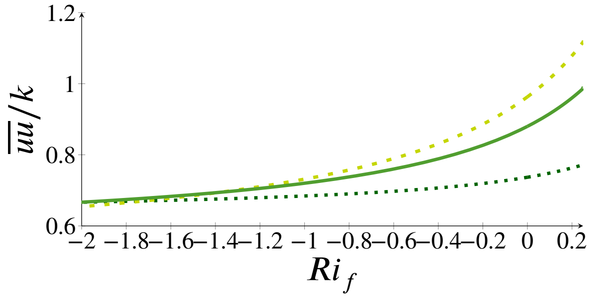

(C) $\langle uu\rangle/k$

Figure 5.1: Algebraic profiles for the distribution of kinetic energy for different models. Results using three different models are compared: the LRR-L model presented in Table 1.4 (- - -), and two Rotta–Monin models respectively with $\mathcal{C}_R = 6.25$, $\mathcal{C}_\Theta = 1.875$ (▬) and $\mathcal{C}_R = 19$, $\mathcal{C}_\Theta = 5.7$ (····).

At this point, preliminary remarks regarding the evolution of the kinetic energy have already been drawn. However, the description of the turbulence has to be completed. Indeed, the value of the kinetic energy has yet to be established. For this purpose, we will focus on the equation of the shear stress Eq. (5.16f) which is constant. Injecting the normal component of the Reynolds tensor in the shear stress equation and replacing the constant fluxes by their values, we get:

$$\frac{u_*^4}{k^2} = -\frac{1}{(1-Ri_f)}\frac{C_k}{C_R} + \frac{\lambda(1-\mathcal{C}_\mathcal{P})}{\mathcal{C}_R}\frac{(1-\mu Ri_f)}{(1-Ri_f)^2} - \frac{Ri_f}{(1-Ri_f)}\frac{(1-\mathcal{C}_\mathcal{G})}{\mathcal{C}_R}\frac{\langle u\theta\rangle}{u_*\theta_*}\frac{u_*^2}{k}, \tag{5.18a}$$

$$\frac{u_*^4}{k^2} = \frac{1}{(1-Ri_f)^2}\left(\underbrace{\frac{\lambda(1-\mathcal{C}_\mathcal{P})-C_k}{\mathcal{C}_R}}_{\alpha_1}\left(1-\frac{\lambda(1-\mathcal{C}_\mathcal{P})\mu}{\lambda(1-\mathcal{C}_\mathcal{P})-C_k}Ri_f\right)+\frac{C_k}{C_R}Ri_f\right) \tag{5.18b}$$

$$- \frac{Ri_f}{(1-Ri_f)}\frac{(1-\mathcal{C}_\mathcal{G})}{\mathcal{C}_R}\frac{\langle u\theta\rangle}{u_*\theta_*}\frac{u_*^2}{k},$$

$$\frac{u_*^4}{k^2} = \frac{\alpha_1\left(1-\overbrace{\left(\frac{\lambda(1-\mathcal{C}_\mathcal{P})\mu}{\lambda(1-\mathcal{C}_\mathcal{P})-C_k}-\frac{C_k}{\mathcal{C}_R\alpha_1}\right)}^{\mu_{xz}}Ri_f\right)}{(1-Ri_f)^2} - \frac{Ri_f}{(1-Ri_f)}\frac{(1-\mathcal{C}_\mathcal{G})}{\mathcal{C}_R}\frac{\langle u\theta\rangle}{u_*\theta_*}\frac{u_*^2}{k}, \tag{5.18c}$$

where $\alpha_1^{-1} \simeq \mathcal{C}_\mu^{-1}$ is the square of the dimensionless kinetic energy in the neutral situation. As we can see on the second RHS terms of this equation, the kinetic energy to shear stress ratio depends on the horizontal turbulent scalar fluxes.

5.1.1.3 Modelling of the Turbulent Heat Fluxes and Impacts on the Dynamics

5.1.1.3.1 Estimation of the Turbulent Heat Fluxes

The Reynolds tensor being coupled not only with the known normal component of the turbulent heat fluxes but also with its horizontal one, we will now focus on the turbulent fluxes to determine the kinetic energy. The transport equation for the turbulent heat fluxes is recalled here:

$$\frac{D\langle u_i\theta\rangle}{Dt} - \mathcal{D}_{\langle u_i\theta\rangle} = \underbrace{-\langle u_j\theta\rangle\frac{\partial\langle U_i\rangle}{x_j}}_{\mathcal{P}^U_{\theta,i}} \underbrace{-\langle u_i u_j\rangle\frac{\partial\langle\Theta\rangle}{x_j}}_{\mathcal{P}^\Theta_{\theta,i}} \underbrace{-\beta_0\langle\theta^2\rangle g_i}_{G_{\theta,i}} + \Pi_{\theta,i} - \epsilon_{\theta,i}, \tag{5.19}$$

Considering the weak equilibrium and the production-dissipation equilibrium the LHS terms are null. The resulting algebraic model is then given by:

$$\langle u_i\theta\rangle = \frac{k}{\epsilon}\left(\frac{1-\mathcal{C}_{\theta_2}}{\mathcal{C}_{\theta_1}}\mathcal{P}^U_{\theta,i} + \frac{1-\mathcal{C}_{\theta'_2}}{\mathcal{C}_{\theta_1}}\mathcal{P}^\Theta_{\theta,i} + \frac{1-\mathcal{C}_{\theta_3}}{\mathcal{C}_{\theta_1}}G_{\theta,i}\right), \tag{5.20}$$

which on each component reads:

$$\langle u\theta\rangle = -\frac{k}{\epsilon}\left(\frac{1-\mathcal{C}_{\theta_2}}{\mathcal{C}_{\theta_1}}\langle w\theta\rangle\frac{\partial\langle U\rangle}{\partial z} + \frac{1-\mathcal{C}_{\theta'_2}}{\mathcal{C}_{\theta_1}}\langle uw\rangle\frac{\partial\langle\Theta\rangle}{\partial z}\right), \tag{5.21a}$$

$$\langle v\theta\rangle = -\frac{k}{\epsilon}\left(\frac{1-\mathcal{C}_{\theta'_2}}{\mathcal{C}_{\theta_1}}\langle vw\rangle\frac{\partial\langle\Theta\rangle}{\partial z}\right), \tag{5.21b}$$

$$\langle w\theta\rangle = -\frac{k}{\epsilon}\left(\frac{1-\mathcal{C}_{\theta'_2}}{\mathcal{C}_{\theta_1}}\langle ww\rangle\frac{\partial\langle\Theta\rangle}{\partial z} - \frac{1-\mathcal{C}_{\theta_3}}{\mathcal{C}_{\theta_1}}g\beta_0\langle\theta^2\rangle\right). \tag{5.21c}$$

Replacing the constant fluxes and the potential temperature gradient by their expressions and injecting the dissipation rate relation Eq. (5.8), the normal component of the Reynolds tensor Eq. (5.17c) and the thermal variance Eq. (5.11c) in the normal turbulent heat fluxes Eq. (5.21c), we can have access to the turbulent Prandtl number:

$$u_*\theta_* = \frac{u_*\theta_*}{(1-Ri_f)^2}\frac{k^2}{u_*^4}\left(\frac{1-\mathcal{C}_{\theta'_2}}{\mathcal{C}_{\theta_1}}\lambda(1-\mu Ri_f)Pr_t - \frac{1-\mathcal{C}_{\theta_3}}{\mathcal{C}_{\theta_1}\mathcal{C}_\Theta}\underbrace{\overbrace{\frac{g\beta_0\theta_*\kappa}{u_*^2}}^{1/L_{MO}}\frac{z}{\varphi_m}}_{Ri_f}Pr_t\right), \tag{5.22a}$$

$$Pr_t = \frac{\varphi_h}{\varphi_m} = \frac{u_*^4}{k^2}\frac{(1-Ri_f)^2}{\underbrace{\frac{1-\mathcal{C}_{\theta'_2}}{\mathcal{C}_{\theta_1}}\lambda}_{\beta_1}\left(1-Ri_f\underbrace{\left(\mu+\frac{1-\mathcal{C}_{\theta_3}}{(1-\mathcal{C}_{\theta'_2})\mathcal{C}_\Theta\lambda}\right)}_{\beta_2}\right)} = \frac{u_*^4}{k^2}\frac{(1-Ri_f)^2}{\beta_1(1-\beta_2 Ri_f)}. \tag{5.22b}$$

In order to ensure that this turbulent Prandtl number is well defined one must ensure that we have $\beta_1 > 0$ and $\beta_2 < 1/Ri_f^{cr}$. Furthermore, injecting the horizontal shear $\langle uv\rangle$ Eq. (5.16d), the dissipation rate Eq. (5.8) and of the turbulent Prandtl number Eq. (5.22b) at equilibrium in the spanwise turbulent fluxes Eq. (5.21b), we get after simplification:

$$\forall Ri_f, \langle v\theta \rangle \left(1 - Ri_f \left(\beta_2 - \frac{1-\mathcal{C}_{\mathcal{G}}}{\lambda \mathcal{C}_R}\right)\right) = 0 \tag{5.23a}$$

$$\langle v\theta \rangle = 0. \tag{5.23b}$$

As expected, the spanwise terms $\langle v\theta \rangle$ and $\langle uv \rangle$ are null as they do not depend on thermal nor shear effects. Furthermore, injecting the known quantities in the streamwise turbulent heat flux, we get:

$$\langle u\theta \rangle = \frac{k}{u_*^2} \frac{u_* \theta_*}{1 - Ri_f} \left(\frac{1-\mathcal{C}_{\theta_2}}{\mathcal{C}_{\theta_1}} + \frac{1}{\lambda} \frac{u_*^4}{k^2} \frac{(1-Ri_f)^2}{(1-\beta_2 Ri_f)} \right). \tag{5.24}$$

5.1.1.3.2 Derivation of the Universal Functions for Turbulent Quantities

For the shear stress, injecting Eq. (5.24) in Eq. (5.18c), we can then obtain:

$$\frac{u_*^4}{k^2} = \frac{1}{(1-Ri_f)^2} \Bigg(\alpha_1 \left(1 - \mu_{xz} Ri_f\right) \tag{5.25a}$$

$$- Ri_f \left(\frac{(1-\mathcal{C}_{\mathcal{G}})}{\mathcal{C}_R} \frac{1-\mathcal{C}_{\theta_2}}{\mathcal{C}_{\theta_1}} + \frac{(1-\mathcal{C}_{\mathcal{G}})}{\mathcal{C}_R} \frac{1-\mathcal{C}_{\theta'_2}}{\mathcal{C}_{\theta_1}} \frac{u_*^4}{k^2} \frac{(1-Ri_f)^2}{\beta_1(1-\beta_2 Ri_f)} \right) \Bigg), \tag{5.25b}$$

$$\frac{u_*^4}{k^2}(1-Ri_f)^2 = \alpha_1 \Bigg(1 - Ri_f \underbrace{\left(\frac{\lambda(1-\mathcal{C}_{\mathcal{P}})\mu}{\lambda(1-\mathcal{C}_{\mathcal{P}}) - \mathcal{C}_k} - \frac{\mathcal{C}_k}{\mathcal{C}_R \alpha_1} + \frac{(1-\mathcal{C}_{\mathcal{G}})(1-\mathcal{C}_{\theta_2})}{\mathcal{C}_R \mathcal{C}_{\theta_1} \alpha_1} \right)}_{\alpha_2} \Bigg)$$

$$- \frac{u_*^4}{k^2} Ri_f \frac{(1-Ri_f)^2}{(1-\beta_2 Ri_f)} \underbrace{\left(\frac{(1-\mathcal{C}_{\mathcal{G}})(1-\mathcal{C}'_{\theta_2})}{\mathcal{C}_R \mathcal{C}_{\theta_1} \beta_1} \right)}_{\alpha_3 = \frac{(1-\mathcal{C}_{\mathcal{G}})}{\lambda \mathcal{C}_R}}, \tag{5.25c}$$

$$\boxed{\varphi_k = \frac{k}{u_*^2} = (1-Ri_f) \sqrt{\frac{(1-(\beta_2-\alpha_3)Ri_f)}{\alpha_1(1-\beta_2 Ri_f)(1-\alpha_2 Ri_f)}}.} \tag{5.25d}$$

The modelling of the Reynolds tensor, turbulent heat fluxes and potential temperature variance allows us to derive a relation between the kinetic energy and the flux Richardson number. As expected, for convective SBLs, the buoyancy effects increase the overall kinetic energy as we observe in Figure 5.2A. For stable cases, the situation is more ambiguous. Notwithstanding the fact that thermal stratification has the effect of suppressing turbulent fluctuations in the normal direction, it has been demonstrated that the TKE also increases in this situation when certain constants are considered. This result, which may appear paradoxical at first glance, is in agreement with experimental data (see, e.g., Nieuwstadt [1984]). This can be explained by the fact that the destruction of normal velocity fluctuations also decreases the shear stress, thus, to maintain a given shear stress more energy is necessary particularly in the streamwise direction.

Furthermore, being a function of the flux Richardson number, which is not uniform, the kinetic energy is not uniform either except in the neutral and stable limits. Thus, the corresponding diffusion term is not null, and the assumption of production-dissipation equilibrium is not exactly respected. Nevertheless, for the time being, we continue to assume that the influence of the diffusion remains relatively minor, and thus the production-equilibrium assumption is still considered.

Injecting the kinetic energy Eq. (5.25) into the relative distribution of TKE Eqs 5.17 we can access the diagonal Reynolds tensor components adimensioned by the shear stress:

$$\boxed{\begin{aligned}
\varphi_{\langle uu\rangle} &= \frac{\langle uu\rangle}{u_*^2} = \lambda_x(1-\mu_x Ri_f)\sqrt{\frac{(1-(\beta_2-\alpha_3)Ri_f)}{\alpha_1(1-\beta_2 Ri_f)(1-\alpha_2 Ri_f)}}, && (5.26a)\\
\varphi_{\langle vv\rangle} &= \frac{\langle vv\rangle}{u_*^2} = \lambda(1-\mu_y Ri_f)\sqrt{\frac{(1-(\beta_2-\alpha_3)Ri_f)}{\alpha_1(1-\beta_2 Ri_f)(1-\alpha_2 Ri_f)}}, && (5.26b)\\
\varphi_{\langle ww\rangle} &= \frac{\langle ww\rangle}{u_*^2} = \lambda(1-\mu Ri_f)\sqrt{\frac{(1-(\beta_2-\alpha_3)Ri_f)}{\alpha_1(1-\beta_2 Ri_f)(1-\alpha_2 Ri_f)}}. && (5.26c)
\end{aligned}}$$

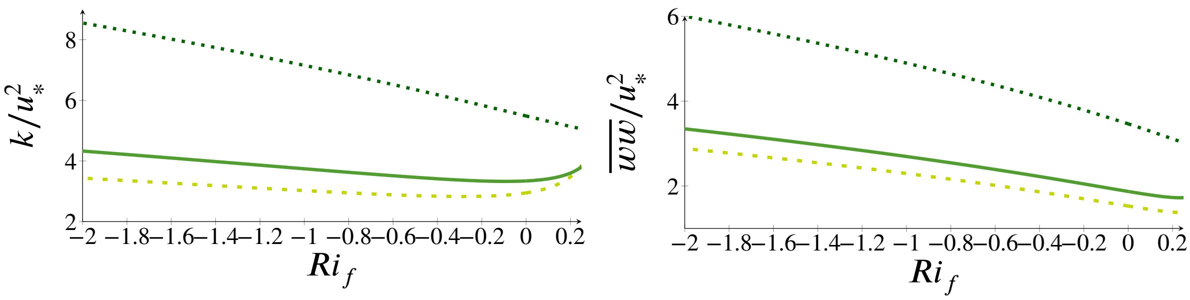

(A) k/u_*^2

(B) $\langle ww\rangle/u_*^2$

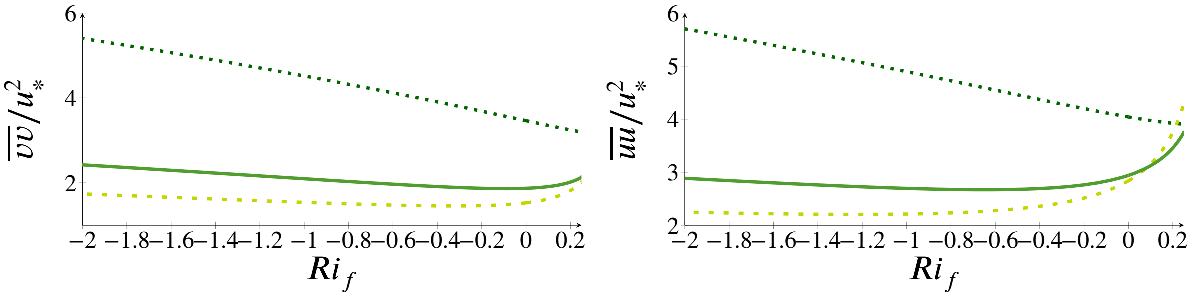

(C) $\langle vv\rangle/u_*^2$

(D) $\langle uu\rangle/u_*^2$

Figure 5.2: Evolution of the kinetic energy and Reynolds tensor diagonal terms with the flux Richardson number for different algebraic models. Results using three different models are compared: the LRR-L model presented in Table 1.4 (- - -), and two Rotta–Monin models respectively with $\mathcal{C}_R = 6.25$, $\mathcal{C}_\Theta = 1.875$ (▬) and $\mathcal{C}_R = 19$, $\mathcal{C}_\Theta = 5.7$ (····).

Furthermore, the universal function of the TKE Eq. (5.25) can be injected respectively in the streamwise turbulent heat fluxes Eq. (5.24), in the turbulent Prandtl number Eq. (5.22b) and in the potential temperature variance Eq. (5.11c) to obtain a relation between these thermal quantities and the flux Richardson number as:

$$\begin{aligned}\varphi_{\langle u\theta\rangle} = \frac{\langle u\theta\rangle}{u_*\theta_*} &= \frac{1-\mathcal{C}_{\theta_2}}{\mathcal{C}_{\theta_1}}\sqrt{\frac{(1-(\beta_2-\alpha_3)Ri_f)}{\alpha_1(1-\beta_2 Ri_f)(1-\alpha_2 Ri_f)}} \\ &\quad + \frac{1}{\lambda}\sqrt{\frac{\alpha_1(1-\alpha_2 Ri_f)}{(1-\beta_2 Ri_f)\,(1-(\beta_2-\alpha_3)Ri_f)}}, \qquad (5.27)\\ Pr_t = \frac{\varphi_h}{\varphi_m} &= \frac{\alpha_1(1-\alpha_2 Ri_f)}{\beta_1\,(1-(\beta_2-\alpha_3)Ri_f)}, \qquad (5.28)\\ \varphi_{\langle\theta^2\rangle} = \frac{\langle\theta\rangle^2}{\theta_*^2} &= \frac{1}{\beta_1\mathcal{C}_\Theta}\sqrt{\frac{\alpha_1(1-\alpha_2 Ri_f)}{(1-\beta_2 Ri_f)\,(1-(\beta_2-\alpha_3)Ri_f)}}. \qquad (5.29)\end{aligned}$$

The corresponding evolution for the turbulent thermal quantities is presented in Figure 5.3

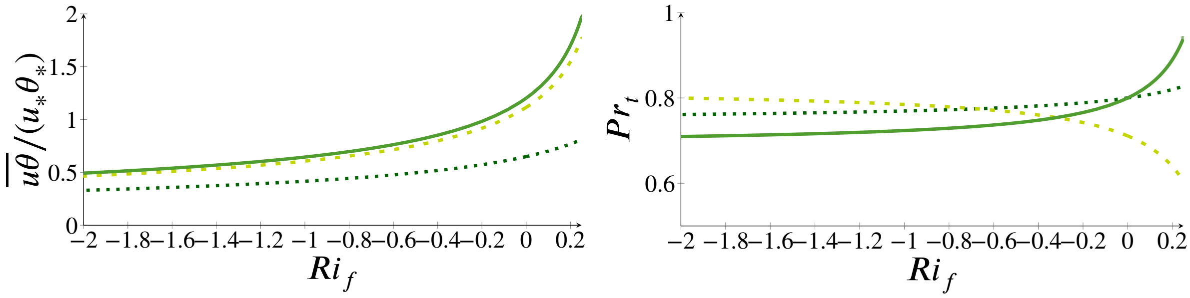

(A) $\langle u\theta\rangle/u_*\theta_*$

(B) Pr_t

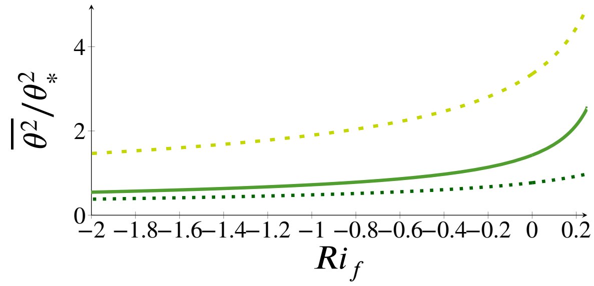

(C) $\langle\theta^2\rangle/\theta_*^2$

Figure 5.3: Evolution of the turbulent heat fluxes with the flux Richardson number for different algebraic models. Results using three different models are compared: the LRR-L model presented in Table 1.4 (- - -), and two Rotta–Monin models respectively with $\mathcal{C}_R = 6.25$, $\mathcal{C}_\Theta = 1.875$ (—) and $\mathcal{C}_R = 19$, $\mathcal{C}_\Theta = 5.7$ (⋯⋯).

Let us take an instant to focus on the asymptotic behaviours of the turbulent quantities derived from Eq. (5.25) to Eq. (5.29). In the stable limit, as the quantities depend solely on the flux Richardson number, which tends towards a finite limit when ζ tends towards infinity, all these quantities tend towards constant value as predicted by Monin–Obukhov theory. Furthermore, in the convective limit the flux Richardson number tends towards minus infinity. It is clear from Eq. (5.25) to Eq. (5.26c) that the diagonal components of the Reynolds tensor expand due to thermal forcing at the expected rate $(-Ri_f)^{1/2}$. Moreover, the potential temperature variance Eq. (5.29) and the normal fluxes Eq. (5.27) decrease also with $(-Ri_f)^{-1/2}$ according to the Monin–Obukhov predictions. In the neutral situation, all the properties converge towards the known neutral values and the dynamics is independent of the modelling selected for the thermal quantities.

5.1.1.3.3 Estimation of the Constant $\mathcal{C}_\Theta$ based on the Near Neutral Turbulent Prandtl Number.

In the near-neutral situation, the algebraic solution for turbulent Prandtl number in the class of models considered Paragraph 5.1.1.1.1 equals to:

$$Pr_t^0 = \frac{\alpha_1}{\beta_1} = \frac{(1-\mathcal{C}_\mathcal{P})}{1-\mathcal{C}_{\theta_2'}}\frac{\mathcal{C}_{\theta_1}}{\mathcal{C}_R} - \frac{3\mathcal{C}_k\mathcal{C}_{\theta_1}}{2(1-\mathcal{C}_{\theta_2'})(\mathcal{C}_R-(1-\mathcal{C}_\mathcal{P}))}. \tag{5.30}$$

This relation might be used to fix some constants in a coherent manner. In the case where a Rotta–Monin model is selected, this equation is simplified into:

$$Pr_t^0 = \frac{\alpha_1}{\beta_1} = \frac{\mathcal{C}_{\theta_1}}{\mathcal{C}_R}. \tag{5.31}$$

Based on modelling consistency, the Lagrangian stochastic counterpart of the Rotta–Monin model is SLM–IEM model. Thus, it results from Eqs 1.228, that considering these models we have $\mathcal{C}_{\theta_1} = \mathcal{C}_{u\theta} = \mathcal{C}_\Theta + \frac{1}{2}\mathcal{C}_R$ and then we retrieve the result obtained by Pozorski et al. [2003a]:

$$\mathcal{C}_\Theta = \mathcal{C}_R(Pr_t^0 - \frac{1}{2}). \tag{5.32}$$

So as to retrieve the value $Pr_t^0 = 0.8$ (see Zilitinkevich et al. [2008], Zilitinkevich et al. [2010], Freire et al. [2019]), given a value $\mathcal{C}_R = 6.25$ to obtain a proper production of kinetic energy we obtain a value $\mathcal{C}_\Theta = 1.875$ which will be our reference value.

5.1.2 Derivation of the Momentum Universal Function issued from the Dissipation Rate Equation

As seen in Section 5.1.1 from Eq. (5.25) to Eq. (5.29), for any modelling of the Reynolds tensor and turbulent heat fluxes in the class treated, algebraic solutions have been found for all second-order statistics. They provide universal functions that depend solely on model constants and on the flux Richardson number. However, the system remains for now unclosed as the latter is still unknown. To close this system, we will consider the modelling of the dissipation rate which will furnish an additional equation. This equation will enable the estimation of the momentum universal function by providing a scale for the distance to the ground. The dissipation rate is governed by:

$$-\mathcal{D}_\epsilon = \frac{\epsilon}{k}\left(\mathcal{C}_{\epsilon_1}\mathcal{P} + \mathcal{G}_\epsilon\right) - \mathcal{C}_{\epsilon_2}\frac{\epsilon^2}{k}, \tag{5.33}$$

where the temporal evolution and advection by mean velocity $\frac{D\epsilon}{Dt}$ is null since we consider a stationary simple sheared flow. However, for the dissipation rate, no local algebraic solution is searched as the diffusion term should be considered. Indeed, it is the only non-local term in the set of equations treated. Therefore, it provides a notion of length scale for the distance to the wall which is necessary to derive the momentum universal function. Then, both the buoyancy effects on the dissipation rate $\mathcal{G}_\epsilon$ and the diffusion term $\mathcal{D}_\epsilon$ must be modelled. The corresponding modelling will be discussed respectively in Section 5.1.2.1 and Section 5.1.2.2. The implicit solution consistent with the modelling considered for this system will be presented in Section 5.1.2.3.

5.1.2.1 Relation between the Modelling of the Buoyant Effects on the Dissipation Rate and Asymptotic Flux Richardson Number

Let us first focus on the treatment of the thermal effects on the dissipation rate. Two models will be presented for this term: first a model linear in $\mathcal{G}$ followed by a model quadratic in $\mathcal{G}$. For each of these models, we will exhibit the value coherent with the asymptotic turbulent behaviour.

5.1.2.1.1 Linear Modelling of the Buoyant Effects on the Dissipation Rate

We first consider the most common modelling of the impacts of the thermal effects on the dissipation rate: $\mathcal{G}_\epsilon = \mathcal{G}_\epsilon^{lin} = \mathcal{C}_{\epsilon 3}\frac{\mathcal{G}\epsilon}{k}$ (see e.g. Wyngaard et al. [1975], Lumley and Khajeh-Nouri [1975]). In stable situations, the destruction of dissipation by buoyancy effects is often considered as negligible compared to the sink term ($\mathcal{C}_{\epsilon_3} = 0$), whereas in unstable situations the production of dissipation by thermal effects has to be considered. Furthermore, in this case, the contributions of thermal and mean strain productions are often considered analogues, resulting in the choice $\mathcal{C}_{\epsilon_3} = \mathcal{C}_{\epsilon_1}$ (see discussion in Hanjalić and Launder [2022]). It is worth noticing that the modelling of this contribution and the value for this constant are still subject to debate. We will consider the two asymptotic limit cases.

Conv. lim. The convective limit case corresponds to the situation encountered on hot days without wind. In this case, the production by shear can be considered null. Thus, we should have an equilibrium between the dissipation rate, the production of energy by thermal effects which is constant in all the domain and finally the TKE diffusion. As presented in Paragraph 1.2.2.3.2, in this situation the latter one should also tend towards a positive constant $\mathcal{D}_k^{-\infty}$ (see Monin and Yaglom [1971][Chapter 7.5]). Thus, at all heights, the dissipation rate equation becomes:

$$\frac{\epsilon}{k}\left(\mathcal{C}_{\epsilon 3}\mathcal{G} - \mathcal{C}_{\epsilon_2}\epsilon\right) = \frac{\epsilon}{k}\mathcal{G}\left(\mathcal{C}_{\epsilon_3} - \mathcal{C}_{\epsilon_2}\left(1 + \frac{\mathcal{D}_k^{-\infty}}{\mathcal{G}}\right)\right) = 0. \tag{5.34}$$

Neglecting the TKE diffusion, in this limit, the dissipation rate is in competition with the production by buoyancy and tends towards the latter. For this reason, it has been chosen to provide similar weight to both these processes by setting $\mathcal{C}_{\epsilon_3} = \mathcal{C}_{\epsilon_2}$. This choice has been made in an optic to obtain a proper decrease of the momentum universal function, considering the approach developed here, as further explained in Paragraph 5.1.2.3.2.

Stable lim. Let us assume a stable boundary layer with the Monin–Obukhov length scale tending positively towards zero. For all heights the dimensionless parameter ζ tends towards infinity and the corresponding Richardson number is equal to its critical value at all heights ($\forall z,\ Ri_f(z) = Ri_f^{cr}$). Then, given Eq. (5.8), ϵ is constant at all heights and its diffusion term is then null. Moreover, the destruction of the dissipation rate by thermal effects is also null, i.e. ($\mathcal{C}_{\epsilon_3} = 0$). The dissipation rate equation is then simplified into:

$$\frac{\epsilon}{k}\left(\mathcal{C}_{\epsilon_1}\mathcal{P} - \mathcal{C}_{\epsilon_2}\mathcal{P}(1 - Ri_f^{cr})\right) = 0, \tag{5.35a}$$

$$\mathcal{C}_{\epsilon_1} = \mathcal{C}_{\epsilon_2}(1 - Ri_f^{cr}), \tag{5.35b}$$

$$Ri_f^{cr} = 1 - \frac{\mathcal{C}_{\epsilon_1}}{\mathcal{C}_{\epsilon_2}}. \tag{5.35c}$$

Thus, the choice of $\mathcal{C}_{\epsilon_1}$ and $\mathcal{C}_{\epsilon_2}$ (respectively, for the production by shear and the dissipation of the dissipation rate) restricts the value of the critical Richardson number (see Duynkerke [1988]). Using the literature value of respectively $C_{\epsilon_1} = 1.44$ and $C_{\epsilon_2} = 1.92$ we get $Ri_f^{cr} = 0.25$ as expected.

5.1.2.1.2 Quadratic Modelling of the Buoyant Effects on the Dissipation Rate

A second proposition made by Wyngaard [1975] for atmospheric flows is to consider that $\mathcal{G}_\epsilon$ is a quadratic function of $\mathcal{G}$ which can be written $\mathcal{G}_\epsilon = \mathcal{G}_\epsilon^{quad} = \mathcal{C}_{\epsilon 3}\mathcal{G} + \mathcal{C}_{\epsilon 4}\frac{\mathcal{G}^2}{\epsilon}$. In doing so, for stable situations where $\mathcal{G}$ is negative, the linear and quadratic terms tend to compensate each other. In contrast, for convective flows, both produce dissipation rate. Such a modelling allows us to keep a single set of constants, no matter the value of the flux Richardson number. In addition, it represents the physics at stake, i.e. the predominant role played by the thermal effect on the dissipation rate in convective situations (see Duynkerke [1988]).

Conv. lim. Let us once more consider the convective asymptotic behaviour. As previously, in this case, the dissipation rate diffusion and the TKE production by shear can be neglected. The dissipation rate equation becomes:

$$\frac{\epsilon}{k}\left(\mathcal{C}_{\epsilon 3}\mathcal{G} + \mathcal{C}_{\epsilon 4}\frac{\mathcal{G}^2}{\epsilon} - \mathcal{C}_{\epsilon 2}\epsilon\right) = 0. \tag{5.36}$$

In absence of TKE diffusion, in this limit, the dissipation rate is in competition only with the production by buoyancy and tends towards the latter. For this reason, it has also been chosen to provide similar weight to both of these processes by setting $\mathcal{C}_{\epsilon_3} + \mathcal{C}_{\epsilon_4} = \mathcal{C}_{\epsilon_2}$. This choice is also made in an optic to obtain a proper decrease in the momentum universal function, considering the approach developed here, as further explained in Paragraph 5.1.2.3.2. Let us note that the production of TKE by buoyant effects is inferior to the dissipation rate under the production-dissipation equilibrium because of the positive sign of the production by shear stress (which here becomes negligible). Thus, with this choice of modelling the production of dissipation rate by thermal effects is weaker than considering a linear modelling of $\mathcal{G}_\epsilon$. It results that the momentum universal function value expected using the quadratic approach is lower in the convective situation than the one obtained with the linear approach.

Stable lim. Let us now focus on the stable asymptotic behaviour. As previously the diffusion effects can be neglected as the dissipation becomes uniform at equilibrium when the flux Richardson number tends towards its critical value Ri_f^{cr}. The dissipation rate equation becomes:

$$\frac{\epsilon^2}{k}\left(\mathcal{C}_{\epsilon 1}\frac{\mathcal{P}}{\epsilon} + \mathcal{C}_{\epsilon 3}\frac{\mathcal{G}}{\epsilon} + \mathcal{C}_{\epsilon 4}\frac{\mathcal{G}^2}{\epsilon^2} - \mathcal{C}_{\epsilon 2}\right) = 0, \tag{5.37a}$$

$$\text{i.e.,} \quad \frac{1}{1 - Ri_f^{cr}}\left(\mathcal{C}_{\epsilon_1} - \mathcal{C}_{\epsilon_3}Ri_f^{cr} + \mathcal{C}_{\epsilon_4}\frac{(Ri_f^{cr})^2}{1 - Ri_f^{cr}} - \mathcal{C}_{\epsilon_2}(1 - Ri_f^{cr})\right) = 0, \tag{5.37b}$$

$$\text{i.e.,} \quad \mathcal{C}_{\epsilon_1} - \mathcal{C}_{\epsilon_2} + (2\mathcal{C}_{\epsilon_2} - \mathcal{C}_{\epsilon_3} - \mathcal{C}_{\epsilon_1})Ri_f^{cr} + (\mathcal{C}_{\epsilon_4} + \mathcal{C}_{\epsilon_3} - \mathcal{C}_{\epsilon_2})(Ri_f^{cr})^2 = 0. \tag{5.37c}$$

In this situation, we consider that all model constants are fixed and we have $\mathcal{C}_{\epsilon_4} + \mathcal{C}_{\epsilon_3} = \mathcal{C}_{\epsilon_2}$. Then, the quadratic term in flux Richardson number disappears and we have:

$$Ri_f^{cr} = \frac{\mathcal{C}_{\epsilon_2} - \mathcal{C}_{\epsilon_1}}{2\mathcal{C}_{\epsilon_2} - \mathcal{C}_{\epsilon_3} - \mathcal{C}_{\epsilon_1}}. \tag{5.38}$$

In this case, the critical value of the flux Richardson number associated with our model depends on three constants namely $\mathcal{C}_{\epsilon_1}$, $\mathcal{C}_{\epsilon_2}$ and $\mathcal{C}_{\epsilon_3}$. As we only want to influence the behaviour of the model regarding the thermal effects without modifying the behaviour in the neutral case, the two first constants will remain unchanged compared to the reference model. It is then possible to obtain $\mathcal{C}_{\epsilon_3}$ as a function of these two constants and of the Ri_f^{cr} as:

$$\mathcal{C}_{\epsilon_3} = \frac{\mathcal{C}_{\epsilon_1} - \mathcal{C}_{\epsilon_2}}{Ri_f^{cr}} + 2\mathcal{C}_{\epsilon_2} - \mathcal{C}_{\epsilon_1}. \tag{5.39}$$

Using as previously $\mathcal{C}_{\epsilon_1} = 1.44$ and $\mathcal{C}_{\epsilon_2} = 1.92$ from Launder and Spalding [1974], and imposing $Ri_f^{cr} = 0.25$ in agreement with the linear model and the experimental estimation, we get $\mathcal{C}_{\epsilon_3} = 0.25\mathcal{C}_{\epsilon_2} = 0.48$ and thus $\mathcal{C}_{\epsilon_4} = \mathcal{C}_{\epsilon_1} = 0.75\mathcal{C}_{\epsilon_2} = 1.44$.

In the following, we will write the equation of ϵ in the most generic form:

$$-\mathcal{D}_\epsilon = \frac{\epsilon^2}{k}\left(\mathcal{C}_{\epsilon_1}\frac{\mathcal{P}}{\epsilon} + \mathcal{C}_{\epsilon_3}\frac{\mathcal{G}}{\epsilon} + \mathcal{C}_{\epsilon_4}\frac{\mathcal{G}^2}{\epsilon^2} - \mathcal{C}_{\epsilon_2}\right). \tag{5.40}$$

with the value of the constants appearing in the RHS terms recalled in Table 5.1.

	$\mathcal{C}_{\epsilon_1}$	$\mathcal{C}_{\epsilon_2}$	$\mathcal{C}_{\epsilon_3}$	$\mathcal{C}_{\epsilon_4}$
$\mathcal{G}_\epsilon^{lin}$	1.44	1.92	$\begin{cases} 1.92 & \text{if } L_{MO} < 0 \\ 0 & \text{if } L_{MO} > 0 \end{cases}$	0
$\mathcal{G}_\epsilon^{quad}$			0.48	1.44

Table 5.1: Coefficient values associated with the two models presented for the RHS of the dissipation rate transport equation.

5.1.2.2 Estimation of Dissipation Rate Diffusion Term

In contrast to the Reynolds stress tensor, the turbulent heat fluxes and the temperature variance, the dissipation rate diffusion term is not neglected outside the two aforementioned limit situations. Knowing the value of this term one can obtain a further equation on the kinetic energy, thereby completing the system of equations. The transport equation of the dissipation rate Eq. (5.33) can then be written:

$$\mathcal{D}_\epsilon = \overbrace{\frac{u_*^6}{k\kappa^2 L_{MO}^2}\left(\frac{1 - Ri_f}{Ri_f}\right)^2}^{\epsilon^2/k} \overbrace{\left(\frac{\mathcal{C}_{\epsilon_2} - \mathcal{C}_{\epsilon_1} - (2\mathcal{C}_{\epsilon_2} - \mathcal{C}_{\epsilon_3} - \mathcal{C}_{\epsilon_1})Ri_f + (\mathcal{C}_{\epsilon_2} - \mathcal{C}_{\epsilon_4} - \mathcal{C}_{\epsilon_3})Ri_f^2}{(1 - Ri_f)^2}\right)}^{-\left(\mathcal{C}_{\epsilon_1}\frac{\mathcal{P}}{\epsilon} + \mathcal{C}_{\epsilon_3}\frac{\mathcal{G}}{\epsilon} + \mathcal{C}_{\epsilon_4}\frac{\mathcal{G}^2}{\epsilon^2} - \mathcal{C}_{\epsilon_2}\right)}, \tag{5.41a}$$

$$\frac{k^3}{u_*^6} = \frac{\mathcal{C}_{\epsilon_2} - \mathcal{C}_{\epsilon_1}}{\kappa^2}\frac{k^2}{\mathcal{D}_\epsilon L_{MO}^2 Ri_f^2}\left(1 - \gamma_1 Ri_f + \gamma_2 Ri_f^2\right), \tag{5.41b}$$

with $\gamma_1 = \frac{2\mathcal{C}_{\epsilon_2} - \mathcal{C}_{\epsilon_3} - \mathcal{C}_{\epsilon_1}}{\mathcal{C}_{\epsilon_2} - \mathcal{C}_{\epsilon_1}}$ $\gamma_2 = \frac{\mathcal{C}_{\epsilon_2} - \mathcal{C}_{\epsilon_4} - \mathcal{C}_{\epsilon_3}}{\mathcal{C}_{\epsilon_2} - \mathcal{C}_{\epsilon_1}}$. Furthermore, the diffusion term has still to be modelled and the results using both the Shir and the Daly–Harlow model are presented here.

Estimation of $\mathcal{D}_\epsilon$ using the Shir Model
We have then to model the diffusion term, considering first the Shir model, it can be written as:

$$\begin{aligned}\mathcal{D}_\epsilon^S &= \frac{\mathrm{d}\left(\mathcal{C}_\epsilon^S \frac{k^2}{\epsilon}\frac{\mathrm{d}\epsilon}{\mathrm{d}z}\right)}{\mathrm{d}z}, \qquad &(5.42\text{a})\\ &= \mathcal{C}_\epsilon^S \frac{k^2}{L_{MO}^2} \frac{1}{Ri_f^2(1 - Ri_f)^2} \underbrace{\left(Ri_f'^2 - Ri_f\left(Ri_f'' + 2Ri_f'^2\right) + Ri_f^2 Ri_f''\right)}_{\mathscr{F}^S(Ri_f)}. \qquad &(5.42\text{b})\end{aligned}$$

Injecting this equation in Eq. (5.41b), it results from the neutral equilibrium that:

$$\mathcal{C}_\epsilon^S = \frac{\mathcal{C}_\mu}{\sigma_\epsilon} = \frac{(\mathcal{C}_{\epsilon_2} - \mathcal{C}_{\epsilon_1})\alpha_1^{3/2}}{\kappa^2}. \tag{5.43}$$

Estimation of $\mathcal{D}_\epsilon$ using the Daly–Harlow Model
In the scope of Daly–Harlow model, we have:

$$\mathcal{D}_\epsilon = \frac{\mathrm{d}\left(\mathcal{C}_\epsilon^{DH} \frac{k}{\epsilon}\langle ww\rangle \frac{\mathrm{d}\epsilon}{\mathrm{d}z}\right)}{\mathrm{d}z}. \tag{5.44}$$

Injecting $\langle ww\rangle/k$ from Eq. (5.17c), one can find:

$$\begin{aligned}\mathcal{D}_\epsilon = \mathcal{C}_\epsilon^{DH}\lambda \frac{k^2}{L_{MO}^2} &\frac{1}{(1 - Ri_f)^3 Ri_f^2}\\ &\underbrace{\left(Ri_f'^2 - Ri_f(Ri_f'' + 3Ri_f'^2) + Ri_f^2(2\mu Ri_f'^2 + Ri_f''(1 + \mu)) - \mu Ri_f^3 Ri_f''\right)}_{\mathscr{F}^{DH}(Ri_f,\mu)}.\end{aligned} \tag{5.45}$$

Injecting this equation in Eq. (5.41b), it results from the neutral equilibrium that:

$$\mathcal{C}_\epsilon^S = \lambda\mathcal{C}_\epsilon^{DH} = \frac{(\mathcal{C}_{\epsilon_2} - \mathcal{C}_{\epsilon_1})\alpha_1^{3/2}}{\kappa^2}. \tag{5.46}$$

5.1.2.3 Analytical Differential Equation for the Flux Richardson Number

5.1.2.3.1 Derivation of the Equation

Two equations have been derived to represent the kinetic energy. The first one Eq. (5.25) is derived in Section 5.1 from the algebraic solution of the shear stress equation. The second one Eq. (5.41b) is obtained in this section from the transport equation of the dissipation rate. Injecting in this equation, the dissipation rate diffusion term estimated either with a Shir model in Eqs 5.42 or treated with a Daly–Harlow model in Eq. (5.45). Using these two equations, we can close the system and we obtain an ordinary differential equation for the flux Richardson number as:

$$\begin{aligned}\mathscr{F}(Ri_f, \upmu)(1-Ri_f)^{1-\updelta_{DH}}\left(1-(\upbeta_2-\upalpha_3)Ri_f\right)^{3/2} \\ = \left(1-\upgamma_1 Ri_f+\upgamma_2 Ri_f^2\right)(1-\upalpha_2 Ri_f)^{3/2}(1-\upbeta_2 Ri_f)^{3/2},\end{aligned} \tag{5.47}$$

with:

$$\mathscr{F}(Ri_f, \mu) = \begin{cases} \mathscr{F}^S(Ri_f) & = Ri_f'^2 - Ri_f\left(Ri_f'' + 2Ri_f'^2\right) + Ri_f^2 Ri_f'' \qquad \text{using Shir model,} \\ \mathscr{F}^{DH}(Ri_f, \upmu) & = Ri_f'^2 - Ri_f(Ri_f'' + 3Ri_f'^2) + Ri_f^2(2\upmu Ri_f'^2 + Ri_f''(1+\upmu)) - \upmu Ri_f^3 Ri_f'' \\ & \quad \text{using Daly–Harlow model,} \end{cases} \tag{5.48}$$

and:

$$\updelta_{DH} = \begin{cases} 0 & \text{using Shir model,} \\ 1 & \text{using Daly–Harlow model.} \end{cases} \tag{5.49}$$

Due to the complex form of this implicit definition, it is not possible to provide an analytical solution for the flux Richardson number. Indeed, this equation is a second-order ordinary differential equation (ODE) due to the second derivative function. The two main difficulties in its resolution reside in the fact that this ODE is non-linear due to the presence of the squared derivative function and product between the flux Richardson and its derivatives. Moreover, polynomial terms of relatively high power are also present. From this equation and the relation $Ri_f(\zeta) = \frac{\zeta}{\varphi_m}(\zeta)$, it is also possible to derive an implicit definition for the momentum universal function. Yet, its structure is more complex making it impossible to determine explicit analytical solutions.

5.1.2.3.2 Analysis of the Asymptotic Behaviour

It is however still possible to study the asymptotic behaviour to ensure that the modelling considered is coherent with the Monin–Obukhov theory.

Neutral limit First, we can notice that the neutral limit is respected as $Ri_f'^2(0) = \frac{1}{\varphi_m^2(0)} = 1$ with $Ri_f = 0$ are solutions of Eq. (5.48). A question arising is then how φ_m evolves near the neutral situation. To this end, for near-neutral stratification, we will consider a first-order Taylor expansion: $\varphi_m = 1 + \varphi_m'(0)\zeta$. As the convective and stable situations correspond to two different turbulent regimes, let us note that the right derivative $\varphi'_m(0)^+$ in stable situations may *a priori* differ from the left derivative $\varphi'_m(0)^-$ for convective cases (see Monin and Yaglom [1971][Chapter 7.3] for further discussion). Keeping only this first-order term in the Taylor expansion and injecting it in Eq. (5.48), we get the relation:

$$1 - \left(2\varphi'_m(0) + 3 + \frac{3}{2}(\beta_2 - \alpha_3)\right)\zeta = 1 - \left(\gamma_1 + \frac{3}{2}(\alpha_2 + \beta_2)\right)\zeta + o(\zeta) \tag{5.50a}$$

$$\varphi'_m(0) = \frac{\gamma_1}{2} + \frac{3}{4}(\alpha_2 + \alpha_3 - 2) \tag{5.50b}$$

Thus, for the derivation of the momentum universal function to be continuous it is necessary for $\mathcal{C}_{\epsilon_3}$ to be constant around zero. This is the case using the quadratic modelling of $\mathcal{G}_\epsilon$. On the contrary, with a linear modelling of $\mathcal{G}_\epsilon$, two different values respectively $\varphi'_m(0^-)$ and $\varphi'_m(0^+)$ may be obtained for the left and right limits. In this case φ_m is expected to be continuous but not its gradient.

Remark 5.1.1. The choice to consider $\mathcal{C}_{\epsilon_4} + \mathcal{C}_{\epsilon_3} = \mathcal{C}_{\epsilon_2}$ has now impact on this Taylor development near-neutral situation. Indeed, without this relation, the additional terms would be neglected due to its higher order.

Stable limit Moreover, through the selection of a first free constant, we have ensured that the stable limit is well respected (see Section 5.1.2.1). Indeed, the flux Richardson number tends towards a critical value Ri_f^{cr}, thus φ_m is linear in ζ with a slope $\left(Ri_f^{cr}\right)^{-1}$

Conv. limit Furthermore, we have ensured that a steady state can be reached when the Richardson number tends negatively towards infinity. This corresponds to a natural convection situation where the mean streamwise velocity and thus the production by shear is null. Thereby we have $\lim\limits_{\zeta\to-\infty} \varphi_m = 0$. We can wonder if the rate of decrease of φ_m imposed by our choice of modelling is correct. For this purpose, we will consider that at high flux Richardson number, the latter one can be considered polynomial and keep only the highest order term such as $(-Ri_f) = \mathcal{C}_{Ri_f}^{-\infty}(-\zeta)^\eta$. As the momentum universal function tends towards zero, we know that η is greater than unity. Thus, keeping only the highest order terms in Eq. (5.48) we get:

$$(-\zeta)^{\frac{11}{2}\eta-2}\left(\mathcal{C}_{Ri_f}^{-\infty}\right)^{\frac{3}{2}}(1+(\mu-1)\delta_{DH})\eta(\eta+1)(\beta_2-\alpha_3)^{\frac{3}{2}} = (-\zeta)^{4\eta}\gamma_1\alpha_2^{\frac{3}{2}}\beta_2^{\frac{3}{2}}+(-\zeta)^{5\eta}\mathcal{C}_{Ri_f}^{-\infty}\gamma_2\alpha_2^{\frac{3}{2}}\beta_2^{\frac{3}{2}} \tag{5.51}$$

With the modelling considered, we have in convetive situations $\gamma_2 = 0$, then we obtain both the polynomial power η and the constant $\mathcal{C}_{Ri_f}^{-\infty}$ as:

$$\begin{cases} \eta = \frac{4}{3}, \\ \mathcal{C}_{Ri_f}^{-\infty} = \frac{\alpha_2\beta_2}{\beta_2-\alpha_3}\left(\frac{9\gamma_1}{28(1+(\mu-1)\delta_{DH})}\right)^{\frac{2}{3}}. \end{cases} \tag{5.52}$$

As we can see the power 4/3 issued of the Monin–Obukhov theory is retrieved. Moreover, the turbulent Prandtl number Eq. (5.28) converging towards a constant value the temperature gradient also converges with the proper rate. Furthermore, as discussed in Paragraph 5.1.1.3.2, all turbulent quantities evolving coherently with the flux Richardson number, which is properly retrieved, their asymptotics is also in agreement with Monin–Obukhov theory.

Remark 5.1.2. In this situation, the choice of the relation $\mathcal{C}_{\epsilon_4} + \mathcal{C}_{\epsilon_3} = \mathcal{C}_{\epsilon_2}$ is of major importance. Indeed, without this choice of modelling, a term of higher order and the power on the RHS of Eq. (5.51) would be 5η. This would result in having $\eta = 4$ i.e., a decrease of the momentum universal function proportionally to $(-\zeta)^3$ way too rapid compared to the expected power of $1/3$.

To sum-up, given an adequate choice of constants for the TKE dissipation rate equation, all asymptotic behaviours agree with the Monin–Obukhov theory. Thus, determining the momentum universal function from the dissipation rate equation seems to be a promising way to close the set of equations considered in a coherent manner. However, given the complexity of Eq. (5.48) no analytical solution has been exhibited. A numerical method will then be used to resolve dissipation rate equation and to furnish the value of momentum universal function as we will see in Section 5.1.2.4.

5.1.2.4 Numerical Estimation of the Momentum Universal Function

5.1.2.4.1 Description of the Iterative Resolution of the Dissipation Rate Equation

So as to have access to a value for the flux-Richardson number, one may want to integrate numerically the dissipation rate equation and then use the relation at the equilibrium between this quantity and the momentum universal function to close the system. The domain is vertically discretised into N cells. Using the divergence theorem, we get:

$$-\left(K_{i+\frac{1}{2}}\left(\frac{\partial \epsilon}{\partial z}\right)_{i+\frac{1}{2}} - K_{i-\frac{1}{2}}\left(\frac{\partial \epsilon}{\partial z}\right)_{i-\frac{1}{2}}\right) = \Delta_z\left(\frac{\epsilon_i}{k_i}\left(\mathcal{C}_{\epsilon_1}\mathcal{P}_i + \mathcal{G}_{\epsilon_i}\right) - \mathcal{C}_{\epsilon_2}\frac{\epsilon_i^2}{k_i}\right), \tag{5.53}$$

where $K_{i+\frac{1}{2}}$ is the turbulent viscosity at the face between the cell i and $i+1$ defined as:

$$K_{i+\frac{1}{2}} = \begin{cases} \frac{\mathcal{C}_\epsilon}{2}\left(\frac{(k_i)^2}{\epsilon_i} + \frac{(k_{i+1})^2}{\epsilon_{i+1}}\right) & \text{using Shir model,} \\ \frac{\mathcal{C}_\epsilon}{2}\left(\frac{(k_i)^2}{\epsilon_i}\frac{1-\mu Ri_{f_i}}{1-Ri_{f_i}} + \frac{(k_{i+1})^2}{\epsilon_{i+1}}\frac{1-\mu Ri_{f_{i+1}}}{1-Ri_{f_{i+1}}}\right) & \text{using Daly–Harlow model.} \end{cases} \tag{5.54}$$

In the bulk of the flow, we can numerically estimate the gradient as:

$$K_{i+\frac{1}{2}}\frac{\epsilon_i - \epsilon_{i+1}}{\Delta_z} + K_{i-\frac{1}{2}}\frac{\epsilon_i - \epsilon_{i-1}}{\Delta_z} = \Delta_z\left(\frac{\epsilon_i}{k_i}(\mathcal{C}_{\epsilon_1}\mathcal{P}_i + \mathcal{C}_{\epsilon_3}\mathcal{G} + \mathcal{C}_{\epsilon_4}\frac{\mathcal{G}^2}{\epsilon_i}) - \mathcal{C}_{\epsilon_2}\frac{\epsilon_i^2}{k_i}\right). \tag{5.55}$$

Keeping all the dissipation and destruction terms implicit (on the LHS) and the production terms explicit (on the RHS), this equation can be written:

$$\begin{aligned} -K_{i+\frac{1}{2}}\epsilon_{i+1} - K_{i-\frac{1}{2}}\epsilon_{i-1} + &\left(K_{i+\frac{1}{2}} + K_{i-\frac{1}{2}} + \mathcal{C}_{\epsilon_2}\frac{\epsilon_i}{k_i}\Delta_z^2 + \max(0, -\mathcal{C}_{\epsilon_3}\frac{\mathcal{G}}{\epsilon_i})\right)\epsilon_i \\ &= \Delta_z^2\frac{\epsilon_i}{k_i}\left(\mathcal{C}_{\epsilon_1}\mathcal{P}_i + \max(0, \mathcal{C}_{\epsilon_3}\mathcal{G}) + \mathcal{C}_{\epsilon_4}\frac{\mathcal{G}^2}{\epsilon_i}\right). \end{aligned} \tag{5.56}$$

On top of the domain, we impose:

$$-K_{top}\left(\frac{\partial \epsilon}{\partial z}\right)_{top} = -K_{top}\left(\frac{\partial \epsilon}{\partial Ri_f}\,\frac{\partial Ri_f}{\partial z}\right)_{top} = K_{top}\frac{u_*^3}{\kappa L_{MO} Ri_{f_{top}}^2}\left(\frac{\partial Ri_f}{\partial z}\right)_{top}, \tag{5.57a}$$

$$\simeq \mathcal{C}_\epsilon^S \frac{k_N^2}{\epsilon_N}\frac{\mathcal{G}}{\Delta_z Ri_{f_N}^2}\left(Ri_{f_{N-1}} - Ri_{f_N}\right). \tag{5.57b}$$

This term should always be positive, so it will be kept implicit.

Moreover, at the lower part of the domain, we can consider that the situation is almost neutral. The boundary condition is treated in coherence with the method used within code_saturne which aims at reaching a second-order accuracy (see Saturne [2023]) :

$$K_{bot}\left(\frac{\partial \epsilon}{\partial z}\right)_{bot} = -\mathcal{C}_\epsilon^S \frac{k_1^2}{\epsilon_1}\frac{u_*^3}{\kappa(0.25\Delta_z + z_0)^2}. \tag{5.58}$$

Let us note that the treatment of the dissipation flux near wall is cumbersome, as we want to study its behaviour in the vicinity of a singular point. This leads to a relatively high numerical error which can be lowered by resolving a quantity such as the turbulent timescale $\mathcal{T}_k = \frac{k}{\epsilon}$ (see e.g., Speziale et al. [1992]) or the turbulent Reynolds number $Re_t = \frac{k^2}{\epsilon\nu}$ (see e.g., Zhang et al. [2020]). Indeed, these quantities tend smoothly towards zero and may therefore be numerically estimated with greater accuracy. Yet, in order to remain as close as possible to the solution obtained with the CFD solver, this resolution based on the dissipation rate is maintained. This system can then be written as:

$$\underbrace{\begin{pmatrix}
\Lambda_1 & -K_{1.5} & & & & & \\
-K_{1.5} & \Lambda_2 & -K_{2.5} & & & & \\
 & \ddots & \ddots & \ddots & & & \\
 & & -K_{i-\frac{1}{2}} & \Lambda_i & -K_{i+\frac{1}{2}} & & \\
 & & & \ddots & \ddots & \ddots & \\
 & & & & -K_{N-1.5} & \Lambda_{N-1} & -K_{N-\frac{1}{2}} \\
 & & & & & -K_{N-\frac{1}{2}} & \Lambda_N
\end{pmatrix}}_{\underline{\underline{\boldsymbol{M}}}}
\underbrace{\begin{pmatrix}
\epsilon_1 \\ \epsilon_2 \\ \vdots \\ \epsilon_i \\ \vdots \\ \epsilon_{N-1} \\ \epsilon_N
\end{pmatrix}}_{\underline{\boldsymbol{\epsilon}}}
=
\underbrace{\begin{pmatrix}
\frac{k_1^2}{\epsilon_1}\frac{\mathcal{C}_\epsilon u_*^3}{\kappa(0.25\Delta_z+z_0)^2} + \frac{\epsilon_1}{k_1}\left(\mathcal{C}_{\epsilon_1}\mathcal{P}_1 + \max(0,\mathcal{C}_{\epsilon_3}\mathcal{G}) + \mathcal{C}_{\epsilon_4}\frac{\mathcal{G}^2}{\epsilon_1}\right)\Delta_z^2 \\
\frac{\epsilon_2}{k_2}\left(\mathcal{C}_{\epsilon_1}\mathcal{P}_2 + \max(0,\mathcal{C}_{\epsilon_3}\mathcal{G}) + \mathcal{C}_{\epsilon_4}\frac{\mathcal{G}^2}{\epsilon_2}\right)\Delta_z^2 \\
\vdots \\
\frac{\epsilon_i}{k_i}\left(\mathcal{C}_{\epsilon_1}\mathcal{P}_i + \max(0,\mathcal{C}_{\epsilon_3}\mathcal{G})\mathcal{C}_{\epsilon_4}\frac{\mathcal{G}^2}{\epsilon_i}\right)\Delta_z^2 \\
\vdots \\
\frac{\epsilon_{N-1}}{k_{N-1}}\left(\mathcal{C}_{\epsilon_1}\mathcal{P}_{N-1} + \max(0,\mathcal{C}_{\epsilon_3}\mathcal{G}) + \mathcal{C}_{\epsilon_4}\frac{\mathcal{G}^2}{\epsilon_{N-1}}\right)\Delta_z^2 \\
\frac{\epsilon_N}{k_N}\left(\mathcal{C}_{\epsilon_1}\mathcal{P}_+ \max(0,\mathcal{C}_{\epsilon_3}\mathcal{G}) + \mathcal{C}_{\epsilon_4}\frac{\mathcal{G}^2}{\epsilon_N}\right)\Delta_z^2
\end{pmatrix}}_{\underline{\boldsymbol{RHS}}}, \tag{5.59}$$

where we have:

$$\Lambda_i = \begin{cases}
K_{1.5} + \frac{\epsilon_1}{k_1}\Delta_z^2\left(\mathcal{C}_{\epsilon_2} + \max(0, -\mathcal{C}_{\epsilon_3}\frac{\mathcal{G}}{\epsilon_1})\right) & \text{if} \quad i = 1, \\
K_{i-\frac{1}{2}} + K_{i+\frac{1}{2}} + \frac{\epsilon_i}{k_i}\Delta_z^2\left(\mathcal{C}_{\epsilon_2} + \max(0, -\mathcal{C}_{\epsilon_3}\frac{\mathcal{G}}{\epsilon_i})\right) & \text{if} \quad 1 < i < N, \\
K_{N-\frac{1}{2}}\frac{\epsilon_N}{k_N}\Delta_z^2\left(\mathcal{C}_{\epsilon_2} + \max(0, -\mathcal{C}_{\epsilon_3}\frac{\mathcal{G}}{\epsilon_N})\right) + \mathcal{C}_\epsilon^S\frac{k_N^2}{\epsilon_N^2}\frac{\mathcal{G}}{\Delta_z Ri_{f_N}^2}\left(Ri_{f_{N-1}} - Ri_{f_N}\right) & \text{if} \quad i = N.
\end{cases} \tag{5.60}$$

This system can simply be written:

$$\underline{\underline{\boldsymbol{M}}}\;\underline{\boldsymbol{\epsilon}} = \underline{\boldsymbol{RHS}}, \tag{5.61}$$

where $\underline{\underline{\boldsymbol{M}}}$ is reversible as it is a diagonally dominant matrix. We should then resolve:

$$\underline{\boldsymbol{\epsilon}} = \underline{\underline{\boldsymbol{M}}}^{-1}\ \underline{\boldsymbol{RHS}}. \tag{5.62}$$

Once the dissipation rate is obtained it is possible to access the flux Richardson number at equilibrium as:

$$Ri_f = \frac{-1}{\left(\frac{\epsilon}{\mathcal{G}} - 1\right)}. \tag{5.63}$$

However, $\underline{\underline{\boldsymbol{M}}}$ and $\underline{\boldsymbol{RHS}}$ being functions of ϵ, we have to use an iterative process to solve this equation using the superscript n to denote the iteration index.

5.1.2.4.2 Constraints on the Flux Richardson Number

Before convergence of the iterative process, it is possible for the equilibrium assumption not to be fulfilled. In order to avoid getting non-physical results based on non-physical intermediate values for the Richardson number, further constraints should be imposed.

Cond. 1 The dissipation rate should remain positive:

$$\epsilon > 0 \tag{5.64}$$

Cond. 2 Since the production induced by shear is positive, the flux Richardson number and the production by convection should be of opposite signs:

$$Ri_f \mathcal{G} < 0, \tag{5.65}$$

Cond. 3 The Richardson number is upper bounded by a critical value Ri_f^{cr}:

$$Ri_f < Ri_f^{cr}. \tag{5.66}$$

We will evaluate the consequences of these conditions for both stable and unstable situations:

Stable sit. In the stable case, the convective effects tend to dump the kinetic energy, i.e. $\mathcal{G} < 0$. Compliance with the first condition implies then compliance with the second. The third condition requires in each point i and at each iteration n to have:

$$\frac{1}{\left(1 - \frac{\epsilon_i^n}{\mathcal{G}}\right)} < Ri_f^{cr}, \tag{5.67}$$

$$\epsilon_i^n > \mathcal{G}\left(1 - \frac{1}{Ri_f^{cr}}\right) \geq 0. \tag{5.68}$$

This last condition is the most restrictive, and is the one that should be in place.

Conv. sit. In this case the convective effects tend to fuel the kinetic energy, i.e., $\mathcal{G} > 0$. The second condition, requiring the Richardson number to be negative, is the most constraining ($Ri_f^{cr} > 0 > Ri_f$). It is therefore sufficient to ensure that the dissipation is greater than the production by convection at each point i and at each iteration n :

$$\epsilon_i^n > \mathcal{G} > 0 \tag{5.69}$$

To ensure that the system under consideration respects Eq. (5.68) and Eq. (5.69) which can be both written $\epsilon^n_i > \mathcal{G}d \geq 0$, the term $\underline{\widehat{\boldsymbol{\epsilon^n}}} = \underline{\boldsymbol{\epsilon^n}} - \mathcal{G}d\underline{\boldsymbol{I}}$ is made implicit. We have then:

$$-K^n_{i+\frac{1}{2}}(\epsilon^{n+1}_{i+1} - \mathcal{G}d) - K^n_{i-\frac{1}{2}}(\epsilon^{n+1}_{i-1} - \mathcal{G}d) + \widehat{\Lambda^n_i}(\epsilon^{n+1}_i - \mathcal{G}d) = \delta_z^2 \frac{\epsilon^n_i}{k^n_i}\left(\mathcal{C}_{\epsilon_1}\mathcal{P}^n_i + \max\left(0, \mathcal{C}_{\epsilon_3}\mathcal{G}\right)\right), \tag{5.70}$$

with :

$$\widehat{\Lambda^n_i} = K^n_{i+\frac{1}{2}} + K^n_{i-\frac{1}{2}} + \frac{\epsilon^n_i}{k^n_i}\delta_z^2\left(\mathcal{C}_{\epsilon_2}\left(1 + \frac{\mathcal{G}d}{\epsilon^n_i - \mathcal{G}d}\right) + \max\left(0, -\mathcal{C}_{\epsilon_3}\frac{\epsilon^n_i}{\epsilon^n_i - \mathcal{G}d}\right)\right) \tag{5.71}$$

The system resolved is then:

$$\underline{\widehat{\boldsymbol{\epsilon^{n+1}}}} = (\underline{\underline{\widehat{\boldsymbol{M^n}}}})^{-1}\underline{\boldsymbol{RHS^n}}. \tag{5.72}$$

The matrix $\underline{\underline{\widehat{\boldsymbol{M^n}}}}$ being a diagonally dominant matrix and all components of $\underline{\boldsymbol{RHS^n}}$ being positive, this resolution ensures that all components of $\underline{\widehat{\boldsymbol{\epsilon^n}}}$ remain positive. Thus, the respect of the three conditions presented is ensured by resolving $\underline{\widehat{\boldsymbol{\epsilon^n}}}$ instead of $\underline{\boldsymbol{\epsilon^n}}$.

5.1.2.4.3 Numerical Corrections near Ground

In the purpose of exhibiting universal functions, let us consider a Rotta–Monin model with respectively $\mathcal{C}_R = 6.25$ to retrieve the proper production of TKE in neutral case, and $\mathcal{C}_\Theta = 1.875$ selected in coherence with $\mathcal{C}_R$ so as to retrieve $Pr^0_t = 0.8$. This choice of model for the fluctuating pressure induced redistributive terms is made in coherence with the SLM–IEM model selected within the Lagrangian stochastic methods. Furthermore, a Shir model is kept for the diffusion term. Using the iterative process presented in this section, a 1-D 100 m high SBL is modelled with 100 cells, for neutral stable and unstable situations with respectively a Monin–Obukhov length scale $L_{MO} = \infty$, $L_{MO} = 20$, and $L_{MO} = -20$.

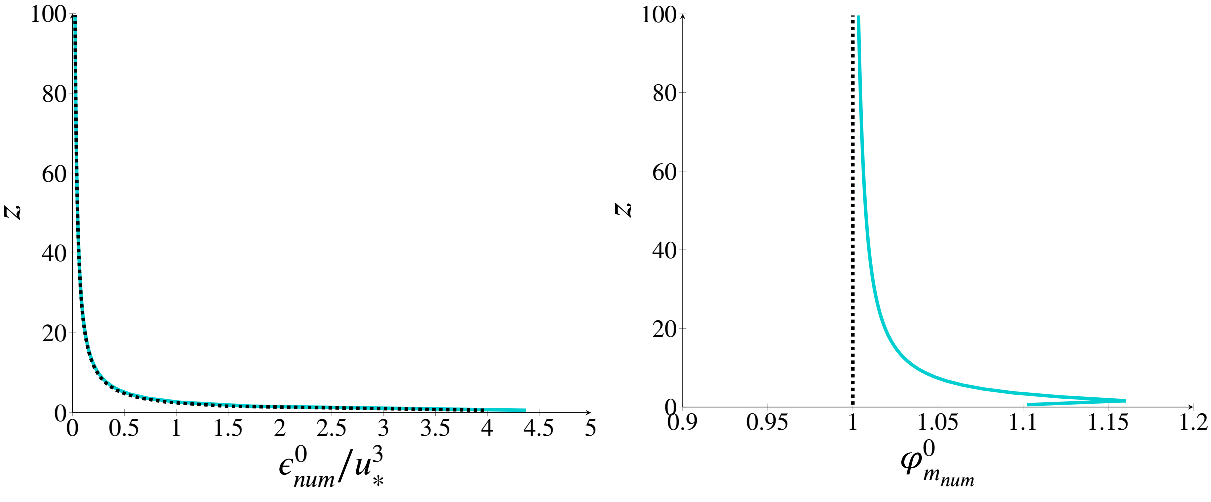

(A) Dissipation rate ϵ.

(B) Momentum universal function φ_m.

Figure 5.4: Vertical profiles obtained with the iterative process presented for neutral situation. These results (—) are compared to the analytical solution (.....).

Let us note that the results obtained are impaired by numerical error even in the neutral case. Indeed, as we can see in Figure 5.4, where a 1-D the numerical solution $\underline{\boldsymbol{\epsilon}}^0_{num}$ tends to be

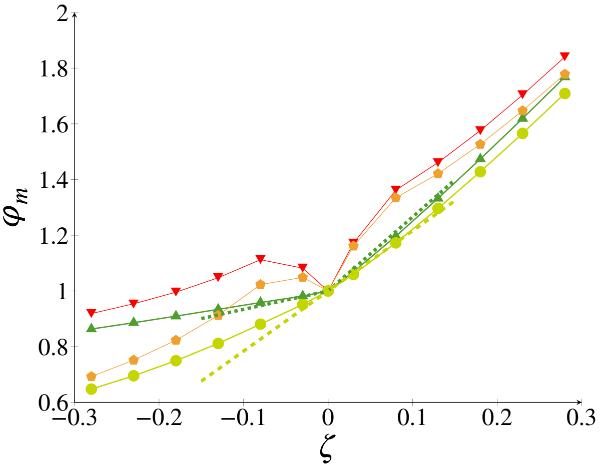

Figure 5.5: Focus on the near-neutral momentum universal function profiles obtained using the iterative methods presented resolving respectively a 100 m high convective and stable SBL with 100 cells and $|L_{MO}| = 20$ m. The results before correction using the linear modelling of the thermal term (▼—▼) and quadratic modelling (⬟—⬟) are compared to their corrected version respectively (▲—▲) and (●—●). These results are also compared to the expected behaviour from the first-order Taylor expansion presented in Eq. (5.50b), respectively (····) and (- - -).

overestimated near ground. In this case, the momentum universal function is derived from this estimation of the dissipation rate as $\varphi^0_{m_{num}}(z) = \frac{\epsilon^0_{num}(z)\kappa z}{u_*^3}$. It is not constant nor equal to one but noticeably overestimated near ground as shown in Figure 5.4B. $\varphi^0_{m_{num}}(z)$ can be seen as a measure of the numerical error resulting from the treatment of the flux of dissipation rate at the bottom of the domain. For this reason, it is expected to obtain better results, using methods transporting of the turbulent timescale $\mathcal{T}_k = \frac{k}{\epsilon}$ instead of the dissipation rate as this timescale has a smoother behaviour near wall (see as proposed by Speziale et al. [1992]). This error in the estimation of the dissipation rate near ground also impacts the results obtained in this zone in thermally stratified situations.

As we can see in Figure 5.5, it results in a spurious overestimation of the universal function in the vicinity of the wall. As the velocity gradient evolves proportionally to φ_m/z, the shape of the momentum function in the vicinity of the ground is of major importance. To mitigate the error near ground, a correction is proposed. It is based on the fact that, near ground, the flow can be considered almost neutral. Thus, the numerical error impacting the resolution of $\underline{\boldsymbol{\epsilon}}_{num}$ is close to its counterpart in neutral flows $\underline{\boldsymbol{\epsilon}}^0_{num}$. In order to measure the altitude over which we can consider the thermal effects sufficiently small to have a flow somewhat similar to the neutral situation, we can simply use the Monin–Obukhov length derived in this precise purpose. Then a blending is proposed as a post-treatment of the value obtained from the iterative process:

$$\epsilon^{cor}_{num_i} = \frac{\epsilon_{num_i}}{\varphi^0_{m_{num}}(z_i)e^{-\left|\frac{z_i}{L_{MO}}\right|} + \left(1 - e^{-\left|\frac{z_i}{L_{MO}}\right|}\right)}. \tag{5.73}$$

With this correction the slope near ground is better retrieved, as we can see in Table 5.2. We can compare the numerical gradient obtained with the asymptotic one Eq. (5.50b) corresponding to the implicit solution Eq. (5.48). The correction proposed enables to obtain a smoother more physical solution keeping in mind that the momentum universal function is meant to be a strictly increasing function of ζ. Yet the numerical estimation seems to underestimate the slope theoretically expected, especially with a quadratic modelling of the buoyant effects on the dissipation rate as shown in 5.2. Moreover, the expected near-neutral momentum universal function gradients are small compared to literature ones Eqs 1.155 to Eqs 1.159 which all agree for a value close to 4.75. Let us note that other choice of modelling would provide other solutions, yet, the standard LRR-IP modelling 1.4 provides similar value for the near-neutral gradients increased by around 0.4.

	$\varphi'_m(0^-)$			$\varphi'_m(0^+)$		
	theor. Eq. (5.50b)	num. cor.	num. uncor.	theor. Eq. (5.50b)	num. cor.	num. uncor.
$\mathcal{G}_\epsilon^{lin}$	0.6607	0.62	-2.73	2.6607	2.29	5.72
$\mathcal{G}_\epsilon^{quad}$	2.1607	1.62	-1.63	2.1607	1.97	5.38

Table 5.2: Theoretical and numerical values for the gradient of φ_m in near-neutral situation obtained resolving respectively a 100 m high convective and stable SBL with 100 cells and $|L_{MO}| = 20$ m.

Finally, the whole iterative process can be summed up as follows:

```
Input:
  Physical properties: domain size $H$, Monin-Obukhov length $L_{MO}$, friction velocity $u_\star$
  Modelling choices: model constants $(\alpha_i,\ \beta_i)$, and model for the diffusion of $\epsilon$
  Numerical choices: threshold $\xi$, cell number $N$
  ------------------------------------------------------------
  Initialize iteration id n = 1
  Compute buoyant term $\mathcal{G} = -\frac{u_*^3}{\kappa L_{MO}}$ and $d$ depending on $L_{MO}$ (see Eq. (5.68) and Eq. (5.69))
  Initialization based on the neutral state i.e, $\epsilon_i^1 = \frac{u_*^3}{\kappa (i-0.5)\frac{H}{N}} + \mathcal{G}d$
  ------------------------------------------------------------
  do
      Estimate $\boldsymbol{Ri_f^n}$ based on $\underline{\boldsymbol{\epsilon^n}}$ and the relation under equilibrium assumption Eq. (5.8)
      Estimate $\underline{\boldsymbol{k^n}}(\underline{\boldsymbol{Ri_f^n}})$ based on algebraic model Eq. (5.25)
      Estimate $\widehat{\underline{\underline{\boldsymbol{M^n}}}}(\underline{\boldsymbol{\epsilon^n}}, \underline{\boldsymbol{k^n}})$ and $\widehat{\underline{\boldsymbol{RHS^n}}}(\underline{\boldsymbol{\epsilon^n}}, \underline{\boldsymbol{k^n}})$ Eq. (5.70) and Eq. (5.71)
      Inverse the system $\widehat{\underline{\boldsymbol{\epsilon^{n+1}}}} = \left(\widehat{\underline{\underline{\boldsymbol{M^n}}}}\right)^{-1} \cdot \underline{\boldsymbol{RHS^n}}$
      Estimate $\underline{\boldsymbol{\epsilon^{n+1}}} = \widehat{\underline{\boldsymbol{\epsilon^{n+1}}}} + \mathcal{G}d$
      Increment the iteration id: n++
  while Convergence is not reached i.e. max(abs($\underline{\boldsymbol{\epsilon^n}} - \underline{\boldsymbol{\epsilon^{n-1}}}$)) > $\xi$
  ------------------------------------------------------------
  Correct $\underline{\boldsymbol{\epsilon^n}}$ based on $\underline{\boldsymbol{\varphi^0_{m_{num}}}}$ (get by using this algorithm with $L_{MO} = \infty$) and Eq. (5.73)
  Estimate universal functions based on equilibrium assumption Eq. (5.8) and algebraic solutions of the model selected from Eq. (5.25) to Eq. (5.29)
  ------------------------------------------------------------
Output:
```

Physical quantities on the mesh: $\underline{\boldsymbol{\varphi_m}}$, $\underline{\boldsymbol{\varphi_h}}$, $\underline{\boldsymbol{Ri_f}}$, $\underline{\boldsymbol{Pr_t}}$,$\underline{\boldsymbol{k}}$, $\underline{\boldsymbol{\langle uu\rangle}}$, $\underline{\boldsymbol{\langle vv\rangle}}$, $\underline{\boldsymbol{\langle ww\rangle}}$, $\underline{\boldsymbol{\epsilon}}$, $\underline{\boldsymbol{\theta^2}}$, $\underline{\boldsymbol{\langle u\theta\rangle}}$.;

5.1.3 Verification of the Universal Functions Derived

5.1.3.1 Momentum Universal Function Derived from the Iterative Method

We will now examine the solutions derived from the iterative solver. Considering that the TKE is at equilibrium we simply have: $\varphi_m = \varphi_\epsilon + \zeta$ with $\varphi_\epsilon = \frac{\epsilon\kappa z}{u_*^3}$. The results displayed are obtained using the simulations presented in Section 5.1.2.4.3. Most of the difference between the two models of the buoyant term appears in the convective context as illustrated in Figure 5.7. Indeed, as expected, in this situation, the quadratic modelling of the buoyant term results in a reduction in the production of dissipation rate compared to a linear modelling. Thus, the corresponding momentum universal function is also diminished. Furthermore, as demonstrated in Figure 5.6A, the asymptotic decrease of both these solutions is proportional to $\zeta^{-1/3}$. In this figure, in order to substantiate this proper rate of decrease, additional simulations are carried out until larger values of ζ (in norm) are reached. This decrease, coherent with Monin–Obukhov theory, is faster than the one proposed by Businger et al. [1971] and Högström [1988] who assumed a power -1/4. As previously stated, Figure 5.7A shows that, in the close vicinity of neutral situations, the slope of the model-consistent universal functions is less steep than the one experimentally encountered. Yet, in the stable case, as these solutions are coherently modelled to avoid crossing of the critical fluxes Richardson number, they increase faster than literature profiles which do not respect this constraint as shown in Figure 5.7C and Figure 5.6B. As the momentum universal function converged well so does the flux Richardson number. Moreover, as discussed in Section 5.1.1, all the turbulent quantities converge coherently with the flux Richardson number, and then also with ζ. Thus, all the quantities characterising the flow seem to converge adequately with the assumption considered.

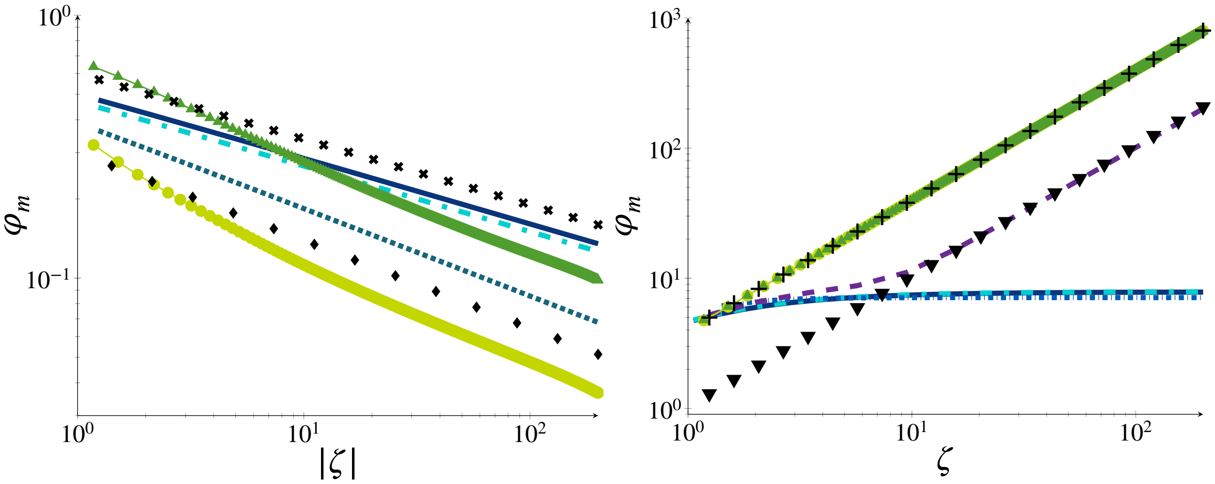

(A) Convective case.

(B) Stable case.

Figure 5.6: Asymptotic profiles for the momentum universal function derived by resolving an iterative process on the dissipation rate in coherence with the algebraic solutions of the Rotta–Monin model with $\mathcal{C}_R = 6.25$ and $\mathcal{C}_\Theta = 1.875$. Two universal profiles are derived either considering a linear modelling of the dissipation rate buoyant term (▲—▲) or a quadratic modelling of this term (●—●). These functions are compared with the literature universal functions: Businger et al. [1971] (▬▬); Carl et al. [1973] (▪▪▪▪▪); Högström [1988] (▬ ▪); Chenge and Brutsaert [2005] (▪·▪·▪); Hartogensis and De Bruin [2005] (▬ ▬). To estimate the proper asymptotic behaviours, the functions $\varphi_m = \zeta$ (▼); $\varphi_m = \zeta/Ri_f^{cr}$ (+) with $Ri_f^{cr} = 0.25$ are plotted in the stable case as well as the functions $\varphi_m = 0.6|\zeta|^{-1/4}$ (✖) and $\varphi_m = 0.3|\zeta|^{-1/3}$ (◆) in the convective case. Theoretical asymptotic behaviours are retrieved.

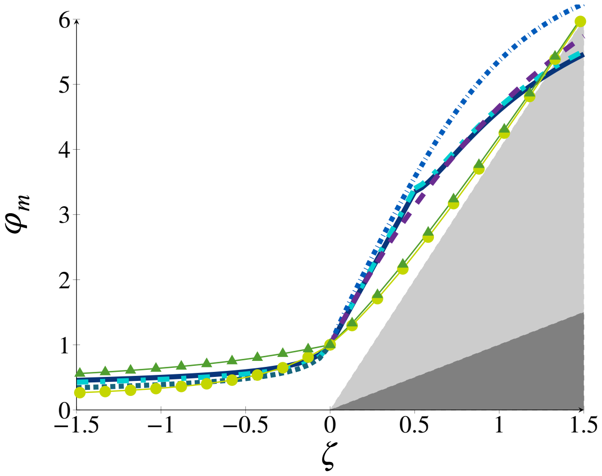

(A) Near neutral case.

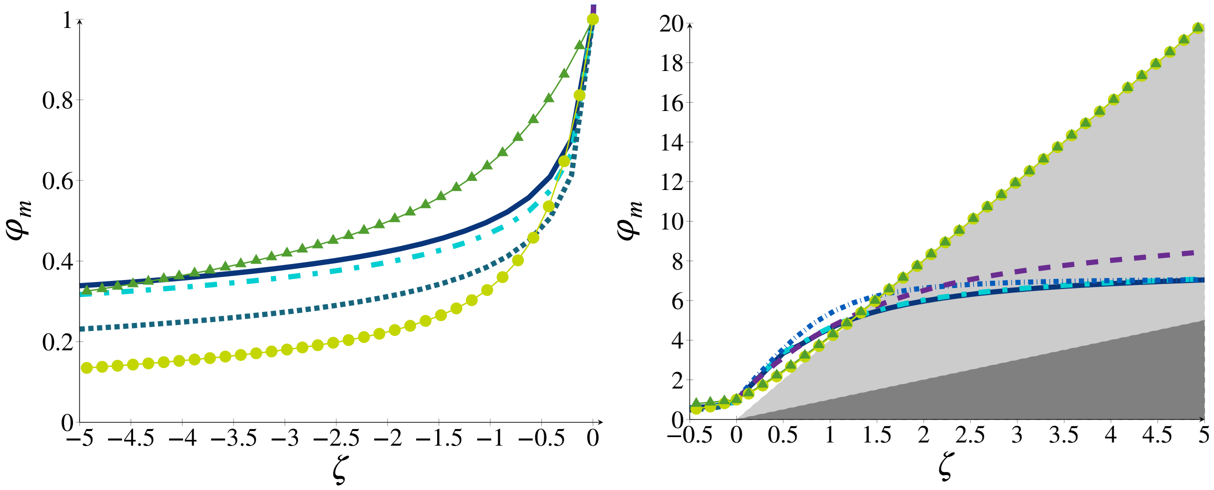

(B) Convective case.

(C) Stable case.

Figure 5.7: Profiles for the momentum universal function derived by resolving an iterative process on the dissipation rate in coherence with algebraic solutions of the Rotta–Monin model with $\mathcal{C}_R = 6.25$ and $\mathcal{C}_\Theta = 1.875$. Two universal profiles are derived either considering a linear modelling of the dissipation rate buoyant term (▲—▲) or a quadratic modelling of this term (●—●). These functions are compared with the literature universal functions: Businger et al. [1971] (▬▬); Carl et al. [1973] (▪▪▪▪▪); Högström [1988] (▬ ▪); Chenge and Brutsaert [2005] (▪·▪·▪); Hartogensis and De Bruin [2005] (▬ ▬). The light grey zone represents the area defined by $Ri_f > Ri_f^{cr}$ with $Ri_f^{cr} = 0.25$, and the dark grey one the area defined by $Ri_f > 1$, both these zones should be inaccessible to universal functions.

5.1.3.2 Comparison with CFD results obtained with code_saturne

A numerical derivation of all the turbulent and mean profiles, characterising stratified SBL flows has been obtained in agreement with the modelling selected and the underlying algebraic solutions. In this context, all the diffusive terms have been neglected except for the dissipation rate where a Shir model is considered. The goal of the present section is to compare the aforementioned profiles with the solutions of the CFD solver code_saturne. In the latter, unless otherwise stated, diffusive terms are also computed for the Reynolds tensor, the turbulent heat fluxes and the potential temperature variance. All these terms will be computed using the isotropic assumption of the Shir model. We will focus on the most common linear modelling of the buoyant effects on the dissipation rate keeping however $\mathcal{C}_{\epsilon_3} = \mathcal{C}_{\epsilon_2}$. So as to remain consistent with the SLM–IEM model considered, we will continue working with a Rotta–Monin model. The full set of constants considered is recalled in Table 5.3.

$\mathcal{C}_S$	$\mathcal{C}_R$	$\mathcal{C}_\mathcal{P}$	$\mathcal{C}_\mathcal{G}$	$\mathcal{C}_\Theta$	$\mathcal{C}_\theta^\mathcal{D}$	$\mathcal{C}_{\theta_1}$	$\mathcal{C}_{\theta_2}$	$\mathcal{C}'_{\theta_2}$	$\mathcal{C}'_{\theta_3}$	$\mathcal{C}_\epsilon^S$	$\mathcal{C}_{\epsilon_1}$	$\mathcal{C}_{\epsilon_2}$	$\mathcal{C}_{\epsilon_3}$	$\mathcal{C}_{\epsilon_4}$
0.11	6.25	0	0	1.875	0.31	5	0	0	0	0.73	1.44	1.92	1.92 (conv.)) 0 (stab.)	0

Table 5.3: Set of constants considered in the treatment of surface-boundary flows within code_saturne simulations.

The test case taken into account is still the modelling of a 1-D 100 m high stratified SBL flow. The roughness height z_0 is equal to 0.1 m and the shear velocity is $u_* = 0.2\ \mathrm{m\,s^{-1}}$ with a temperature at ground of 15°C. To see the behaviour in the asymptotic in very stable and convective situations, we will study two simulations with respectively a Monin–Obukhov length scale of 20 m and -20 m. The time step kept equals to 0.1 s for stability reasons and as a way to ensure $\sqrt{ww}\Delta t/\Delta z < 0.5$. At the bottom of the domain, the algebraic solution is imposed. On top of the domain, the temperature obtained with the algebraic model, the shear stress and the turbulent heat fluxes are imposed. For other quantities, the flux is imposed based on algebraic solutions. In the horizontal directions periodic conditions are imposed.

5.1.3.2.1 Treatment of Stable Surface-Boundary Layer

We will first focus on the results obtained in the stable situation considering L_{MO}= 20 m. In order to ensure that the algebraic solution derived is close to the solution of the CFD solver, we initialise the flow with a state corresponding to the algebraic solution of a $k-\epsilon$ model (see Appendix 5.A) with a universal function proposed by Chenge and Brutsaert [2005] and observe whether it converges towards the expected solution. Despite the presence of small numerical oscillations, in this case the velocity and temperature gradients obtained using code_saturne are found to be close to the solutions obtained with the new methodology, as evidenced in Figure 5.8.

Moreover, the diffusion terms (with the exception of the dissipation rate) are sufficiently small to allow for the accurate retrieval of turbulent quantities, as evidenced in Figure 5.9. A small difference between the proposed methodology and CFD results is still discernible in the centre of the domain where the CFD profiles are slightly smoother due to diffusive effects. Furthermore, numerical oscillations can be observed on the first-order moment derivatives as already stated, but also on the turbulent Prandtl number where they are more pronounced. This suggest the necessity for the development of stable integration methods for DRSM–DFM models (see e.g. Ferrand et al. [2023]).

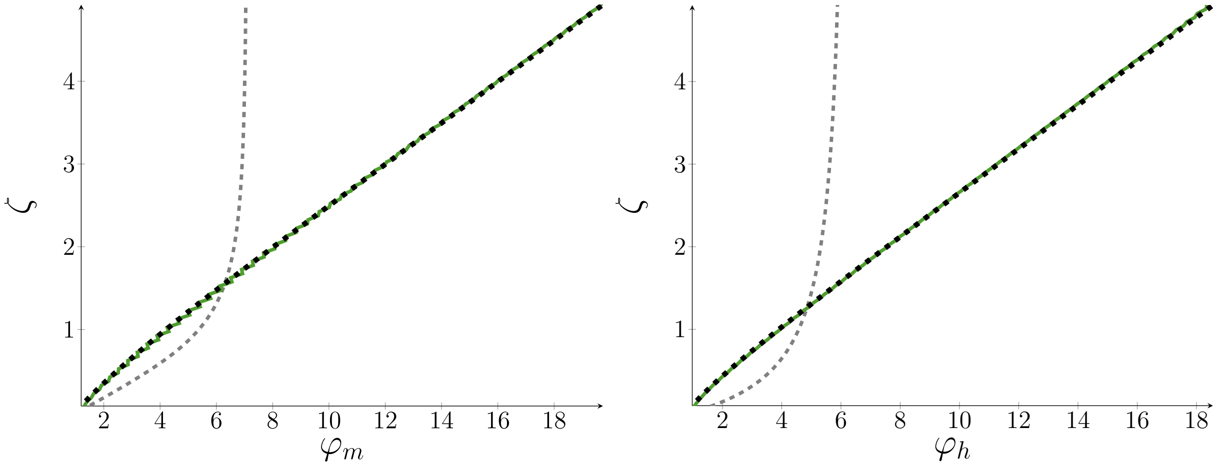

(A) Momentum universal function.

(B) Heat universal function.

Figure 5.8: Comparison between algebraic (⋯) and computed first-order universal functions at convergence (—) in a stable case. The initial state (- - -) corresponds to Chenge and Brutsaert [2005] universal functions with algebraic solutions corresponding to the $k-\epsilon$ model see Appendix 5.A.

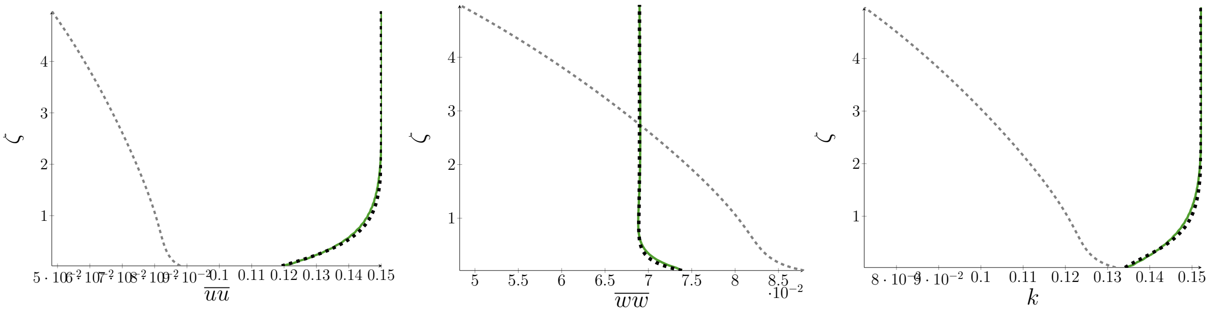

(A) Streamwise kinetic energy.

(B) Normal kinetic case.

(C) Overall TKE.

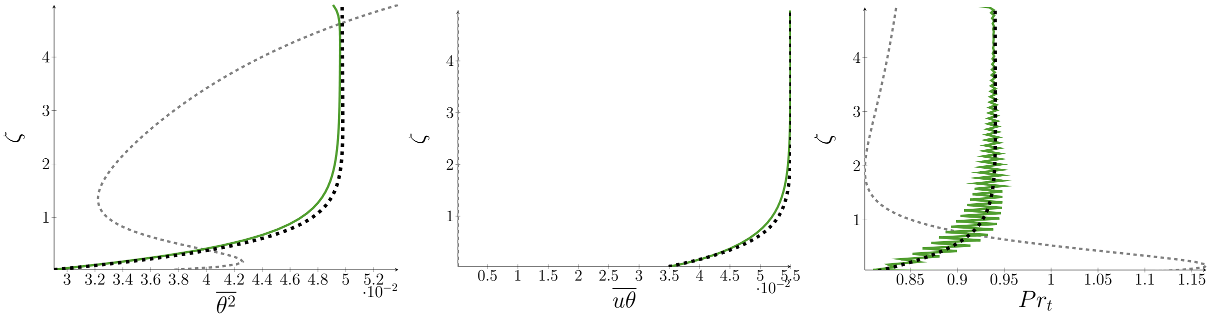

(D) Pot. temperature variance.

(E) Streamwise turb. heat fluxes.

(F) Turbulent Prandtl number.

Figure 5.9: Comparison between algebraic (⋯) and computed turbulent universal functions at convergence (—) in stable case. The initial state (- - -) corresponds to Chenge and Brutsaert [2005] universal functions with algebraic solution corresponding to the $k-\epsilon$ model see Appendix 5.A.

We can consider that the methodology proposed here offers a highly accurate and model-consistent representation of the stable SBL. It could then be employed to fuel CFD simulations by providing suitable idealised boundary conditions. Moreover, the significant disparity in behaviour between the initial state and the final one underscores the necessity to provide boundary conditions that align with the model's underlying assumptions.

5.1.3.2.2 Treatment of Convective Surface-Boundary Layer

In the convective SBL obtained with L_{MO} = -20 m, the numerical error becomes stronger, highly deteriorating the CFD simulation, as we can see on the very noisy first-order profiles Figure 5.10. Such numerical oscillations might testimony for inconsistency in the boundary conditions.

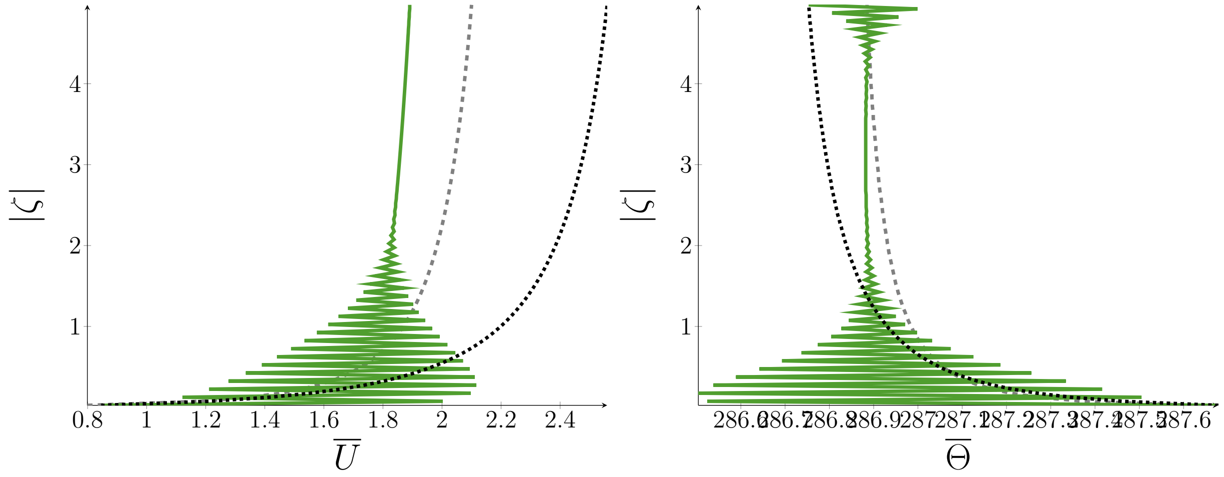

(A) Momentum universal function.

(B) Heat universal function.

Figure 5.10: Comparison between algebraic (...); initial state (- - -) based on Högström [1988] universal functions and computed mean quantities at convergence (—)in a convective situation.

To get rid of these spurious oscillations, the shear stress, the normal fluxes but also the mean velocity, mean temperature and the initial state are imposed based on algebraic solutions. Imposing these fields, it is possible for the CFD simulations to run without diffusive terms in code_saturne. The results with and without these diffusive terms are compared considering either algebraic-solution-consistent Dirichlet condition or Neumann condition on top of the domain. The goal is then to determine what kind of condition should be imposed. As we can see in Figure 5.11, except on bottom of the domain where spurious numerical oscillations are still present, the algebraic solution is perfectly retrieved without diffusive terms when considering Dirichlet condition on top of the domain. A slight drift appears in this case when imposing a Neumann condition. The first-order moment being imposed, these first results attest the proper derivation of the algebraic solution. However, in this convective situation, the treatment of the upper boundary condition is less straightforward taking into account diffusive effects on the Reynolds tensor, the turbulent heat fluxes and the potential temperature variance. Indeed, the presence of diffusive terms modifies quite noticeably the shape of the solution obtained using code_saturne. In this case, it seems that we are outside the validity domain of the equilibrium hypothesis as the thermally forced vertical gradient fuels the diffusive effects modifying totally the slope near wall. It results that even though imposing a Neumann condition on top of the domain enables to retrieve proper gradient on the upper half of the domain, the CFD results converge towards a solution quite different from the one obtained using the algebraic solution. It is possible to limit this difference between algebraic and CFD solution by imposing a Dirichlet condition on top of the domain, but this condition is too strong and more difficult to justify on physical grounds. A further study in this situation should be carried out. Let us emphasise that these results have been obtained with boundary conditions fuelled by the external resolution of the iterative process aforementioned, which does not take into account the diffusive effects. A first conclusion that can be drawn is that, in convective cases, the estimation of the solutions used to set the boundary conditions should include the diffusive effects on the second-order moments. Doing so, both the values and the gradients to impose would be modified compared to the results presented here.

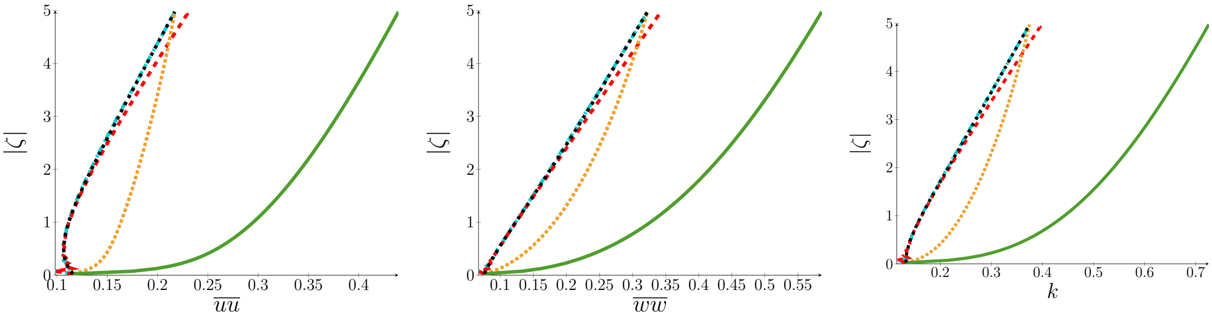

(A) Streamwise kinetic energy. (B) Normal kinetic case. (C) Overall turbulent kinetic.

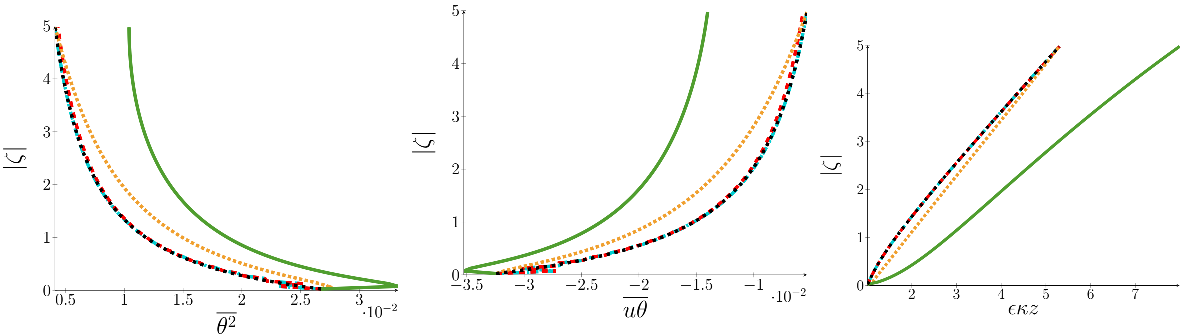

(D) Pot. temperature variance. (E) Horizontal turbulent heat fluxes. (F) Dissipation rate.

Figure 5.11: Comparison between algebraic (.....) and computed turbulent universal functions at convergence. The results imposing a Neumann condition on the upper part of the domain with (───) and without (- -) diffusive terms are presented along the results obtained with Dirichlet condition with (.....) and without diffusion term (- - -). The shear flux, normal turbulent heat fluxes mean velocity and potential temperature are imposed to ensure stability.

5.1.4 Local Conclusions and Perspectives

Considering a class of linear modelling for the fluctuating pressure induced redistribution terms, a description of the stratified SBL has been proposed based on algebraic solutions of the Reynolds tensor, turbulent heat fluxes and potential temperature variance. In this process, equilibrium assumptions have been made, which implies neglecting the dissipation term for these quantities. Doing so, in the scope of Monin–Obukhov theory, it is possible to extract universal functions for all these second-order moments which depend only on the flux Richardson number or equivalently on the momentum universal function. Having established these algebraic solutions, so as to estimate the flux Richardson number, an iterative numerical resolution of the dissipation rate has been carried out. Being the sole equation in which a diffusion term is considered, it provides a notion of length to the wall necessary to compute the flux Richardson number. This approach enables to close the system considered and to provide a description of the stratified SBL coherent with Monin–Obukhov theory even in both stable and convective limits. It has been verified that the solutions obtained in this manner are very close to the solution of the CFD solution in stable conditions, as the diffusive effects remain negligible. In contrast, the equilibrium assumptions considered (assuming a zero diffusivity condition for the Reynolds tensor, turbulent heat fluxes and potential temperature variance) do not hold in the case of convective boundary layers. In view of this, the results obtained using the methodology proposed are quite far from the one obtained using the CFD code taking into account the diffusive effects. A further study is then necessary to properly treat these situations. Better results might be obtained considering the TKE diffusion in the iterative process used to resolve the diffusion rate. Moreover, it might also be possible to consider the diffusive effects in the derivation of an algebraic solution by considering correlations between these terms and the local ones. It is possible, for example, in a first approach, to simply consider diffusive effects proportional to the buoyant effects as proposed by Takeuchi and Yokoyama [1963]. Doing so, algebraic solutions with a similar structure might be obtained replacing some constants (e.g. α_i and β_i) by functions depending on model constant and on the flux Richardson number. To directly take into consideration the diffusive terms, the resolution of such a 1-D system could be carried out directly within code_saturne, to obtain the coherent universal function, instead of using an external iterative solver as presented here. Furthermore, to obtain accurate results in convective situations, a more detailed analysis of the boundary condition considered and their implementation but also of the stability of the numerical integration scheme selected should be carried out.

5.2 Analysis of Particle/Mesh PDF Methods for Thermally Stratified Surface-Boundary-Layers Flows

Contents

The goal of the present section is to propose an extension of the work presented in Chapter 3, for thermally stratified wall boundary flows. We will place ourselves in the stable state studied in Paragraph 5.1.3.2.1, i.e. consider a 100 m high SBL with a Monin–Obukhov length of 20 m. In this case, the solution of the algebraic model represents quite well the dynamics of the flow and will be used for the mean carrier fields. The simulations are carried out during a physical time of 1000 s with a time step of 0.05 s and using 200,000 particles initially uniformly distributed.

In Section 5.2.1, we will first examine the influence of the correct wall boundary condition for instantaneous potential temperature on thermal quantities and concentration are emphasised. In Section 5.2.2, a particular interest is directed towards the spatial error that is induced by the interpolation of mean potential temperature at the location of the particles. Finally, the error impairing the estimation of the statistics due to the lack of statistical uniformity in the averaging bins is presented in Section 5.2.3.

5.2.1 Verification of the Wall-boundary Condition on Potential Temperature

We will first present the necessity to use an an-elastic wall boundary condition (WBC) for the instantaneous potential temperature presented in Paragraph 1.3.3.2.4 and first proposed for the real temperature by Pozorski et al. [2003b]. The corresponding results will be compared to the elastic WBC where the potential temperature is unchanged by the crossing of the rebound plane. For the dynamics, the standard an-elastic boundary condition is considered in both cases. We first consider a mesh containing 100 cells and a roughness height of 0.1 m. As for the neutral situation similar results are obtained with smooth and rough walls in high Reynolds flows. Indeed, the boundary conditions imposed in the Lagrangian stochastic methods are based on the respect of the proper fluxes near wall (see Section 3.1.2). As previously, in order to limit the spatial numerical error discussed hereafter, the rebound plane is placed at an altitude of 5 m. The values plotted are adimensionised by the friction velocity u_*, the friction temperature θ_* and the mean concentration over the height. They are then indexed with the superscript $^+$. For the mean potential temperature, the dimensionless difference between local and ground value $\langle \delta\Theta \rangle^+ = (\langle \Theta \rangle - \Theta_0)/\theta_*$ is presented.

The an-elastic WBC on potential temperature being designed to retrieve the correct normal turbulent fluxes near wall, the latter is properly described using this condition as we can see in Figure 5.12C. Additionally, a less noticeable effect also appears on the mean potential temperature profiles in Figure 5.12A. Indeed, using an elastic rebound, the mean potential temperature gradient being assumed null at the rebound plane (instead of positive in this stable situation), it results in an overproduction of potential temperature. At the contrary to the dynamics, where the WBC used has no effect on the concentration in one dimensional SBL flows, the elastic rebound on potential temperature triggers an error on the concentration profile highlighted in Figure 5.12B. Indeed, the temperature profile being poorly retrieved, it results in an inaccurate estimation of the buoyant effects which are no longer in equilibrium with the local pressure gradient. In the stable case, where the elastic WBC on potential temperature induces an overestimation of the latter, a decay in the particle concentration near ground appears. Similar processes are expected in the convective situation leading to opposite effects, namely the accumulation of particles near the ground. Finally, the impacts of the elastic rebounds may also be noticed on second-order quantities such as the potential temperature variance in Figure 5.12D and turbulent heat fluxes in Figure 5.12C. Indeed, the elastic boundary condition imposing a null thermal gradient, the production terms of these second-order moments are underestimated which in turn leads to their underestimation (in norm). This issue is analogous to the one affecting the streamwise component of the Reynolds stress tensor in the neutral case, see Section 3.1.2, where an elastic rebound on the streamwise velocity results in an underestimation of both shear stress and streamwise component of the Reynolds stress tensor. These results demonstrate that the an-elastic boundary condition should also be applied to the instantaneous potential temperature.

5.2.2 Influence of Mean Field Interpolation at Particle Positions

A second source of error is the interpolation of the mean carrier fields at particle locations, which tarnishes the evolution of the instantaneous properties associated with the particles. In order to dampen this error, the interpolation method should respect the three conditions: Placing the rebound plane directly on the bottom of the domain and using a coarser spatial discretisation with 20 cells over the height of the latter, we will compare the results obtained using four different interpolation methods:

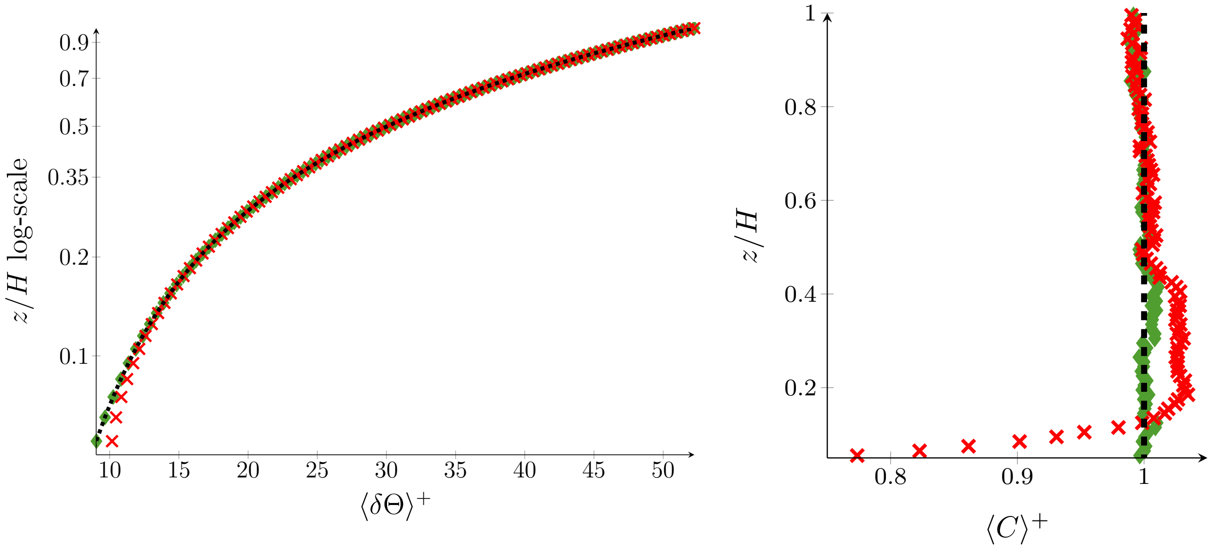

(A) Normalised increase of potential temperature.

(B) Normalised concentration.

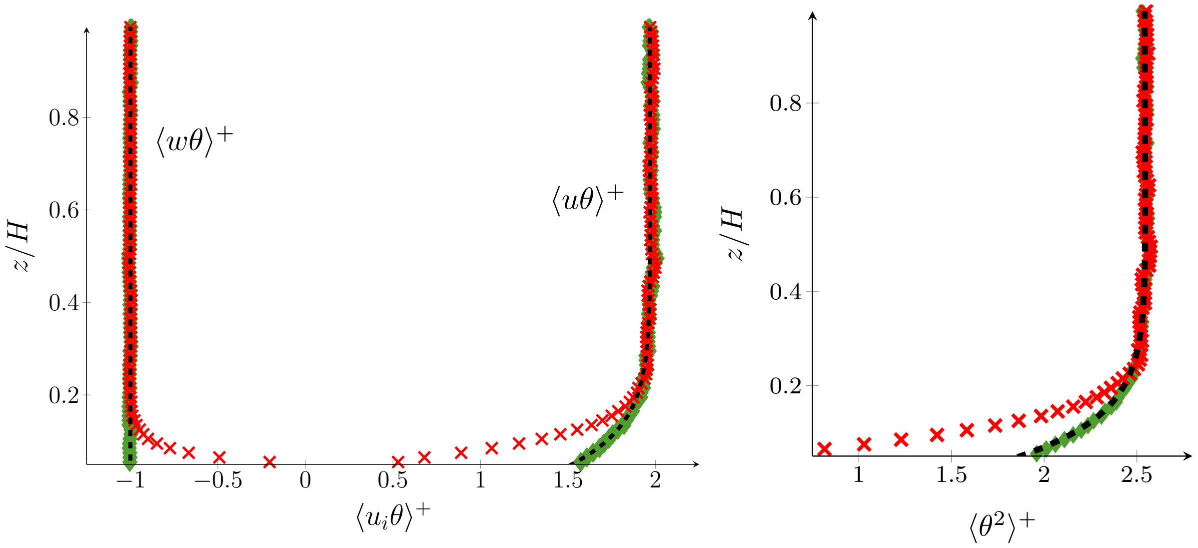

(C) Normalised turbulent heat fluxes.

(D) Potential temperature variance.

Figure 5.12: Comparison of the vertical profiles obtained using both the standard an-elastic wall-boundary condition (♦) and the elastic one (✖). These results are obtained in a stably stratified SBL. Only the an-elastic rebound respects the well-mixed criterion and enables to retrieve proper thermal quantities compared to the algebraic or analytical solutions (▪▪▪).

Interp. A A piece-wise uniform interpolation of the mean velocity, the potential temperature and the Lagrangian timescale fields.

Similarly to the neutral situation discussed in Section 3.2.1, this condition is not coherent with the condition Cond. ii, stating the necessity to have an interpolation more accurate than piece-wise uniform near wall for the mean velocity nor the mean potential temperature. This condition is necessary to reproduce well the first-order moments but mostly the corresponding gradients and the resulting production terms. Moreover, this interpolation is not coherent with Cond. iii either. The latter one asserts that the interpolation should be consistent with production dissipation equilibrium near wall. The piece-wise uniform interpolation on the mean velocity triggers a poor interpolation of the TKE production by shear, but also a poor interpolation of the production term in the streamwise turbulent heat fluxes. Similar issue arises with the piece-wise uniform interpolation on the mean potential temperature triggering a poor interpolation of the production terms in the turbulent heat fluxes equations but also in the temperature variance equation.

Interp. B A piece-wise linear interpolation of the mean velocity, with a piece-wise uniform interpolation of the potential temperature and the Lagrangian timescale fields.

This interpolation method aims at separating the error caused by the interpolation of the mean velocity and mean temperature. Assuming that the normal turbulent heat fluxes are properly retrieved, this scheme is coherent to properly treat the TKE equation. Yet, due to the poor interpolation of the mean potential temperature, the normal turbulent heat fluxes and thermal variance are expected to remain unaltered in comparison to the previous interpolation method.

Interp. C A piece-wise linear interpolation of the mean velocity and the potential temperature with a piece-wise uniform interpolation of the Lagrangian timescale fields.

This interpolation is coherent with respect to the production-dissipation equilibrium near wall for the TKE but also turbulent heat fluxes and potential temperature. An important remark is that, in the velocity equation, the mean pressure gradient can be decomposed into a mechanical component resulting from the constraints imposed by the flow and in a hydrostatic one in equilibrium with the weight. Within the FV solver, the mean carrier fields are assumed uniform within a cell, so the mean hydrostatic pressure gradient furnished is locally in equilibrium with a piecewise uniform interpolation of the mean buoyant term. However, in this case, a finer interpolation of the mean carrier potential temperature and then of the mean buoyant term is provided at the position of the particles. In order to prevent spurious accumulation of particles either at the face or at the centre of the cell (depending on the stability considered), the local interpolation of the mean pressure gradient should locally be at equilibrium with the buoyant term. Assuming a Boussinesq approximation, it is then necessary to modify the mean pressure gradient as follows:

$$\left[\frac{\partial \overline{P}}{\partial x_i}\right](\underline{\boldsymbol{X}}) = \frac{\partial \overline{P}}{\partial x_i}(\underline{\boldsymbol{X}}^c) - \rho_0 g_i \beta \left([\overline{\Theta}](\underline{\boldsymbol{X}}) - \overline{\Theta}(\underline{\boldsymbol{X}}^c)\right), \tag{5.74}$$

where the quantities within brackets are interpolated quantities obtained with an interpolation scheme to define. Furthermore, we have $\underline{\boldsymbol{X}}$ and $(\underline{\boldsymbol{X}}^c)$ which are respectively the positions of the particle and of the centre of the cell. Thus, considering a piecewise linear interpolation of the potential temperature we should consider:

$$\left[\frac{\partial \overline{P}}{\partial x_i}\right](\underline{\boldsymbol{X}}) = \frac{\partial \overline{P}}{\partial x_i}(\underline{\boldsymbol{X}}^c) - \rho_0 g_i \beta \frac{\partial \overline{\Theta}}{\partial x_j}(X_j - X_j^c). \tag{5.75}$$

As in Chapter 3, the mechanical component of the pressure gradient is still considered uniform within each cell.

Interp. D An interpolation based on the estimated universal functions for the mean velocity, the potential temperature and the Lagrangian timescale fields near ground.

In order to achieve a more accurate description than a piece-wise linear interpolation, one may wish to utilise an analytic solution in the wall cells. However, in thermally stratified SBLs, the analytical solution is not directly accessible. In order to derive a pseudo-analytical interpolation we should resort to estimated universal functions. Using an integration by parts, we have:

$$\Psi(z) = \int_{z_0}^{z+z_0} \frac{\varphi}{z} \mathrm{d}z, \tag{5.76a}$$

$$= \varphi(z+z_0)\log(z+z_0) - \varphi(z_0)\log(z_0) - \int_{z_0}^{z+z_0} \frac{\partial \varphi}{\partial z} \log(z) \mathrm{d}z. \tag{5.76b}$$

Assuming a linear evolution for the universal function on the mean gradient, we get:

$$[U]_\Psi(z) = \frac{u_*}{\kappa}\Bigg([\varphi_m]_1(z+z_0)\log(z+z_0) - [\varphi_m]_1(z_0)\log(z_0) - \frac{(\varphi_m(z_c)-1)}{(z_c+z_0)}\Big((z+z_0)\log(z+z_0) - z_0\log(z_0) - z\Big)\Bigg), \tag{5.77}$$

$$[\Theta]_\Psi(z) = \frac{\theta_*}{\kappa}\Bigg([\varphi_h]_1(z+z_0)\log(z+z_0) - [\varphi_h]_1(z_0)\log(z_0) - \frac{(\varphi_h(z_c)-1)}{(z_c+z_0)}\Big((z+z_0)\log(z+z_0) - z_0\log(z_0) - z\Big)\Bigg). \tag{5.78}$$

Let us note that different limits of this interpolation may be put forward. A first source of error arises from the selection of the universal function to be considered. In this instance, we use the functions derived from the solutions presented in Section 5.1. As the latter ones are stored only in the computation points, a further interpolation of these values is necessarily associated with additional error. Furthermore, in order to remain consistent with this interpolation for the first-order moments, the Lagrangian timescale is also estimated based on the algebraic solutions within the wall cells. Note that here again the hydrostatic part of the mean pressure gradient should be corrected respecting Eq. (5.74) in coherence with the interpolation procedure outlined in Eq. (5.78).

The results obtained near wall with these different propositions of interpolation are presented in Figure 5.13, where the statistics associated with the particles estimated on a partition of the domain 10 times finer than the FV mesh are plotted. In order to circumvent any potential inaccuracy resulting from the estimation of the statistics (treated for neutral SBL in Section 3.3.1), the statistics on display were originally computed on a sub-mesh 1000 times finer than the FV mesh and then spatially averaged on a sub-mesh 10 times finer than the FV one. The error impacting the post-treatment of the statistics when the latter are not uniform in the averaging bins will be further discussed for stratified flows in Section 5.2.3.

Comparing the Interp. A and Interp. B in Figure 5.13, we can see that the interpolation method for the mean velocity field at particles location has an impact on the streamwise component of the Reynolds tensor and horizontal fluxes due to the production by mean velocity appearing in these equations. Using a piece-wise constant interpolation, a spurious behaviour appears. It is characterised by an overproduction of gradients and production terms in proximity to cell interfaces with an underestimation in the vicinity of the cell centres. This phenomenon is

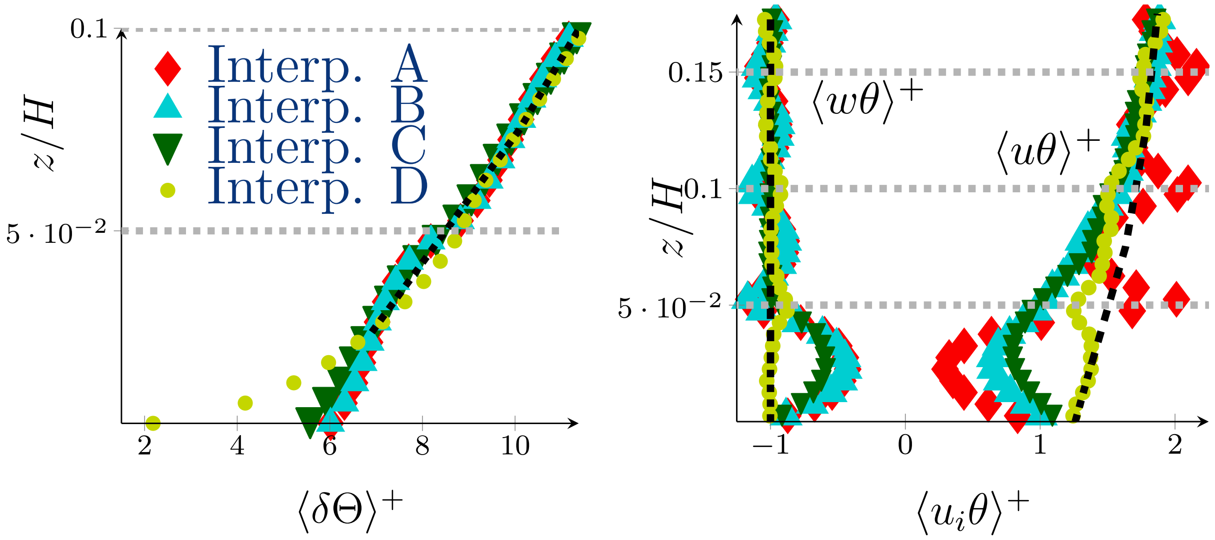

(A) Normalised potential temperature.

(B) Normalised turbulent heat fluxes.

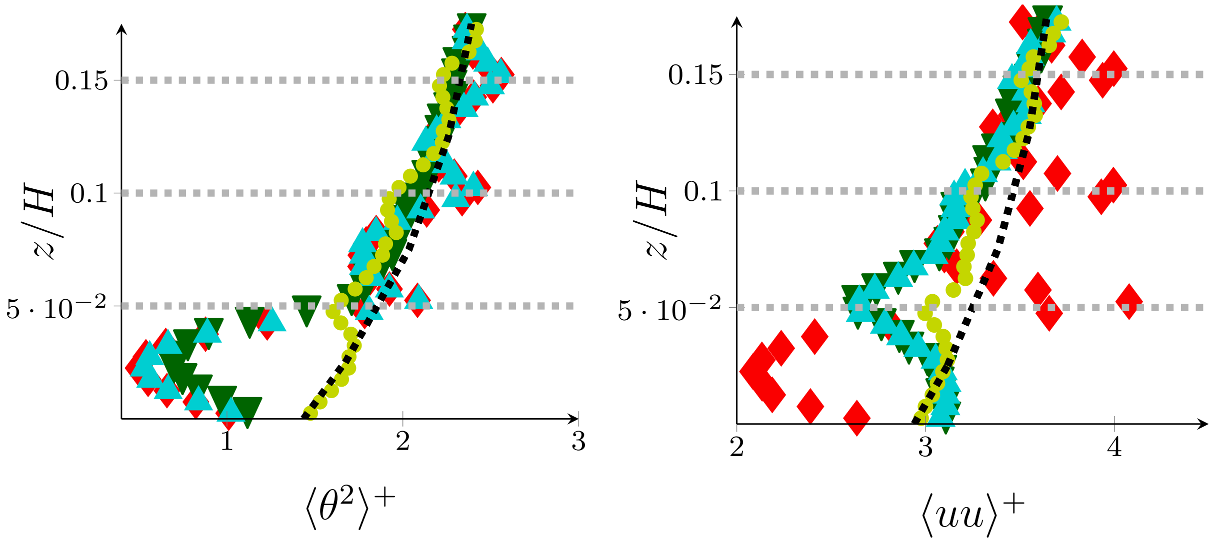

(C) Normalised potential temperature variance.

(D) Normalised streamwise TKE.

Figure 5.13: Vertical profiles near wall in a stably stratified SBL flow for different interpolation methods. The results obtained with four interpolation methods are compared: Interp. A which is a piece-wise constant interpolation for all mean fields(♦); Interp. B which is a piece-wise linear interpolation on mean velocity fields and a piece-wise constant interpolation on both the potential temperature and mean Lagrangian timescale (▲); Interp. C which is a piece-wise linear interpolation on both mean velocity and potential temperature fields and piece-wise constant for other fields (▼); Interp. D which is an interpolation based on estimation pseudo-analytical solutions for the mean velocity, potential temperature fields and Lagrangian timescale field in the cell at wall. The latter (●) is similar to Interp. C otherwise. These statistics are compared to the analytical solution (▪▪▪). Note that a specific statistical treatment has been made to avoid the statistical error discussed on Section 3.3 and in Section 5.2.3.

particularly evident in the context of the mean velocity, as observed in the streamwise component of the Reynolds tensor and turbulent heat fluxes. A similar pattern caused by interpolation error on the mean potential temperature emerges when examining the potential temperature variance and the normal turbulent heat fluxes. This error on thermal quantities is of a lesser amplitude than the one on the dynamics. These interpolation errors decrease as we move towards the upper part of the SBL. This improvement in the particles dynamics is due to the increase of the Lagrangian timescale. The latter becomes sufficiently high for a proper turbulent mixing between particles issued from different cells to take place. Moreover, such spurious effects seem to be properly damped using a piece-wise linear interpolation proposed in Interp. C. Nevertheless, quite big interpolation errors are still discernible on the first or two first cells near wall depending on the field considered. To enhance these outcomes, one may want to use the pseudo-analytical interpolation scheme Interp. D. This scheme enables the accurate retrieval of results in proximity to the wall within the first cell. This underscores the necessity for a rigorous derivation of the pseudo-analytical solution proposed. Nevertheless, the effects of the discontinuity of the mean carrier fields at the first cell upper interface are still discernible. They are characterised by an underproduction of the second-order moments at the interfaces. Moreover, outside the wall cell, the errors induced by the piece-wise linear interpolation are still noticeable, in the few first cells.

5.2.3 Analysis of Statistical Bias Induced by Local Spatial Averaging

We will now take a closer look at the errors introduced by estimating statistics on coarse averaging bins within where the flow is not statistically uniform. To this end we will focus on results obtained with the interpolation Interp. C (i.e., piece-wise linear for the mean velocity and potential temperature and piece-wise constant for the other quantities). As discussed in Section 3.3.1.1, there is no systematic error in the estimation of first-order moments from the set of particles. However, an error appears in the estimation of the covariances as highlighted in Eq. (3.10). Indeed, the covariances obtained directly on the coarse averaging bins correspond to the sum of the true covariances of interest, but also to the spatial covariances of the mean fields associated with the particles. The latter biases the obtained statistics. In the case of neutral SBL, since the velocity gradient decreases proportionally to the inverse of the height, this error affects the streamwise component of the Reynolds tensor only near wall and disappears in the bulk. However, in the case of stably stratified flows, as both the mean potential temperature gradient and the streamwise velocity gradient tend to become uniform, this systematic error impairs the estimation of covariances in the whole flow and the resulting error tends to become uniform. The latter affects the streamwise TKE and turbulent heat fluxes but also the potential temperature variance, as one can see in Figure 5.14. In this figure, for a given set of particles obtained using the interpolation methods Interp. C (i.e. with the same dynamics and thermal evolution of the particles), the statistics are estimated on different averaging bins. Although the interpolation error is still present close to the wall, the statistical error converges well, as one can see in the bulk. This highlights the relative importance of this source of error in such flows.

So as to avoid considering a cumbersome second partition of the domain to estimate the statistics, one may want to estimate the spurious spatial covariance of the mean fields directly onto the coarse original mesh as discussed in Section 3.3.2. Considering a linear estimation of the mean fields one can use the reconstruction Reconst. lin. With this choice of reconstruction, the correction is given by Eq. (3.14). The latter is non null only for Ψ and Φ representing the mean streamwise velocity and/or the mean potential temperature, yielding to a bias only on the streamwise TKE, streamwise turbulent heat fluxes and potential temperature variance. As presented in Figure 5.15, this source of error associated with the estimation of the statistics is properly corrected in the whole domain with an error subsisting near ground due to too a poor interpolation of the first-order carrier fields at particle location.

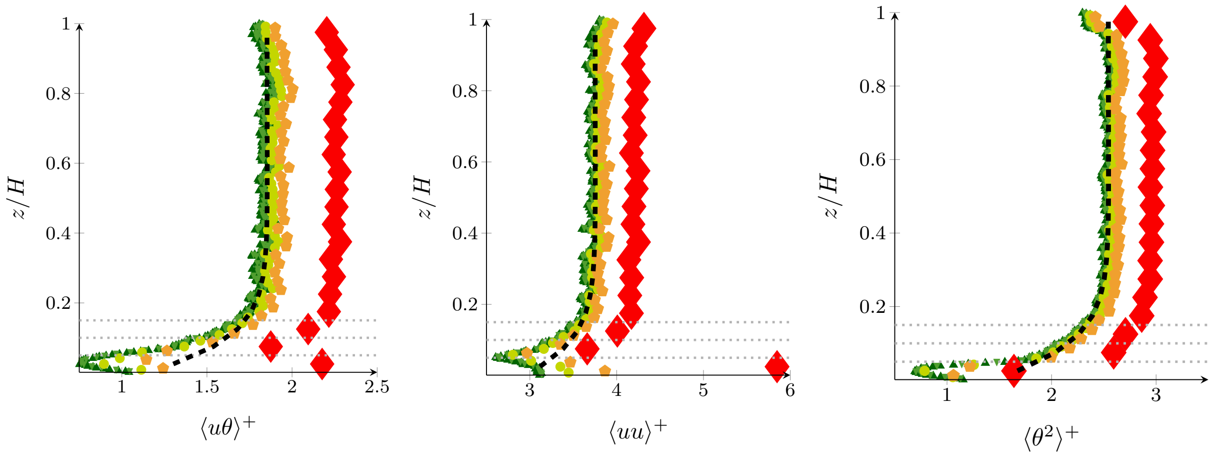

(A) Streamwise turb. heat flux.

(B) Streamwise TKE.

(C) Pot. temperature variance.

Figure 5.14: Vertical profiles of the statistical estimator of the thermal and dynamical variances and covariances using different spatial bins for the local averaging compared to the algebraic solutions (- - -). Compared to the FV cells (indicated by the grey dotted lines), the bins are respectively: of the same size (♦); 2 times finer (⬟); 3 times finer (●); 10 times finer (▼); 20 times finer (▲). Note that these observed statistical estimators are extracted from the same particle set, i.e. they correspond to identical particle dynamics and thermal evolution.

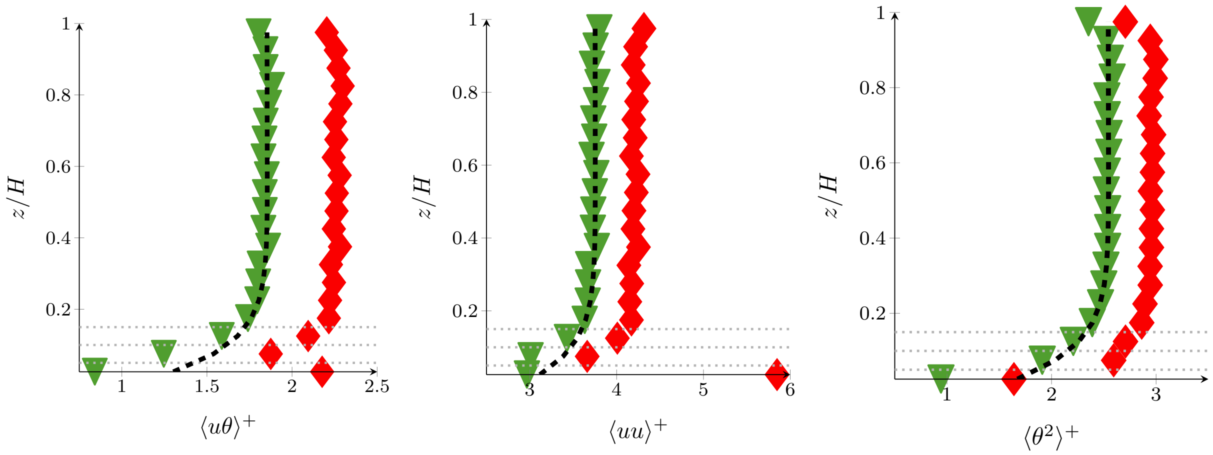

(A) Streamwise turb. heat flux.

(B) Streamwise TKE.

(C) Pot. temperature variance.

Figure 5.15: Vertical profiles of the statistical estimators of the thermal and dynamical variances and covariances with and without correction. Both profiles correspond to the same set of particles obtained using a linear interpolation of the mean velocity and potential temperature is considered. The uncorrected results (♦) are compared with the results obtained when correcting the post-treatment of the statistics based on linear assumption for the evolution of the mean fields (▼) and with algebraic solutions (- - -).

5.2.4 Local Conclusions

In this section, an extension of the work presented in Chapter 3 to stratified flows has been proposed. It has been applied to a stably stratified SBL flow.

In this case, the importance of using a consistent modelling of the boundary condition for the instantaneous thermal properties has been verified in Section 5.2.1 using the an-elastic rebound presented in Eq. (1.239) following the work of Pozorski et al. [2003b]'s work. Indeed, considering an elastic rebound for the potential temperature is equivalent to imposing a zero-flux condition on this quantity, resulting in the destruction of the turbulent heat fluxes. This is in contradiction with the physical phenomena at stake in the SBL. Moreover, the overestimation of the potential temperature in stable flows results in an erroneous depletion of concentration near wall and then to the non-respect of the well-mixed criterion. In convective situations, the use of the elastic rebound for the instantaneous potential temperature would result in an underestimation of the latter and in an accumulation of the particles near wall.

In addition, similarly to the issue presented in Section 3.2.2, it has been shown in Section 5.2.2 that the interpolation method used to estimate the mean carrier fields at the particle location should be more accurate than piece-wise uniform for the mean velocity and potential temperature fields especially near the wall. Moreover, considering an interpolation finer than piecewise uniform for the mean carrier thermal property appearing in the buoyancy term, it is necessary to adjust the hydrostatic part of the mean pressure gradient, in order to respect the local hydrostatic equilibrium. For the time being, a linear interpolation method is considered for the mean velocity and potential temperature fields.

Finally, the error induced by the estimation of second-order statistics on coarse averaging bins is put forward. In the neutral case, presented in Section 3.3, where the velocity gradient decreases as the inverse of the distance from the wall, this error occurs only in the vicinity of the wall. In contrast, in stably stratified flows, where the first-order gradients tend towards a non-zero constant in the bulk, this error impacts the estimation of the statistics everywhere. A first solution to limit this error is to use a finer partition of the domain to estimate the statistics. Yet, to avoid the cumbersome tracking of particles on two different meshes, it has been shown that this error can be properly corrected directly on the original mesh. To do so and because the first-order moments are estimated only in the centre of the cells, an assumption to reconstruct them everywhere is necessary. This assumption should be coherent with the interpolation methods considered. Thus, if one wants to correct the covariance estimators on the original coarse mesh with another interpolation scheme, the reconstruction of the mean fields associated with the particles and the resulting correction should be adapted accordingly.

5.3 Linear Dispersion in 2-D Thermally Stratified-Boundary-Layer Flows

Contents

5.3.1 Study of the Plume Shapes in Stratified Surface-Boundary-Layer Flows

The goal of this section is to present a case of 2-D linear dispersion in stratified SBL flows. It is based on the work of Monin [1959], who showed that pollutant plumes must have a finite dimension. Indeed, the spatial amplitude of a plume is limited by the velocity of the fastest vertical eddies which remain finite. Such a constraint is not verified by EVM or Gaussian methods, in which the diffusive terms transport pollutants throughout the entire domain at infinite speed. Moreover, Monin demonstrated that the shape of the plume in stationary and horizontally homogeneous SBL flows does not depend on the mean velocity characterised by the friction velocity u_* but solely on the stability measured through the Monin–Obukhov length scale L_{MO}. In order to verify the numerical results obtained and the effects of the atmospheric stability on pollutant dispersion, we will consider a linear emission at the ground with a roughness height $z_0 = 0.1$ m. Different stability conditions, from very convective to very stable situations, are considered with Monin–Obukhov length-scale going from -10 m to 20 m. The friction velocity considered equals to 0.2 $\mathrm{m\,s^{-1}}$ for the thermally stratified flows and different values from 0.2 $\mathrm{m\,s^{-1}}$ to 1 $\mathrm{m\,s^{-1}}$ are compared for neutral flows. The domain considered is a 140 m long and 200 m high rectangular domain, meshed using a uniform Cartesian mesh containing 200×200 cells. The pollutant is injected on the ground at a distance of 14 m downstream of the inlet. The height of this domain can be large compared to the physical height of the SBL especially in stable situations where it can be limited to a few dozens of metres. The dynamics of the upper part of the domain might suffer from neglecting Coriolis effects and assuming constant fluxes. Based on physical grounds, such assumptions should no longer be considered in such area. However, we only consider the near source dispersion over a distance within which the pollutant plume remains in the SBL. Thus, it is assumed that the dynamics in the upper region has little impacts on the dispersion in the lower part of the domain. The simulations are performed with a time step of 0.5 s and injecting 1000 particles per second (i.e., 500 per iteration) within the Lagrangian stochastic method.

The numerical results obtained using both a second-order FV solver and particle solver are then verified. So as to characterise the limit of the plume, we consider that it corresponds to the volume encompassing 99% of the pollutant mass. Such a restriction of the plume dimension is necessary in Lagrangian methods as we should only consider statistics associated with a sufficient number of particles. The 1% particles outside the plume may correspond to very specific stochastic trajectories of notional particles whose dynamics is not representative of the plume physics.

5.3.1.1 Results Obtained using the Moment Approach

First, in the scope of the moment approach, the universal functions derived in Section 5.3 are imposed at the inlet but also on both the lower and upper cells. In these simulations, a DRSM-DFM model is considered with a Shir model for the diffusion term and a Rotta–Monin model for the pressure-induced redistribution terms. From the green curves in Figure 5.16 representing plume shapes in neutral situations for three friction velocities, we can see that the latter are indeed independent of this parameter. This may at first glance seem paradoxical, however, both the transport velocities in the horizontal and normal direction are proportional to the friction velocity. Thus, increasing the shear stress will increase the advection which is the main source of transport in the horizontal direction but also the turbulent transport in a similar manner. As a result, the angle made by the plume remains unchanged, as does its shape (see Monin [1959] for further discussion).

Looking at the evolution of the plume shape with the Monin–Obukhov length scale for a constant value of the friction velocity $u_* = 0.2\ \mathrm{m\,s^{-1}}$, it is retrieved that the stability plays a major role in the shape of the pollutant as discussed in Paragraph 1.2.2.2.4. In stable flows, the thermal effects tend to kill normal fluctuations of velocity lowering the vertical transport. Consequently, as stability increases, plume sizes shrink while pollutant concentration increases. In contrast, in convective SBLs, the normal fluctuations are enhanced by thermal effects. In such a case, it is also retrieved that the plumes widen and the concentrations in their midst decrease due to a better turbulent mixing.

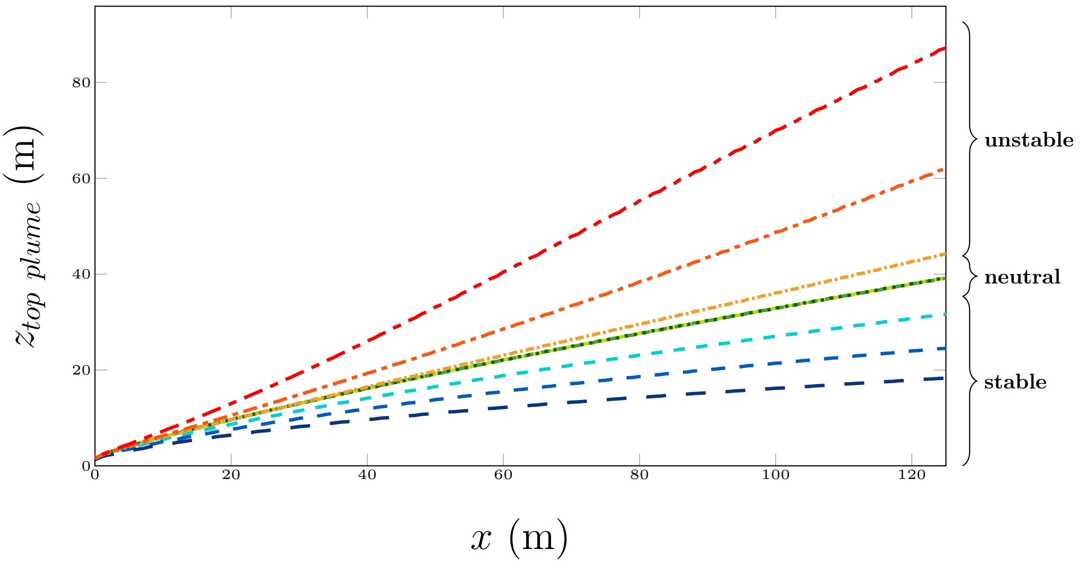

Figure 5.16: Pollutant plume shapes obtained using a Rotta–Monin model, for different friction velocities and Monin–Obukhov length scales. The limit of the plume is characterised by the zone below which 99% of the pollutant is encompassed. Three neutral flows with different friction velocities are compared: $u_* = 0.2\ \mathrm{m\,s^{-1}}$ (——), $u_* = 0.56\ \mathrm{m\,s^{-1}}$ (- - - -), $u_* = 1\ \mathrm{m\,s^{-1}}$ (.......). Furthermore, the plume shapes obtained with a friction velocity $u_* = 0.2\ \mathrm{m\,s^{-1}}$ are plotted for different stability situation, respectively $L_{MO} = 200$ m (- - -); $L_{MO} = 50$ m (– – ·); $L_{MO} = 20$ m (– –); $L_{MO} = -50$ m (-·-·-·-); $L_{MO} = -20$ m (-·-·-); $L_{MO} = -10$ m (– · – ·). The plume is independent of u_* but its amplitude depends strongly on the stability.

5.3.1.2 Results Obtained using the Lagrangian Stochastic Methods

We will now consider the results obtained using the Lagrangian stochastic methods. In coherence with the Rotta–Monin model taken into account in the FV simulations, a SLM–IEM model is considered with $\mathcal{C}_0 = 3.5$ and $\mathcal{C}_\Theta = 1.875$ to retrieve a proper Prandtl number. In order to avoid errors induced by the resolution of the FV solver, we will use the universal functions derived from Section 5.1, to provide the mean carrier fields. Such a choice might be questionable in the case of convective SBL flows where the diffusion of TKE should not be neglected. Yet, this source of error should be weighed against the errors arising from the resolution of the FV solver. It is true that using the solution issued from the FV solver the errors obtained would be smaller than those encountered in Section 5.1.3.2, since it is easier to maintain the profile injected at inlet than to retrieve it from upper and lower boundary conditions. Nevertheless, the solutions from the methodology developed in Section 5.1 are used to fuel the mean carrier fields, we can see in Figure 5.17, that results obtained are similar to the one obtained using a DRSM-DFM modelling. The independence of the plume shape with regards to the friction velocity is properly captured as well as the qualitative effects of the dynamics on the stability.

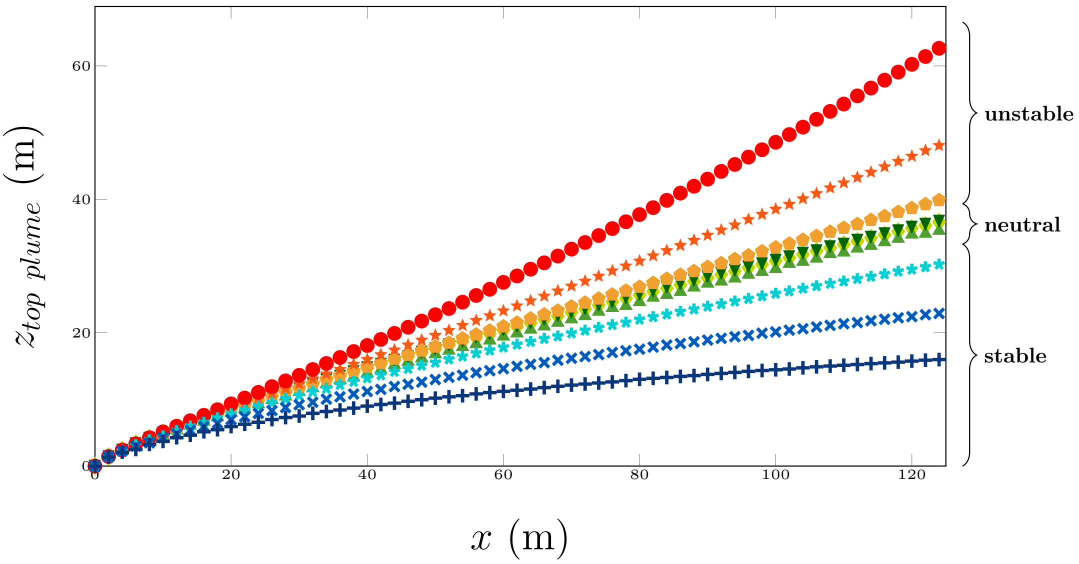

Figure 5.17: Pollutant plume shapes obtained using a SLM–IEM model, for different friction velocities and Monin–Obukhov length scales. The limit of the plume is characterised by the zone below which 99% of the pollutant is encompassed. Three neutral flows with different friction velocities are compared: $u_* = 0.2\ \mathrm{m\,s^{-1}}$ (♦), $u_* = 0.56\ \mathrm{m\,s^{-1}}$ (▲), $u_* = 1\ \mathrm{m\,s^{-1}}$ (▼). Furthermore, the plume shapes obtained with a friction velocity $u_* = 0.2\ \mathrm{m\,s^{-1}}$ are plotted for different stability situation, respectively $L_{MO} = 200$ m (✱); $L_{MO} = 50$ m (✖); $L_{MO} = 20$ m (✚); $L_{MO} = -50$ m (⬟); $L_{MO} = -20$ m (★); $L_{MO} = -10$ m (●). The plume is independent of u_* but increases with the thermal effects.

Impacts of the Thermal Modelling on the Plume

Our aim here is to measure the effects of properly modelling the instantaneous potential temperature within the Lagrangian stochastic approach. To do so, using the same mean carrier fields, the results obtained with three modelling variants of this quantity are compared in Figure 5.18:

- In the first simulation, in Figure 5.18A, as in Figure 5.17, we consider an IEM model with a finite relaxation time characterised by the choice $\mathcal{C}_\Theta = 1.875$. This value is selected in coherence with the constant $\mathcal{C}_0 = 3.5$ and the turbulent Prandtl number in neutral case an will be considered as the reference situation.

- The second simulation corresponds to an instantaneous relaxation time for the potential temperature obtained by taking $\mathcal{C}_\Theta = 0$. The potential temperature associated with the particles then remains constant over their trajectories. As we can see in Figure 5.18B, with this modelling the deviation of the particle potential temperature compared to the local mean flow is not dampened. This results in overestimated stability effects, with plumes that are too diffuse in convective situations and overly confined in stable situations.

- Finally, an instantaneous relaxation time is assumed by setting $\mathcal{C}_\Theta = \infty$. Such a modelling is often used in the scope of atmospheric dispersion with Lagrangian stochastic methods (see e.g. Tinarelli et al. [2012], Massimo et al. [2013], Pisso et al. [2019]). In this situation, where the potential temperature associated with the particle corresponds to the local mean fields without any memory of the particle trajectory, the stability effects are underestimated, resulting in a smaller variation of the plume shape with L_{M0}. At the opposite of the infinite relaxation time, we can see that the stable plumes are more diffuse than in the reference case, whereas they are less diffuse in the convective situations and all the plume shapes come closer to the neutral setup.

We can then see that the relative importance of the stability on the plume shape depends, as expected, on the Monin-Obukhov length scale, but also on the modelling of the potential temperature. The latter impacts are enhanced by taking larger relaxation times and diminished by taking smaller ones. Thus, although this issue is often overlooked in the context of atmospheric dispersion, the modelling of the instantaneous thermal quantities and the selection of a suitable relaxation time should be seen as of significant importance.

5.3.2 Impacts of the Thermal Modelling on the Dynamic of a Buoyant Plume

To discuss the implications of the thermal modelling of plume rise, we will now consider the simulation of a weakly buoyant plume in a stably stratified flow with $L_{MO} = 20$ m. The difference between the ground potential temperature and the potential temperature of the injected flow equals to $3.5°C$, the reason explaining this choice of a small temperature difference is twofold. First, the effects of the pollutant dispersion on the background flow are not taken into account, thus, to be physically sound, relatively small buoyancy effects should be considered. Secondly, since we want to remain as much as possible in the SBL, we want a moderate rise of the plume. Furthermore, to be able to discuss the shape of these plumes with more ease, we will consider an emission at a height of 25 m. As previously, the carrier fields selected are derived from the solutions presented in Section 5.1. The corresponding potential temperature at the injection altitude is equal to ground temperature plus 2.5°C, while the isotherm at ground temperature plus 3.5° C is reached at 39 m. To illustrate the importance of the instantaneous potential temperature modelling, the lower limit but also the centre and the upper limit of pollutant plumes are plotted in Figure 5.19. Each of these limits represents respectively the altitude below which 1%, 50% and 99% of the pollutant is located. As in the previous paragraph, the three plumes plotted are obtained with the same mean carrier flow and three modelling variants of the instantaneous potential temperature corresponding to three limit relaxation times.

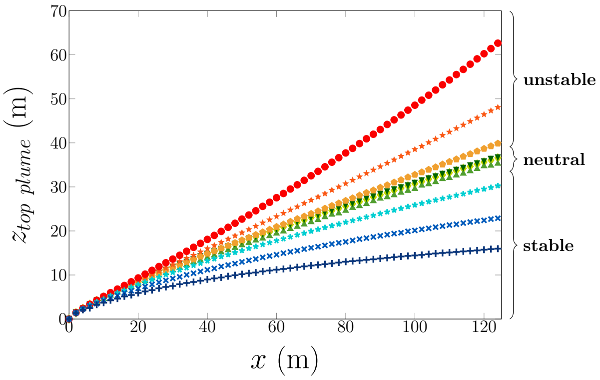

(A) Finite relaxation time

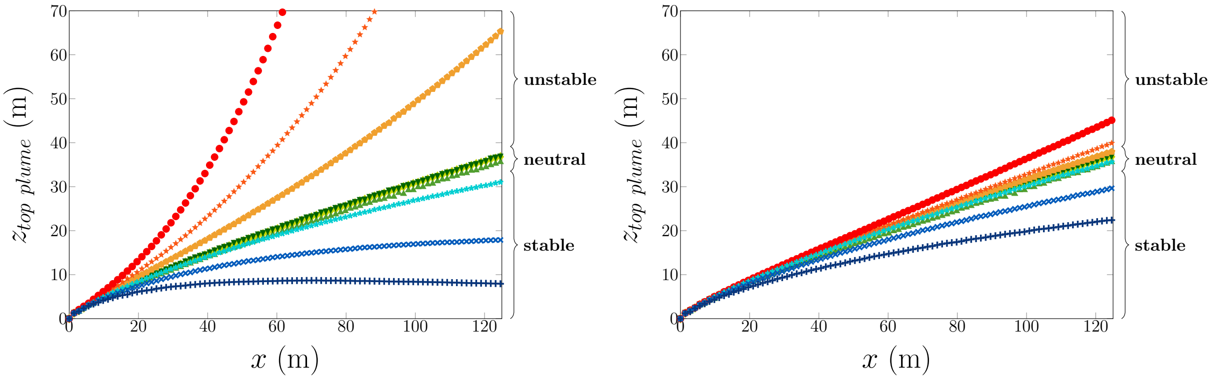

(B) Infinite relaxation time

(C) Instantaneous relaxation time

Figure 5.18: Pollutant plume shapes obtained using different thermal relaxation times, for different friction velocities and Monin–Obukhov length scales. The limit of the plume is characterised by the zone below which 99% of the pollutant is encompassed. Three neutral flows with different friction velocities are compared: $u_* = 0.2 \text{ m s}^{-1}$ (♦), $u_* = 0.56 \text{ m s}^{-1}$ (▲), $u_* = 1 \text{ m s}^{-1}$ (▼). Furthermore, the plume shapes obtained with a friction velocity $u_* = 0.2 \text{ m s}^{-1}$ are plotted for different stability situation, respectively $L_{MO} = 200$ m (✱); $L_{MO} = 50$ m (✖); $L_{MO} = 20$ m (✚); $L_{MO} = -50$ m (⬟); $L_{MO} = -20$ m (★); $L_{MO} = -10$ m (●). The plume shape is independent of u_* but increases with the thermal effects and the relaxation time.

- In the first simulation (in green), considering an IEM method, we have $\mathcal{C}_\Theta = 1.875$, this value is selected in coherence with the carrier fields considered. In this situation, particle instantaneous potential temperature tends towards the local mean temperature with a finite relaxation time $\mathcal{T}_\Theta = \frac{k}{\mathcal{C}_\Theta \epsilon}$. As expected, in Figure 5.19, the centre of the plume rises due to thermal effects until a relatively constant altitude located in between the injection height and the height corresponding to the isotherm of injection temperature. From there, the centre of the plume tends to remain fairly constant, although there is a tendency for this quantity to decrease. The latter could be explained by the asymmetric nature of the flow around its mean location, which is noticeable by the asymmetric shape of the plume. Indeed, the flow on the upper part being faster than on the lower part, the pollutant is evacuated more quickly there, causing this slow decrease of the centre of the plume.

- Second (in red), a simulation is carried out considering $\mathcal{C}_\Theta = 0$. In this case the relaxation time for the potential temperature is infinite. Thus, the potential temperature associated with the particles remains constant over their trajectories and the plume rises until it reaches the altitude associated with the injection temperature isotherm. Moreover, in this case, for all the particles, the buoyant terms can be at equilibrium only when the particles are in the vicinity of this constant target location. The buoyancy introduces then a restoring effect pushing particles towards this position. This leads to a dampening of the potential deviation to this location and thus to a less diffusive shape of the plume.

- Finally, a simulation (in blue) is considered with $\mathcal{C}_{\Theta} = \infty$. In this case, the instantaneous potential temperature relaxes instantaneously towards the local mean potential temperature. Due to this choice, the plume rise is not naturally treated by the buoyancy effects and an *ad hoc* parameterisation should be applied. For this reason, in the case studied where no such specific modelling of the buoyant rise is considered, the height of the centre of the plume remains fairly constant near the injection. Over larger distances, reflection of the particles at wall triggers an elevation of the mean level of the centre of the plume. A second element of interest is that in this case the buoyant effects do not oppose at all the vertical dispersion yielding to a more diffuse and broader plume.

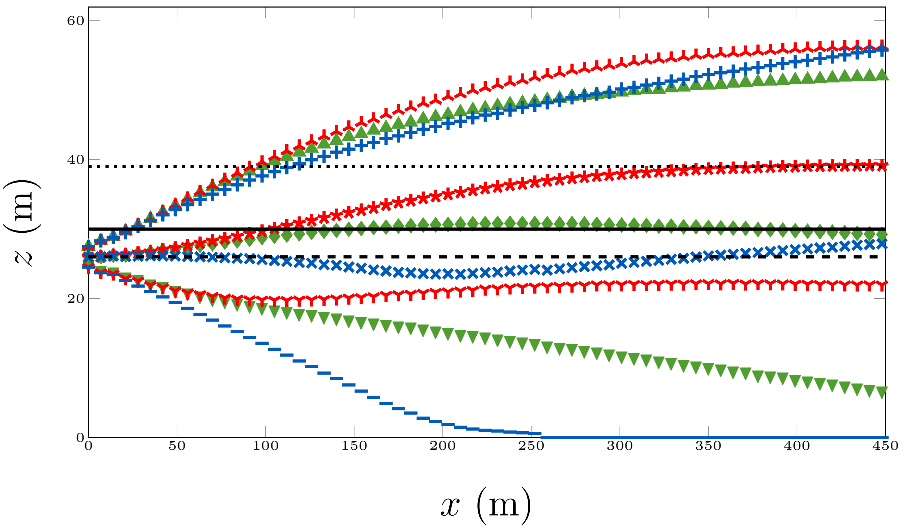

Figure 5.19: Buoyant plume shape obtained with different relaxation times. The first relaxation times tackled is $\frac{k}{\mathcal{C}_{\theta}\epsilon}$ with $\mathcal{C}_{\theta} = 1.875$ (in green), the top of the plume (▲), its centre (♦), and its bottom (▼) are plotted. The upper limit (✚), centre (✖) lower limit (−) of the plume obtained with an instantaneous relaxation are plotted in blue whereas the plume corresponding to an infinite relaxation time is plotted in red with respectively (⅄) for its upper limit, (✱) for its centre and (Y) for its lower limits. These limits represent respectively the altitude below which 99%, 50%, 1% of the concentration is located. It is clear that the position of the plume centre and the dispersion around this value depend on the modelling considered for the instantaneous potential temperature.

In all the three plumes, due to the non-uniformity of both the mean flow and the turbulent fields, the pollutant plume is not symmetric around its mean location. Over longer distances, these effects may result in a shift of the mean location of the plume, mainly because the upper region sees a faster velocity fields. Such phenomena cannot be properly handled by Gaussian methods often used to simulate the dispersion far from the source.

5.3.3 Local Conclusions and Perspectives

In this section, it has been demonstrated that the shape of the pollutant plumes in stationary horizontally uniform SBL flows does not depend on the friction velocity characterising the flow velocity. The only parameter impacting this shape is the Monin–Obukhov length-scale which is representative of the thermal effects. Indeed, in stable flows, the latter killing the vertical fluctuations of velocity, the plume remains narrow and concentrated. In contrast, in convective flows, the thermal effects enhancing the vertical velocity fluctuations, they have a mixing effect triggering the production of broad and diffuse plumes. This result is properly retrieved both using the FV solver with a Rotta–Monin model and a Lagrangian stochastic one with a SLM–IEM model. It has been showed that the proper modelling of the thermal relaxation is of major importance to retrieve a proper plume dynamics, both to describe their central position or the dispersion around this value. Assuming an instantaneous thermal relaxation time does not enable to obtain a proper rise of the plume and strongly overestimates the width of the latter in a stable case. Unfortunately, the treatment of highly buoyant plumes such as encountered during a fire remains out of the scope of the present work. Indeed, in order to consider the effects of highly buoyant plumes treated with the Lagrangian solver on the background flow, a stronger coupling between particle quantities and the carrier flow should be ensured. Such a two-way coupling is out of the scope of the present work. Moreover, such buoyant plumes would rise above the SBL in a zone where the hypotheses considered to estimate the carrier fields are no longer respected and are also out of the scope of the present work.

Local Appendix

5.A Derivation of Algebraic Solutions for Lower Order Modelling

In this section, a complement of Section 5.1 is presented with methods of lower order compared to the DRSM-DFM methods presented. We still consider the case of a horizontally uniform and stationary stratified SBL flow. First, the results for the kinetic energy obtained with the standard $k - \epsilon$ model are presented. Then, the results obtained using respectively a SGDH and a GGDH closures for the turbulent heat fluxes are displayed.

5.A.1 Algebraic Closure for the Turbulent Kinetic Energy using a Standard $k - \epsilon$ Modelling

Using a $k - \epsilon$ modelling of the turbulence, the closure gives:

$$\nu_t = -\frac{\langle uw \rangle}{\frac{\partial \langle U \rangle}{\partial z}} = \frac{u_* \kappa z}{\varphi_m} = \frac{\mathcal{C}_\mu k^2}{\epsilon}. \tag{5.79}$$

Under the TKE equilibrium assumption, injecting the dissipation of the dissipation rate Eq. (5.8), we get the equation:

$$\frac{k^2}{u_*^4} = \frac{1}{\mathcal{C}_\mu}\left(1 - Ri_f\right) = \frac{\left(1 - Ri_f\right)^2 \left(1 - (\beta_2 - \alpha_3) Ri_f\right)}{\alpha_1 (1 - \beta_2 Ri_f)(1 - \alpha_2 Ri_f)}, \tag{5.80}$$

where the result obtained with the $k - \epsilon$ model is compared with Eq. (5.25) obtained in the broader case of DRSM models. Thus, the notation used in Section 5.1 can still be used by setting for example $\alpha_1 = \mathcal{C}_\mu$ and $\alpha_2 = 0$ $\alpha_3 = \beta_2 = 1$. This might be of importance, as only the algebraic solution on the TKE is necessary to fuel the iterative process on the dissipation rate. Thus, the latter method can be directly extended to EVM models.

Furthermore, if one wants to have an idea of the TKE distribution one may assume as a first approach:

$$\frac{\langle u_i u_j \rangle}{k} = \frac{2}{3}\delta_{ij} - \frac{\nu_t}{k}\left(\frac{\partial U_i}{\partial x_j} + \frac{\partial U_j}{\partial x_i}\right). \tag{5.81a}$$

In this case, we have $\frac{\langle uu \rangle}{k} = \frac{\langle vv \rangle}{k} = \frac{\langle ww \rangle}{k} = \frac{2}{3}$. Thus, with $\lambda = \lambda_x = \frac{2}{3}$ and $\mu_x = \mu_y = \mu_z$ the notation used in Eqs 5.17 might still be used.

If one wants to take into account the thermal effects in the distribution of TKE, the Reynolds tensor might be modelled as:

$$\begin{aligned}
\frac{\langle u_i u_j \rangle}{k} =& \frac{2}{3}\delta_{ij} - \frac{\nu_t}{k}\left(\frac{\partial U_i}{\partial x_j} + \frac{\partial U_j}{\partial x_i}\right) + \mathcal{C}_\theta^{k-\epsilon}\frac{(\mathcal{G}_{ij} - \frac{2}{3}\mathcal{G}\delta_{ij})}{\epsilon}, && (5.82a)\\
=& \frac{\frac{2}{3}\delta_{ij} - \frac{\nu_t}{k}\left(\frac{\partial U_i}{\partial x_j} + \frac{\partial U_j}{\partial x_i}\right)}{1 - Ri_f}\left(1 - \frac{\frac{2}{3}\delta_{ij} - \frac{\nu_t}{k}\left(\frac{\partial U_i}{\partial x_j} + \frac{\partial U_j}{\partial x_i}\right) + \mathcal{C}_\theta^{k-\epsilon}\frac{\mathcal{G}_{ij} - \frac{2}{3}\mathcal{G}}{\mathcal{G}}}{\frac{2}{3}\delta_{ij} - \frac{\nu_t}{k}\left(\frac{\partial U_i}{\partial x_j} + \frac{\partial U_j}{\partial x_i}\right)} Ri_f\right). && (5.82b)
\end{aligned}$$

Thus, for the diagonal terms, we would have:

$$\begin{aligned}
\frac{\langle uu \rangle}{k} &= \frac{\frac{2}{3}}{1 - Ri_f}\left(1 - \left(1 - \mathcal{C}_\theta^{k-\epsilon}\right) Ri_f\right), && (5.83a)\\
\frac{\langle vv \rangle}{k} &= \frac{\frac{2}{3}}{1 - Ri_f}\left(1 - \left(1 - \mathcal{C}_\theta^{k-\epsilon}\right) Ri_f\right), && (5.83b)\\
\frac{\langle ww \rangle}{k} &= \frac{\frac{2}{3}}{1 - Ri_f}\left(1 - \left(1 + 2\mathcal{C}_\theta^{k-\epsilon}\right) Ri_f\right). && (5.83c)
\end{aligned}$$

Here again, the notation introduced in Eqs 5.17 can be retained with $\lambda_x = \lambda = 2/3$, $\mu_x = \mu_y = 1 - \mathcal{C}_\theta^{k-\epsilon}$ and $\mu = 1 + 2\mathcal{C}_\theta^{k-\epsilon}$. Moreover, as a $k-\epsilon$ can only be consistent with a SGDH modelling of the turbulent heat fluxes, we would also have a consistent behaviour for the shear stress.

5.A.2 Algebraic Closure considering a SGDH Modelling for the Turbulent Heat Fluxes

Modelling for the turbulent heat fluxes with the SGDH model, we have:

$$\langle u_i \theta \rangle = -K_t \frac{\partial \langle \Theta \rangle}{\partial x_i}. \tag{5.84}$$

The streamwise turbulent heat fluxes are then null and the equation Eq. (5.18c) for the shear stress gives:

$$\frac{k^2}{u_*^4} = \frac{1}{\mathcal{C}_\mu}\frac{(1 - Ri_f)^2}{(1 - \mu Ri_f)} = \frac{(1 - Ri_f)^2 (1 - (\beta_2 - \alpha_3) Ri_f)}{a_1 (1 - \beta_2 Ri_f)(1 - \alpha_2 Ri_f)}. \tag{5.85}$$

Using for example the set of constants: $\alpha_1 = \mathcal{C}_\mu$, $\alpha_2 = \mu$, $\alpha_3 = 0$ and $\beta_2 = 1$, we can obtain the solution for k with a similar form as Eq. (5.25) to fuel the iterative solver on the dissipation rate. Furthermore, considering $K_t = \frac{\nu_t}{Pr_t^0} = \frac{\mathcal{C}_\theta^{SGDH} k^2}{\epsilon}$ with $\mathcal{C}_\theta^{SGDH} = \frac{\mathcal{C}_\mu}{Pr_t^0}$ and Pr_t^0 a constant we have:

$$
\begin{aligned}
-\langle w\theta\rangle = u_*\theta_* = K_t \frac{\partial \Theta}{\partial z} &= \frac{\mathcal{C}_\theta^{SGDH} k^2}{\epsilon} \frac{\theta_*}{\kappa z} \varphi_h, && (5.86a)\\
\frac{u_*^4}{k^2} = \mathcal{C}_\theta^{SGDH} \frac{\varphi_h}{\varphi_m} \frac{1}{1 - Ri_f} &= \frac{\mathcal{C}_\theta^{SGDH} Pr_t}{1 - Ri_f}, && (5.86b)\\
Pr_t =& \frac{u_*^4}{k^2} \frac{(1 - Ri_f)}{\mathcal{C}_\theta^{SGDH}}. && (5.86c)
\end{aligned}
$$

5.A.3 Algebraic Closure considering a GGDH Modelling for the Turbulent Heat Fluxes

Modelling the turbulent heat fluxes with a GGDH model, we have:

$$
\langle u_i \theta\rangle = -\mathcal{C}_\theta^{GGDH} \frac{k}{\epsilon} \langle u_i u_k\rangle \frac{\partial \langle\Theta\rangle}{\partial x_k}. \qquad (5.87)
$$

The equation Eq. (5.18c) becomes then:

$$
\begin{aligned}
\frac{u_*^4}{k^2} =& \alpha_1 \frac{1 - \mu_{xz} Ri_f}{(1 - Ri_f)^2} - \frac{Ri_f}{(1 - Ri_f)} \frac{(1 - \mathcal{C}_G)\mathcal{C}_\theta^{GGDH}}{\mathcal{C}_R} \frac{u_*^3}{\epsilon\theta_*} \frac{\partial\langle\Theta\rangle}{\partial z}, && (5.88a)\\
=& \alpha_1 \frac{1 - \mu_{xz} Ri_f}{(1 - Ri_f)^2} - Pr_t \frac{Ri_f}{(1 - Ri_f)^2} \frac{(1 - \mathcal{C}_G)\mathcal{C}_\theta^{GGDH}}{\mathcal{C}_R}. && (5.88b)
\end{aligned}
$$

The kinetic energy depends then on the turbulent Prandtl number which can be obtained thanks to the equation driving the normal turbulent heat fluxes as:

$$
\begin{aligned}
-\langle w\theta\rangle = u_*\theta_* &= \mathcal{C}_\theta^{GGDH} \langle ww\rangle \frac{k}{\epsilon} \frac{\partial\langle\Theta\rangle}{\partial z}, && (5.89a)\\
\frac{u_*^4}{k^2} &= \mathcal{C}_\theta^{GGDH} \lambda (1 - \mu Ri_f) \frac{1}{(1 - Ri_f)^2} Pr_t, && (5.89b)\\
Pr_t &= \frac{u_*^4}{k^2} \frac{(1 - Ri_f)^2}{\mathcal{C}_\theta^{GGDH} \lambda (1 - \mu Ri_f)}. && (5.89c)
\end{aligned}
$$

Injecting this equation in the equation of turbulent energy Eqs 5.88, we get:

$$
\begin{aligned}
\frac{u_*^4}{k^2} \left(1 + \frac{Ri_f}{1 - \mu Ri_f} \underbrace{\frac{(1 - \mathcal{C}_G)}{\mathcal{C}_R \lambda}}_{\frac{3\mu}{4} - \frac{1}{2\lambda}}\right) =& \frac{\alpha_1 (1 - \mu_{xz} Ri_f)}{(1 - Ri_f)^2}, && (5.90a)\\
\frac{k^2}{u_*^4} = \frac{(1 - Ri_f)^2 \left(1 - Ri_f \left(\frac{\mu}{4} + \frac{1}{2\lambda}\right)\right)}{\alpha_1 (1 - \mu Ri_f)(1 - \mu_{xz} Ri_f)} =& \frac{(1 - Ri_f)^2 (1 - (\beta_2 - \alpha_3) Ri_f)}{a_1 (1 - \beta_2 Ri_f)(1 - \alpha_2 Ri_f)}. && (5.90b)
\end{aligned}
$$

We can keep the same structure as in Eq. (5.25) in the iterative process by taking: $\alpha_1 = \mathcal{C}_\mu$, $\alpha_2 = \mu_{xz}$, $\alpha_3 = \frac{3}{4}\mu - \frac{1}{2\lambda}$, $\beta_2 = \mu$.

Furthermore, we have:

$$Pr_t = \frac{\alpha_1}{\mathcal{C}_\theta^{GGDH}\lambda} \frac{(1 - \mu_{xz} Ri_f)}{\left(1 - Ri_f\left(\frac{\mu}{4} + \frac{1}{2\lambda}\right)\right)}, \tag{5.91a}$$

$$\frac{\langle u\theta \rangle}{u_* \theta_*} = \sqrt{\frac{\alpha_1}{\lambda^2} \frac{(1 - \mu_{xz} Ri_f)}{(1 - \mu Ri_f)\left(1 - Ri_f\left(\frac{\mu}{4} + \frac{1}{2\lambda}\right)\right)}}. \tag{5.91b}$$

CHAPTER 6

Conclusions and Perspectives

In this work, a first axis of study considered has been the analysis of the numerical error that may arise when considering Lagrangian stochastic methods based on particle/mesh formulations. In this scope, in Chapter 2, the question of the interplay between temporal and spatial errors has been raised. Indeed, considering only the local mean carrier fields associated to the initial location may introduce error, as the evolution of the mean fields along particle path over a time step is not taken into account. Such an error may be particularly noticeable should we consider highly varying mean fields or time steps long compared to the local CFL number. To limit this source of error, a time-step-robust time-splitting method, enabling for each particle to estimate the travelling time in each cell, has been developed. This algorithm enables to dynamically update the mean carrier fields associated to the particle location with local values, every time a particle enters a new cell. However, as a Lagrangian stochastic method based on Itô formulation is used, the major concern of anticipation error has raised. In this matter, this chapter has been a good vector to discuss and analyse precisely the spurious biases that may arise when introducing mismanaged anticipating terms in Lagrangian stochastic methods. Indeed, because of Itô definition for the stochastic integrals, it is necessary for the quantities integrated to be selected at the previous time step and independently from the stochastic draws associated to the current time step. Estimating the particle time of residence in a cell, based on draw-dependent information, would then introduce an anticipation error when integrating over this time period. To avoid the occurrence of such mismanaged anticipation error, it has been chosen to consider a deterministic virtual particle associated to each stochastic one and whose free-of-bias trajectory has been used to estimate the travelling time of each particle in each cell. This algorithm has then been verified on two representative test cases ensuring both the correct computation of the stochastic integrals but also the proper update of the mean carrier fields along the particle trajectory. It has been shown that the latter may greatly diminish the computational error. This issue led to the publication of a first scientific article (see Balvet et al. [2023a]).

Furthermore, still in a purpose of characterising and lowering the numerical error that may impact the results obtained using PDF methods, a detailed investigation of the spatial numerical error has been carried out. This issue has first been studied in detail in Chapter 3 for neutral-surface boundary-layer (SBL) flows and has later been extended to thermally stratified SBL flows in Section 5.2. The inquiry in neutral SBL was the subject of a second published article (see

Balvet et al. [2023b]). It has been demonstrated that the spatial error encountered is twofold. First, an error in the interpolation of the mean carrier fields at the location of the particles impais the evolution of the instantaneous quantities associated to the particles. It has been exposed that, especially near the wall, it is necessary to use an interpolation method more accurate than piecewise constant for the mean velocity and potential temperature so that the corresponding local gradient can be adequately estimated. The poor estimation of this gradient would impact the mean first-order moments, but also and mostly the corresponding second-order moments, as their production terms would be greatly tarnished. Moreover, it has been prescribed to use an interpolation for the Lagrangian timescale coherent with the choice made for the first-order moments and the respect of the production-dissipation equilibrium for both the TKE and the potential temperature variance. Considering these constraints and the necessity to use a cell-based method (i.e., based only on information stored in the particle cell), to be able to treat complex unstructured 3-D meshes, different interpolations methods have been proposed. Using a linear piecewise interpolation enables to improve greatly the results and has the advantage of being general and easy to implement. However, it is still possible to improve these results near wall by using locally a more accurate interpolation e.g., a pseudo-analytical interpolation of the mean fields. In both cases, a remaining issue is the discontinuity of such interpolation, when particles cross cell interfaces. To ensure such a continuity for a local interpolation method, a further inquiry should be realised potentially relying on the use of compatible discrete operator (CDO) schemes (see e.g. Bonelle [2014]). Let us note that such a choice would require a consequent modification of the tracking algorithm. The second source of spatial numerical error exhibited is the error impacting the estimation of the statistics from the set of particles. As we have considered a hybrid formulation, in which the statistics estimated are not injected in the particle dynamics, this error only impacts the observable post-treated and provided to the user. Using a stand-alone method, it would also introduce a bias in the instantaneous evolution of the quantities associated to the particles. It has been proved that computing the ensemble statistics on coarse averaging bins, within which the statistics associated to the particles are not uniform, results in the introduction of an error in the estimation of the covariances. Indeed, the covariances obtained in such a manner correspond to the sum of the covariances of interest with the local spatial covariances of the mean first-order fields. Two solutions are proposed to get rid of the second covariances spoiling the user observables. The first one is to use an intermediate finer mesh to estimate the statistics and spatially average resulting statistics onto the coarser mesh. However, such a method is cumbersome as it requires to introduce a second auxiliary mesh and then to track the particle location on both meshes leading to a non-negligible increase of computational cost. To avoid such an issue, it is then proposed to correct the estimation of the covariances directly on the coarse mesh by estimating the local spatial covariances of the corresponding mean fields directly on this mesh. To do so, it is necessary to reconstruct the mean fields profiles within the cells knowing solely their values stored at the centre of cells. It is highlighted that proper results are retrieved when considering a reconstruction scheme for the mean fields associated to the particle set coherent with the interpolation methods used to estimate the mean carrier fields.

The second axis of this study, dealing with the modelling of atmospheric SBL flows with Lagrangian stochastic methods, is also introduced. In this purpose, in Section 3.1 for the dynamics and in Section 5.2.1 for the thermal effects, a special interest is provided for the treatment of wall boundary conditions used in the particle solver. As we have considered only a model valid for high Reynolds number flows, and as the particles can be arbitrarily close to the limit of the domain, the wall boundary condition should be implemented in a zone where the viscous effects are negligible (i.e., for the neutral case in the logarithmic zone). It has been verified that for both the instantaneous streamwise velocity and the instantaneous potential temperature an an-elastic rebound should be considered when the particles cross the limit of the domain. The latter is necessary to retrieve proper normal fluxes (respectively the shear stress and normal turbulent heat fluxes). Indeed, considering an elastic rebound amounts to impose a zero-gradient on the first-order terms and a zero flux condition at the boundary condition. Such specular rebounds are then in opposition with the physical phenomena at stake near wall and result in a poor estimation of both the resulting first and second-order moment. Even though the use of a specular rebound on the mean velocity does not impact the concentration profiles in 1-D periodic flows, the elastic rebound on the potential temperature triggers a mistreatment of the potential temperature profiles, and then also a mistreatment of the buoyant terms. The latter ones are then no longer in equilibrium with the pressure gradient. Near the wall, this results in a spurious accumulation of particles for thermally unstable conditions and in a spurious depletion of particles for stable flows. This is in clear violation with the well mixed criterion. At the opposite it has been further verified that using the an-elastic boundary condition proposed by Dreeben and Pope [1997b] and Pozorski and Minier [1998] proper results are retrieved.

In the continuation of the design to better model the atmospheric flows and in the scope of hybrid modelling, a model-consistent description of the SBL has been derived in Section 5.1 to provide proper mean carrier flows. Placing ourselves in the scope of the Monin–Obukhov theory, this description is based on the algebraic solutions derived from a class of second-order models within which the fluctuating pressure induced redistribution terms are modelled taking into account linear contributions of the physical processes at stake. To do so, except for the dissipation rate, the diffusion terms of turbulent quantities are neglected under equilibrium assumptions. Doing so, it is possible to determine the universal functions characterising all the first-order and second-order statistics except for the mean velocity. All these universal functions depend solely on the flux Richardson number and then on the momentum universal function. In order to estimate the latter, the turbulent kinetic energy dissipation rate equation is considered. This is the only equation for which the diffusive term is considered. It is thus the only non-local equation providing a scale for the distance to the wall necessary to estimate the momentum universal function and to close the system. Even though it is possible to derive an implicit solution for the flux Richardson number and then the momentum fluxes, the latter are too complex to be resolved analytically. An iterative resolution of the dissipation rate equation has then been considered, based on the algebraic solution previously obtained. Doing so, it has been possible to exhibit a description of the SBL flows which agrees with Monin–Obukhov similarity theory respecting both the theoretical stable and convective asymptotic behaviours. It has been verified that the results obtained are coherent with results obtained using the CFD solver code_saturne in stable situations. These situations are of most interest, as they are the most penalising for a dispersion of pollutant. In contrast, in the case of convective flows multiple difficulties have emerged. First, numerical discrepancies occur, the latter may stem from a poor implementation of the boundary conditions or from the necessity to use more stable numerical scheme for second-order methods. Moreover, it seems that in this situation the equilibrium assumptions considered neglecting the effects of the diffusive terms are no longer valid. Yet, it has been demonstrated that without the diffusive terms the algebraic solution proposed is retrieved. Let us note that the algebraic solution is used to fuel the boundary condition of the CFD simulations. A further work should then be made to properly characterise such situations. In this scope, the effects of the TKE diffusion on the dissipation rate should be implemented within the iterative resolution of the latter. Moreover, it would be pertinent to try to estimate the effects of the diffusive terms based on correlation between local terms and the diffusive terms. This work still paves the way for the development of model-consistent derivation of universal functions which aims at maintaining profiles injected as boundary conditions at inlet by providing profiles close to the solution of the FV simulation.

Finally, the third axis of study of this work is the description of plume obtained using hybrid PDF methods and where only the particles issued from the pollutant source are simulated. This issue is first introduced for neutral flows in Chapter 4, comparing simulation results with experimental data of Gamel [2015] obtained in a channel flow. Two cases are considered first a dispersion in an unobstructed flow and then a dispersion in the wake of an isolated obstacles. It is shown that, in the scope of hybrid moment/PDF methods, the mean concentration but also of the scalar fluxes might be estimated directly by simulating only the particles issued from the source and neglecting the micro-mixing effects. However, the consideration of the latter is of major importance to be able to estimate the scalar variance. Without this modelling of the micro-mixing, the scalar variance is grossly overestimated. It is however possible to obtain a quite adequate description of the scalar variance scale, considering only particles issued from the source, by using the volumetric particles approach proposed by Cassiani [2013]. Although the aforementioned improvements proposed in this thesis have a noticeable effect near wall, the latter remains of secondary order compared to the impact of a proper estimation of the mean carrier fields. In this case where there are no duplicated fields between moment and PDF approaches, it is put forward that the error induced by the lack of consistency in the modelling selected might be weak compared to the gain of using non-consistent models which better capture the recirculation zone and the physics of the carrier flow. Moreover, the choice of modelling selected for the PDF methods also seems to have a preponderant effect on the pollutant dispersion. Indeed, the isotropic turbulent timescale and the isotropic production of turbulent fluctuations might induce an overestimation of the normal fluctuations near wall. The latter results in overly diffusive plumes. Furthermore, in these flows, signals of the potential presence of 3-D effects have been addressed, yet only a 2-D study has been performed. A further study on the effect of secondary flows should be carried out using a 3-D simulation. Finally, the thermal effects on the plume shapes have been qualitatively assessed in stratified SBL flows in Section 5.3. Following Monin [1959], it has been verified that in these flows the plume shapes do not depend directly on the wind velocity characterised by the friction velocity but solely on the atmospheric stability characterised by the Monin–Obukhov length scale. Indeed, in stable flows the thermal effects tend to kill the vertical fluctuations of velocity whereas they are enhanced in convective situation. This results in a direct impact on the plume shapes going from small and concentrated plumes for very stable situations to large diffuse plumes mixed by turbulent effects in convective situations. Such qualitative results are properly captured in the simulations carried out. Moreover, the impact of the thermal relaxation time modelling on rise and diffusion of plumes has been exposed using a weakly buoyant plume. The simulations carried out properly retrieve the physical behaviours expected and illustrate the importance of a proper consideration of the thermal modelling on both the plume rise and dispersion.

In the continuation of the work proposed by Bahlali [2018], from both a numerical and theoretical point of view, this study has furnished a detailed characterisation of the neutral and stratified SBL flows using Lagrangian stochastic methods. It aims at providing guidelines and explanations for a better use of such methods for atmospheric dispersion using the open source CFD solver code_saturne. However, besides the perspectives already stated other ones are still to be considered, from numerical, modelling and theoretical scopes.

First, from a numerical point a view, a further study on DRSM and DFM methods should be tackled to obtain more stable schemes with a better implementation of the boundary conditions. The proper resolution of these methods, which transports explicitly the Reynolds stress tensor and turbulent heat fluxes, is of great importance as, using a Langevin standpoint, GLM methods are intrinsically consistent with such approaches. This work on the boundary-condition implementation and on the numerical scheme might then substantially improve the estimation of the mean carrier flows provided to the particle solver. Furthermore, within the latter solver, a temporal numerical error is still present when considering fluid particles in the diffusive regime with a varying Lagrangian timescale. Such a situation is classically encountered in the near ground region imposing to use a very small time step for all particles. This triggers a great increase in the computational cost which remains a limitation of the method presented. The implementation and verification of the extended scheme proposed by Minier [2016] are a promising way to release an important lock in the use and development of this approach with the exponential temporal scheme considered.

Furthermore, from a modelling perspective, it is worth noting that the SLM model selected is coherent with a Rotta model. Both assume an isotropic redistribution of the kinetic energy, which is not representative of the situation encountered near wall where more energy is directed towards the streamwise direction. Such a model might result in too diffusive plumes. The extension to the GLM class of model might be of great interest especially given that the methods used to derive model-consistent universal functions is directly applicable for a wide range of GLM model. Yet, it is worth noticing that such an extension is not direct as it would require a modification of the temporal scheme considered. For now, the integration in each spatial direction is treated independently. Yet, using anisotropic GLM models the evolution in one direction might depend on the integration in the other direction and would require a specific change of basis to be able to consider an integration scheme like the one actually implemented. Moreover, in the scope of developing a proper GLM model for atmospheric purposes, one may either consider the implementation of the Lagrangian counterpart of the standard SRQM model, but one may also derive a model specifically fitted to treat such flows. To this end, for models of the class studied, it would be required to confront the algebraic solutions derived with experimental data to validate the modelling proposed.

In addition, the approach developed has only considered Boussinesq assumption; and an extension to an anelastic description of the atmosphere could be tackled. In this perspective, we consider a deviation compared to the adiabatic flow instead of a deviation compared to a constant flow for the treatment of buoyancy. This description is indeed physically sounder in the context of atmospheric flows. This is of particular importance mostly if one aims at going upper in the atmosphere where the adiabatic variation of density might become non-negligible. Indeed, the scope of this work is limited to the SBL due to the conceptual framework considered based on the Monin–Obukhov theory. Yet, the flow within the Eckman layer is of great importance in the description of the dispersion at longer scales. In order to be able to consider such scales, an extension of the Monin–Obukhov theory should be inquired to treat the Coriolis effects but also the decrease of the shear stress and turbulent heat fluxes with altitude.

Furthermore, so as to be physically more accurate, the consideration of the humidity should be investigated as for now only dry atmosphere have been considered. Such a study will show more of the method potential if we also take into account the atmospheric chemistry for which such methods are particularly well fitted. In addition, we may also take into account the inertial particles, for which the work presented can be directly extended, to see the effect of segregation based on particles mass and inertia (see Minier and Peirano [2001], Minier [2016]). Indeed, these methods are well equipped to treat such poly-disperse flows, and to model deposition phenomena whether they are dry or humid.

Moreover, in the perspective of using such methods for accidental purpose, we may consider the case of buoyant or highly buoyant release which may occur in case of fire. Lagrangian stochastic methods might be of great interest to treat such cases as the poly-disperse creation of ashes, soot, chemical compounds and the corresponding radiation might be taken into account explicitly. However, in this end, first a specific inquiry on the mechanisms at stake near the fire source should be considered. Moreover, a stronger coupling (two-way coupling) between the particle solver and FV approach should be considered to characterise the effects of the fire on the mean carrier flows. Finally the proper treatment of the Ekman layer should be seen as a prerequisite if one wants to simulate such dispersion over relatively short distances.

Bibliography

K. E. Akihiro Tominaga, Iehisa Nezu and H. Nakagawa. Three-dimensional turbulent structure in straight open channel flows. Journal of Hydraulic Research, 27(1):149–173, 1989. doi: 10.1080/00221688909499249. URL https://doi.org/10.1080/00221688909499249.

D. Anfossi, D. Öttl, G. Degrazia, and A. Goulart. An analysis of sonic anemometer observations in low wind speed conditions. Boundary-Layer Meteorology, 114:179–203, 2005.

F. Archambeau, N. Méchitoua, and M. Sakiz. Code Saturne: A finite volume code for the computation of turbulent incompressible flows-Industrial applications. International Journal on Finite Volumes, 1(1), 2004. URL https://ijfv.math.cnrs.fr/spip.php?article3.

L. Arnold. Stochastic Differential Equations: Theory and Applications. Wiley-Interscience [John Wiley & Sons], New York, 1974.

P. Arya. Introduction to Micrometeorology. 2nd Edition. Academic Press, San Diego, 1998.

P. Arya. Air Pollution Meteorology and Dispersion. Oxford University Press, Oxford, 1999.

M. Bahlali. Adaptation de la modélisation hybride eulérienne/lagrangienne stochastique de Code_Saturne à la dispersion atmosphérique de polluants à l'échelle micro-météorologique et comparaison à la méthode eulérienne. PhD thesis, Université Paris Est, 2018. URL http://www.theses.fr/2018PESC1047. Thèse de doctorat dirigée par B. Carissimo, Bertrand Sciences et Techniques de l'Environnement Paris Est 2018.

M. L. Bahlali, E. Dupont, and B. Carissimo. Atmospheric dispersion using a Lagrangian stochastic approach: Application to an idealized urban area under neutral and stable meteorological conditions. Journal of Wind Engineering and Industrial Aerodynamics, 193: 103976, Aug. 2019. doi: 10.1016/j.jweia.2019.103976. URL https://enpc.hal.science/hal-02898281.

M. L. Bahlali, C. Henry, and B. Carissimo. On the well-mixed condition and consistency issues in hybrid Eulerian/Lagrangian stochastic models of dispersion. Boundary-Layer Meteorology, 174(2):275–296, 2020. doi: 10.1007/s10546-019-00486-9.

G. Balvet, J.-P. Minier, C. Henry, Y. Roustan, and M. Ferrand. A time-step-robust algorithm to compute particle trajectories in 3-d unstructured meshes for lagrangian stochastic methods. Monte Carlo Methods and Applications, 29(2):95–126, 2023a. doi: doi:10.1515/mcma-2023-2002. URL https://doi.org/10.1515/mcma-2023-2002.

G. Balvet, J.-P. Minier, Y. Roustan, and M. Ferrand. Analysis of wall-modelled particle/mesh pdf methods for turbulent parietal flows. Monte Carlo Methods and Applications, 29 (4):275–305, 2023b. doi: doi:10.1515/mcma-2023-2017. URL https://doi.org/10.1515/mcma-2023-2017.

J. Barlow and O. Coceal. A review of urban roughness sublayer turbulence. Technical report, UK Met Office, 01 2009.

A. Bisignano and B. J. Devenish. A model for temperature fluctuations in a buoyant plume. Boundary-Layer Meteorology, 157(2):157–172, 2015.

J. Bonelle. Opérateurs discrets compatibles pour la discrétisation sur maillages polyédriques des équations elliptiques et de Stokes. PhD thesis, Université Paris Est, 2014. URL http://www.theses.fr/2014PEST1078. Thèse de doctorat dirigée par E. Alexandre Mathématiques Paris Est 2014.

C. E. Brennen. Fundamentals of Multiphase Flow. Cambridge University Press, 2005. ISBN 9780521848046.

G. A. Briggs. A plume rise model compared with observations. Journal of the Air Pollution Control Association, 15(9):433–438, 1965. doi: 10.1080/00022470.1965.10468404. URL https://doi.org/10.1080/00022470.1965.10468404.

R. E. Britter and S. R. Hanna. Flow and dispersion in urban areas. Annual Review of Fluid Mechanics, 35(1):469–496, 2003. doi: 10.1146/annurev.fluid.35.101101.161147. URL https://doi.org/10.1146/annurev.fluid.35.101101.161147.

Y. Brunet. Turbulent flow in plant canopies: Historical perspective and overview. Boundary-Layer Meteorology, 177(2-3):315–364, 2020.

J. A. Businger, J. C. Wyngaard, Y. Izumi, and E. F. Bradley. Flux-Profile Relationships in the Atmospheric Surface Layer. Journal of the Atmospheric Sciences, 28(2):181–189, Mar. 1971. ISSN 0022-4928, 1520-0469. doi: 10.1175/1520-0469(1971)028<0181:FPRITA>2.0.CO;2. URL https://journals.ametsoc.org/view/journals/atsc/28/2/1520-0469_1971_028_0181_fprita_2_0_co_2.xml. Publisher: American Meteorological Society Section: Journal of the Atmospheric Sciences.

D. M. Carl, T. C. Tarbell, and H. A. Panofsky. Profiles of Wind and Temperature from Towers over Homogeneous Terrain. Journal of the Atmospheric Sciences, 30(5):788–794, July 1973. ISSN 0022-4928, 1520-0469. doi: 10.1175/1520-0469(1973)030<0788:POWATF>2.0.CO;2. URL http://journals.ametsoc.org/doi/10.1175/1520-0469(1973)030<0788:POWATF>2.0.CO;2.

M. Cassiani. The volumetric particle approach for concentration fluctuations and chemical reactions in lagrangian particle and particle-grid models. Boundary-Layer Meteorology, 146 (2):207–233, 2013.

M. Cassiani, P. Franzese, and U. Giostra. A pdf micromixing model of dispersion for atmospheric flow. part i: development of the model, application to homogeneous turbulence and to neutral boundary layer. Atmospheric Environment (1994), 39(8):1457–1469, 2005.

Y. Chenge and W. Brutsaert. Flux-profile Relationships for Wind Speed and Temperature in the Stable Atmospheric Boundary Layer. Boundary-Layer Meteorology, 114(3):519–538, Mar. 2005. ISSN 0006-8314, 1573-1472. doi: 10.1007/s10546-004-1425-4. URL http://link.springer.com/10.1007/s10546-004-1425-4.

S. Chibbaro and J.-P. Minier. A note on the consistency of hybrid Eulerian/Lagrangian approach to multiphase flows. International Journal of Multiphase Flow, 37(3):293–297, 2011. doi: 10.1016/j.ijmultiphaseflow.2010.10.010.

R. Clift, J. R. Grace, and M. E. Weber. Bubbles, Drops, and Particles. Dover Civil and Mechanical Engineering Series. Dover Publications, 2005. ISBN 9780486445809. URL https://books.google.fr/books?id=UUr0mD8niUQC.

T. comity ISO/TC 20. Standard atmosphere. Standard, International Organization for Standardization, Geneva, CH, Mar. 1975.

B. J. Daly and F. H. Harlow. Transport equations in turbulence. The Physics of Fluids, 13(11): 2634–2649, 1970. doi: https://doi.org/10.1063/1.1692845.

S. Das and P. Durbin. A Lagrangian stochastic model for dispersion in stratified turbulence. Physics of Fluids - PHYS FLUIDS, 17, 02 2005. doi: 10.1063/1.1849184.

J. W. Deardorff. On the magnitude of the subgrid scale eddy coefficient. Journal of Computational Physics, 7(1):120–133, 1971.

J. W. Deardorff. Numerical Investigation of Neutral and Unstable Planetary Boundary Layers. Journal of the Atmospheric Sciences, 29(1):91–115, Jan. 1972. ISSN 0022-4928, 1520-0469. doi: 10.1175/1520-0469(1972)029<0091:NIONAU>2.0.CO;2. URL http://journals.ametsoc.org/doi/10.1175/1520-0469(1972)029<0091:NIONAU>2.0.CO;2.

F. Dehoux. Modélisation statistique des écoulements turbulents en convection forcée, mixte et naturelle. PhD thesis, Poitiers, 2012. URL https://www.theses.fr/2012POIT2276.

F. Dehoux, Y. Lecocq, S. Benhamadouche, R. Manceau, and L. Brizzi. Algebraic modeling of the turbulent heat fluxes using the elliptic blending approach—application to forced and mixed convection regimes. Flow, Turbulence and Combustion, 88:77–100, 03 2011. doi: 10.1007/s10494-011-9366-8.

B. J. Delarue and S. B. Pope. Application of pdf methods to compressible turbulent flows. Physics of Fluids (1994), 9(9):2704–2715, 1997.

A. O. Demuren and W. Rodi. Calculation of turbulence-driven secondary motion in non-circular ducts. Journal of Fluid Mechanics, 140:189–222, 1984. doi: 10.1017/S0022112084000574.

H. W. Detering and D. Etling. Application of the E-ϵ turbulence model to the atmospheric boundary layer. Boundary-Layer Meteorology, 33(2):113–133, 1985.

T. D. Dreeben and S. B. Pope. Probability density function and Reynolds-stress modeling of near-wall turbulent flows. Physics of Fluids, 9:154–163, 1997a.

T. D. Dreeben and S. B. Pope. Wall-function treatment in pdf methods for turbulent flows. Physics of Fluids, 9(9):2692–2703, 1997b. doi: 10.1063/1.869381.

T. D. Dreeben and S. B. Pope. Probability density function/Monte Carlo simulation of near-wall turbulent flows. Journal of Fluid Mechanics, 357:141–166, 1998. doi: 10.1017/S0022112097008008.

P. G. Duynkerke. Application of the E $-\epsilon$ Turbulence Closure Model to the Neutral and Stable Atmospheric Boundary Layer. Journal of the Atmospheric Sciences, 45(5):865–880, Mar. 1988. ISSN 0022-4928, 1520-0469. doi: 10.1175/1520-0469(1988)045<0865:AOTTCM>2.0.CO;2. URL https://journals.ametsoc.org/view/journals/atsc/45/5/1520-0469_1988_045_0865_aottcm_2_0_co_2.xml.

A. J. Dyer. A review of flux-profile relationships. Boundary-Layer Meteorology, 7(3):363–372, 1974.

A. Einstein. Über die von der molekularkinetischen Theorie der Wärme geforderte Bewegung von in ruhenden Flüssigkeiten suspendierten Teilchen. Annalen der Physik, 322(8):549–560, Jan. 1905. doi: 10.1002/andp.19053220806.

S. Elghobashi and B. Launder. Turbulent time scales and the dissipation rate of temperature variance in the thermal mixing layer. Physics of Fluids, 26, 09 1983. doi: 10.1063/1.865423.

R. Eymard, G. Henry, R. Herbin, F. Hubert, R. Klöfkorn, and G. Manzini. 3D benchmark on discretization schemes for anisotropic diffusion problems on general grids. In Finite Volumes for Complex Applications VI Problems & Perspectives, pages 895–930. Springer, 2011. doi: 10.1007/978-3-642-20671-9_89.

M. Ferrand and D. Violeau. A family of explicit algebraic models for Reynolds stresses and passive scalar fluxes. Journal of Hydraulic Research, 50(5):494–505, 2012.

M. Ferrand, J.-M. Hérard, T. Norddine, and R. Simon. Stable schemes for second-moment turbulent models for incompressible flows. Comptes Rendus Mécanique, 351:337–353, 09 2023.

A. Fick. On liquid diffusion. The London, Edinburgh, and Dublin Philosophical Magazine and Journal of Science, 10(63):30–39, 1855. doi: 10.1080/14786445508641925. URL https://doi.org/10.1080/14786445508641925.

J. J. Finnigan. Chapter two - the turbulent wind in plant and forest canopies. In E. A. Johnson and K. Miyanishi, editors, Plant Disturbance Ecology (Second Edition), pages 17–63. Academic Press, San Diego, second edition edition, 2021. ISBN 978-0-12-818813-2. doi: https://doi.org/10.1016/B978-0-12-818813-2.00002-2. URL https://www.sciencedirect.com/science/article/pii/B9780128188132000022.

B. Fisher, E. Metcalfe, I. Vince, and A. Yates. Modelling plume rise and dispersion from pool fires. Atmospheric Environment, 35(12):2101–2110, 2001.

J. B. J. Fourier, G. Darboux, et al. Théorie analytique de la chaleur, volume 504. Didot Paris, 1822. doi: https://doi.org/10.1017/CBO9780511693229.

J. Franke, A. Hellsten, K. Schlünzen, and B. Carissimo. Best practice guideline for the cfd simulation of flows in the urban environment - a summary. In 11th Conference on Harmonisation within Atmospheric Dispersion Modelling for Regulatory Purposes, Cambridge, UK, July 2007, United Kingdom, 2007. Cambridge Environmental Research Consultants.

L. S. Freire, M. Chamecki, E. Bou-Zeid, and N. L. Dias. Critical flux Richardson number for Kolmogorov turbulence enabled by tke transport. Quarterly Journal of the Royal Meteorological Society, 145(721):1551–1558, 2019. doi: https://doi.org/10.1002/qj.3511. URL https://rmets.onlinelibrary.wiley.com/doi/abs/10.1002/qj.3511.

H. Gamel. Caractérisation expérimentale de l'écoulement et de la dispersion autour d'un obstacle bidimensionnel. PhD thesis, Ecole Centrale de Lyon, 2015. URL http://www.theses.fr/2015ECDL0002. Thèse de doctorat dirigée par P. Richard Mécanique Ecully, Ecole centrale de Lyon 2015.

C. W. Gardiner. Handbook of Stochastic Methods, volume 3. Springer Berlin, 1985.

M. Germano, U. Piomelli, P. Moin, and W. H. Cabot. A dynamic subgrid-scale eddy viscosity model. Physics of Fluids. A, Fluid dynamics, 3(7):1760–1765, 1991.

M. M. Gibson and B. E. Launder. Ground effects on pressure fluctuations in the atmospheric boundary layer. Journal of Fluid Mechanics, 86(3):491–511, June 1978. ISSN 0022-1120, 1469-7645. doi: 10.1017/S0022112078001251. URL https://www.cambridge.org/core/product/identifier/S0022112078001251/type/journal_article.

P. Glasserman. Monte Carlo Methods in Financial Engineering. Stochastic Modelling and Applied Probability. Springer New York, 2013. ISBN 9780387216171.

S.-E. Gryning, E. Batchvarova, B. Brümmer, H. Jørgensen, and S. Larsen. On the extension of the wind profile over homogeneous terrain beyond the surface boundary layer. Boundary-Layer Meteorology, 124(2):251–268, 2007. Publisher: Springer.

M. Haeffelin, L. Barthès, O. Bock, C. Boitel, S. Bony, D. Bouniol, H. Chepfer, M. Chiriaco, J. Cuesta, J. Delanoë, P. Drobinski, J.-L. Dufresne, C. Flamant, M. Grall, A. Hodzic, F. Hourdin, F. Lapouge, Y. Lemaître, A. Mathieu, Y. Morille, C. Naud, V. Noël, W. O'Hirok, J. Pelon, C. Pietras, A. Protat, B. Romand, G. Scialom, and R. Vautard. Sirta, a ground-based atmospheric observatory for cloud and aerosol research. Ann. Geophys., 23:253–275, 2005. doi: 10.5194/angeo-23-253-2005.

K. Hanjalić and B. Launder. Modelling Turbulence in Engineering and the Environment: Rational Alternative Routes to Closure. Cambridge University Press, 2 edition, 2022. doi: 10.1017/9781108875400.

K. Hanjalić and B. E. Launder. A Reynolds stress model of turbulence and its application to thin shear flows. Journal of Fluid Mechanics, 52(4):609–638, Apr. 1972. ISSN 0022-1120, 1469-7645. doi: 10.1017/S002211207200268X. URL https://www.cambridge.org/core/product/identifier/S002211207200268X/type/journal_article.

S. Hanna, G. A. Briggs, R. P. Hosker, and J. S. Smith. Handbook on atmospheric diffusion. Technical report, National Oceanic and Atmospheric Administration, Oak Ridge, TN, 1982. URL https://api.semanticscholar.org/CorpusID:128993711.

O. K. Hartogensis and H. A. R. De Bruin. Monin–Obukhov Similarity Functions of the Structure Parameter of Temperature and Turbulent Kinetic Energy Dissipation Rate in the Stable Boundary Layer. Boundary-Layer Meteorology, 116(2):253–276, Aug. 2005. ISSN 0006-8314, 1573-1472. doi: 10.1007/s10546-004-2817-1. URL http://link.springer.com/10.1007/s10546-004-2817-1.

D. C. Haworth. Progress in probability density function methods for turbulent reacting flows. Progress in Energy and Combustion Science, 36(2):168–259, 2010. doi: 10.1016/j.pecs.2009.09.003.

D. C. Haworth and S. B. Pope. A generalized Langevin model for turbulent flows. The Physics of Fluids, 29(2):387–405, 1986. doi: 10.1063/1.865723.

C. Henry, J.-P. Minier, M. Mohaupt, C. Profeta, J. Pozorski, and A. Tanière. A stochastic approach for the simulation of collisions between colloidal particles at large time steps. International Journal of Multiphase Flow, 61:94–107, 2014. ISSN 0301-9322. doi: https://doi.org/10.1016/j.ijmultiphaseflow.2014.01.007. URL https://www.sciencedirect.com/science/article/pii/S0301932214000135.

R. Hockney. Computer experiment of anomalous diffusion. The Physics of Fluids, 9(9):1826–1835, 1966. doi: 10.1063/1.1761939.

R. W. Hockney and J. W. Eastwood. Computer Simulation using Particles. CRC Press, 1988. doi: 10.1201/9780367806934.

M. Hutchinson, H. Oh, and W. Chen. A review of source term estimation methods for atmospheric dispersion events using static or mobile sensors. Information Fusion, 36:130–148, 2016.

U. L. F. Högström. Non-Dimensional Wind and Temperature Profiles in the Atmospheric Surface Layer: A Re-Evaluation. In B. B. Hicks, editor, Topics in Micrometeorology. A Festschrift for Arch Dyer, pages 55–78. Springer Netherlands, Dordrecht, 1988. ISBN 978-94-010-7822-1 978-94-009-2935-7. doi: 10.1007/978-94-009-2935-7-6. URL http://link.springer.com/10.1007/978-94-009-2935-7_6.

A. Innocenti, C. Marchioli, and S. Chibbaro. Lagrangian filtered density function for LES-based stochastic modelling of turbulent particle-laden flows. Physics of Fluids (1994), 28(11), 2016.

A. Innocenti, N. Mordant, N. Stelzenmuller, and S. Chibbaro. Lagrangian stochastic modelling of acceleration in turbulent wall-bounded flows. Journal of Fluid Mechanics, 892, 2020. doi: /10.1017/jfm.2020.203.

A. Innocenti, R. O. Fox, and S. Chibbaro. A Lagrangian probability-density-function model for turbulent particle-laden channel flow in the dense regime. Physics of Fluids, 33(5):053308, 2021. doi: 10.1063/5.0045690.

M. Z. Jacobson. Fundamentals of Atmospheric Modeling. Cambridge University Press, 2 edition, 2005. doi: 10.1017/CBO9781139165389.

P. Jenny, S. Pope, M. Muradoglu, and D. Caughey. A Hybrid Algorithm for the Joint PDF Equation of Turbulent Reactive Flows. Journal of Computational Physics, 166(2):218–252, Jan. 2001. ISSN 00219991. doi: 10.1006/jcph.2000.6646. URL https://linkinghub.elsevier.com/retrieve/pii/S0021999100966464.

W. Jones and B. Launder. The prediction of laminarization with a two-equation model of turbulence. International Journal of Heat and Mass Transfer, 15(2):301–314, Feb. 1972. ISSN 00179310. doi: 10.1016/0017-9310(72)90076-2. URL https://linkinghub.elsevier.com/retrieve/pii/0017931072900762.

M. Kadivar, D. Tormey, and G. McGranaghan. A review on turbulent flow over rough surfaces: Fundamentals and theories. International Journal of Thermofluids, 10:100077, 2021.

S. Kenjereš, S. Gunarjo, and K. Hanjalić. Contribution to elliptic relaxation modelling of turbulent natural and mixed convection. International Journal of Heat and Fluid Flow, 26 (4):569–586, 2005. ISSN 0142-727X. doi: https://doi.org/10.1016/j.ijheatfluidflow.2005.03.007. URL https://www.sciencedirect.com/science/article/pii/S0142727X05000342. CHT'04.

Y. Kitamura, A. Hori, and T. Yagi. Flux Richardson Number and Turbulent Prandtl Number in a Developing Stable Boundary Layer. Journal of the Meteorological Society of Japan. Ser. II, 91(5):655–666, 2013. ISSN 0026-1165, 2186-9057. doi: 10.2151/jmsj.2013-507. URL https://www.jstage.jst.go.jp/article/jmsj/91/5/91_2013-507/_article.

M. Klein, A. Sadiki, and J. Janicka. A digital filter based generation of inflow data for spatially developing direct numerical or large eddy simulations. Journal of Computational Physics, 186 (2):652–665, 2003.

A. Kolmogorov. The Local Structure of Turbulence in Incompressible Viscous Fluid for Very Large Reynolds' Numbers. Akademiia Nauk SSSR Doklady, 30:301–305, Jan. 1941.

A. N. Kolmogorov. A refinement of previous hypotheses concerning the local structure of turbulence in a viscous incompressible fluid at high reynolds number. Journal of Fluid Mechanics, 13(1):82–85, 1962. doi: 10.1017/S0022112062000518.

L. Landau and E. Lifshitz. Chapter vi - diffusion. In Fluid Mechanics, pages 227–237. Pergamon, second edition, 1987. ISBN 978-0-08-033933-7. doi: https://doi.org/10.1016/B978-0-08-033933-7.50014-3. URL https://www.sciencedirect.com/science/article/pii/B9780080339337500143.

P. Langevin. Sur la théorie du mouvement brownien. Comptes Rendus de l'Académie des Sciences, 1908. URL https://fr.wikisource.org/wiki/Sur_la_th%C3%A9orie_du_mouvement_brownien.

B. Launder and D. Spalding. The numerical computation of turbulent flows. Computer Methods in Applied Mechanics and Engineering, 3(2):269–289, 1974. ISSN 0045-7825. doi: https://doi.org/10.1016/0045-7825(74)90029-2. URL https://www.sciencedirect.com/science/article/pii/0045782574900292.

B. E. Launder. On the effects of a gravitational field on the turbulent transport of heat and momentum. Journal of Fluid Mechanics, 67(3):569–581, 1975. doi: 10.1017/S002211207500047X.

B. E. Launder, G. J. Reece, and W. Rodi. Progress in the development of a Reynolds-stress turbulence closure. Journal of Fluid Mechanics, 68(3):537–566, 1975. doi: 10.1017/S0022112075001814.

A. Leelóssy, I. Lagzi, A. Kovács, and R. Mészáros. A review of numerical models to predict the atmospheric dispersion of radionuclides. Journal of Environmental Radioactivity, 182:20–33, 2018.

D. Li. Turbulent Prandtl number in the atmospheric boundary layer - where are we now? Atmospheric Research, 216:86–105, 2019. ISSN 0169-8095. doi: https://doi.org/10.1016/j.atmosres.2018.09.015. URL https://www.sciencedirect.com/science/article/pii/S0169809518307324.

D. K. Lilly. A proposed modification of the Germano subgrid-scale closure method. Physics of Fluids A: Fluid Dynamics, 4(3):633–635, 1992. doi: 10.1063/1.858280. URL https://doi.org/10.1063/1.858280.

K. E. Lilly. The representation of small-scale turbulence in numerical simulation experiments. In Proceedings of IBM Scientific Computing Symposium on Environmental Sciences, pages 195–210, 1966. URL https://api.semanticscholar.org/CorpusID:122042262.

R. Löhner and J. Ambrosiano. A vectorized particle tracer for unstructured grids. Journal of Computational Physics, 91(1):22–31, 1990. doi: 10.1016/0021-9991(90)90002-I.

J. L. Lumley. Computational Modeling of Turbulent Flows, volume 18 of Advances in Applied Mechanics. Elsevier, 1979. doi: https://doi.org/10.1016/S0065-2156(08)70266-7. URL https://www.sciencedirect.com/science/article/pii/S0065215608702667.

J. L. Lumley and B. Khajeh-Nouri. Computational Modeling of Turbulent Transport, volume 18. Elsevier, 1975. doi: 10.1016/S0065-2687(08)60460-4.

M. Massimo, P. Salizzoni, C. François-Xavier, I. Korsakissok, E. Danzi, and L. Soulhac. Plume rise and spread in buoyant releases from elevated sources in the lower atmosphere. Environmental Fluid Mechanics, 14, 08 2013. doi: 10.1007/s10652-013-9300-9.

R. McDermott and S. Pope. The parabolic edge reconstruction method (PERM) for Lagrangian particle advection. Journal of Computational Physics, 227(11):5447–5491, May 2008. ISSN 00219991. doi: 10.1016/j.jcp.2008.01.045. URL https://linkinghub.elsevier.com/retrieve/pii/S0021999108000843.

J. McInnes and F. Bracco. Stochastic particle dispersion modeling and the tracer-particle limit. Physics of Fluids A, page 2809, 1992.

A. Melling and J. H. Whitelaw. Turbulent flow in a rectangular duct. Journal of Fluid Mechanics, 78(2):289–315, 1976. doi: 10.1017/S0022112076002450.

G. L. Mellor and H. J. Herring. A survey of the mean turbulent field closure models. AIAA Journal, 11(5):590–599, May 1973. ISSN 0001-1452, 1533-385X. doi: 10.2514/3.6803. URL https://arc.aiaa.org/doi/10.2514/3.6803.

J.-P. Minier. On Lagrangian stochastic methods for turbulent polydisperse two-phase reactive flows. Progress in Energy and Combustion Science, 50:1–62, 2015. doi: 10.1016/j.pecs.2015.02.003.

J.-P. Minier. Statistical descriptions of polydisperse turbulent two-phase flows. Physics Reports, 665:1–122, 2016. doi: 10.1016/j.physrep.2016.10.007.

J.-P. Minier. A methodology to devise consistent probability density function models for particle dynamics in turbulent dispersed two-phase flows. Physics of Fluids, 33(2):023312, 2021. doi: 10.1063/5.0039249.

J.-P. Minier and E. Peirano. The pdf approach to turbulent polydispersed two-phase flows. Physics Reports, 352(1-3):1–214, 2001. doi: 10.1016/S0370-1573(01)00011-4.

J.-P. Minier and J. Pozorski. Derivation of a PDF model for turbulent flows based on principles from statistical physics. Physics of Fluids, 9(6):1748–1753, 1997. doi: 10.1063/1.869291.

J.-P. Minier and J. Pozorski. Wall-boundary conditions in probability density function methods and application to a turbulent channel flow. Physics of Fluids, 11(9):2632–2644, 1999. doi: 10.1063/1.870125.

J.-P. Minier, R. Cao, and S. Pope. Comment on the article “An effective particle tracing scheme on structured/unstructured grids in hybrid finite volume/PDF Monte Carlo methods” by Li and Modest. Journal of Computational Physics, 186(1):356–358, 2003a. doi: 10.1016/S0021-9991(03)00006-8.

J.-P. Minier, E. Peirano, and S. Chibbaro. Weak first-and second-order numerical schemes for stochastic differential equations appearing in Lagrangian two-phase flow modeling. Monte Carlo Methods and Applications, 9(2):93–133, 2003b. doi: 10.1515/156939603322663312.

J.-P. Minier, E. Peirano, and S. Chibbaro. PDF model based on Langevin equation for polydispersed two-phase flows applied to a bluff-body gas-solid flow. Physics of Fluids, 16(7):2419–2431, 2004. doi: 10.1063/1.1718972.

J.-P. Minier, S. Chibbaro, and S. B. Pope. Guidelines for the formulation of Lagrangian stochastic models for particle simulations of single-phase and dispersed two-phase turbulent flows. Physics of Fluids, 26(11):113303, 2014. doi: 10.1063/1.4901315.

M. Mohaupt, J.-P. Minier, and A. Tanière. A new approach for the detection of particle interactions for large-inertia and colloidal particles in a turbulent flow. International Journal of Multiphase Flow, 37(7):746–755, 2011. ISSN 0301-9322. doi: https://doi.org/10.1016/j.ijmultiphaseflow.2011.02.003. URL https://www.sciencedirect.com/science/article/pii/S0301932211000486.

T. Möller and B. Trumbore. Fast, minimum storage ray-triangle intersection. Journal of Graphics Tools, 2(1):21–28, 1997. doi: 10.1080/10867651.1997.10487468.

A. Monin. Smoke propagation in the surface layer of the atmosphere. Advances in Geophysics, 6:331–343, 1959. ISSN 0065-2687. doi: https://doi.org/10.1016/S0065-2687(08)60121-1. URL https://www.sciencedirect.com/science/article/pii/S0065268708601211.

A. Monin and A. M. Obukhov. Basic laws of turbulent mixing in the ground layer of atmosphere. Tr. Akad. Nauk SSSR Geophiz. Inst, 1954. URL https://api.semanticscholar.org/CorpusID:123571221.

A. Monin and A. Yaglom. Statistical Fluid Mechanics, Vol. I, Mechanics of Turbulence. MIT Press, Cambridge, MA, 1971.

A. Monin and A. Yaglom. Statistical Fluid Mechanics, Vol. II, Mechanics of Turbulence. MIT Press, Cambridge, MA, 1975.

L. Mortarini, E. Ferrero, S. Falabino, S. Trini Castelli, R. Richiardone, and D. Anfossi. Low-frequency processes and turbulence structure in a perturbed boundary layer. Quarterly Journal of the Royal Meteorological Society, 139(673):1059–1072, 2013.

M. Muradoglu and S. Pope. Local time-stepping algorithm for solving probability density function turbulence model equations. AIAA journal, 40(9):1755–1763, 2002. doi: 10.2514/2.1880.

M. Muradoglu, P. Jenny, S. B. Pope, and D. A. Caughey. A consistent hybrid finite-volume/particle method for the PDF equations of turbulent reactive flows. Journal of Computational Physics, 154(2):342–371, 1999. doi: 10.1006/jcph.1999.6316.

G. R. Newman, B. E. Launder, and J. L. Lumley. Modelling the behaviour of homogeneous scalar turbulence. Journal of Fluid Mechanics, 111:217–232, 1981. doi: 10.1017/S002211208100236X.

F. T. M. Nieuwstadt. The Turbulent Structure of the Stable, Nocturnal Boundary Layer. Journal of the Atmospheric Sciences, 41(14):2202–2216, July 1984. ISSN 0022-4928, 1520-0469. doi: 10.1175/1520-0469(1984)041<2202:TTSOTS>2.0.CO;2. URL http://journals.ametsoc.org/doi/10.1175/1520-0469(1984)041<2202:TTSOTS>2.0.CO;2.

T. Norddine, M. Ferrand, and S. Benhamadouche. Realizability-preserving time-stepping for the differential Reynolds stress turbulence models. Journal of Computational Physics, 494:112511, 2023. ISSN 0021-9991. doi: https://doi.org/10.1016/j.jcp.2023.112511. URL https://www.sciencedirect.com/science/article/pii/S002199912300606X.

A. M. Obukhov. Turbulence in an atmosphere with a non-uniform temperature. Boundary-Layer Meteorology, 2(1):7–29, Mar. 1971. doi: 10.1007/BF00718085.

B. Øksendal. Stochastic Differential Equations, pages 65–84. Springer Berlin Heidelberg, Berlin, Heidelberg, 1995. ISBN 978-3-642-14394-6. doi: 10.1007/978-3-642-14394-6_5. URL https://doi.org/10.1007/978-3-642-14394-6_5.

H. Öttinger. Stochastic Processes in Polymeric Fluids: Tools and Examples for Developing Simulation Algorithms. Springer Berlin Heidelberg, 1996. ISBN 9783642582905. URL https://books.google.fr/books?id=b1rrCAAAQBAJ.

H. A. Panofsky, H. Tennekes, D. H. Lenschow, and J. C. Wyngaard. The characteristics of turbulent velocity components in the surface layer under convective conditions. Boundary-Layer Meteorology, 11(3):355–361, 1977.

E. Peirano and J.-P. Minier. Probabilistic formalism and hierarchy of models for polydispersed turbulent two-phase flows. Physical Review E, 65(4):046301, 2002. doi: 10.1103/PhysRevE.65.046301.

E. Peirano, S. Chibbaro, J. Pozorski, and J.-P. Minier. Mean-field/PDF numerical approach for polydispersed turbulent two-phase flows. Progress in Energy and Combustion Science, 32(3):315–371, 2006. doi: 10.1016/j.pecs.2005.07.002.

I. Pisso, E. Sollum, H. Grythe, N. I. Kristiansen, M. Cassiani, S. Eckhardt, D. Arnold, D. Morton, R. L. Thompson, C. D. Groot Zwaaftink, N. Evangeliou, H. Sodemann, L. Haimberger, S. Henne, D. Brunner, J. F. Burkhart, A. Fouilloux, J. Brioude, A. Philipp, P. Seibert, and A. Stohl. The lagrangian particle dispersion model flexpart version 10.4. Geoscientific Model Development, 12(12):4955–4997, 2019. doi: 10.5194/gmd-12-4955-2019. URL https://gmd.copernicus.org/articles/12/4955/2019/.

R. Poletto, T. Craft, and A. Revell. A new divergence free synthetic eddy method for the reproduction of inlet flow conditions for les. Flow, Turbulence and Combustion, 91(3):519–539, 2013.

S. Pope. The relationship between the probability approach and particle models for reaction in homogeneous turbulence. Combustion and Flame, 35:41–45, 1979. ISSN 00102180. doi: 10.1016/0010-2180(79)90005-1. URL https://linkinghub.elsevier.com/retrieve/pii/0010218079900051.

S. Pope. Application of the velocity-dissipation probability density function model to inhomogeneous turbulent flows. Physics of Fluids A: Fluid Dynamics, 3(8):1947–1957, 1991. doi: 10.1063/1.857925.

S. Pope. Turbulent Flows. Cambridge University Press, 2000. ISBN 9780521598866.

S. Pope and Y. Chen. The velocity-dissipation probability density function model for turbulent flows. Physics of Fluids A: Fluid Dynamics, 2(8):1437–1449, 1990. doi: 10.1063/1.857592.

S. B. Pope. A Monte Carlo method for the PDF equations of turbulent reactive flow. Combustion Science and Technology, 25(5-6):159–174, 1981. doi: 10.1080/00102208108547500.

S. B. Pope. A Lagrangian two-time probability density function equation for inhomogeneous turbulent flows. The Physics of Fluids, 26(12):3448–3450, 1983. doi: 10.1063/1.864125.

S. B. Pope. PDF methods for turbulent reactive flows. Progress in Energy and Combustion Science, 11(2):119–192, 1985. doi: 10.1016/0360-1285(85)90002-4.

S. B. Pope. Consistency conditions for random-walk models of turbulent dispersion. Physics of Fluids, 30(8):2374, 1987. ISSN 00319171. doi: 10.1063/1.866127. URL https://aip.scitation.org/doi/10.1063/1.866127.

S. B. Pope. Lagrangian PDF methods for turbulent flows. Annual Review of Fluid Mechanics, 26(1):23–63, 1994a. doi: 10.1146/annurev.fl.26.010194.000323.

S. B. Pope. On the relationship between stochastic Lagrangian models of turbulence and second-moment closures. Physics of Fluids, 6(2):973–985, 1994b. doi: 10.1063/1.868329.

P. P. Popov, R. McDermott, and S. B. Pope. An accurate time advancement algorithm for particle tracking. Journal of Computational Physics, 227(20):8792–8806, 2008. doi: 10.1016/j.jcp.2008.06.021.

J. Pozorski and J.-P. Minier. On the Lagrangian turbulent dispersion models based on the Langevin equation. International Journal of Multiphase Flow, 24(6):913–945, 1998. doi: 10.1016/S0301-9322(98)00016-0.

J. Pozorski and M. Wacławczyk. Mixing in Turbulent Flows: An Overview of Physics and Modelling. Processes, 8(11):1379, Oct. 2020. ISSN 2227-9717. doi: 10.3390/pr8111379. URL https://www.mdpi.com/2227-9717/8/11/1379.

J. Pozorski, M. Waclawczyk, and J.-P. Minier. Probability density function computation of heated turbulent channel flow with the bounded Langevin model. Journal of Turbulence, 4:N11, Apr. 2003a. ISSN 1468-5248. doi: 10.1088/1468-5248/4/1/011. URL http://www.informaworld.com/openurl?genre=article&doi=10.1088/1468-5248/4/1/011&magic=crossref||D404A21C5BB053405B1A640AFFD44AE3.

J. Pozorski, M. Wacławczyk, and J.-P. Minier. Full velocity-scalar probability density function computation of heated channel flow with wall function approach. Physics of Fluids, 15(5):1220–1232, May 2003b. ISSN 1070-6631, 1089-7666. doi: 10.1063/1.1564827. URL https://pubs.aip.org/pof/article/15/5/1220/255114/Full-velocity-scalar-probability-density-function.

L. Prandtl. Bericht über Untersuchungen zur ausgebildeten Turbulenz. Zeitschrift Angewandte Mathematik und Mechanik, 5(2):136–139, Jan. 1925. doi: 10.1002/zamm.19250050212.

A. Reynolds. Superstatistical lagrangian stochastic modeling. Physica A Statistical Mechanics and its Applications, 340(1):298–308, 2004. ISSN 0378-4371. doi: https://doi.org/10.1016/j.physa.2004.04.020. URL https://www.sciencedirect.com/science/article/pii/S0378437104004285. News and Expectations in Thermostatistics.

A. M. Reynolds. Third-order lagrangian stochastic modeling. Physics of Fluids (1994), 15(9):2773–2777, 2003.

O. Reynolds. On the dynamical theory of incompressible viscous fluids and the determination of the criterion. Proceedings: Mathematical and Physical Sciences, 451(1941):5–47, 1895. ISSN 09628444. URL http://www.jstor.org/stable/52792.

L. F. Richardson. Weather Prediction by Numerical Process. Cambridge University Press, 1922. doi: 10.1017/CBO9780511618291.

O. F. T. Roberts. The Theoretical Scattering of Smoke in a Turbulent Atmosphere. Proceedings of the Royal Society of London, 104(728):640–654, 12 1923. doi: https://doi.org/10.1098/rspa.1923.0132.

H. C. Rodean. Stochastic lagrangian models of turbulent diffusion. Meteorological Monographs, 26(48):1 – 84, 1996. doi: https://doi.org/10.1175/0065-9401-26.48.1. URL https://journals.ametsoc.org/view/journals/amsm/26/48/0065-9401-26_48_1.xml.

W. Rodi. Turbulence Models and Their Application in Hydraulics (1st ed.). Routledge, 2000. doi: https://doi.org/10.1201/9780203734896.

M. W. Rotach. On the influence of the urban roughness sublayer on turbulence and dispersion. Atmospheric Environment (1994), 33(24):4001–4008, 1999.

J. Rotta. Statistische Theorie nichthomogener Turbulenz. Zeitschrift fur Physik, 129(6):547–572, Nov. 1951. doi: 10.1007/BF01330059.

K. K. Sabelfeld. Random fields and Stochastic Lagrangian models: analysis and applications in turbulence and porous media. Walter de Gruyter, Berlin/Boston, 2012.

C. Saturne. Theory guide, EDF R&D, 2023. Technical report, EDF R&D, 2023. URL https://www.code-saturne.org/documentation/7.0/theory.pdf.

B. L. Sawford. Generalized random forcing in random-walk turbulent dispersion models. Physics of Fluids, 29(11):3582, 1986. ISSN 00319171. doi: 10.1063/1.865784. URL https://aip.scitation.org/doi/10.1063/1.865784.

D. P. Schmidt and C. Rutland. A new droplet collision algorithm. Journal of Computational Physics, 164(1):62–80, 2000. doi: 10.1006/jcph.2000.6568.

U. Schumann. Realizability of Reynolds-stress turbulence models. The Physics of Fluids (1958), 20(5):721–725, 1977.

C. C. Shir. A preliminary numerical study of atmospheric turbulent flows in the idealized planetary boundary layer. Journal of Atmospheric Sciences, 30(7):1327 – 1339, 1973. doi: 10.1175/1520-0469(1973)030<1327:APNSOA>2.0.CO;2. URL https://journals.ametsoc.org/view/journals/atsc/30/7/1520-0469_1973_030_1327_apnsoa_2_0_co_2.xml.

H. Sigurgeirsson, A. Stuart, and W.-L. Wan. Algorithms for particle-field simulations with collisions. Journal of Computational Physics, 172(2):766–807, 2001. doi: 10.1006/jcph.2001.6858.

J. Smagorinsky. General circulation experiments with the primitive equations: I. the basic experiment. Monthly Weather Review, 91(3):99 – 164, 1963. doi: https://doi.org/10.1175/1520-0493(1963)091<0099:GCEWTP>2.3.CO;2. URL https://journals.ametsoc.org/view/journals/mwre/91/3/1520-0493_1963_091_0099_gcewtp_2_3_co_2.xml.

P. Spalart and S. Allmaras. A one-equation turbulence model for aerodynamic flows. AIAA Journal, 439, 01 1992. doi: 10.2514/6.1992-439.

C. G. Speziale, S. Sarkar, and T. B. Gatski. Modelling the pressure–strain correlation of turbulence: an invariant dynamical systems approach. Journal of Fluid Mechanics, 227:245–272, 1991. doi: 10.1017/S0022112091000101.

C. G. Speziale, R. Abid, and E. C. Anderson. Critical evaluation of two-equation models for near-wall turbulence. AIAA Journal, 30(2):324–331, Feb. 1992. ISSN 0001-1452, 1533-385X. doi: 10.2514/3.10922. URL https://arc.aiaa.org/doi/10.2514/3.10922.

E. A. Spiegel and G. Veronis. On the boussinesq approximation for a compressible fluid. The Astrophysical Journal, 131:442, 1960. URL https://api.semanticscholar.org/CorpusID:121803237.

B. Sportisse. A review of parameterizations for modelling dry deposition and scavenging of radionuclides. Atmospheric Environment, 41(13):2683–2698, Apr. 2007. doi: 10.1016/j.atmosenv.2006.11.057. URL https://inria.hal.science/inria-00633841.

K. D. Squires and J. K. Eaton. Lagrangian and Eulerian statistics obtained from direct numerical simulations of homogeneous turbulence. Physics of Fluids A, 3(1):130–143, Jan. 1991. doi: 10.1063/1.857872.

C. Srinivasan and D. V. Papavassiliou. Prediction of the Turbulent Prandtl Number in Wall Flows with Lagrangian Simulations. Industrial & Engineering Chemistry Research, 50(15): 8881–8891, Aug. 2011. ISSN 0888-5885, 1520-5045. doi: 10.1021/ie1019497. URL https://pubs.acs.org/doi/10.1021/ie1019497.

J. M. Stockie. The mathematics of atmospheric dispersion modeling. SIAM Review, 53(2): 349–372, 2011. doi: 10.1137/10080991X. URL https://doi.org/10.1137/10080991X.

G. Stokes. On the theories of the internal friction of fluids in motion and of the equilibrium and motion of elastic solids. Trans. Cambridge Philos. Soc., 8(2):287–319., 1845.

R. Stull. An Introduction to Boundary Layer Meteorology. Kluwer Academic Publishers,, Dordrecht, Boston and London, 1988. doi: http://dx.doi.org/10.1007/978-94-009-3027-8.

S. Subramaniam and D. Haworth. A probability density function method for turbulent mixing and combustion on three-dimensional unstructured deforming meshes. International Journal of Engine Research, 1(2):171–190, 2000. doi: 10.1243/1468087001545128.

K. Takeuchi and O. Yokoyama. The scale of turbulence and the wind profile in the surface boundary layer. Journal of the Meteorological Society of Japan. Ser. II, 41(2):108–117, 1963.

G. I. Taylor. Diffusion by Continuous Movements. Proceedings of the London Mathematical Society, s2-20(1):196–212, 01 1922. ISSN 0024-6115. doi: 10.1112/plms/s2-20.1.196. URL https://doi.org/10.1112/plms/s2-20.1.196.

G. I. Taylor. Statistical theory of turbulence. Proceedings of the Royal Society of London. Series A, Mathematical and Physical Sciences, 151(873):421–444, 1935. ISSN 00804630. URL http://www.jstor.org/stable/96557.

H. Tennekes and J. Lumley. A First Course in Turbulence. MIT Press, Cambridge, MA, 1972.

D. J. Thomson. Criteria for the selection of stochastic models of particle trajectories in turbulent flows. Journal of Fluid Mechanics, 180(-1):529, July 1987. ISSN 0022-1120, 1469-7645. doi: 10.1017/S0022112087001940. URL http://www.journals.cambridge.org/abstract_S0022112087001940.

D. J. Thomson and J. D. Wilson. History of Lagrangian Stochastic Models for Turbulent Dispersion. In J. Lin, D. Brunner, C. Gerbig, A. Stohl, A. Luhar, and P. Webley, editors, Geophysical Monograph Series, pages 19–36. American Geophysical Union, Washington, D. C., Mar. 2013. ISBN 9781118704578 9780875904900. doi: 10.1029/2012GM001238. URL http://doi.wiley.com/10.1029/2012GM001238.

G. Tinarelli, L. Mortarini, S. T. Castelli, G. Carlino, J. Moussafir, C. Olry, P. Armand, and D. Anfossi. Review and Validation of MicroSpray, a Lagrangian Particle Model of Turbulent Dispersion, chapter 25, pages 311–328. American Geophysical Union (AGU), 2012. ISBN 9781118704578. doi: https://doi.org/10.1029/2012GM001242. URL https://agupubs.onlinelibrary.wiley.com/doi/abs/10.1029/2012GM001242.

L. Valiño and C. Dopazo. A binomial Langevin model for turbulent mixing. Physics of Fluids A: Fluid Dynamics, 3(12):3034–3037, Dec. 1991. ISSN 0899-8213. doi: 10.1063/1.857847. URL https://pubs.aip.org/pof/article/3/12/3034/402166/A-binomial-Langevin-model-for-turbulent-mixing.

G. K. Vallis. Atmospheric and Oceanic Fluid Dynamics: Fundamentals and Large-Scale Circulation. Cambridge University Press, 2 edition, 2017. doi: 10.1017/9781107588417.

H. Van Dop. Buoyant plume rise in a lagrangian framework. Boundary-Layer Meteorology, 62 (1-4):97–105, 1993.

D. Violeau. Fluid Mechanics and the SPH Method: Theory and Applications. Oxford University Press, 05 2012. ISBN 9780199655526. doi: 10.1093/acprof:oso/9780199655526.001.0001. URL https://doi.org/10.1093/acprof:oso/9780199655526.001.0001.

S. Viswanathan, H. Wang, and S. B. Pope. Numerical implementation of mixing and molecular transport in LES/PDF studies of turbulent reacting flows. Journal of Computational Physics, 230(17):6916–6957, July 2011. ISSN 00219991. doi: 10.1016/j.jcp.2011.05.020. URL https://linkinghub.elsevier.com/retrieve/pii/S002199911100324X.

T. Von Karman and L. Howarth. On the statistical theory of isotropic turbulence. Proceedings of the Royal Society of London. Series A - Mathematical and Physical Sciences, 164(917): 192–215, 1938. doi: 10.1098/rspa.1938.0013. URL https://royalsocietypublishing.org/doi/abs/10.1098/rspa.1938.0013.

M. Wacławczyk, J. Pozorski, and J.-P. Minier. Probability density function computation of turbulent flows with a new near-wall model. Physics of Fluids (1994), 16(5):1410–1422, 2004.

D. C. Wilcox. Reassessment of the scale-determining equation for advanced turbulence models. AIAA Journal, 26(6):1299–1310, Nov. 1988. doi: 10.2514/3.10041.

J. D. Wilson and B. L. Sawford. Review of Lagrangian stochastic models for trajectories in the turbulent atmosphere. Boundary-Layer Meteorology, 78(1-2):191–210, feb 1996. ISSN 0006-8314, 1573-1472. doi: 10.1007/BF00122492. URL http://link.springer.com/10.1007/BF00122492.

J. Wyngaard, O. Coté, and K. Rao. Modeling the atmospheric boundary layer. In Advances in Geophysics, volume 18, pages 193–211. Elsevier, 1975. ISBN 9780120188185. doi: 10.1016/S0065-2687(08)60461-6. URL https://linkinghub.elsevier.com/retrieve/pii/S0065268708604616.

J. C. Wyngaard. Modeling the planetary boundary layer — extension to the stable case. Boundary-Layer Meteorology, 9(4):441–460, 1975. ISSN 0006-8314, 1573-1472. doi: 10.1007/BF00223393. URL http://link.springer.com/10.1007/BF00223393.

J. C. Wyngaard and O. R. Coté. The evolution of a convective planetary boundary layer — A higher-order-closure model study. Boundary-Layer Meteorology, 7(3):289–308, 1974. doi: 10.1007/BF00240833.

J. Xu and S. Pope. Assessment of numerical accuracy of PDF/Monte Carlo methods for turbulent reacting flows. Journal of Computational Physics, 152(1):192–230, 1999. doi: 10.1006/jcph.1999.6241.

T. Yang, Y. Yin, H. Zhou, and Z. Ren. Review of Lagrangian stochastic models for turbulent combustion. Acta Mechanica Sinica, 37(10):1467–1488, Oct. 2021. doi: 10.1007/s10409-021-01142-7.

P. K. Yeung and S. B. Pope. Lagrangian statistics from direct numerical simulations of isotropic turbulence. Journal of Fluid Mechanics, 207:531–586, 1989. doi: 10.1017/S0022112089002697.

Y. Zhang, M. M. Rahman, and G. Chen. Development of k-r turbulence model for wall-bounded flows. Aerospace Science and Technology, 98:105681, 2020.

S. Zilitinkevich and D. Chalikov. Determining the universal wind-velocity and temperature profiles in the atmospheric boundary layer. Izvestiya, Atmos. Ocean. Phys, 4:165–170, 1968.

S. S. Zilitinkevich. On the determination of the height of the Ekman boundary layer. Boundary-Layer Meteorology, 3(2):141–145, Dec. 1972. ISSN 0006-8314, 1573-1472. doi: 10.1007/BF02033914. URL http://link.springer.com/10.1007/BF02033914.

S. S. Zilitinkevich, T. Elperin, N. Kleeorin, I. Rogachevskii, I. Esau, T. Mauritsen, and M. W. Miles. Turbulence energetics in stably stratified geophysical flows: Strong and weak mixing regimes. Quarterly Journal of the Royal Meteorological Society, 134(633):793–799, Apr. 2008. ISSN 00359009, 1477870X. doi: 10.1002/qj.264. URL https://onlinelibrary.wiley.com/doi/10.1002/qj.264.

S. S. Zilitinkevich, I. Esau, N. Kleeorin, I. Rogachevskii, and R. D. Kouznetsov. On the Velocity Gradient in Stably Stratified Sheared Flows. Part 1: Asymptotic Analysis and Applications. Boundary-Layer Meteorology, 135(3):505–511, June 2010. doi: 10.1007/s10546-010-9488-x.

C. Zonato, A. Vidili, R. Pastorino, and D. M. De Faveri. Plume rise of smoke coming from free burning fires. Journal of Hazardous Materials, 34(1):69–79, 1993.